



Universiteit
Leiden
The Netherlands

Dynamical Structure and Evolution of Stellar Systems

Ven, Glenn van de

Citation

Ven, G. van de. (2005, December 1). *Dynamical Structure and Evolution of Stellar Systems*. Retrieved from <https://hdl.handle.net/1887/3740>

Version: Corrected Publisher's Version

License: [Licence agreement concerning inclusion of doctoral thesis in the Institutional Repository of the University of Leiden](#)

Downloaded from: <https://hdl.handle.net/1887/3740>

Note: To cite this publication please use the final published version (if applicable).

DYNAMICAL STRUCTURE AND EVOLUTION
OF STELLAR SYSTEMS

DYNAMICAL STRUCTURE AND EVOLUTION OF STELLAR SYSTEMS

Proefschrift

ter verkrijging van
de graad van Doctor aan de Universiteit Leiden,
op gezag van de Rector Magnificus Dr. D.D. Breimer,
hoogleraar in de faculteit der Wiskunde en
Natuurwetenschappen en die der Geneeskunde,
volgens besluit van het College voor Promoties
te verdedigen op donderdag 1 december 2005
klokke 15.15 uur

door

Petrus Martinus van de Ven

geboren te Mill en Sint Hubert
in 1977

Promotiecommissie

Promotor: Prof. dr. P.T. de Zeeuw

Referent: Prof. dr. K.C. Freeman (Australian National University)

Overige leden: Prof. dr. P.G. van Dokkum (Yale University, USA)
Prof. dr. M. Franx
Prof. dr. H.J. Habing
Dr. A. Helmi (Rijksuniversiteit Groningen)
Prof. dr. C. Hunter (Florida State University, USA)
Prof. dr. K. Kuijken

Omslag: Zonsondergang in Amboseli National Park, Kenia. Deze foto met op de achtergrond de Kilimanjaro is genomen tijdens mijn huwelijksreis in mei 2005.

TABLE OF CONTENTS

	Page
CHAPTER 1. INTRODUCTION	1
1 Stellar systems	1
2 Surface brightness	2
3 Two-dimensional kinematics	3
4 Dynamical models	4
5 Dynamical structure and evolution	6
6 This thesis	7
7 Future prospects	10
CHAPTER 2. THE DYNAMICAL DISTANCE AND STRUCTURE OF ω CENTAURI	13
1 Introduction	14
2 Observations	15
3 Selection	20
4 Kinematics	24
5 Schwarzschild's method	33
6 Tests	36
7 Dynamical models for ω Cen	41
8 Best-fit parameters	47
9 Intrinsic structure	50
10 Conclusions	60
A Maximum likelihood estimation velocity moments	64
B Polar grid of apertures	66
C Simple distance estimate	68
CHAPTER 3. A BAR SIGNATURE AND CENTRAL DISK IN NGC 5448	71
1 Introduction	72
2 The data	73
3 Analyzing gas velocity fields	75
4 A bar model for NGC 5448	78
5 Results	80
6 Discussion and conclusions	85
CHAPTER 4. RECOVERY OF THREE-INTEGRAL GALAXY MODELS	89
1 Introduction	90
2 Triaxial Abel models	92
3 Observables	98
4 Triaxial three-integral galaxy models	102
5 Axisymmetric three-integral galaxy models	109
6 Recovery of triaxial galaxy models	112
7 Recovery of axisymmetric galaxy models	120
8 Discussion and conclusions	123
A Limiting cases	127

B	The function $\mathcal{M}(s, i, j; a, b, \phi)$	130
C	Conversion from true moments to Gauss-Hermite moments	132
CHAPTER 5. GENERAL SOLUTION OF THE JEANS EQUATIONS		137
1	Introduction	138
2	The Jeans equations for separable models	139
3	The two-dimensional case	151
4	The general case	169
5	Discussion and conclusions	187
A	Solving for the difference in stress	190
CHAPTER 6. THE EINSTEIN CROSS: LENSING VS. STELLAR DYNAMICS		195
1	Introduction	196
2	Observations	197
3	Analysis	199
4	Results	206
5	Discussion	208
6	Conclusions	209
CHAPTER 7. FP AND M/L EVOLUTION OF LENS GALAXIES		213
1	Introduction	214
2	FP parameters	215
3	Transformation to restframe	218
4	FP and M/L evolution	220
5	Stellar population ages	223
6	Colors	227
7	Summary and conclusions	229
LIST OF PUBLICATIONS		233
NEDERLANDSE SAMENVATTING		235
CURRICULUM VITAE		246
NAWOORD		247
APPENDIX: COLOR FIGURES		249

CHAPTER 1

INTRODUCTION

1 STELLAR SYSTEMS

THE universe formed in a 'Big Bang', after which it began expanding. Places with more dark matter than their surroundings collapsed under gravity and collected gas, from which the first stars were born. Depending on the distribution of the dark matter, these stars ended up in systems of different sizes and shapes. The stars inside these stellar systems evolve: most stars fade out at the end of their life, but the more massive stars explode. New stars can be formed from their debris. Also, the systems themselves evolve by interacting and merging. This leads to the question: Can we find out how the different stellar systems evolved from the Big Bang to the present day?

One way to answer this question is to observe objects at very large distances. Since light needs time to travel, by looking at objects very far away, we see how they were a long time ago. However, with increasing distance, these objects quickly become smaller and fainter, such that very large telescopes with the ability to make very sharp images are needed. Another approach is to study nearby stellar systems and try to uncover, like an archaeologist, the 'fossil record' of their formation and evolution. Because they are close, they are also brighter, and the motions and composition of the stars in these systems can be observed in great detail. We can try to reconstruct the three-dimensional stellar system by fitting theoretical models, based on Newton's law of gravity, to these observations. In this way, we can 'look' inside stellar systems and search for features, i.e. 'fossils', in their structure and internal motions related to their formation history.

The most suitable stellar systems to study the fossil record are those for which the stars are not hidden from sight by clouds of gas and dust, and which are not 'polluted' by recent star formation. Globular clusters are the cleanest stellar systems, containing of the order of a million very old stars, which formed from the same collapsing matter very soon after the Big Bang. In addition, they are simple, nearly spherical objects and we can observe them from nearby as they also surround our own Milky Way galaxy. We can resolve many of the individual stars in these clusters and observe their velocities along the line-of-sight and even in the plane of the sky ('proper motions') by measuring the small changes in their positions with time. Reliable kinematic measurements of individual stars are currently only possible for the nearest objects and for the stars inside the Milky Way.

In the beginning of the twentieth century it became clear that the Milky Way is just one of the 'island universes' that can be seen in the night sky. Photographic observations showed that these galaxies come in different flavors. This led Hubble (1936) to classify them into four distinct groups, according to their apparent shape. In the resulting Hubble sequence (or Hubble diagram or Hubble tuning fork) the Milky Way belongs to the group of disk-like galaxies which are called *spirals* according to

their prominent spiral arms. At the other end of the sequence, we find the *elliptical* galaxies that seemingly have little or no structure. *Lenticular* galaxies are placed in between, having a disk but no prominent spiral arms, and a spheroidal stellar distribution. The fourth group consists of galaxies without a regular shape, which appropriately were named *irregulars*. At that time, it was thought that the complex spirals were formed from the simple ellipticals. Although we now know that galaxy formation and evolution happens the other way around, the spirals are still called late-type galaxies, and ellipticals and lenticulars are known as early-type galaxies.

The late-type galaxies, including the Milky Way, contain significant amounts of gas and dust, and this material is converted into stars by continuous, and often intensive star formation, which makes it very hard to recover their formation history. Early-type galaxies do not contain much gas and dust, and consequently have no recent star formation, so that they are well suited to study galaxy formation and evolution. For the nearby (< 100 Mpc) early-type galaxies, we can investigate the fossil record of their formation in detail. Although we are in general unable to resolve their individual stars, we can obtain accurate and spatially-resolved photometric and kinematic measurements from the integrated light of stars along the line-of-sight.

2 SURFACE BRIGHTNESS

To first order, the surface brightness of early-type galaxies is well described by a simple function of radius along elliptical isophotes. Although the photometry of early-type galaxies seems to be rather simple, this does not mean that their intrinsic dynamical structure can also be derived and described in a straightforward way.

The conversion from a surface brightness measured on the plane of the sky to an intrinsic luminous density is in general non-unique. This deprojection is unique for spherical objects, but only very few galaxies have a round appearance, and even then they need not be intrinsically spherical. In the case of flattened objects with axial symmetry, the deprojection is only unique for a viewing direction in the plane normal to the axis of symmetry, better known as an edge-on viewing direction and often described by an inclination angle $i = 90^\circ$ (Rybicki 1987). However, a stellar system in equilibrium can also be of triaxial shape (Binney 1976). The deprojection then becomes highly non-unique, with the viewing direction described by two viewing angles. In contrast with axisymmetric objects, the orientation of the elliptical isophotes may vary with radius for triaxial shapes (Stark 1977). Very soon after this was realized, isophotal twists were indeed observed in real galaxies (e.g., Carter 1978; King 1978; Williams & Schwarzschild 1979; Leach 1981).

In the case of axisymmetric objects, the flattening might be in part caused by rotation, similar to the flattening of the Earth. Instead of this gravitational support by ordered motion, random motion, acting as a kind of pressure, can also prevent a stellar system against gravitational collapse. This random motion is measured from the mean velocity dispersion of the stars. The components in three orthogonal directions, often referred to as the semi-axis lengths of the velocity ellipsoid, can be different so that the stellar system is anisotropic, and can vary throughout the stellar system, even for an axisymmetric or spherical stellar system.

These dynamical properties cannot be inferred from photometry and require kinematic measurements, e.g., from spectroscopic observations. The development of telescopes and instruments in the mid-seventies and early eighties of the twentieth cen-

tury made it possible to measure the ordered-over-random motion ratios, V/σ , of early-type galaxies. From these kinematic measurements it became clear that these systems in general rotate too slowly for pure rotational support (e.g., Bertola & Cappaccioli 1975; Illingworth 1977). Further observations revealed that lenticulars and low-luminosity ellipticals have disk-like isophotes and show clear rotation, while giant ellipticals seem to have boxy isophotes and often hardly show any rotation (Davies et al. 1983; Bender 1988). The reason behind this dichotomy is ascribed to the different underlying dynamical structures, with faint early-type galaxies comparable to isotropic oblate rotators and luminous early-type galaxies consistent with anisotropic triaxial stellar systems (e.g., Davies et al. 1983; Bender & Nieto 1990; de Zeeuw & Franx 1991; Faber et al. 1997).

However, recent (N-body) simulations of merging galaxies seem to suggest the opposite concerning the degree of anisotropy, producing faint anisotropic and luminous isotropic early-type galaxies (Burkert & Naab 2005). Based on a detailed study of the orbital structure inferred from dynamical models of two dozen early-type galaxies, Cappellari et al. (2005a) come to the same conclusions. It is evident that such detailed simulations and dynamical models of galaxies are crucial to understand their formation history. At the same time, the improvement in the determination of the intrinsic dynamical structure would not have been possible without the aid of two-dimensional kinematic measurements and realistic dynamical modeling.

3 TWO-DIMENSIONAL KINEMATICS

Early-type galaxies can in general be assumed to be collisionless stellar systems in equilibrium. Only in the center can the stellar density become high enough for stars to significantly perturb each other's orbits; everywhere else the stellar system is collisionless. Except for the outskirts the dynamical time scale of the stars is short enough for the stellar system to have reached equilibrium in the time passed since its formation. These assumptions are also valid for many globular clusters, except for their cores, where two-body relaxation can play an important role. When a stellar system is collisionless and in equilibrium, its dynamical state is completely described by the (time-independent) distribution function (DF) of the stars in the six-dimensional phase space of positions and velocities.

For stars in the Milky Way and in nearby globular clusters, we can measure the line-of-sight velocity and proper motions as a function of position on the plane of the sky. The determination of the sixth dimension, the distance, is in general very difficult and relatively uncertain. Moreover, due to obscuration by gas and dust and limited spatial and spectral instrumental resolution, observations are not complete, although future space missions like *GAIA* are expected to provide a stereoscopic census of a significant part of the Milky-Way and its surroundings (Perryman et al. 2001).

Even at astronomically small distances it becomes no longer possible to resolve individual stars with current telescopes. We can still measure the projected surface brightness and (for the nearby galaxies) the line-of-sight velocity distribution of the integrated stellar light as a function of position on the plane of the sky. In the last two decades a major step forward has been made in the latter observations with the introduction of integral-field spectrographs. Via an array of lenses, a bundle of fibers or a set of adjacent slits, the integrated light from different positions on the plane of the sky is dispersed in the wavelength direction. In this way, integral-field

spectrographs provide a spectrum at each position within a two-dimensional area, from which we can simultaneously extract the kinematics of the stars and gas, as well as line-strength measurements, as a function of position on the plane of the sky.

Due to the high quality of modern spectroscopic observations, it is often possible to also measure the higher-order line-of-sight velocity moments of the DF, in addition to the mean velocity and velocity dispersion. These moments are often expressed in terms of the Gauss-Hermite moments, which are less sensitive to the noise in the wings than the true velocity moments (van der Marel & Franx 1993; Gerhard 1993). The measurement of these higher-order velocity moments are also important to break the so called mass-anisotropy degeneracy: a change in the observed line-of-sight velocity dispersion can be due to (a combination of) a change in the velocity ellipsoid, i.e., a change in anisotropy, or a change in mass. Since we cannot observe the velocity dispersion in the plane of the sky, we need the higher order line-of-sight velocity moments to constrain a possible change in the velocity ellipsoid. On the other hand, to measure a change in mass we need to know the mass-to-light ratio M/L to convert the observed surface brightness into a mass distribution. Unfortunately, we do not know the value of M/L , which moreover may vary throughout the galaxy due to a change in the properties of the underlying stellar populations, or due to the presence of non-luminous matter in the form of a central black hole and/or an extended dark halo. To overcome these problems, realistic and detailed dynamical models, which make full use of the information that is present in the photometric and (two-dimensional) kinematic observations, are crucial.

4 DYNAMICAL MODELS

Integral-field spectroscopy has (literally) added a new dimension to observations of nearby early-type galaxies. The resulting kinematic maps provide us with three-dimensional information on the DF. Still, taking into account the uncertainties in the maps due to inevitable noise in the observations, together with the unknown viewing direction, M/L , and possible dark matter contribution, it seems almost hopeless to recover the DF in the six-dimensional phase space. Fortunately, for stationary equilibrium stellar systems the DF depends in general on fewer than six parameters.

4.1 INTEGRALS OF MOTION

According to Jeans (1915) theorem the DF is a function of the isolating integrals of motion admitted by the potential (Lynden-Bell 1962b; Binney 1982). In a spherical symmetric potential these integrals of motion are the energy E and the three components of the angular momentum vector \mathbf{L} . In axisymmetric geometry orbits have two exact integrals of motion, the energy E and the angular momentum component L_z parallel to the symmetry z -axis. All regular orbits furthermore obey a third integral I_3 , which in general is not known in closed form. In the triaxial case, E is conserved and all regular orbits have two additional integrals of motion, I_2 and I_3 , both of which in general are not known explicitly.

If, in addition to the potential, the DF itself is also spherically symmetric, it depends only on the magnitude L of the angular momentum vector and not on its direction, i.e., $f = f(E, L^2)$. Such models have anisotropic velocity distributions, but if $f = f(E)$, the stars are in isotropic equilibrium. Eddington (1916) showed that in this case $f(E)$ can uniquely be recovered from the intrinsic mass density $\rho(r)$. Although

anisotropic spherical models can sometimes be found by a similar analytic inversion (e.g., Dejonghe 1987), most of them are constructed by assumption of a special functional form for $f(E, L^2)$ (e.g., Binney & Tremaine 1987). Well-known spherical models are for example those considered by Osipkov (1979) and Merritt (1985), with a DF of the form $f(E \pm L^2/r_a^2)$, where r_a is a constant scale length.

For axisymmetric models with $f = f(E, L_z)$, inversion formulas have been known for a long time in the case where the density $\rho(R, z)$ can be expressed explicitly in terms of the underlying gravitational potential V as $\rho(R, V)$ (e.g., Lynden-Bell 1962; Hunter 1975; Dejonghe 1986). In spite of the latter limitation, many $f(E, L_z)$ models have been derived in this way (e.g., de Zeeuw 1994), including for example the exact DF for the Kuzmin-Kutuzov (1962) model by Dejonghe & de Zeeuw (1988). With the method derived by Hunter & Qian (1993) it became possible to obtain the two-integral DF directly from $\rho(R, z)$. While $\rho(R, z)$ constrains only the part of the DF that is even in the velocities, i.e., $f = f(E, L_z^2)$, the odd part can be found once the mean azimuthal velocity field $v_\phi(R, z)$ is known. Although these two-integral axisymmetric models have already significantly improved our understanding of the dynamical structure of stellar systems (e.g., Qian et al. 1995), for more realistic models we need to include the third integral of motion. How to do this is not evident because this third integral of motion is in general unknown. The construction of triaxial models with two non-classical integrals of motion is even more complex.

An exception is provided by the special family of models with a gravitational potential of Stäckel form, for which all three integrals of motion are exact and known explicitly. The associated densities have a large range of possible shapes, but they all have cores rather than central cusps, and hence are inadequate for describing the central parts of galaxies with massive black holes. Even so, their kinematic properties are as rich as those seen in the main body of early-type galaxies (Statler 1991, 1994a; Arnold et al. 1994). Several (numerical and analytic) DFs have been constructed for these separable models (e.g., Bishop 1986; Dejonghe & de Zeeuw 1988; Hunter & de Zeeuw 1992). These also include the Abel models, first introduced by Dejonghe & Laurent (1991) and extended by Mathieu & Dejonghe (1999), which generalize the spherical Osipkov-Merritt models and axisymmetric Kuzmin-Kutuzov models (Chapter 4).

4.2 VELOCITY MOMENTS

A way to avoid the unknown non-classical integrals of motion and even the DF is to solve the continuity equation and Jeans equations that follow by taking velocity moments of the collisionless Boltzmann equation. The continuity equation connects the first moments (mean streaming) and the Jeans equations connect the second moments (or the velocity dispersions, if the mean streaming is known) directly to the density and the gravitational potential, without the need to know the DF.

Unfortunately, in nearly all cases there are fewer equations than velocity moments, so that additional assumptions have to be made about the degree of anisotropy. The Jeans equations in the spherical case with a simple form for the anisotropy parameter (e.g., Binney & Tremaine 1987) are widely used to model a large variety of dynamical systems. Kinematic measurements of stellar systems have also been successfully fitted by using the solution of the Jeans equation in axisymmetric geometry with the DF assumed to be independent of the third integral of motion, $f(E, L_z)$, corresponding to isotropy in the meridional (R, z) -plane (e.g., Hunter 1977; Satoh 1980; Binney, Davies & Illingworth 1990; van der Marel 1991).

Such ad-hoc assumptions are not needed in the case of separable Stäckel models. For each orbit in a Stäckel potential, at most one component of the streaming motion is non-zero and all mixed second moments vanish in the coordinate system in which the equations of motion separate. Consequently, the continuity equation can be readily solved for the one non-vanishing first moment (Statler 1994a), and used to provide constraints on the intrinsic shapes of individual galaxies (e.g., Statler 1994b, 2001; Statler et al. 2004). The Jeans equations form a closed system with as many equations as non-vanishing second moments. The solution of these equations in axisymmetric geometry has been known for a while (e.g., Evans & Lynden-Bell 1989), and the solution for the triaxial case is presented in Chapter 5.

4.3 EQUATIONS OF MOTION

Although much has been learned about the dynamical structure of stellar systems by modeling their observed surface brightness and kinematics with solutions of the continuity equation and the Jeans equations (e.g., Binney & Tremaine 1987), the results need to be interpreted with care since the moment solutions may not correspond to a physical distribution function $f \geq 0$. A non-physical DF can be avoided, without actually specifying the DF, by solving directly the equations of motions in a given potential, and fitting the resulting density and velocity distribution to the observed surface brightness and kinematics. Analytically this is only possible for (very) special choices of the potential or in an approximate way by restricting to the lower-order (linear) terms in the equations of motions (e.g., Binney & Tremaine 1987; Chapter 3). Numerically, a very powerful tool is provided by Schwarzschild's (1979, 1982) orbit superposition method, originally designed to reproduce triaxial mass distributions.

Schwarzschild's method allows for an arbitrary gravitational potential, with possible contributions from dark components. The equations of motion are integrated for a representative library of orbits, and then the orbital weights are determined for which the combined and projected density and higher order velocity moments of the orbits best fit the observed surface brightness and (two-dimensional) kinematics. The resulting best-fit distribution of (positive) orbital weights represents the DF (cf. Vandervoort 1984), which is thus guaranteed to be everywhere non-negative.

A number of groups have developed independent numerical implementations of Schwarzschild's method in axisymmetric geometry and determined black hole masses, mass-to-light ratios, dark matter profiles as well as the DF of early-type galaxies by fitting in detail their projected surface brightness and line-of-sight velocity distributions (see § 1 of Chapter 4 for an overview and references). By including proper motion measurements the distance and dynamical structure of nearby globular clusters can be determined (Chapter 2; van den Bosch et al. 2005). The non-trivial extension of Schwarzschild's method to triaxial geometry (Chapter 4; van den Bosch et al. 2006) allows the modeling of giant ellipticals with significant features of triaxiality both in their observed photometry (isophotal twist) and in their observed kinematics (kinematic misalignment, kinematically decoupled components, etc.).

5 DYNAMICAL STRUCTURE AND EVOLUTION

Above we presented three different approaches to model stellar systems: analytically computing the DF specified as a function of the known integrals of motion; solving the continuity equation and Jeans equations for the velocity moments; and integrating

the equations of motion. In this order, the approaches show an increase in freedom and flexibility, but at the same time an increase in complexity and a corresponding increase in (computational) effort to find the best-fit dynamical model. For triaxial geometries in particular, the first two approaches can be very useful to constrain the large parameter space before applying the more general but computationally expensive Schwarzschild method. Such a combination of modeling techniques applied to two-dimensional observations provides a very powerful tool to investigate the fossil record of formation in nearby globular clusters and early-type galaxies.

The gravitational potential forms the basis of all dynamical models, and in general is inferred from the observed surface brightness. This involves a deprojection and a conversion from light to mass, for given viewing angle(s) and mass-to-light ratio M/L , which enter the model as free parameters. The deprojection is nearly always non-unique and mass does not have to follow light, because of varying properties of the underlying stellar population or the presence of dark matter, so that M/L does not have to be constant. Although the inferred gravitational potential might thus be different from the true one, various tests seem to suggest that the parameters as well as the DF are recovered well, as long as there are enough accurate photometric and kinematic constraints (Chapters 2 and 4).

A unique way to get a more direct handle on the gravitational potential is via strong gravitational lensing. The mass of a foreground galaxy bends the light of a distant quasar behind it, resulting in multiple images. From the separation and relative fluxes of the images the total mass distribution (including possible dark matter) of the lens galaxy, and hence the potential, can be constrained. Next, by constructing a dynamical model of the lens galaxy that fits the observed surface brightness and kinematics, the dark matter distribution in the lens galaxy can be studied. Only very few of the known lens galaxies are close enough to obtain sufficient photometric and (two-dimensional) kinematic measurements for a detailed dynamical study (Chapter 6).

At higher redshift, measurements of stellar systems are limited to their global properties. Often only photometric properties such as luminosity, color and size are readily accessible, because kinematic measurements from spectra become very challenging due to the dimming of the light. Strong gravitational lensing provides a way out here: since the velocity dispersion of the lens galaxy is related to its mass, the (central) velocity dispersion can be estimated from the separation of the quasar images (e.g., Schneider et al. 1992). Once the global properties of several stellar systems are known, these stellar systems can be linked and their evolution investigated by means of scaling relations such as the Fundamental Plane. The change with redshift of the latter tight relation between the structural parameters and velocity dispersion of early-type galaxies, provides a measurement of the M/L evolution (Chapter 7). Comparing such measurements of the change in the global (dynamical) properties of early-type galaxies with time, with the detailed determinations of the (dynamical) properties of nearby early-type galaxies, allows a better understanding of the dynamical structure and evolution of stellar systems from the Big Bang to the present day.

6 THIS THESIS

In CHAPTER TWO, we determine the dynamical distance D , inclination i , mass-to-light ratio M/L and intrinsic orbital structure of the Milky Way globular cluster ω Centauri, by fitting axisymmetric dynamical models to the ground-based proper motions of van

Leeuwen et al. (2000) and line-of-sight velocities from four independent data-sets. We correct the observed velocities for perspective rotation caused by the space motion of the cluster, and show that the residual solid-body rotation component in the proper motions can be taken out without any modeling other than assuming axisymmetry. This also provides a tight constraint on $D \tan i$. The corrected mean velocity fields are consistent with regular rotation, and the velocity dispersion fields display significant deviations from isotropy.

We model ω Centauri with an axisymmetric implementation of Schwarzschild's orbit superposition method. We bin the individual measurements on the plane of the sky to search efficiently through the parameter space of the models. Tests on an analytic model demonstrate that this approach is capable of measuring the cluster distance to an accuracy of about 6 per cent. Application to ω Centauri reveals no dynamical evidence for a significant radial dependence of M/L , in harmony with the relatively long relaxation time of the cluster. The best-fit dynamical model has a stellar V -band mass-to-light ratio $M/L_V = 2.5 \pm 0.1 M_\odot/L_\odot$ and an inclination $i = 50^\circ \pm 4^\circ$, which corresponds to an average intrinsic axial ratio of 0.78 ± 0.03 . The best-fit dynamical distance $D = 4.8 \pm 0.3$ kpc (distance modulus 13.75 ± 0.13 mag) is significantly larger than obtained by means of simple spherical or constant-anisotropy axisymmetric dynamical models, and is consistent with the canonical value 5.0 ± 0.2 kpc obtained by photometric methods. The total mass of the cluster is $(2.5 \pm 0.3) \times 10^6 M_\odot$. The best-fit model is close to isotropic inside a radius of about 10 arcmin and becomes increasingly tangentially anisotropic in the outer region, which displays significant mean rotation. This phase-space structure may well be caused by the effects of the tidal field of the Milky Way. The cluster contains a separate disk-like component in the radial range between 1 and 3 arcmin, contributing about 4% to the total mass.

In CHAPTER THREE, we analyze spatially resolved SAURON kinematic maps of the inner kpc of the nearby early-type barred spiral galaxy NGC 5448. The observed morphology and kinematics of the emission-line gas are patchy and perturbed, indicating clear departures from circular motion. The kinematics of the stars are more regular, and display a small inner disk-like system embedded in a large-scale rotating structure. We focus on the [O III] gas, and use a harmonic decomposition formalism to analyze the gas velocity field. The higher-order harmonic terms and the main kinematic features of the observed data are consistent with a simple bar model. We construct a bar model by solving the linearized equations of motion, considering an $m = 2$ perturbation mode, and with parameters which are consistent with the large-scale bar detected via imaging. Optical and near infra-red images reveal asymmetric extinction in NGC 5448, and we recognize that some of the deviations between the data and the analytical bar model may be due to these complex dust features. Our study illustrates how the harmonic decomposition formalism can be used as a powerful tool to quantify non-circular motions in observed gas velocity fields.

In CHAPTER FOUR, we construct axisymmetric and triaxial galaxy models with a phase-space distribution function that depends on linear combinations of the three exact integrals of motion for a separable potential. For these Abel models the density and higher velocity moments can be calculated efficiently, and they capture much of the rich internal dynamics of early-type galaxies. We use these models to mimic the two-dimensional kinematics obtained with integral-field spectrographs such as SAURON. We fit the simulated observations with axisymmetric and triaxial dynamical models obtained with our numerical implementation of Schwarzschild's orbit-

superposition method, while varying the viewing direction and the mass-to-light ratio. We find that Schwarzschild's method is able to recover the internal dynamical structure of early-type galaxies and to accurately determine the mass-to-light ratio, but additional information is needed to constrain better the viewing direction.

In CHAPTER FIVE, we continue our analysis of galaxy models with separable potentials and derive the general solution of the Jeans equations. The Jeans equations relate the second-order velocity moments to the density and potential of a stellar system, without making any assumptions about the distribution function. For general three-dimensional stellar systems, there are three equations and six independent moments. By assuming that the potential is triaxial and of separable Stäckel form, the mixed moments vanish in confocal ellipsoidal coordinates. Consequently, the three Jeans equations and three remaining non-vanishing moments form a closed system of three highly-symmetric coupled first-order partial differential equations in three variables. These equations were first derived by Lynden-Bell (1960), but have resisted solution by standard methods for a long time. We present the general solution here.

We consider the two-dimensional limiting cases first. We solve their Jeans equations by a new method which superposes singular solutions. The resulting solutions of the Jeans equations give the second moments throughout the system in terms of prescribed boundary values of certain second moments. The two-dimensional solutions are applied to non-axisymmetric disks, oblate and prolate spheroids, and also to the scale-free triaxial limit. We then extend the method of singular solutions to the triaxial case, and obtain a full solution, again in terms of prescribed boundary values of second moments. The general solution can be expressed in terms of complete (hyper)elliptic integrals which can be evaluated in a straightforward way, and provides the full set of second moments which can support a triaxial density distribution in a separable triaxial potential.

In CHAPTER SIX, we investigate the total mass distribution in the inner parts of the strong gravitational lens system QSO 2237+0305, well-known as the Einstein Cross. In this system, a distant quasar is lensed by the bulge of an early-type spiral at a redshift $z \sim 0.04$ (i.e., at a distance of about 160 Mpc). We obtain a realistic luminosity density of the lens galaxy by deprojecting its observed surface brightness, and we construct a lens model that accurately fits the positions and relative fluxes of the four quasar images. We combine both to build axisymmetric dynamical models that fit preliminary two-dimensional stellar kinematics derived from recent observations with the integral-field spectrograph GMOS. We find that the stellar velocity dispersion measurements with a mean value of $167 \pm 10 \text{ km s}^{-1}$ within the Einstein radius $R_E = 0.90''$, are in agreement with predictions from our and previous lens models. From the best-fit dynamical model, with I -band mass-to-light ratio $M/L = 3.6 M_\odot/L_\odot$, the Einstein mass is consistent with $M_E = 1.60 \times 10^{10} M_\odot$ from our lens model. The shapes of the density inferred from the lens model and from the surface brightness are very similar, but further improvement on the preliminary kinematic data is needed, before firm conclusions on the total mass distribution can be drawn.

In CHAPTER SEVEN, we consider in addition to the Einstein Cross twenty-five strong gravitational lens galaxies with redshifts up to $z \sim 1$. At such large distances, we are limited to the global properties of these lens galaxies, which effectively form a mass-selected sample of early-type galaxies in environments of relatively low density. We analyze their Fundamental Plane and use it, under the assumption that early-type galaxies are a homologous family, to measure the M/L ratio evolution.

If we assume that the M/L ratios of field early-type galaxies evolve as power-laws, we find for the lens galaxies an evolution rate $d \log(M/L)/dz = -0.62 \pm 0.13$ in the rest-frame B -band for a flat cosmology with $\Omega_M = 0.3$ and $\Omega_\Lambda = 0.7$. For a Salpeter (1955) Initial Mass Function and Solar metallicity, these results correspond to a mean stellar formation redshift of $\langle z_\star \rangle = 1.8_{-0.5}^{+1.4}$. After correction for maximum progenitor bias, van Dokkum & Franx (2001) find for cluster galaxies $\langle z_\star^{cl} \rangle = 2.0_{-0.2}^{+0.3}$, which is not significantly different from that found for the lens galaxies. However, without progenitor bias correction and imposing the constraint that lens and cluster galaxies that are of the same age have equal M/L ratios, the difference is significant and the stellar populations of the lens galaxies are 10–15% younger than those of the cluster galaxies. Furthermore, we find that both the M/L ratios as well as the restframe colors of the lens galaxies show significant scatter. About half of the lens galaxies are consistent with an old cluster-like stellar population, but the other galaxies are bluer and best fit by single burst models with stellar formation redshifts as low as $z_\star \sim 1$. Moreover, the scatter in color is correlated with the scatter in M/L ratio. We interpret this as evidence of a significant age spread among the stellar populations of lens galaxies, whereas those in cluster galaxies are well approximated by a single formation epoch.

7 FUTURE PROSPECTS

An important part of the work presented in this thesis concerns the extension of dynamical modeling to triaxial geometry. This is in particular important for the giant ellipticals, many of which show clear signatures of non-axisymmetry in their kinematics as observed with integral-field spectrograph such as SAURON (Emsellem et al. 2004). Triaxial models of these giant ellipticals, together with axisymmetric models of other ellipticals and lenticulars (Cappellari et al. 2005b), will allow us to study in detail the clean fossil record of their formation.

Because SAURON typically observes the bright inner parts of galaxies, we need additional information to investigate the extended dark matter distribution predicted by current theories of galaxy formation (e.g., Kauffmann & van den Bosch 2002). We saw that strong gravitational lensing can place constraints on the dark matter, but only very few lens galaxies are close enough for detailed dynamical modeling. Currently we are investigating the use of the large field-of-view of SAURON to obtain stellar kinematic measurements in the faint outer parts. Further kinematic constraints are provided by HI and X-ray observations as well as velocities of globular clusters and planetary nebulae at large radii. We have started extending our modeling software to allow the inclusion of both integrated and discrete kinematics. This is also important for the dynamical modeling of stars and stellar systems in the Milky Way.

For nearby globular clusters such as ω Centauri, such discrete modeling software will enable us to fit directly the three-dimensional velocity measurements of the individual stars, and even incorporate measurements of their age and metallicity. By fitting an orbit-based model simultaneously to all these observations, different stellar populations can be separated in phase-space, after which their structure and dynamics can be studied separately. This will be important for solving the puzzle of the multiple stellar populations in ω Centauri (e.g., Freeman & Rodgers 1975; Bedin et al. 2004) and to reveal its formation history. Moreover, fitting directly the proper motion measurements in the very center of globular clusters, provided by observations with the Hubble Space Telescope (e.g., King & Anderson 2002), will allow us to investigate

the presence of a possible intermediate-mass black hole.

The modeling of the stars in the Milky Way is complicated by dust extinction and the presence of a rotating bar, which requires a non-trivial extension of our existing steady-state modeling software. In a preliminary study (Habing et al. 2005), we use the very accurate line-of-sight velocities of more than a thousand OH/IR and SiO masers to show that with such an extension we can model the dynamical structure in the inner Milky Way and provide direct evidence for the existence of a bar. Moreover, this extension will make it possible to model other rotating and barred galaxies, including the early-type and late-type spirals observed with SAURON (Falcón-Barroso et al. 2005; Ganda et al. 2005), and link the stellar and gas kinematics.

The large amount of already available photometric and kinematic data will grow rapidly with existing and future instruments and space missions, such as RAVE, GAIA and SIM, which will provide data for millions of stars, as well as VIMOS, SINFONI, MUSE and other integral-field spectrographs, which will provide two-dimensional data for many nearby galaxies. At the same time, the rapid increase of telescope size and instrument sensitivity will allow an ever deeper look into the universe, with a direct view on the evolution and even formation of stellar systems. The work presented in this thesis provides a step forward in the development and application of dynamical models to deduce from this wealth of data how the different stellar systems evolved from the Big Bang to the present day.

REFERENCES

- Arnold R., de Zeeuw P. T., Hunter C., 1994, *MNRAS*, 271, 924
Bedin L. R., Piotto G., Anderson J., Cassisi S., King I. R., Momany Y., Carraro G., 2004, *ApJ*, 605, L125
Bender R., 1988, *A&A*, 193, L7
Bender R., Nieto J.-L., 1990, *A&A*, 239, 97
Bertola F., Capaccioli M., 1975, *ApJ*, 200, 439
Binney J., 1976, *MNRAS*, 177, 19
Binney J., 1982, *MNRAS*, 201, 15
Binney J., Tremaine S., 1987, *Galactic Dynamics*. Princeton, NJ, Princeton University Press
Binney J. J., Davies R. L., Illingworth G. D., 1990, *ApJ*, 361, 78
Bishop J. L., 1986, *ApJ*, 305, 14
Burkert A., Naab T., 2005, *MNRAS*, accepted, astro-ph/0504595
Cappellari M., et al. 2005a, astro-ph/0509470
Cappellari M., et al. 2005b, *MNRAS*, submitted, astro-ph/0505042
Carter D., 1978, *MNRAS*, 182, 797
Davies R. L., Efstathiou G., Fall S. M., Illingworth G., Schechter P. L., 1983, *ApJ*, 266, 41
de Zeeuw P. T., 1994, in *The Formation and Evolution of Galaxies*, eds. C. Muñoz-Tuñón and F. Sánchez, p. 231
de Zeeuw P. T., Franx M., 1991, *ARA&A*, 29, 239
Dejonghe H., 1986, *Phys. Rep.*, 133, 217
Dejonghe H., 1987, *MNRAS*, 224, 13
Dejonghe H., de Zeeuw P. T., 1988, *ApJ*, 333, 90
Dejonghe H., Laurent D., 1991, *MNRAS*, 252, 606
Eddington A. S., 1916, *MNRAS*, 76, 572
Emsellem E., et al. 2004, *MNRAS*, 352, 721
Evans N. W., Lynden-Bell D., 1989, *MNRAS*, 236, 801
Faber S. M., Tremaine S., Ajhar E. A., Byun Y.-I., Dressler A., Gebhardt K., Grillmair C., Kormendy J., Lauer T. R., Richstone D., 1997, *AJ*, 114, 1771
Falcón-Barroso J., et al. 2005, *MNRAS*, submitted

- Freeman K. C., Rodgers A. W., 1975, *ApJ*, 201, L71
Ganda K., et al. 2005, *MNRAS*, submitted
Gerhard O. E., 1993, *MNRAS*, 265, 213
Habing H. J., Sevenster M. N., Messineo M., van de Ven G., Kuijken K., 2005, *A&A*, submitted
Hubble E. P., 1936, *Realm of the Nebulae*. Yale University Press
Hunter C., 1975, *AJ*, 80, 783
Hunter C., 1977, *AJ*, 82, 271
Hunter C., de Zeeuw P. T., 1992, *ApJ*, 389, 79
Hunter C., Qian E., 1993, *MNRAS*, 262, 401
Illingworth G., 1977, *ApJ*, 218, L43
Jeans J. H., 1915, *MNRAS*, 76, 70
Kauffmann G., van den Bosch F., 2002, *Scientific American*, 286, 36
King I. R., 1978, *ApJ*, 222, 1
King I. R., Anderson J., 2002, in *ASP Conf. Ser. 265: Omega Centauri, A Unique Window into Astrophysics*, eds. F. van Leeuwen, J. D. Hughes, G. Piotto, p. 21
Kuzmin G. G., Kutuzov S. A., 1962, *Bull. Abastumani Astroph. Obs.*, 27, 82
Leach R., 1981, *ApJ*, 248, 485
Lynden-Bell D., 1960, PhD thesis, Cambridge University
Lynden-Bell D., 1962a, *MNRAS*, 123, 447
Lynden-Bell D., 1962b, *MNRAS*, 124, 95
Mathieu A., Dejonghe H., 1999, *MNRAS*, 303, 455
Merritt D., 1985, *AJ*, 90, 1027
Osipkov L. P., 1979, *Pis ma Astronomicheskii Zhurnal*, 5, 77
Perryman M. A. C., de Boer K. S., Gilmore G., Høg E., Lattanzi M. G., Lindegren L., Luri X., Mignard F., Pace O., de Zeeuw P. T., 2001, *A&A*, 369, 339
Qian E. E., de Zeeuw P. T., van der Marel R. P., Hunter C., 1995, *MNRAS*, 274, 602
Rybicki G. B., 1987, in *IAU Symp. 127: Structure and Dynamics of Elliptical Galaxies*, ed. P. T. de Zeeuw, p. 397
Salpeter E. E., 1955, *ApJ*, 121, 161
Sato C., 1980, *PASJ*, 32, 41
Schneider P., Ehlers J., Falco E. E., 1992, *Gravitational Lenses*. Springer-Verlag Berlin Heidelberg New York
Schwarzschild M., 1979, *ApJ*, 232, 236
Schwarzschild M., 1982, *ApJ*, 263, 599
Stark A. A., 1977, *ApJ*, 213, 368
Statler T. S., 1991, *AJ*, 102, 882
Statler T. S., 1994a, *ApJ*, 425, 458
Statler T. S., 1994b, *ApJ*, 425, 500
Statler T. S., 2001, *AJ*, 121, 244
Statler T. S., Emsellem E., Peletier R. F., Bacon R., 2004, *MNRAS*, 353, 1
van den Bosch R. C. E., de Zeeuw P. T., Gebhardt K., Noyola E., van de Ven G., 2005, *ApJ*, submitted
van den Bosch R. C. E., van de Ven G., Verolme E. K., Cappellari M., de Zeeuw P. T., 2006, *MNRAS*, to be submitted
van der Marel R. P., 1991, *MNRAS*, 253, 710
van der Marel R. P., Franx M., 1993, *ApJ*, 407, 525
van Dokkum P. G., Franx M., 2001, *ApJ*, 553, 90
van Leeuwen F., Le Poole R. S., Reijns R. A., Freeman K. C., de Zeeuw P. T., 2000, *A&A*, 360, 472
Vandervoort P. O., 1984, *ApJ*, 287, 475
Williams T. B., Schwarzschild M., 1979, *ApJ*, 227, 56

THE DYNAMICAL DISTANCE AND INTRINSIC STRUCTURE OF THE GLOBULAR CLUSTER ω CENTAURI

ABSTRACT

We determine the dynamical distance D , inclination i , mass-to-light ratio M/L and the intrinsic orbital structure of the globular cluster ω Cen, by fitting axisymmetric dynamical models to the ground-based proper motions of van Leeuwen et al. (2000) and line-of-sight velocities from four independent data-sets. We bring the kinematic measurements onto a common coordinate system, and select on cluster membership and on measurement error. This provides a homogeneous data-set of 2295 stars with proper motions accurate to 0.20 mas yr^{-1} and 2163 stars with line-of-sight velocities accurate to 2 km s^{-1} , out to about half the tidal radius.

We correct the observed velocities for perspective rotation caused by the space motion of the cluster, and show that the residual solid-body rotation component in the proper motions (caused by relative rotation of the photographic plates from which they were derived) can be taken out without any modeling other than assuming axisymmetry. This also provides a tight constraint on $D \tan i$. The corrected mean velocity fields are consistent with regular rotation, and the velocity dispersion fields display significant deviations from isotropy.

We model ω Cen with an axisymmetric implementation of Schwarzschild's orbit superposition method, which accurately fits the surface brightness distribution, makes no assumptions about the degree of velocity anisotropy in the cluster, and allows for radial variations in M/L . We bin the individual measurements on the plane of the sky to search efficiently through the parameter space of the models. Tests on an analytic model demonstrate that this approach is capable of measuring the cluster distance to an accuracy of about 6 per cent. Application to ω Cen reveals no dynamical evidence for a significant radial dependence of M/L , in harmony with the relatively long relaxation time of the cluster. The best-fit dynamical model has a stellar V -band mass-to-light ratio $M/L_V = 2.5 \pm 0.1 \text{ M}_\odot/L_\odot$ and an inclination $i = 50^\circ \pm 4^\circ$, which corresponds to an average intrinsic axial ratio of 0.78 ± 0.03 . The best-fit dynamical distance $D = 4.8 \pm 0.3 \text{ kpc}$ (distance modulus $13.75 \pm 0.13 \text{ mag}$) is significantly larger than obtained by means of simple spherical or constant-anisotropy axisymmetric dynamical models, and is consistent with the canonical value $5.0 \pm 0.2 \text{ kpc}$ obtained by photometric methods. The total mass of the cluster is $(2.5 \pm 0.3) \times 10^6 \text{ M}_\odot$.

The best-fit model is close to isotropic inside a radius of about 10 arcmin and becomes increasingly tangentially anisotropic in the outer region, which displays significant mean rotation. This phase-space structure may well be caused by the effects of the tidal field of the Milky Way. The cluster contains a separate disk-like component in the radial range between 1 and 3 arcmin, contributing about 4% to the total mass.

1 INTRODUCTION

THE globular cluster ω Cen (NGC 5139) is a unique window into astrophysics (van Leeuwen, Hughes & Piotto 2002). It is the most massive globular cluster of our Galaxy, with an estimated mass between $2.4 \times 10^6 M_\odot$ (Mandushev, Staneva & Spasova 1991) and $5.1 \times 10^6 M_\odot$ (Meylan et al. 1995). It is also one of the most flattened globular clusters in the Galaxy (e.g., Geyer, Nelles & Hopp 1983) and it shows clear differential rotation in the line-of-sight (Merritt, Meylan & Mayor 1997). Furthermore, multiple stellar populations can be identified (e.g., Freeman & Rodgers 1975; Lee et al. 1999; Pancino et al. 2000; Bedin et al. 2004). Since this is unusual for a globular cluster, a whole range of different formation scenarios of ω Cen have been suggested, from self-enrichment in an isolated cluster or in the nucleus of a tidally stripped dwarf galaxy, to a merger between two or more globular clusters (e.g., Icke & Alcaïno 1988; Freeman 1993; Lee et al. 2002; Tsuchiya, Korchagin & Dinescu 2004).

ω Cen has a core radius of $r_c = 2.6$ arcmin, a half-light (or effective) radius of $r_h = 4.8$ arcmin and a tidal radius of $r_t = 45$ arcmin (e.g., Trager, King & Djorgovski 1995). The resulting concentration index $\log(r_t/r_c) \sim 1.24$ implies that ω Cen is relatively loosely bound. In combination with its relatively small heliocentric distance of 5.0 ± 0.2 kpc (Harris 1996)¹. This makes it possible to observe individual stars over almost the entire extent of the cluster, including the central parts. Indeed, line-of-sight velocity measurements² have been obtained for many thousands of stars in the field of ω Cen (Suntzeff & Kraft 1996, hereafter SK96; Mayor et al. 1997, hereafter M97; Reijns et al. 2005, hereafter Paper II; Xie, Gebhardt et al. in preparation, hereafter XGEA). Recently, also high-quality measurements of proper motions of many thousands of stars in ω Cen have become available, based on ground-based photographic plate observations (van Leeuwen et al. 2000, hereafter Paper I) and Hubble Space Telescope (HST) imaging (King & Anderson 2002).

The combination of proper motions with line-of-sight velocity measurements allows us to obtain a dynamical estimate of the distance to ω Cen and study its internal dynamical structure. While line-of-sight velocity observations are in units of km s^{-1} , proper motions are angular velocities and have units of (milli)arcsec yr^{-1} . A value for the distance is required to convert these angular velocities to km s^{-1} . Once this is done, the proper motion and line-of-sight velocity measurements can be combined into a three-dimensional space velocity, which can be compared to kinematic observables that are predicted by dynamical models. By varying the input parameters of these models, the set of model parameters (including the distance) that provides the best-fit to the observations can be obtained. Similar studies for other globular clusters, based on comparing modest numbers of line-of-sight velocity and proper motion measurements with simple spherical dynamical models, were published for M3 (Cudworth 1979), M22 (Peterson & Cudworth 1994), M4 (Peterson, Rees & Cudworth 1995; see also Rees 1997), and M15 (McNamara, Harrison & Baumgardt 2004).

A number of dynamical models which reproduce the line-of-sight velocity measurements have been published. As no proper motion information was included in these models, the distance could not be fitted and had to be assumed. Furthermore, all

¹Throughout this chapter we use this distance of 5.0 ± 0.2 kpc, obtained with photometric methods, as the canonical distance.

²Instead of the often-used term *radial* velocities, we adopt the term *line-of-sight* velocities, to avoid confusion with the decomposition of the proper motions in the plane of the sky into a radial and tangential component.

these models were limited by the flexibility of the adopted techniques and assumed either spherical geometry (Meylan 1987, Meylan et al. 1995) or an isotropic velocity distribution (Merritt et al. 1997). Neither of these assumptions is true for ω Cen (Geyer et al. 1983; Merrifield & Kent 1990). Recent work, using an axisymmetric implementation of Schwarzschild’s (1979) orbit superposition method, shows that it is possible to fit anisotropic dynamical models to (line-of-sight) kinematic observations of non-spherical galaxies (van der Marel et al. 1998; Cretton et al. 1999; Cappellari et al. 2002; Verolme et al. 2002; Gebhardt et al. 2003; Krajnović et al. 2005). Here, we extend Schwarzschild’s method in such a way that it can deal with a combination of proper motion and line-of-sight velocity measurements of individual stars. This allows us to derive an accurate dynamical distance and to improve our understanding of the internal structure of ω Cen.

It is possible to incorporate the discrete kinematic measurements of ω Cen directly in dynamical models by using maximum likelihood techniques (Merritt & Saha 1993; Merritt 1993; Merritt 1997; Romanowsky & Kochanek 2001; Kleyana et al. 2002), but these methods are non-linear, are not guaranteed to find the global best-fitting model, and are very CPU-intensive for data-sets consisting of several thousands of measurements. We therefore decided to bin the measurements instead and obtain the velocity moments in a set of apertures on the plane of the sky. While this method is (in principle) slightly less accurate, as some information in the data may be lost during the binning process, it is much faster, which allows us to make a thorough investigation of the parameter space of ω Cen in a relatively short time. It should also give a good starting point for a subsequent maximum likelihood model using the individual measurements.

This chapter is organized as follows. In Section 2, we describe the proper motion and line-of-sight velocity measurements and transform them to a common coordinate system. The selection of the kinematic measurements on membership and measurement error is outlined in Section 3. In Section 4, we correct the kinematic measurements for perspective rotation and show that a residual solid-body rotation component in the proper motions can be taken out without any modeling other than assuming axisymmetry. This also provides a tight constraint on the inclination of the cluster. In Section 5, we describe our axisymmetric dynamical modeling method, and test it in Section 6 on an analytical model. In Section 7, we construct the mass model for ω Cen, bin the individual kinematic measurements on the plane of the sky and describe the construction of dynamical models that we fit to these observations. The resulting best-fit parameters for ω Cen are presented in Section 8. We discuss the intrinsic structure of the best-fit model in Section 9, and draw our conclusions in Section 10.

2 OBSERVATIONS

We briefly describe the stellar proper motion and line-of-sight velocity observations of ω Cen that we use to constrain our dynamical models (see Table 1). We then align and transform them to a common coordinate system.

2.1 PROPER MOTIONS

The proper motion study in Paper I is based on 100 photographic plates of ω Cen, obtained with the Yale-Columbia 66 cm refractor telescope. The first-epoch observations were taken between 1931 and 1935, for a variable star survey of ω Cen (Martin

Source	Extent (arcmin)	Observed (#stars)	Selected (#stars)	Precision (km s^{-1})
proper motions				
Paper I	0–30	9847	2295	< 4.7
line-of-sight velocities				
SK96	3–23	360	345	2.2
M97	0–22	471	471	0.6
Paper II	0–38	1966	1588	2.0
XGEA	0–3	4916	1352	1.1
Merged	0–30		2163	< 2.0

TABLE 1 — Overview of the proper motions and line-of-sight velocity data-sets for ω Cen. The last row describes the four different line-of-sight velocity data-sets merged together, using the stars in common. The precision is estimated as the median of the (asymmetric) velocity error distribution. If a selection on the velocity errors is applied (§ 3), the upper limit is given. For the proper motions, we assume a canonical distance of 5 kpc to convert from mas yr^{-1} to km s^{-1} .

1938). Second-epoch plates, specifically meant for the proper motion study, were taken between 1978 and 1983. The plates from both periods were compared and proper motions were measured for 9847 stars. The observations cover a radial range of about 30 arcmin from the cluster center.

2.2 LINE-OF-SIGHT VELOCITIES

We use line-of-sight velocity observations from four different data-sets: the first two, by SK96 and M97, from the literature, the third is described in the companion Paper II and the fourth (XGEA) was provided by Karl Gebhardt in advance of publication.

SK96 used the ARGUS multi-object spectrograph on the CTIO 4 m Blanco telescope to measure, from the Ca II triplet range of the spectrum, the line-of-sight velocities of bright giant and subgiant stars in the field of ω Cen. They found respectively 144 and 199 line-of-sight velocity members, and extended the bright sample to 161 with measurements by Patrick Seitzer. The bright giants cover a radial range from 3 to 22 arcmin, whereas the subgiants vary in distance between 8 and 23 arcmin. From the total data-set of 360 stars, we remove the 6 stars without (positive) velocity error measurement together with the 9 stars for which we do not have a position (see § 2.3.1), leaving a total of 345 stars.

M97 published 471 high-quality line-of-sight velocity measurements of giants in ω Cen, taken with the photoelectric spectrometer CORAVEL, mounted on the 1.5 m Danish telescope at Cerro La Silla. The stars in their sample are located between 10 arcsec and 22 arcmin from the cluster center.

In Paper II, we describe the line-of-sight velocity measurements of 1966 individual stars in the field of ω Cen, going out to about 38 arcmin. Like SK96, we observed with ARGUS, but used the Mg*b* wavelength range. We use the 1589 cluster members, but exclude the single star for which no positive velocity error measurement is available.

Finally, the data-set of XGEA contains the line-of-sight velocities of 4916 stars in the central 3 arcmin of ω Cen. These measurements were obtained in three epochs over a time span of four years, using the Rutgers Imaging Fabry-Perot Spectrophotometer on the CTIO 1.5 m telescope. During the reduction process, some slightly

smear out single stars were accidentally identified as two fainter stars. Also, contaminating light from surrounding stars can lead to offsets in the line-of-sight velocity measurements. To exclude (most of) these misidentifications (Gebhardt, priv. comm.), we select the 1352 stars with a measured (*R*-band) magnitude brighter than 14.5.

2.3 COORDINATE SYSTEM: POSITIONS

We constrain our dynamical models by merging all the above data-sets. We convert all stellar positions to the same projected Cartesian coordinates and align the different data-sets with respect to each other by matching the stars in common between the different data-sets. Next, we rotate the coordinates over the observed position angle of ω Cen to align with its major and minor axis, and give the relation with the intrinsic axisymmetric coordinate system we assume for our models.

2.3.1 Projected Cartesian coordinates (x'' , y'')

The stellar positions in Paper I are given in equatorial coordinates α and δ (in units of degrees for J2000), with the cluster center at $\alpha_0 = 201^\circ.69065$ and $\delta_0 = -47^\circ.47855$. For objects with small apparent sizes, these equatorial coordinates can be converted to Cartesian coordinates by setting $x'' = -\Delta\alpha \cos \delta$ and $y'' = \Delta\delta$, with x'' in the direction of West and y'' in the direction of North, and $\Delta\alpha \equiv \alpha - \alpha_0$ and $\Delta\delta \equiv \delta - \delta_0$. However, this transformation results in severe projection effects for objects that have a large angular diameter or are located at a large distance from the equatorial plane. Since both conditions are true for ω Cen, we must project the coordinates of each star on the plane of the sky along the line-of-sight vector through the cluster center

$$\begin{aligned} x'' &= -r_0 \cos \delta \sin \Delta\alpha, \\ y'' &= r_0 (\sin \delta \cos \delta_0 - \cos \delta \sin \delta_0 \cos \Delta\alpha), \end{aligned} \tag{2.1}$$

with scaling factor $r_0 \equiv 10800/\pi$ to have x'' and y'' in units of arcmin. The cluster center is at $(x'', y'') = (0, 0)$.

The stellar observations by SK96 are tabulated as a function of the projected radius to the center only. However, for each star for which its ROA number (Woolley 1966) appears in the Tables of Paper I or M97, we can reconstruct the positions from these data-sets. In this way, only nine stars are left without a position. The positions of the stars in the M97 data-set are given in terms of the projected polar radius R'' in arcsec from the cluster center and the projected polar angle θ'' in radians from North to East, and can be straightforwardly converted into Cartesian coordinates x'' and y'' . For Paper II, we use the Leiden Identification (LID) number of each star, to obtain the stellar positions from Paper I. The stellar positions in the XGEA data-set are already in the required Cartesian coordinates x'' and y'' .

2.3.2 Alignment between data-sets

Although for all data-sets the stellar positions are now in terms of the projected Cartesian coordinates (x'', y'') , (small) misalignments between the different data-sets are still present. These misalignments can be eliminated using the stars in common between the different data-sets. As the data-set of Paper I covers ω Cen fairly uniformly over much of its extent, we take their stellar positions as a reference frame.

All the positions for the Paper II data-set and most of the positions for the SK96 data-set come directly from Paper I, and hence are already aligned. For the M97 and

XGEA data-set, we use the `DAOMASTER` program (Stetson 1992), to obtain the transformation (horizontal and vertical shift plus rotation) that minimizes the positional difference between the stars that are in common with those in Paper I: 451 for the M97 data-set and 1667 for the XGEA data-set.

2.3.3 Major-minor axis coordinates (x', y')

With all the data-sets aligned, we finally convert the stellar positions into the Cartesian coordinates (x', y') , with the x' -axis and y' -axis aligned with respectively the observed major and minor axis of ω Cen. Therefore we have to rotate (x'', y'') over the position angle of the cluster. This angle is defined in the usual way as the angle between the observed major axis and North (measured counterclockwise through East).

To determine the position angle, we fit elliptic isophotes to the smoothed Digital Sky Survey (DSS) image of ω Cen, while keeping the center fixed. In this way, we find a nearly constant position angle of 100° between 5 and 15 arcmin from the center of the cluster. This is consistent with an estimate by Seitzer (priv. comm.) from a U -band image, close to the value of 96° found by White & Shawl (1987), but significantly larger than the position angle of 91.3° measured in Paper I from star counts.

2.3.4 Intrinsic axisymmetric coordinates (x, y, z)

Now that we have aligned the coordinates in the plane of the sky (x', y') with the observed major and the major axis, the definition of the intrinsic coordinate system of our models and the relation between both becomes straightforward. We assume the cluster to be axisymmetric and express the intrinsic properties of the model in terms of Cartesian coordinates (x, y, z) , with the z -axis the symmetry axis. The relation between the intrinsic and projected coordinates is then given by

$$\begin{aligned} x' &= y, \\ y' &= -x \cos i + z \sin i, \\ z' &= -x \sin i - z \cos i. \end{aligned} \tag{2.2}$$

The z' -axis is along the line-of-sight in the direction away from us³, and i is the inclination along which the object is observed, from $i = 0^\circ$ face-on to $i = 90^\circ$ edge-on.

2.4 COORDINATE SYSTEM: VELOCITIES

After the stellar positions have been transformed to a common coordinate system, we also convert the proper motions and line-of-sight velocities to the same (three-dimensional) Cartesian coordinate system. We center it around zero (mean) velocity by subtracting the systemic velocity in all three directions, and relate it to the intrinsic axisymmetric coordinate system.

2.4.1 Proper motions

The proper motions (in mas yr^{-1}) of Paper I are given in the directions East and North, i.e., in the direction of $-x''$ and y'' respectively. After rotation over the position angle of 100° , we obtain the proper motion components $\mu_{x'}$ and $\mu_{y'}$, aligned with the observed major and minor axis of ω Cen, and similarly, for the proper motion errors.

³In the common (mathematical) definition of a Cartesian coordinate system the z' -axis would point towards us, but here we adopt the astronomical convention to have positive line-of-sight away from us.

2.4.2 Multiple line-of-sight velocity measurements

In Paper II, the measured line-of-sight velocities are compared with those of SK96 and M97 for the stars in common. A systematic offset in velocity between the different data-sets is clearly visible in Fig. 1 of that paper. We measure this offset with respect to the M97 data-set, since it has the highest velocity precision and more than a hundred stars in common with the other three data-sets: 129 with SK96, 312 with Paper II⁴ and 116 with XGEA. As in Paper II, we apply four-sigma clipping, i.e., we exclude all stars for which the measured velocities differ by more than four times the combined velocity error. This leaves respectively 117, 284 and 109 stars in common between M97 and the three data-sets of SK96, Paper II and XGEA. The (weighted⁵) mean velocity offsets of the data-set of M97 minus the three data-sets of SK96, Paper II and XGEA, are respectively $-0.41 \pm 0.08 \text{ km s}^{-1}$, $1.45 \pm 0.07 \text{ km s}^{-1}$ and $0.00 \pm 0.12 \text{ km s}^{-1}$. For each of the latter three data-sets, we add these offsets to all observed line-of-sight velocities.

Next, for each star that is present in more than one data-set, we combine the multiple line-of-sight velocity measurements. Due to non-overlapping radial coverage of the data-set of SK96 and XGEA, there are no stars in common between these two data-sets, and hence no stars that appear in all four data-sets. There are 138 stars with position in common between three data-sets and 386 stars in common between two data-sets.

For the 138 stars in common between three data-sets, we check if the three pairwise velocity differences satisfy the four-sigma clipping criterion. For 6 stars, we find that two of the three pairs satisfy the criterion, and we select the two velocities that are closest to each other. For 7 stars, we only find a single pair that satisfies the criterion, and we select the corresponding two velocities. Similarly, we find for the 386 stars in common between two data-sets, 13 stars for which the velocity difference does not satisfy the criterion, and we choose the measurement with the smallest error. This means from the 524 stars with multiple velocity measurements, for 26 stars (5%) one of the measurements is removed as an outlier. This can be due to a chance combination of large errors, a misidentification or a binary; Mayor et al. (1996) estimated the global frequency of short-period binary systems in ω Cen to be 3–4%.

As pointed out in § 2.6 of Paper II, we can use for the stars in common between (at least) three data-sets, the dispersion of the pairwise differences to calculate the external (instrumental) dispersion for each of the data-sets. In this way, we found in Paper II that the errors tabulated in SK96 are under-estimated by about 40% and hence increased them by this amount, whereas those in M97 are well-calibrated. Unfortunately, there are too few stars in common with the XGEA data-set for a similar (statistically reliable) external error estimate.

In the final sample, we have 125 stars with the weighted mean of three velocity measurements and 373 stars with the weighted mean of two velocity measurements. Together with the 2596 single velocity measurements, this gives a total of 3094 cluster stars with line-of-sight velocities.

⁴In Paper II, we report only 267 stars in common with the data-set of M97. The reason is that there the comparison is based on matching ROA numbers, and since not all stars from Paper II have a ROA number, we find here more stars in common by matching in position.

⁵To calculate the mean and dispersion of a sample, we use the weighted estimators and corresponding uncertainties as described in Appendix A of Paper II.

2.4.3 Systemic velocities

To center the Cartesian velocity system around zero mean velocity, we subtract from both the proper motion data-sets and the merged line-of-sight data-set the (remaining) systemic velocities. In combination with the cluster proper motion values from Table 4 of Paper I, we find the following systemic velocities

$$\begin{aligned}\mu_{x'}^{\text{sys}} &= 3.88 \pm 0.41 \text{ mas yr}^{-1}, \\ \mu_{y'}^{\text{sys}} &= -4.44 \pm 0.41 \text{ mas yr}^{-1}, \\ v_{z'}^{\text{sys}} &= 232.02 \pm 0.03 \text{ km s}^{-1}.\end{aligned}\tag{2.3}$$

2.4.4 Intrinsic axisymmetric coordinate system

In our models, we calculate the velocities in units of km s^{-1} . If we assume a distance D (in units of kpc), the conversion of the proper motions in units of mas yr^{-1} into units of km s^{-1} is given by

$$v_{x'} = 4.74 D \mu_{x'} \quad \text{and} \quad v_{y'} = 4.74 D \mu_{y'}.\tag{2.4}$$

The relation between observed $(v_{x'}, v_{y'}, v_{z'})$ and intrinsic (v_x, v_y, v_z) velocities is the same as in eq. (2.2), with the coordinates replaced by the corresponding velocities.

In addition to Cartesian coordinates, we also describe the intrinsic properties of our axisymmetric models in terms of the usual cylindrical coordinates (R, ϕ, z) , with $x = R \cos \phi$ and $y = R \sin \phi$. In these coordinates the relation between the observed and intrinsic velocities is

$$\begin{aligned}v_{x'} &= v_R \sin \phi + v_\phi \cos \phi, \\ v_{y'} &= (-v_R \cos \phi + v_\phi \sin \phi) \cos i + v_z \sin i, \\ v_{z'} &= (-v_R \cos \phi + v_\phi \sin \phi) \sin i + v_z \cos i.\end{aligned}\tag{2.5}$$

3 SELECTION

We discuss the selection of the cluster members from the different data-sets, as well as some further removal of stars that cause systematic deviations in the kinematics.

3.1 PROPER MOTIONS

In Paper I, a membership probability was assigned to each star. We use the stars for which we also have line-of-sight velocity measurements to investigate the membership determination. Furthermore, in Paper I the image of each star was inspected and classified according to its separation from other stars. We study the effect of the disturbance by a neighboring star on the kinematics. Finally, after selection of the undisturbed cluster members, we exclude the stars with relatively large uncertainties in their proper motion measurements, which cause a systematic overestimation of the mean proper motion dispersion.

3.1.1 Membership determination

The membership probability in Paper I was assigned to each star in the field by assuming that the distribution of stellar velocities is Gaussian. In most studies, this is done by adopting one common distribution for the entire cluster. However, this does not take into account that the internal dispersion, as well as the relative number

of cluster stars decreases with radius. To better incorporate these two effects, the membership probability in Paper I was calculated along concentric rings.

By matching the identification numbers and the positions of stars, we find that there are 3762 stars for which both proper motions and line-of-sight velocities are measured. This allows us to investigate the quality of the membership probability assigned in Paper I, as the separation of cluster and field stars is very clean in line-of-sight velocities (see e.g. Paper II, Fig. 4).

From the line-of-sight velocities, we find that of the 3762 matched stars, 3385 are cluster members. Indeed, most of these cluster stars, 3204 (95%), have a membership probability based on their proper motions of at least 68 per cent. Based on the latter criterion, the remaining 181 (5%) cluster stars are wrongly classified as field stars in Paper I. From the 3762 matched stars, 377 stars are field stars from the line-of-sight velocity data-set of Paper II. Based on a membership probability of 68 per cent, 54 (14%) of these field stars are wrongly classified as cluster members in Paper I. This fraction of field stars misclassified as cluster stars is an upper limit, since the obvious field stars are already removed from the proper motion data-set of Paper I.

Wrongly classifying cluster stars as field stars is relatively harmless for our purpose, since it only reduces the total cluster data-set. However, classifying field stars as members of the cluster introduces stars from a different population with different (kinematical) properties. With a membership probability of 99.7 per cent the fraction of field stars misclassified as cluster stars reduces to 5%. However, at the same time we expect to miss almost 30% of the cluster stars as they are wrongly classified as field stars. Taking also into account that the additional selections on disturbance by neighboring stars and velocity error below remove (part of) the field stars misclassified as cluster stars, we consider stars with a membership probability of at least 68 per cent as cluster members.

While for the 3762 matched stars, the line-of-sight velocities confirm 3385 stars as cluster members, from the remaining 6084 (unmatched) stars of Paper I, 4597 stars have a proper motion membership probability of at least 68 per cent. From the resulting proper motion distribution, we remove 83 outliers with proper motions five times the standard deviation away from the mean, leaving a total of 7899 cluster stars.

3.1.2 Disturbance by neighboring stars

In Paper I, each star was classified according to its separation from other stars on a scale from 0 to 4, from completely free to badly disturbed by a neighboring star. In Fig. 1, we show the effect of the disturbance on the proper motion dispersion. The (smoothed) profiles are constructed by calculating the mean proper motion dispersion of the stars binned in concentric rings, taking the individual measurement errors into account (Appendix A). The proper motions in the x' -direction give rise to the velocity dispersion profiles $\sigma_{x'}$ in the left panel. The proper motions in the y' -direction yield the dispersion profiles $\sigma_{y'}$ in the right panel. The thickest curves are the dispersion profiles for all 7899 cluster stars with proper motion measurements. The other curves show how, especially in the crowded center of ω Cen, the dispersion decreases significantly when sequentially stars of class 4 (severely disturbed) to class 1 (slightly disturbed) are removed. We select the 4415 undisturbed stars of class 0.

The membership determination is cleaner for undisturbed stars, so that above fraction of 5% of the cluster stars misclassified as field stars becomes smaller than 3% if only stars of class 0 are selected. The dispersion profiles $\sigma_{x'}$ and $\sigma_{y'}$ in Fig. 1

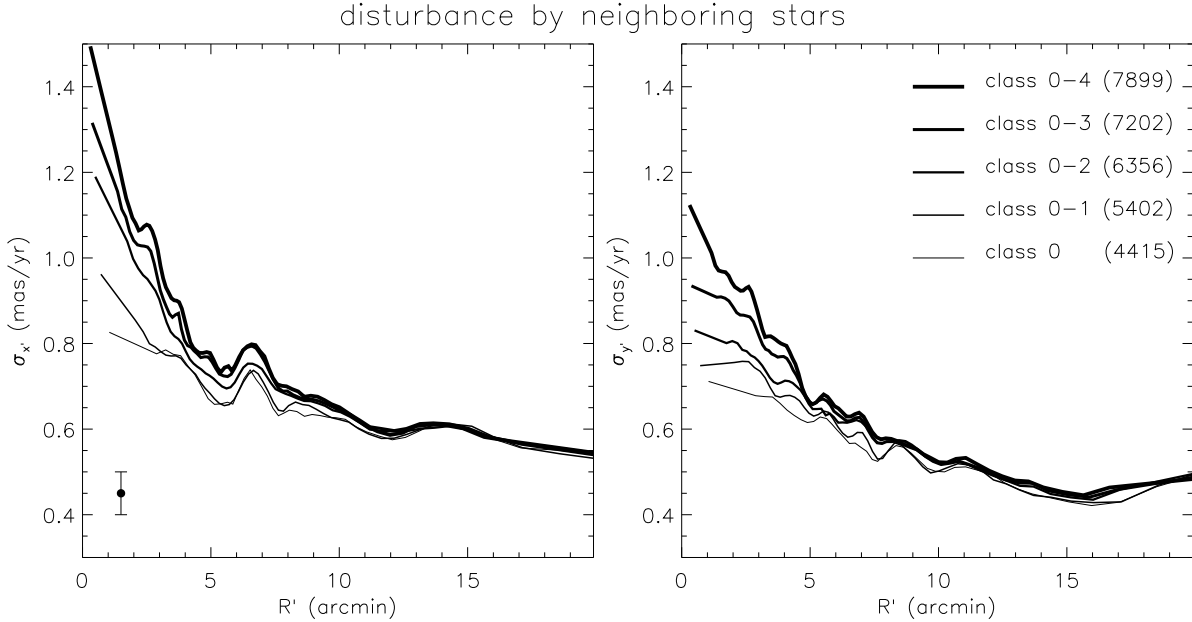


FIGURE 1 — Velocity dispersion profiles, calculated along concentric rings, from the proper motions of Paper I. The dispersion profiles from the proper motions in the x' -direction (y' -direction) are shown in the left (right). The error bar at the bottom-left indicates the typical uncertainty in the velocity dispersion. The thickest curves are the dispersion profiles for all 7899 cluster stars with proper motion measurements. The other curves show how the dispersion decreases significantly, especially in the crowded center of ω Cen, when sequentially stars of class 4 (severely disturbed) to class 1 (slightly disturbed) are removed. We select the 4415 undisturbed stars of class 0.

are systematically offset with respect to each other, demonstrating that the velocity distribution in ω Cen is anisotropic. We discuss this further in § 4.6 and § 9.2.

3.1.3 Selection on proper motion error

After selection of the cluster members that are not disturbed by neighboring stars, it is likely that the sample of 4415 stars still includes (remaining) interlopers and stars with uncertain proper motion measurements, which can lead to systematic deviations in the kinematics. Fig. 2 shows that the proper motion dispersion profiles decrease if we sequentially select a smaller number of stars by setting a tighter limit on the allowed error in their proper motion measurements.

Since the proper motion errors are larger for the fainter stars (see also Fig. 11 of Paper I), a similar effect happens if we select on magnitude instead. The decrease in dispersion is most prominent at larger radii as the above selection on disturbance by a neighboring star already removed the uncertain proper motion measurements in the crowded center of ω Cen. All dispersion profiles in the above are corrected for the broadening due to the individual proper motion errors (cf. Appendix A). The effect of this broadening, indicated by the dotted curve, is less than the decrease in the dispersion profiles due to the selection on proper motion error.

Since the kinematics do not change anymore significantly for a limit on the proper motion errors lower than 0.20 mas yr^{-1} , we select the 2295 stars with proper motion errors below this limit. The preliminary HST proper motions of King & Anderson

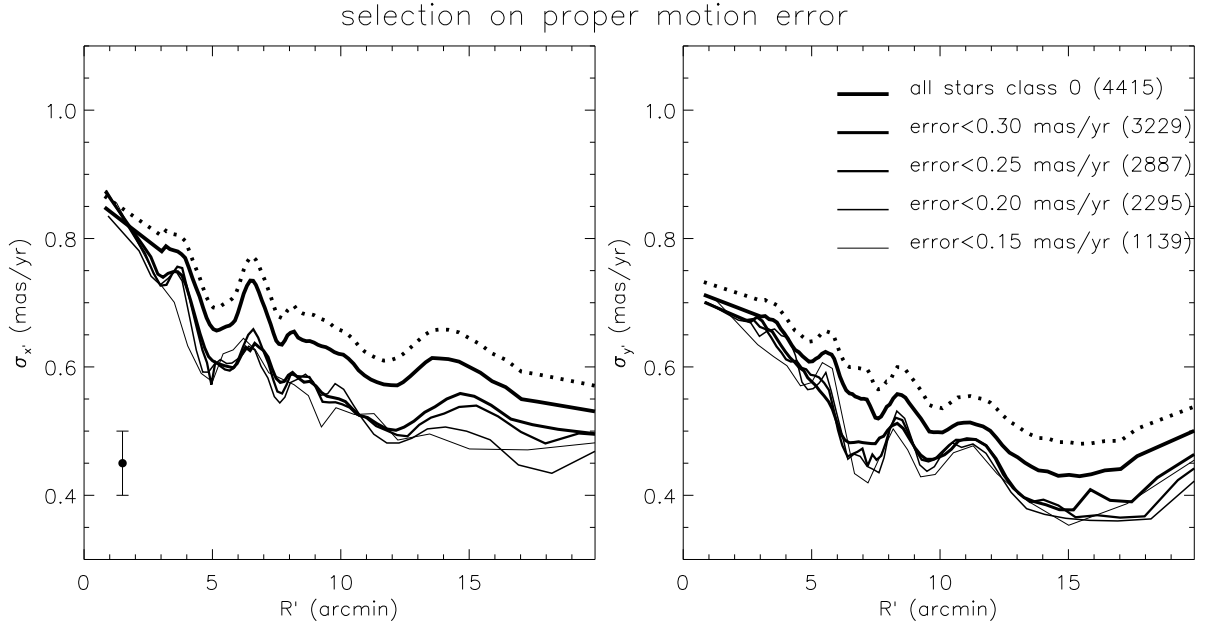


FIGURE 2 — Proper motion dispersion profiles as in Fig. 1. Starting with all undisturbed (class 0) cluster stars (thickest solid curve), sequentially a smaller number of stars is selected by setting a tighter limit on the allowed error in their proper motion measurements. The dispersion decreases if the stars with uncertain proper motion measurements are excluded. This effect is significant and larger than the dispersion broadening due to the individual velocity errors, indicated by the dotted curve. We select the 2295 stars with proper motion error smaller than 0.20 mas yr^{-1} , since below this limit the kinematics stay similar.

(2002) in the center of ω Cen ($R' \sim 1$ arcmin) give rise to mean proper motion dispersion $\sigma_{x'} = 0.81 \pm 0.08 \text{ mas yr}^{-1}$ and $\sigma_{y'} = 0.77 \pm 0.08 \text{ mas yr}^{-1}$, depending on the magnitude cut-off. In their outer calibration field ($R' \sim 14$ arcmin), the average dispersion is about $0.41 \pm 0.03 \text{ mas yr}^{-1}$. These values are consistent with the mean proper motion dispersion of the 2295 selected stars at those radii. We are therefore confident that the proper motion kinematics have converged.

The spatial distribution of the selected stars is shown in the left panel of Fig. 4. In the two upper panels of Fig. 5, the distributions of the two proper motion components (left panels) and the corresponding errors (right panels) of the $N_{\text{sel}} = 2295$ selected stars are shown as shaded histograms, on top of the histograms of the $N_{\text{mem}} = 7899$ cluster members. The selection removes the extended tails, making the distribution narrower with an approximately Gaussian shape.

3.2 LINE-OF-SIGHT VELOCITIES

For each of the four different line-of-sight velocity data-sets separately, the velocity dispersion profiles of the selected (cluster) stars (§ 2.2 and Table 1) are shown in Fig. 3. The dotted curve is the dispersion profile of all the 4916 stars observed by XGEA, whereas the dotted-dashed curve is based on the 1352 selected stars with a measured magnitude brighter than 14.5, showing that fainter misidentified stars lead to an under-estimation of the line-of-sight velocity dispersion. Although the dispersion profile of the M97 data-set (long dashed curve) seems to be systematically higher than those of the other data-sets, it is based on a relatively small number of

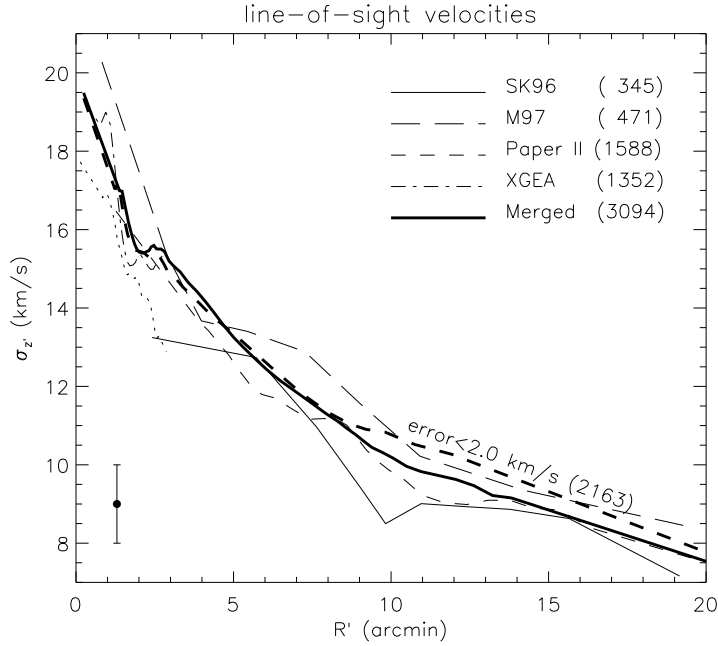


FIGURE 3 — *Velocity dispersion profiles, calculated along concentric rings, for the four different line-of-sight velocity data-sets separately and after they have been merged. The dotted curve shows the under-estimated dispersion for the XGEA data-set if also the faint stars are included. From the merged data-set of 3094 stars we select the 2163 stars with line-of-sight velocity errors smaller than 2.0 km s^{-1} , resulting in a dispersion profile (thick dashed curve) that is not under-estimated due to uncertain line-of-sight velocity measurements.*

stars, similar to the SK96 data-set, and the differences are still within the expected uncertainties indicated by the error bar.

The thick solid curve is the dispersion profile of the 3094 stars after merging the four line-of-sight velocity data-sets (§ 2.4.2). Due to uncertainties in the line-of-sight velocity measurements of especially the fainter stars, the latter dispersion profile is (slightly) under-estimated in the outer parts. By sequentially lowering the limit on the line-of-sight velocity errors, we find that below 2.0 km s^{-1} the velocity dispersion (thick dashed curve) converges. Hence, we select the 2163 stars with line-of-sight velocity errors smaller than 2.0 km s^{-1} .

The spatial distribution of these stars is shown in the right panel Fig. 4. In the bottom panels of Fig. 5, the distribution of the line-of-sight velocities (left) and corresponding errors (right) of the $N_{\text{sel}} = 2163$ selected stars are shown as filled histograms, on top of the histograms of the $N_{\text{mem}} = 3094$ cluster members in the merged data-set.

4 KINEMATICS

We compute the mean velocity fields for the selected stars and correct the kinematic data for perspective rotation and for residual solid-body rotation in the proper motions. At the same time, we place a tight constraint on the inclination. Finally, we calculate the mean velocity dispersion profiles from the corrected kinematic data.

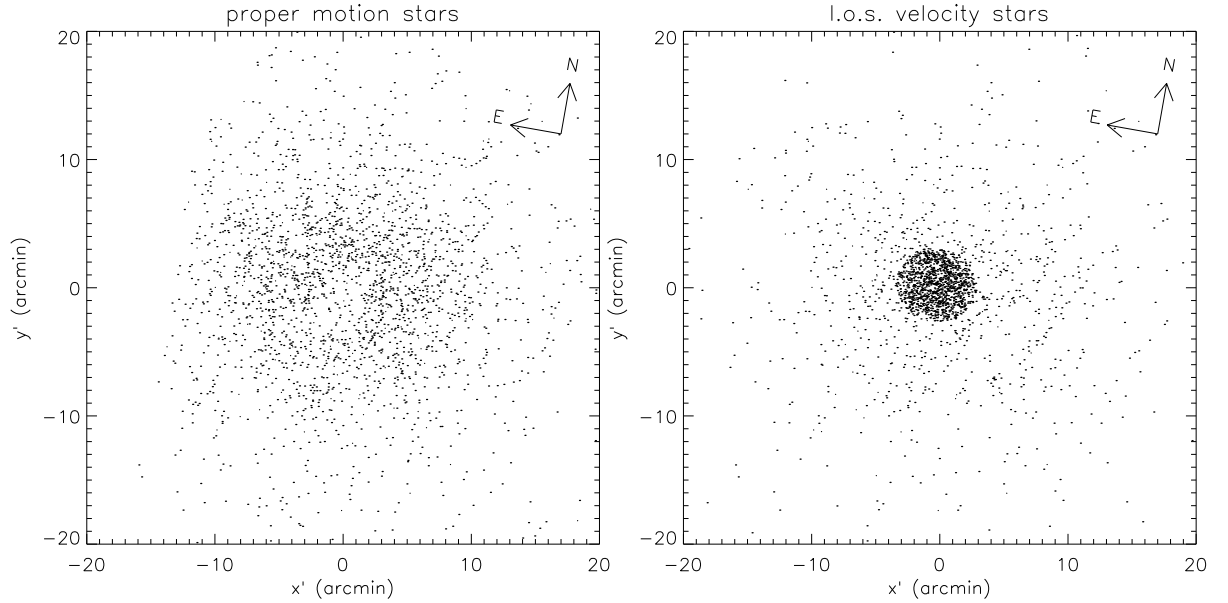


FIGURE 4 — The stars in ω Cen with proper motion measurements (left) and line-of-sight velocity measurements (right), that are used in our analysis. The stellar positions are plotted as a function of the projected Cartesian coordinates x' and y' , with the x' -axis aligned with the observed major axis and the y' -axis aligned with the observed minor axis of ω Cen. The excess of stars with line-of-sight velocities inside the central 3 arcmin in the bottom panel is due to the XGEA data-set.

4.1 SMOOTHED MEAN VELOCITY FIELDS

The left-most panels of Fig. 6 show the smoothed mean velocity fields for the 2295 selected stars with proper motion measurements and the 2163 selected stars with line-of-sight velocity measurements. This adaptive kernel smoothing is done by selecting for each star its 200 nearest neighbors on the plane of the sky, and then calculating the mean velocity (and higher order velocity moments) from the individual velocity measurements (Appendix A). The contribution of each neighbor is weighted with its distance to the star, using a Gaussian distribution with zero mean and the mean distance of the 200 nearest neighbors as the dispersion.

The top-left panel shows the mean proper motion (in mas yr^{-1}) in the major axis x' -direction, i.e., the horizontal component of the streaming motion on the plane of the sky. The grey scale is such that white (black) means that the stars are moving on average to the right (left) and the dashed curve shows the region where the horizontal component of the mean proper motion vanishes. Similarly, the middle-left panel shows the mean proper motion in the minor axis y' -direction, i.e. the vertical component of the streaming motion on the plane of the sky, with white (black) indicating average proper motion upwards (downwards). Finally, the lower-left panel shows the mean velocity (in km s^{-1}) along the line-of-sight z' -axis, where white (black) means that the stars are on average receding (approaching). The (dashed) zero-velocity curve is the rotation axis of ω Cen.

Apart from a twist in the (dashed) zero-velocity curve, the latter line-of-sight velocity field is as expected for a (nearly) axisymmetric stellar system. However, both proper motion fields show a complex structure, with an apparently dynamically de-

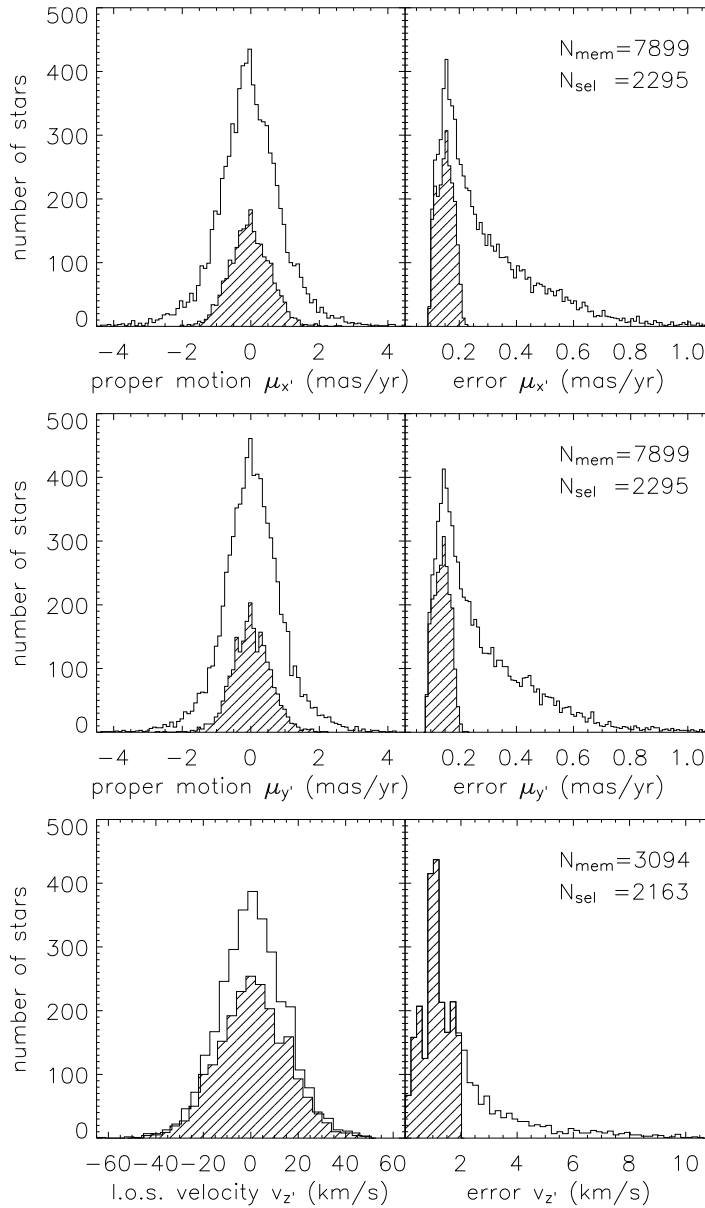


FIGURE 5 — Histograms of measured velocities (left panels) and corresponding velocity errors (right panels). The proper motion components $\mu_{x'}$ (top panels) and $\mu_{y'}$ (middle panels), in the direction of the observed major and minor axis of ω Cen respectively, come from the photographic plate observations in Paper I. The line-of-sight velocities (lower panels) are taken from four different data-sets (§ 2.2). The shaded histograms for the N_{sel} selected stars (§ 3) are overlaid on the histograms of the N_{mem} cluster member stars.

coupled inner part, far from axisymmetric. We now show that it is, in fact, possible to bring these different observations into concordance.

4.2 PERSPECTIVE ROTATION

The non-axisymmetric features in the observed smoothed mean velocity fields in the left-most panels of Fig. 6, might be (partly) caused by perspective rotation. Because

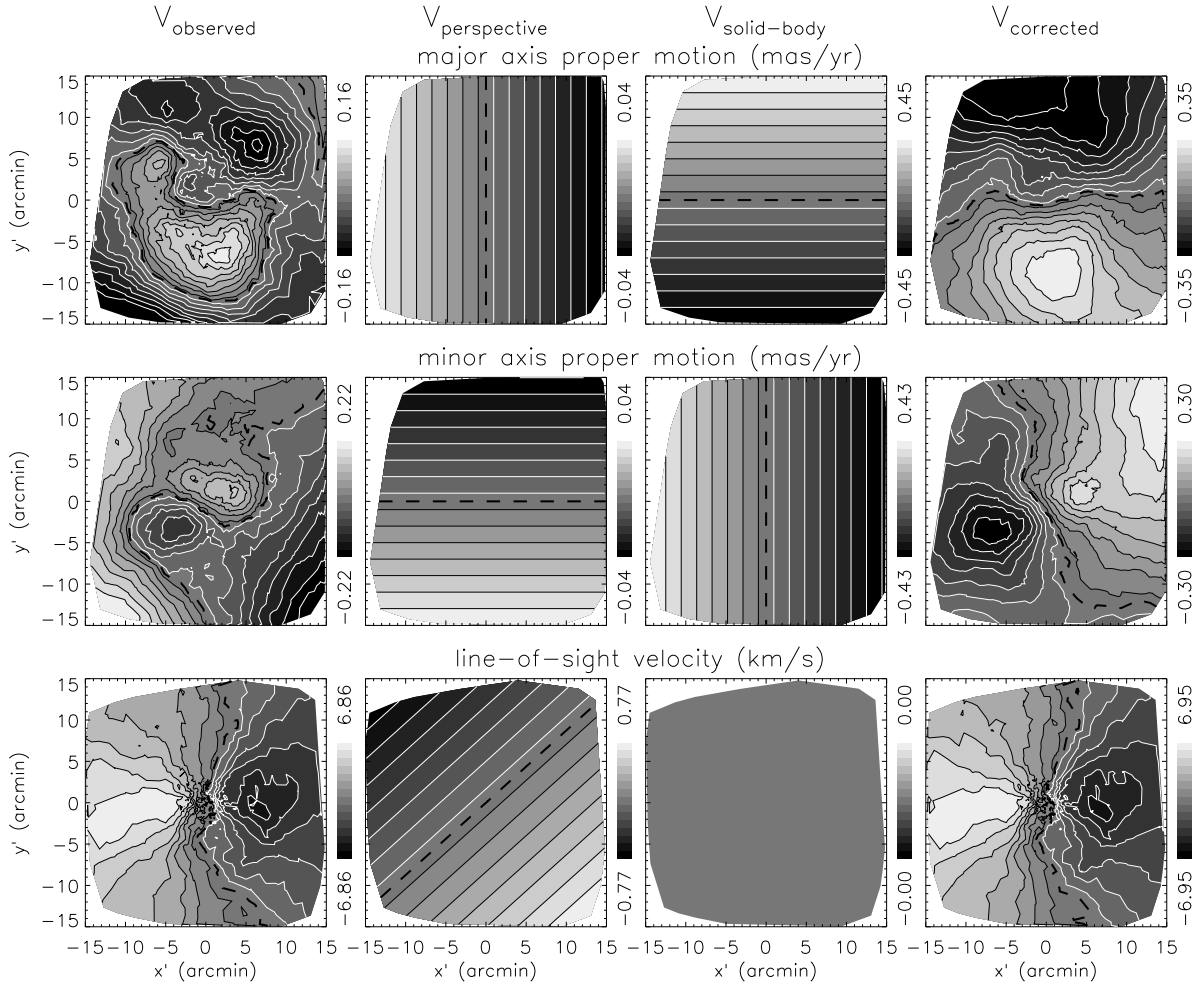


FIGURE 6 — The mean velocity fields of ω Cen corrected for perspective and solid-body rotation. The individual measurements are smoothed using adaptive kernel smoothing. From top to bottom: The mean ground-based proper motion in the major axis x' -direction and in the minor axis y' -direction, and the mean line-of-sight velocity. From left to right: Observed velocity fields of ω Cen, contribution from perspective rotation, contribution from solid-body rotation and the velocity fields after correcting for both. The perspective rotation is caused by the space motion of ω Cen. The solid-body rotation in the proper motions is due to relative rotation of the first and second epoch photographic plates by an amount of $0.029 \text{ mas yr}^{-1} \text{ arcmin}^{-1}$. (See p. 249 for a color version of this figure.)

ω Cen has a large extent on the plane of the sky (with a diameter about twice that of the full moon), its substantial systemic (or space) motion (eq. 2.3) produces a non-negligible amount of apparent rotation: the projection of the space motion onto the principal axis (x', y', z') is different at different positions on the plane of the sky (Feast, Thackeray & Wesselink 1961). We expand this perspective rotation in terms of the reciprocal of the distance D . Ignoring the negligible terms of order $1/D^2$ or smaller, we find the following additional velocities

$$\begin{aligned}
 \mu_{x'}^{\text{pr}} &= -6.1363 \times 10^{-5} x' v_{z'}^{\text{sys}} / D \quad \text{mas yr}^{-1}, \\
 \mu_{y'}^{\text{pr}} &= -6.1363 \times 10^{-5} y' v_{z'}^{\text{sys}} / D \quad \text{mas yr}^{-1}, \\
 v_{z'}^{\text{pr}} &= 1.3790 \times 10^{-3} (x' \mu_{x'}^{\text{sys}} + y' \mu_{y'}^{\text{sys}}) D \quad \text{km s}^{-1},
 \end{aligned} \tag{4.1}$$

with x' and y' in units of arcmin and D in kpc. For the canonical distance of 5 kpc, the systemic motion for ω Cen as given in eq. (2.3) and the data typically extending to 20 arcmin from the cluster center, we find that the maximum amplitude of the perspective rotation for the proper motions is about 0.06 mas yr^{-1} and for the line-of-sight velocity about 0.8 km s^{-1} . These values are a significant fraction of the observed mean velocities (left panels of Fig. 6) and of the same order as the uncertainties in the extracted kinematics (see Appendix B). Therefore, the perspective rotation as shown in the second column panels of Fig. 6, cannot be ignored and we correct the observed stellar velocities by subtracting it. Since we use the more recent and improved values for the systemic proper motion from Paper I, our correction for perspective rotation is different from that of Merritt et al. (1997). The amplitude of the correction is, however, too small to explain all of the complex structure in the proper motion fields and we have to look for an additional cause of non-axisymmetry.

4.3 RESIDUAL SOLID-BODY ROTATION

Van Leeuwen & Le Poole (2002) already showed that a possible residual solid-body rotation component in the ground-based proper motions of Paper I can have an important effect on the kinematics. The astrometric reduction process to measure proper motions removes the ability to observe an overall rotation on the plane of the sky (e.g., Vasilevskis et al. 1979). This solid-body rotation results in a transverse proper motion $v_t = \Omega R'$, with Ω the amount of solid-body rotation (in units of $\text{mas yr}^{-1} \text{ arcmin}^{-1}$) and R' the distance from the cluster center in the plane of the sky (in units of arcmin). Decomposition of v_t along the observed major and minor axis yields

$$\begin{aligned}\mu_{x'}^{\text{sbr}} &= +\Omega y' \text{ mas yr}^{-1}, \\ \mu_{y'}^{\text{sbr}} &= -\Omega x' \text{ mas yr}^{-1}.\end{aligned}\tag{4.2}$$

Any other reference point than the cluster center results in a constant offset in the proper motions, and is removed by setting the systemic proper motions to zero. Also an overall expansion (or contraction) cannot be determined from the measured proper motions, and results in a radial proper motion in the plane of the sky. Although both the amount of overall rotation and expansion are in principle free parameters, they can be constrained from the link between the measured (differential) proper motions to an absolute proper motion system, such as defined by the Hipparcos and Tycho-2 catalogues (Perryman et al. 1997; Høg et al. 2000). In Paper I, using the 56 stars in common with these two catalogues, the allowed amount of residual solid-body rotation was determined to be no more than $\Omega = 0.02 \pm 0.02 \text{ mas yr}^{-1} \text{ arcmin}^{-1}$ and no significant expansion was found.

As the amplitude of the allowed residual solid-body rotation is of the order of the uncertainties in the mean proper motions already close to the center, and can increase beyond the maximum amplitude of the mean proper motions in the outer parts, correcting for it has a very important effect on the proper motions. We use a general relation for axisymmetric objects to constrain Ω , and at the same find a constraint on the inclination.

4.4 THE RESIDUAL SOLID-BODY ROTATION DIRECTLY FROM THE MEAN VELOCITIES

For any axisymmetric system, there is, at each position (x', y') on the plane of the sky, a simple relation between the mean proper motion in the y' -direction $\langle \mu_{y'} \rangle$ and the

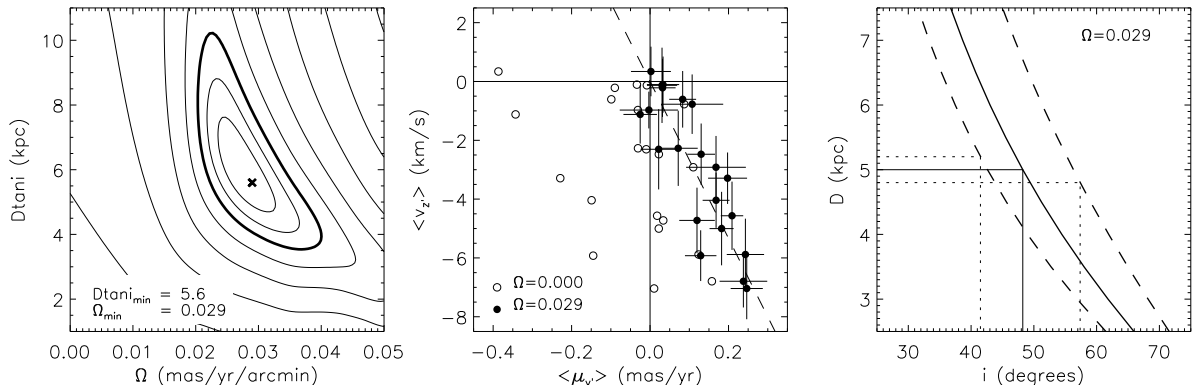


FIGURE 7 — Constraints on the amount of residual solid-body rotation Ω and via $D \tan i$, on the distance D (in kpc) and inclination i (in degrees), using the general relation (4.3) for axisymmetric objects. The left panel shows the contour map of the goodness-of-fit parameter $\Delta\chi^2$. The inner three contours are drawn at the 68.3%, 95.4% and 99.7% (thick contour) levels of a $\Delta\chi^2$ -distribution with two degrees of freedom. Subsequent contours correspond to a factor of two increase in $\Delta\chi^2$. The overall minimum is indicated by the cross. The middle panel shows the mean line-of-sight velocity $\langle v_{z'} \rangle$ and mean short-axis proper motion $\langle \mu_{y'} \rangle$ within the same polar apertures, before (open circles) and after (filled circles) correction for residual solid-body rotation with the best-fit value of $\Omega = 0.029 \pm 0.004 \text{ mas yr}^{-1} \text{ arcmin}^{-1}$. The best-fit value for $D \tan i = 5.6 (+1.9/-1.0) \text{ kpc}$ gives rise to the relation in the right panel (solid line), bracketed (at the 68.3%-level) by the dashed lines. Given the canonical distance of $D = 5.0 \pm 0.2 \text{ kpc}$, the dotted lines indicate the constraint on inclination of $i = 48 (+9/-7) \text{ degrees}$.

mean line-of-sight velocity $\langle v_{z'} \rangle$ (see e.g. Appendix A of Evans & de Zeeuw 1994, hereafter EZ94). Using relation (2.5), with for an axisymmetric system $\langle v_R \rangle = \langle v_z \rangle = 0$, we see that, while the mean velocity component in the x' -direction includes the spatial term $\cos \phi$, those in the y' -direction and line-of-sight z' -direction both contain $\sin \phi$. The latter implies that, by integrating along the line-of-sight to obtain the observed mean velocities, the expressions for $\langle v_{y'} \rangle$ and $\langle v_{z'} \rangle$ only differ by the $\cos i$ and $\sin i$ terms. Going from $\langle v_{y'} \rangle$ to $\langle \mu_{y'} \rangle$ via eq. (2.4), we thus find the following general relation for axisymmetric objects

$$\langle v_{z'} \rangle(x', y') = 4.74 D \tan i \langle \mu_{y'} \rangle(x', y'), \quad (4.3)$$

with distance D (in kpc) and inclination i .

This relation implies that, at each position on the plane of the sky, the only difference between the mean short-axis proper motion field and the mean line-of-sight velocity field should be a constant scaling factor equal to $4.74 D \tan i$. Comparing the left-most middle and bottom panel in Fig. 6 (V_{observed}), this is far from what we see, except perhaps for the inner part. We ascribe this discrepancy to the residual solid-body rotation, which causes a perturbation of $\langle \mu_{y'} \rangle$ increasing with x' as given in eq. (4.2). In this way, we can objectively quantify the amount of solid body rotation Ω needed to satisfy the above relation (4.3), and at the same time find the best-fit value for $D \tan i$.

To compute uncorrelated values (and corresponding errors) for the mean short-axis proper motion $\langle \mu_{y'} \rangle$ and mean line-of-sight velocity $\langle v_{z'} \rangle$ at the same positions on the plane of the sky, we bin the stars with proper motion and line-of-sight velocity measurements in the same polar grid of apertures (see also Appendix B). We plot the resulting values for $\langle v_{z'} \rangle$ against $\langle \mu_{y'} \rangle$ and fit a line (through the origin) by minimizing

the χ^2 , weighted with the errors in both directions (§ 15.3 of Press et al. 1992).

By varying the amount of solid-body rotation Ω and the slope of the line, which is proportional to $D \tan i$ (eq. 4.3), we obtain the $\Delta\chi^2 = \chi^2 - \chi_{\min}^2$ contours in the left panel of Fig. 7. The inner three contours are drawn at the levels containing 68.3%, 95.4% and 99.7% (thick contour) of a $\Delta\chi^2$ -distribution with two degrees of freedom⁶. Subsequent contours correspond to a factor of two increase in $\Delta\chi^2$. The overall minimum χ_{\min}^2 , indicated by a cross, implies (at the 68.3%-level) a best-fit value of $\Omega = 0.029 \pm 0.004 \text{ mas yr}^{-1} \text{ arcmin}^{-1}$. This is fully consistent with the upper limit of $\Omega = 0.02 \pm 0.02 \text{ mas yr}^{-1} \text{ arcmin}^{-1}$ from Paper I.

The middle panel of Fig. 7 shows that without any correction for residual solid-body rotation, the values for $\langle v_{z'} \rangle$ and $\langle \mu_{y'} \rangle$ are scattered (open circles), while they are nicely correlated after correction with $\Omega = 0.029 \text{ mas yr}^{-1} \text{ arcmin}^{-1}$ (filled circles). The resulting solid-body rotation, shown in the third column of Fig. 6, removes the cylindrical rotation that is visible in the outer parts of the observed proper motion fields (first column). After subtracting this residual solid-body rotation, together with the perspective rotation (second column), the complex structures disappear, resulting in (nearly) axisymmetric mean velocity fields in the last column. Although the remaining non-axisymmetric features, such as the twist of the (dashed) zero-velocity curve, might indicate deviations from true axisymmetry, they can also be (partly) artifacts of the smoothing, which, especially in the less dense outer parts, is sensitive to the distribution of stars on the plane of the sky.

This shows that the application of eq. (4.3) to the combination of proper motion and line-of-sight measurements provides a powerful new tool to determine the amount of solid body rotation. At the same time, it also provides a constraint on the inclination.

4.5 CONSTRAINT ON THE INCLINATION

From the left panel of Fig. 7 we obtain (at the 68.3%-level) a best-fit value for $D \tan i$ of $5.6 (+1.9/-1.0)$ kpc. The right panel shows the resulting relation (solid line) between the distance D and the inclination i , where the dashed lines bracket the 68.3%-level uncertainty. If we assume the canonical value $D = 5.0 \pm 0.2$ kpc, then the inclination is constrained to $i = 48 (+9/-7)$ degrees.

Although we apply the same polar grid to the proper motions and line-of-sight velocities, the apertures contain different (numbers of) stars. To test that this does not significantly influence the computed average kinematics and hence the above results, we repeated the analysis but now only include the 718 stars for which both the proper motions and line-of-sight velocity are measured. The results are equivalent, but less tightly constrained due to the smaller number of apertures.

Van Leeuwen & Le Poole (2002) compared, for different values for the amount of residual solid-body rotation Ω , the shape of the radial profile of the mean transverse component of proper motions from Paper I, with that of the mean line-of-sight velocities calculated by Merritt et al. (1997) from the line-of-sight velocity data-set of M97. They found that $\Omega \sim 0.032 \text{ mas yr}^{-1} \text{ arcmin}^{-1}$ provides a plausible agreement. Next, assuming a distribution for the density and the rotational velocities in the cluster, they computed projected transverse proper motion and line-of-sight velocity profiles,

⁶For a Gaussian distribution with dispersion σ , these percentages correspond to the 1σ , 2σ and 3σ confidence intervals respectively. For the (asymmetric) χ^2 -distribution there is in general no simple relation between dispersion and confidence intervals. Nevertheless, the 68.3%, 95.4% and 99.7% levels of the χ^2 -distribution are often referred to as the 1σ , 2σ and 3σ levels.

and by comparing them to the observed profiles, they derived a range for the inclination i from 40 to 60 degrees. Their results are consistent with our best-fit values $\Omega = 0.029 \pm 0.004 \text{ mas yr}^{-1} \text{ arcmin}^{-1}$ and $i = 48 (+9/-7)$ degrees. Our method is based on a general relation for axisymmetric objects, without any further assumptions about the underlying density and velocity distribution. Moreover, instead of comparing shapes of mean velocity profiles, we actually fit the mean velocity fields.

In the above analysis, we assume that all of the solid-body rotation in the proper motion is the result of a (non-physical) residual from the photographic plate reduction in Paper I. This raises the question what happens if a (physical) solid-body rotation component is present in ω Cen. Such a solid-body rotation component is expected to be aligned with the intrinsic rotation axis, inclined at about 48° , and therefore also present in the line-of-sight velocities. Except for the perspective rotation correction, we leave the mean line-of-sight velocities in the above analysis unchanged, so that any such solid-body rotation component should also remain in the proper motion.

Still, since we are fitting the residual solid-body rotation Ω and the slope $D \tan i$ simultaneously, they can become (partly) degenerate. Combining eq. (4.2) with (4.5), we obtain the best-fit values for $D \tan i$ and Ω by minimizing

$$\chi^2 = \sum_j^n \frac{\left[\langle v_{z'}^{\text{obs}} \rangle_j - 4.74 D \tan i \left(\langle \mu_{y'}^{\text{obs}} \rangle_j + \Omega x'_j \right) \right]^2}{\left[\Delta \langle v_{z'}^{\text{obs}} \rangle_j \right]^2 + \left[4.74 D \tan i \Delta \langle \mu_{y'}^{\text{obs}} \rangle_j \right]^2}, \quad (4.4)$$

where $\langle v_{z'}^{\text{obs}} \rangle_j$ and $\langle \mu_{y'}^{\text{obs}} \rangle_j$ are respectively the observed mean line-of-sight velocity and the observed mean proper motion in the y' -direction, measured in aperture j of a total of n apertures, with their centers at x'_j . $\Delta \langle v_{z'}^{\text{obs}} \rangle_j$ and $\Delta \langle \mu_{y'}^{\text{obs}} \rangle_j$ are the corresponding measurement errors. Suppose now the extreme case that all of the observed mean motion is due to solid-body rotation: an amount of Ω_0 residual solid-body rotation in the plane of the sky, and an amount of ω_0 intrinsic solid-body rotation, around the intrinsic z -axis in ω Cen, which we assume to be inclined at i_0 degrees. At a distance D_0 , the combination yields per aperture $\langle v_{z'}^{\text{obs}} \rangle_j = 4.74 D_0 \omega_0 \sin i_0 x'_j$ and $\langle \mu_{y'}^{\text{obs}} \rangle_j = (\omega_0 \cos i_0 - \Omega_0) x'_j$. Substitution of these quantities in the above eq. (4.4), and ignoring the (small) variations in the measurements errors, yields that $\chi^2 = 0$ if

$$D \tan i = D_0 \tan i_0 \left[1 + \frac{\Omega - \Omega_0}{\omega_0 \cos i_0} \right]^{-1}. \quad (4.5)$$

This implies a degeneracy between $D \tan i$ and Ω , which in the left panel of Fig. 7, would result in the same minimum all along a curve. However, in the case the motion in ω Cen consists of more than only solid-body rotation, this degeneracy breaks down and we expect to find a unique minimum. The latter seems to be the case here, and we conclude that the degeneracy and hence the intrinsic solid-body rotation are not dominant, if present at all.

4.6 MEAN VELOCITY DISPERSION PROFILES

In Fig. 8, we show the mean velocity dispersion profiles of the radial $\sigma_{R'}$ (dotted) and tangential $\sigma_{\theta'}$ (dashed) components of the proper motions, together with the line-of-sight velocity dispersion $\sigma_{z'}$ (solid). The dispersions are calculated along concentric rings from the selected sample of 2295 stars with proper motions corrected for perspective and residual solid-body rotation and 2163 stars with line-of-sight velocities

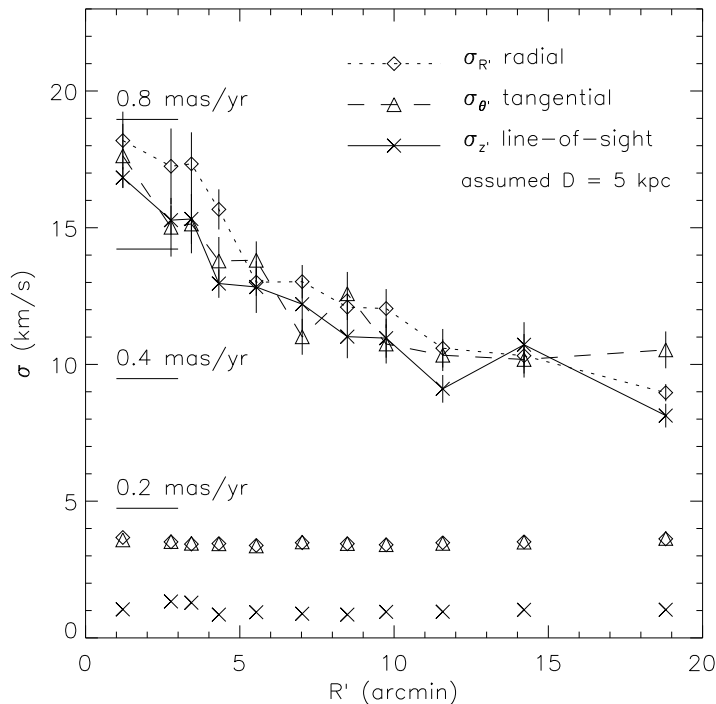


FIGURE 8 — Mean velocity dispersion profiles calculated along concentric rings. Assuming the canonical distance of 5 kpc, the profiles of the radial $\sigma_{R'}$ (dotted curve with diamonds) and tangential $\sigma_{\theta'}$ (dashed curve with triangles) components of the proper motion dispersion are converted into the same units of km s^{-1} as the profile of the line-of-sight velocity dispersion $\sigma_{z'}$ (solid curve with crosses). The horizontal lines indicate the corresponding scale in mas yr^{-1} . The mean velocity error per ring is indicated below the profiles by the corresponding symbols. The diamonds and triangles mostly overlap, as the errors of the radial and tangential components are nearly similar.

corrected for perspective rotation. We obtain similar mean velocity dispersion profiles if we only use the 718 stars for which both proper motions and line-of-sight velocity are measured. We assume the canonical distance of 5 kpc to convert the proper motion dispersion into units of km s^{-1} , while the black horizontal lines indicate the corresponding scale in units of mas yr^{-1} . Below the profiles, the symbols represent the corresponding mean velocity error per ring, showing that the accuracy of the line-of-sight velocity measurements (crosses) is about four times better than the proper motion measurements (diamond and triangles, which mostly overlap since the errors for the two components are similar).

In § 3.1, we already noticed that since the (smoothed) profile of the major-axis proper motion dispersion $\sigma_{x'}$ lies on average above that of the minor-axis proper motion dispersion $\sigma_{y'}$ (Fig. 1 and 2), the velocity distribution of ω Cen cannot be fully isotropic. By comparing in Fig. 8 the radial (dotted) with the tangential (dashed) component of the proper motion dispersion, ω Cen seems to be radial anisotropic towards the center, and there is an indication of tangential anisotropy in the outer parts. Moreover, if ω Cen would be isotropic, the line-of-sight velocity dispersion profile (blue) would have to fall on top of the proper motion dispersion profiles if scaled with the correct distance. A scaling with a distance lower than the canonical 5 kpc

is needed for the line-of-sight dispersion profile to be on average the same as those of both proper motion components.

Hence, it is not surprising that we find a distance as low as $D = 4.6 \pm 0.2$ kpc from the ratio of the average line-of-sight velocity dispersion and the average proper motion dispersion (Appendix C). This often used simple distance estimate is only valid for spherical symmetric objects. Whereas the averaged observed flattening for ω Cen is already as low as $q' = 0.879 \pm 0.007$ (Geyer et al. 1983), an inclination of around 48° (§ 4.5), implies an intrinsic axisymmetric flattening $q < 0.8$.

A model with a constant oblate velocity ellipsoid as in Appendix C, allows for offsets between the mean velocity dispersion profiles. However, the model is not suitable to explain the observed variation in anisotropy with radius. Therefore, we use in what follows Schwarzschild's method to build general axisymmetric anisotropic models.

5 SCHWARZSCHILD'S METHOD

We construct axisymmetric dynamical models using Schwarzschild's (1979) orbit superposition method. This approach is flexible and efficient and does not require any assumptions about the degree of velocity anisotropy. The only crucial approximations are that the object is collisionless and stationary. While these assumptions are generally valid for a galaxy, they may not apply to a globular cluster. The central relaxation time of ω Cen is a few times 10^9 years and the half-mass relaxation time a few times 10^{10} years (see also Fig. 21 below). The collisionless approximation should therefore be fairly accurate.

The implementation that we use here is an extension of the method presented in Verolme et al. (2002). In the next subsections, we outline the method and describe the extensions.

5.1 MASS MODEL

Schwarzschild's method requires a mass parameterization, which we obtain by using the Multi-Gaussian Expansion method (MGE; Monnet, Bacon & Emsellem 1992; Emsellem, Monnet & Bacon 1994; Cappellari 2002). The MGE-method tries to find the collection of two-dimensional Gaussians that best reproduces a given surface brightness profile or a (set) of images. Typically, of the order of ten Gaussians are needed, each with three free parameters: the central surface brightness $\Sigma_{0,j}$, the dispersion along the observed major axis σ'_j and the observed flattening q'_j . Even though Gaussians do not form a complete set of functions, in general the surface brightness is well fitted (see also Fig. 12). Moreover, the MGE-parameterization has the advantage that the deprojection can be performed analytically once the viewing angles (in this case the inclination) are given. Also many intrinsic quantities such as the potential and accelerations can be calculated by means of simple one-dimensional integrals.

5.2 GRAVITATIONAL POTENTIAL

We deproject the set of best-fitting Gaussians by assuming that the cluster is axisymmetric and by choosing a value of the inclination i . The choice of a distance D to the object then allows us to convert angular distances to physical units, and luminosities are transformed to masses by multiplying with the mass-to-light ratio M/L .

The latter quantity is often assumed to be independent of radius. In the inner regions of most galaxies, where two-body relaxation does not play an important role,

this often is a valid assumption. Generally, globular clusters have much shorter relaxation times and may therefore show significant M/L -variations. This has been confirmed for post core-collapse clusters such as M15 (e.g., Dull et al. 1997; van den Bosch et al. 2006). However, ω Cen has a relatively long relaxation time of $> 10^9$ years, implying that little mass segregation has occurred and the mass-to-light ratio should be nearly constant with radius. In our analysis we assume a constant M/L , but we also investigate possible M/L -variations.

The stellar potential is then calculated by applying Poisson's equation to the intrinsic density. The contribution of a dark object such as a collection of stellar remnants or a central black hole may be added at this stage. On the basis of the relation between the black hole mass and the central dispersion (e.g., Tremaine et al. 2002), globular clusters might be expected to harbor central black holes with intermediate mass of the order 10^3 – $10^4 M_\odot$ (e.g., van der Marel 2004). With a central dispersion of nearly 20 km s^{-1} , the expected black hole mass for ω Cen would be $\sim 10^4 M_\odot$. The spatial resolution that is required to observe the kinematical signature of such a black hole is of the order of its radius of influence, which is around 5 arcsec (at the canonical distance of 5 kpc). This is approximately an order of magnitude smaller than the resolution of the ground-based observations we use in our analysis, so that our measurements are insensitive to such a small mass. Hence, we do not include a black hole in our dynamical models of ω Cen.

5.3 INITIAL CONDITIONS AND ORBIT INTEGRATION

After deriving the potential and accelerations, the next step is to find the initial conditions for a representative orbit library. This orbit library must include all types of orbits that the potential can support, to avoid any bias. This is done by choosing orbits through their integrals of motion, which, in this case, are the orbital energy E , the vertical component of the angular momentum L_z and the effective third integral I_3 .

For each energy E , there is one circular orbit in the equatorial plane, with radius R_c that follows from $E = \Phi + \frac{1}{2} R_c \partial \Phi / \partial R_c$ for $z = 0$, and with $\Phi(R, z)$ the underlying (axisymmetric) potential. We sample the energy by choosing the corresponding circular radius R_c from a logarithmic grid. The minimum radius of this grid is determined by the resolution of the data, while the maximum radius is set by the constraint that ≥ 99.9 per cent of the model mass should be included in the grid. L_z is sampled from a linear grid in $\eta = L_z / L_{\max}$, with L_{\max} the angular momentum of the circular orbit. I_3 is parameterized by the starting angle of the orbit and is sampled linearly between zero and the initial position of the so-called thin tube orbit (see Fig. 3 of Cretton et al. 1999).

The orbits in the library are integrated numerically for 200 times the period of a circular orbit with energy E . In order to allow for comparison with the data, the intrinsic density, surface brightness and the three components of the projected velocity are stored on grids. During grid storage, we exploit the symmetries of the projected velocities by folding around the projected axes and store the observables only in the positive quadrant ($x' \geq 0, y' \geq 0$). Since the sizes of the polar apertures on which the average kinematic data is computed (Fig. 13) are much larger than the typical seeing FWHM (1–2 arcsec), we do not have to store the orbital properties on an intermediate grid and after orbit integration convolve with the point spread function (PSF). Instead, the orbital observables are stored directly onto the polar apertures.

5.4 FITTING TO THE OBSERVATIONS

After orbit integration, the orbital predictions are matched to the observational data. We determine the superposition of orbits whose properties best reproduce the observations. If O_{ij} is the contribution of the j th orbit to the i th constraint point, this problem reduces to solving for the orbital weights γ_j in

$$\sum_j^{N_O} \gamma_j O_{ij} = C_i, \quad i = 1, \dots, N_C, \quad (5.1)$$

where N_O is the number of orbits in the library, N_C is the number of constraints to be reproduced and C_i is the i th constraint. Since γ_j determines the mass of each individual orbit in this superposition, it is subject to the additional condition $\gamma_j \geq 0$.

Eq. (5.1) can be solved by using linear or quadratic programming (e.g., Schwarzschild 1979, 1982, 1993; Vandervoort 1984; Dejonghe 1989), maximum entropy methods (e.g., Richstone & Tremaine 1988; Gebhardt et al. 2003) or with a linear least-squares solver [e.g., Non-Negative Least-Squares (NNLS), Lawson & Hanson 1974], which was used in many of the spherical and axisymmetric implementations (e.g., Rix et al. 1997; van der Marel et al. 1998; Cretton et al. 1999; Cappellari et al. 2002; Verolme et al. 2002; Krajnović et al. 2005), and is also used here. NNLS has the advantage that it is guaranteed to find the global best-fitting model and that it converges relatively quickly.

Due to measurement errors, incorrect choices of the model parameters and numerical errors, the agreement between model and data is never perfect. We therefore express the quality of the solution in terms of χ^2 , which is defined as

$$\chi^2 = \sum_{i=1}^{N_C} \left(\frac{C_i^* - C_i}{\Delta C_i} \right)^2. \quad (5.2)$$

Here, C_i^* is the model prediction of the constraint C_i and ΔC_i is the associated error. The value of χ^2 for a single model is of limited value, since the true number of degrees of freedom is generally not known. On the other hand, the difference in χ^2 between a model and the overall minimum value, $\Delta\chi^2 = \chi^2 - \chi_{\min}^2$, is statistically meaningful (see Press et al. 1992, § 15.6), and we can assign the usual confidence levels to the $\Delta\chi^2$ distribution. The probability that a given set of model parameters occurs can be measured by calculating $\Delta\chi^2$ for models with different values of these model parameters. We determine the overall best-fitting model by searching through parameter space.

The orbit distribution for the best-fitting model may vary rapidly for adjacent orbits, which corresponds to a distribution function that is probably not realistic. This can be prevented by imposing additional regularization constraints on the orbital weight distribution. This is usually done by minimizing the n th-order partial derivatives of the orbital weights $\gamma_j(E, L_z, I_3)$, with respect to the integrals of motion E , L_z and I_3 . The degree of smoothing is determined by the order n and by the maximum value Δ that the derivatives are allowed to have, usually referred to as the regularization error. Since the distribution function is well recovered by minimizing the second order derivatives ($n = 2$) and smoothening with $\Delta = 4$ (e.g., Verolme & de Zeeuw 2002; Krajnović et al. 2005; Chapter 4), we adopt these values.

6 TESTS

Before applying our method to observational data, we test it on a theoretical model, the axisymmetric power-law model (EZ94).

6.1 THE POWER-LAW MODEL

The potential Φ of the power-law model is given by

$$\Phi(R, z) = \frac{\Phi_0 R_c^\beta}{(R_c^2 + R^2 + z^2 q_\Phi^{-2})^{\beta/2}}, \quad (6.1)$$

in which (R, z) are cylindrical coordinates, Φ_0 is the central potential, R_c is the core radius and q_Φ is the axial ratio of the spheroidal equipotentials. The parameter β controls the logarithmic gradient of the rotation curve at large radii.

The mass density that follows from applying Poisson's equation to eq. (6.1) can be expanded as a finite sum of powers of the cylindrical radius R and the potential Φ . Such a power-law density implies that the *even* part of the distribution function is a power-law of the two integrals energy E and angular momentum L_z . For the *odd* part of the distribution function, which defines the rotational properties, a prescription for the stellar streaming is needed. We adopt the prescription given in eq. (2.11) of EZ94, with a free parameter k controlling the strength of the stellar streaming, so that the odd part of the distribution function is also a simple power-law of E and L_z . Due to the simple form of the distribution function, the calculation of the power-law observables is straightforward. Analytical expressions for the surface brightness, the three components of the mean velocity and velocity dispersion are given in eqs (3.1)–(3.8) of EZ94.

6.2 OBSERVABLES

We choose the parameters of the power-law model such that its observable properties resemble those of ω Cen. We use $\Phi_0 = 2500 \text{ km}^2 \text{ s}^{-2}$, which sets the unit of velocity of our models, and a core radius of $R_c = 2.5 \text{ arcmin}$, which sets the unit of length. For the flattening of the potential we take $q_\Phi = 0.95$ and we set $\beta = 0.5$, so that the even part of the distribution function is positive (Fig. 1 of EZ94). The requirement that the total distribution function (even plus odd part) should be non-negative places an upper limit on the (positive) parameter k . This upper limit k_{max} is given by eq. (2.22) of EZ94⁷. Their eq. (2.24) gives the value k_{iso} for which the power-law model has a nearly isotropic velocity distribution. In our case $k_{\text{max}} = 1.38$ and $k_{\text{iso}} = 1.44$. We choose $k = 1$, i.e., a power-law model that has a (tangential) anisotropic velocity distribution.

Furthermore, we use an inclination of $i = 50^\circ$, a mass-to-light ratio of $M/L = 2.5 M_\odot/L_\odot$ and a distance of $D = 5 \text{ kpc}$. At this inclination the projected flattening of the potential is $q'_\Phi = 0.97$. The isocontours of the projected surface density are more flattened. Using eq. (2.9) of Evans (1994), the central and asymptotic axis ratios of the isophotes are respectively $q'_0 = 0.96$ and $q'_\infty = 0.86$, i.e., bracketing the average observed flattening of ω Cen of $q' = 0.88$ (Geyer et al. 1983).

Given the above power-law parameters, we calculate the three components of the mean velocity V and velocity dispersion σ on a polar grid of 28 apertures, spanning a radial range of 20 arcmin. Because of axisymmetry we only need to calculate the observables in one quadrant on the plane of the sky, after which we reflect the results

⁷The definition of χ has a typographical error and should be replaced by $\chi = (1 - \beta/2)/|\beta|$.

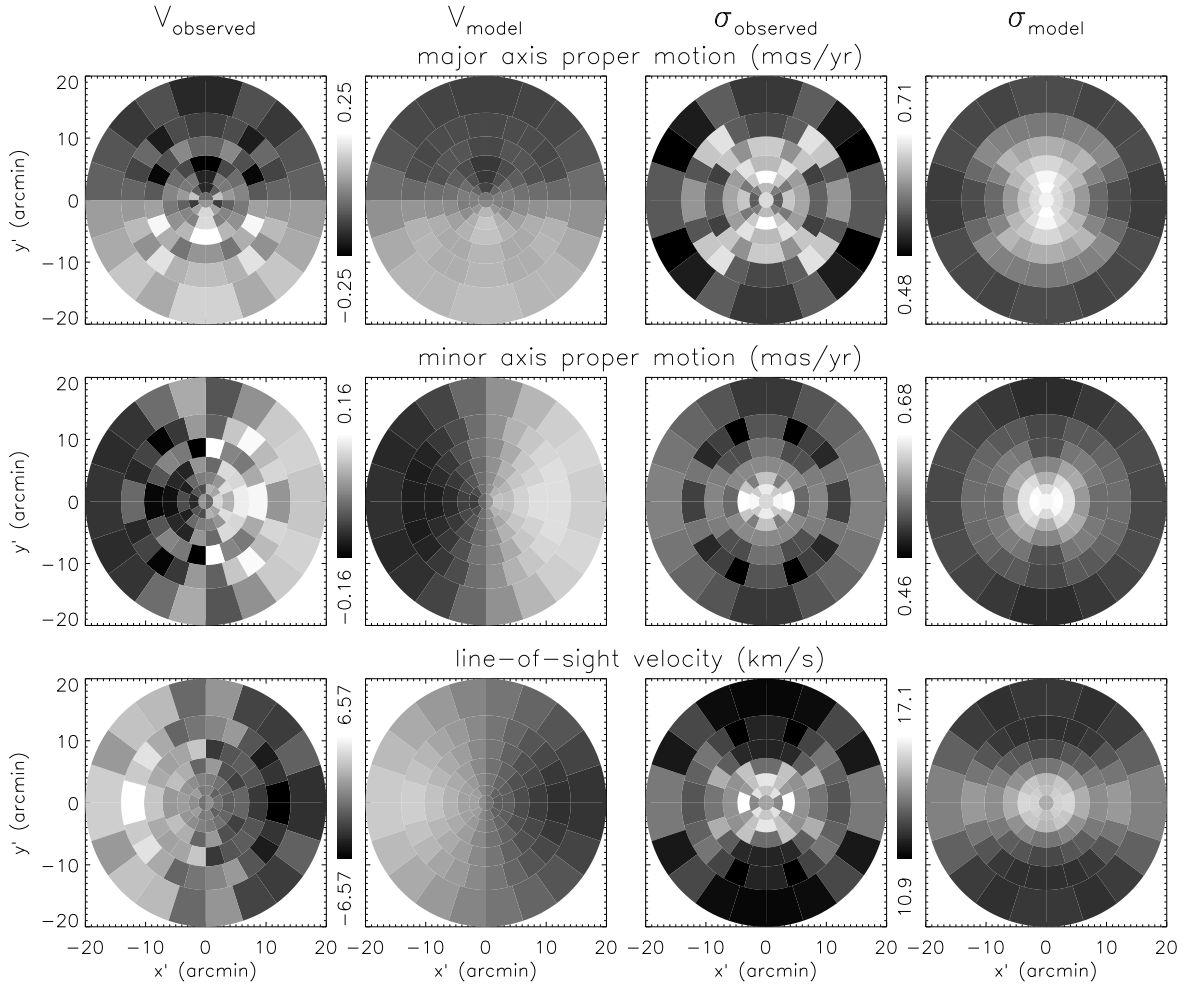


FIGURE 9 — Mean velocity and velocity dispersion calculated from a power-law model (first and third column) and from the best-fit dynamical Schwarzschild model (second and fourth column). The parameters of the power-law model are chosen such that its observables resemble those of ω Cen, including the level of noise, which is obtained by randomizing the observables according to the uncertainties in the measurements of ω Cen (see § 6.2 and Appendix B for details). The average proper motion kinematics in the x' -direction (top row) and y' -direction (middle row), and the average mean line-of-sight kinematics (bottom row), calculated in polar apertures in the first quadrant, are unfolded to the other three quadrants to facilitate the visualization.

to the other quadrants. Next, we use the relative precisions $\Delta V/\sigma \sim 0.11$ and $\Delta\sigma/\sigma \sim 0.08$ as calculated for ω Cen (Appendix B), multiplied with the calculated σ for the power-law model, to attach an error to the power-law observables in each aperture. Finally, we perturb the power-law observables by adding random Gaussian deviates with the corresponding errors as standard deviations.

Without the latter randomization, the power-law observables are as smooth as those predicted by the dynamical Schwarzschild models, so that the goodness-of-fit parameter χ^2 in eq. (5.2), approaches zero. Such a perfect agreement never happens for real data. Including the level of noise representative for ω Cen, allows us to use χ^2 to not only investigate the recovery of the power-law parameters, but, at the same

time, also assesses the accuracy with which we expect to measure the corresponding parameters for ω Cen itself.

The resulting mean velocity V_{observed} and velocity dispersion σ_{observed} fields for the power-law model are shown in respectively the first and third column of Fig. 9. They are unfolded to the other three quadrants to facilitate the visualization.

6.3 SCHWARZSCHILD MODELS

We construct axisymmetric Schwarzschild models based on the power-law potential (6.1). We calculate a library of 2058 orbits by sampling 21 energies E , 14 angular momenta L_z and 7 third integrals I_3 . In this way, the number and variety of the library of orbits is large enough to be representative for a broad range of stellar systems, and the set of eqs (5.1) is still solvable on a machine with 512 Mb memory (including regularization constraints).

The resulting three-integral Schwarzschild models include the special case of dependence on only E and L_z like for the power-law models. Schwarzschild's method requires that the orbits in the library are sampled over a range that includes most of the total mass, whereas all power-law models have infinite mass. To solve this problem at least partially, we ensure that there are enough orbits to constrain the observables at all apertures. We distribute the orbits logarithmically over a radial range from 0.01 to 100 arcmin (five times the outermost aperture radius) and fit the intrinsic density out to a radius of 10^5 arcmin. The orbital velocities are binned in histograms with 150 bins, at a velocity resolution of 2 km s^{-1} .

To test whether and with what precision we can recover the input distance of $D = 5 \text{ kpc}$, the inclination of $i = 50^\circ$ and the mass-to-light ratio $M/L = 2.5 M_\odot/L_\odot$, we calculate models for values of D between 3.5 and 6.5 kpc, i between 35° (the asymptotic isophotal axis ratio $q'_\infty = 0.86$ implies that $i > 30^\circ$) and 70° , and M/L between 1.5 and $3.5 M_\odot/L_\odot$. Additionally, to test how strongly the best-fitting parameters depend on the underlying mass model, we also vary the flattening of the power-law potential q_Φ between 0.90 and 1.00. We then fit each of the dynamical models simultaneously to the calculated observables of the power-law model (with $q_\Phi = 0.95$). Comparing these calculated observables with those predicted by the Schwarzschild models, results for each fitted Schwarzschild model in a goodness-of-fit parameter χ^2 . We use this value to find the best-fit Schwarzschild model and to determine the accuracy of the corresponding best-fit parameters.

Calculating the observables for all orbits in the library requires about an hour on a 1 GHz machine with 512 MB memory and the NNLS-fit takes about half an hour. No distinct models need to be calculated for different values of M/L , as a simple velocity scaling prior to the NNLS-fit is sufficient. Making use of (a cluster of) about 30 computers, the calculations for the full four-parameter grid of Schwarzschild models takes a few days.

6.4 DISTANCE, INCLINATION AND MASS-TO-LIGHT RATIO

The Schwarzschild model that best fits the calculated power-law observables is the one with the (overall) lowest χ^2 -value. After subtraction of this minimum value, we obtain $\Delta\chi^2$ as function of the three parameters D , i and M/L (with $q_\Phi = 0.95$ fixed). To visualize this three-dimensional function, we calculate for a pair of parameters, say D and i , the minimum in $\Delta\chi^2$ as function of the remaining parameter, M/L in

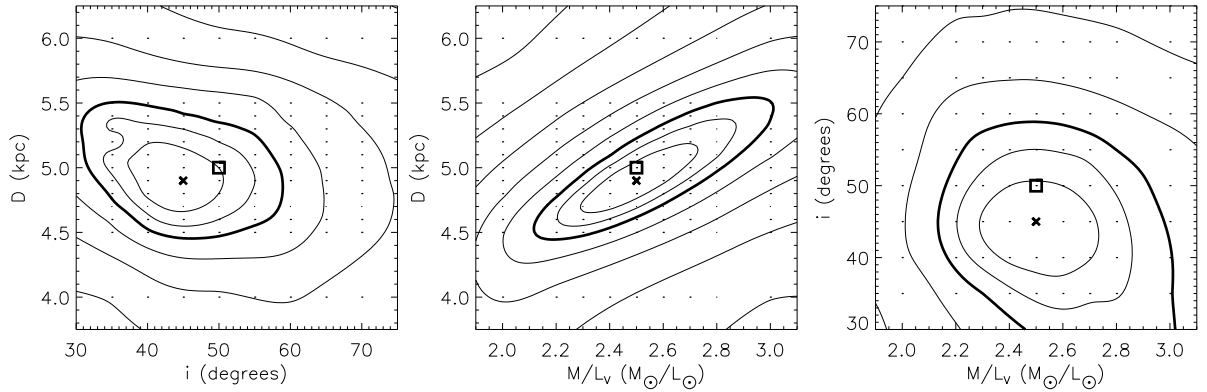


FIGURE 10 — The (marginalized) goodness-of-fit parameter $\Delta\chi^2$ as a function of distance D , inclination i and mass-to-light ratio M/L_V , for different Schwarzschild model fits (indicated by the dots) to an axisymmetric power-law model with observables resembling those of ω Cen (see text for details). The χ^2 -values are offset such that the overall minimum, indicated by the cross, is zero. The contours are drawn at the confidence levels for a $\Delta\chi^2$ -distribution with three degrees of freedom, with inner three contours corresponding to the 68.3%, 95.4% and 99.7% (thick contour) confidence levels. Subsequent contours correspond to a factor of two increase in $\Delta\chi^2$. The input parameters $D = 5.0$ kpc, $i = 50^\circ$ and $M/L = 2.5 M_\odot/L_\odot$, indicated by the open square, are recovered within the 68.3% confidence levels.

this case. The contour plot of the resulting marginalized $\Delta\chi^2$ is shown in the left panel of Fig. 10. The dots indicate the values at which Schwarzschild models have been constructed and fitted to the power-law observables. The contours are drawn at the confidence levels for a $\Delta\chi^2$ -distribution with three degrees of freedom, with inner three contours corresponding to the 68.3%, 95.4% and 99.7% confidence levels. Subsequent contours correspond to a factor of two increase in $\Delta\chi^2$. The minimum ($\Delta\chi^2 = 0$) is indicated by the cross. Similarly, we show in the middle and left panel the contour plots of $\Delta\chi^2$ marginalized for respectively the pair D and M/L and the pair i and M/L .

The input parameters $D = 5.0$ kpc, $i = 50^\circ$ and $M/L = 2.5 M_\odot/L_\odot$, indicated by the open square, are well recovered. The mean velocity V_{model} and velocity dispersion σ_{model} predicted by the best-fit Schwarzschild model are shown in the second and fourth column of Fig. 9. The corresponding power-law observables are well reproduced within the error bars.

Since the parameters of the power-law model are chosen such that its observables and corresponding errors resemble those of ω Cen, the contours in Fig. 10 provide an estimate of the precision with which we expect to measure the best-fitting parameters for ω Cen. At the 68.3%-level (99.7%-level) the distance D , inclination i and mass-to-light ratio M/L are retrieved with an accuracy of respectively 6 (11), 9 (18), 13 (28) per cent. Due the additional complication of infinite mass in the case of the power-law models, these estimates most likely are upper limits to the precision we expect to achieve for ω Cen. This holds especially for the inclination and the mass-to-light ratio as they are sensitive to how well the mass model is fitted. The distance is mainly constrained by the kinematics, so that the corresponding accuracy is probably an accurate estimate of the precision with which we expect to measure the distance to ω Cen.

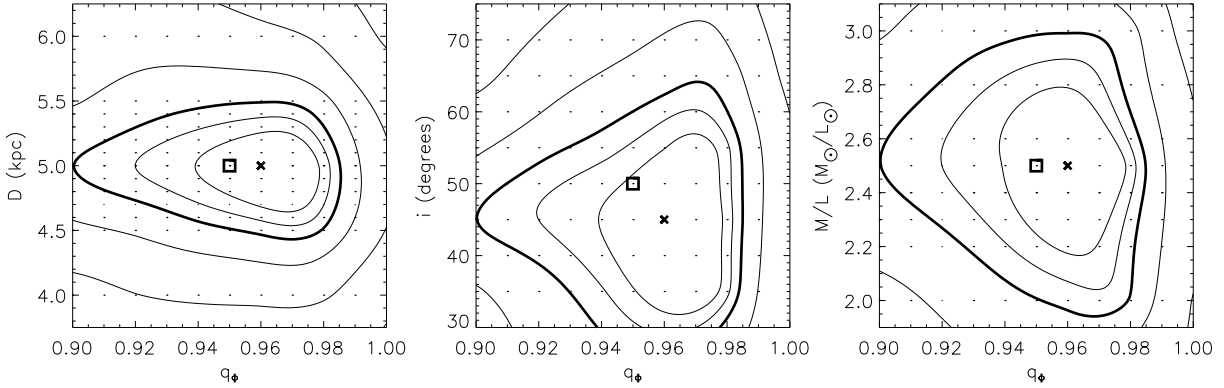


FIGURE 11 — The (marginalized) goodness-of-fit parameter $\Delta\chi^2$ as a function of distance D , inclination i and mass-to-light ratio M/L against the flattening q_Φ of the underlying potential, for different Schwarzschild model fits (indicated by the dots) to the observables of an axisymmetric power-law model resembling those of ω Cen. The contours are as in Fig. 10, but for a $\Delta\chi^2$ -distribution with four degrees of freedom. The cross indicates the overall best-fit model ($\Delta\chi^2 = 0$). The input parameters of the power-law model, $q_\Phi = 0.95$, $D = 5.0$ kpc, $i = 50^\circ$ and $M/L = 2.5 M_\odot/L_\odot$, are indicated by the open square. The input parameters are recovered within the 68.3% confidence levels, even for mass models that assume a (slightly) incorrect value for the flattening. However, spherical models ($q_\Phi = 1.0$) are strongly ruled out.

6.5 FLATTENING

The above investigation of the recovery of the global parameters D , i and M/L is for a known mass model, given by the power-law potential (6.1). In general, we obtain the mass model from a MGE-parameterization of the observed surface brightness (§ 5.1). There is no guarantee that the resulting MGE model provides an accurate description of the true mass distribution. We tested the effect of an incorrect mass model on the best-fit parameters by varying the flattening q_Φ of the power-law potential while keeping the calculated observables (for the power-law model with $q_\Phi = 0.95$) fixed.

Since we use these same values for the other power-law parameters ($\Phi_0 = 2500$ km² s⁻², $R_c = 2.5$ arcmin, $\beta = 0.5$ and $k = 1$), we have to be careful that by varying q_Φ the model is still physical, i.e., that the underlying distribution function is non-negative. For these parameters and q_Φ between 0.9 and 1.0 this is the case (EZ94).

As before, for all Schwarzschild models we calculate $\Delta\chi^2$, which is now a function of the four parameters D , i , M/L and q_Φ . In the three panels of Fig. 11, we show $\Delta\chi^2$ marginalized for respectively D , i and M/L against q_Φ . The symbols and contours are as in Fig. 10, but now for a $\Delta\chi^2$ -distribution with four degrees of freedom. The input parameters of the power-law model (indicated by an open square) are $q_\Phi = 0.95$, $D = 5.0$ kpc, $i = 50^\circ$ and $M/L = 2.5 M_\odot/L_\odot$.

The distance D is well constrained around the input value, even at q_Φ value that are different from the true value of 0.95. This implies that the best-fitting distance is accurate even for mass models that assume a (slightly) incorrect value for the flattening. Whereas a potential with a flattening as low as 0.90 still (just) falls within the contour at the 99.7%-level, we conclude, as in § 4.6, that spherical models ($q_\Phi = 1$) are strongly ruled out. The middle and right panel of Fig. 11 show that the results for respectively the mass-to-light M/L and inclination i are similar, although, as before, they are less well constrained due to the infinite mass of the power-law models.

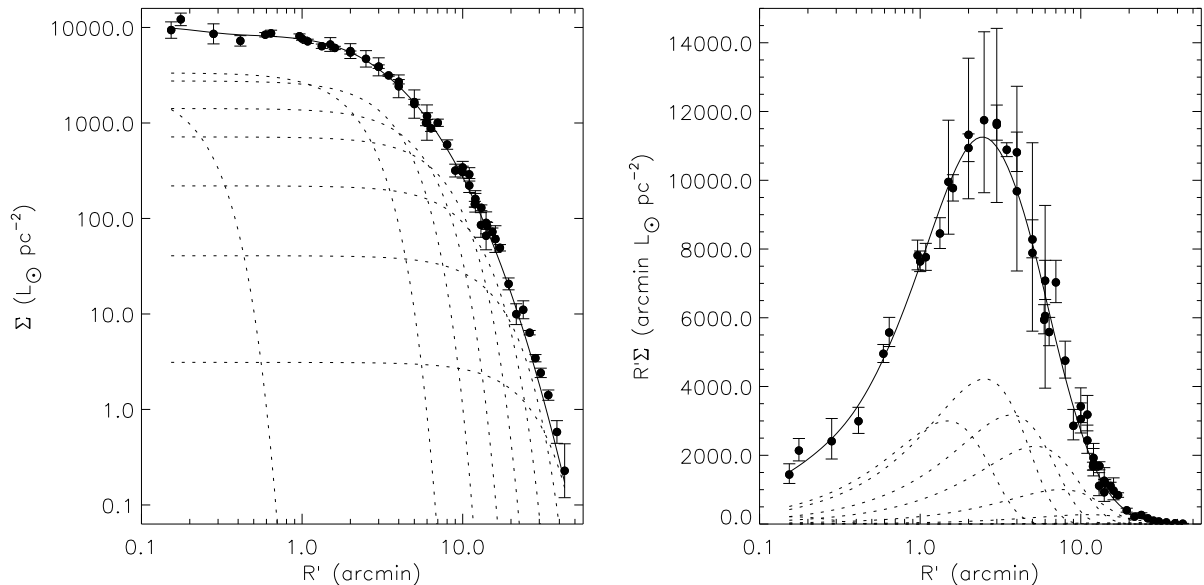


FIGURE 12 — The Multi-Gaussian Expansion (MGE) of the V-band surface brightness profile of ω Cen. The filled circles represent the measurements by Meylan (1987), the dotted curves correspond to the eight Gaussians in the expansion and the solid curve represents their sum. The left panel shows the surface brightness Σ as a function of projected radius R' (in arcmin). Kalnajs (1999) has shown that the quantity $R'\Sigma$ in the right panel is a good diagnostic of the mass that is enclosed at each radius.

7 DYNAMICAL MODELS FOR ω CEN

We use our method as described in § 5, to construct dynamical models for ω Cen. We obtain the mass model from a MGE-parameterization of the observed surface brightness. We compute the mean velocity and velocity dispersion of both proper motion components and along the line-of-sight in polar apertures on the plane of the sky. For a range of distances, inclinations and (constant) mass-to-light ratios, we then simultaneously fit axisymmetric Schwarzschild models to these observations. Additionally, we also allow for radial variation in the mass-to-light ratio.

7.1 MGE MASS MODEL

An MGE-fit is best obtained from a two-dimensional image, which gives direct information about the flattening and any radial variations in the two-dimensional structure of the object. Unfortunately, no such image is available to us, and the only published surface brightness observations of ω Cen consist of radial surface brightness profiles, and an ellipticity profile by Geyer et al. (1983). We therefore perform a one-dimensional MGE-fit to the radial surface brightness profile, and after that use the ellipticity profile to include flattening in the mass model.

We use the V-band surface brightness data from Meylan (1987), who combined various published measurements (Gascoigne & Burr 1956; Da Costa 1979; King et al. 1968). Their data consists of individual measurements along concentric rings, while the MGE-algorithm developed by Cappellari (2002) requires a regular (logarithmic) spacing of the surface brightness measurements. We therefore first describe the profile in terms of a fourth-order polynomial and then fit a set of one-dimensional

j	Σ_{0V} ($L_{\odot} \text{ pc}^{-2}$)	σ' (arcmin)	q'
1	2284.7077	0.15311	1.000000
2	3583.7901	1.47715	0.934102
3	3143.2029	2.52542	0.876713
4	1670.8477	3.69059	0.848062
5	840.86244	5.21905	0.849760
6	262.69433	7.53405	0.835647
7	46.995893	11.0685	0.866259
8	3.3583961	17.5470	0.926328

TABLE 2 — The parameters of the 8 Gaussians from the MGE-fit to the V-band surface brightness profile of ω Cen as derived by Meylan (1987). The second column gives the central surface brightness (in $L_{\odot} \text{ pc}^{-2}$) of each Gaussian component, the third column the dispersion (in arcmin) along the major axis and the fourth column the observed flattening.

Gaussians to this polynomial. Eight Gaussians with different central surface brightness $\Sigma_{0V,j}$ and dispersion σ'_j are required by the MGE-fit (second and third column of Table 2). Fig. 12 shows that this MGE-model provides an excellent fit, not only to the surface brightness Σ , but also to $R'\Sigma$ (cf. Kalnajs 1999).

The MGE-parameterization is converted into a two-dimensional luminosity distribution by assigning an observed flattening q'_j to each Gaussian in the superposition. We take into account that the observed flattening of ω Cen varies as a function of radius (cf. Geyer et al. 1983). This is done by assuming that the flattening of the j th Gaussian q'_j is equal to the observed flattening at a projected radius $R' = \sigma'_j$. This is justified by the fact that a given Gaussian contributes most at radii close to its dispersion σ'_j . Although small deviations from the true two-dimensional light distribution in ω Cen may still occur, we showed in § 6.5 that this approximation does not significantly influence the derived intrinsic parameters for ω Cen. Moreover, a two-dimensional MGE-fit to the combination of the surface brightness profile from Meylan (1987) and the ellipticity profile from Geyer et al. (1983), yields nearly equivalent MGE parameters as those in Table 2, although the fit to the observed surface brightness profile is less good.

To conserve the total luminosity, we increase the central surface brightness of each Gaussian by $1/q'_j$. Taking into account a reddening of $E(B - V) = 0.11$ for ω Cen (Lub 2002), the total V-band luminosity of our mass model, at the canonical distance of 5.0 ± 0.2 kpc, is $L_V = 1.0 \pm 0.1 \times 10^6 L_{\odot}$. This compares well with other estimates of the total luminosity of ω Cen of $0.8 \times 10^6 L_{\odot}$ (Carraro & Lia 2000), $1.1 \times 10^6 L_{\odot}$ (Seitzer 1983) and $1.3 \times 10^6 L_{\odot}$ (Meylan 1987). The most flattened Gaussian in the superposition ($j = 7$) places a mathematical lower limit on the inclination of 33° . This is safely below the constraint of 41–57 degrees found in § 4.5.

7.2 MEAN VELOCITY AND VELOCITY DISPERSION

We construct a polar aperture grid for the proper motions and line-of-sight velocities, as shown in Fig. 13. The dots in the left panel represent the positions, folded to the first quadrant, of the 2295 selected stars with ground-based proper motions. The overlaid polar grid, extending to about 20 arcmin, consists of 28 apertures.

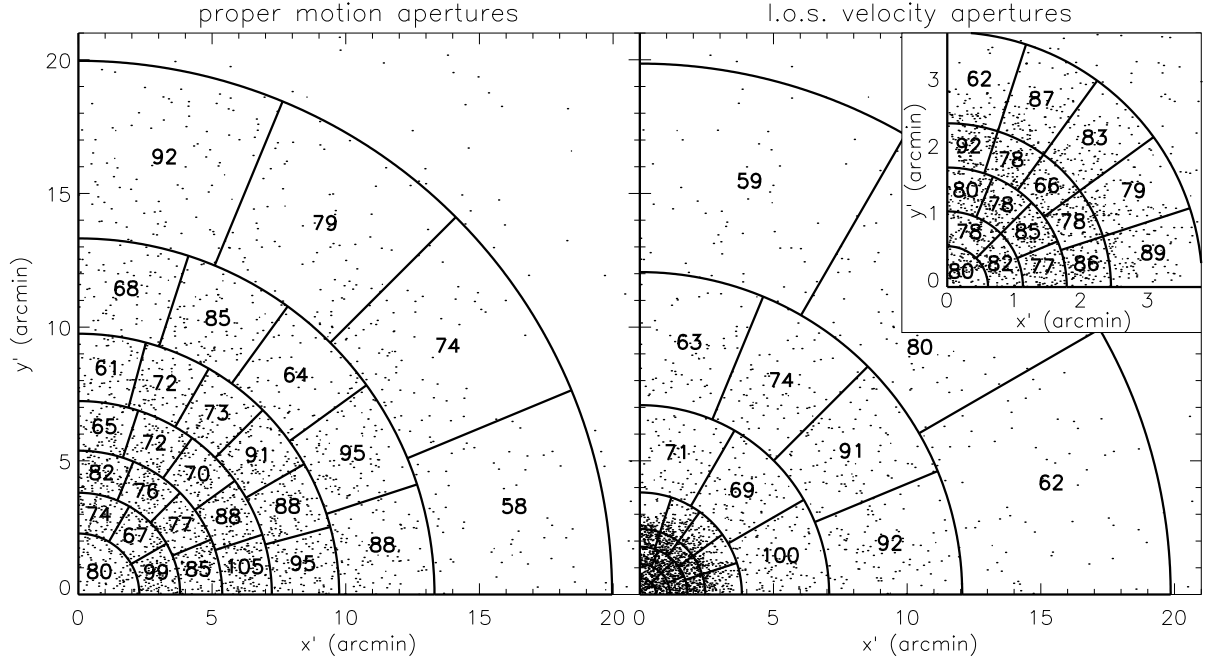


FIGURE 13 — The polar aperture grid for the proper motions (left panel) and for the line-of-sight velocities (right panel). The dots represent the individual stars, with positions folded to the first quadrant, while the solid lines indicate the locations of the apertures. The number of stars included are indicated in each aperture. An enlargement of the inner part of the line-of-sight polar grid is shown in the top-right corner of the right panel.

Per aperture, the number of stars is indicated, adding up to a total of 2223 stars. Similarly, the right panel shows the 2163 selected stars with line-of-sight velocities. The different number of stars and spatial distribution results in a polar grid of 27 apertures, which includes in total 2121 stars.

For each aperture, we use the maximum likelihood method (Appendix A) to compute the mean velocity V and velocity dispersion σ for both proper motion components on along the line-of-sight. We calculate corresponding errors by means of the Monte Carlo bootstrap method.

Each aperture contains around 50 to 100 stars. In Appendix B, we find that this is a good compromise between precision in the observables and spatial resolution. Including more stars per aperture by increasing its size decreases the uncertainties in the observables (and hence makes the resulting kinematic fields smoother). At the same time, since the apertures should not overlap to assure uncorrelated observables, this means less apertures in the polar grid and hence a loss in spatial resolution.

The properties of the apertures and corresponding mean kinematics are given in Table 3 for the proper motions and in Table 4 for the line-of-sight velocities. The mean velocity V_{observed} and velocity dispersion σ_{observed} fields are shown in the first and third column of Fig. 14 respectively. Although the average kinematics are only calculated in the first quadrant, we use the assumed axisymmetric geometry to unfold them to the other three quadrants to facilitate the visualization.

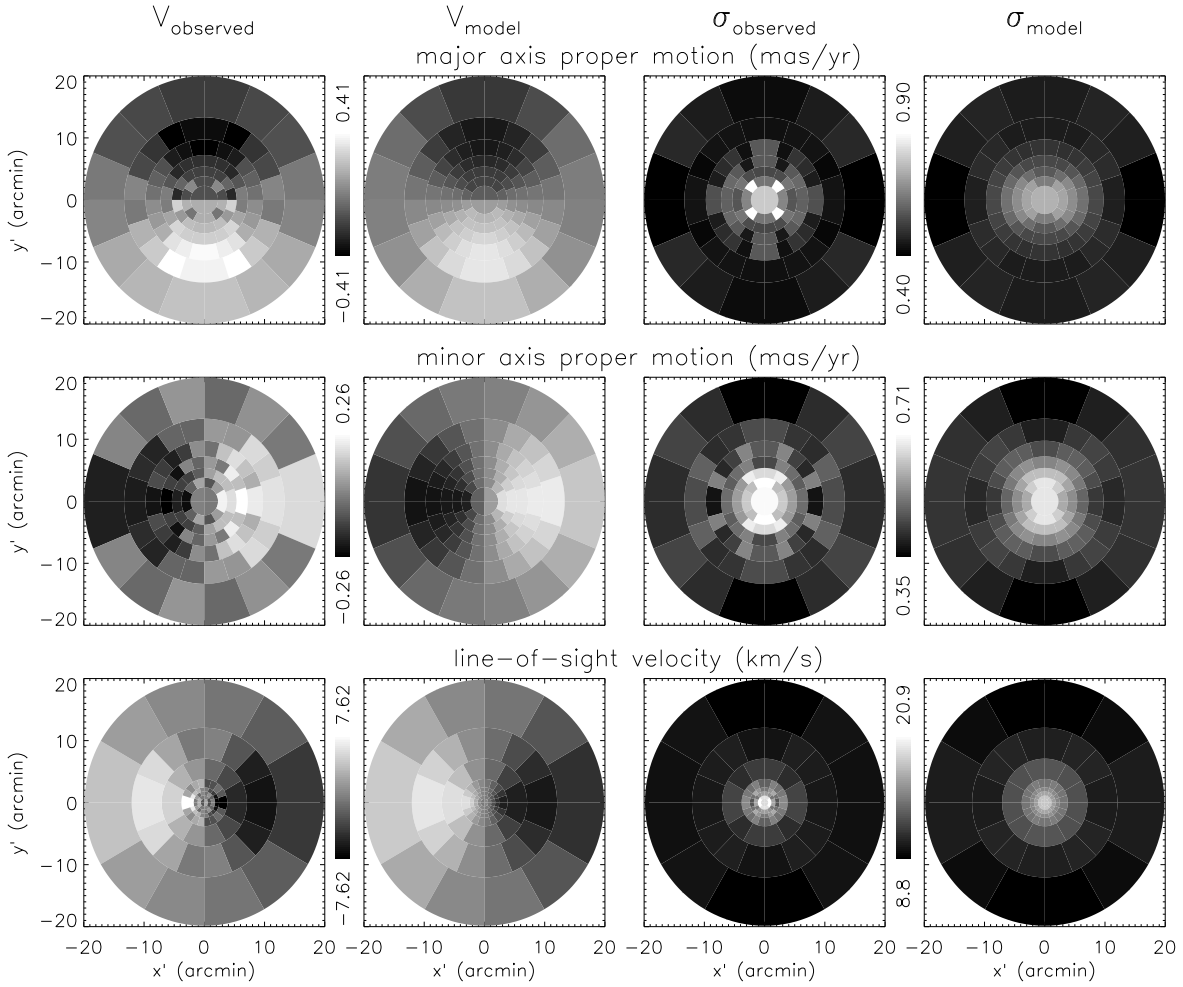


FIGURE 14 — Mean velocity and velocity dispersion calculated from the observations of ω Cen (first and third column) and from the best-fit dynamical model with $D = 4.8$ kpc, $i = 50^\circ$ and $M/L_V = 2.5 M_\odot/L_\odot$ (second and fourth column). The mean proper motion kinematics in the x' -direction (top row) and y' -direction (middle row), and the mean line-of-sight kinematics (bottom row), calculated in polar apertures in the first quadrant, are unfolded to the other three quadrants to facilitate the visualization.

7.3 CONSTRUCTING DYNAMICAL MODELS

First, we calculate models for a range of values in distance D , inclination i and constant V -band mass-to-light ratio M/L_V . Next, fixing D and i at their measured best-fit values, we calculate a large set of models in which we allow M/L_V to vary with radius.

We sample the orbits on a grid of $21 \times 14 \times 7$ values in (E, L_z, I_3) on a radial range from 0.01 to 63 arcmin. This grid extends beyond the tidal radius of 45 arcmin (Trager et al. 1995), so that all mass is included. No PSF-convolution is used and the observables are stored directly onto the apertures.

We (linearly) sample D between 3.5 and 6.5 kpc in steps of 0.5 kpc, and additionally we refine the grid between 4.0 and 5.5 kpc to steps of 0.1 kpc. We vary i between 35 (close to the lower limit of 33 degrees imposed by the flattening, see § 7.1) and 90 degrees in steps of five degrees, and we refine between 40 and 50 degrees to steps of one degree. We choose the constant M/L_V values between 2.0 and 4.0 M_\odot/L_\odot with steps 0.5 M_\odot/L_\odot , and we refine between 2.0 and 3.0 M_\odot/L_\odot to steps of 0.1 M_\odot/L_\odot .

	n_*	r_0	θ_0	Δr	$\Delta\theta$	$V_{x'}$	$\Delta V_{x'}$	$\sigma_{x'}$	$\Delta\sigma_{x'}$	$V_{y'}$	$\Delta V_{y'}$	$\sigma_{y'}$	$\Delta\sigma_{y'}$
1	80	1.14	45.0	2.28	90.0	-0.15	0.09	0.80	0.07	-0.01	0.09	0.70	0.05
2	99	3.04	15.0	1.53	30.0	-0.16	0.07	0.66	0.04	0.23	0.07	0.64	0.05
3	67	3.04	45.0	1.53	30.0	0.03	0.12	0.90	0.07	0.06	0.08	0.62	0.05
4	74	3.04	75.0	1.53	30.0	-0.15	0.08	0.64	0.07	-0.08	0.09	0.71	0.06
5	85	4.59	11.2	1.57	22.5	-0.27	0.06	0.57	0.03	0.19	0.06	0.57	0.05
6	77	4.59	33.7	1.57	22.5	-0.08	0.07	0.63	0.05	0.13	0.06	0.57	0.08
7	76	4.59	56.2	1.57	22.5	-0.20	0.07	0.55	0.05	0.13	0.08	0.69	0.06
8	82	4.59	78.7	1.57	22.5	-0.19	0.05	0.55	0.04	0.07	0.07	0.66	0.06
9	105	6.31	9.0	1.86	18.0	0.00	0.06	0.60	0.04	0.26	0.05	0.50	0.04
10	88	6.31	27.0	1.86	18.0	-0.13	0.07	0.61	0.04	0.13	0.05	0.48	0.05
11	70	6.31	45.0	1.86	18.0	-0.28	0.07	0.58	0.07	0.23	0.06	0.50	0.06
12	72	6.31	63.0	1.86	18.0	-0.25	0.05	0.45	0.04	-0.01	0.06	0.53	0.05
13	65	6.31	81.0	1.86	18.0	-0.25	0.07	0.58	0.05	0.05	0.06	0.45	0.03
14	95	8.49	7.5	2.52	15.0	-0.04	0.05	0.56	0.04	0.22	0.04	0.38	0.02
15	88	8.49	22.5	2.52	15.0	-0.09	0.05	0.46	0.04	0.10	0.07	0.53	0.07
16	91	8.49	37.5	2.52	15.0	-0.15	0.05	0.49	0.04	0.14	0.04	0.41	0.03
17	73	8.49	52.5	2.52	15.0	-0.31	0.06	0.51	0.06	0.19	0.05	0.44	0.03
18	72	8.49	67.5	2.52	15.0	-0.35	0.05	0.44	0.04	0.14	0.06	0.54	0.05
19	61	8.49	82.5	2.52	15.0	-0.40	0.07	0.58	0.05	-0.03	0.07	0.48	0.04
20	88	11.54	9.0	3.56	18.0	0.02	0.05	0.44	0.04	0.20	0.05	0.46	0.04
21	95	11.54	27.0	3.56	18.0	-0.17	0.04	0.42	0.04	0.17	0.05	0.49	0.04
22	64	11.54	45.0	3.56	18.0	-0.24	0.05	0.44	0.04	0.18	0.05	0.41	0.03
23	85	11.54	63.0	3.56	18.0	-0.41	0.05	0.44	0.03	0.05	0.04	0.43	0.03
24	68	11.54	81.0	3.56	18.0	-0.36	0.05	0.43	0.03	0.05	0.05	0.46	0.03
25	58	16.64	11.2	6.64	22.5	-0.02	0.06	0.40	0.04	0.19	0.06	0.41	0.05
26	74	16.64	33.7	6.64	22.5	-0.14	0.06	0.48	0.05	-0.01	0.06	0.45	0.04
27	79	16.64	56.2	6.64	22.5	-0.17	0.05	0.46	0.03	0.04	0.04	0.41	0.04
28	92	16.64	78.7	6.64	22.5	-0.21	0.05	0.43	0.03	-0.05	0.04	0.35	0.03

TABLE 3 — *The mean velocity and velocity dispersion calculated in polar apertures on the plane of sky from the proper motion observations. Per row the information per aperture is given. The first column labels the aperture and the second column gives the number of stars n_* that fall in the aperture. Columns 3–6 list the polar coordinates r (in arcmin) and the angle θ (in degrees) of the centroid of the aperture and the corresponding widths Δr (in arcmin) and $\Delta\theta$ (in degrees). The remaining columns present the average proper motion kinematics in units of mas yr^{-1} . The mean velocity V with error ΔV and velocity dispersion σ with error $\Delta\sigma$ are given in columns 7–10 for the proper motion component in the x' -direction and in columns 11–14 for the proper motion component in the y' -direction.*

To investigate possible variation in M/L_V with radius, we make use of the eight Gaussian components of the MGE mass model (§ 7.1). In case of constant M/L_V , we obtain the intrinsic density by multiplying all the (deprojected) components with the same constant M/L_V value. To construct a mass model with a radial M/L_V profile, we multiply each component with its own M/L_V value, as in this way the calculation of the potential is still efficient. However, to reduce the number of free parameters (to make a search through parameter space feasible) and to enforce a continuous profile, we only vary the M/L_V values for the first, second, fourth and

	n_*	r_0	θ_0	Δr	$\Delta\theta$	$V_{z'}$	$\Delta V_{z'}$	$\sigma_{z'}$	$\Delta\sigma_{z'}$
1	80	0.31	45.0	0.61	90.0	2.4	2.2	19.0	1.5
2	82	0.87	22.5	0.52	45.0	-3.1	2.1	20.9	1.4
3	78	0.87	67.5	0.52	45.0	0.2	1.9	19.5	1.4
4	77	1.46	11.2	0.66	22.5	0.0	1.9	16.7	1.3
5	85	1.46	33.7	0.66	22.5	-1.8	1.7	14.4	0.8
6	78	1.46	56.2	0.66	22.5	1.0	1.8	15.6	1.5
7	80	1.46	78.7	0.66	22.5	-0.7	1.7	16.2	1.2
8	86	2.12	9.0	0.66	18.0	-7.6	1.5	12.8	1.1
9	78	2.12	27.0	0.66	18.0	-6.4	1.6	14.3	0.8
10	66	2.12	45.0	0.66	18.0	-3.8	1.9	16.8	1.2
11	78	2.12	63.0	0.66	18.0	-3.0	1.7	15.9	1.0
12	92	2.12	81.0	0.66	18.0	-0.3	1.7	14.5	1.0
13	89	3.13	9.0	1.37	18.0	-7.6	1.6	15.3	1.0
14	79	3.13	27.0	1.37	18.0	-2.2	1.5	14.6	1.0
15	83	3.13	45.0	1.37	18.0	-1.0	1.4	14.1	0.8
16	87	3.13	63.0	1.37	18.0	-2.6	1.4	15.0	0.8
17	62	3.13	81.0	1.37	18.0	-2.9	1.9	13.4	1.3
18	100	5.45	15.0	3.27	30.0	-5.0	1.2	12.0	1.0
19	69	5.45	45.0	3.27	30.0	-3.1	1.3	10.9	1.1
20	71	5.45	75.0	3.27	30.0	-1.4	1.2	11.8	1.0
21	92	9.57	11.2	4.98	22.5	-6.2	1.0	10.0	0.9
22	91	9.57	33.7	4.98	22.5	-5.5	1.1	10.3	1.0
23	74	9.57	56.2	4.98	22.5	-2.4	1.2	10.3	0.9
24	63	9.57	78.7	4.98	22.5	0.2	1.3	9.8	0.9
25	62	15.96	15.0	7.80	30.0	-4.1	1.2	9.6	1.1
26	80	15.96	45.0	7.80	30.0	-1.9	1.2	9.8	0.7
27	59	15.96	75.0	7.80	30.0	-0.6	1.2	8.8	0.9

TABLE 4 — The mean velocity and velocity dispersion calculated in polar apertures on the plane of sky from the line-of-sight velocity observations. Columns 1–6 are as in Table 3 and the remaining columns present the average line-of-sight kinematics in km s^{-1} .

sixth component. For the third and fifth component, we interpolate between the M/L values of the neighboring components. To the outer two components we assign the same M/L_V value as the sixth component, because their individual M/L_V values are not well constrained due to the small number of kinematic measurements at these radii. With the distance and inclination fixed at their best-fit values from the case of constant mass-to-light ratio, we are left with a four-dimensional space to search through, requiring again a few days on (a cluster of) about 30 computers.

All dynamical models are fitted simultaneously to the two-dimensional light distribution of ω Cen (§ 7.1), and to the mean velocity and velocity dispersion of both proper motions components and along the line-of-sight, calculated in polar apertures on the plane of the sky (Fig. 14). Comparing the predicted values with the observations, results for each fitted model in a goodness-of-fit parameter χ^2 , which we use to find the best-fit model and to determine the accuracy of the corresponding best-fit parameters.

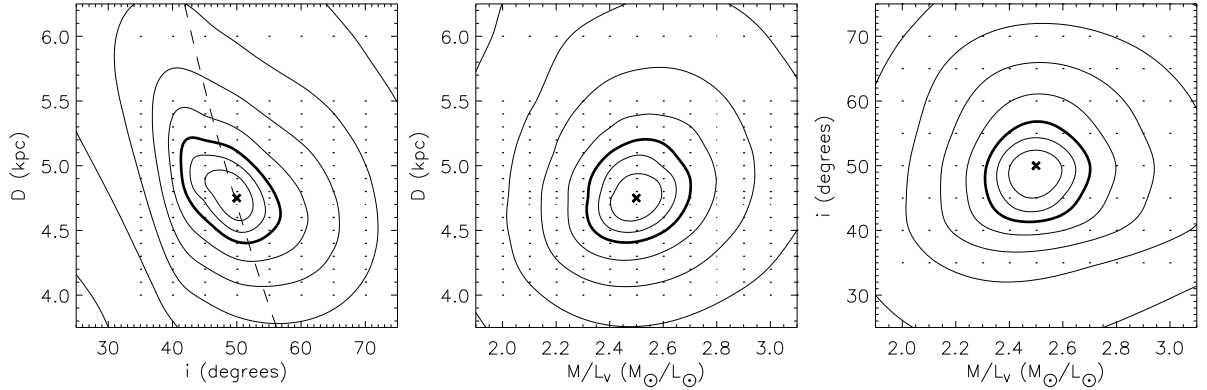


FIGURE 15 — The (marginalized) goodness-of-fit parameter $\Delta\chi^2$ as a function of distance D , inclination i and mass-to-light ratio M/L_V , for different dynamical model fits (indicated by the dots) to the kinematics of ω Cen. The contours are as in Fig. 10. The best-fit dynamical model is at $D = 4.8$ kpc, $i = 50^\circ$ and $M/L_V = 2.5 M_\odot/L_\odot$, indicated by the cross. The dashed curve shows the $D \tan i = 5.6$ kpc constraint from the mean velocities (§ 4.5).

8 BEST-FIT PARAMETERS

In Fig. 15, we show $\Delta\chi^2$ as a (marginalized) function of the distance D , inclination i and constant mass-to-light ratio M/L_V . The dots represent the values at which dynamical models have been constructed and fitted to the two-dimensional (photometric and kinematic) observations of ω Cen. The cross indicates the over-all best-fit model. The contours show that all three parameters are tightly constrained, with at the 68.3%-level (99.7%-level): $D = 4.8 \pm 0.3$ (± 0.5) kpc, $i = 50 \pm 3$ (± 5) degrees and $M/L_V = 2.5 \pm 0.1$ (± 0.2) M_\odot/L_\odot . As an illustration that our best-fit model indeed reproduces the observations, the mean velocity and velocity dispersion in polar apertures on the plane of the sky as they follow from this model are shown in respectively the second and fourth column of Fig. 14. The model fits the observations within the uncertainties given in Table 3 and 4.

After the discussion on the set of models where we allow the mass-to-light ratio M/L_V to vary with radius, we compare our best-fit values for the (constant) mass-to-light ratio, inclination and distance with results from previous studies.

8.1 MASS-TO-LIGHT RATIO VARIATION

Fig. 16 summarizes the results from fitting models in which we allowed the mass-to-light ratio M/L_V to vary with radius in the way described in § 7.3. The filled circles represent the eight Gaussian components, with the best-fit M/L_V value of each component plotted against their dispersions along the major axis (see column three of Table 2). The error bars represent the 68.3% confidence level.

The uncertainty on the innermost point around 0.15 arcmin is relatively large since at that small radius there are only a few observations (see Fig. 13) to constrain the M/L_V value. Nevertheless, the resulting M/L_V profile only shows a small variation, which is not significantly different from the best-fit constant M/L_V of $2.5 M_\odot/L_\odot$.

In the above experiment, we fixed the distance and inclination at the best-fit values of $D = 4.8$ kpc and $i = 50^\circ$ from the case of constant M/L_V . Although an important constraint is that all eight Gaussian components have to be at the same distance,

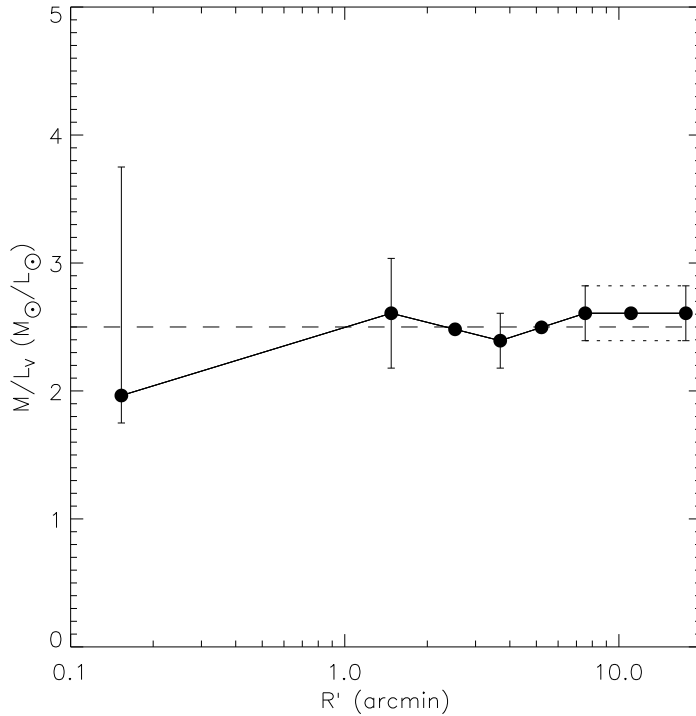


FIGURE 16 — Variation in mass-to-light ratio M/L_V with projected radius R' . The filled circles represent the eight Gaussian components of the MGE mass model, with the best-fit M/L_V value of each component plotted against its dispersion along the major axis. With the distance and inclination fixed at $D = 4.8$ kpc and $i = 50$ degrees, we allowed variation in the M/L_V values for the four inner points with error bar, while the two outer points were shifted vertically similar to the fourth point, and the remaining two points were interpolated between the two neighboring points. Each of the models was simultaneously fitted to the photometric and kinematic observations of ω Cen. The error bars represent the 68.3% confidence level for the corresponding $\Delta\chi^2$ -distribution with four degrees of freedom. The variation in the resulting M/L_V profile is small with no significant deviation from the best-fit constant M/L_V of $2.5 M_\odot/L_\odot$ (horizontal dashed line).

its precise value, as well as that of the inclination, is not crucial. We tested that a reasonable variation in these fixed values (within the 99.7% confidence level in Fig. 15) does not significantly change the best-fit M/L_V profile. We conclude that a constant mass-to-light ratio for ω Cen is a valid assumption.

8.2 MASS-TO-LIGHT RATIO

Our best-fit mass-to-light ratio of $M/L_V = 2.5 \pm 0.1 M_\odot/L_\odot$ lies in between the estimates by Seitzer (1983) of $2.3 M_\odot/L_\odot$ and by Meylan (1987) of $2.9 M_\odot/L_\odot$. Meylan et al. (1995) derived a value of $4.1 M_\odot/L_\odot$, based on a spherical, radial anisotropic King-Michie dynamical model, while we find that ω Cen is flattened and outwards tangentially anisotropic (see § 9.2). Moreover, their adopted central value of the line-of-sight velocity dispersion is significantly higher than ours, even if we use the same data-set by M97.

Meylan et al. (1995) estimated the total mass of ω Cen to be $5.1 \times 10^6 M_\odot$, which is also significantly higher than what we derive. After multiplication with the total luminosity of our mass model of $L = 1.0 \times 10^6 L_\odot$ (at the best-fit distance of $D = 4.8 \pm 0.3$

kpc), we find a total mass of $M = (2.5 \pm 0.3) \times 10^6 M_{\odot}$. This is consistent with the value by Mandushev et al. (1991) of $2.4 \times 10^6 M_{\odot}$ and Seitzer (1983) of $2.8 \times 10^6 M_{\odot}$. The estimate by Meylan (1987) of $3.9 \times 10^6 M_{\odot}$ is higher, but again based on a spherical King-Michie model.

8.3 INCLINATION

The dashed curve in the left panel of Fig. 15 shows the $D \tan i = 5.6$ kpc constraint from the mean velocities derived in § 4.5. This constraint can be used to eliminate either the distance or the inclination and hence reduce the parameter space. Although we do not use this constraint in the dynamical models, it is clear that the above best-fit D and i yield $D \tan i = 5.6 \pm 0.2$ kpc, which is consistent with the value derived from the mean velocities.

The best-fit inclination of $i = 50 \pm 3$ degrees falls within the range of 30–60 degrees that was derived in Paper I from the amplitude of the proper motions, but is slightly higher than the estimate by van Leeuwen & Le Poole (2002) between 40 and 60 degrees. However, as discussed in § 4.5, they used models of modest complexity and freedom which require strong assumptions, whereas our method is more general and robust.

Our best-fit inclination implies that ω Cen is intrinsically even more non-spherical than the average observed flattening of $q' = 0.879 \pm 0.007$ (Geyer et al. 1983) already indicates. Using the relation $q^2 \sin^2 i = q'^2 - \cos^2 i$ for axisymmetric objects, we find an average intrinsic axial ratio $q = 0.78 \pm 0.03$.

8.4 DISTANCE

Adopting a reddening of $E(B - V) = 0.11$ for ω Cen (Lub 2002), the best-fit dynamical distance corresponds to a distance modulus of $(m - M)_V = 13.75 \pm 0.13$ (± 0.22 at the 99.7%-level). This is consistent with the (canonical) distance modulus of $(m - M)_V = 13.84$ by photometric methods, as given in the globular cluster catalog of Harris (1996), together with the uncertainty estimate of about 0.1 magnitude by Benedict et al. (2002), using the absolute magnitude of RR Lyrae stars. Using the infrared color versus surface brightness relation for the eclipsing binary OGLEC 17, Thompson et al. (2001) find a larger distance modulus of $(m - M)_V = 14.05 \pm 0.11$. However, their distance modulus estimates based on the measured bolometric luminosity of the binary components, are on average lower, ranging from 13.66 to 14.06.

Although our dynamical distance estimate is consistent with that by other methods, it is at the lower end. A lower value for the distance is expected if the proper motion dispersion is over-estimated and/or the line-of-sight velocity dispersion underestimated (see also Appendix C, eq. C.1). As we saw in § 3, both are likely in the case of ω Cen if the kinematic data is not properly selected. The correction in § 4 for perspective rotation and especially for the residual solid-body rotation is crucial for the construction of a realistic dynamical model and a reliable distance estimate.

An impression of the effect of the selection and correction of the kinematic data on the distance estimate follows from the range of dynamical models we constructed for ω Cen. Before any selection and correction, the kinematics of the cluster stars give rise to a best-fit dynamical model at a distance as low as ~ 3.5 kpc. After removing from the proper motion data-set the stars disturbed by their neighbors, i.e., only selecting class 0 stars, the best-fit distance becomes ~ 4.0 kpc. The correction for perspective and solid-body rotation increase the best-fit distance to ~ 4.5 kpc. Fi-

nally, after the additional selection on velocity errors, we find our best-fit dynamical distance of 4.8 ± 0.3 kpc.

An even tighter selection does not significantly change the best-fit dynamical model and corresponding distance. The same is true if we use a different polar grid, with fewer or more stars per aperture, and if we restrict to only fitting the average kinematics in the inner or outer parts. Still, e.g. remaining interlopers in the proper motion data-set can cause a (small) under-estimation of the distance. Moreover, Platais et al. (2003) argue that possibly a (non-physical) residual proper motion color/magnitude dependence in the data-set of Paper I causes the systematic offset between the proper motions of the metal-rich RGB-a stars and those of the dominant HB and metal-poor RGB stars, noticed by Ferraro, Bellazzini & Pancino (2002). Since we do not correct for this possible systematic offset, the proper motion dispersion might be over-estimated and hence our distance estimate can be systematically too low. However, the effect is expected to be small since the number of RGB-a stars in the data-set is small. A deeper proper motion catalog, like that of King & Anderson (2002) obtained with the HST, is needed to better quantify (non-physical and physical) differences in the proper motions among the multiple stellar populations observed in ω Cen.

Although the distance and inclination are tightly linked through the mean velocities (§ 4.5), a small under-estimation of the distance only results in a slight over-estimation of the inclination (see also the solid curve in the right panel of Fig. 7). Similarly, the mass-to-light ratio is nearly insensitive to small changes in the distance.

9 INTRINSIC STRUCTURE

We use the intrinsic velocity moments of our best-fit dynamical model to investigate the importance of rotation and the degree of anisotropy in ω Cen. Additionally, the distribution of the orbital weights allows us to study the phase-space distribution function of ω Cen.

9.1 ROTATION

We calculate the intrinsic velocity moments of our best-fit model by combining the appropriate moments of the orbits that receive weight in the superposition. We consider the first and second order velocity moments, for which $\langle v_R \rangle = \langle v_\theta \rangle = \langle v_R v_\phi \rangle = \langle v_\theta v_\phi \rangle = 0$ because of axisymmetry. We define the radial, angular and azimuthal velocity dispersion respectively as $\sigma_R^2 = \langle v_R^2 \rangle$, $\sigma_\theta^2 = \langle v_\theta^2 \rangle$, $\sigma_\phi^2 = \langle v_\phi^2 \rangle - \langle v_\phi \rangle^2$. The only non-vanishing cross-term is $\sigma_{R\theta}^2 = \langle v_R v_\theta \rangle$. The average root-mean-square velocity dispersion σ_{RMS} is given by $\sigma_{\text{RMS}}^2 = (\sigma_R^2 + \sigma_\theta^2 + \sigma_\phi^2)/3$.

A common way to establish the importance of rotation in elliptical galaxies and bulges of disk galaxies, is to determine their position in the $(V/\sigma, \epsilon)$ -diagram (e.g., Davies et al. 1983). The *observational* quantities that are used for V , σ and ϵ are respectively the maximum (line-of-sight) velocity along the major axis, the average velocity dispersion within half the effective radius and the ellipticity at the effective radius. We obtain for ω Cen the observational quantities $V \sim 8 \text{ km s}^{-1}$ (at a radius of ~ 8 arcmin), $\sigma \sim 16 \text{ km s}^{-1}$ and $\epsilon \sim 0.15$ (Geyer et al. 1983). These values result in $(V/\sigma, \epsilon) \sim (0.5, 0.15)$, placing ω Cen just above the curve for isotropic oblate rotators.

On the other hand, the intrinsic velocity moments from our best-fit dynamical model for ω Cen, allow us to investigate *intrinsically* the importance of rotation. The grey scale in Fig. 17 show the ratio of the mean (azimuthal) rotation $\langle v_\phi \rangle$ over the

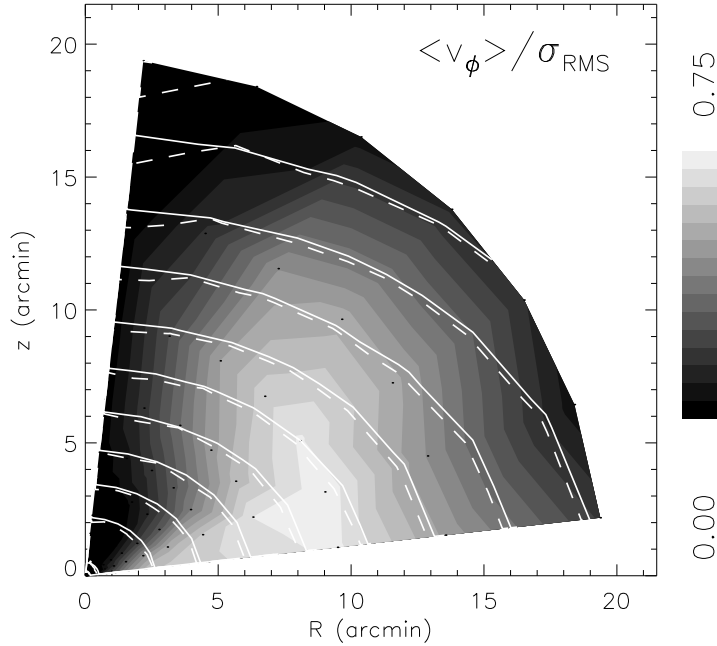


FIGURE 17 — The grey scale represents the mean azimuthal rotation $\langle v_\phi \rangle$ in the meridional plane as a function of equatorial plane radius R and height z , and normalized by σ_{RMS} (excluding the axes to avoid numerical problems). The white curves are contours of constant mass density in steps of one magnitude, from the mass model (solid) and from the best-fit model (dashed), showing that the mass is well fitted. (See p. 250 for a color version of this figure.)

average root-mean-square velocity dispersion σ_{RMS} , as function of the position in the meridional plane. Near the equatorial plane and between radii of about 5 to 15 arcmin, this ratio is > 0.5 . The maximum of ~ 0.7 around 8 arcmin coincides with the peak in the mean line-of-sight velocity field. Within this region in the meridional plane rotational support is important. However, more inwards and further outwards this ratio rapidly drops below 0.5 and ω Cen is at least partly pressure supported. We conclude that rotation is important in ω Cen, but it is not a simple isotropic oblate rotator.

9.2 ANISOTROPY

For the velocity distribution in ω Cen to be isotropic all three velocity dispersion components σ_R , σ_θ and σ_ϕ have to be equal and the cross-term $\sigma_{R\theta}$ has to vanish. Fig. 18 shows that this is not the case.

In the top panels, we show the degree of anisotropy in the meridional plane. The top-left panel shows the radial over the angular velocity dispersion σ_R/σ_θ . This ratio does however not include the non-zero cross-term $\sigma_{R\theta}$. The latter causes the velocity ellipsoid to be rotated with respect to the R and θ coordinates. Taking this into account the semi-axis lengths of the velocity ellipsoid in the meridional plane are given by $\sigma_\pm^2 = (\sigma_R^2 + \sigma_\theta^2)/2 \pm \sqrt{(\sigma_R^2 - \sigma_\theta^2)^2/4 + \sigma_{R\theta}^4}$. In the top-right panel, we show the ratio of this minor σ_- and major σ_+ semi-axis length of the velocity ellipsoid (which is by definition in the range from zero to unity). This demonstrates that the velocity distribution of ω Cen is nearly isotropic near the equatorial plane, but becomes increasingly

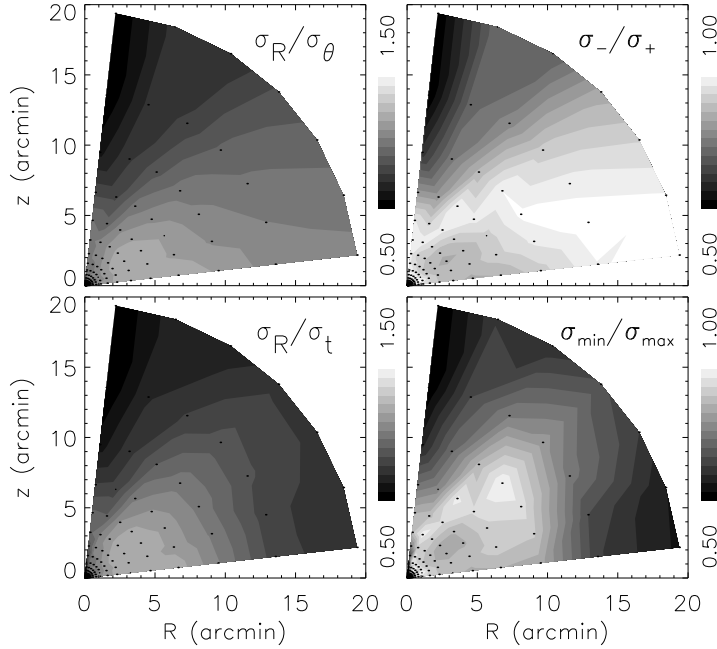


FIGURE 18 — Degree of anisotropy as function of the equatorial plane radius R and height z (excluding the axes to avoid numerical problems). The top panels show the degree of anisotropy in the meridional plane: left the radial over the angular velocity dispersion and right the minor σ_- over the major σ_+ semi-axis length of the velocity ellipsoid, taking into account the cross-term $\sigma_{R\theta}$. The bottom panels include the azimuthal velocity dispersion: left the radial over the tangential velocity dispersion, with $\sigma_t^2 = (\sigma_\theta^2 + \sigma_\phi^2)/2$, and right the minimum over the maximum of the three semi-axis lengths σ_+ , σ_- and σ_ϕ of the velocity ellipsoid. See text for further details.

tangential anisotropic towards the symmetry axis.

In the bottom panels we also include the azimuthal velocity dispersion σ_ϕ . The bottom-left panel shows the radial over the tangential velocity dispersion, where the latter is defined as $\sigma_t^2 = (\sigma_\theta^2 + \sigma_\phi^2)/2$. Again this ratio does not take into account the cross-term $\sigma_{R\theta}$. The actual degree of anisotropy is given by the three semi-axis lengths σ_+ , σ_- and σ_ϕ of the velocity ellipsoid. In the bottom-right panel, we show, as a function of the position in the meridional plane, the minimum over the maximum of these three semi-axis lengths. Except for the region near the equatorial plane and within 10 arcmin, the best-fit model for ω Cen is clearly not isotropic. Even within this region, between about 3 and 5 arcmin, it is (slightly) radially anisotropic. Outside this region ω Cen becomes increasingly tangentially anisotropic.

Clearly, isotropic models are not suitable to model ω Cen. Also dynamical models with a two-integral distribution function of the form $F(E, L_z)$, with $L_z = R\langle v_\phi \rangle$ the angular momentum component along the symmetry z -axis, are not able to describe the complex dynamical structure of ω Cen. For these models the solution of the Jeans equations can be used to construct dynamical models in a straightforward way (e.g., Satoh 1980; Binney, Davies & Illingworth 1990) and they allow for azimuthal anisotropy. However, for these models $\sigma_R = \sigma_\theta$ and $\sigma_{R\theta} = 0$, i.e., isotropy in the full meridional plane, which is not the case for ω Cen (top panels of Fig. 18). Our axisymmetric dynamical models do not have these restrictions as they are based on a

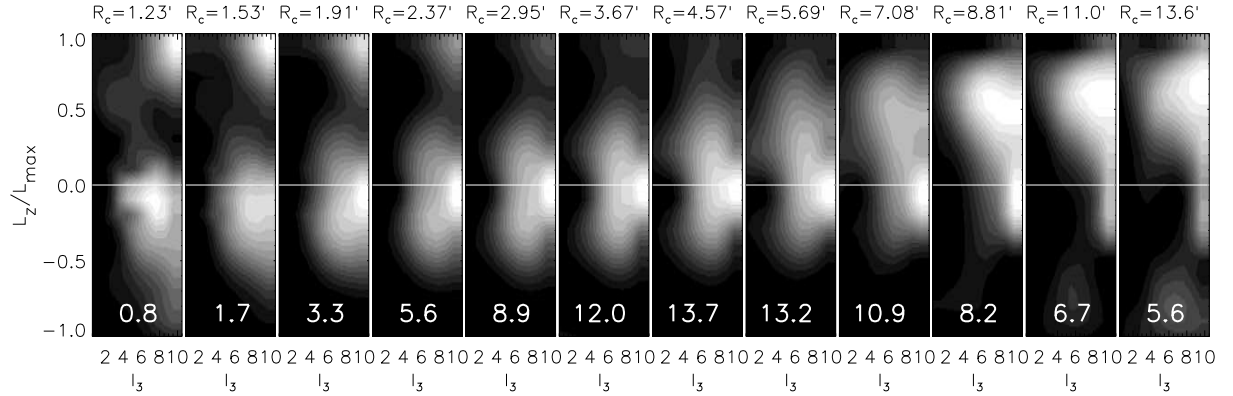


FIGURE 19 — The orbital weight distribution for our best-fit model of ω Cen. From left to right, the panels show the orbital weight distribution at increasing distance from the center, which corresponds to increasing energy. The radius R_c (in arcmin) of the circular orbit at the corresponding energy is given above each panel. The radial range that is shown is constrained by the observations and contains more than 90% of the total cluster mass. The vertical axis represents the angular momentum L_z in units of L_{\max} , the angular momentum of the circular orbit. The horizontal axis represents the third integral I_3 , parameterized by the number of the (linearly sampled) starting angle of the orbit. Black shading corresponds to zero orbital weights, and white corresponds to the maximum orbital weight in each panel. At the bottom of each panel the fraction (in %) of the included mass with respect to the total mass is indicated. (See p. 250 for a color version of this figure.)

general three-integral distribution function $F(E, L_z, I_3)$, which we investigate next for our best-fit model.

9.3 DISTRIBUTION FUNCTION

Each orbit in our models is characterized by the three integrals of motion E , L_z and I_3 . As function of these three integrals, we show in Fig. 19 for our best-fit model of ω Cen the distribution of the (mass) weights that were assigned to the different orbits in the NNLS-fit. The energy E is sampled through the radius R_c (in arcmin) of the circular orbit (different panels), of which we show the range that is constrained by the observations and that contains more than 90% of the total cluster mass. The angular momentum L_z (vertical) is in units of L_{\max} , the angular momentum of the circular orbit. The third integral I_3 (horizontal) is parameterized by the linearly sampled starting angle of the orbit, from the equatorial plane towards the symmetry axis, and of which the number is given.

In each panel, the orbital weights are scaled with respect to the maximum orbital weight in that panel, indicated by the white color, whereas black corresponds to zero orbital weight. The fraction of the sum of the mass weights in each panel with respect to total mass in all panels is given at the bottom of each panel (in %). To avoid an unrealistic orbital weight distribution that fluctuates rapidly for adjacent orbits, we regularize our models (§ 5.4). For values of the smoothing parameter below $\Delta = 4$ and even without regularization, we find the same best-fit parameters and although the distribution function becomes spiky, the main features of Fig. 19 remain.

Most of the mass in the orbital weight distribution is in the component that is prominent in all panels. With increasing radius, the average angular momentum L_z of this component increases from nearly zero to a significant (positive) value in

the outer parts. This reflects the outwards increasing tangential anisotropy already seen in the bottom-left panel of Fig. 18. An almost non-rotating part is still present beyond 5 arcmin, attached to the rotating component, which becomes the dominant component (in mass). There is also a separate component at $L_z/L_{\max} \sim 1$ that is clearly visible between about 1 and 3 arcmin. Within this radial range, this maximum rotating component contributes almost 20% of the mass, and it includes about 4% of the total mass, i.e., its mass is of the order of $10^5 M_\odot$.

In the right-most panels of Fig. 19 there is a (weak) signature of a component with $L_z/L_{\max} \sim -1$, which we expect to be a spurious feature due to insufficient observational constraints. Whereas (nearly) circular orbits ($|L_z|/L_{\max} \sim 1$) are confined in radius to R_c , orbits with lower $|L_z|$ can go further inwards, so that they have most of their contribution (their cusps) at a smaller radius than R_c (e.g., Cappellari et al. 2004). Hence, the apparent feature at $L_z/L_{\max} \sim -1$ in the most-right panel is only constrained by data around and beyond the radius $R_c = 13.6$ arcmin, where the coverage of the data is sparse with only a few polar bins (see Fig. 13). The main component in this panel at $L_z/L_{\max} \sim 0.5$ is (mostly) constrained by data at smaller radii, where there is good data coverage. The separate maximum rotating component between 1 and 3 arcmin is constrained by only a few proper motion apertures, but is strongly constrained by the line-of-sight velocity data.

Due to the difference in spatial coverage between the proper motion and line-of-sight velocity data, the two data-sets (better) constrain different parts of the orbital weight distribution. By fitting besides the light distribution of ω Cen the mean velocity and velocity dispersion of only the proper motion components, we find a less prominent separate component between 1 and 3 arcmin, but it is still present. In the case of only fitting the mean line-of-sight velocity and velocity dispersion, this separate component is clearly visible and even extends into the outer rotating main component. The transition between the main non-rotating and rotating component is in the case of only line-of-sight data more abrupt than in Fig. 19. However, the proper motion data, which has a better coverage in the outer parts, shows a similar smooth transition. We conclude that, although the spatial coverage is different, both data-sets give rise to the same main features in the orbital weight distribution.

9.4 DYNAMICAL SUBSTRUCTURES

Within 5 arcmin the main component has on average a high value of I_3 . In combination with the low value of L_z , we interpret this as a non-rotating spheroidal structure. Beyond 5 arcmin, L_z increases and I_3 decreases, and the main component flattens and rotates faster. The smaller component attached to it may well be the signature of the fading non-rotating spheroidal component.

For the separate component between 1 and 3 arcmin, L_z approaches its maximum value. As a result, the zero-velocity curve shrinks towards the circular orbit in the equatorial plane, and the corresponding orbits are all flat, irrespective of the (high) value of I_3 (see also Fig. 3 of Cretton et al. 1999). Hence, this fast-rotating component is likely to be an inner disk, which fades away into the more massive main rotating component at larger radius.

We compute the spatial distribution and average kinematics of these possible substructures in the phase-space of ω Cen. To this end we select the orbits from our best-fit model that contribute non-zero weight to three different parts of the distribution function in Fig. 19. We select the *inner* main component in the 7 left-most panels,

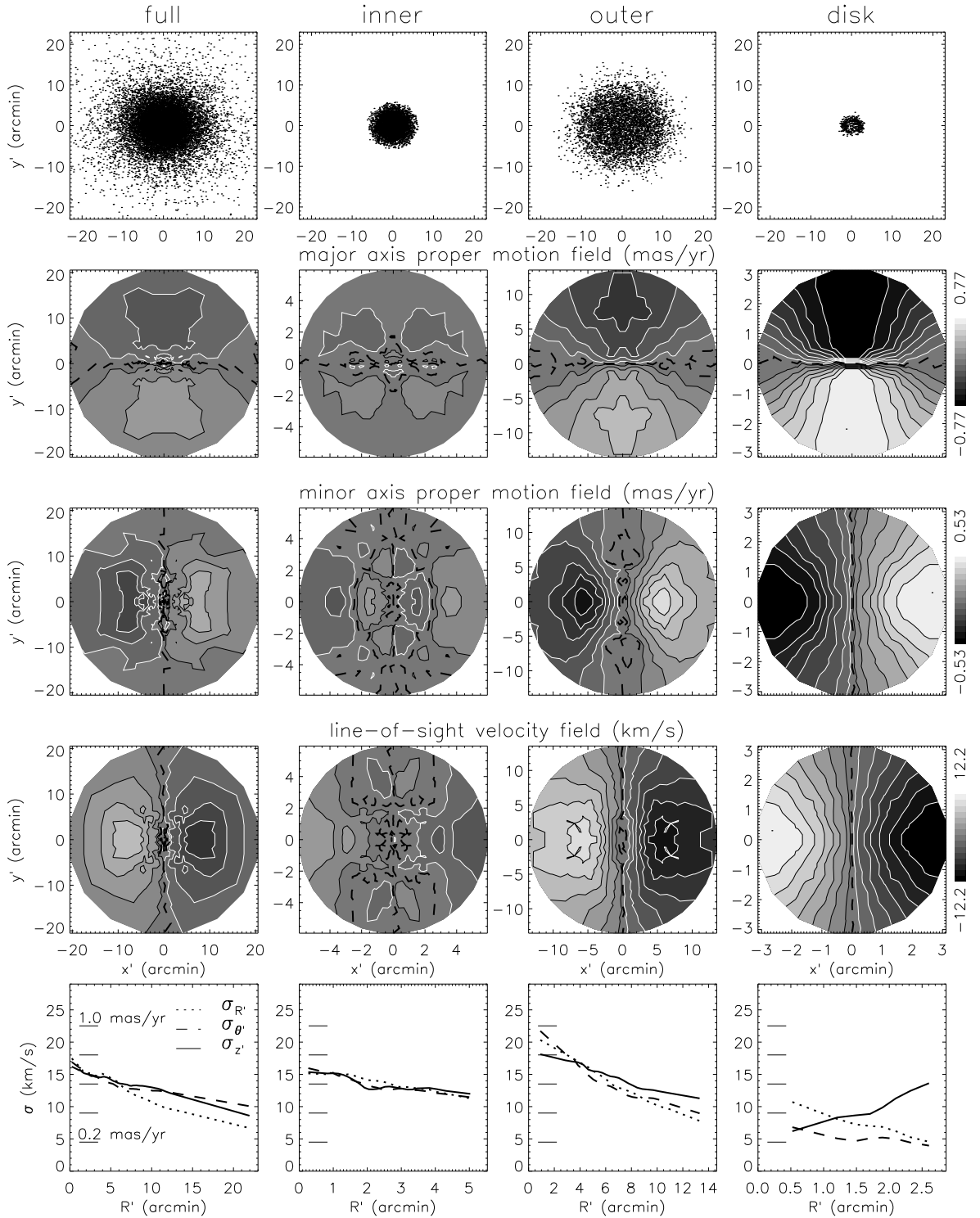


FIGURE 20 — Kinematics of different components in the distribution function of our best-fit model for ω Cen. From left to right: full distribution function, main inner component, main outer component and separate disk component between 1 and 3 arcmin (see text for details). From top to bottom: spatial distribution, mean velocity fields in the direction of the major x' -axis, the minor y' -axis and the line-of-sight z' -axis, and mean velocity dispersion profiles. The radial dispersion $\sigma_{R'}$ (dotted) and tangential dispersion $\sigma_{\theta'}$ (dashed) are on the plane of the sky and $\sigma_{z'}$ (solid) is the line-of-sight dispersion. (See p. 251 for a color version of this figure.)

excluding the separate *disk* component in the 5 left-most panels, and the *outer* main component in the 3 right-most panels (excluding the weak feature in the bottom). For each orbit with non-zero weight, we then randomly draw points along its numerically integrated orbit, with the number of drawings proportional to its relative weight. In this way, we make an (N-body) realization of our best-fit model consisting of a couple of tens of thousands of particles, representing the stars in ω Cen. For each of these stars, we determine the position on the plane of the sky and the three velocity components; the two proper motion components in the plane of the sky and the line-of-sight velocity. For the stars that belong to a certain part or substructure of phase-space, we then calculate the spatial distribution and mean kinematics.

Fig. 20 shows the results for all stars, those in the inner and outer main component and those in the separate disk component, respectively, per column from left to right. The first row shows the spatial distribution. The flattening of the spatial distribution of all stars and of the outer main component are both about 0.88, similar to the average observed flattening for ω Cen. The inner main component, going out to a radius of about 6 arcmin, is rounder with a flattening of about 0.94. The spatial distribution of the disk component only extends to a radius of about 3 arcmin, has an average flattening as low as 0.60 and is less dense in the center as this maximum rotating disk consists of stars on (nearly) circular orbits which avoid the center. The second to fourth row show the mean velocity fields in respectively the direction of the major x' -axis and the minor y' -axis on the plane of the sky and the line-of-sight z' -axis. In each panel the axes are scaled with respect to the spatial extent of each component. Whereas the inner main component indeed hardly shows any rotation, the outer main component clearly rotates and the separate disk component rotates even faster. In the last row, the velocity dispersion profiles are presented, radial (dotted) and tangential (dashed) on the plane of the sky and along the line-of-sight (solid). Even though the outer main component is flatter and rotates faster than the inner main component, it is not kinematically colder due to the mixture of orbits with different L_z values. On the other hand, the maximum rotating disk is the kinematically coldest component. Whereas the inner main component is nearly isotropic, the outer main component is anisotropic and the disk component is even stronger anisotropic.

The presence of dynamical substructures implies that the formation history of ω Cen is more complicated than expected for a typical globular cluster. However, the interpretation of these different components in the distribution function is very difficult. In what follows we investigate the possible effects due to the tidal interaction between ω Cen and the Milky Way (§ 9.5), and the possible link to the observed multiple stellar populations in ω Cen (§ 9.6).

9.5 TIDAL INTERACTION

Based on its current position and motion in the Milky Way (MW), Dinescu, Girard & van Altena (1999) simulated the orbit of ω Cen around the Galactic Center (GC). They found that the average orbit is inclined by only 17° with respect to the Galactic plane, has a period of $P \sim 122$ Myr and an angular momentum of about $406 \text{ kpc km s}^{-1}$. Assuming that the average orbit of ω Cen is circular, we thus find a radius $R_{OC} \sim 2.8$ kpc and a velocity of about 143 km s^{-1} , of which the component perpendicular to Galactic plane $v_\perp \sim 42 \text{ km s}^{-1}$. Since the scale height of the MW disk is typically 250 pc, it takes about $t_{\text{enc}} \sim 12$ Myr for ω Cen to cross the MW disk. This means that for nearly 10% of its time ω Cen is immersed in the disk and feels the additional

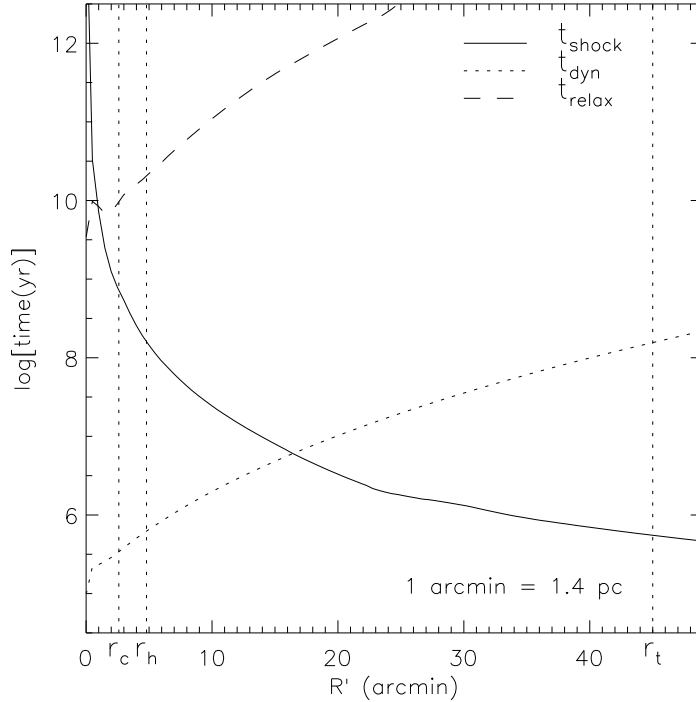


FIGURE 21 — Timescales as function of the projected radius R' . The solid curve represents the timescale on which shocks, caused by successive passages of ω Cen through the MW disk, change the mean-squared velocity of a cluster star by the order of the (local) velocity dispersion of the cluster. The dotted and dashed curves show respectively the dynamical time t_{dyn} and relaxation time t_{relax} . The vertical dashed lines indicate with increasing distance the core radius r_c , the half-light radius r_h and the tidal radius r_t of ω Cen.

gravitational field.

To investigate what effect the MW tidal field has on the stars in ω Cen, we use the impulse approximation as described by Binney & Tremaine (1987, p. 446), with the typical properties of the MW from their Tables 1-1 and 1-2. We assume a Cartesian coordinate system with its origin at the center of ω Cen and the z -axis perpendicular to the MW disk. If ω Cen goes through the MW disk, the effect on the velocity component perpendicular to the disk is the largest. Hence, the velocity of a cluster star changes on average by $|\Delta v| \sim z|g_z(R)|/v_{\perp}$, where g_z is the z -component of the gravitational field of the MW disk. The cumulative effect of successive passages through the MW disk becomes of the order of the (local) velocity dispersion σ of the cluster on a timescale of $t_{\text{shock}} \sim P\sigma^2 v_{\perp}^2 / (8z^2 g_z^2)$.

An infinite disk with surface density Σ generates a gravitational field $g_z = 2\pi G\Sigma$. In the solar neighborhood the MW disk has a surface density of $\Sigma_{\odot} \sim 75 M_{\odot} \text{pc}^{-2}$. Assuming that the MW disk falls off as $\exp(-R/R_d)$ in the radial coordinate, with $R_d = 3.5 \text{ kpc}$, we find that at the mean circular radius $R = R_{\text{OC}}$ of ω Cen's orbit around the GC, $g_z \sim 2.9 \times 10^{-13} \text{ km s}^{-2}$. For a spherical shell of stars of radius r , we have that on average $z^2 = r^2/3$. We thus find that the timescale on which disk shocking becomes important is

$$t_{\text{shock}} \sim 21 \left(\frac{\sigma}{\text{km s}^{-1}} \right)^2 \left(\frac{r}{\text{arcmin}} \right)^{-2} \text{ Myr.} \quad (9.1)$$

Fig. 21 shows t_{shock} (solid curve) as function of the projected radius R' (in arcmin). We used the line-of-sight velocity dispersion as given in Fig. 8, smoothed and extrapolated to larger radii using measurements by Scarpa, Marconi & Gilmozzi (2003) between about 20 and 30 arcmin⁸. In the same figure we have also plotted the dynamical time t_{dyn} (dotted curve; Binney & Tremaine 1987, eq. 2-30) and the relaxation time t_{relax} (dashed curve; Spitzer & Hart 1971; Binney & Tremaine 1987, eq. 8-71). The three vertical dashed lines indicate respectively the core radius $r_c = 2.6$ arcmin, the half-light radius $r_h = 4.8$ arcmin and the tidal radius $r_t = 45$ arcmin (e.g., Trager et al. 1995).

Clearly, the impulse approximation is not valid near the center of ω Cen, where the period of the stellar orbits $T \equiv 4t_{\text{dyn}}$ is much smaller than the duration of the passage through the disk $t_{\text{enc}} \sim 12$ Myr. Disk shocking is thus unimportant at the center of ω Cen: the orbits evolve adiabatically and emerge unharmed from the encounter. Around a radius of 16 arcmin, where T is about twice t_{enc} , disk shocks begin to play an important role since the disk shocking time becomes of the order of the dynamical time $t_{\text{shock}} \sim t_{\text{dyn}} \sim 6$ Myr. At the tidal radius of 45 arcmin, the MW disk gravitational field becomes dominant.

The effect that the MW tidal field has on the internal dynamics of ω Cen also strongly depends on the relative orientation and spinning direction of the angular momentum vector of the stars in ω Cen (internal) and the angular momentum vector of its orbit around the GC (external). We found that the rotation axis is about 50° inclined with respect the line-of-sight (the z' -axis) in the direction South⁹. On the plane of sky, the rotation axis projects onto the minor y' -axis, which makes an angle of about 10° away from North in the direction East. The equatorial coordinates of ω Cen are $\alpha_0 = 13^{\text{h}}26^{\text{m}}46^{\text{s}}$ and $\delta_0 = -47^\circ28'43''$ (J2000), which correspond to a Galactic longitude and latitude of $l = 309^\circ$ and $b = 15^\circ$. Hence, the rotation axis is nearly parallel (angle $< 3^\circ$) to the equatorial plane, and makes an angle of about 65° with respect to the Galactic plane. Seen from the North Galactic pole, ω Cen is moving in anti-clockwise direction around the GC. The rotation inside ω Cen is dominated by orbits with positive L_z values in Fig. 19, which correspond to clockwise rotation.

We thus find that the internal and external angular momentum vector are for more than 90% parallel with respect to each other with opposite spinning direction. From mergers of spinning galaxies it is well known that if the spins are anti-parallel as in this case, the orbital disruption is much less than in the case of parallel spins (e.g., Toomre & Toomre 1972). Hence, in the past ω Cen might have contained a significant number of stars on orbits with negative L_z (parallel spin), which then were removed from the cluster during its successive passages through the MW disk. Stars on orbits with positive L_z (anti-parallel spin) had a bigger chance to survive.

Furthermore, the stars on more radial orbits (those with smaller values of L_z) cover a broader range in radius, with the influence of the MW tidal field becoming stronger at increasing radius. In the course of time, these radial orbits thus have a bigger chance of being disrupted than the more tangential orbits with similar mean radius.

⁸Taking into account the measurement error of about 1 km s^{-1} and the perspective rotation that can be as large as 1.5 km s^{-1} at those radii (eq. 4.1).

⁹This means that in the common definition of the inclination, as in eq. (2.2), the best-fit inclination is -50° . This also explains the sign difference of $\langle v_{z'} \rangle$ in eq. (4.3) and along the vertical axis of the plot in the middle panel of Fig. 7. However, we decided to adopt the usual convention to take the value for the inclination in the range from 0° (face-on) to 90° (edge-on).

Both effects (together) might explain the prominent rotating main component in the distribution function in Fig. 19 beyond a radius of 10 arcmin, while the non-rotating main component that dominates inwards, fades away. The removal of the more radial orbits also naturally explains the outwards increasing tangential anisotropy in our best-fit model of ω Cen (§ 9.2).

The above analysis shows that the frequent passages of ω Cen through the MW disk most likely have played a crucial role in the evolution of this cluster. At least part of the phase-space structure of ω Cen may well be caused by the tidal field of the MW. Detailed (N-body) simulations are needed to further quantify this.

9.6 MULTIPLE STELLAR POPULATIONS

Among the Galactic globular clusters, ω Cen especially stands out because of its chemical inhomogeneity, first revealed in photometric investigations by Dickens & Woolley (1967) and spectroscopically confirmed by Freeman & Rodgers (1975). Besides the main population of metal-poor stars ($\sim 65\%$ of all stars with $[\text{Ca}/\text{H}] \sim -1.4$) and an intermediate population ($\sim 30\%$, $[\text{Ca}/\text{H}] \sim -1.0$), recently also a separate metal-rich population ($\sim 5\%$, $[\text{Ca}/\text{H}] \sim -0.5$) has been identified (Lee et al. 1999; Pancino et al. 2000), and even the main sequence of ω Cen is bifurcated (Bedin et al. 2004).

These different stellar populations also appear to have a different spatial distribution. Whereas the metal-poor stars seem to follow the observed flattening of ω Cen in the East-West direction, the more metal-rich stars are elongated in the North-South direction and also more centrally concentrated (e.g., Pancino et al. 2003). There are also indications of differences in the kinematics of the stellar populations. Norris et al. (1997) find that the metal-poor populations have on average a higher line-of-sight velocity dispersion and exhibit a well-defined line-of-sight rotation, while the metal-rich populations show no significant rotation. Ferraro et al. (2002) claim that the separate metal-rich population has a coherent bulk proper motion significantly different from the other cluster stars.

We use the empirical relation in eq. (15) of Paper I to estimate the $[\text{Ca}/\text{H}]$ abundances of stars in our analysis with V -band magnitude and $B-V$ color measurements consistent with the top of the red giant branch ($V < 13.5$ and $B-V > 0.7$). The resulting $[\text{Ca}/\text{H}]$ histograms for the proper motion and line-of-sight velocity stars both show a distribution with a broad peak around $[\text{Ca}/\text{H}] \sim -1.2$ and a long tail extending beyond $[\text{Ca}/\text{H}] \sim -0.5$. In both cases the peak shows a small dip, so that we might divide the stars into a metal-poor population with $[\text{Ca}/\text{H}] \leq -1.2$ and a metal-rich population with $[\text{Ca}/\text{H}] > -1.2$, similar to Norris et al. (1997).

Comparing the mean line-of-sight kinematics of the metal-poor and metal-rich stars, we confirm the result of Norris et al. (1997) that the more centrally concentrated metal-rich stars are on *average* kinematically cooler and nearly non-rotating. The line-of-sight velocity dispersion *profile* is steeper for the metal-richer stars than for the metal-poor stars, such that that in the center the metal-richer stars are even (slightly) kinematically warmer. The proper motions seem to imply a similar difference in the slope of the velocity dispersion profiles. However, with the proper motion errors on average four times larger than those of the line-of-sight velocities (see also Fig. 8), there are no significant differences between the kinematics of the metal-poor and metal-rich stellar populations.

The above correlations between the kinematics and chemical properties of stars in ω Cen, are expected to show up in the distribution function (see also Freeman

2002). The centrally concentrated non-rotating metal-rich stars would lie near the bottom of the potential well at the lower values of E found in the cluster, symmetrically distributed over positive and negative values of L_z , and towards higher values of I_3 . The rotating metal-poor stars would span the entire range of E , with an asymmetric distribution in L_z and towards lower I_3 .

These expectations are consistent with the orbital weight distribution of our best-fit dynamical model of ω Cen (Fig. 19 and 20). Whereas the metal-richer stars might well be associated with the inner non-rotating part of the main component, we might see the kinematical signatures of the metal-poorer stars becoming dominant when the main component flattens and rotates faster in the outer parts. Still, we have to be careful as these are (indirect) indications of a link between substructures in the distribution function and the different stellar populations.

To investigate directly the distribution function of the different stellar populations, one can try to construct separate dynamical (Schwarzschild) models. However, since the separation into different stellar populations is not evident, separate mass models are needed and the separate kinematic constraints are based on much fewer stars, this is very difficult with the current data-set. A more feasible approach is to model together, in a consistent way, the observed kinematics and physical properties of the stars. For example, by labeling the orbits in the model with different colors, the observed color (averaged per aperture) can be used to constrain the model in addition to the photometry and kinematics. On the other hand, now that we have constrained the global parameters (distance, inclination and mass-to-light ratio) considerably, it has become feasible to use non-linear maximum likelihood techniques to directly incorporate discrete stellar measurements. In this way, for the model that best fits (simultaneously) the measured kinematics and age and metallicity indicators of individual stars, the different stellar populations can be cleanly separated in phase-space. This extension, which we leave for a future paper, will provide an important contribution to solving the stellar population puzzle in ω Cen, and clarify its formation history.

10 CONCLUSIONS

We used an extension of Schwarzschild's (1979) orbit superposition method to construct realistic axisymmetric dynamical models for ω Cen with an arbitrary anisotropic velocity distribution. By fitting these models simultaneously to proper motion and line-of-sight velocity measurements, we measured the radial mass-to-light profile, the inclination and the distance to ω Cen, which is needed to convert the proper motions to physical units. This dynamical distance estimate can provide a useful calibration for the photometric distance ladder.

We used the ground-based proper motions from Paper I and the line-of-sight velocities from four independent data-sets. We brought the kinematic measurements onto a common coordinate system and carefully selected on cluster membership and on measurement error. This provided a homogeneous data-set of 2295 stars with proper motions accurate to 0.20 mas yr^{-1} and 2163 stars with line-of-sight velocities accurate to 2 km s^{-1} , covering a radial range out to about half the tidal radius of the cluster. We corrected the kinematic measurements for perspective rotation and removed a residual solid-body rotation component in the proper motions. We showed that the latter can be measured without any modeling other than assuming axisymmetry and at the same time we obtained a tight constraint on $D \tan i$ of $5.6 (+1.9/-1.0) \text{ kpc}$, pro-

viding a unique way to estimate the inclination i of a nearly spherical object once the distance D is known. The corrected mean velocity fields are consistent with regular rotation, and the mean velocity dispersions display significant deviations from isotropy.

We binned the individual measurements on the plane of the sky to search efficiently through the parameter space of the models. Tests on an analytic model demonstrated that our approach is capable of measuring the cluster distance to an accuracy of about 6 per cent. Application to ω Cen revealed no dynamical evidence for a significant radial dependence of the (V -band) stellar mass-to-light ratio M/L_V , in harmony with the relatively long relaxation time of the cluster. We found that our best-fit dynamical model has $M/L_V = 2.5 \pm 0.1 M_\odot/L_\odot$ and $i = 50^\circ \pm 4^\circ$, which corresponds to an average intrinsic axial ratio of 0.78 ± 0.03 . The best-fit dynamical distance $D = 4.8 \pm 0.3$ kpc (distance modulus 13.75 ± 0.13 mag) is significantly larger than obtained by means of simple spherical or constant-anisotropy axisymmetric dynamical models, and is consistent with the canonical value 5.0 ± 0.2 kpc obtained by photometric methods. The total mass of the cluster is $(2.5 \pm 0.3) \times 10^6 M_\odot$.

Schwarzschild's approach also provides an insight into the intrinsic orbital structure of the cluster. Our best-fit model implies that ω Cen is close to isotropic inside a radius of about 10 arcmin and becomes increasingly tangentially anisotropic in the outer region, which displays significant mean rotation. We found that this may well be caused by the effects of the tidal field of the Milky Way. Furthermore, the best-fit model contains a separate disk-like component between 1 and 3 arcmin, contributing about 4% to the total mass. This phase-space structure, which might be linked to the multiple stellar populations observed in ω Cen, is expected to provide important constraints on its formation history.

We might improve our best-fit dynamical model of ω Cen and better constrain the distance and the other parameters, by extending the data-set with e.g. proper motions derived from HST images. Whereas with the ground-based proper motions we were unable to probe the center of ω Cen due to crowding, the high spatial resolution and high sensitivity of HST, results in many proper motion measurements in the very center, which allows the investigation of a possible central mass concentration in ω Cen.

We may also increase the kinematic constraints on our dynamical models by including mean correlated and higher-order velocity moments. With the parameter range considerably constrained, it now becomes also feasible to use non-linear maximum likelihood techniques to directly incorporate the discrete kinematic measurements. These techniques not only allow correlated and higher-order velocity moments to be included in a straightforward way, but also provide a natural way to incorporate measurements of age and metallicity indicators of individual stars in addition to their photometry and kinematics. By fitting an orbit-based model simultaneously to all these observations, different stellar populations can be separated in phase-space, after which their structure and dynamics can be studied separately.

We have shown that with the method described in this paper, we were able to measure the global parameters of ω Cen, including its distance, and investigate its intrinsic orbital structure. This method can also be applied to study other globular clusters and stellar clusters in the Milky Way, provided that accurate velocity measurements are available. With the amount of (photometric and kinematic) data quickly increasing, we expect this method to become an important tool to model these stellar systems and gain insight in their formation and evolution.

ACKNOWLEDGMENTS

This project would not have been possible without the extensive plate collection of ω Cen obtained in the nineteen thirties by Willem Christiaan Martin, which, together with the plates taken in the eighties by Ken Freeman and Pat Seitzer and the massive subsequent effort by Rudolph Le Poole and Floor van Leeuwen, produced the proper motions reported in Paper I. The line-of-sight velocities used here include those obtained at CTIO in the early nineties by Renate Reijns and Pat Seitzer, as reported in Paper II. We are also grateful to Karl Gebhardt for allowing us to use his unpublished Fabry–Perot measurements, and to Jay Anderson & Ivan King for providing their preliminary HST proper motions. It is a pleasure to thank Thijs Kouwenhoven for assistance in the initial phase of the work reported here, to thank Jesús Falcón-Barroso, Ken Freeman, Floor van Leeuwen, and Scott Tremaine for useful discussions and suggestions during the course of this work, and to thank Michele Cappellari, Richard McDermid and Anne-Marie Weijmans for a critical reading of the manuscript. We also thank the referee for constructive comments and suggestions that improved the presentation of the manuscript. This research was supported in part by NWO through grant 614.000.301, and by the Netherlands Research School for Astronomy NOVA.

REFERENCES

- Andrews D. F., Bickel P. J., Hampel F. R., Rogers W., Tukey J., 1972, *Robust Estimates of Locations: Survey and Advances*. Princeton University, Princeton
- Bedin L. R., Piotto G., Anderson J., Cassisi S., King I. R., Momany Y., Carraro G., 2004, *ApJ*, 605, L125
- Beers T. C., Flynn K., Gebhardt K., 1990, *AJ*, 100, 32
- Benedict G. F., et al. 2002, *AJ*, 123, 473
- Binney J., Tremaine S., 1987, *Galactic Dynamics*. Princeton, NJ, Princeton University Press
- Binney J. J., Davies R. L., Illingworth G. D., 1990, *ApJ*, 361, 78
- Cappellari M., 2002, *MNRAS*, 333, 400
- Cappellari M., et al. 2004, in *Carnegie Centennial Symposium I: Co-evolution of Black Holes and Galaxies*, ed. L. Ho
- Cappellari M., Verolme E. K., van der Marel R. P., Kleijn G. A. V., Illingworth G. D., Franx M., Carollo C. M., de Zeeuw P. T., 2002, *ApJ*, 578, 787
- Carraro G., Lia C., 2000, *A&A*, 357, 977
- Cretton N., de Zeeuw P. T., van der Marel R. P., Rix H., 1999, *ApJS*, 124, 383
- Cudworth K. M., 1979, *AJ*, 84, 1312
- Da Costa G. S., 1979, *AJ*, 84, 505
- Davies R. L., Efstathiou G., Fall S. M., Illingworth G., Schechter P. L., 1983, *ApJ*, 266, 41
- Dejonghe H., 1989, *ApJ*, 343, 113
- Dickens R. J., Woolley R. v. d. R., 1967, *Royal Greenwich Observatory Bulletin*, 128, 255
- Dinescu D. I., Girard T. M., van Altena W. F., 1999, *AJ*, 117, 1792
- Dull J. D., Cohn H. N., Lugger P. M., Murphy B. W., Seitzer P. O., Callanan P. J., Rutten R. G. M., Charles P. A., 1997, *ApJ*, 481, 267
- Emsellem E., Monnet G., Bacon R., 1994, *A&A*, 285, 723
- Evans N. W., 1994, *MNRAS*, 267, 333
- Evans N. W., de Zeeuw P. T., 1994, *MNRAS*, 271, oc202
- Feast M. W., Thackeray A. D., Wesselink A. J., 1961, *MNRAS*, 122, 433
- Ferraro F. R., Bellazzini M., Pancino E., 2002, *ApJ*, 573, L95
- Freeman K. C., 1993, in *ASP Conf. Ser. 48*, eds. G. H. Smith, J. P. Brodie, p. 608
- Freeman K. C., 2002, in *ASP Conf. Ser. 265*, eds. F. van Leeuwen, J. D. Hughes, G. Piotto, p. 423
- Freeman K. C., Rodgers A. W., 1975, *ApJ*, 201, L71

- Gascoigne S. C. B., Burr E. J., 1956, MNRAS, 116, 570
Gebhardt K., et al. 2003, ApJ, 583, 92
Gerhard O. E., 1993, MNRAS, 265, 213
Geyer E. H., Nelles B., Hopp U., 1983, A&A, 125, 359
Harris W. E., 1996, AJ, 112, 1487
Høg E., et al. 2000, VizieR Online Data Catalog, 1259, 0
Icke V., Alcaïno G., 1988, A&A, 204, 115
Kalnajs A. J., 1999, in ASP Conf. Ser. 165, eds. B. K. Gibson, T. S. Axelrod, M. E. Putman, p. 325
Kenney J. F., Keeping E. S., 1951, The Distribution of the Standard Deviation. § 7.8 in *Mathematics of Statistics*, Pt. 2, 2nd ed. Princeton, NJ: Van Nostrand
King I. R., Anderson J., 2002, in ASP Conf. Ser. 265, eds. F. van Leeuwen, J. D. Hughes, G. Piotto, p. 21
King I. R., Hedemann E. J., Hodge S. M., White R. E., 1968, AJ, 73, 456
Kleyna J., Wilkinson M. I., Evans N. W., Gilmore G., Frayn C., 2002, MNRAS, 330, 792
Krajnović D., Cappellari M., Emsellem E., McDermid R. M., de Zeeuw P. T., 2005, MNRAS, 357, 1113
Lawson C. L., Hanson R. J., 1974, Solving least squares problems. Prentice-Hall Series in Automatic Computation, Englewood Cliffs: Prentice-Hall, 1974
Lee Y.-W., Joo J.-M., Sohn Y.-J., Rey S.-C., Lee H.-C., Walker A. R., 1999, Nature, 402, 55
Lee Y.-W., Rey S.-C., Ree C. H., Joo J.-M., Sohn Y.-J., Yoon S.-J., 2002, in ASP Conf. Ser. 265, eds. F. van Leeuwen, J. D. Hughes, G. Piotto, p. 305
Lub J., 2002, in ASP Conf. Ser. 265, eds. F. van Leeuwen, J. D. Hughes, G. Piotto, p. 95
Lucy L. B., 1974, AJ, 79, 745
Mandushev G., Staneva A., Spasova N., 1991, A&A, 252, 94
Martin W. C., 1938, Annalen van de Sterrewacht te Leiden, 17, 1
Mayor M., et al. 1996, in ASP Conf. Ser. 90, eds. E. F. Milone, J.-C. Mermilliod, p. 190
Mayor M., et al. 1997, AJ, 114, 1087 [M97]
McNamara B. J., Harrison T. E., Baumgardt H., 2004, ApJ, 602, 264
Merrifield M. R., Kent S. M., 1990, AJ, 99, 1548
Merritt D., 1993, ApJ, 413, 79
Merritt D., 1997, AJ, 114, 228
Merritt D., Meylan G., Mayor M., 1997, AJ, 114, 1074
Merritt D., Saha P., 1993, ApJ, 409, 75
Meylan G., 1987, A&A, 184, 144
Meylan G., Mayor M., Duquenois A., Dubath P., 1995, A&A, 303, 761
Monnet G., Bacon R., Emsellem E., 1992, A&A, 253, 366
Norris J. E., Freeman K. C., Mayor M., Seitzer P., 1997, ApJ, 487, L187
Pancino E., Ferraro F. R., Bellazzini M., Piotto G., Zoccali M., 2000, ApJ, 534, L83
Pancino E., Seleznev A., Ferraro F. R., Bellazzini M., Piotto G., 2003, MNRAS, 345, 683
Perryman M. A. C., ESA 1997, The HIPPARCOS and TYCHO catalogues. ESA SP 1200
Peterson R. C., Cudworth K. M., 1994, ApJ, 420, 612
Peterson R. C., Rees R. F., Cudworth K. M., 1995, ApJ, 443, 124
Platais I., Wyse R. F. G., Hebb L., Lee Y., Rey S., 2003, ApJ, 591, L127
Press W. H., Teukolsky S. A., Vetterling W. T., Flannery B. P., 1992, Numerical Recipes. Cambridge Univ. Press, Cambridge
Rees R. F., 1997, in ASP Conf. Ser. 127, ed. R. M. Humphreys, p. 109
Reijns R. A., Seitzer P., Arnold R., Freeman K. C., Ingerson T., van den Bosch R. C. E., van de Ven G., de Zeeuw P. T., 2005, A&A, pp in press, astro-ph/0509227 [Paper II]
Richstone D. O., Tremaine S., 1988, ApJ, 327, 82
Rix H., de Zeeuw P. T., Cretton N., van der Marel R. P., Carollo C. M., 1997, ApJ, 488, 702
Romanowsky A. J., Kochanek C. S., 2001, ApJ, 553, 722
Sato C., 1980, PASJ, 32, 41
Scarpa R., Marconi G., Gilmozzi R., 2003, A&A, 405, L15

- Schwarzschild M., 1979, ApJ, 232, 236
 Schwarzschild M., 1982, ApJ, 263, 599
 Schwarzschild M., 1993, ApJ, 409, 563
 Seitzer P. O., 1983, Ph.D. Thesis, Australian National Univ.
 Spitzer L. J., Hart M. H., 1971, ApJ, 164, 399
 Stetson P. B., 1993, in IAU Colloq. 136, eds. C. J. Butler, I. Elliott, p. 291
 Suntzeff N. B., Kraft R. P., 1996, AJ, 111, 1913 [SK96]
 Thompson I. B., Kaluzny J., Pych W., Burley G., Krzeminski W., Paczyński B., Persson S. E., Preston G. W., 2001, AJ, 121, 3089
 Toomre A., Toomre J., 1972, ApJ, 178, 623
 Trager S. C., King I. R., Djorgovski S., 1995, AJ, 109, 218
 Tremaine S., et al. 2002, ApJ, 574, 740
 Tsuchiya T., Korchagin V. I., Dinescu D. I., 2004, MNRAS, 350, 1141
 van den Bosch R. C. E., de Zeeuw P. T., Gebhardt K., Noyola E., van de Ven G., 2005, ApJ, submitted
 van der Marel R. P., 2004, in Carnegie Centennial Symposium I: Co-evolution of Black Holes and Galaxies, ed. L. Ho, p. 37
 van der Marel R. P., Cretton N., de Zeeuw P. T., Rix H., 1998, ApJ, 493, 613
 van der Marel R. P., Franx M., 1993, ApJ, 407, 525
 van Leeuwen F., Hughes J. D., Piotto G., eds, 2002, Omega Centauri, A Unique Window into Astrophysics, ASP Conf. Ser. 265
 van Leeuwen F., Le Poole R. S., 2002, in ASP Conf. Ser. 265, eds. F. van Leeuwen, J. D. Hughes, G. Piotto, p. 41
 van Leeuwen F., Le Poole R. S., Reijns R. A., Freeman K. C., de Zeeuw P. T., 2000, A&A, 360, 472 [Paper I]
 Vandervoort P. O., 1984, ApJ, 287, 475
 Vasilevskis S., van Leeuwen F., Nicholson W., Murray C. A., 1979, A&AS, 37, 333
 Verolme E. K., de Zeeuw P. T., 2002, MNRAS, 331, 959
 Verolme E. K., et al. 2002, MNRAS, 335, 517
 White R. E., Shawl S. J., 1987, ApJ, 317, 246
 Woolley R. v. d. R., 1966, Royal Observatory Annals, 2, 1

APPENDIX A MAXIMUM LIKELIHOOD ESTIMATION VELOCITY MOMENTS

We use the average kinematics of stars that fall within apertures on the plane of the sky. This is comparable to the kinematics from the integrated spectra of galaxies in an aperture. A very important difference is, however, that we have to take into account the errors on the individual velocity measurements.

A possible way to measure the mean velocity and velocity dispersion, is to fit a Gaussian distribution to the velocity histogram of the stars that fall within an aperture. Whereas the mean velocity V is well estimated, the best-fit mean velocity dispersion σ_{fit} is too large, as the Gaussian distribution is broadened due to the velocity errors. This additional 'instrumental' dispersion σ_{ins} can be estimated by the mean of the velocity errors. The corrected mean velocity dispersion σ then follows from $\sigma^2 = \sigma_{\text{fit}}^2 - \sigma_{\text{ins}}^2$. Since this is only an approximate correction, we use a maximum likelihood estimate of the velocity moments that at the same time corrects for each individual velocity error.

Suppose $\mathcal{L}(v)$ is the (intrinsic) velocity distribution of the stars in an aperture, in one of the three principal directions. We can consider each stellar velocity measurement v_i in that aperture as drawn from this distribution, or alternatively, the product of $\mathcal{L}(v)$ with a delta function around v_i , integrated over all velocities. Due to (instrumental) uncertainties this delta-function is broadened, and we assume that it can

be described by a Gaussian around v_i , with the corresponding velocity error σ_i as the standard deviation. For a sufficient number of draws N , i.e. velocity measurements in the aperture, we can then recover the (unknown) velocity distribution $\mathcal{L}(v)$ by maximizing the likelihood

$$L(V, \sigma, \dots) = \prod_{i=1}^N \int_{-\infty}^{\infty} \mathcal{L}(v) \frac{e^{-\frac{1}{2} \left(\frac{v_i - v}{\sigma_i} \right)^2}}{\sqrt{2\pi} \sigma_i} dv, \quad (\text{A.1})$$

or, equivalently, minimizing $\Lambda \equiv -2 \ln(L)$, with respect to the mean velocity V , mean velocity dispersion σ and possible higher-order velocity moments.

It is possible to recover $\mathcal{L}(v)$ in a non-parametric way using (extensions of) Lucy's (1974) method, but exploiting the fact that Gaussians are good low-order approximations, the velocity distribution is often parameterized by a Gauss-Hermite (GH) series (van der Marel & Franx, 1993; Gerhard, 1993). It has the advantage that it only requires the storage of the velocity moments ($V, \sigma, h_3, h_4, \dots$) instead of the full velocity distribution. Furthermore, it allows a simple velocity scaling of the model, which is useful when investigating the effect of a change in the stellar mass-to-light ratio.

Another advantage of parameterizing $\mathcal{L}(v)$ comes from the observation that the integral in (A.1) is the *convolution* of the velocity distribution and the Gaussian of each velocity measurement. For a Gaussian velocity distribution this convolution is straightforward, but also in the case that $\mathcal{L}(v)$ is described by a GH series, the convolution can be carried out analytically. This makes it feasible to apply the method to a large number of discrete measurements and to estimate the uncertainties on the extracted velocity moments by means of the Monte Carlo bootstrap method (§ 15.6 of Press et al. 1992).

In the case of no measurement errors, the maximum likelihood estimator of the standard deviation σ , given by

$$\hat{\sigma} = \sqrt{\frac{1}{n} \sum_{i=1}^n (v_i - \bar{v})^2}, \quad \text{with } \bar{v} = \sum_{i=1}^n v_i, \quad (\text{A.2})$$

is a biased estimator, underestimating the true σ by a factor (see also e.g. Kenney & Keeping 1951, p. 171)

$$b(n) = \sqrt{\frac{2}{n} \frac{\Gamma(\frac{n}{2})}{\Gamma(\frac{n-1}{2})}} = 1 - \frac{3}{4n} - \frac{7}{32n^2} - \dots \quad (\text{A.3})$$

where Γ is the gamma function. When we consider the measurement errors σ_i , there is no such simple analytical bias correction as (A.3). However, we can use the latter result to derive the following approximate corrected standard deviation estimator

$$\tilde{\sigma} \approx \frac{1}{b(n)} \sqrt{\hat{\sigma}^2 + [1 - b^2(n)] \overline{\sigma^2}}, \quad (\text{A.4})$$

where $\hat{\sigma}$ is the maximum likelihood estimated dispersion and $\overline{\sigma^2} = \frac{1}{n} \sum_{i=1}^n \sigma_i^2$ the average measurement error.

APPENDIX B POLAR GRID OF APERTURES

We use Monte Carlo simulations of the observed stellar velocities and corresponding errors to investigate the recovery of their average kinematics. We mimic the stellar velocity observations by randomly drawing from an assumed intrinsic Gaussian velocity distribution, with given mean velocity V_0 and velocity dispersion σ_0 . This set of intrinsic velocities, is then 'instrumentally' broadened by adding to each velocity a random drawing from a Gaussian with zero mean and the velocity error as standard deviation. These velocity errors are simulated by randomly drawing from the observed velocity error distribution (right panels of Fig. 5). For the latter we use the *rejection method* (§ 7.3 of Press et al. 1992), with a Lorentzian distribution as comparison function. In this way, we create, for a given number of stars, 500 sets of simulated velocities and corresponding errors.

Next, we use the maximum likelihood method of Appendix A to calculate the mean velocity and velocity dispersion for each simulated set separately. In Fig. B.1, we compare the (biweight¹⁰) mean (filled circles) of these 500 mean velocity and velocity dispersion measurements with V_0 and σ_0 (horizontal lines) of the given intrinsic Gaussian velocity distribution. The error bars are the (biweight) standard deviation of the kinematic measurements, and indicate the precision with which the kinematics can be measured, given the observed velocity error distribution. The precision increases with increasing number of stars per bin. The precision also increases with decreasing intrinsic mean velocity dispersion σ_0 . To remove the latter dependency, we give *relative* kinematic measurements and corresponding errors, i.e., divided by the (arbitrarily) chosen value for σ_0 .

Both the mean velocity and velocity dispersion are recovered well. To obtain a better precision, we can increase the number of stars per aperture, but at the same time the spatial resolution decreases, as we have to increase the size of the apertures. We find that between 50 and 100 stars per aperture is a good compromise. For the proper motions this implies a (relative) precision for the mean velocity V and velocity dispersion σ of respectively $\Delta V/\sigma \sim 0.12$ and $\Delta\sigma/\sigma \sim 0.09$. For the line-of-sight velocities we find similar values, respectively $\Delta V/\sigma \sim 0.12$ and $\Delta\sigma/\sigma \sim 0.08$.

Given the average proper motion dispersion of about 0.5 mas yr^{-1} for ω Cen (§ 7.2), this means we expect to measure the mean proper motion and dispersions with an average (absolute) precision of respectively 0.06 mas yr^{-1} and 0.05 mas yr^{-1} . Similarly, with an average line-of-sight velocity dispersion of about 14 km s^{-1} for ω Cen, we expect to measure the mean line-of-sight velocity and dispersion with an average precision of respectively 1.7 km s^{-1} and 1.1 km s^{-1} .

Indeed, the average of the uncertainties in the kinematics given in Table 3 and 4 are consistent with these expectations. Moreover, as predicted, the decrease in the uncertainties with radius is proportional to the decrease in dispersion. In other words, if we divide the uncertainties by the corresponding dispersions, we find nearly constant (relative) precisions, $\Delta V/\sigma \sim 0.11$ and $\Delta\sigma/\sigma \sim 0.08$ for both proper motions and line-of-sight velocities, consistent with the above simulated precisions.

To enhance the signal-to-noise of the observations, we first reflect all measurements back to the first quadrant ($x' \geq 0, y' \geq 0$). We exploit the fact that for an axisym-

¹⁰The biweight mean and biweight standard deviation (e.g., Andrews et al. 1972; Beers, Flynn & Gebhardt 1990) are robust estimators for a broad range of non-Gaussian underlying populations and are less sensitive to outliers than other moment estimators.

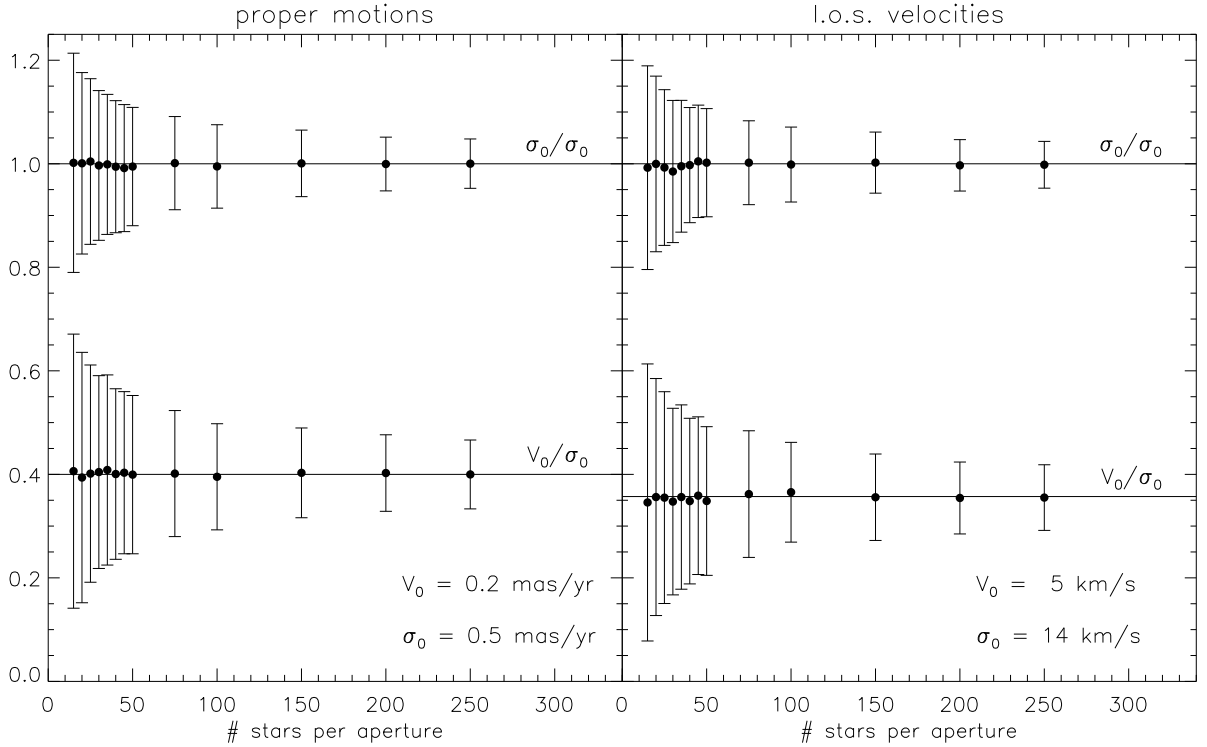


FIGURE B.1 — Recovery of maximum-likelihood-estimated kinematics from proper motions (left panel) and line-of-sight velocities (right panel). For a given number of stars per aperture, velocities and corresponding errors are simulated by randomly drawing from an intrinsic Gaussian distribution with mean velocity V_0 and velocity dispersion σ_0 , broadened by velocity errors randomly drawn from the observed velocity error distributions (left panels Fig. 5). Each filled circle with error bar shows the mean and standard deviation of the measured kinematics from 500 such simulations. As a compromise between lower precision (larger error bars) for a small number of stars per aperture, and lower spatial resolution (larger bins) for a larger number of stars, we choose to have between 50 and 100 stars per bin.

metric object, the proper motions in the x' -direction are symmetric in the projected minor axis, while the proper motions in the y' -direction as well as the line-of-sight velocities are symmetric in the projected major axis. Since our models are intrinsically axisymmetric, it is equivalent to fit either to the original or to the reflected data.

We use a polar grid of apertures on (the first quadrant of) the plane of the sky to better approximate the shape of photometric and kinematic observations. Every aperture is characterized by its central radius $r_0 > 0$ and angle $0^\circ < \theta_0 < 90^\circ$, together with its radial and angular width, denoted by Δr and $\Delta\theta$, respectively. We construct the polar grids such that each aperture has (at least) 50 stars, together with the requirement that the apertures are as 'round' as possible in the sense that $\Delta r \approx r_0 \Delta\theta$. The latter avoids (very) radial or angular elongated apertures, which would include stars from (very) different positions, with probably different (kinematical) properties than the stars near the center of the aperture.

APPENDIX C SIMPLE DISTANCE ESTIMATE

The most straightforward way to obtain a dynamical distance estimate is from the ratio of the line-of-sight velocity dispersion σ_{los} and the proper motion velocity dispersion σ_{pm} for spherically symmetric objects (e.g., Binney & Tremaine 1987, p. 280)

$$D \text{ (kpc)} = \frac{\sigma_{\text{los}} \text{ (km s}^{-1}\text{)}}{4.74 \sigma_{\text{pm}} \text{ (mas yr}^{-1}\text{)}}. \quad (\text{C.1})$$

Using, from the 2295 selected stars with proper motions and 2163 selected stars with line-of-sight velocities, the 718 stars for which all three velocity components are measured, we find for the two mean proper motion dispersion components $\sigma_{x'} = 0.58 \pm 0.02$ mas yr⁻¹ and $\sigma_{y'} = 0.55 \pm 0.02$ mas yr⁻¹, and for the mean line-of-sight velocity dispersion $\sigma_{z'} = 12.3 \pm 0.3$ km s⁻¹. Substituting the latter value together with the average proper motion dispersion in (C.1), we obtain a distance of $D = 4.6 \pm 0.2$ kpc.

This value is below the canonical distance $D = 5.0 \pm 0.2$ (Harris et al. 1996). The above simple distance estimate is not valid for ω Cen, which is not spherically symmetric. Moreover, although the above average values for $\sigma_{x'}$ and $\sigma_{y'}$ are just consistent with each other, from the left panel of Fig. C.1 it is clear that the profile of the mean proper motion dispersion profile of $\sigma_{x'}$ (dotted) lies systematically above that of $\sigma_{y'}$ (dashed). A non-spherical anisotropic model is needed to explain these observations. Here we consider a simple model with constant anisotropy.

If we make the (ad-hoc) assumption that the velocity ellipsoid is oblate with intrinsic semi-axis lengths $\sigma_x = \sigma_y \equiv \sigma$ and $\sigma_z = q_{\text{ve}} \sigma$ (all in km s⁻¹), where q_{ve} is the average intrinsic flattening, the observed velocity dispersions are given by

$$\begin{aligned} \sigma_{x'} &= \sigma / 4.74 D \text{ mas yr}^{-1}, \\ \sigma_{y'} &= q'_{\text{ve}} \sigma / 4.74 D \text{ mas yr}^{-1}, \\ \sigma_{z'} &= [1 - (1 - q'^2_{\text{ve}}) \cot^2 i]^{1/2} \sigma \text{ km s}^{-1}, \end{aligned} \quad (\text{C.2})$$

where we have used eq. (2.2) and the relation $q^2 \sin^2 i = q'^2 - \cos^2 i$. Using the best-fit value for $D \tan i$ of 5.6 kpc (§ 4.5), we eliminate the inclination i . Next, by fitting the ratios of the line-of-sight velocity dispersion over the proper motion dispersion components, $\sigma_{z'}/\sigma_{x'}$ and $\sigma_{z'}/\sigma_{y'}$, to the observations in the left panel of Fig. 8, we determine the best-fit values for the remaining two free parameters: the distance D and the (projected) flattening of the velocity ellipsoid q'_{ve} .

Since we use the full dispersion profiles and we allow for an anisotropic velocity distribution, this simple way to obtain a dynamical distance estimate goes beyond the above spherical symmetric approach. If $q'_{\text{ve}} = 1$ in eq. (C.2), we recover this approach in which both ratios are equal and the distance follows from eq. (C.1).

We show in the right panel of Fig. C.1 the $\Delta\chi^2$ contours for a range of q'_{ve} and D . The overall minimum, indicated by a cross, corresponds to the best-fit values $q'_{\text{ve}} = 0.92 \pm 0.05$ and $D = 4.54 \pm 0.14$ kpc. The isotropic case ($q'_{\text{ve}} = 1$) is excluded at about the 95.4%-level. The best-fit (projected) flattening of the velocity ellipsoid is less than the average observed flattening $q' = 0.879 \pm 0.007$ (hashed region) from the stellar photometry of ω Cen (Geyer et al. 1983), although an equivalent value is not excluded (at the 68.3%-level). The velocity distribution is expected to be less flattened, since it traces more directly the potential, which in general is rounder than the light distribution (see e.g. p. 48 of Binney & Tremaine 1987).

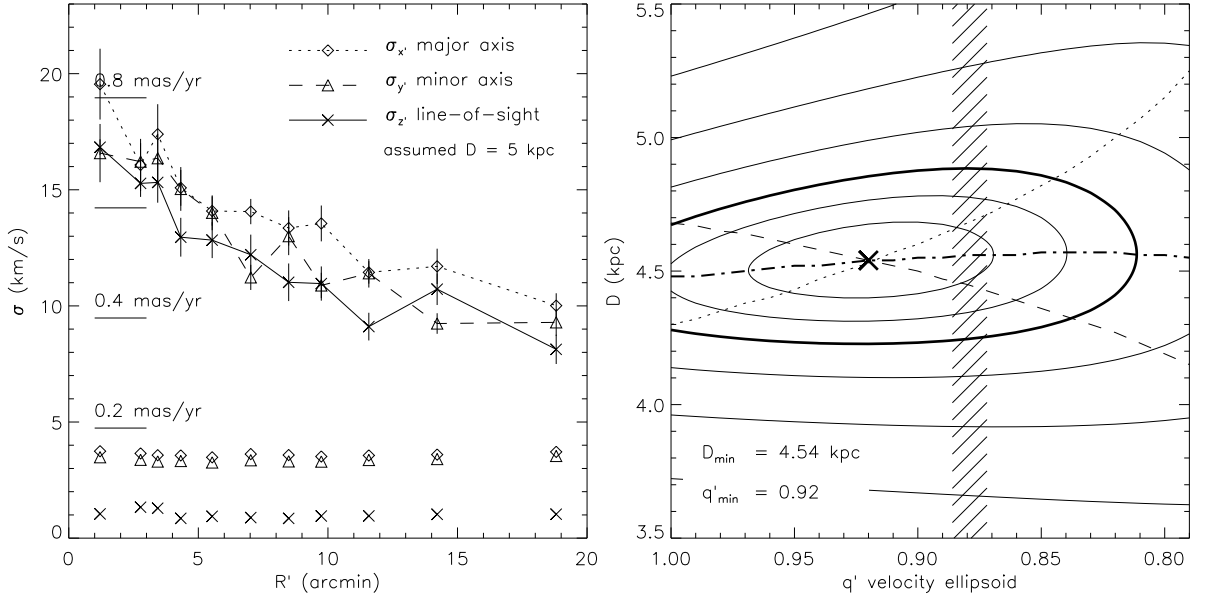


FIGURE C.1 — Left panel: velocity dispersion profiles calculated along concentric rings. Assuming the canonical distance of 5 kpc, the profiles of the proper motion components in the x' -direction (dotted curve with diamonds) and y' -direction (dashed curve with triangles) are converted into the same units of km s^{-1} as the line-of-sight profile in the z' -direction (solid curve with crosses). The black horizontal lines indicate the corresponding scale in mas yr^{-1} . Below the profiles, the mean velocity error per ring is indicated by the corresponding symbols. Right panel: Assuming an oblate velocity ellipsoid with constant (projected) flattening, the ratio of the line-of-sight over the proper motion velocity dispersion profiles yields an estimate for the dynamical distance D . The best-fit values correspond to the minimum (cross) in the $\Delta\chi^2$ contour plot, where the inner three contours are drawn at the 68.3%, 95.4% and 99.7% (thick contour) levels, and subsequent contours correspond to a factor of two increase in $\Delta\chi^2$. For increasing flattening of the velocity ellipsoid, starting with the isotropic case on the left axis, the dotted (dashed) curve shows the corresponding best-fit distance if only the profile of the proper motion in the x' -direction (y' -direction) is used, and the dotted-dashed curve if both are used. The observed flattening from the stellar photometry (Geyer et al. 1983) is indicated by the hashed region.

If we only fit the ratio $\sigma_{z'}/\sigma_{x'}$, the dotted curve shows the best-fit distance at given flattening. While in this case the distance increases with flattening, almost exactly the opposite happens if we only fit the ratio $\sigma_{z'}/\sigma_{y'}$ (dashed curve). Simultaneously fitting both ratios does not provide a good fit (the χ^2 value is larger than the number of degrees of freedom) and the resulting best-fit distance (dotted-dashed curve) of about 4.5 kpc is significantly below the canonical distance of 5.0 kpc.

We conclude that both the simple distance estimate (C.1) and the above constant-anisotropy axisymmetric model are not valid for ω Cen and underestimate its distance. To explain the observed kinematics of ω Cen and obtain a reliable distance estimate, one needs a non-spherical dynamical model with varying anisotropy, like the Schwarzschild modeling technique used here.

CHAPTER 3

A BAR SIGNATURE AND CENTRAL DISK IN THE GASEOUS AND STELLAR VELOCITY FIELDS OF NGC 5448

ABSTRACT

We analyze SAURON kinematic maps of the inner kpc of the early-type (Sa) barred spiral galaxy NGC 5448. The observed morphology and kinematics of the emission-line gas is patchy and perturbed, indicating clear departures from circular motion. The kinematics of the stars is more regular, and display a small inner disk-like system embedded in a large-scale rotating structure. We focus on the [O III] gas, and use a harmonic decomposition formalism to analyze the gas velocity field. The higher-order harmonic terms and the main kinematic features of the observed data are consistent with an analytically constructed simple bar model. The bar model is derived using linear theory, considering an $m = 2$ perturbation mode, and with bar parameters which are consistent with the large-scale bar detected via imaging. We also study optical and near infra-red images to reveal the asymmetric extinction in NGC 5448, and we recognize that some of the deviations between the data and the analytical bar model may be due to these complex dust features. Our study illustrates how the harmonic decomposition formalism can be used as a powerful tool to quantify non-circular motions in observed gas velocity fields.

K. Fathi, G. van de Ven, R.F. Peletier, E. Emsellem,
J. Falc3n-Barroso, M. Cappellari, P.T. de Zeeuw
MNRAS, in press (2005)

1 INTRODUCTION

DYNAMICAL studies of spiral galaxies often make the distinction between the bulge and the disk: the bulge is associated with the hot ‘spheroidal’ component which mainly contains stars, and the disk is a rapidly rotating thin structure which also contains a substantial fraction of the total amount of interstellar gas. Line-of-sight velocity distributions are efficient probes of the dynamical structures of these systems, and can be used to derive the mass distribution, structural properties, and perturbations of the gravitational potential linked to $m = 1$ or $m = 2$ modes, or to external triggers such as interactions. These can be obtained with classical long-slit spectrography, although it requires a-priori assumptions for the orientation of the slits. A time-consuming way to obtain velocity fields through single slits is to spatially scan the galaxy with successive individual exposures (e.g., Statler 1994; Ohtani 1995). Integral field spectrography in the optical (IFS, Adam et al. 1989; Afanasiev et al. 1990; Bacon et al. 1995; Davies et al. 1997; García-Lorenzo, Arribas & Mediavilla 2000; Roth, Laux & Heilemann 2000; Bacon et al. 2001; Bershady et al. 2004) was designed to uniformly cover the field of view which makes it possible to study these systems in a much improved way: the analysis is not constrained by a priori choices of slit position, and the gaseous and stellar components can be observed simultaneously. Optical IFS is often used complementary to HI and Fabry-Perot scanning interferometers, (e.g., van Gorkom et al. 1986; Plana & Boulesteix 1996) as the latter usually have excellent spatial coverage but a limited spectral domain, only probing a couple of lines (mostly in emission).

Although circular rotation is the dominant kinematic feature of the disk component, previous observational as well as theoretical studies have shown the presence of non-circular motions (e.g., Freeman 1965; Combes & Gerin 1985; Shlosman, Frank & Begelman 1989; Athanassoula 1994; Shlosman & Noguchi 1993; Moiseev 2000; Regan & Teuben 2004; Wong, Blitz & Bosma 2004). Cold disk-like systems are more prone than bulges to perturbations and instabilities, the dissipative gaseous component being more responsive than the stellar component (e.g., Thielheim & Wolff 1982). Perturbations of the gas dynamics can lead to significant galaxy evolution via, e.g., redistribution of the angular momentum, triggering of star formation, or building of a central mass concentration.

Bars are potential actors in this context as they can drive mass inwards or outwards, and may participate in the complex process which eventually leads to the fueling of an active nucleus (e.g., Simkin, Su & Schwarz 1980, Sakamoto, Baker & Scoville 2000). The presence of large-scale bars has been correlated with starbursts (e.g., Martinet & Friedli 1997) and nuclear rings (Shlosman 1999), but only weakly if at all with nuclear activity (e.g., Knapen et al. 2000). This may not be so surprising as the fueling of an active galactic nucleus (AGN), i.e., gas accretion onto a massive black hole, involves rather small spatial and short time-scales, so might not be related to the kpc scale bar. Inner small bars (Shlosman et al. 1989) may sometimes help to link the different spatial scales (Emsellem, Goudfrooij & Ferruit 2003), but they probably cannot serve as a universal mechanism. AGN activity is short-lived and occurs in the central astronomical units of galaxies, whereas current studies have focused on long-lived phenomena influencing the central kpc scale. In order to properly study the influence of a bar on the redistribution of mass in the central kpc of a galaxy, we need to obtain constraints both on the source of the underlying gravitational potential and

Field of View	41"×33"
Pixel Size	0".8
Instrumental Disp.	108km s ⁻¹
Spectral Range	[4820 - 5280]Å
Spectral Features	H β , [O III], Fe5015, Mgb, [N I], Fe5270

TABLE 1 — *SAURON* data characteristics.

on some tracer of the on-going perturbations. This can be achieved by simultaneously studying the stellar and gas dynamics.

We have observed 24 early-type spiral (Sa) galaxies with the *SAURON* Integral Field Spectrograph (Bacon et al. 2001), mounted at the 4.2m William Herschel Telescope of the Observatorio del Roque de los Muchachos at La Palma (de Zeeuw et al. 2002). Most of these galaxies are found to have gas velocity fields that strongly deviate from that of a simple rotating disk. For the present study, we selected NGC 5448 out of the Sa *SAURON* sample which shows a clear sign of the presence of a bar in its photometry and which has a significant amount of ionized-gas (Falcón-Barroso et al. 2005). In this chapter, we analyze both the stellar and gas kinematics obtained with *SAURON*, and quantify the non-circular gaseous motions in NGC 5448. To this aim, we build models with elliptical streaming motion and compare the resulting velocity structures with our observational data, using a harmonic decomposition technique. In Section 2, we present our data. Section 3 outlines our analysis method of the gas kinematics. In Section 4, we build a bar model for NGC 5448, and we present and discuss the corresponding results in Sections 5 and 6.

2 THE DATA

NGC 5448 is a barred Sa active galaxy with prominent irregular dust lanes at different spatial scales. The RC3 classification of NGC 5448 is (R)SAB(r)a, with inclination of 64°, systemic velocity of 1971 km s⁻¹, position angle (PA) of 115°, and total *B*-band magnitude of 11.93. Photometry shows that this galaxy hosts a large-scale bar with two well-defined spiral arms emerging near the ends of the bar (Eskridge et al. 2002). The inner parts of the arms are somewhat patchy and form a broken ring, the outer parts of the arms being smoother (Sandage & Bedke 1994). This galaxy has a nuclear elongated feature of about 10" (Fathi & Peletier 2003) with bluer *V* – *H* color than its surroundings (Carollo et al. 2002). Ho, Filippenko, & Sargent (1995) classified the nucleus as an AGN: its central aperture spectrum exhibits a clear broad-line emitting region. Laine et al. (2002) classified NGC 5448 as a non-Seyfert.

2.1 SAURON OBSERVATIONS

We observed NGC 5448 with *SAURON* on April the fourteenth 2004. Detailed specifications for the instrument, data, reduction procedure, and the data preparation procedure can be found in Bacon et al. (2001), de Zeeuw et al. (2002), and Emsellem et al. (2004). A brief summary of the instrument and data characteristics is presented in Table 1. We obtained 4 exposures of 1800 s each, producing a total of 1431 simultaneous galaxy spectra per frame, together with 146 sky spectra 1'.9 away from the main field. We also observed standard stars to be used for accurate velocity, flux,

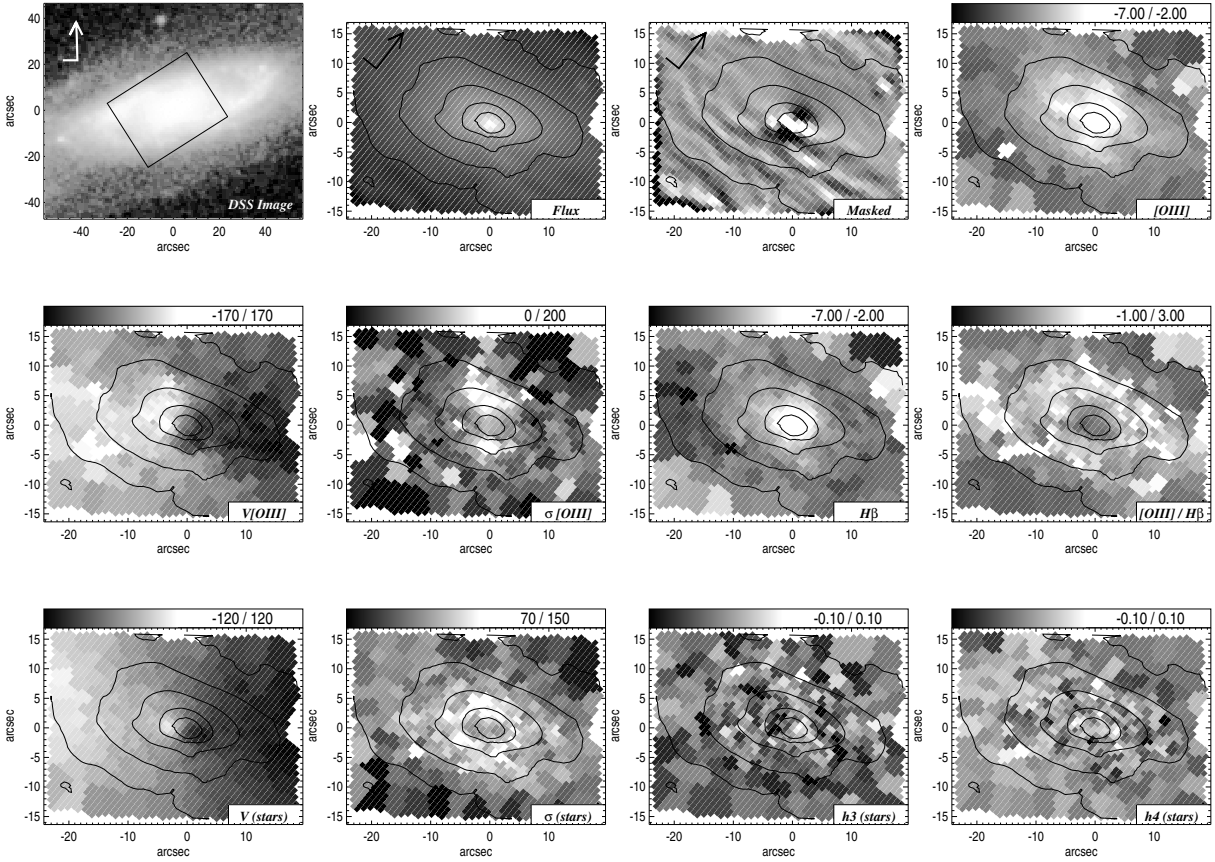


FIGURE 1 — *Top Left: Digitized Sky Survey image of NGC 5448 with SAURON footprint and north-east orientation arrow. All other panels show the SAURON data. The stellar flux map and unsharp-masked SAURON image are given in mag arcsec⁻² with arbitrary zero point, and north-east direction as indicated. The titles are indicated at the bottom right corner of each panel, and the plotting ranges are given at the top. All SAURON maps have the same orientation with overplotted stellar contours in magnitude steps of 0.25, and all velocities and velocity dispersions are given in km s⁻¹. (See p. 252 for a color version of this figure.)*

and line-strength calibration of our observed galaxy. Wavelength calibration was done using arc lamp exposures taken before and after each target exposure. The standard reduction was performed using the xSauron software package developed at the CRAL (Lyon), providing a fully calibrated datacube for each individual exposure. We merged the 4 spatially dithered exposures after a resampling to a common spatial scale of $0''.8 \times 0''.8$ per pixel, leading to a total of 1973 spectra within our field.

2.2 STELLAR AND GASEOUS KINEMATIC MAPS

The signal-to-noise (S/N) ratio of individual spectra varies considerably throughout the field: in order to homogenize the S/N we applied the adaptive spatial 2D-binning scheme of Cappellari & Copin (2003). We have set a target S/N value of 60 to be able to derive reliable higher-order moments of the stellar velocity distribution. Penalized Pixel Fitting (pPXF, Cappellari & Emsellem 2004) was used to derive the stellar line-of-sight velocity distribution parametrized by a Gauss-Hermite series up to and including the fourth order (van der Marel & Franx 1993; Gerhard 1993). The optimal stellar

template in pPXF was built with a combination of stellar spectra from Jones (1997) and synthesis spectra from Vazdekis (1999) as in Emsellem et al. (2004). The derived stellar mean velocity V , mean velocity dispersion σ , and higher order velocity moments h_3 and h_4 maps, are presented in bottom row of Fig. 1. We discuss the maps in Section 5.

The method which we have applied to derive the emission-line kinematics is described and validated in Sarzi et al. (2005) and Falc3n-Barroso et al. (2005). It consists of iteratively searching for the emission-line velocities and velocity dispersions, while solving at each step for both their amplitudes and the optimal combination of the stellar templates over the full SAURON wavelength range. No masking of the regions affected by emission is thus required.

Our binning scheme was optimized for the derivation of reliable stellar kinematics, but is not necessarily well adapted to analyze the emission-line gas. Since the gaseous component commonly rotates faster than the stellar component, to obtain reliable gas kinematics, in general a lower S/N is required. Moreover, gas and stars do not necessarily share the same spatial distributions. As a consequence, the stellar bins are often larger than necessary for the gas, implying a loss of spatial information for analyzing the gaseous component (Fathi 2004). Accordingly, the data that we present here has a minimum stellar S/N of 60 and a minimum emission-line amplitude-over-noise of 3.

Finally, we have carefully inspected the emission-line profiles to search for possible asymmetric profiles but have not found any significant deviation from a pure Gaussian, nor any significant indication for more than one component being present in the profiles, at least at the instrumental resolution of SAURON. We know from other SAURON studies of e.g., NGC 1068 (Emsellem et al. 2005) that we can resolve several components in very strong AGNs.

3 ANALYZING GAS VELOCITY FIELDS

3.1 CIRCULAR AND NON-CIRCULAR KINEMATICS

In this section we start with a simple mathematical model, and then add complexity as required by the observational constraints. In the simplest model, the galactic disk is purely rotational, has negligible velocity dispersion, and is infinitesimally thin. In the presence of axisymmetric radial and vertical velocities, and when taking into account the effect of projection and the convention that positive line-of-sight velocities correspond to recession, the line-of-sight velocities V_{los} can be represented by

$$V_{\text{los}}(R, \psi, i) = V_{\text{sys}} + V_{\text{rot}}(R) \cos \psi \sin i + V_{\text{rad}}(R) \sin \psi \sin i + V_z(R) \cos i, \quad (3.1)$$

where V_{sys} is the systemic velocity of the galaxy, V_{rot} and V_{rad} are the rotational and radial velocities, and V_z is the vertical velocity component, which we set to zero throughout this chapter. The inclination i of the galaxy ranges from $i = 0^\circ$ for a face-on viewing and $i = 90^\circ$ for an edge-on viewing. Furthermore, (R, ψ) are polar coordinates in the plane of the galaxy related to observable Cartesian coordinates x and y (in the plane of the sky) by

$$\begin{cases} R \cos \psi & = -(x - X_{\text{cen}}) \sin \phi_0 + (y - Y_{\text{cen}}) \cos \phi_0, \\ R \sin \psi \cos i & = -(x - X_{\text{cen}}) \cos \phi_0 - (y - Y_{\text{cen}}) \sin \phi_0, \end{cases} \quad (3.2)$$

where X_{cen} and Y_{cen} are the coordinates for the center, and ϕ_0 is the PA of the projected major axis of the disk, measured with respect to north in counterclockwise direction. This simple model cannot explain most observed velocity fields. The gas kinematics in real galaxies exhibits radial and/or vertical motions due to, e.g., the presence of bars, spiral arms, which create angle-dependent velocities which cannot be explained using eq. (3.1), and hence additional ingredients in the analysis method are required.

Several attempts have been made to investigate more complex velocity fields (Sakhibov & Smirnov 1989; Canzian 1993; Schoenmakers, Franx & de Zeeuw 1997 [hereafter SFdZ]; Fridman & Khoruzhii 2003; Wong et al. 2004; Krajnović et al. 2005). The main idea of these techniques is to deal separately with the ‘unperturbed’ underlying component and the residual velocity field, obtained by subtracting the reconstructed unperturbed velocity field from the data. To solve the problem, as stated, one would have to know the unperturbed velocity component at a given radius. Unfortunately we do not know beforehand the unperturbed velocity field. A powerful technique for unveiling the perturbations makes use of the expansion of the velocity information in Fourier harmonic components. Following the terminology of SFdZ (see their appendix for the detailed derivation), given that the line-of-sight velocity can be expressed as a two-dimensional analytic function of galactocentric coordinates, it can be written as a Fourier series:

$$V_{\text{los}} = V_{\text{sys}} + \sum_{n=1}^k [c_n(R) \cos n\psi + s_n(R) \sin n\psi] \sin i, \quad (3.3)$$

where k is the number of harmonics, and c_n and s_n give us information about the nature of the perturbations, and they are tightly connected to the underlying potential. Note that $c_1 = V_{\text{rot}}$ and $s_1 = V_{\text{rad}}$. Furthermore, numerical simulations by Burlak et al. (2000) have shown that this formalism is very stable and its results are rather insensitive to the presence of holes in the velocity field.

3.2 TILTED-RING AND HARMONIC DECOMPOSITION

Our quantitative analysis uses the formalism of eq. (3.3) combined with the tilted-ring method (Rogstad, Lockart & Wright 1974; Rogstad, Wright & Lockart 1976), inspired from the ROTCUR routine in the GIPSY package (Begeman 1987; van der Hulst et al. 1992). Accordingly, we divide the galaxy disk into concentric ellipses within which we fit the rotation velocity and the set of geometric parameters of eq. (3.3). The method assumes that each pixel in the velocity field is identified with a unique position in the galaxy and that circular rotation is the dominant feature. We assume that our measurements refer to positions on a single inclined disk, i.e., that we do not expect a strong warp and/or overlapping spiral arms within the observed field. Accounting for harmonic perturbations up to order 3, this method results in a large parameter-space problem, and it requires some additional assumptions to obtain a physically meaningful solution. We obtain the parameters by proceeding as follows:

- i. We start from a simple inclined two-dimensional disk. In case of erroneous inclination, one would detect systematics in the residual field as explained in Section 3.3. Using a two-dimensional disk produces a robust model, in the sense that warps and other deviations from this basic model should be prominent in the residual maps.

- ii. Secondly, we fix the dynamical center of the galaxy to coincide with the photometric center. The photometric center is obtained by fixing the center of the H band image, since the H -band image is less affected by dust. The HST V -band image and the SAURON image are then aligned with the HST H -band image.
- iii. At every radius, we fit $V_{\text{los}} = c_0 + c_1 \cos \psi \sin i$, varying c_0 , PA, and c_1 . The result is used to fix the systemic velocity ($V_{\text{sys}} = c_0$) simply as the mean value over radius, using Tukey's bi-weight mean formalism (Mosteller & Tukey 1977), which is particularly advantageous for being non-sensitive to outliers. After V_{sys} , we fit the PA and c_1 , followed by fixing the PA in the same way as the V_{sys} was fixed.
- iv. For each ring, we import the values derived according to the recipe above, and fit the rotation curve and the higher harmonic components (up to order 3) applying a χ^2 -minimization scheme. The results are presented in Fig. 2.

Analyzing the first, second, and third harmonic components only, is an efficient way to analyze specific elements of the perturbations on the underlying potential. A perturbation of order m creates $m - 1$ and $m + 1$ line-of-sight velocity terms (see e.g., Canzian 1993 and SFdZ). As a result, our fitted c_1 , s_1 , c_3 , and s_3 terms contain information about possible $m = 2$ perturbations.

When sectioning the field into concentric rings, the radial extent of each ring is a free parameter which has to be pre-determined. For a range of possible ring radii, we have examined the fitted velocity information. Determination of the radial thickness of the rings becomes a trade-off between smoothness of the fitted velocity field, and robustness of the fit. Radially thin rings result in smooth fits, and thus smooth residual (Data - Fit) fields, whereas radially thick rings result in lower errors for the fitted parameters. Patchy gas distribution causes non-uniform distribution of points, and it is important to make sure that all the rings include enough points to fit harmonic parameters to reasonable accuracy. This is particularly important in the innermost and outermost points. We adopt a geometric increase of the ring radii (meaning that the radial width of the rings is increased by a factor $1 + \text{step}$). Here, we adopt a step of 0.2, and only fit the inner $30''$ of the SAURON velocity field, since rings larger than this radius are not sufficiently covered and hence do not deliver reliably derived parameters. Finally, since we are simultaneously fitting 6 harmonic components, we make sure that each ellipse contains at least 25 data points, in order to obtain reliable errors.

3.3 ERRORS

Warner et al. (1973) and van der Kruit & Allen (1978) showed that assuming wrong input disk parameters could cause recognizable signatures in the residual velocity fields. SFdZ quantified these signatures in terms of harmonic expansion, and showed that the Fourier components due to non-circular motions will mix with those due to erroneous disk parameters X_{cen} , Y_{cen} , i , and PA. Errors in the kinematic center translate to the c_0 , c_2 and s_2 terms, while PA errors appear in the s_1 and s_3 terms, and inclination errors in the c_1 and c_3 terms. In the case of erroneous kinematic center, the c_0 and the c_2 terms fall off as $\frac{1}{R}$ whereas the presence of a radius-independent $m = 1$ mode shows the relation $c_0 \sim 3c_2$ (Schoenmakers 1999). Our chosen center coordinates do not deliver any of these situations. Another source of error is 'pixel sampling' for which errors propagate onto the c_1 (as the rotation curve rises more gradually) and the c_3 term (as if inclination changes). This effect may also propagate onto the s_1 and

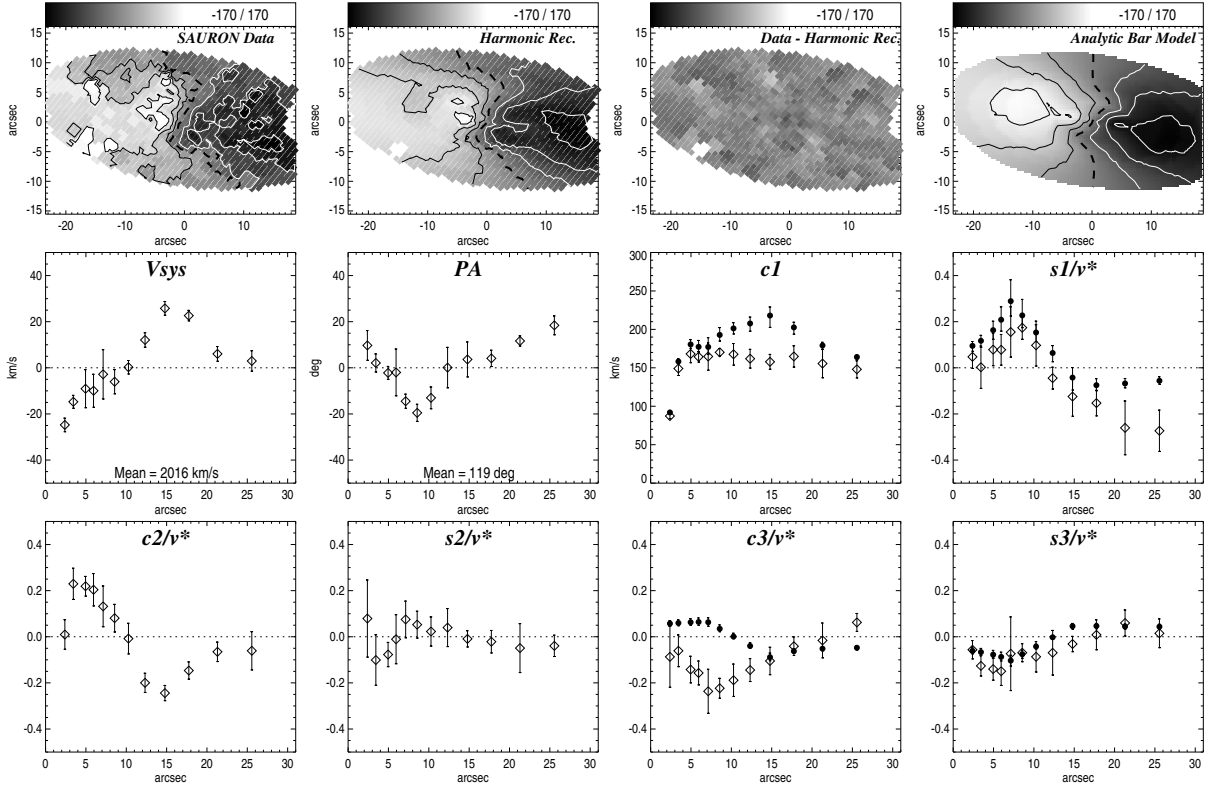


FIGURE 2 — Top row, from left to right: observed *SAURON* gas velocity field of NGC 5448; reconstruction based on the harmonic decomposition of the *SAURON* gas velocity field; residual field (data - harmonic reconstruction); and the analytic bar model, which reproduces best the main kinematic features of the observed gas velocity field. Middle and bottom row: the harmonic parameters as a function of outer radius of each ring, and $v^* = c_1 \sin i$. The over-plotted filled circles are the analytically calculated first and third harmonic terms for the bar model (the second terms are zero by construction), with the error bars corresponding to the 99.7% confidence level (see Section 4 for details). The orientation of the maps is the same as in Fig. 1, and the mean PA value is given in the north-east direction.

s_3 parameters, although not significantly (Wong 2000). Our data and analysis does not require consideration of this effect since our spatial resolution is high enough.

Our data extraction code delivers error measurements for each individual pixel (Falc3n-Barroso et al. 2005). We calculate the errors for the tilted-ring and harmonic parameters by means of Monte Carlo simulations. Repeated application of the tilted-ring method to the Gaussian randomized gas velocity field yields the uncertainties on the harmonic parameters. Our 500 simulations show that choosing geometrically increasing ring radii with steps of 0.2 indeed yields satisfactory errors. The errors are low, and the parameter profiles are represented by an adequate number of points.

4 A BAR MODEL FOR NGC 5448

The SFdZ formalism is a very powerful tool for analyzing velocity fields. One can analytically derive the higher-order harmonic parameters for potentials of desired form. Schoenmakers (1999) derived the harmonic parameters for a lopsided potential, and a more extensive expansion was done by Wong et al. (2004), who derived the higher-order harmonics for simple bar and two-armed spiral perturbations.

We import their model for a globally elongated gravitational potential, which, in the plane of the galaxy, consists of an axisymmetric component $\Phi_0(R)$ from Kuijken & Tremaine (1994), with a bi-symmetric potential of the form $\Phi_2(R) \cos 2\theta$ added to it. In the case of flat rotation curve, the potential is written as

$$\begin{cases} \Phi_0(R) = v_c^2 \ln R, \\ \Phi_2(R) = -\varepsilon v_c^2 / 2, \end{cases} \quad (4.1)$$

where v_c is the circular velocity and ε is the elongation of the potential. Introducing a constant damping term into the equations of motion and considering only the $m = 2$ perturbation term (Lindblad & Lindblad 1994; Wada 1994), linear epicyclic approximation of Lin & Shu (1964) was applied to obtain an analytical solution for gaseous orbits in this barred potential. Since this model is restricted to $m = 2$ perturbation, it affects only the first and third harmonic parameters (c_1 , s_1 , c_3 , and s_3). These depend on the amplitude of the damping term (λ), the ellipticity of the potential (ε), the corotation radius (CR), and the viewing angle of the bar (θ), where $\theta = 0$ corresponds to end-on view.

We use these analytic harmonic parameters to reconstruct the signatures of prominent non-circular motions in the observed velocity fields. We build a library of models with varying bar parameters ($0 < \varepsilon < 0.5$, $0 < \lambda < 0.5$ and a range of bar sizes), viewed from different angles ($0^\circ \leq \theta \leq 180^\circ$). The effects of λ and ε on the velocity field are predictable. The bar signature is weaker for a larger damping factor and/or a smaller flattening of the potential. However, the effect of varying θ is not straightforward.

Investigating our library of dissipative bar models, we find that only for a certain combination of parameters the model exhibits a strong twist of the gas zero-velocity curve similar to our data (Fig. 1). We quantify the comparison by calculating, for each bar model in our library, the discrepancy between the reconstructed velocity field and the observed velocity field, in terms of the goodness-of-fit parameter χ^2 . Care has to be taken at the inner Lindblad resonance (ILR), since there the linear epicyclic theory breaks down. At the ILR the weak-bar model is not expected to reproduce the velocity field, due to the presence of non-linear terms, which are not accounted for by the analytic epicyclic theory. Hence, for a small region around the ILR, we interpolate the bar models.

The minimum goodness-of-fit parameter χ_{\min}^2 yields the best-fit bar model, for which we show in Fig. 2 the reconstructed velocity field and harmonic terms (filled circles). The best-fit model accounts for an $m = 2$ perturbation of a single bar, with potential ellipticity $\varepsilon = 0.15 \pm 0.02$, damping term $\lambda = 0.12 \pm 0.03$, viewing angle $\theta = 19 \pm 3^\circ$, and CR = $37 \pm 4''$. The errors on the bar parameters follow from the bar models for which the difference between the corresponding χ^2 and χ_{\min}^2 is below the 99.7% level. From the harmonic terms of these bar models, we also obtain an estimate on the uncertainty in c_1 , s_1 , c_3 and s_3 , indicated by the error bars on the corresponding filled circles in Fig. 2. Given the significant second harmonic term and the simplicity of the analytic bar model, it is not surprising that it cannot provide a perfect fit to the data. Still, this generic bar model does reproduce the main features in the observed velocity field, as well as the overall behavior of the first and third harmonic terms. This supports the case of a bar as the main driver behind the observed non-circular motions.

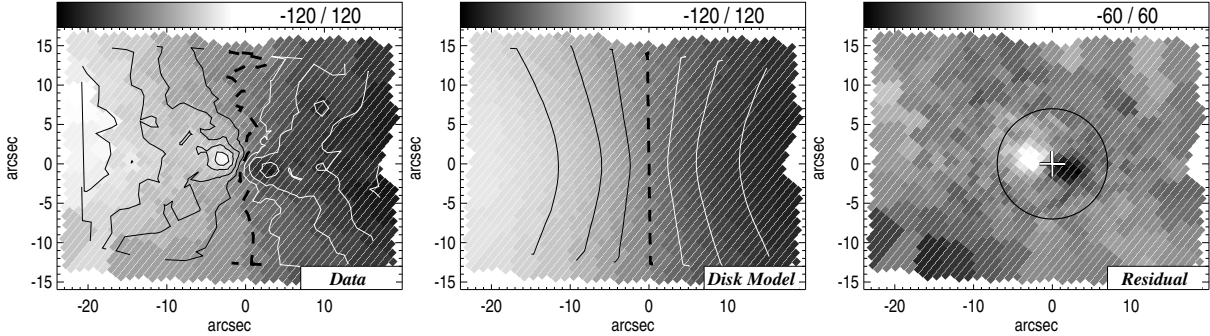


FIGURE 3 — A thin isothermal disk model for the stellar velocity field of NGC 5448. The circle marks the $7''$ region within which we find a disk-like structure. The disk model, fitted to the field outside this region, implies for the outer disk a scale length of $18''$, $V_{\text{sys}} = 2002 \text{ km s}^{-1}$, and $\text{PA} = 91^\circ$. The orientation of the maps is the same as in Fig. 1. (See p. 252 for a color version of this figure.)

5 RESULTS

The gas velocity field decomposition of Section 3.2 provides the radial profiles for the primary disk parameters and the higher order harmonic terms. Assuming the inclination $i = 64^\circ$ from the RC3 catalog (de Vaucouleurs et al. 1991), we apply this method to our observed gas velocity field in an iterative manner by first varying the V_{sys} and PA. We then fix these parameter to their mean values and we proceed by deriving the V_{rot} and higher harmonic terms (see Fig. 2). We detect a varying zeroth harmonic term (V_{sys}) with variation amplitude up to 40 km s^{-1} in the central $10''$. We find a strong PA twist of about 30° in the central $10''$, and outside this radius the PA goes back to the central values. The circular velocity component c_1 rises steeply and peaks at $5''$ radius, followed by a very slow decline out to the outer radii. We find that the behavior of the s_1 term could be compared with the V_{sys} or the PA: the s_1 term changes sign at around $12''$, and at the same galactocentric radius, the V_{sys} and the PA change sign around their mean values. The s_1 exhibits amplitudes of the order of $0.2 c_1 \sin i$. The bottom row in Fig. 2 shows that, apart from the s_2 term, the higher harmonic terms significantly deviate from zero, and indeed account for the considerable deviation of the velocity field of NGC 5448 from pure rotation. In the following sections, we describe the distinct features that we find in our kinematic maps.

5.1 THE STELLAR COMPONENT

The SAURON flux map in Fig. 1 displays a smooth stellar distribution and the presence of prominent dust lanes to the south of the nucleus. The stellar kinematics shows a prominent regular disk-like rotation with a smaller inner stellar disk within the central $7''$ radius. The stellar velocity dispersion decreases towards the center, and at the location of the maximum line-of-sight velocities for the central structure, h_3 anti-correlates with V which supports the argument that the central component of NGC 5448 is a central disk. We approximate the stellar velocity field with that of an exponential thin disk (Freeman 1970) to emphasize the kinematic signatures of the central disk. Fig. 3 shows this simple inclined disk model, where the inner stellar disk rotates faster than the outer disk. The best-fit model for the outer stellar disk, omitting the central $7''$ and assuming an inclination fixed to the RC3 catalog value,

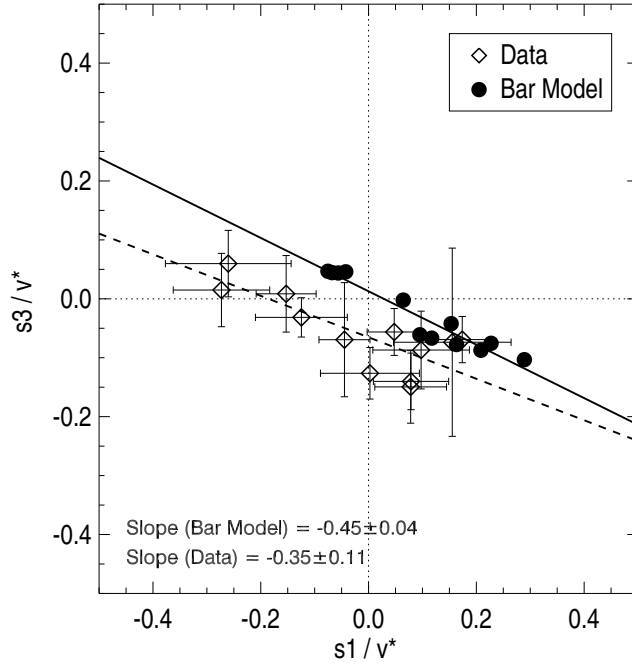


FIGURE 4 — First and third sinusoidal harmonic terms normalized to $v^* = c_1 \sin i$. Both the data and the bar model show a negative slope (dashed and solid line respectively), indicating that elliptical streaming, due to the bar potential, is the main driver of the radial motions observed in the gas velocity field of NGC 5448.

yields $V_{\text{sys}} = 2002 \text{ km s}^{-1}$, a disk scale length $18''$, and a disk $\text{PA} = 91^\circ$. Repeating the same exercise for the region inside $7''$, we find that the central disk is misaligned with respect to the outer disk by $\sim 13^\circ$.

5.2 GAS DISTRIBUTION AND KINEMATICS

Fig. 1 demonstrates that along the strong dust lanes, the gas shows a patchy distribution, with an asymmetric elongation of [O III] gas towards the east as well as the galactic poles. The $\text{H}\beta$ distribution is more regular. All kinematic features of the [O III] gas are accompanied by $\text{H}\beta$ emitting gas. The [O III]/ $\text{H}\beta$ map in Fig. 1 displays a prominent ring-like structure at $5''$ – $15''$, indicating high ionization of the gas in this region.

The gas velocity map clearly shows very prominent ‘S’-shaped zero-velocity curve with very sharp edges indicating very strong non-circular gas motions (Peterson & Huntley 1980). This ‘S’-shaped gaseous zero-velocity curve is confirmed by the PA variation derived by the tilted-ring decomposition in Fig. 2. Zero-velocity curve twists can be indicative of strong radial motions, created by, e.g., interactions, mergers or elliptical streaming due to a barred potential. Wong (2000) distinguished differences between radial motion mechanisms by comparing the s_3 versus s_1 harmonic terms, and found that the behavior of s_3 versus s_1 is different between a bar model and a pure axisymmetric or warped model. As demonstrated in Wong et al. (2004, Fig. 5) the s_3 versus s_1 of a warped disk lie on a positive slope. Moreover in case of an externally triggered radial flow, the points in the s_3 versus s_1 graph should lie on a zero-slope. Setting up the same diagnostics, in Fig. 4, we find that for our data the s_3 versus s_1 curve has a negative slope very similar to that of the bar model presented in Fig. 2. This confirms the signature of elliptical streaming in the gas velocity field of NGC 5448.

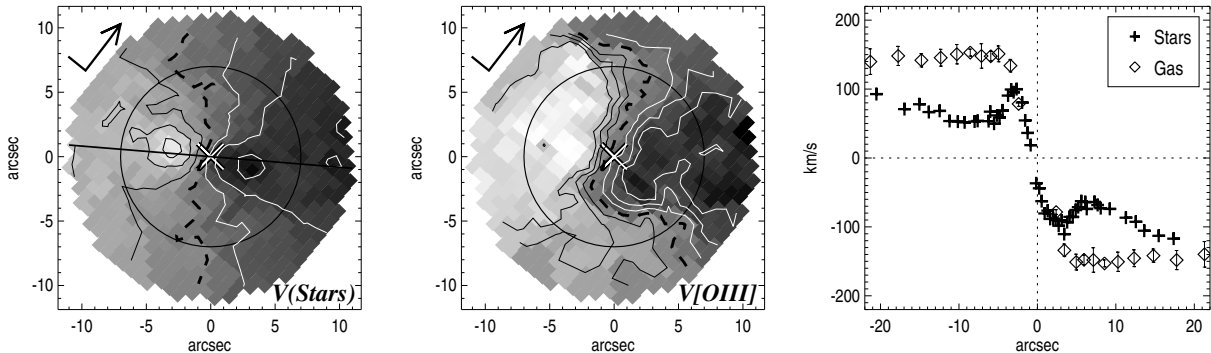


FIGURE 5 — Zooming into the central few arcseconds of the stellar and gaseous velocity maps of NGC 5448, using the same velocity range as in Fig. 1. Indicated are the north-east direction (arrow), the photometric PA (straight line) and the photometric center (cross). The over-plotted circle indicates the $7''$ radius for comparison with Fig. 3. In the right panel, we present the stellar rotation curve (extracted along the photometric PA) together with the gas rotation curve derived from tilted-ring decomposition. (See p. 253 for a color version of this figure.)

Comparing the stellar maps with the gas maps, we find that the gas velocities are considerably higher: This is confirmed by the rotation curve presented in Fig. 5. We find that the gaseous σ map displays some features comparable to the stellar σ map. Although the stellar velocity dispersion is more steeply rising toward the center, both maps show a prominent dip in the center. This supports the hypothesis of the presence of a central dynamically cold disk-like structure, present both in the stellar and gaseous component. Both maps also show a dispersion increase in bi-polar directions just a few arcseconds from the center. This is much more prominent in the gas map, as its σ reaches values $\simeq 250 \text{ km s}^{-1}$. This may be indicative of significant outflows in this AGN host.

5.3 POSITION ANGLE VALUES

The projected and deprojected PA profiles from Laine et al. (2002) in Fig. 6 display strong variations in the central few arcseconds. The HST images display asymmetrically distributed dust within the central few arcseconds, which may cause these strong central PA variations (also found by Kornreich et al. 2001). At larger radii, we find that the PA profile shows a variation of the order of 10° , but overall it stays fairly constant around the nominal RC3 value, i.e. 115° . Our tilted-ring decomposition of the gaseous velocity field, yields a mean gas kinematic PA of $119 \pm 5^\circ$, which is consistent with the photometric PA from RC3. In the case of the large stellar disk, as described in Section 5.1, we find an offset of $\sim 25^\circ$ between the stellar kinematic PA and the photometric mean PAs. This misalignment could be due to the effect of the bar on the observed stellar velocity field.

5.4 THE INNER FEW ARCSECONDS

In Fig. 5 we zoom into the central few arcseconds of the stellar and the gaseous velocity fields of NGC 5448 to emphasize the observed kinematic differences between the two components. The gaseous component exhibits a strongly twisting (dashed) zero-velocity curve, and the gas rotates faster than the stars. We find that the inner stellar disk not only is misaligned with the outer stellar disk, but is also slightly

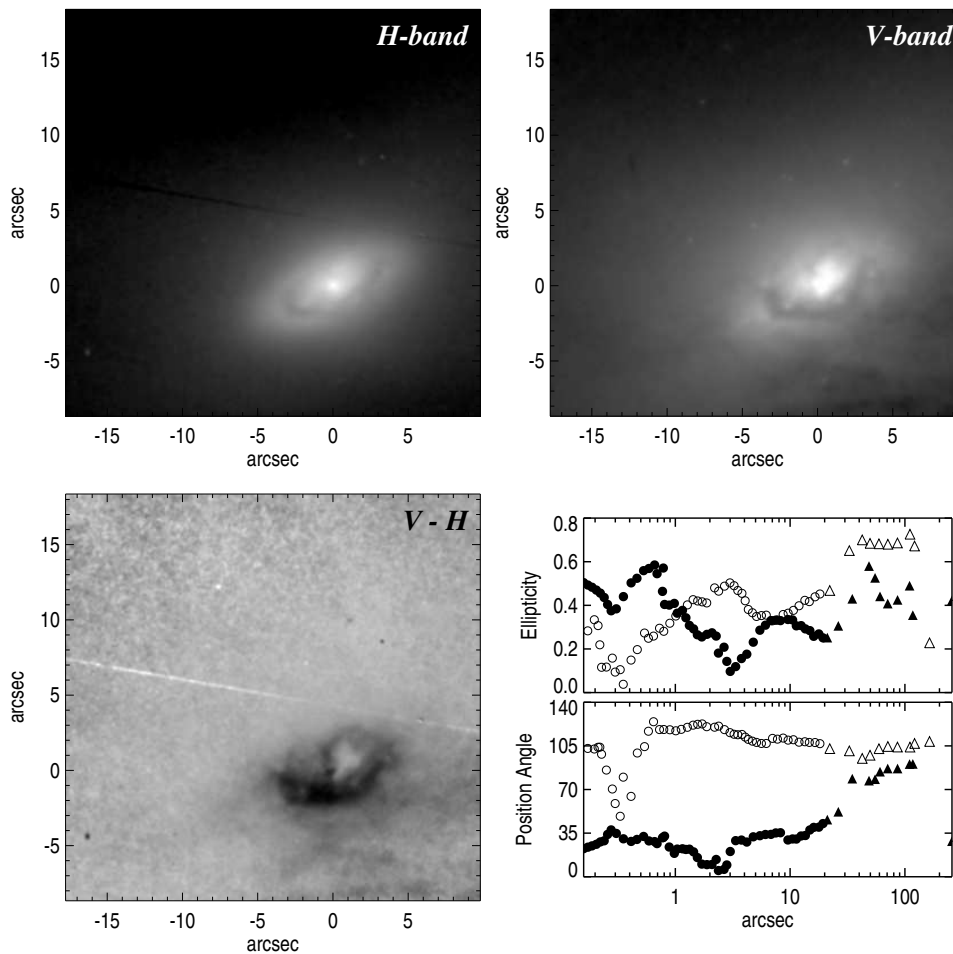


FIGURE 6 — The top panels show *HST/NICMOS H-band (F160W)* and *WFPC2 V-band (F606W)* images of NGC 5448. The bottom left panel is the $V - H$ map obtained by convolving the *H-band* image with the *V-band* image PSF and vice versa, and subtracting one from the other. All maps have pixel-size of $0''.0455$, and the same orientation as the *DSS* image. The bottom right profiles are the observed (open symbols) and deprojected (filled symbols) ellipticity and PA profiles from Laine et al. (2002). Circles represent values derived from the *NICMOS* image, and triangles show the values derived using the *DSS* image. Here we focus on the region beyond $1''$.

shifted to the south-east. In contrast, we find from the photometric profiles in Fig. 6, that the ellipticity of the central disk is similar to that of the outer disk (~ 0.55), as well as their PAs. The prominent dust lanes at the south of this galaxy may explain the kinematic misalignment between the outer and inner stellar disks. In the central $\sim 4''$ the gas isovelocity contours are comparatively straight and parallel. The tilted-ring decomposition of the gas velocity field provides the gas rotation curve illustrated in Fig. 5. The gas rotates about 70 km s^{-1} faster than the stars outside $\sim 4''$, with some indication that outside this radius the negative velocities reach lower values than the positive line-of-sight velocities. This asymmetry could be caused by complex dust distribution or attributed to a signature of lopsidedness.

5.5 DUST EFFECTS OR LOPSIDEDNESS?

Although the unsharp-masked SAURON image shows strong signature of dust-lanes in the region south of the nucleus, the central dust distribution is easier to study when

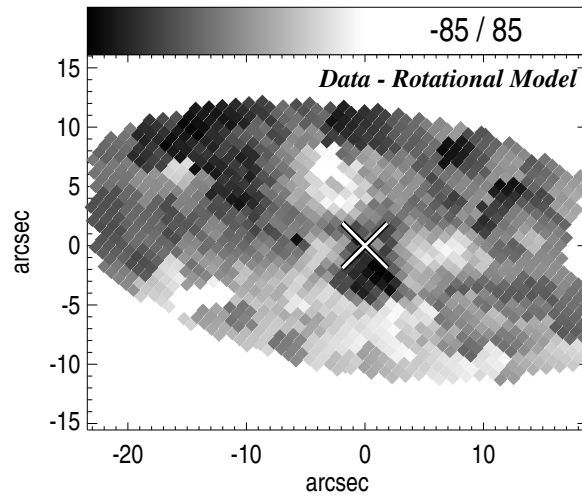


FIGURE 7 — Residual field after subtracting the best-fit rotational model from the observed gas velocity field. This map reveals the strong non-circular motions in NGC 5448, however, no ring-like feature is found.

looking at the HST images and the $V - H$ color map in Fig. 6. The color map shows a strong dust lane about $1''$ at the south-east of the galaxy nucleus as well as an asymmetrically distributed overall dust distribution. The larger scale WFPC2 image shows that this central dust lane is accompanied by several other dust lanes further away from the nucleus. Using the Galactic extinction law of Rieke & Lebofsky (1985), the HST images yield an average extinction value of $A_V \simeq 0.5$ over the central $3''$, with a maximum value of 1.5. The extinction increases significantly towards the center, with a prominent peak a few arcseconds south of the nucleus (see Fig. 6).

Some of the observational effects of the asymmetrical dust distribution could be interpreted as signatures of lopsidedness. Lopsidedness in galaxies has been investigated by e.g., Baldwin, Lynden-Bell & Sancisi (1980) and Swaters et al. (1999). The amplitude of this effect may depend on galactocentric radius, and viewed from different viewing angles will produce different signatures in the observed velocity field. These studies have shown that the residuals are dominated by the zeroth harmonic term for viewing angle of 90° , and by the second harmonic term for viewing angle of 0° . In the special case of radius-dependent lopsidedness $c_0 \sim 3c_2$. NGC 5448 has a large inclination, thus the zeroth term dominates, and we find no correlation between the c_0 and the c_2 terms. Our harmonic decomposition results display strongly varying zeroth and second terms. This was shown by SFdZ to be a possible indication of an $m = 1$ perturbation, i.e. lopsidedness (c.f., Fig 2. in SFdZ). In this case, subtracting the rotational component from the perturbed velocity field, one should find a ring-like feature. In Fig. 7, we present this residual field for NGC 5448 and find no ring-like feature. Therefore, not lopsidedness, but dust is most likely the cause for the asymmetric features that we observe in NGC 5448.

5.6 THE LARGE-SCALE BAR

In Fig 2, we find that the harmonic parameters derived from the data are consistent with the bar model outlined in Section 4. Our simple model is limited to an $m = 2$ perturbation. Complicated flow patterns in bars studied by, e.g., Lindblad (1999), imply a significant contribution from $m = 4$ and higher-order modes. The third harmonic

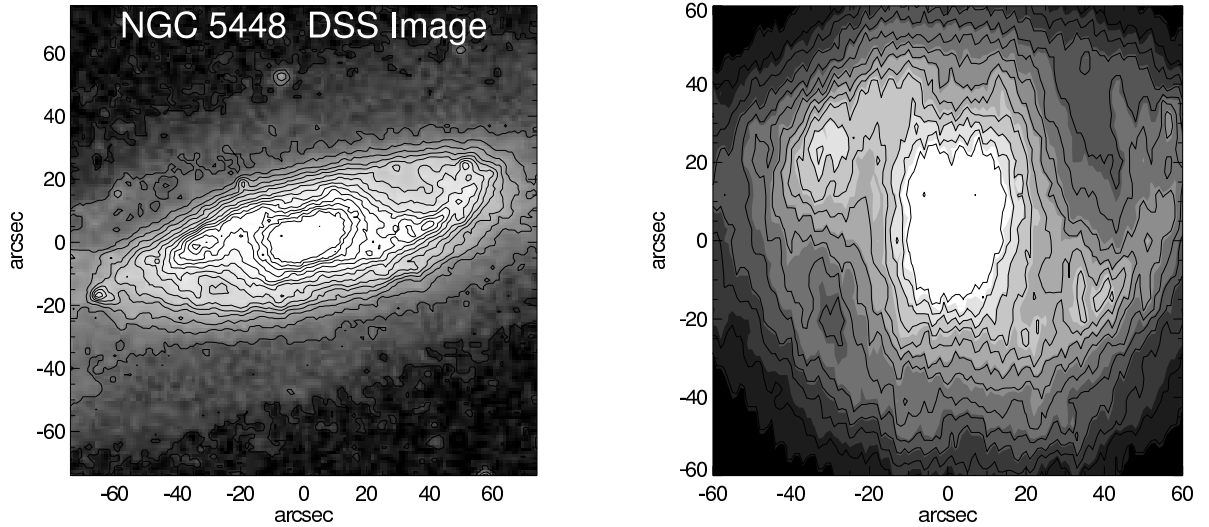


FIGURE 8 — Observed (left) and deprojected (right) DSS image of NGC 5448. The inclination of 64° and PA of 115° from the RC3 catalog have been used to deproject the image according to the two-dimensional deprojection of a circular thin disk.

terms are also influenced by $m = 4$, which could explain the differences between our model bar and the data for these parameters, but a detailed model is beyond the scope of the current analysis.

We now compare the modeled bar with the deprojected Digitized Sky Survey (DSS) image. The inclination from the RC3 and the PA from our tilted-ring model were used to deproject the DSS image in a simple way by assuming that the galaxy disk is thin. The outer spiral arms are clearly emphasized in the deprojected DSS image (Fig. 8).

It is somewhat difficult to identify the size of the large-scale bar from the image. From our bar model we find a CR of about $37''$. In practice, this is done by assuming that at CR the circular frequency of the axisymmetric potential is identical to bar angular frequency. According to this definition and since we use a flat rotation curve, the ILR is located at $1 - 1/\sqrt{2}$ of the CR, i.e., at about $11''$. If we assume that the bar in NGC 5448 ends close to the starting point of the spiral arms (Sanders & Huntley 1976), we can associate its CR with the inner radius of the arms. Fig. 8 shows that our analytic bar model is of reasonable size. The assumed CR radius is confirmed by the ellipticity profile presented in Fig. 6, since the high ellipticity plateau starts at around this radius. At around the ILR (i.e., $11''$), there is a good agreement between the s_1 profiles from the data and the model, with in both cases a change in sign at the ILR.

6 DISCUSSION AND CONCLUSIONS

We have used linear theory to construct a bar model ($m = 2$ mode) for NGC 5448. The best-fit model considers the effects of a single weak bar with a potential ellipticity $\varepsilon = 0.15$ and a damping amplitude of $\lambda = 0.12$. We compare the harmonic terms of the model with those derived from the data and find an overall consistency (see Fig. 2). Using this model, we have been able to associate the radial motion of gas with that of the large-scale bar (see Fig. 4).

NGC 5448 exhibits clear signatures of the presence of other components than a single bar, which affect the observed velocity field. Inspecting the photometry and

the central parts of the gaseous and stellar velocity field, we have detected a central rotating disk-like stellar component embedded in the larger disk (see Fig. 3). The WFPC2 image shows one very sharp dust lane $1''$ from the center of this galaxy. This image also shows three more fuzzy and almost parallel dust lanes further out in the south-east direction. The dusty center is also apparent in the $V - H$ image in Fig. 6. Dust is inhomogeneously distributed and continues down to the very bright nucleus. Light from the central light source is absorbed by the dust asymmetrically and the center appears to be located at the north-west of its actual position.

Investigating the projected and deprojected ellipticity profiles derived from the H -band data from Laine et al. (2002) confirms the presence of a central disk in the inner $7''$. Although the projected ellipticity profile decreases at $\sim 4''$ and outwards, we cannot pin down the exact size of the central disk. The observed ellipticity decrease could be partly caused by the strongly asymmetric dust distribution. The stellar kinematic maps show that the central disk rotates faster than the main disk, and our observed gas distribution and kinematics indicate that this central disk also hosts gas which rotates faster than its stellar counterpart. This is not unexpected, since due to its dissipative nature, the gas is not slowed down by asymmetric drift. It is important to note that, in NGC 5448, the gas velocities are well ordered but larger in magnitude than the stellar velocities. However, Fig. 5 indicates that this velocity difference dies out at larger radii. The difference between the stellar and gas velocities can be easily explained as due to the fact that the stars are in a thicker structure (bulge) in the central regions, while at larger radii both the gas and the stars are in a flatter disk, and both move closer to the circular velocity.

It is known that bars are efficient in transferring mass towards the inner regions of their host galaxies. The centrally concentrated matter may be able to form a central disk (Yuan & Yen 2004), or an inner bar (e.g., Maciejewski & Sparke 2000, Englmaier & Shlosman 2004). Our analysis has shown that the non-circular gas kinematics in NGC 5448 could be driven by the large-scale bar. The central disk could then have been formed as a result of the gas accumulation at the center.

To conclude, we have been able to analytically model the bar signatures in the AGN host NGC 5448. We have unveiled a central disk, and have distinguished the effects of a lopsided perturbation from strong dust features. NGC 5448 hosts considerable amounts of dust which is asymmetrically distributed all the way to the center, resembling the ‘Evil Eye’ galaxy (Braun, Walterbos & Kennicutt 1992). This study shows the power of the harmonic decomposition formalism to quantify non-circular motions in observed velocity fields, and we plan to apply this approach to the full set of Sa galaxies observed with SAURON.

ACKNOWLEDGMENTS

It is a pleasure to acknowledge the entire SAURON team for their efforts in carrying out the observations and data preparation, for lively interactions and many fruitful discussions. The SAURON project is made possible through grants 614.13.003 and 781.74.203 from ASTRON/NWO and financial contributions from the Institut National des Sciences de l’Univers, the Université Claude Bernard Lyon I, the universities of Durham and Leiden, the British Council, PPARC grant ‘Extragalactic Astronomy & Cosmology at Durham 1998–2002’, and the Netherlands Research School for Astronomy NOVA. Jesús Falcón-Barroso acknowledges support from the Euro3D

Research Training Network. Kambiz Fathi acknowledges support for Proposal number HST-GO 09782.01 provided by NASA through a grant from the STScI, which is operated by the Association of Universities for Research in Astronomy, Incorporated, under NASA contract NAS5-26555. Kambiz Fathi is also grateful to Isaac Shlosman for stimulating and insightful discussions. Finally, we thank the referee for constructive comments which improved the manuscript.

REFERENCES

- Adam, G., Bacon, R., Courtes, G., Georgelin, Y., Monnet, G., Pecontal, E. 1989, *A&A* L, 208, 15
Afanasiev, V.L., Dodonov, S.N., Sil'chenko, O.K., Vlasyuk, V.V. 1990, SAO preprint, N54
Athanasoula, E. 1994, in *Mass-Transfer Induced Activity in Galaxies*, ed. I. Shlosman, Cambridge University Press, p.143
Bacon, R. et al. 1995, *A&AS*, 113, 347
Bacon, R. et al. 2001, *MNRAS*, 326, 23
Baldwin, J. E., Lynden-Bell, D., Sancisi, R. 1980, *MNRAS*, 193, 313
Begeman, K. G. 1987, PhD Thesis, University of Groningen
Bershady, M. A., Andersen, D. R., Harker, J., Ramsey, L. W., Verheijen, M. A. W. 2004, *PASP*, 116, 565
Braun, R., Walterbos, R. A. M., Kennicutt, R. C., Jr. 1992, *Nature*, 360, 442
Burlak, A. N., Zasov, A. V., Fridman, A. M., Khoruzhi, O. V. 2000, *AstL*, 26, 809
Canzian, B., 1993, *ApJ*, 414.617
Cappellari, M., Copin, Y. 2003, *MNRAS*, 342, 345
Cappellari, M., Emsellem, E. 2004, *PASP*, 116, 138
Carollo, C. M., Stiavelli, M., Seigar, M., de Zeeuw, P. T., Dejonghe, H. 2002, *AJ*, 123, 159
Combes, F., Gerin, M. 1985, *A&A*, 150, 327
Davies, R. L. et al. 1997, *SPIE*, 2871, 1099
de Vaucouleurs, G., de Vaucouleurs, A., Corwin, H. G., Buta, R. J., Paturel, G., Fouque, P. 1991: *Third Reference Catalogue of Bright Galaxies*, Springer-Verlag, New York
de Zeeuw, P. T. et al. 2002, *MNRAS*, 329, 513
Emsellem, E., Goudfrooij, P., Ferruit, P. 2003, *MNRAS*, 345, 1297
Emsellem, E. et al. 2004, *MNRAS*, 352, 721
Emsellem, E. et al. 2005, *MNRAS*, submitted
Eskridge, P. B. et al. 2002, *ApJS*, 143, 73
Englmaier, P., Shlosman, I. 2004, *ApJ*, 617, 105
Falcón-Barroso, J. et al. 2005, *MNRAS*, submitted
Fathi, K., Peletier, R. F. 2003, *A&A*, 407, 61
Fathi, K. 2004, PhD Thesis, University of Groningen
Freeman, K. C. 1965, *MNRAS*, 130, 183
Freeman, K. C. 1970, *ApJ*, 160, 811
Fridman, A. M., Khoruzhii, O. V. 2003, *SSRv*, 105, 1
García-Lorenzo, B., Arribas, S., Mediavilla, E. 2000, *INGN*, 3, 25
Gerhard O. E., 1993, *MNRAS*, 265, 213
Ho, L. C., Filippenko, A. V., Sargent, W. L. 1995, *ApJS*, 98, 477
Jones, L. A. 1997, PhD Thesis, University of North Carolina, Chapel Hill
Knapen, J. H., Shlosman, I., Heller, C. H., Rand, R. J., Beckman, J. E., Rozas, M. 2000, *ApJ*, 528, 219
Kornreich, D. A., Haynes, M. P., Jore, K. P., Lovelace, R. V. E. 2001, *AJ*, 121, 1358
Krajnović, D. et al. 2005, *MNRAS*, submitted
Kuijken, K., Tremaine, S. 1994, *ApJ*, 421, 178
Laine, S., Shlosman, I., Knapen, J. H., Peletier, R. F. 2002, *ApJ*, 567, 97
Lin, C. C., Shu, F. H. 1964, *ApJ*, 140, 646
Lindblad, P. O., Lindblad, P. A. B. 1994, in *Physics of the Gaseous and Stellar Disks of the Galaxy*, ASP Conf. Ser. 66, ed. I.R. King, p. 29

- Lindblad, P. O. 1999, *A&ARv*, 9, 221
- Maciejewski, W., Sparke, L. S. 2000, *MNRAS*, 313, 745
- Martinet, L., Friedli, D. 1997, *A&A*, 323, 363
- Moiseev, A. V. 2000, *A&A*, 363, 843
- Mosteller, F., Tukey, J. 1977, *Data Analysis and Regression*, Addison-Wesley
- Ohtani, H. 1995, in *Tridimensional Optical Spectroscopic Methods in Astrophysics*, ASP Conf. Ser., 71, eds. G. Comte, M. Marcelin, p. 149
- Peterson, C. J., Huntley, J. M. 1980, *ApJ*, 242, 913
- Plana, H., Boulesteix, J. 1996, *IAUS*, 171, 432
- Regan, M. W., Teuben, P. J. 2004, *ApJ*, 600, 595
- Rieke G. H., Lebofsky M. J., 1985, *ApJ*, 288, 618
- Rogstad, D. H., Lockart, I. A., Wright, M. C. H. 1974, *ApJ*, 193, 309
- Rogstad, D. H., Wright, M. C. H., Lockart, I. A. 1976, *ApJ*, 204, 703
- Roth, M. M., Laux, U., Heilemann, W. 2000, *SPIE*, 4008, 485
- Sakamoto, K. Baker, A. J., Scoville, N. Z. 2000, *ApJ*, 533, 149
- Sakhibov, F. K., Smirnov, M. A. 1989, *AZh*, 66, 921
- Sandage, A., Bedke, J. 1994, *The Carnegie atlas of galaxies*, Washington, DC: Carnegie Institute of Washington
- Sanders, R. H., Huntley, J. M. 1976, *ApJ*, 209, 53
- Sarzi, M. et al. 2005, *MNRAS*, submitted
- Simkin, S. M., Su, H. J., Schwarz, M. P. 1980, *ApJ*, 237, 404
- Shlosman, I., Frank, J., Begelman, M. 1989, *Nature*, 338, 45
- Shlosman, I., Noguchi, M. 1993, *ApJ*, 414, 474
- Shlosman, I. 1999, in *The Evolution of Galaxies on Cosmological Timescales*, ASP Conf. Ser. 187, eds. J. E. Beckman, T. J. Mahoney, p.100
- Schoenmakers, R. H. M., Franx, M., de Zeeuw, P. T. 1997, *MNRAS*, 292, 349 [SFdZ]
- Schoenmakers, R. H. M. 1999, PhD Thesis, University of Groningen
- Statler, T. 1994, *ApJ*, 425, 500
- Swaters, R. A., Schoenmakers, R. H. M., Sancisi, R., van Albada, T. S. 1999, *MNRAS*, 304, 330
- Thielheim, K. O., Wolff, H. 1982, *MNRAS*, 199, 151
- van der Hulst, J. M., Terlouw, J. P., Begeman, K. G., Zwitter, W., Roelfsema, P. R. 1992, in *Astronomical Data Analysis Software and Systems I*, ASP Conf. Ser. 25, eds. D. M. Worrall, C. Biemesderfer, J. Barnes, p.131
- van der Kruit, P. C., Allen, R. J. 1978, *ARA&A*, 16, 103
- van der Marel R. P., Franx M., 1993, *ApJ*, 407, 525
- van Gorkom, J. H., Knapp, G. R., Raimond, E., Faber, S. M., Gallagher, J. S. 1986, *AJ*, 91, 791
- Vazdekis, A. 1999, *ApJ*, 513, 224
- Wada, K. 1994, *PASJ*, 46, 165
- Warner, P. J., Wright, M. C. H., Baldwin, J. E. 1973, *MNRAS*, 163, 163
- Wong, T. 2000, PhD Thesis, University of California, Berkeley
- Wong, T., Blitz, L., Bosma, A. 2004, *ApJ*, 605, 183
- Yuan, C., Yen, D. C. C. 2004, in *Penetrating Bars Through Masks of Cosmic Dust*, *A&S Sci. Lib.* vol. 319, eds. D. Block, I. Puerari, K. C. Freeman, R. Groess, E. K. Block

CHAPTER 4

RECOVERY OF THREE-INTEGRAL GALAXY MODELS

ABSTRACT

We construct axisymmetric and triaxial galaxy models with a phase-space distribution function that depends on linear combinations of the three exact integrals of motion for a separable potential. These Abel models, first introduced by Dejonghe & Laurent and subsequently extended by Mathieu & Dejonghe, are the axisymmetric and triaxial generalizations of the well-known spherical Osipkov–Merritt models. Their density and higher velocity moments can be calculated efficiently and we show that they capture much of the rich internal dynamics of early-type galaxies. We use these models to mimic the high-quality two-dimensional kinematic observations that are obtained with integral-field spectrographs such as SAURON. We fit the simulated observations with axisymmetric and triaxial dynamical models obtained with our numerical implementation of Schwarzschild’s orbit-superposition method, while varying the viewing direction and the mass-to-light ratio. We find that Schwarzschild’s method is able to recover the internal dynamical structure of early-type galaxies and to accurately determine the mass-to-light ratio, but additional information is needed to constrain better the viewing direction.

1 INTRODUCTION

THE equilibrium state of a collisionless stellar system such as an elliptical or lenticular galaxy is completely described by its distribution function (DF) in the six-dimensional phase space of positions and velocities. The recovery of the DF from observations is difficult, as for galaxies other than our own, we can usually only measure the projected surface brightness and the line-of-sight velocity distribution of the integrated light as a function of position on the plane of the sky. Moreover, we generally do not know the intrinsic shape of the galaxy, nor the viewing direction, or the contribution to the gravitational potential provided by a supermassive central black hole and/or an extended halo of dark matter. By Jeans (1915) theorem, the DF is a function of the isolating integrals of motion admitted by the potential, but it is not evident how to take advantage of this property other than for the limiting case of spherical systems. Orbits in axisymmetric geometry have two exact integrals of motion, the energy E and the angular momentum component L_z parallel to the symmetry axis, but the third effective or non-classical integral I_3 obeyed by all regular orbits is generally not known in closed form. In stationary triaxial geometry E is conserved, but regular orbits now have two additional effective integrals of motion, I_2 and I_3 , which are not known explicitly.

Schwarzschild (1979, 1982) devised a numerical method which sidesteps our ignorance about the non-classical integrals of motion. It allows for an arbitrary gravitational potential, which may include contributions from dark components, integrates the equations of motion for a representative library of orbits, computes the density distribution of each orbit, and then determines the orbital weights such that the combined orbital densities reproduce the density of the system. The best-fitting orbital weights represent the DF (cf. Vandervoort 1984). Pfenniger (1984) and Richstone & Tremaine (1984) included kinematic moments in this method, and Rix et al. (1997) showed how to include the line-of-sight velocity profiles. A number of groups have developed independent numerical implementations of Schwarzschild's method for axisymmetric geometry which fit the projected surface brightness and line-of-sight velocity distributions of early-type galaxies in detail (van der Marel et al. 1998; Cretton et al. 1999; Gebhardt et al. 2000, Cappellari et al. 2002; Valluri, Merritt & Emsellem 2004; Thomas et al. 2004). Applications include the determination of central black hole masses (see also van der Marel et al. 1997; Cretton & van den Bosch 1999; Verolme et al. 2002; Gebhardt et al. 2003; Copin, Cretton & Emsellem 2004), very accurate global dynamical mass-to-light ratios (Cappellari et al. 2005), as well as dark matter profiles as a function of radius (Cretton, Rix & de Zeeuw 2000; Thomas et al. 2005), and recovery of the DF (Krajnović et al. 2005). Finally, van de Ven et al. (2005) included proper motion measurements in order to model nearby globular clusters, and Verolme et al. (2003) and van den Bosch et al. (2006) describe an extension to triaxial geometry that includes all line-of-sight kinematics.

Although Schwarzschild models have significantly increased our understanding of the dynamical structure and evolution of early-type galaxies, questions remain about the uniqueness and the accuracy with which they are able to recover the global parameters as well as the internal dynamics of these galaxies. Many tests have been done to establish how the axisymmetric code recovers known input models, but these generally have been limited to spherical geometry or to an input axisymmetric DF that is a function of E and L_z only (van der Marel et al. 1998; Cretton et al. 1999;

Verolme & de Zeeuw 2002; Valluri et al. 2004; Cretton & Emsellem 2004; Thomas et al. 2004; Krajnović et al. 2005). The code for triaxial geometry so far has been tested for densities consistent with a DF that depends on E only.

One could construct a numerical galaxy model with Schwarzschild’s method itself, compute the observables, and then use these as input for the code and determine how well it recovers the input model. This is useful, but does not provide a fully independent test of the software. An alternative is to consider the special family of models with gravitational potential of Stäckel form, for which all three integrals of motion are exact and known explicitly. The potentials of these models have a core rather than a central cusp, so the models cannot include a central black hole, and are inadequate for describing galactic nuclei. However, they can be constructed for a large range of axis ratios (Statler 1987), and their observed kinematic properties are as rich as those seen in the main body of early-type galaxies (Statler 1991, 1994; Arnold, de Zeeuw & Hunter 1994).

A small number of analytic DFs have been constructed for triaxial separable models. The ‘thin-orbit’ models (Hunter & de Zeeuw 1992) have the maximum possible streaming motions, but their DF contains delta functions, and they are therefore not particularly useful for a test of general-purpose numerical machinery. Dejonghe & Laurent (1991, hereafter DL91) constructed separable triaxial models in which the DF depends on a single parameter $S = E + wI_2 + uI_3$, which is a linear combination of the three exact integrals E , I_2 and I_3 admitted by these potentials, and is quadratic in the velocity components. For a given radial density profile, the DF follows by simple inversion of an Abel integral equation. These so-called Abel models have no net mean streaming motions, and are the axisymmetric and triaxial generalizations of the well-known spherical Osipkov–Merritt models (Osipkov 1979; Merritt 1985), for which the observables can be calculated easily (Carollo, de Zeeuw & van der Marel 1995). Mathieu & Dejonghe (1999, hereafter MD99) generalized the results of DL91 by including two families of DF components with net internal mean motions around the long and the short axis, respectively, and compared the resulting models with observations of Centaurus A. Although the Abel character of the non-rotating components is no longer conserved, the expressions for the velocity moments in these more general models can still be evaluated in a straightforward way. When the entire DF depends on the same single variable S the famous ellipsoidal hypothesis (e.g., Eddington 1915; Chandrasekhar 1940) applies, so that self-consistency is only possible in the spherical case (Eddington 1916; Camm 1941). This does not hold for Abel models with a DF that is a sum of components for which the variable S has different values of the parameters w and u . Such multi-component Abel models can provide (nearly) self-consistent models with a large variety of shapes and dynamics.

Here, we construct axisymmetric and triaxial Abel models to test our numerical implementation of Schwarzschild’s method. We assume a convenient form for the gravitational potential, and construct the DF that reproduces a realistic surface brightness distribution. We compute the resulting intrinsic moments of the models, and then derive two-dimensional maps of the observed kinematics. We show that, despite the simple form of the DF, these models display the large variety of features observed in early-type galaxies with integral-field spectrographs such as SAURON (Emsellem et al. 2004). We fit axisymmetric and triaxial Schwarzschild dynamical models to the resulting simulated observables to investigate the accuracy of the recovery of the internal dynamics and the DF, and determine how well the intrinsic shape, orientation

and mass-to-light ratio are constrained. The oblate limiting case provides a new and convenient three-integral test for the axisymmetric code. We find that Schwarzschild's method is able to recover the internal dynamical structure of early-type galaxies and is able to accurately measure the mass-to-light ratio, but the viewing angles are only weakly constrained.

This chapter is organized as follows. In Section 2 we summarize the properties of the triaxial Abel models of DL91 and MD99 in a form which facilitates their numerical implementation. In Section 3 we describe the conversion to observables, and in Section 4 we construct a specific triaxial galaxy model. In Section 5 we consider the axisymmetric limit and construct a three-integral oblate galaxy model. In Section 6 and 7 we fit the observables of both Abel models with our numerical Schwarzschild models, and investigate how well the intrinsic moments and three-integral DF as well as the values of the global parameters are recovered. We summarize our conclusions in Section 8. In Appendix A we describe the simpler Abel models for the elliptic disk, large distance and spherical limit, and link them to the classical Osipkov–Merritt solutions for spheres. Readers who are mainly interested in the tests of the Schwarzschild method may skip Sections 2–5 on the first reading.

2 TRIAXIAL ABEL MODELS

The triaxial Abel models introduced by DL91 have gravitational potentials of Stäckel form, for which the equations of motion separate in confocal ellipsoidal coordinates. We briefly describe these potentials, and refer for further details to de Zeeuw (1985a). We then make a specific choice for the DF, for which the velocity moments simplify.

2.1 STÄCKEL POTENTIALS

We define confocal ellipsoidal coordinates (λ, μ, ν) as the three roots for τ of

$$\frac{x^2}{\tau + \alpha} + \frac{y^2}{\tau + \beta} + \frac{z^2}{\tau + \gamma} = 1, \quad (2.1)$$

with (x, y, z) the usual Cartesian coordinates, and with constants α, β and γ such that $-\gamma \leq \nu \leq -\beta \leq \mu \leq -\alpha \leq \lambda$. From the inverse relations

$$x^2 = \frac{(\lambda + \alpha)(\mu + \alpha)(\nu + \alpha)}{(\alpha - \beta)(\alpha - \gamma)}, \quad (2.2)$$

and similarly for y^2 and z^2 by cyclic permutation of $\alpha \rightarrow \beta \rightarrow \gamma \rightarrow \alpha$, it follows that a combination (λ, μ, ν) generally corresponds to eight different points $(\pm x, \pm y, \pm z)$. In these coordinates, the Stäckel potentials have the following form (Weinacht 1924)

$$V_S(\lambda, \mu, \nu) = \frac{U(\lambda)}{(\lambda - \mu)(\lambda - \nu)} + \frac{U(\mu)}{(\mu - \nu)(\mu - \lambda)} + \frac{U(\nu)}{(\nu - \lambda)(\nu - \mu)}, \quad (2.3)$$

where $U(\tau)$ is an arbitrary smooth function ($\tau = \lambda, \mu, \nu$). The right-hand side of eq. (2.3) can be recognized as the second order divided difference of $U(\tau)$. Henceforth, we denote it with the customary expression $U[\lambda, \mu, \nu]$, which is symmetric in its arguments (see Hunter & de Zeeuw 1992, eqs 2.1–2.3, 2.13 and 2.14). Addition of an arbitrary linear function of τ to $U(\tau)$ does not change V_S .

The density ρ_S that corresponds to V_S can be found from Poisson's equation

$$4\pi G\rho_S(\lambda, \mu, \nu) = \nabla^2 V_S(\lambda, \mu, \nu), \quad (2.4)$$

or alternatively by application of Kuzmin's (1973) formula (see de Zeeuw 1985b). This formula shows that, once we have chosen the confocal coordinate system and the density along the short axis, the mass model is fixed everywhere by the requirement of separability¹. For centrally concentrated mass models, V_S has the x -axis as long-axis and the z -axis as short-axis. In most cases this is also true for the associated density (de Zeeuw, Peletier & Franx 1986).

2.2 ORBITAL STRUCTURE

The Hamilton-Jacobi equation separates in (λ, μ, ν) for the potentials (2.3), so that every orbit has three exact integrals of motion (cf. de Zeeuw & Lynden-Bell 1985)

$$\begin{aligned} E &= \frac{1}{2}(v_x^2 + v_y^2 + v_z^2) + U[\lambda, \mu, \nu], \\ I_2 &= \frac{1}{2}TL_y^2 + \frac{1}{2}L_z^2 + \frac{1}{2}(\alpha - \beta)v_x^2 - (\beta - \alpha)x^2U[\lambda, \mu, \nu, -\alpha], \\ I_3 &= \frac{1}{2}L_x^2 + \frac{1}{2}(1 - T)L_y^2 + \frac{1}{2}(\gamma - \beta)v_z^2 + (\gamma - \beta)z^2U[\lambda, \mu, \nu, -\gamma], \end{aligned} \quad (2.5)$$

where v_x , v_y and v_z are the velocity components in the Cartesian coordinate system, and from $L_x = yv_z - zv_y$, the component of the angular momentum vector parallel to the x -axis, L_y and L_z follow by cyclic permutation of $x \rightarrow y \rightarrow z \rightarrow x$ and $v_x \rightarrow v_y \rightarrow v_z \rightarrow v_x$. Furthermore, T is a triaxiality parameter defined as

$$T = (\beta - \alpha)/(\gamma - \alpha), \quad (2.6)$$

and $U[\lambda, \mu, \nu, \sigma]$ is the third-order divided difference of $U(\tau)$. All models for which $U'''(\tau) > 0$, have similar orbital structure and support four families of regular orbits: boxes (B) with no net rotation, inner (I) and outer (O) long-axis tubes with net rotation around the x -axis, and short-axis (S) tubes with net rotation around the z -axis (Kuzmin 1973; de Zeeuw 1985a; Hunter & de Zeeuw 1992).

According to Jeans (1915) theorem the phase-space distribution function (DF) is a function $f(E, I_2, I_3)$ of the isolating integrals of motion (cf. Lynden-Bell 1962; Binney 1982). The velocity moments of the DF are defined as

$$\mu_{lmn}(\lambda, \mu, \nu) = \iiint v_\lambda^l v_\mu^m v_\nu^n f(E, I_2, I_3) dv_\lambda dv_\mu dv_\nu, \quad (2.7)$$

where l , m and n are non-negative integers, and v_λ , v_μ and v_ν are the velocity components in the confocal ellipsoidal coordinate system. Many of the velocity moments vanish due to the symmetry of the orbits in these coordinates. The zeroth-order velocity moment is the mass density that corresponds to the DF

$$\rho_\star(\lambda, \mu, \nu) = \mu_{000}(\lambda, \mu, \nu). \quad (2.8)$$

In self-consistent models, ρ_\star must equal ρ_S given in eq. (2.4), the mass density that is related to the potential V_S by Poisson's equation.

¹A third method for the calculation of the density is to use $\rho_S = H[\lambda, \lambda, \mu, \mu, \nu, \nu]$, where the fifth-order divided difference is of the function $H(\tau) = 4a(\tau)U'(\tau) - 2a'(\tau)U(\tau)$ with $a(\tau) = (\tau + \alpha)(\tau + \beta)(\tau + \gamma)$ and $U(\tau)$ defines the potential as in eq. (2.3). This result was obtained by Hunter in 1989 (priv. comm.), and by Mathieu & Dejonghe (1996). Similar expressions exist for the related families of potential-density pairs introduced in de Zeeuw & Pfenniger (1988).

2.3 ABEL DISTRIBUTION FUNCTION

Following DL91, we choose the DF to be a function of the three integrals of motion E , I_2 and I_3 as given in eq. (2.5) through one variable

$$f(E, I_2, I_3) = f(S), \quad \text{with} \quad S = -E + w I_2 + u I_3, \quad (2.9)$$

and w and u are two parameters². This choice for the DF is equivalent to the celebrated ellipsoidal hypothesis (e.g., Eddington 1915; Chandrasekhar 1940). Self-consistency is only possible in the spherical case (Eddington 1916; Camm 1941). On the other hand, these DFs can produce realistic (luminous) mass densities ρ_* , which differ from the (total) mass density ρ_S , as in galaxies with dark matter (but see § 3.4 below when we combine DFs of the form [2.9] with different values for w and u .)

DL91 and MD99 divided the DF into three types of components. The non-rotating (NR) type is made of box orbits and tube orbits with both senses of rotation populated equally. The two rotating types, LR and SR, consist of tube orbits, and have net rotation around either the long axis or the short axis.

2.3.1 Velocity moments

Due to the choice (2.9) of the DF, the general expression (2.7) for the velocity moments can be simplified, as shown by DL91 for the non-rotating component and by MD99 for the rotating components. We recast their results into a different form to facilitate the numerical implementation. The resulting velocity moments are given by

$$\mu_{lmn}(\lambda, \mu, \nu) = \sqrt{\frac{2^{l+m+n+3}}{H_{\mu\nu}^{l+1} H_{\nu\lambda}^{m+1} H_{\lambda\mu}^{n+1}}} \int_{S_{\min}}^{S_{\max}} T_{lmn} [S_{\text{top}}(\lambda, \mu, \nu) - S]^{(l+m+n+1)/2} f(S) dS, \quad (2.10)$$

and set to zero at positions for which $S_{\max} \leq S_{\min}$. The terms $H_{\mu\nu}$, $H_{\nu\lambda}$ and $H_{\lambda\mu}$ in the square root in front of the integral are defined as

$$H_{\sigma\tau} = 1 + \frac{(\sigma + \alpha)(\tau + \alpha)}{\gamma - \alpha} w + \frac{(\sigma + \gamma)(\tau + \gamma)}{\alpha - \gamma} u, \quad (2.11)$$

with $\sigma, \tau = \lambda, \mu, \nu$. Orbits are confined to the region of space for which all three terms are non-negative. In general, this condition will not be satisfied for all points, so that the Abel components have finite extent. From the requirement that at least the origin $(\lambda, \mu, \nu) = (-\alpha, -\beta, -\gamma)$ should be included, we find the following limits on w and u

$$w \geq -\frac{1}{\beta - \alpha} \quad \text{and} \quad u \leq \frac{1}{\gamma - \beta}. \quad (2.12)$$

The factor T_{lmn} in the integrand as well as the upper limit S_{\max} of the integral are different for each of the three Abel component types NR, LR and SR, and are discussed in §§ 2.3.2–2.3.4 below. The lower limit of the integral S_{\min} has to be at least as large as the smallest value possible for the variable S . This limiting value S_{lim} depends on the choice of the DF parameters w and u (eq. 2.9), as is shown in Fig. 2 (cf. Fig. 7 of DL91). The boundaries follow from (2.12) and the separatrices L_1 and L_2 are given by

$$L_1 : w = \frac{u^2 U(\frac{1}{u} - \gamma)}{(\beta - \alpha)[1 - (\gamma - \alpha)u]}, \quad L_2 : w = \frac{u}{1 - (\gamma - \alpha)u}. \quad (2.13)$$

²In contrast with DL91 and MD99, we choose $V_S \leq 0$ and $E \leq 0$, consistent with e.g. de Zeeuw (1985a).

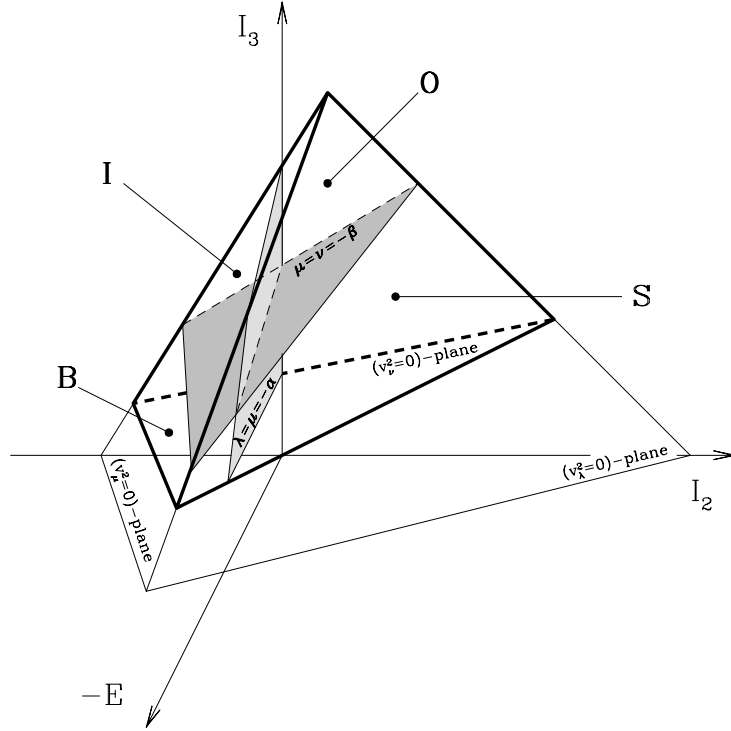


FIGURE 1 — The tetrahedron shows all accessible points in integral space (E, I_2, I_3) for a given position (λ, μ, ν) . The tetrahedron is bounded by the planes for which $v_\lambda^2 = 0$, $v_\mu^2 = 0$, $v_\nu^2 = 0$ and $E = 0$, respectively. The two shaded planes, which are given by $v_\lambda^2 = v_\mu^2 = 0$ at $\lambda = \mu = -\alpha$ and $v_\mu^2 = v_\nu^2 = 0$ at $\mu = \nu = -\beta$, divide the tetrahedron into the parts corresponding to the four general orbit families in a triaxial separable potential: box (B) orbits, inner (I) and outer (O) long-axis tube orbits and short-axis (S) tube orbits.

At a given position (λ, μ, ν) , orbits with different values of the integrals of motion E , I_2 and I_3 , and hence different values of S , can contribute to the integral (2.10). The restriction to bound orbits ($E \leq 0$) together with the requirement that v_λ^2 , v_μ^2 and v_ν^2 all three have to be non-negative determines the part of the integral space that is accessible by orbits that go through (λ, μ, ν) . An example of the resulting tetrahedron in the (E, I_2, I_3) -space is shown in Fig. 1 (cf. Fig. 1 of MD99). The largest possible value of S is given by the top of this tetrahedron

$$S_{\text{top}}(\lambda, \mu, \nu) = -U[\lambda, \mu, \nu] - w \frac{(\lambda + \alpha)(\mu + \alpha)(\nu + \alpha)}{\gamma - \alpha} U[\lambda, \mu, \nu, -\alpha] - u \frac{(\lambda + \gamma)(\mu + \gamma)(\nu + \gamma)}{\alpha - \gamma} U[\lambda, \mu, \nu, -\gamma], \quad (2.14)$$

which is thus a function of the position (λ, μ, ν) . At the origin $S_{\text{top}}(-\alpha, -\beta, -\gamma) = U[-\alpha, -\beta, -\gamma]$, which is the central value of the potential V_S . In what follows, we normalize V_S by setting $U[-\alpha, -\beta, -\gamma] = -1$, so that $0 \leq S_{\text{top}} \leq 1$.

2.3.2 Non-rotating components (NR)

Since the non-rotating component type can exist everywhere in the accessible integral space (the tetrahedron in Fig. 1), we simply have that $S_{\text{max}} = S_{\text{top}}(\lambda, \mu, \nu)$. Spatially the

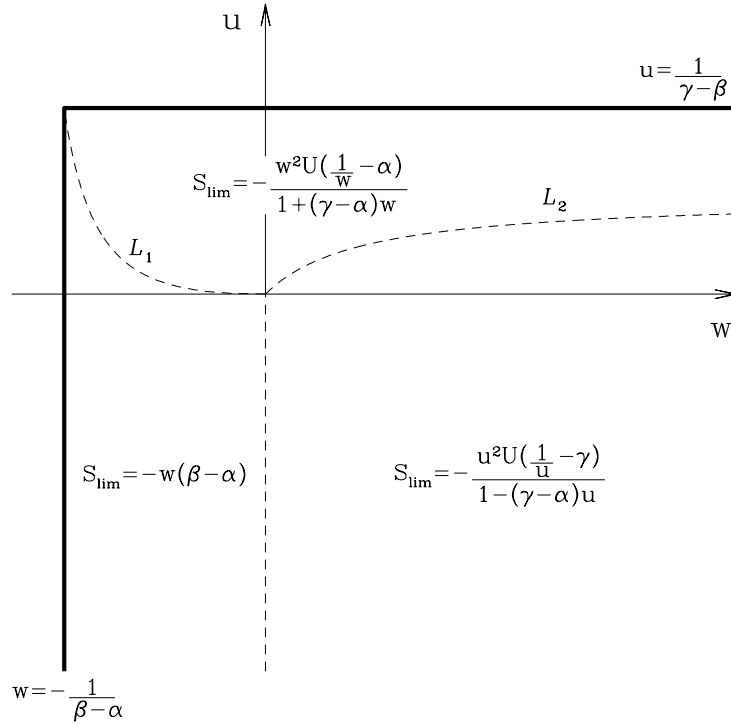


FIGURE 2 — The limiting value S_{lim} of the variable $S = -E + w I_2 + u I_3$ as function of the parameters w and u . The physical region is bounded by the relations (2.12), indicated by the thick solid lines. The dashed curves divide this region into three parts, each with a different expression for S_{lim} . The relations for the separatrices L_1 and L_2 are given in eq. (2.13).

NR components are thus bounded by the surface $S_{\text{top}}(\lambda, \mu, \nu) = S_{\text{min}}$.

The factor T_{lmn} follows from the cross section of the S -plane within the tetrahedron and can be written in compact form as (cf. DL91)

$$T_{lmn}^{\text{NR}} = B\left(\frac{l+1}{2}, \frac{m+1}{2}, \frac{n+1}{2}\right), \quad (2.15)$$

where B is the beta function of three variables³. Since T_{lmn}^{NR} is independent of S it can be taken out of the integral, which then becomes of Abel form. Unfortunately, the inversion of eq. (2.10) for any chosen moment $\mu_{lmn}(\lambda, \mu, \nu)$, including the case $l = m = n = 0$, is generally impossible, as the left-hand side is a function of three variables, while the DF depends on only one variable, S . The density ρ_* specified along any given curve will define a different $f(S)$. A case of particular interest is to choose the density along the short axis to be $\rho_*(0, 0, z) = \rho_S(0, 0, z)$. This defines a unique $f(S)$, and hence gives ρ_* everywhere. Kuzmin's formula applied to $\rho_S(0, 0, z)$ similarly defines the density ρ_S everywhere. For single Abel DF components these will not be the same, except in the spherical limit (see Appendix A.3)

Since the orbits have no net rotation, the velocity moments μ_{lmn}^{NR} are only non-zero when l, m and n are all three even, and vanish in all other cases.

³The beta function of k variables is defined in terms of the complete gamma function Γ as $B(\beta_1, \dots, \beta_k) = \Gamma(\beta_1) \cdots \Gamma(\beta_k) / \Gamma(\beta_1 + \dots + \beta_k)$.

2.3.3 Long-axis rotating components (LR)

The long-axis rotating component type only exists in the part of the integral space that is accessible by the (inner and outer) long-axis tube orbits. Within the tetrahedron for all orbits this is the region for which $v_\nu^2 \geq 0$ at $\nu = -\beta$. It follows that $S_{\max} = S_{\text{top}}(\lambda, \mu, -\beta) \leq S_{\text{top}}(\lambda, \mu, \nu)$, so that the spatial extent of the LR components is generally smaller than the NR components.

The term T_{lmn} follows from the cross section of the S -plane within the tetrahedron and with the above boundary plane $v_\nu^2 = 0$ at $\nu = -\beta$, resulting in

$$T_{lmn}^{\text{LR}} = \frac{(-2)^{(l+m+4)/2} \sqrt{a_0^{l+1} b_0^{m+1}} \mathcal{M}_0^{\text{LR}}}{(s+1)(s-1) \dots (s+1-(l+m))}, \quad (2.16)$$

with $s = l + m + n$, the parameters a_0 and b_0 defined as

$$a_0 = \frac{(\lambda + \beta) H_{\mu\nu} [S_{\text{top}}(\lambda, \mu, -\beta) - S]}{(\lambda - \nu) H_{\mu(-\beta)} [S_{\text{top}}(\lambda, \mu, \nu) - S]}, \quad b_0 = \frac{(\mu + \beta) H_{\nu\lambda} [S_{\text{top}}(\lambda, \mu, -\beta) - S]}{(\mu - \nu) H_{(-\beta)\lambda} [S_{\text{top}}(\lambda, \mu, \nu) - S]}, \quad (2.17)$$

and

$$\mathcal{M}_0^{\text{LR}} = \begin{cases} \mathcal{M}(s, \frac{l}{2}, \frac{m}{2}; a_0, b_0, \frac{\pi}{2}), & a_0 \leq b_0, \\ \mathcal{M}(s, \frac{m}{2}, \frac{l}{2}; b_0, a_0, \frac{\pi}{2}), & a_0 > b_0. \end{cases} \quad (2.18)$$

The function \mathcal{M} is defined in Appendix B, where we evaluate it in terms of elementary functions (odd s) and elliptic integrals (even s).

The orbits have net rotation around the long axis, but the motion parallel to the intermediate axis and short axis cancels. As a result, the velocity moments μ_{lmn}^{LR} vanish when l or m are odd. To invert the net rotation around the long-axis, μ_{lmn}^{LR} has to be multiplied with $(-1)^n$, i.e. the non-zero odd velocity moments have opposite sign.

2.3.4 Short-axis rotating components (SR)

The short-axis component type reaches the part of integral space accessible by the short-axis tube orbits. Within the tetrahedron for all orbits this is the region for which $v_\mu^2 \geq 0$ both at $\mu = -\beta$ and $\mu = -\alpha$ (Fig. 1). The latter requirement is equivalent to $I_2 \geq 0$. In this case, $S_{\max} = S_{\text{top}}(\lambda, -\alpha, \nu) \leq S_{\text{top}}(\lambda, \mu, \nu)$, and the spatial extent of the SR components is generally smaller than the NR components.

The form of the term T_{lmn} depends on the cross section of the S -plane within the tetrahedron and with the above two boundary planes. It is given by

$$T_{lmn}^{\text{SR}} = \frac{(-2)^{(l+n+4)/2} \sum_{i=1}^2 \sqrt{a_i^{l+1} b_i^{n+1}} \mathcal{M}_i^{\text{SR}}}{(s+1)(s-1) \dots (s+1-(l+n))}. \quad (2.19)$$

The parameters a_1 and b_1 follow from a_0 and b_0 defined in (2.17) by interchanging $\nu \leftrightarrow \mu$, and in turn a_2 and b_2 follow from a_1 and b_1 by interchanging $\beta \leftrightarrow \alpha$. For the terms $\mathcal{M}_i^{\text{SR}}$ we have two possibilities, I and II,

$$\mathcal{M}_I^{\text{SR}} = \begin{cases} \mathcal{M}(s, \frac{l}{2}, \frac{n}{2}; a_I, b_I, \theta_I), & a_I \leq b_I, \\ \mathcal{M}(s, \frac{n}{2}, \frac{l}{2}; b_I, a_I, \frac{\pi}{2}) - \mathcal{M}(s, \frac{n}{2}, \frac{l}{2}; b_I, a_I, \frac{\pi}{2} - \theta_I), & a_I > b_I, \end{cases} \quad (2.20)$$

$$\mathcal{M}_{II}^{\text{SR}} = \begin{cases} \mathcal{M}(s, \frac{l}{2}, \frac{n}{2}; a_{II}, b_{II}, \frac{\pi}{2}) - \mathcal{M}(s, \frac{l}{2}, \frac{n}{2}; a_{II}, b_{II}, \theta_{II}), & a_{II} \leq b_{II}, \\ \mathcal{M}(s, \frac{n}{2}, \frac{l}{2}; b_{II}, a_{II}, \frac{\pi}{2} - \theta_{II}), & a_{II} > b_{II}, \end{cases} \quad (2.21)$$

where \mathcal{M} is given in Appendix B, and θ_I and θ_{II} follow from

$$\tan^2 \theta_I = \frac{b_{II}(a_I - a_{II})}{a_{II}(b_{II} - b_I)} \quad \text{and} \quad \tan^2 \theta_{II} = \frac{b_I(a_{II} - a_I)}{a_I(b_I - b_{II})}. \quad (2.22)$$

For the assignment of the labels I and II , we discriminate between four cases

$$\begin{aligned} a_1 \leq a_2, \quad b_1 \geq b_2 & : I \rightarrow 1, \quad II \rightarrow 2, \\ a_1 \geq a_2, \quad b_1 \leq b_2 & : I \rightarrow 2, \quad II \rightarrow 1, \\ a_1 \leq a_2, \quad b_1 \leq b_2 & : I \rightarrow 1, \quad \theta_I = \pi/2, \quad C_2^{\text{SR}} = 0, \\ a_1 \geq a_2, \quad b_1 \geq b_2 & : I \rightarrow 2, \quad \theta_I = \pi/2, \quad C_1^{\text{SR}} = 0. \end{aligned} \quad (2.23)$$

The orbits only have net rotation around the short axis, so that the velocity moments μ_{lmn}^{SR} vanish when l or n are odd. Multiplying μ_{lmn}^{SR} with $(-1)^m$ results in net rotation around the short axis in the opposite direction.

3 OBSERVABLES

We now describe how to convert the intrinsic velocity moments $\mu_{lmn}(\lambda, \mu, \nu)$ to observable quantities on the plane of the sky: the surface brightness (SB) and the mean line-of-sight velocity V , velocity dispersion σ , as well as higher-order moments of the line-of-sight velocity distribution.

3.1 FROM INTRINSIC TO OBSERVER'S COORDINATE SYSTEM

In order to calculate the projected velocity moments, we introduce a new Cartesian coordinate system (x'', y'', z'') , with x'' and y'' in the plane of the sky and the z'' -axis along the line-of-sight. Choosing the x'' -axis in the (x, y) -plane of the intrinsic coordinate system (cf. de Zeeuw & Franx 1989 and their Fig. 2), the transformation between both coordinate systems is known once two viewing angles, the polar angle ϑ and azimuthal angle φ , are specified. The intrinsic z -axis projects onto the y'' -axis, which for an axisymmetric galaxy model aligns with the short axis of the projected surface density Σ . However, for a triaxial galaxy model the y'' -axis in general lies at an angle ψ with respect to the short axis of Σ . This misalignment ψ can be expressed in terms of the viewing angles ϑ and φ and the triaxiality parameter T (defined in eq. 2.6) as follows (cf. eq. B9 of Franx 1988)

$$\tan 2\psi = -\frac{T \sin 2\varphi \cos \vartheta}{\sin^2 \vartheta - T (\cos^2 \varphi - \sin^2 \varphi \cos^2 \vartheta)} \quad (3.1)$$

with $\sin 2\psi \sin 2\varphi \cos \vartheta \leq 0$ and $-\pi/2 \leq \psi \leq \pi/2$. A rotation over ψ transforms the coordinate system (x'', y'', z'') to (x', y', z') , with the x' -axis and y' -axis aligned with respectively the major and minor axis of Σ , whereas $z' = z''$ is along the line-of-sight.

The expressions in § 2.3 involve the velocity components in the confocal coordinate system (λ, μ, ν) . The conversion to line-of-sight quantities can be done by four successive matrix transformations. First, we obtain the velocity components in the first octant of the intrinsic Cartesian coordinate system (x, y, z) by applying the matrix \mathbf{Q} , of which the first element is given by (cf. DL91)

$$Q_{11} = \text{sign}(\lambda + \alpha) \sqrt{\frac{(\mu + \alpha)(\nu + \alpha)(\lambda + \beta)(\lambda + \gamma)}{(\alpha - \beta)(\alpha - \gamma)(\lambda - \mu)(\lambda - \nu)}}, \quad (3.2)$$

and the other elements follow horizontally by cyclic permutation of $\lambda \rightarrow \mu \rightarrow \nu \rightarrow \lambda$ and vertically by cyclic permutation of $\alpha \rightarrow \beta \rightarrow \gamma \rightarrow \alpha$. The second matrix uses the symmetries of the orbits to compute the appropriate signs of the intrinsic Cartesian velocities in the other octants. The result depends on whether or not the orbit has a definite sense of rotation in one of the confocal coordinates. For the three types of Abel components this results in the following matrices

$$\begin{aligned} \text{NR} &: \mathbf{S} = \text{diag}[\text{sgn}(x), \text{sgn}(y), \text{sgn}(z)] \\ \text{LR} &: \mathbf{S} = \text{diag}[\text{sgn}(xyz), \text{sgn}(z), \text{sgn}(y)] \\ \text{SR} &: \mathbf{S} = \text{diag}[\text{sgn}(y), \text{sgn}(x), \text{sgn}(xyz)] \end{aligned} \quad (3.3)$$

Finally, the conversion from the intrinsic to the observer's Cartesian velocities involves the same projection and rotation as for the coordinates. We represent these two coordinate transformations respectively by the projection matrix

$$\mathbf{P} = \begin{pmatrix} -\sin \varphi & \cos \varphi & 0 \\ -\cos \vartheta \cos \varphi & -\cos \vartheta \sin \varphi & \sin \vartheta \\ \sin \vartheta \cos \varphi & \sin \vartheta \sin \varphi & \cos \vartheta \end{pmatrix}, \quad (3.4)$$

and the rotation matrix

$$\mathbf{R} = \begin{pmatrix} \cos \psi & -\sin \psi & 0 \\ \sin \psi & \cos \psi & 0 \\ 0 & 0 & 1 \end{pmatrix}. \quad (3.5)$$

In this way, we arrive at the following relation

$$\begin{pmatrix} v_{x'} \\ v_{y'} \\ v_{z'} \end{pmatrix} = \mathbf{M} \begin{pmatrix} v_{\lambda} \\ v_{\mu} \\ v_{\nu} \end{pmatrix}, \quad \text{with } \mathbf{M} \equiv \mathbf{SPQR}, \quad (3.6)$$

where the full transformation matrix \mathbf{M} is thus a function of (λ, μ, ν) , the constants (α, β, γ) and the viewing angles $(\vartheta, \varphi, \psi)$.

We can now write each velocity moment in the observer's Cartesian coordinate system (x', y', z') as a linear combination of the velocity moments in the confocal ellipsoidal coordinate system

$$\mu_{ijk}(x', y', z') = \sum_{l,m,n} c_{l,m,n} \mu_{lmn}(\lambda, \mu, \nu), \quad (3.7)$$

with $i + j + k = l + m + n$. The coefficients $c_{l,m,n}$ are combinations of elements of \mathbf{M} , and can be obtained recursively as

$$c_{l,m,n} = c_{l-1,m,n} + c_{l,m-1,n} + c_{l,m,n-1}, \quad (3.8)$$

with the first order expressions given by

$$c_{1,0,0} = M_{e_s 1}, \quad c_{0,1,0} = M_{e_s 2}, \quad c_{0,0,1} = M_{e_s 3}, \quad (3.9)$$

and the index e_s is the s th element ($s = l + m + n$) of the vector $\mathbf{e} = [1, \dots, 1, 2, \dots, 2, 3, \dots, 3]$. The number of integers 1 ($\#1$) is equal to the value of the velocity moment index i , and similarly $\#2 = j$ and $\#3 = k$. For the density μ_{000} we have $c_{0,0,0} = 1$.

3.2 LINE-OF-SIGHT VELOCITY MOMENTS

Spectroscopic observations of the integrated light of galaxies provide the line-of-sight velocity distribution (LOSVD) as a function of position on the sky plane:

$$\mathcal{L}(x', y', v_{z'}) = \iiint f(E, I_2, I_3) dv_{x'} dv_{y'} dz'. \quad (3.10)$$

The velocity moments of the LOSVD are

$$\mu_k(x', y') = \int_{-\infty}^{\infty} v_{z'}^k \mathcal{L}(x', y', v_{z'}) dv_{z'} \quad (3.11)$$

$$= \int_{-\infty}^{\infty} \mu_{00k}(x', y', z') dz'. \quad (3.12)$$

The latter form follows upon substitution of the definition (3.10), rearranging the sequence of integration and using the definition of the intrinsic velocity moments of the DF. The lowest order velocity moments μ_0 , μ_1 and μ_2 provide the surface mass density Σ , the mean line-of-sight velocity V and dispersion σ by

$$\Sigma = \mu_0, \quad V = \frac{\mu_1}{\mu_0}, \quad \text{and} \quad \sigma^2 = \frac{\mu_0 \mu_2 - \mu_1^2}{\mu_0^2}, \quad (3.13)$$

as a function of (x', y') .

The triple integral on the right-hand side of (3.10) can be evaluated relatively easily for the Abel DF (2.9), but is numerically cumbersome. On the other hand, the moments of the LOSVD follow by the single integration (3.12) and can be computed efficiently, even though the expressions for μ_{00k} are somewhat lengthy.

Whereas Σ , V and σ can be measured routinely, determinations of the higher order moments (μ_3 , μ_4 , ...), are in general more uncertain as they depend significantly on the wings of the LOSVD, which become quickly dominated by the noise in the observations. Instead of these true higher-order moments, one often uses the Gauss-Hermite moments (h_3 , h_4 , ...), which are much less sensitive to the wings of the LOSVD (van der Marel & Franx 1993; Gerhard 1993).

There is no simple (analytic) relation between the true moments (3.13) and the Gauss-Hermite moments, including the lower order moments Σ_{GH} , V_{GH} and σ_{GH} (but see eq. 18 of van der Marel & Franx 1993 for approximate relations to lowest order in h_3 and h_4). For this reason, we derive the Gauss-Hermite moments numerically. One way is to find the Gauss-Hermite LOSVD of which the numerically calculated true moments best-fit those from the Abel model. In Appendix C, we show however that this direct fitting of the true moments has various (numerical) problems, which can cause the resulting Gauss-Hermite moments to be significantly different from their true values. Instead, we (re)construct the LOSVD from the true moments by means of an Edgeworth expansion and then fit a Gauss-Hermite series to it. With this alternative method the Gauss-Hermite moments can be computed accurately and efficiently.

3.3 SURFACE BRIGHTNESS

The surface brightness follows upon integration of the luminosity density along the line-of-sight. The luminosity density in turn is related to the mass density ρ_* via the

stellar mass-to-light ratio M_*/L . Whereas ρ_* is the zeroth-order velocity moment of the DF (eq. 2.8) that describes the distribution of the luminous matter, ρ_S is associated to the potential V_S and hence contains all matter, including possible dark matter. This means that in general the surface brightness cannot be obtained from ρ_S (or from V_S) and vice versa, without knowing (or assuming) the distribution of the dark matter. However, when the dark matter fraction is assumed to be constant, we only have to multiply ρ_S by a constant factor (<1) to obtain ρ_* . This means that ρ_S is related to the luminosity density via a total mass-to-light ratio M/L which is M_*/L multiplied by the same factor. When in addition M_*/L does not change (e.g., due to variation in the underlying stellar populations), M/L is constant, i.e., mass follows light.

While in the outer parts of late-type galaxies the presence of dark matter, as predicted by the cold dark matter paradigm for galaxy formation (e.g., Kauffmann & van den Bosch 2002), was demonstrated convincingly already more than two decades ago (e.g., van Albada et al. 1985), the proof in the outer parts of early-type galaxies remains uncertain (e.g., Romanowsky et al. 2003), mainly due to a lack of kinematic constraints. As a consequence, in the outer parts of galaxies, commonly a simple functional form for the dark matter distribution is assumed, often the universal profile from the CDM paradigm (Navarro, Frenk & White 1997).

The dark matter distribution in the inner parts of galaxies is probably even more poorly understood (e.g., Primack 2004). Comparing the (total) M/L from dynamical modeling with the (stellar) M_*/L from color and absorption line-strength measurements can constrain the dark matter distribution (e.g., Cappellari et al. 2005). But due to uncertainties in the stellar population models, even the dark matter fraction is uncertain, let alone the shape of the dark matter distribution. The use of strong gravitational lensing to constrain the total mass distribution, in combination with dynamical modeling seems to be a promising way to study in detail the fraction and shape of the dark matter in the inner parts of galaxies (e.g., Treu & Koopmans 2004; see also Chapter 6 of this thesis). However, in current dynamical studies of the central parts of early-type galaxies, it is commonly assumed that mass follows light. As we saw above, after deprojection of the observed surface brightness for a given viewing direction, a simple scaling with the constant M/L then yields the total mass density ρ_S , from which the potential can be determined by solving Poisson's equation.

In the case of a constant mass-to-light ratio, we can also first multiply the surface brightness with this mass-to-light ratio and then deproject the resulting *surface* mass density to obtain the *intrinsic* mass density. The surface mass density that corresponds to the DF is Σ , defined in eq. (3.13). The surface mass density Σ_S related to the potential V_S has concentric isodensity contours that show no twist (e.g., Franx 1988).

3.4 COMBINATION OF MULTIPLE DF COMPONENTS

Until now, we have chosen the Abel DF to be a function of a single variable $S = -E + wI_2 + uI_3$, and we have separated it in three component types, non-rotating (NR), long-axis rotating (LR) and short-axis rotating (SR), but we have not made any assumption about the form of the DF (apart from the obvious requirement that it has to be non-negative everywhere and that it decreases to zero at large radii). Following MD99, we choose the DF to be a linear combination of basis functions of the form

$$f_\delta(S) = \left(\frac{S - S_{\min}}{1 - S_{\min}} \right)^\delta, \quad (3.14)$$

with δ a positive constant and $S_{\text{lim}} \leq S_{\text{min}} \leq S \leq 1$, and S_{lim} given in Fig. 2.

Once the potential V_S is known, we use the relations from § 2.3 together with the expressions in Appendix B, to compute the intrinsic velocity moments for the NR, SR and LR components in an efficient way, where at most the integral over S has to be evaluated numerically. For the NR components this integral can even be evaluated explicitly, resulting in

$$\mu_{lmn,\delta}^{\text{NR}}(\lambda, \mu, \nu) = \sqrt{\frac{[2(S_{\text{max}} - S_{\text{min}})]^{l+m+n+3}}{H_{\mu\nu}^{l+1} H_{\nu\lambda}^{m+1} H_{\lambda\mu}^{n+1}}} \left(\frac{S_{\text{max}} - S_{\text{min}}}{1 - S_{\text{min}}} \right)^\delta B\left(\frac{l+1}{2}, \frac{m+1}{2}, \frac{n+1}{2}, \delta+1\right), \quad (3.15)$$

where $S_{\text{max}} = S_{\text{top}}(\lambda, \mu, \nu)$ (cf. eq. 2.14). For a given viewing direction and mass-to-light ratio, we can then convert the intrinsic velocity moments to observable quantities as described in § 3.1–3.3. The observables depend on the choice of the DF parameters w , u and δ , they are different for each component type, and for the rotating components (LR and SR), they also depend on the sense of rotation around the axis of symmetry⁴. By combining the observables for a set of such DF components, we can construct realistic galaxy models. Since the mean line-of-sight velocity, velocity dispersion and higher order Gauss-Hermite velocity moments, are non-linear functions of the DF, we cannot directly combine these observables in a linear way.

Instead, we use the projected velocity moments (eq. 3.12) of the DF components, which we add together after multiplying each of them with a constant weight. We convert the resulting combined projected velocity moments to observables. Since the mass included in each DF component is different, we multiply the weights with the mass of the corresponding DF component, divided by the total (luminous) mass. In this way, we obtain the mass fractions per DF component.

4 TRIAXIAL THREE-INTEGRAL GALAXY MODELS

After choosing a Stäckel potential, we investigate the shape of the density generated by the Abel DF components, and use these components to construct a triaxial galaxy model with three integrals of motion.

4.1 ISOCHRONE POTENTIAL AND DENSITY

There are various choices for the potential and density that provide useful test models for comparison with the kinematics of triaxial elliptical galaxies (e.g., Arnold et al. 1994). One option is to consider the so-called perfect ellipsoid, for which Statler (1987) already computed numerical Schwarzschild models and Hunter & de Zeeuw (1992) investigated the maximum streaming thin orbit models. It has a density distribution stratified on similar concentric ellipsoids, but the potential function $U(\tau)$ contains elliptic integrals, which slows down numerical calculations. An alternative is to consider the set of models introduced by de Zeeuw & Pfenniger (1988), which have nearly ellipsoidal density figures, and have a potential and density that are evaluated easily and swiftly. They are defined by the choice:

$$U(\tau) = -GM(\sqrt{\tau} - \sqrt{-\alpha})(\sqrt{\tau} - \sqrt{-\gamma}) \left(\sqrt{\tau} + \frac{\sqrt{\alpha\gamma} - \beta}{\sqrt{-\alpha} + \sqrt{-\gamma}} \right), \quad (4.1)$$

⁴To change only the sense of rotation, the observables do not have to be recomputed, as a simple change in the sign of the odd velocity moments is sufficient.

so that the triaxial Stäckel potential has the elegant form

$$V_S(\lambda, \mu, \nu) = \frac{-GM \left(\sqrt{\lambda\mu} + \sqrt{\mu\nu} + \sqrt{\nu\lambda} - \beta \right)}{(\sqrt{\lambda} + \sqrt{\mu})(\sqrt{\mu} + \sqrt{\nu})(\sqrt{\nu} + \sqrt{\lambda})}, \quad (4.2)$$

where we set $GM = \sqrt{-\gamma} + \sqrt{-\alpha}$ to normalize V_S to -1 in the center. In the oblate axisymmetric limit this potential is that of the Kuzmin-Kutuzov (1962) models of Dejonghe & de Zeeuw (1988), and in the spherical limit it reduces to Hénon's (1959) isochrone. For all these models, V_S along the short z -axis is identical to the isochrone potential $-GM/(\sqrt{\tau} + \sqrt{-\alpha})$. We therefore refer to models with $U(\tau)$ of the form (4.1) as isochrone models. Since the potential falls off as $1/r$ at large radii, all these models have finite total mass.

The expressions for the integrals of motion are given in (2.5), where $U[\lambda, \mu, \nu] = V_S$ and the third order divided difference $U[\lambda, \mu, \nu, \sigma]$ is given by the symmetric expression

$$U[\lambda, \mu, \nu, \sigma] = -GM \frac{\sqrt{\lambda\mu\nu} + \sqrt{\mu\nu\sigma} + \sqrt{\nu\sigma\lambda} + \sqrt{\sigma\lambda\mu} - \beta(\sqrt{\lambda} + \sqrt{\mu} + \sqrt{\nu} + \sqrt{\sigma})}{(\sqrt{\lambda} + \sqrt{\mu})(\sqrt{\lambda} + \sqrt{\nu})(\sqrt{\lambda} + \sqrt{\sigma})(\sqrt{\mu} + \sqrt{\nu})(\sqrt{\mu} + \sqrt{\sigma})(\sqrt{\nu} + \sqrt{\sigma})}. \quad (4.3)$$

These isochrone models have the convenient property that the expressions for the potential and the integrals of motion contain only elementary functions of the (confocal ellipsoidal) coordinates and have no singularities.

The same is true for the associated mass density ρ_S , of which the expression is given in Appendix C of de Zeeuw & Pfenniger (1988), and a contour plot of ρ_S in the (x, z) -plane is shown in their Fig. 2. These authors also derive the axis ratios of ρ_S in the center (their eq. C7) and at large radii (their eq. C11), in terms of the axis ratios ζ and ξ of the confocal ellipsoidal coordinate system, defined as

$$\zeta^2 = \beta/\alpha, \quad \xi^2 = \gamma/\alpha. \quad (4.4)$$

Although ρ_S becomes slightly rounder at larger radii, its axis ratios remain smaller than unity (for $\xi < \zeta < 1$) because at large radii $\rho_S \sim 1/r^4$. Characteristic values for the axis ratios can be obtained from the (normalized) moments of inertia along the principal axes of the density,

$$a^2 = \frac{\int x^2 \rho(x, 0, 0) dx}{\int \rho(x, 0, 0) dx}, \quad (4.5)$$

where the intermediate and short semi-axis length, b and c , of the inertia ellipsoid follow from the long semi-axis length a by replacing x with y and z respectively. Taking for example $\zeta = 0.8$ and $\xi = 0.64$, the semi-axis lengths of the inertia ellipsoid result in the characteristic axis ratios $b_S/a_S = 0.89$ and $c_S/a_S = 0.82$ for the density ρ_S . The contours of the projected density are nearly elliptic with slowly varying axis ratios.

4.2 THE SHAPE OF THE LUMINOUS MASS DENSITY

Whereas the shape of the (total) mass density ρ_S is fixed by the choice of the potential V_S , and ζ and ξ (4.4), the shape of the (luminous) density ρ_* , which is the zeroth order velocity moment of the DF (eq. 2.8), also depends on the DF parameters w , u and δ , and the type of component. For $\zeta = 0.8$ and $\xi = 0.64$, we show in Fig. 3 for non-rotating DF components the characteristic axis ratios of the corresponding density, as

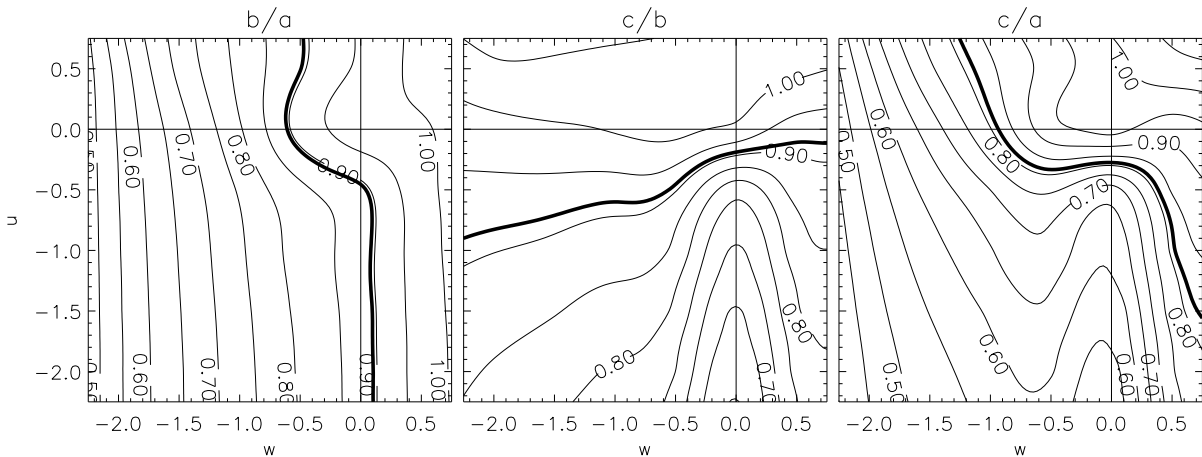


FIGURE 3 — The characteristic axis ratios of the luminous mass density for a non-rotating Abel component, as function of the DF parameters w and u , and $\delta = 1$. The axis ratios of the confocal ellipsoidal coordinate system are $\zeta = 0.8$ and $\xi = 0.64$. The thick contours are drawn at the levels that correspond to the characteristic axis ratios of the total mass density ρ_S , associated with the underlying isochrone Stäckel potential (4.2). The intermediate-over-long axis ratio b/a depends mainly on w , the short-over-intermediate axis ratio c/b depends mainly on u , and c/a is the product of the previous two.

function of w and u . We have set $\delta = 1$, but the axis ratios depend only weakly on it, with ρ_* becoming slightly flatter for increasing δ . The thick contours are drawn at the levels that correspond to the values of the characteristic axis ratios of ρ_S , respectively $a_S/b_S = 0.89$, $c_S/b_S = 0.91$ and $c_S/a_S = 0.82$. These values are independent of w and u (as well as the other DF parameters).

While the intermediate-over-long axis ratio b/a increases with increasing w , its value is nearly independent of u . By contrast, the short-over-intermediate axis ratio c/b , is nearly independent of w , and increases with increasing u . The short-over-long axis ratio c/a is the product of the previous two axis ratios and thus depends on both w and u . When both w and u are negative, the density ρ_* has its long-axis along the x -axis and its short-axis along the z -axis, in the same way as the potential V_S and the associated density ρ_S . Above certain positive values of either w or u , the axis ratios become larger than unity, which means that ρ_* is no longer aligned with the underlying coordinate system in the same way as V_S and ρ_S . For example, when $w = -0.5$ and $u = 0.5$, $b/a < 1$ but $c/b > 1$, so that in this case ρ_* has its short axis along the y -axis.

A change in the sign of w and u has a strong effect on the radial slope of ρ_* . In Fig. 4, the radial profiles of ρ_* along the principal axes are shown for four combinations of w and u . The density is normalized to the central value ρ_0 . To set the dimension of the radius r , we have set the scale length l_α , defined as

$$l_\alpha = \sqrt{-\alpha}, \quad (4.6)$$

to $10''$. For given axis ratios ζ and ξ of the confocal ellipsoidal coordinate system, we calculate all quantities with respect to unit scale length. At the end we scale the resulting Abel model, depending on the value of l_α (in arcsec) and the assumed distance D (in Mpc). The profiles along the y -axis (dotted curves) and along the z -axis (dashed curves) are arbitrarily offset vertically with respect to the profile along the

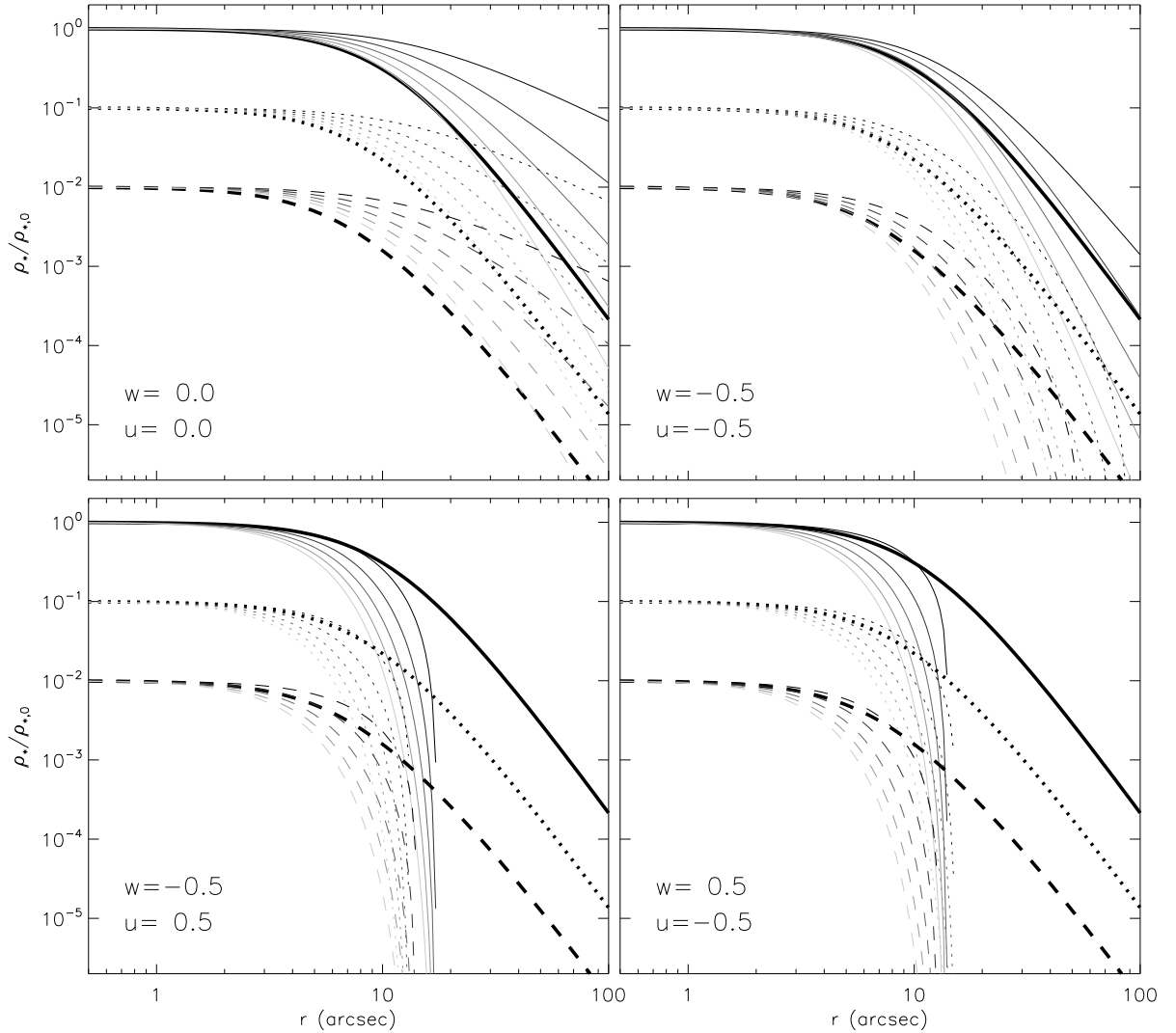


FIGURE 4 — Principal axes profiles of the luminous mass density ρ_* for a non-rotating Abel component, normalized to the central value $\rho_{*,0}$. Each panel is for a different combination of the DF parameters w and u , while the grey scale indicates variation in δ from zero (darkest curve) to four (lightest curve), in unity steps. The profiles along the y -axis (dotted curves) and along the z -axis (dashed curves) are arbitrarily offset vertically with respect to the profile along the x -axis (solid curves) to enhance the visualization. The thick black curves show the profiles for the (total) mass density ρ_S , associated with the underlying isochrone Stäckel potential (4.2), with $\zeta = 0.8$ and $\xi = 0.64$, and scale length $a = 10''$. When the value of either w or u is positive (bottom panels), the profiles show a break at around the scale-length, so that these compact components may be used to represent kinematically decoupled components.

x -axis (solid curves) to enhance the visualization. The thin curves are the profiles of the (luminous) mass density ρ_* for varying δ , from $\delta = 0$ (darkest curve) to $\delta = 4$ (lightest curve), in unit steps. The thick black curves show the profiles for the (total) mass density ρ_S , which is independent of w , u and δ .

The profiles of ρ_* become steeper for increasing δ and for increasing absolute values of w and u . In particular, when either w or u becomes positive (bottom panels), the

profiles suddenly become much steeper and drop to zero already at relatively small radii. The resulting Abel components are thus compact and, as we saw above, can be different in shape and orientation from the main body of the galaxy model. Therefore, they can be used to represent kinematically decoupled components. When both $w \leq 0$ and $u \leq 0$ (top panels), ρ_* falls off much more gently and the Abel components cover a larger region. When $w = u = 0$ (top left panel), so that the DF only depends on energy, the profiles as well as the shape (Fig. 3) of ρ_* can even be flatter than those of ρ_S . However, already for small non-zero values of w and u , generally $\rho_* \leq \rho_S$ everywhere in the galaxy model, and $\rho_* < \rho_S$ in the outer parts. Although self-consistency $\rho_* = \rho_S$ is only possible in the spherical case (for fixed values of w and u , see § 2.3), we can choose the parameters w , u and δ so that $\rho_* \sim \rho_S$. At the same time, having $\rho_* < \rho_S$ in the outer parts of the galaxy model, allows us to take into account a dark halo contribution.

The shape of ρ_* can furthermore change due to the additional contribution from long-axis rotating and short-axis rotating components. Although these components have no density along respectively the long-axis and short-axis, the behavior of their overall shape as function of w , u and δ is similar as above for the corresponding non-rotating components.

The above analysis shows that, given the triaxial isochrone potential (4.2), we can use Abel components to construct a galaxy model with a realistic density. Depending on the choice of w , u and δ , the galaxy model can contain compact (kinematically decoupled) components and account for possible dark matter (in the outer parts). Furthermore, we show below that even with a small number DF components, enough kinematic variation is possible to mimic the two-dimensional kinematic maps of early-type galaxies provided by observations with integral-field spectrographs such as SAURON. This means that we can construct simple but realistic galaxy models to test our Schwarzschild software (§ 6 and 7).

4.3 A TRIAXIAL ABEL MODEL

As before, we choose the isochrone Stäckel potential (4.2), we take $\zeta = 0.8$ and $\xi = 0.64$ for the axis ratios of the coordinate system (4.4), resulting in a triaxiality parameter (2.6) of about $T = 0.61$, and we set the scale length (4.6) to $l_\alpha = 10''$. Assuming a distance of $D = 20$ Mpc and a total mass of $10^{11} M_\odot$ results in a central value for the potential $V_0 \sim 2.5 \times 10^6 \text{ km}^2 \text{ s}^{-2}$, which also sets the unit of velocity. We restrict the number of DF components to three, one of each type. For the first component of type NR we set $w = -0.5$, $u = -0.5$ and $\delta = 1$, so that the shape of the corresponding density is similar to that of ρ_S , except in the outer parts where a steeper profile mimics the presence of dark matter (see Figs. 3 and 4). For the second and third component, respectively of type LR and SR, we adopt the same parameters, expect that we take $u = 0.5$ for the SR component, which therefore is more compact than the NR and LR component.

For each DF component, we calculate the intrinsic true velocity moments up to fifth ($s = 5$) order and integrate them along the line-of-sight, which we set by choosing $\vartheta = 70^\circ$ and $\varphi = 30^\circ$ for the viewing angles. After rotation over the misalignment angle $\psi = 101^\circ$ (3.1), we obtain the projected true velocity moments μ_k ($k = 0, \dots, 5$) shown in Fig. 5. The parameters of each DF component are given on the right. The grey scale indicates the range of the true velocity moment in each panel, from minimum (black) to maximum value (white). The NR component has zero odd velocity moments. For the LR and SR component, the even velocity moments show a decrease in the center,

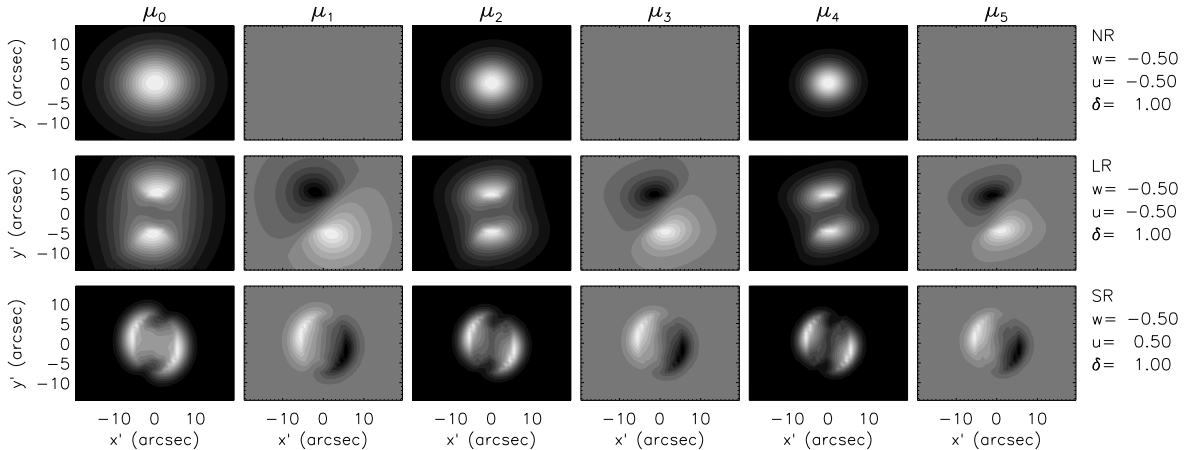


FIGURE 5 — From left to right: Projected true moments μ_k ($k = 0, \dots, 5$) of Abel DF components for a model with the triaxial separable isochrone potential (4.2) with $\zeta = 0.8$ and $\xi = 0.64$ ($T = 0.61$), and scale length $a = 10''$. The model is placed at a distance of $D = 20$ Mpc and the adopted viewing angles are $\vartheta = 70^\circ$ and $\varphi = 30^\circ$. From top to bottom: A non-rotating (NR), long-axis rotating (LR) and short-axis rotating (SR) Abel component, with the corresponding DF parameters w , u and δ given on the right.

because these components have zero density along respectively the intrinsic long and short axis. We add the true velocity moments of the NR, LR and SR components, weighted with mass fractions of respectively 80%, 10% and 10%. From the resulting combined true velocity moments, we construct the Edgeworth LOSVD and fit a Gauss-Hermite series (see Appendix C), to obtain maps of the mean line-of-sight surface mass density Σ , velocity V , velocity dispersion σ and higher-order moments h_3 and h_4 . We convert Σ to the surface brightness by dividing by a constant stellar mass-to-light ratio of $M_*/L = 4 M_\odot/L_\odot$.

To convert these ‘perfect’ kinematics to ‘realistic’ observations, similar to those obtained with SAURON (Bacon et al. 2001), we finally apply the following steps. Each of the maps consist of 30 by 40 square pixels of $1''$ in size. Using the adaptive spatial 2D-binning scheme of Cappellari & Copin (2003), we bin the pixels according to the criterion that each of the resulting (Voronoi) bins contains a minimum in signal-to-noise (S/N), which we take proportional to the square root of the surface brightness. For the mean errors in the kinematics we adopt the typical values of 10 km s^{-1} for V and σ and 0.03 for h_3 and h_4 in the kinematics of a representative sample of early-type galaxies observed with SAURON (Emsellem et al. 2004). We then weigh these values with the S/N in each bin to mimic the observed variation in measurement errors across the field. Finally, we use the computed measurement errors to (Gaussian) randomize the kinematic maps. In this way, we include the randomness that is always present in real observations. The resulting kinematic maps are shown in the top panels of Fig. 6. Because of the eight-fold symmetry of the triaxial model, the maps are always point-symmetric, apart from the noise added.

4.4 REALISTIC GALAXY MODELS WITH MULTIPLE DF COMPONENTS

In the above triaxial Abel model we only use three DF components to obtain a transparent (test) galaxy model, but with rich enough internal dynamics to provide observ-

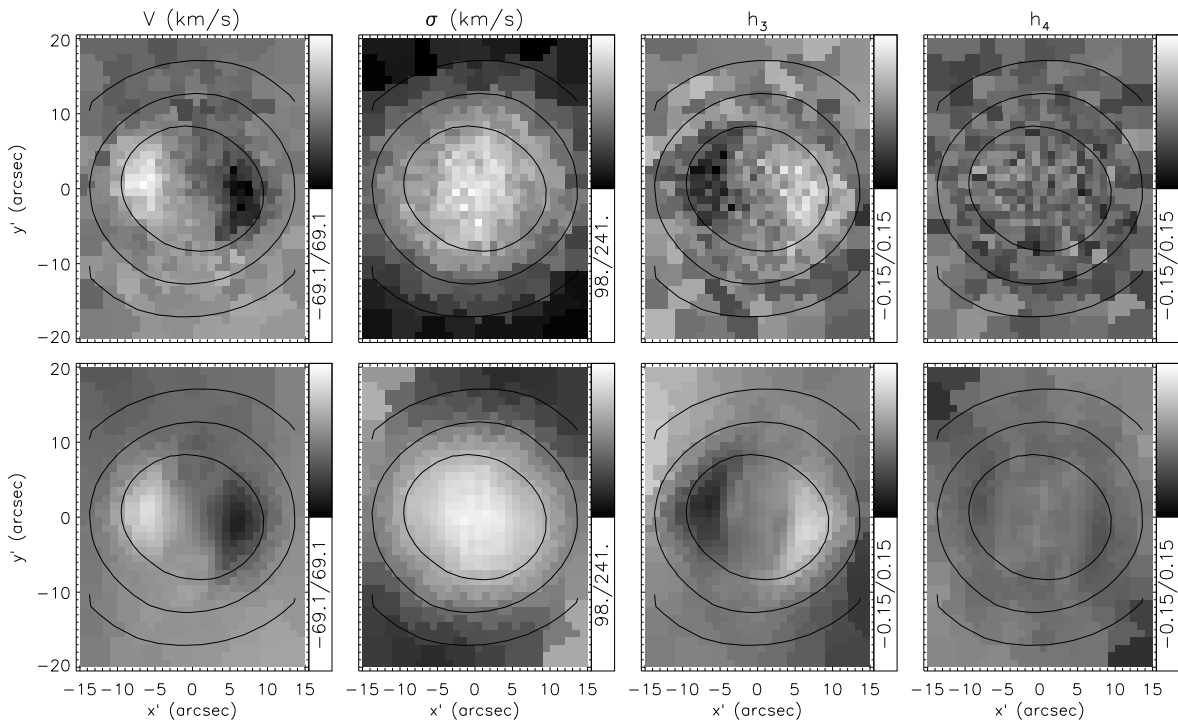


FIGURE 6 — Kinematic maps for a triaxial Abel model (top; see § 4.3) and for the best-fit triaxial Schwarzschild model (bottom; see § 6). From left to right: mean line-of-sight velocity V (in km s^{-1}), velocity dispersion σ (in km s^{-1}) and Gauss-Hermite moments h_3 and h_4 . The line-of-sight kinematics of the input Abel model have been converted to observables with realistic measurement errors as described in the text. Isophotes of the surface brightness of the Abel model are overplotted in each map. At the right side of each map, the (linear) scale of the corresponding kinematics is indicated by the grey scale bar, and the limits are given below. (See p. 253 for a color version of this figure.)

ables that mimic the kinematics of real early-type galaxies. More general Abel models can be obtained by a (linear) combination of more DF components, with varying functional forms of the variable S and different values of the parameters w and u . We saw in § 4.2 that by changing w and u the DF components can have a large range in different shapes, and the same is true for the corresponding intrinsic velocity moments (see also Fig. 9–11 of DL91).

By summing a series of DF components over w and u [with possibly different functional dependences of $f(S)$], one might expect to cover a large fraction of all physical DFs. Due to the different values of w and u , such a sum of DF components is no longer a function of the same, single variable S , so that the ellipsoidal hypothesis does not apply. Consequently, it becomes possible to construct (nearly) self-consistent dynamical models, with the (combined) luminous mass density ρ_* equal (or close) to the mass density ρ_S associated to the potential.

This combination of DF components provides an elegant way to (numerically) build three-integral galaxy models. Nuyten (2005, MSc thesis) used thirty DF components to fit the kinematic maps of the decoupled core galaxy NGC 4365 provided by observations with the integral-field spectrograph SAURON (Davies et al. 2001). The best-fit is reasonable, but deviates especially in the center due to the presence of a massive

black hole. We find constraints on the viewing direction and mass-to-light ratio, as well as a first estimate of the masses and a description of the intrinsic dynamical structure of the different orbital components, consistent with an independent determination by Statler et al. (2004). This preliminary investigation shows that Abel models with a few DF components, as in § 4.3, already provide quite a good representation of real early-type galaxies (see also MD96 for a similar application to Centaurus A).

5 AXISYMMETRIC THREE-INTEGRAL GALAXY MODELS

We now consider three-integral galaxy models in the axisymmetric limit. Various groups have successfully developed independent axisymmetric implementations of Schwarzschild's method and verified their codes in a number of ways. The published tests to recover a known (analytical) input model have been limited to spherical geometry or to an axisymmetric DF that is a function of the two integrals of motion E and L_z only. Here we present the velocity moments of the three-integral Abel DF in the axisymmetric limit and we choose again the isochrone form (4.1) for the potential. The properties of the resulting three-integral Kuzmin-Kutuzov models can be expressed explicitly in cylindrical coordinates. In § 7, we fit Schwarzschild models to the resulting observables to test our axisymmetric implementation of Schwarzschild's method.

5.1 VELOCITY MOMENTS OF AXISYMMETRIC ABEL MODELS

When two of the three constants α , β or γ are equal, the confocal ellipsoidal coordinates (λ, μ, ν) reduce to spheroidal coordinates and the triaxial Stäckel potential (2.3) becomes axisymmetric.

When $\beta = \alpha \neq \gamma$, we cannot use μ as a coordinate and replace it by the azimuthal angle ϕ , defined as $\tan \phi = y/x$. The relation between (λ, ϕ, ν) and the usual cylindrical coordinates (R, ϕ, z) is given by

$$R^2 = \frac{(\lambda + \alpha)(\nu + \alpha)}{\alpha - \gamma}, \quad z^2 = \frac{(\lambda + \gamma)(\nu + \gamma)}{\gamma - \alpha}. \quad (5.1)$$

The Stäckel potential $V_S(\lambda, \nu) = U[\lambda, -\alpha, \nu]$ is *oblate axisymmetric*. The corresponding integrals of motion follow by substitution of $\mu = -\beta = -\alpha$ in the expressions (2.5). The second integral of motion reduces to $I_2 = \frac{1}{2}L_z^2$ and the triaxiality parameter $T = 0$.

With the choice (2.9) for the DF, the expression for the velocity moments becomes

$$\mu_{lmn}(\lambda, \nu) = \sqrt{\frac{2^{l+m+n+3}}{H_{(-\alpha)\nu}^{l+1} H_{\nu\lambda}^{m+1} H_{\lambda(-\alpha)}^{n+1}}} \int_{S_{\min}}^{S_{\max}} T_{lmn} [S_{\text{top}}(\lambda, -\alpha, \nu) - S]^{(l+m+n+1)/2} f(S) dS, \quad (5.2)$$

where $H_{\sigma\tau}$ is defined in eq. (2.11) and $S_{\min} \geq S_{\text{lim}}$, which follows from Fig. 2 for $\beta = \alpha$. The lower limit on w vanishes, so that it can have any value.

For the NR type of components $S_{\max} = S_{\text{top}}(\lambda, -\alpha, \nu)$, defined in eq. (2.14), and the expression for T_{lmn}^{NR} is as in eq. (2.15). The NR velocity moments $\mu_{lmb}^{\text{NR}}(\lambda, \nu)$ vanish when either l , m or n is odd. Since the only family of orbits that exists are the short-axis tube orbits, we can introduce net rotation (around the z -axis) by setting the DF to zero for $L_z < 0$, so that $\mu_{lmn}^{\text{SR}}(\lambda, \nu) = \frac{1}{2}\mu_{lmn}^{\text{NR}}(\lambda, \nu)$. These SR velocity moments vanish when either l or n is odd, but are non-zero if m is odd. They should be multiplied with $(-1)^m$ for net rotation in the opposite direction.

In the conversion to observables described in § 3, the matrix \mathbf{Q} , which transforms the velocity components $(v_\lambda, v_\phi, v_\nu)$ to (v_x, v_y, v_z) , reduces to

$$\mathbf{Q} = \begin{pmatrix} A \cos \phi & -\sin \phi & -B \cos \phi \\ A \sin \phi & \cos \phi & -B \sin \phi \\ B & 0 & A \end{pmatrix}, \quad (5.3)$$

where A and B are defined as

$$A^2 = \frac{(\lambda + \gamma)(\nu + \alpha)}{(\lambda - \nu)(\alpha - \gamma)}, \quad B^2 = \frac{(\lambda + \alpha)(\nu + \gamma)}{(\lambda - \nu)(\gamma - \alpha)}. \quad (5.4)$$

Because of the symmetry around the short-axis, the azimuthal viewing angle φ loses its meaning and the misalignment angle $\psi = 0^\circ$. We are left with only the polar viewing angle ϑ , which is commonly referred to as the inclination i . As a consequence, the projection matrix \mathbf{P} is a function of i only and follows by substituting $\vartheta = i$ and $\varphi = 0$ in eq. (3.4), while the rotation matrix \mathbf{R} in eq. (3.5) reduces to the identity matrix.

When $\beta = \gamma \neq \alpha$, we replace the coordinate ν by the angle χ , defined as $\tan \chi = z/y$. The resulting coordinates (λ, μ, χ) follow from the above coordinates (λ, ϕ, ν) by taking $\nu \rightarrow \mu$, $\phi \rightarrow \chi$, and $\gamma \rightarrow \alpha \rightarrow \beta$. The Stäckel potential $V_S(\lambda, \mu) = U[\lambda, \mu, -\gamma]$ is now *prolate axisymmetric*, and for the integrals of motion we set $\nu = -\beta = -\gamma$ in the expressions (2.5), so that $I_3 = \frac{1}{2}L_x^2$ and $T = 1$. The intrinsic velocity moments $\mu_{lmn}(\lambda, \mu)$ follow from eq. (5.2) by interchanging $\nu \leftrightarrow \mu$, $\gamma \leftrightarrow \alpha$ and $m \leftrightarrow n$. Taking $\beta = \gamma$ in Fig. 2, we see that now the upper limit on u vanishes. In this case, $S_{\max} = S_{\text{top}}(\lambda, \mu, -\gamma)$ for the NR components, and since we only have the long-axis tube orbits, we can introduce net rotation (around the x -axis) by setting the DF to zero for $L_x < 0$, so that $\mu_{lmn}^{\text{LR}}(\lambda, \mu) = \frac{1}{2}\mu_{lmn}^{\text{NR}}(\lambda, \mu)$. The LR velocity moments vanish if either l or m is odd and multiplication with $(-1)^n$ yields net rotation in the opposite direction. The matrix \mathbf{Q} , which transforms $(v_\lambda, v_\mu, v_\chi)$ to (v_x, v_y, v_z) , in this case reduces to

$$\mathbf{Q} = \begin{pmatrix} C & -D & 0 \\ D \cos \chi & C \cos \chi & -\sin \chi \\ D \sin \chi & C \sin \chi & \cos \chi \end{pmatrix}, \quad (5.5)$$

where C and D follow from respectively A and B in (5.4) by replacing ν by μ . We substitute $\vartheta = \pi/2 - i$ and $\varphi = 0$ in eq. (3.4) to obtain the projection matrix \mathbf{P} . The rotation matrix \mathbf{R} again reduces to the identity matrix.

5.2 KUZMIN-KUTUZOV POTENTIAL AND DENSITY

In the axisymmetric limit, the form (4.1) for $U(\tau)$ results in the Kuzmin-Kutuzov (1962) potential. We give the properties relevant for our analysis, while further details can be found in Dejonghe & de Zeeuw (1988), including expressions and plots of the mass density ρ_S , its axis ratios, and the two-integral DF $f(E, L_z^2)$ consistent with ρ_S [see also Batsleer & Dejonghe (1993), who also corrected a typographical error in $f(E, L_z^2)$].

When $\beta = \alpha$, the oblate axisymmetric potential $V_S(\lambda, \nu) = U[\lambda, -\alpha, \nu]$ and the third order divided difference $U[\lambda, -\alpha, \nu, \sigma]$, which both appear in the expressions for the integral of motions (2.5), have the simple forms

$$V_S(\lambda, \nu) = \frac{-GM}{\sqrt{\lambda} + \sqrt{\nu}}, \quad (5.6)$$

$$U[\lambda, -\alpha, \nu, \sigma] = \frac{-GM}{(\sqrt{\lambda} + \sqrt{\nu})(\sqrt{\lambda} + \sqrt{\sigma})(\sqrt{\nu} + \sqrt{\sigma})}, \quad (5.7)$$

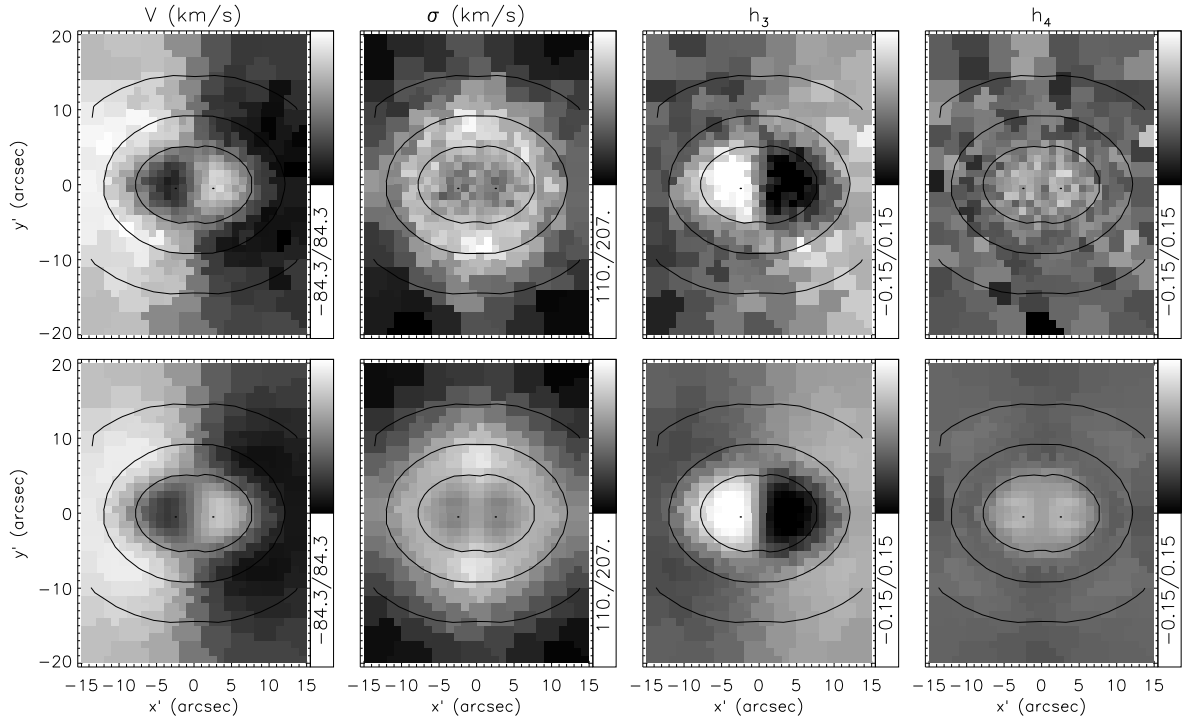


FIGURE 7 — Kinematic maps for an oblate axisymmetric Abel model (top; see § 5.3) and for the fitted axisymmetric Schwarzschild model (bottom; see § 7). Parameters and grey scale are as in Fig. 6. (See p. 255 for a color version of this figure.)

where again $GM = \sqrt{-\gamma} + \sqrt{-\alpha}$, so that $V_S = -1$ in the center. By means of the relations

$$\lambda + \nu = R^2 + z^2 - \alpha - \gamma, \quad \lambda\nu = \alpha\gamma - \gamma R^2 - \alpha z^2, \quad (5.8)$$

and $(\sqrt{\lambda} + \sqrt{\nu})^2 = \lambda + \nu + 2\sqrt{\lambda\nu}$ and $(\sqrt{\lambda} + \sqrt{\sigma})(\sqrt{\nu} + \sqrt{\sigma}) = \sqrt{\lambda\nu} + \sqrt{\sigma}(\sqrt{\lambda} + \sqrt{\nu}) + \sigma$, we can write the potential and integrals of motion explicitly as elementary expressions in the usual cylindrical coordinates.

When $\beta = \gamma$, the prolate potential $V_S(\lambda, \mu) = U[\lambda, \mu, -\gamma]$ and the third order divided difference $U[\lambda, \mu, -\gamma, \sigma]$ follow respectively from (5.6) and (5.7) by replacing ν by μ .

5.3 AN AXISYMMETRIC ABEL MODEL

The above constructed triaxial Abel model (§ 4.3) transforms into an oblate axisymmetric Abel model if we let ζ approach unity, while keeping $\xi = 0.64$ fixed. We keep the NR component with the same parameters, $u = w = -0.5$ and $\delta = 1$, but we exclude the LR component since long-axis tube orbits do not exist in an oblate axisymmetric galaxy. We include two SR components, one with the same parameters as the NR component, and for the other we set $u = 0.5$ and choose the sense of rotation in the opposite direction. The latter implies a compact counter-rotating component, which is clearly visible in the kinematic maps shown in the top panels of Fig. 7. The inclination is the same value as the polar angle ϑ for the triaxial Abel model, i.e. $i = 70^\circ$, and the mass fractions of the three DF components are respectively 20%, 60% and 20%. Due to axisymmetry all maps are bi-symmetric and the velocity field shows a straight zero-velocity curve. The signatures of the counter-rotation are similar in the velocity

field and h_3 (but anti-correlated), and result in a decrease of σ and an increase of h_4 in the center.

6 RECOVERY OF TRIAXIAL GALAXY MODELS

We briefly describe our numerical implementation of Schwarzschild's method in triaxial geometry (see van den Bosch et al. 2006 for a full description), which we then use to fit the observables of the triaxial Abel model constructed in § 4.3. We investigate the recovery of the intrinsic velocity moments and, through the distribution of the orbital mass weights, the recovery of the three-integral DF. We also determine the constraints placed on the viewing direction and the mass-to-light ratio.

6.1 TRIAXIAL SCHWARZSCHILD MODELS

The first step is to infer the gravitational potential from the observed surface brightness. This is done by means of the Multi-Gaussian Expansion method (MGE; e.g., Cappellari 2002), which allows for possible position angle twists and ellipticity variations in the surface brightness. For a given set of viewing angles $(\vartheta, \varphi, \psi)$ (see § 3.1), the surface brightness is deprojected and multiplied by a mass-to-light ratio M/L to yield the intrinsic mass density, from which the gravitational potential then follows by solving Poisson's equation. Orbits are calculated numerically in the resulting gravitational potential. To obtain a representative library of orbits, the integrals of motion have to be sampled well. The energy can be sampled directly, but since the other integrals of motion are generally not known, we start, at a given energy, orbits from a polar grid in the (x, z) -plane, which is crossed perpendicularly by all families of (regular) orbits. To have enough box orbits to support the triaxial shape, we also start orbits by dropping them from the equipotential surface (Schwarzschild 1979, 1993).

Assigning a mass weight γ_j to each orbit j from the library, we compute their combined properties and find the weighted superposition that best fits the observed surface brightness and (two-dimensional) kinematics. However, the resulting orbital weight distribution may vary rapidly, and hence probably corresponds to an unrealistic DF. To obtain a smoothly varying DF, we both dither the orbits by considering a bundle of integrated orbits that were started close to each other, and we regularize when looking for the best-fit set of orbital weights by requiring them to vary smoothly between neighboring orbits (in integral space). The best-fit Schwarzschild model follows from the minimum in

$$\chi^2 = \sum_{i=1}^{N_O} \left(\frac{O_i - O_i^*}{\Delta O_i} \right)^2, \quad (6.1)$$

where N_O is the number of (photometric and kinematic) observables O_i with associated error ΔO_i and O_i^* is the corresponding model prediction.

In this case, we can use directly the isochrone Stäckel potential V_S of the triaxial Abel model. However, to closely simulate the Schwarzschild modeling of real galaxies, we infer the potential from a deprojection of an MGE fit of the surface mass density Σ_S generated by V_S . The resulting potential reproduces V_S to high precision.

We compute a library of orbits by sampling 21 energies E via a logarithmic grid in radius from $1''$ to $224''$ that contains ≥ 99.9 per cent of the total mass. At each energy, we construct a uniform polar grid of 7 radii by 8 angles within the region in the first quadrant of the (x, z) -plane that is enclosed by the equipotential and the thin orbit

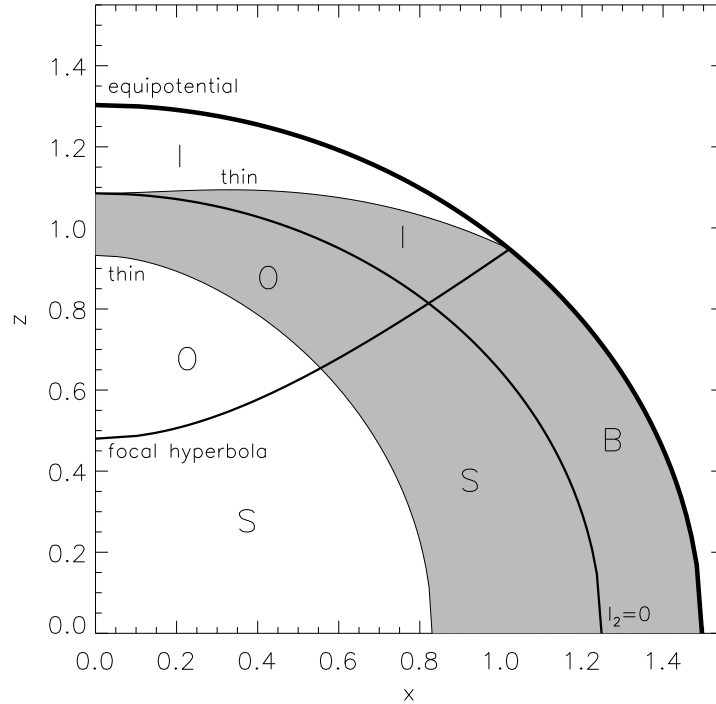


FIGURE 8 — The (x, z) -plane for a triaxial isochrone potential (4.2) with $\zeta = 0.8$ and $\xi = 0.64$, at a given energy E (cf. Schwarzschild 1993). The region inside the equipotential (solid curve) is crossed perpendicularly by the four general orbit families: box (B) orbits, inner (I) and outer (O) long-axis tube orbits and short-axis (S) tube orbits. They are separated by the focal hyperbola of the ellipsoidal coordinate system in which the equations of motion separate, and the curve on which the second integral of motion I_2 is zero. The thin orbits with maximum streaming divide the regions of the tube orbits in two parts, each of which is crossed once by each tube orbit. By considering only the grey region, we sample all orbits without duplication.

curves (Fig. 8). In addition, we drop box orbits from a similar uniform polar grid on the equipotential surface in the first octant. This results in a total of $21 \times 7 \times 8 \times 2 = 2352$ starting positions, from each of which a bundle of 6^3 orbits are started. Taking into account the two senses of rotation of the tube orbits, this results in a total 762048 orbits that are numerically integrated in the potential.

The velocities of each bundle of orbits are summed in histograms with 201 bins, at a velocity resolution of 10 km s^{-1} . The weighted sum of the velocity histograms is fitted to the intrinsic density ρ_* and simultaneously their projected values are fitted to the observed surface brightness and higher-order velocity moments. At the same time, the orbital weights are regularized in E and in the starting positions by minimizing their second order derivatives and requiring that these derivatives are smaller than the smoothing parameter (e.g., Cretton et al. 1999), which we set to $\Delta = 4$.

6.2 INTRINSIC MOMENTS

We calculate the intrinsic first and second order velocity moments of the Schwarzschild model by combining the appropriate moments of the orbits that receive weight in the superposition, and investigate how well they compare with the intrinsic veloc-

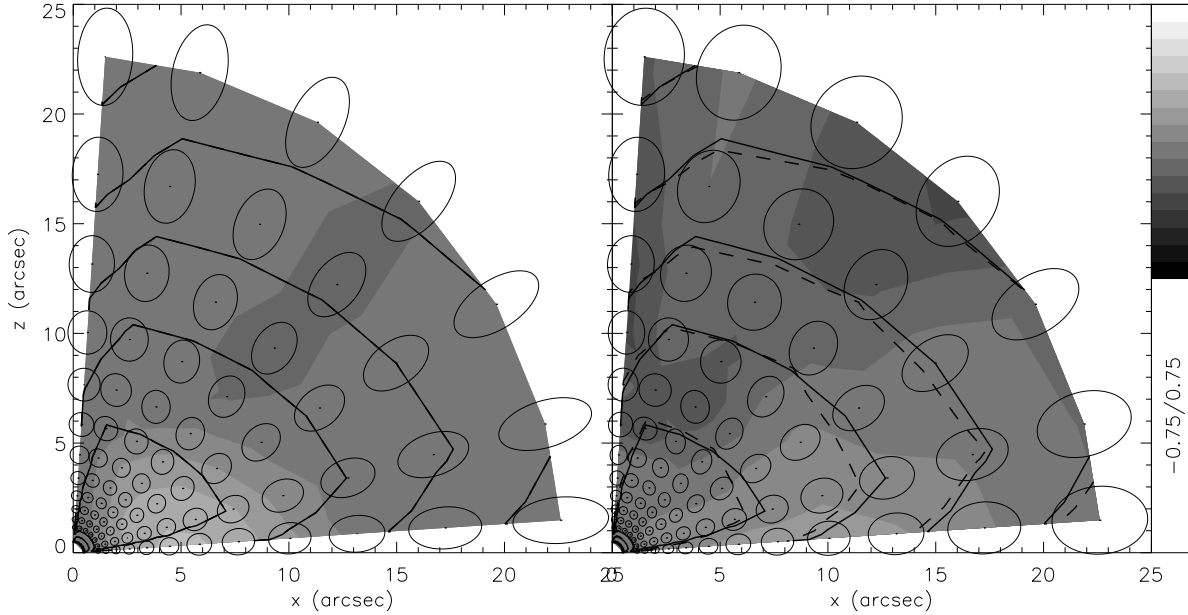


FIGURE 9 — The grey scale represents the mean motion $\langle v_y \rangle$ perpendicular to the (x, z) -plane, normalized by σ_{RMS} (excluding the axes to avoid numerical problems), for a triaxial Abel model (left) and for the best-fit triaxial Schwarzschild model (right). The ellipses are cross sections of the velocity ellipsoid with the (x, z) -plane. The black curves are contours of constant mass density in steps of one magnitude, for the input Abel model (solid) and for the fitted Schwarzschild model (dashed). See § 6.2 for details. (See p. 254 for a color version of this figure.)

ity moments of the Abel model. In general, there are three first $\langle v_t \rangle$ and six second order velocity moments $\langle v_s v_t \rangle$ ($s, t = x, y, z$). Combining them yields the six dispersion components σ_{st} of the velocity ellipsoid, where $\sigma_{st}^2 \equiv \langle v_s v_t \rangle - \langle v_s \rangle \langle v_t \rangle$.

To facilitate visualization, we restrict the analysis to a single plane. We choose the (x, z) -plane, as it is crossed perpendicularly by all four (major) orbit families. Because $\langle v_x \rangle = \langle v_z \rangle = \sigma_{xy} = \sigma_{yz} = 0$, we are left with $\langle v_y \rangle$ perpendicular to the (x, z) -plane as the only non-vanishing mean motion and σ_{zx} in the (x, z) -plane as the only non-vanishing cross-term. The average root-mean-square velocity dispersion σ_{RMS} is given by $\sigma_{\text{RMS}}^2 = (\sigma_x^2 + \sigma_y^2 + \sigma_z^2)/3$, where $\sigma_x \equiv \sigma_{xx}$, $\sigma_y \equiv \sigma_{yy}$ and $\sigma_z \equiv \sigma_{zz}$.

The ratio $\langle v_y \rangle / \sigma_{\text{RMS}}$ of ordered over random motion is a measure of the importance of rotation for the gravitational support of a galaxy. In Fig. 9, the grey scale shows the values of this ratio in the (x, z) -plane, for the triaxial Abel model (left panel) and for the fitted triaxial Schwarzschild model (right panel). The ellipses show the cross sections of the velocity ellipsoid with the (x, z) -plane. In a Stäckel potential the axes of the velocity ellipsoid are aligned with the confocal ellipsoidal coordinate system (e.g., Eddington 1915; van de Ven et al. 2003). As a result, one of the axes of the velocity ellipsoid is perpendicular to the (x, z) -plane, with semi-axis length σ_y . The other two axes lie in the (x, z) -plane and have semi-axis lengths given by

$$\sigma_{\pm}^2 = \frac{1}{2}(\sigma_x^2 + \sigma_y^2) \pm \sqrt{\frac{1}{4}(\sigma_x^2 - \sigma_y^2)^2 + \sigma_{xy}^4}. \quad (6.2)$$

The ellipses are radially elongated, corresponding to a radial anisotropic velocity distribution. Finally, the black curves are contours of constant luminous mass density in steps of one magnitude.

The density of the triaxial Abel model (solid curve) is well fitted by the triaxial Schwarzschild model (dashed curve). In both the Abel model and the fitted Schwarzschild model $\langle v_y \rangle / \sigma_{\text{RMS}}$ is relatively low. The Abel model shows an increase to a value of 0.3 near the x -axis, caused by the decoupled core (Fig. 6). This enhancement is not well reproduced by the Schwarzschild model, which moreover shows a slight decrease of $\langle v_y \rangle / \sigma_{\text{RMS}}$ towards the z -axis. In this region the ellipses are also rounder than in the Abel model, but towards the equatorial plane the ellipses are very similar. The orientation of the ellipses agrees over most of the (x, z) -plane. This shows that, although there is still room for improvement by refining for example the orbit sampling, the main intrinsic dynamical properties of the Abel model are recovered reasonably well.

6.3 DISTRIBUTION FUNCTION

The fitted triaxial Schwarzschild model results in a mass weight γ per orbit. These mass weights are a function of the three integrals of motion (E, I_2, I_3) . In general, only the energy is exact, but for a separable potential I_2 and I_3 are also known explicitly and given by (2.5). The orbital mass weights are related to the DF $f(E, I_2, I_3)$ via the phase-space volume (see Vandervoort 1984)

$$\gamma(E, I_2, I_3) = \iiint_{\text{cell}} f(E, I_2, I_3) \Delta V(E, I_2, I_3) dE dI_2 dI_3, \quad (6.3)$$

where the integration is over the cell in integral space represented by the orbit. The DF of the input Abel model is given in § 2.3. We first calculate ΔV and the integration volume, and then return to the comparison of the orbital mass weights.

6.3.1 Phase-space volume

The expression for the phase-space volume $\Delta V(E, I_2, I_3)$ can be deduced from the relations in § 7.1 of de Zeeuw (1985a). It is given by

$$\Delta V(E, I_2, I_3) = \frac{\gamma - \alpha}{2\sqrt{2}} \iiint_{\Omega} \sqrt{\frac{(\lambda + \beta)(\mu + \beta)(\nu + \beta)}{[E - V_{\text{eff}}(\lambda)][E - V_{\text{eff}}(\mu)][E - V_{\text{eff}}(\nu)]}} \times \frac{(\lambda - \mu)(\mu - \nu)(\nu - \lambda) d\lambda d\mu d\nu}{(\lambda + \alpha)(\lambda + \beta)(\lambda + \gamma)(\mu + \alpha)(\mu + \beta)(\mu + \gamma)(\nu + \alpha)(\nu + \beta)(\nu + \gamma)}, \quad (6.4)$$

where the effective potential V_{eff} is defined as⁵

$$V_{\text{eff}}(\tau) = \frac{I_2}{\tau + \alpha} + \frac{I_3}{\tau + \gamma} + \frac{U(\tau)}{(\tau + \alpha)(\tau + \gamma)}, \quad (6.5)$$

and Ω is the configuration space volume accessible by the orbit in the triaxial separable potential that obeys the three integrals of motion (E, I_2, I_3) .

Because of the separability of the equations of motion, each orbit in a triaxial separable potential can be considered as a sum of three independent motions. Each of these one-dimensional motions is either an oscillation or rotation in one of the three

⁵ $U(\tau)$ is defined up to an arbitrary linear function, and can always be written as $-(\tau + \alpha)(\tau + \gamma)G(\tau)$, with $-G(\tau)$ the potential along the intermediate axis, so that the third term in (6.5) is well defined. The sign convention here is consistent with de Zeeuw (1985a)

orbit	I_2	E	λ	μ	ν
B	< 0	$V_{\text{eff}}(-\beta) \dots 0$	$[-\alpha, \lambda_{\text{max}}]$	$[-\beta, \mu_{\text{max}}]$	$[-\gamma, \nu_{\text{max}}]$
I	< 0	$\min[V_{\text{eff}}(\mu)] \dots V_{\text{eff}}(-\beta)$	$[-\alpha, \lambda_{\text{max}}]$	$[\mu_{\text{min}}, \mu_{\text{max}}]$	$[-\gamma, -\beta]$
O	> 0	$\min[V_{\text{eff}}(\lambda)] \dots V_{\text{eff}}(-\beta)$	$[\lambda_{\text{min}}, \lambda_{\text{max}}]$	$[\mu_{\text{min}}, -\alpha]$	$[-\gamma, -\beta]$
S	> 0	$\max\{V_{\text{eff}}(-\beta), \min[V_{\text{eff}}(\lambda)]\} \dots 0$	$[\lambda_{\text{min}}, \lambda_{\text{max}}]$	$[-\beta, -\alpha]$	$[-\gamma, \nu_{\text{max}}]$

TABLE 1 — Configuration space Ω for the four families of regular orbits.

confocal ellipsoidal coordinates (λ, μ, ν) , such that the configuration space volume Ω is bounded by the corresponding coordinate surfaces. The values of (λ, μ, ν) that correspond to these bounding surfaces can be found from Table 1 for the four families of regular orbits: boxes (B), inner (I) and outer (O) long-axis tubes, and short-axis (S) tubes. Whereas α , β and γ are the limits on (λ, μ, ν) set by the foci of the confocal ellipsoidal coordinate system, the other limits are the solutions of $E = V_{\text{eff}}(\tau)$ (see Fig. 7 of de Zeeuw 1985a). In the case of the triaxial isochrone Stäckel potential (4.2), we can write this equation as a fourth-order polynomial in $\sqrt{\tau}$. The solutions are then the squares of three of the four roots of this polynomial (the fourth root is always negative).

For each orbit in our Schwarzschild model, we compute (E, I_2, I_3) by substituting the starting position and velocities of the orbit into the expressions (2.5). From the value of E and the sign of I_2 (while always $I_3 \geq 0$), we determine to which orbit family it belongs. The corresponding configuration space volume Ω is then given by the boundaries for λ , μ and ν in the last three columns of Table 1. The phase-space volume $\Delta V(E, I_2, I_3)$ follows by numerical evaluation of the right-hand side of eq. (6.4).

The integrand in (6.4) contains singularities at the integration limits, which can be removed for a triaxial isochrone potential. We write the integrand completely in terms of $(\sqrt{\sigma} \pm \sqrt{\tau})^{1/2}$, where $\sigma, \tau = \lambda, \mu, \nu$ or a constant value. Suppose now that the integral over λ ranges from λ_0 to λ_1 and the terms $(\sqrt{\lambda} - \sqrt{\lambda_0})^{1/2}$ and $(\sqrt{\lambda_1} - \sqrt{\lambda})^{1/2}$ appear in the denominator. The substitution $\sqrt{\lambda} = \sqrt{\lambda_0} + (\sqrt{\lambda_1} - \sqrt{\lambda_0}) \sin^2 \eta$ then removes both singularities since $d\lambda / [(\sqrt{\lambda} - \sqrt{\lambda_0})(\sqrt{\lambda_1} - \sqrt{\lambda})]^{1/2} = 4\sqrt{\lambda} d\eta$.

6.3.2 Cell in integral space

We approximate the triple integration over the cell in integral space in eq. (6.3) by the volume $\Delta E \Delta(I_{2,3})$. Here ΔE is the (logarithmic) range in E between subsequent sets of orbits at different energies (see § 6.1), with outer boundaries given by the central potential and $E = 0$. Because we do not directly sample I_2 and I_3 in our implementation of Schwarzschild's method, as their expressions are in general unknown, we cannot directly calculate the area $\Delta(I_{2,3})$. Instead, we compute the Voronoi diagram of the points in the (I_2, I_3) -plane that correspond to the starting position and velocities of each orbit, at a given energy E . An example is given in the left panel of Fig. 10. The area of the Voronoi bins approximates the area $\Delta(I_{2,3})$ for each orbit.

The four families of regular orbits are separated by two lines that follow from $I_2 = 0$ and $E = V_{\text{eff}}(-\beta)$. The latter provides also part of the boundary on I_2 and I_3 . The remainder is given by the positivity constraint on I_3 and by the solution of $E = V_{\text{eff}}(\kappa_0)$ and $dV_{\text{eff}}(\kappa_0)/d\kappa = 0$, with $\kappa_0 \geq -\beta$ (cf. eqs 64 and 65 of de Zeeuw 1985a).

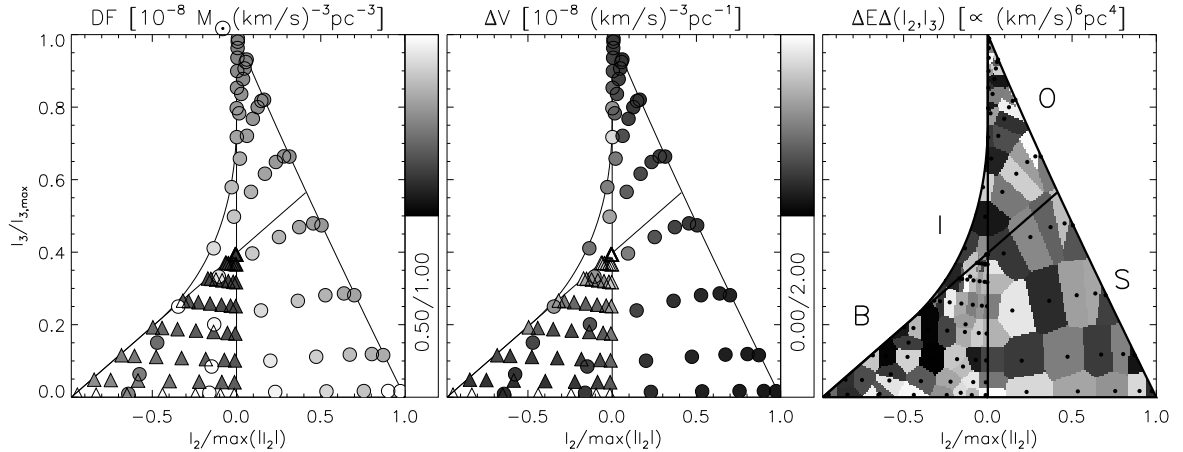


FIGURE 10 — Three quantities involved in the calculation of the orbital mass weights for a triaxial Abel model with an isochrone potential. For a given energy E , in each panel, the values of the second and third integral of motion, I_2 and I_3 , are shown that correspond to the orbital starting position and velocities in the triaxial Schwarzschild model that is fitted to the observables of this triaxial Abel model. The circles refer to orbits started in the (x, z) -plane and the triangles represent the additional set of orbits dropped from the equipotential surface (see § 6.1). The grey scale in the left panel indicates the value of the DF $f(E, I_2, I_3)$ for each orbit. The grey scale in the middle panel represents the values of the phase-space volume $\Delta V(E, I_2, I_3)$. The area of each Voronoi bin in the right panel, multiplied by the range in energy E , approximates the cell $\Delta E \Delta(I_2, I_3)$ in integral space for each orbit. The product of these three values provides an estimate of the mass weight $\gamma(E, I_2, I_3)$ for each orbit. The solid curves bound and separate the regions of the box (B) orbits, inner (I) and outer (O) long-axis tube orbits and short-axis (S) tube orbits.

For $-\beta \leq \kappa_0 \leq -\alpha$ the solution describes the boundary curve for which $I_2 \leq 0$ and corresponds to the thin I tube orbits. For $\kappa_0 \geq -\alpha$ we find the boundary curve for which $I_2 \geq 0$, corresponding to the thin O and S tube orbits.

There are limits on the values of κ_0 depending on the value of E , and sometimes there are no valid solutions for κ_0 , which implies that the corresponding tube orbits do not contribute at that energy. These limits can be obtained from the thin orbit curves in the (x, z) -plane (Fig. 8). From the expressions for the integrals of motion (2.5) in this plane, we find that the thin orbit curves follow by solving $E = U[\lambda, \kappa_0, \kappa_0]$ for I tubes and $E = U[\kappa_0, \kappa_0, \kappa]$, with $\kappa = \mu$ for O tubes and $\kappa = \nu$ for S tubes. In general these equations have to be solved numerically, but in the case of the triaxial isochrone potential (4.2), they reduce to a second order polynomial in $\sqrt{\kappa_0}$ and the solutions simply follow from the roots of the polynomial.

6.3.3 Orbital mass weight distribution

Once we have computed for each orbit the DF $f(E, I_2, I_3)$, the phase-space volume $\Delta V(E, I_2, I_3)$ and the cell $\Delta E \Delta(I_2, I_3)$ in integral space (Fig. 10), its (approximate) mass weight $\gamma(E, I_2, I_3)$ follows by multiplication of these three quantities. The resulting orbital mass weight distribution of the input triaxial Abel model is shown in the top panels of Fig. 11, and that of the fitted triaxial Schwarzschild model in the bottom panels. The energy E increases from left to right, which corresponds to increasing distance from the center as is indicated by the radius R_E (in arcsec) at the top of each

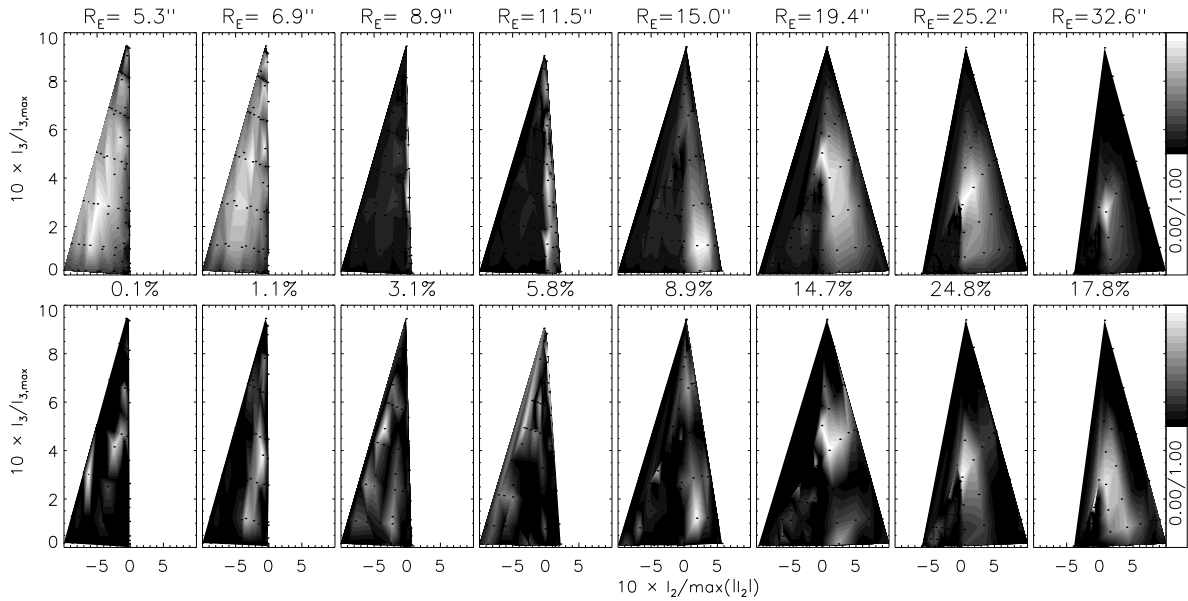


FIGURE 11 — The orbital mass weight distribution for the input triaxial Abel model (top) and for the fitted triaxial Schwarzschild model (bottom). From left to right the energy increases, corresponding to increasing distance from the center, indicated by the radius R_E (in arcsec) of the thin short-axis tube orbit on the x -axis. The vertical and horizontal axes represent respectively the second and third integral of motion, I_2 and I_3 , normalized by their maximum amplitude (for given E). Between the two rows of panels, the fraction (in %) of the included mass with respect to the total mass is indicated. (See p. 254 for a color version of this figure.)

panel. For this representative radius we use the radius of the corresponding thin (S) tube orbit on the long x -axis (Fig. 8). The values of I_2 and I_3 on the horizontal and vertical axes respectively, are both normalized with respect to their maximum amplitude at the given energy. In each panel the mass weight values are normalized with respect to the maximum in that panel. Between the two rows of panels, the fraction of the summed values in each panel with respect to the total mass weight in all panels is given as a percentage.

The four panels with the largest fraction in mass, with R_E between about $15''$ and $30''$, are best constrained by the kinematic observables, taking into account that even orbits that extend beyond the maximum radius covered by the data can contribute significantly at lower radii. In these panels, the main features of the orbital mass weight distribution of the triaxial Abel model are recovered reasonably well. In the inner panels the orbital mass weight distribution in the Schwarzschild model is relatively noisy, which is mostly the consequence of the discreteness of the orbit library as well as the numerical nature of the method. In the outer parts the Schwarzschild model is still constrained by the mass model, which extends to a radius of about hundred arcseconds, but the orbital mass weight distribution deviates from that of the input Abel model due to the lack of kinematic constraints.

6.4 GLOBAL PARAMETERS

In the experiments described in the above, we computed the best-fit Schwarzschild model for the viewing angles $(\vartheta, \varphi, \psi) = (70^\circ, 30^\circ, 101^\circ)$ and mass-to-light ratio $M/L =$

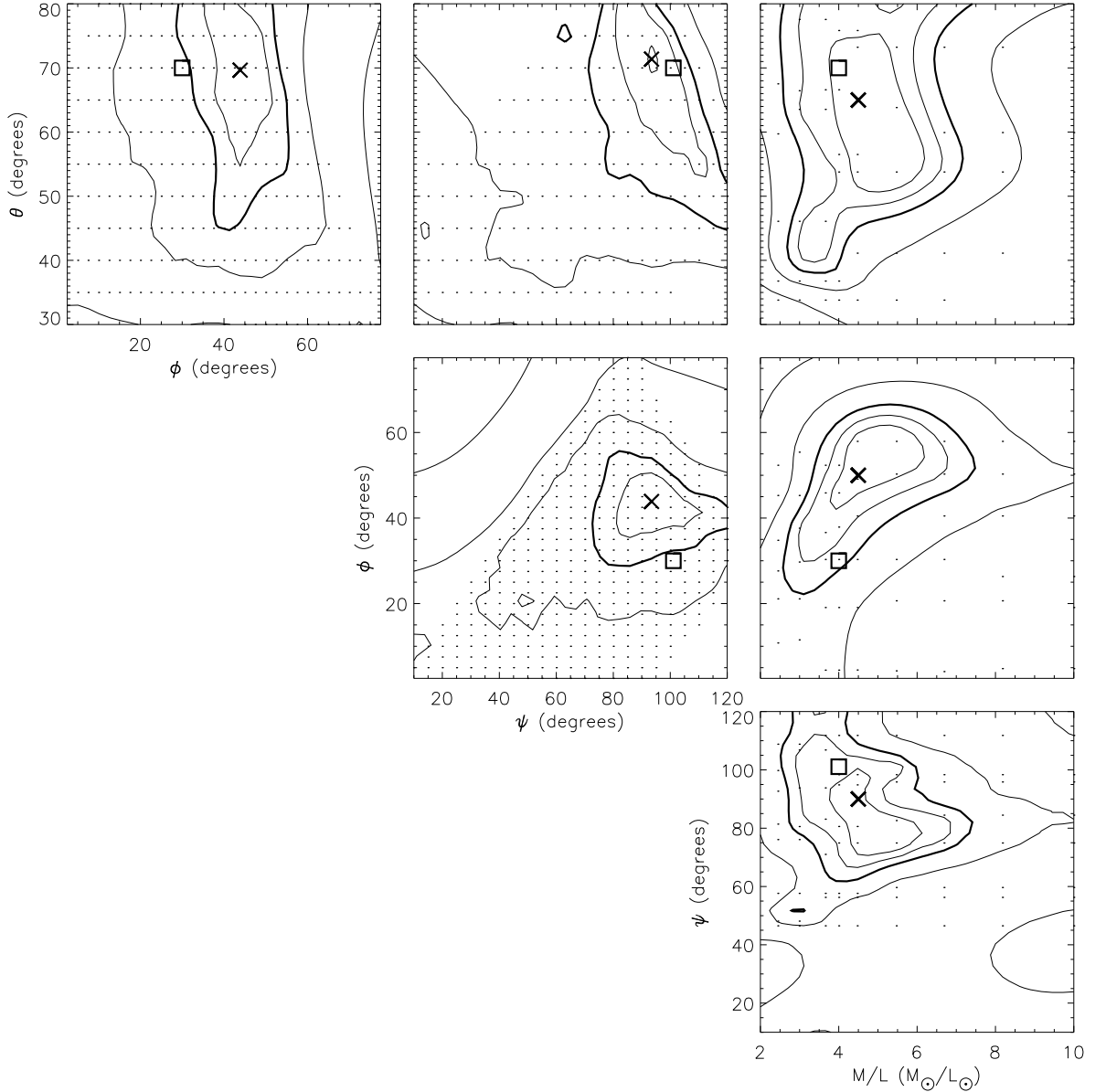


FIGURE 12 — The (marginalized) goodness-of-fit parameter $\Delta\chi^2$ as a function of viewing angles (ϑ, φ, ψ) and mass-to-light ratio M/L , for different triaxial Schwarzschild model fits to a triaxial Abel model (see text for details). The χ^2 -values are offset such that the overall minimum, indicated by the cross, is zero. The contours are drawn at the confidence levels for a $\Delta\chi^2$ -distribution with four degrees of freedom, with inner three contours corresponding to the 68.3%, 95.4% and 99.7% (thick contour) confidence levels. Subsequent contours correspond to a factor of two increase in $\Delta\chi^2$. The parameters of the input Abel model, $(\vartheta, \varphi, \psi) = (70^\circ, 30^\circ, 101^\circ)$ and $M/L = 4 M_{\odot}/L_{\odot}$, are indicated by the open square.

$4 M_{\odot}/L_{\odot}$ for which the simulated observables of the triaxial Abel model were obtained. We recalculated the best-fit Schwarzschild model for a range of these parameters, and compared the resulting χ^2 -values (6.1) in order to establish which models (still) provide an acceptable fit. We quantify the quality of each fit by the difference

$\Delta\chi^2(\vartheta, \varphi, \psi, M/L)$ with respect to the overall minimum χ^2 value. To visualize this four-dimensional function, we calculate for a pair of parameters, say ϑ and φ , the minimum in $\Delta\chi^2$ as function of the remaining parameters, ψ and M/L in this case. The contour plots of the resulting marginalized $\Delta\chi^2$ for all different pairs of parameters are shown in Fig. 12. The contours are drawn at the confidence levels for a $\Delta\chi^2$ -distribution with four degrees of freedom, with the inner three contours corresponding to the 68.3%, 95.4% and 99.7% (thick contour) confidence levels. Subsequent contours correspond to a factor of two increase in $\Delta\chi^2$. In each panel, the overall minimum ($\Delta\chi^2 = 0$) is indicated by the cross, while the open square corresponds to the parameters of the input Abel model.

A range of viewing angles is excluded as they lead to nonphysical deprojections of the MGE fit to the projected luminosity density (or surface brightness). Since the observables depend in a non-linear way on the viewing angles, we do not sample the viewing angles uniformly. Instead, we sample uniformly in the characteristic (4.5) axis ratios b/a , c/a and a'/a for a given observed flattening b'/a' , resulting in an irregular grid in the viewing angles. In this way, we keep the number of viewing angles relatively low and still have a representative sampling. Since the Schwarzschild method is computationally expensive, such an optimization allows a full search through parameter space within a reasonable time. A parallel search on thirty desktop computers through three hundred combinations of viewing angles and ten different M/L values, currently takes about one week. To calculate the marginalized $\Delta\chi^2$ we need to interpolate (linearly) in the irregular grid of viewing angles. The dots in Fig. 12 show the corresponding (regular) grid of viewing angles, together with the (regular) sampling in M/L .

We find that the input M/L is well recovered, with a typical uncertainty of order 10%. The viewing angles of the input model are recovered to within 10 degrees, but the allowed range in ϑ is about 35 degrees, and for φ and ψ it is almost 20 degrees. While Schwarzschild models with global parameters in this range provide an acceptable fit to the observables, their intrinsic moments and orbital mass weight distribution can deviate significantly from those of the input Abel model. We return to this apparent degeneracy in the viewing direction in § 8.

7 RECOVERY OF AXISYMMETRIC GALAXY MODELS

We now describe the application of our axisymmetric implementation of Schwarzschild's method to the observables of the oblate Abel model of § 5.3, while highlighting the differences with the above application in triaxial geometry.

7.1 AXISYMMETRIC SCHWARZSCHILD MODELS

Our implementation of Schwarzschild's method in axisymmetric geometry is described in detail in Cappellari et al. (2005). The main differences with respect to our triaxial implementation are certain simplifications due to the extra symmetry. There are no twists in the surface brightness. We use the same set-up as in the triaxial case, but since the box orbits are not present, the additional dropping of orbits from the equipotential surface is not needed.

7.2 INTRINSIC MOMENTS

It is convenient to analyze the intrinsic velocity moments of (oblate) axisymmetric models in cylindrical coordinates (R, ϕ, z) . Because of axisymmetry the models are

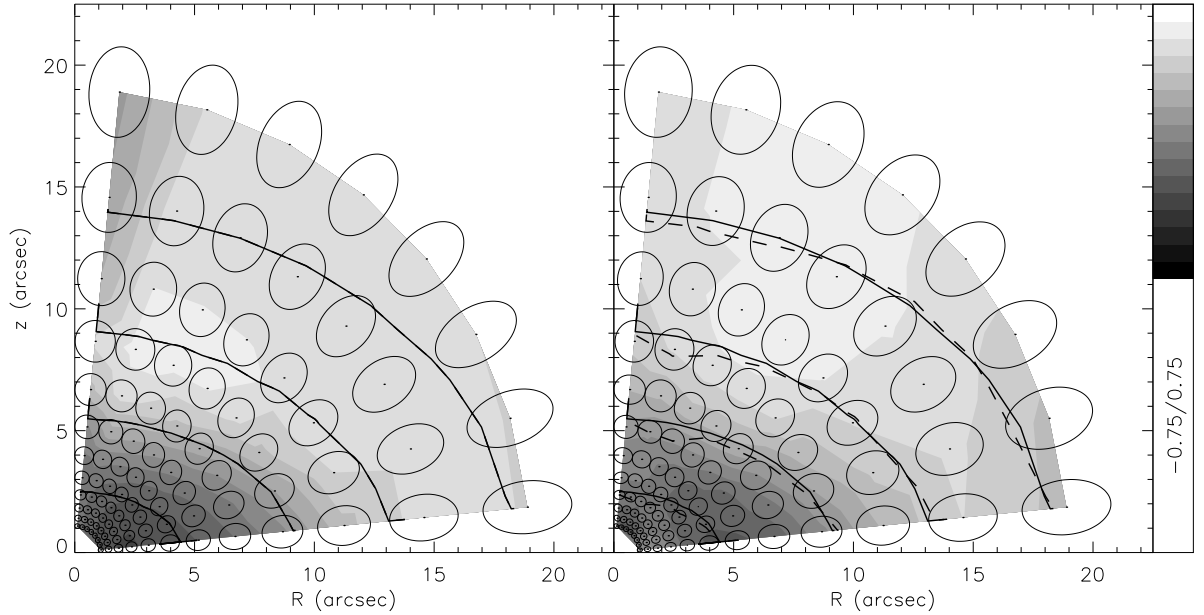


FIGURE 13 — The mean azimuthal motion $\langle v_\phi \rangle$ perpendicular to the meridional plane, normalized by σ_{RMS} , for an oblate axisymmetric Abel model (left) and for the best-fit axisymmetric Schwarzschild model (right). Parameters and grey scale are as in Fig. 9. (See p. 255 for a color version of this figure.)

independent of the azimuthal angle ϕ , and it is sufficient to consider the meridional (R, z) -plane. The analysis of the intrinsic velocity moments in the (R, z) -plane is similar to that for the triaxial case in the (x, z) -plane (§ 6.2). In this case, the mean azimuthal rotation $\langle v_\phi \rangle$, perpendicular to the meridional plane, is the only non-vanishing first order velocity moment. In Fig. 13, we compare the values of $\langle v_\phi \rangle / \sigma_{\text{RMS}}$, indicated by the grey scale, for the Abel model (left panel) with those for the fitted Schwarzschild model (right panel). The root-mean-square velocity dispersion σ_{RMS} is defined as $\sigma_{\text{RMS}}^2 = (\sigma_R^2 + \sigma_\phi^2 + \sigma_z^2)/3$. The azimuthal axis of the velocity ellipsoid, with semi-axis length σ_ϕ defined as $\sigma_\phi^2 = \langle v_\phi^2 \rangle - \langle v_\phi \rangle^2$, is perpendicular to the meridional plane. The cross sections with the meridional plane are indicated by the ellipses in Fig. 13, where the semi-axis lengths follow from (6.2) by replacing (x, z) with (R, z) .

As in the triaxial case the density (solid curve) is well fitted by the axisymmetric Schwarzschild model (dashed curve). The Abel model shows a strong gradient in $\langle v_\phi \rangle / \sigma_{\text{RMS}}$, which is accurately recovered by the axisymmetric Schwarzschild model. The absolute difference is on average less than 0.07, except near the symmetry z -axis. This is likely the result of numerical difficulties due to the small fraction of mass contributed in this region by the short-axis tube orbits. The shape and orientation of the ellipses are nearly identical, indicating that the anisotropic velocity distribution of the Abel model is recovered to high accuracy. The lengths of the axes of the velocity ellipsoid deviate on average by only 5 km s^{-1} , i.e., well within the typical error of 10 km s^{-1} assigned to the simulated velocity dispersion of the Abel model (§ 5.3).

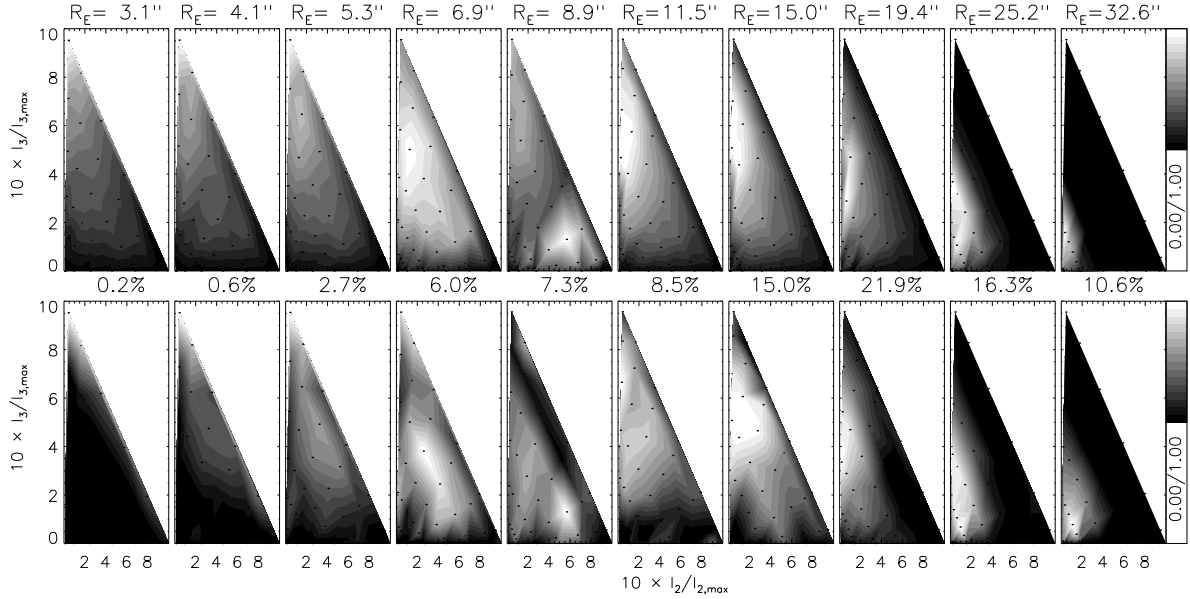


FIGURE 14 — *The mass weight distribution for an oblate axisymmetric Abel model (top) and for the fitted axisymmetric Schwarzschild model (bottom). Parameters and grey scale are the same as in Fig. 11. In this case, the second integral of motion $I_2 = \frac{1}{2}L_z^2$, where L_z is the component of the angular momentum parallel to the symmetry z -axis. (See p. 256 for a color version of this figure.)*

7.3 DISTRIBUTION FUNCTION

In the oblate axisymmetric case, all (regular) orbits are short-axis tube orbits with $I_2 = \frac{1}{2}L_z^2$ and energy E ranging from $\min[V_{\text{eff}}(\lambda)]$ to zero. The expression (6.4) for the phase-space volume reduces to

$$\Delta V(E, L_z, I_3) = \frac{\pi}{2|L_z|} \int_{-\gamma}^{\nu_{\max}} \int_{\lambda_{\min}}^{\lambda_{\max}} \sqrt{\frac{(\lambda+\alpha)(\nu+\alpha)}{[E-V_{\text{eff}}(\lambda)][E-V_{\text{eff}}(\nu)]}} \frac{(\nu-\lambda) d\lambda d\nu}{(\lambda+\alpha)(\lambda+\gamma)(\nu+\alpha)(\nu+\gamma)}, \quad (7.1)$$

where as before ν_{\max} , λ_{\min} and λ_{\max} are the solutions of $E = V_{\text{eff}}(\tau)$ (see Fig. 23 of de Zeeuw 1985a). The factor in front of the double integral includes the factor 2π from the integration over the azimuthal angle ϕ . In Fig. 14, we show in the top panels the orbital mass weight distribution of the oblate axisymmetric Abel model, and in the bottom panels that of the fitted axisymmetric Schwarzschild model.

The three-integral mass weight distributions are very similar, even in the panels with a relatively low mass content. The average fractional error is around 20%, and if we consider in each panel the mass weights above the mean value, which together contribute nearly half of the total mass, the fractional error decreases to around 15%. A similar good recovery was found by Krajnović et al. (2005) for the case of a two-integral DF $f(E, L_z)$, which implies an isotropic velocity distribution in the meridional plane. Thomas et al. (2005) showed that their independent axisymmetric numerical implementation of Schwarzschild's method is similarly able to recover an analytical $f(E, L_z)$. Our results show that the orbital mass weight distribution that follows from a fully three-integral DF $f(E, L_z, I_3)$ can be recovered with high accuracy as well.

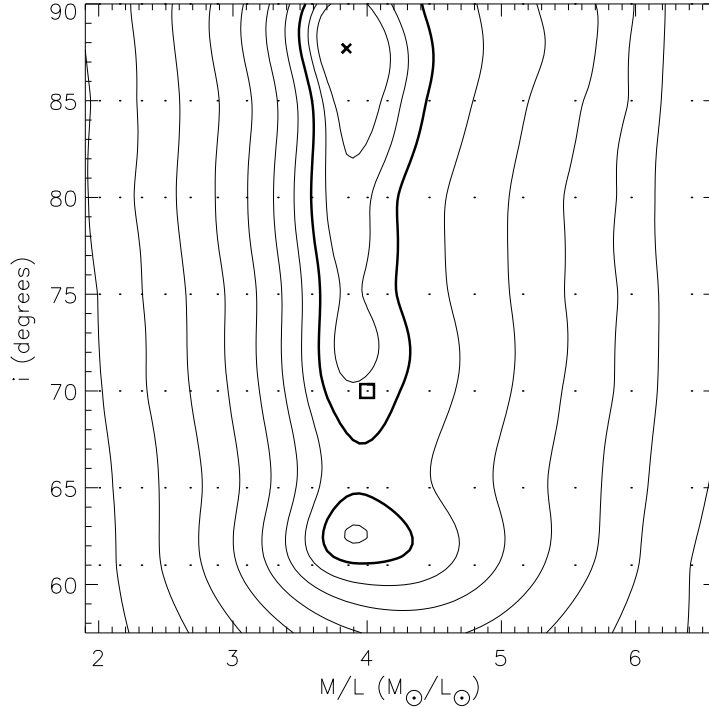


FIGURE 15 — The goodness-of-fit parameter $\Delta\chi^2$ as a function of inclination i and mass-to-light ratio M/L , for different axisymmetric Schwarzschild model fits (indicated by the dots) to an oblate axisymmetric Abel model (see text for details). The contours are as in Fig. 12, but for a $\Delta\chi^2$ -distribution with two degrees of freedom. The cross indicates the overall best-fit model ($\Delta\chi^2 = 0$). The parameters of the input Abel model, $i = 70^\circ$ and $M/L = 4 M_\odot/L_\odot$, are indicated by the open square.

7.4 GLOBAL PARAMETERS

In the axisymmetric case we only have the inclination i as viewing angle, so that, together with the mass-to-light ratio, there are two global parameters. For a range of these global parameters, we fit axisymmetric Schwarzschild models to the simulated observables of the oblate axisymmetric Abel model, and compare the corresponding goodness-of-fit χ^2 -values. In Fig. 15, we show the resulting differences $\Delta\chi^2$ with respect to the overall best-fit Schwarzschild model, indicated by the cross. The contours are now for a $\Delta\chi^2$ -distribution with two degrees of freedom. The $M/L = 4 M_\odot/L_\odot$ of the input Abel model is recovered accurately, with an average fractional error of less than 10%. However, for the inclination nearly all values within the allowed range by the flattening ($i > 60$) are allowed, including the value of $i = 70^\circ$ used to compute the observables of the Abel models. Krajnović et al. (2005) and Cappellari et al. (2005) found similar evidence for a possible degeneracy in the inclination.

8 DISCUSSION AND CONCLUSIONS

We have extended the Abel models introduced by DL91 and generalized by MD99, and used them to construct realistic axisymmetric and triaxial galaxy models to test the accuracy of Schwarzschild’s orbit superposition method.

Although Abel models have separable potentials with a central core and assume

a specific functional form for the (three-integral) DF, they can have a large range of shapes and their observables, which can be calculated easily, include many of the features seen in the kinematic maps of early-type galaxies. We have used an isochrone Stäckel potential that in the axisymmetric limit reduces to the Kuzmin-Kutuzov model and becomes Hénon's isochrone in the spherical limit. Because of the simple form of the isochrone potential, the resulting Abel models are ideally suited to test numerical implementations of the Schwarzschild orbit superposition method. The calculation of the phase-space volume, needed when comparing the orbital mass weight distribution of the Schwarzschild models with the three-integral DF of the Abel models, simplifies significantly for this case.

Integral-field observations in principle provide the LOSVD as a function of position on the sky, so that it is a function $\mathcal{L}(x', y', v_{z'})$ that depends on three variables. Our oblate axisymmetric and triaxial model galaxies have a DF which is a sum of Abel components $f(S) = f(-E + wI_2 + uI_3)$ with different values of the parameters w and u , so that the DF is a function of three variables as well, namely the integrals of motion E , I_2 and I_3 . We have shown that by fitting Schwarzschild models to the simulated observables of these models, $f(E, I_2, I_3)$ is well recovered for the input value of the mass-to-light ratio M/L and the correct viewing angle(s). By varying these global parameters, we have found that the best-fit M/L is close to the input value, but the viewing direction is less well determined.

First consider three-integral oblate models, i.e., with a DF that is a function $f(E, L_z, I_3)$ and the viewing direction defined by the inclination. The value of M/L is recovered to within 10% for all models, but the inclination is poorly constrained. Since we assume M/L is constant, the total luminosity of the model is fixed, and the total mass follows from the virial theorem, it is not surprising that the value of M/L is insensitive to a change in inclination. If the inclination is wrong, then, in order to fit the observed surface brightness, the deprojected mass model requires a different intrinsic flattening. Our results show that there is sufficient freedom in $f(E, L_z, I_3)$ to still fit the observed (moments of) $\mathcal{L}(x', y', v_{z'})$, so that the inclination is not well-determined.

The observed ellipticity of the surface brightness places a lower limit on the inclinations that provide a physical deprojection. In some galaxies the presence of a gas or dust disk provides a further constraint. An embedded disk of stars, which is not directly visible in the observed surface brightness (e.g., Rix & White 1992), might constrain the inclination as well. This can be tested by fitting the observables of an Abel model that contains a disk-like DF component. Work along these lines is in progress.

If, instead of having a three-integral DF $f(E, L_z, I_3)$, a galaxy happens to be well approximated by a two-integral DF $f(E, L_z)$, the range of inclinations that leads to an acceptable fit of the three-parameter $\mathcal{L}(x', y', v_{z'})$ is expected to shrink. The density $\rho(R, z)$ of an axisymmetric model uniquely determines the even part of $f(E, L_z)$ and the mean streaming $\rho\langle v_\phi \rangle$ in the meridional plane fixes the part of $f(E, L_z)$ that is odd in L_z (Dejonghe 1986). Ignoring non-uniqueness in the deprojection of the surface density Σ (Rybicki 1987) and the mean streaming motion V on the plane of the sky, these two quantities define a two-integral DF completely. The observed velocity dispersion and higher moments of $\mathcal{L}(x', y', v_{z'})$ will not be fitted, except at the correct inclination. In this way, e.g. by fitting a two-integral Jeans model [i.e., solution of the Jeans equations assuming the DF is of the form $f(E, L_z)$] to the observed velocity dispersion field of a galaxy, an apparent best fit at a certain inclination can be found (e.g., Cappellari et al. 2005). However, the reliability of the derived best-fit inclination,

of course, depends on the correctness of the assumption of a two-integral DF.

In the triaxial case, the DF is again a function of three integrals of motion, but the orbital structure in these models is substantially richer than in the oblate axisymmetric models, with four major orbit families, instead of only one. This introduces a fundamental non-uniqueness in the recovery of the DF. Whereas in the oblate axisymmetric case $\rho(R, z)$ uniquely defines the even part of $f(E, L_z)$, in the (separable) triaxial case the density $\rho(x, y, z)$ does *not* uniquely determine the even part of $f(E, I_2, I_3)$, although both of these are functions of three variables (Hunter & de Zeeuw 1992). It is not known whether specification of $\mathcal{L}(x', y', v_{z'})$ can narrow down the range of possible DFs further, even ignoring the non-uniqueness caused by the required deprojection of the surface brightness. Our results show that the Schwarzschild method recovers the correct orbital mass weight distribution for the input values of the three viewing angles $(\vartheta, \varphi, \psi)$ and the mass-to-light ratio M/L . Given the very large freedom in orbit choice for this case, the modest resolution of our orbit library, and the resulting approximations in the evaluation of the phase space volume, the agreement between the orbital mass weights found in § 6.3 is in fact remarkable. It may be possible to improve the DF recovery further by refining the sampling of the orbits and the regularization of the orbital mass weights.

By varying the four global parameters, we have seen that the M/L value is again well-determined. A range of $(\vartheta, \varphi, \psi)$ is excluded as they lead to nonphysical deprojections of the observed surface brightness. In particular the presence of twists in the position angle of the isophotes can substantially constrain the viewing direction. But given the availability of four major orbit families, it is not surprising that, within the allowed space of viewing angles, there is sufficient freedom to adapt $f(E, I_2, I_3)$ to fit the observables, even if the viewing angles are wrong. This degeneracy is similar to that in the axisymmetric case. As before, in some galaxies the presence of a disk might provide a constraint on the viewing direction. Furthermore, assuming the potential is nearly separable, which might be appropriate outside the nuclear region, and use of the continuity equation (as done by Statler 1994), or the Jeans equation solutions of van de Ven et al (2003), might appear to constrain the viewing angles, but at the expense of assuming a mean streaming field or dispersion field in the (x, z) -plane. If this happens to be (very close to) the right choice, then the inferred viewing angles (and intrinsic structure) are correct, but this is not known a priori. A similar conclusion applies to model fits with a limited number of Abel DF components. By including the full range of Abel DF components, one would presumably recover the larger range of allowed viewing angles also found by Schwarzschild's method.

We conclude that Schwarzschild's method is able to recover the internal dynamical structure of early-type galaxies and allows an accurate determination of the mass-to-light ratio, but additional information is needed to constrain better the viewing direction. The axisymmetric Schwarzschild method has already been successfully applied by us and other groups to determine the black hole mass, mass-to-light ratio, dark matter profile as well as the (three-integral) DF of early-type galaxies. With our extension to triaxial geometry we are now able to model early-type galaxies — and in particular the giant ellipticals — which show clear signatures of non-axisymmetry, including isophote twist, kinematic misalignment and kinematic decoupled components. Moreover, since triaxial galaxies may appear axisymmetric (or even spherical) in projection, we can investigate the effect of intrinsic triaxiality on the measurements of e.g. black hole masses based on axisymmetric model fits to observations of galaxies.

REFERENCES

- Arnold R., 1990, *MNRAS*, 244, 465
- Arnold R., de Zeeuw P. T., Hunter C., 1994, *MNRAS*, 271, 924
- Bacon R., et al. 2001, *MNRAS*, 326, 23
- Batsleer P., Dejonghe H., 1993, *A&A*, 271, 104
- Binney J., 1982, *MNRAS*, 201, 15
- Blinnikov S., Moessner R., 1998, *A&AS*, 130, 193
- Camm G. L., 1941, *MNRAS*, 101, 195
- Cappellari M., 2002, *MNRAS*, 333, 400
- Cappellari M., Copin Y., 2003, *MNRAS*, 342, 345
- Cappellari M., et al. 2005, *MNRAS*, submitted, astro-ph/0505042
- Cappellari M., Verolme E. K., van der Marel R. P., Verdoes Kleijn G. A., Illingworth G. D., Franx M., Carollo C. M., de Zeeuw P. T., 2002, *ApJ*, 578, 787
- Carlson B. C., 1977, *Special Functions of Applied Mathematics*. Academic Press, New York San Francisco London
- Carollo C. M., de Zeeuw P. T., van der Marel R. P., 1995, *MNRAS*, 276, 1131
- Chandrasekhar S., 1940, *ApJ*, 92, 441
- Copin Y., Cretton N., Emsellem E., 2004, *A&A*, 415, 889
- Cretton N., de Zeeuw P. T., van der Marel R. P., Rix H., 1999, *ApJS*, 124, 383
- Cretton N., Emsellem E., 2004, *MNRAS*, 347, L31
- Cretton N., Rix H.-W., de Zeeuw P. T., 2000, *ApJ*, 536, 319
- Cretton N., van den Bosch F. C., 1999, *ApJ*, 514, 704
- Davies R. L., et al. 2001, *ApJ*, 548, L33
- de Zeeuw P. T., 1985a, *MNRAS*, 216, 273
- de Zeeuw P. T., 1985b, *MNRAS*, 216, 599
- de Zeeuw P. T., Franx M., 1989, *ApJ*, 343, 617
- de Zeeuw P. T., Hunter C., Schwarzschild M., 1987, *ApJ*, 317, 607
- de Zeeuw P. T., Lynden-Bell D., 1985, *MNRAS*, 215, 713
- de Zeeuw P. T., Peletier R., Franx M., 1986, *MNRAS*, 221, 1001
- de Zeeuw P. T., Pfenniger D., 1988, *MNRAS*, 235, 949
- Dejonghe H., 1986, *Phys. Rep.*, 133, 217
- Dejonghe H., de Zeeuw P. T., 1988, *ApJ*, 333, 90
- Dejonghe H., Laurent D., 1991, *MNRAS*, 252, 606 [DL91]
- Eddington A. S., 1915, *MNRAS*, 76, 37
- Eddington A. S., 1916, *MNRAS*, 76, 572
- Edgeworth F. Y., 1905, *Cambridge Philos. Soc.*, 20, 36
- Emsellem E., et al. 2004, *MNRAS*, 352, 721
- Franx M., 1988, *MNRAS*, 231, 285
- Gebhardt K., et al. 2000, *AJ*, 119, 1157
- Gebhardt K., et al. 2003, *ApJ*, 583, 92
- Gerhard O. E., 1993, *MNRAS*, 265, 213
- Gradshteyn I. S., Ryzhik I. M., 1994, *Table of Integrals, Series and Products*. Academic Press, San Diego
- Henon M., 1959, *Annales d'Astrophysique*, 22, 126
- Hunter C., de Zeeuw P. T., 1992, *ApJ*, 389, 79
- Jeans J. H., 1915, *MNRAS*, 76, 70
- Kauffmann G., van den Bosch F., 2002, *Scientific American*, 286, 36
- Krajnović D., Cappellari M., Emsellem E., McDermid R. M., de Zeeuw P. T., 2005, *MNRAS*, 357, 1113
- Kuzmin G. G., 1973, in *Proc. All-Union Conf., Dynamics of Galaxies and Clusters*. ed. T. B. Omarov (Alma Ata: Akad. Nauk Kazakhskoj SSR), 71 (English transl. in *IAU Symp. 127, Structure and Dynamics of Ell. Galaxies*, ed. P.T. de Zeeuw [Dordrecht: Reidel], 553)
- Kuzmin G. G., Kutuzov S. A., 1962, *Bull. Abastumani Astroph. Obs.*, 27, 82
- Lynden-Bell D., 1962, *MNRAS*, 124, 1

- Mathieu A., Dejonghe H., 1996, *A&A*, 314, 25
 Mathieu A., Dejonghe H., 1999, *MNRAS*, 303, 455 [MD99]
 Mathieu A., Dejonghe H., Hui X., 1996, *A&A*, 309, 30
 Merritt D., 1985, *AJ*, 90, 1027
 Navarro J. F., Frenk C. S., White S. D. M., 1997, *ApJ*, 490, 493
 Osipkov L. P., 1979, *Pis'ma v Astronomicheskii Zhurnal*, 5, 77
 Pfenniger D., 1984, *A&A*, 134, 373
 Primack J. R., 2004, in *IAU Symp. 220: Dark Matter in Galaxies*, eds. S. D. Ryder, D. J. Pisano, M. A. Walker, and K. C. Freeman, p. 53
 Richstone D. O., Tremaine S., 1984, *ApJ*, 286, 27
 Rix H., de Zeeuw P. T., Cretton N., van der Marel R. P., Carollo C. M., 1997, *ApJ*, 488, 702
 Rix H.-W., White S. D. M., 1992, *MNRAS*, 254, 389
 Romanowsky A. J., Douglas N. G., Arnaboldi M., Kuijken K., Merrifield M. R., Napolitano N. R., Capaccioli M., Freeman K. C., 2003, *Science*, 301, 1696
 Rybicki G. B., 1987, in *IAU Symp. 127: Structure and Dynamics of Elliptical Galaxies*, ed. P. T. de Zeeuw, p. 397
 Schwarzschild M., 1979, *ApJ*, 232, 236
 Schwarzschild M., 1982, *ApJ*, 263, 599
 Schwarzschild M., 1993, *ApJ*, 409, 563
 Scorza C., Bender R., 1995, *A&A*, 293, 20
 Statler T. S., 1987, *ApJ*, 321, 113
 Statler T. S., 1991, *AJ*, 102, 882
 Statler T. S., 1994, *ApJ*, 425, 458
 Statler T. S., Emsellem E., Peletier R. F., Bacon R., 2004, *MNRAS*, 353, 1
 Teuben P., 1987, *MNRAS*, 227, 815
 Thomas J., Saglia R. P., Bender R., Thomas D., Gebhardt K., Magorrian J., Corsini E. M., Wegner G., 2005, *MNRAS*, 360, 1355
 Thomas J., Saglia R. P., Bender R., Thomas D., Gebhardt K., Magorrian J., Richstone D., 2004, *MNRAS*, 353, 391
 Treu T., Koopmans L. V. E., 2004, *ApJ*, 611, 739
 Valluri M., Merritt D., Emsellem E., 2004, *ApJ*, 602, 66
 van Albada T. S., Bahcall J. N., Begeman K., Sancisi R., 1985, *ApJ*, 295, 305
 van de Ven G., Hunter C., Verolme E. K., de Zeeuw P. T., 2003, *MNRAS*, 342, 1056 (Chapter 5)
 van de Ven G., van den Bosch R. C. E., Verolme E. K., de Zeeuw P. T., 2005, *A&A*, in press, astro-ph/0509228 (Chapter 2)
 van den Bosch R. C. E., van de Ven G., Verolme E. K., Cappellari M., de Zeeuw P. T., 2006, *MNRAS*, to be submitted
 van der Marel R. P., Cretton N., de Zeeuw P. T., Rix H., 1998, *ApJ*, 493, 613
 van der Marel R. P., de Zeeuw P., Rix H.-W., Quinlan G. D., 1997, *Nature*, 385, 610
 van der Marel R. P., Franx M., 1993, *ApJ*, 407, 525
 Vandervoort P. O., 1984, *ApJ*, 287, 475
 Verolme E. K., de Zeeuw P. T., 2002, *MNRAS*, 331, 959
 Verolme E. K., et al. 2002, *MNRAS*, 335, 517
 Verolme E. K., et al. 2003, in *Galaxies and Chaos*, eds. G. Contopoulos and N. Voglis, LNP vol. 626, p. 279
 Weinacht J., 1924, *Math. Ann.*, 91, 279

APPENDIX A LIMITING CASES

When two or all three of the constants α , β or γ that define the confocal coordinate system are equal, the triaxial Abel models reduce to limiting cases with more symmetry and thus with fewer degrees of freedom. The oblate and prolate axisymmetric limits are described in § 5.1. DL91 derived the non-rotating Abel models for elliptic disks and in the spherical limit. We summarize their results and give the rotating

Abel models for these limiting cases. At the same time, we also derive the properties of the non-rotating and rotating Abel models in the limit of large radii.

A.1 ELLIPTIC DISK POTENTIAL

The two-dimensional analogues of the triaxial Abel models are the elliptic Abel disks with Stäckel potential $V_S(\lambda, \mu) = U[\lambda, \mu]$ in confocal elliptic coordinates (λ, μ) . The relations with (x, y) follow from those in § 2.1 by setting $z = 0$ and $\nu = -\beta = -\gamma$. Choosing the DF as $f(E, I_2) = f(S)$, with $S = -E + w I_2$, with the two integrals of motion

$$E = \frac{1}{2} (v_x^2 + v_y^2) + U[\lambda, \mu], \quad I_2 = \frac{1}{2} L_x^2 + \frac{1}{2} (\beta - \alpha) v_x^2 + (\beta - \alpha) x^2 U[\lambda, \mu, -\alpha], \quad (\text{A.1})$$

the velocity moments can be evaluated as

$$\mu_{lm}(\lambda, \mu) = \sqrt{\frac{2^{l+m+2}}{[1 - (\lambda + \alpha)w]^{l+1} [1 - (\mu + \alpha)w]^{m+1}}} \int_{S_{\min}}^{S_{\max}} T_{mn} [S_{\text{top}}(\lambda, \mu) - S]^{(l+m)/2} f(S) dS, \quad (\text{A.2})$$

As in the general triaxial case, $S_{\min} \geq S_{\text{lim}}$, where the expression of the latter is given along the w -axis ($u = 0$) in Fig. 2. The accessible part of the (E, I_2) -integral space is now a triangle, the top of which is $S_{\text{top}}(\lambda, \mu) = -U[\lambda, \mu] + w(\lambda + \alpha)(\mu + \alpha)U[\lambda, \mu, -\alpha]$.

For the NR part $S_{\max} = S_{\text{top}}(\lambda, \mu)$ and $T_{lm}^{\text{NR}} = B(\frac{l+1}{2}, \frac{m+1}{2})$. Of the two possible orbit families, the box orbits have no net rotation and the tube orbits rotate around the axis perpendicular to the disk (the z -axis). Since this is similar to the short-axis tube orbits in the general triaxial case, we refer to the rotating part as the SR part. This SR part reaches the region of the accessible integral space (the triangle) for which $v_\mu^2 \geq 0$ at $\mu = -\alpha$ (or $I_2 \geq 0$). Therefore, $S_{\max} = S_{\text{top}}(\lambda, -\alpha)$ and

$$T_{lm}^{\text{SR}} = 2 \int_0^{\arcsin(\sqrt{a_0})} \sin^l \theta \cos^m \theta d\theta, \quad a_0 = \frac{(\lambda + \alpha) [1 - (\mu + \alpha)w] [S_{\text{top}}(\lambda, -\alpha) - S]}{(\lambda - \mu) [S_{\text{top}}(\lambda, \mu) - S]}. \quad (\text{A.3})$$

The integral can be evaluated in terms of elementary functions (see e.g. Gradshteyn & Ryzhik 1994, relations 2.513 on p.160–162).

The NR velocity moments $\mu_{lm}^{\text{NR}}(\lambda, \mu)$ vanish when either l or m is odd, and the SR velocity moments $\mu_{lm}^{\text{SR}}(\lambda, \mu)$ only when l is odd. The latter should be multiplied with $(-1)^m$ for net rotation in the opposite direction. Further information on elliptic Stäckel disks can be found in Teuben (1987) and de Zeeuw, Hunter & Schwarzschild (1987).

A.2 LARGE DISTANCE LIMIT

At large radii, $\lambda \rightarrow r^2 \gg -\alpha$, so that the confocal ellipsoidal coordinates of § 2.1 reduce to conical coordinates (r, μ, ν) , with r the usual distance to the origin, i.e., $r^2 = x^2 + y^2 + z^2$ and μ and ν angular coordinates on the sphere. In these coordinates the Stäckel potential is of the form $V_S(r, \mu, \nu) = V(r) + U[\mu, \nu]/r^2$, where $V(r)$ is an arbitrary smooth function of r . The corresponding integrals of motion are given by

$$\begin{aligned} E &= \frac{1}{2} (v_x^2 + v_y^2 + v_z^2) + V_S(r, \mu, \nu), \\ I_2 &= \frac{1}{2} T L_y^2 + \frac{1}{2} L_z^2 - (\beta - \alpha) \frac{x^2}{r^2} U[\mu, \nu, -\alpha], \\ I_3 &= \frac{1}{2} L_x^2 + \frac{1}{2} (1 - T) L_y^2 + (\gamma - \beta) \frac{z^2}{r^2} U[\mu, \nu, -\gamma]. \end{aligned} \quad (\text{A.4})$$

With the choice (2.9) for the DF, the expression for the velocity moments becomes

$$\mu_{lmn}(r, \mu, \nu) = \frac{1}{r^{m+n+2}} \sqrt{\frac{2^{l+m+n+3}}{F_\nu^{m+1} F_\mu^{n+1}}} \int_{S_{\min}}^{S_{\max}} T_{lmn} [S_{\text{top}}(r, \mu, \nu) - S]^{(l+m+n+1)/2} f(S) dS, \quad (\text{A.5})$$

where F_μ and F_ν are defined as

$$F_\tau = \frac{1}{r^2} + \frac{(\tau + \alpha)w - (\tau + \gamma)u}{\gamma - \alpha}, \quad \tau = \mu, \nu. \quad (\text{A.6})$$

As in the general triaxial case, $S_{\min} \geq S_{\text{lim}}$, where S_{lim} can be obtained from Fig. 2. The expressions of S_{\max} and T_{lmn} for the NR, LR and SR parts are those given in §§ 2.3.2–2.3.4 respectively, but with $S_{\text{top}}(\lambda, \mu, \nu)$ (eq. 2.14) replaced by

$$S_{\text{top}}(r, \mu, \nu) = -V_S(r, \mu, \nu) - w \frac{(\mu + \alpha)(\nu + \alpha)}{\gamma - \alpha} U[\mu, \nu, -\alpha] - u \frac{(\mu + \gamma)(\nu + \gamma)}{\alpha - \gamma} U[\mu, \nu, -\gamma] \quad (\text{A.7})$$

and the parameters a_0 and b_0 (2.17) reduce to

$$a_0 = \frac{S_{\text{top}}(r, \mu, -\beta) - S}{S_{\text{top}}(r, \mu, \nu) - S}, \quad b_0 = \frac{(\mu + \beta) F_\nu [S_{\text{top}}(r, \mu, -\beta) - S]}{(\mu - \nu) F_{(-\beta)} [S_{\text{top}}(r, \mu, \nu) - S]}, \quad (\text{A.8})$$

which by interchanging $\nu \leftrightarrow \mu$ become a_1 and b_1 , and in turn a_2 and b_2 follow by $\beta \leftrightarrow \alpha$. The conversion to observables follows from § 3, with v_λ replaced by v_r and in the matrix \mathbf{Q} all terms $\lambda + \sigma$ ($\sigma = -\alpha, -\beta, -\gamma, \mu, \nu$) cancel out (cf. eq. 25 of Statler 1994).

Suppose now that at large radii r , the function $V(r)$ in the Stäckel potential decreases and we keep in the above expressions only the dominant terms. In this case, F_μ , F_ν and S_{top} reduce to functions of μ and ν only. As a result, the velocity moments (A.5) are independent of r , except for the prefactor $1/r^{m+n+2}$, and therefore are scale-free. Once we have calculated the velocity moments at a radius r , those at radius $r' = qr$, with q a constant, follow by a simple scaling, $\mu_{lmn}(r', \mu, \nu) = \mu_{lmn}(r, \mu, \nu)/q^{m+n+2}$.

A.3 SPHERICAL POTENTIAL

When $\alpha = \beta = \gamma$, both μ and ν lose their meaning and we replace them by the customary polar angle θ and azimuthal angle ϕ . The expressions for the Abel models in these spherical coordinates (r, θ, ϕ) follow in a straightforward way from those in § A.2 for the large distance limit in conical coordinates (r, μ, ν) .

The Stäckel potential $V_S = V(r)$ is spherical symmetric. The expressions for the integrals of motion follow from (A.4), where for I_2 and I_3 the right-most terms vanish. The triaxiality parameter T is now a free parameter, so that, together with the parameters w and u , we can rewrite $S = -E + w I_2 + u I_3$ as

$$S = -E + \frac{1}{2}uL_x^2 + \frac{1}{2}[(1 - T)u + Tw]L_y^2 + \frac{1}{2}wL_z^2. \quad (\text{A.9})$$

This means that with the choice (2.9) for the DF, we cover the most general homogeneous quadratic form in the velocities that is allowed by the integrals of motion in a spherical symmetric potential, i.e., the energy E and all three components of the angular momentum vector \mathbf{L} (cf. DL91). These include the models considered by Osipkov (1979) and Merritt (1985) with the DF of the form $f(E \pm L^2/r_a^2)$ and those studied by

Arnold (1990) with a more general DF of the form $f(E \pm L^2/r_a^2 \pm L_z^2/r_b^2)$. These models follow by setting $u = \pm 2/r_a^2$, and $w = u$ or $w = u \pm 2/r_b^2$ respectively.

The velocity moments follow from eq. (A.5), with

$$F_\tau = \frac{1}{2}(w - u) \left[\cos^2 \theta + T(\sin^2 \theta \sin^2 \phi - 1) \pm \sqrt{\Lambda} \right] - \frac{1}{2}(w + u) + \frac{1}{r^2}. \quad (\text{A.10})$$

where the positive and negative sign are for F_μ and F_ν respectively, and

$$\Lambda = [\sin^2 \theta + T(\sin^2 \theta \sin^2 \phi - 1)]^2 + 4T \sin^2 \theta \cos^2 \theta \sin^2 \phi. \quad (\text{A.11})$$

Taking $\alpha = \beta = \gamma$ in Fig. 2, we see that the boundaries on w and u both vanish. The separatrices L_1 and L_2 , defined in eq. (2.13), reduce to the negative w -axis and the line $w = u$, respectively. Furthermore, $S_{\max} = S_{\text{top}} = V(r)$, and for T_{lmn} we use the expression (2.15). The resulting velocity moments $\mu_{lmn}(r, \theta, \phi)$, which are in general not spherical symmetric, vanish when either l , m or n is odd.

The latter implies no net rotation, which is the case when the (conserved) angular momentum vectors \mathbf{L} for the orbits are randomly oriented. We can introduce net rotation if we assume that (a fraction of) the orbits have a preferred sense of rotation around an angular momentum vector \mathbf{L}_0 that points in a specific direction given by θ_0 and ϕ_0 . Using the projection matrix P in § 3.1 with $\vartheta = \theta_0$ and $\varphi = \phi_0$, we transform to the coordinate system $(r' = r, \theta', \phi')$, in which \mathbf{L}_0 is aligned with the z' -axis. If we next set the DF to zero for $L_{z'} < 0$, we find $\mu'_{lmn}(r, \theta', \phi') = \frac{1}{2}\mu_{lmn}(r, \theta', \phi')$, which does still vanish when l or m is odd, but is non-zero when n is odd, resulting in net rotation (and after multiplication with $(-1)^n$ in opposite direction). With the inverse of the projection matrix, we can then transform these velocity moments to the original coordinates system (r, θ, ϕ) . In this way, we can build spherical Abel models, which in addition to a non-rotating part consist of a component or several components with a preferred rotation axis. Mathieu, Dejonghe & Hui (1996) used this approach to construct a spherical model of Centaurus A, including DF components with rotation around the apparent long and short axis.

APPENDIX B THE FUNCTION $\mathcal{M}(s, i, j; a, b, \phi)$

The function \mathcal{M} that appears in the velocity moments of the rotating Abel components is defined as

$$\mathcal{M}(s, i, j; a, b, \phi) = \int_0^\phi \left(\frac{\partial}{\partial a} \right)^i \left(\frac{\partial}{\partial b} \right)^j \frac{[1 - \sqrt{[1 - p(\theta)]^{s+1}}]}{p(\theta)} d\theta, \quad (\text{B.1})$$

with $p(\theta) \equiv a \cos^2 \theta + b \sin^2 \theta$. For odd s , corresponding to odd velocity moments, the integral can be evaluated in a straightforward way in terms of elementary functions. In Table B.1, we give the resulting expressions for $s = 1, 3, 5$.

For even s , the integral can be evaluated in terms of the (incomplete) elliptic integrals. To simplify the numerical evaluation we use Carlson's (1977) symmetrical forms R_F , R_D and R_J (for the relations between both forms see e.g. de Zeeuw & Pfenniger 1988). In Table B.2, we give the expressions for $s = 0, 2, 4$, where we have introduced

$s i j$	$\mathcal{M}(s, i, j; a, b, \phi)$
100	ϕ
300	$\frac{1}{2}(4 - a - b)\phi + \frac{1}{4}(b - a)\sin 2\phi$
310	$-\frac{1}{2}\phi - \frac{1}{4}\sin 2\phi$
301	$-\frac{1}{2}\phi + \frac{1}{4}\sin 2\phi$
500	$\frac{1}{8}(24 - 12a - 12b + 3a^2 + 3b^2 + 2ab)\phi$ $+ \frac{1}{4}(b - a)(3 - a - b)\sin 2\phi + \frac{1}{32}(b - a)^2\sin 4\phi$
510	$-\frac{1}{4}(6 - 3a - b)\phi - \frac{1}{4}(3 - 2a)\sin 2\phi - \frac{1}{16}(b - a)\sin 4\phi$
501	$-\frac{1}{4}(6 - 3b - a)\phi + \frac{1}{4}(3 - 2b)\sin 2\phi + \frac{1}{16}(b - a)\sin 4\phi$
520	$\frac{3}{4}\phi + \frac{1}{2}\sin 2\phi + \frac{1}{16}\sin 4\phi$
511	$\frac{1}{4}\phi - \frac{1}{16}\sin 4\phi$
502	$\frac{3}{4}\phi - \frac{1}{2}\sin 2\phi + \frac{1}{16}\sin 4\phi$

TABLE B.1 — *The function \mathcal{M} for odd s .*

the following quantities based on these symmetric elliptic integrals

$$\begin{aligned}
F &= \frac{\sqrt{1-a}\sin\phi}{a} R_F(\cos^2\phi, \Delta^2, 1), \\
D &= \frac{\sin^3\phi}{3\sqrt{1-a}} R_D(\cos^2\phi, \Delta^2, 1), \\
J &= \frac{(b-a)\sin^3\phi}{3a^2\sqrt{1-a}} R_J(\cos^2\phi, \Delta^2, 1, \frac{p(\phi)}{a}),
\end{aligned} \tag{B.2}$$

with $\Delta^2 = [1 - p(\phi)]/(1 - a)$, and we have defined the terms

$$\begin{aligned}
A &= \frac{1}{\sqrt{ab}} \arctan\left(\sqrt{\frac{b}{a}} \tan\phi\right), \\
P &= \sin\phi \cos\phi \sqrt{1 - p(\phi)}, \\
Q &= \sin\phi \cos\phi \frac{1 - \sqrt{1 - p(\phi)}}{p(\phi)}.
\end{aligned} \tag{B.3}$$

In Fig. B.1, we show the $\mathcal{M}(s, i, j; a, b, \phi)$ as function of ϕ for the case that $a = 0.5$ and $b = 0.8$, up to order $s = 5$.

We now consider some special cases. When either a or b is zero, the corresponding velocity moments vanish (eqs 2.16 and 2.19), and when $a_i > b_i$ the arguments of the function \mathcal{M} are interchanged (eqs 2.18, 2.20 and 2.21). This means we only have to consider the range $0 < a \leq b$, together with $0 < \phi \leq \pi/2$, since \mathcal{M} vanishes when $\phi = 0$.

When $a = b$, it follows that $p(\theta) = a$ in eq. (B.1), and henceforth we can separate $\mathcal{M}(s, i, j; a, a, \phi) = \mathcal{M}_1(s, i, j; a) \mathcal{M}_2(i, j; \phi)$, where

$$\mathcal{M}_1(s, i, j; a) = \frac{d^{i+j}}{da^{i+j}} \frac{[1 - \sqrt{(1-a)^{s+1}}]}{a}, \quad \mathcal{M}_2(i, j; \phi) = \int_0^\phi \cos^{2i}\theta \sin^{2j}\theta d\theta. \tag{B.4}$$

sij	$\mathcal{M}(s, i, j; a, b, \phi)$
000	$A - F + J$
200	$A - (1 - a)F - (b - a)D + J$
210	$-\frac{1}{2a} [A + Q - (1 + a)F + (1 - a)D + J]$
201	$-\frac{1}{2b} [A - Q - F - (1 - b)D + J]$
400	$A + \frac{1}{3}(b - a)P - \frac{1}{3}(2a^2 + ab - 6a + 3)F + \frac{1}{3}(2a + 2b - 7)(b - a)D + J$
410	$-\frac{1}{2a} [A + aP + Q - (1 + 2a)(1 - a)F + (2a^2 - 2a - ab + 1)D + J]$
401	$-\frac{1}{2b} [A - bP - Q - (1 - ab)F - (2b^2 - 2b - ab + 1)D + J]$
420	$\frac{3}{4a^2} \left\{ A + \frac{a^2 p(\phi) - ab}{3(b-a)p(\phi)} P + \frac{5a \cos^2 \phi + 3b \sin^2 \phi}{3p(\phi)} Q + \frac{2a^3 - 3a^2 b + 4a^2 + 3a - 3ab - 3b}{3(b-a)} F \right.$ $\left. - \frac{(2a^2 + 5a - 4ab - 3b)(1-a)}{3(b-a)} D + J \right\}$
411	$\frac{1}{4ab} \left\{ A + \frac{ab - ab p(\phi)}{(b-a)p(\phi)} P + \frac{b \sin^2 \phi - a \cos^2 \phi}{p(\phi)} Q + \frac{a^2 b - ab + a - b}{b-a} F + \frac{a^2 b + ab^2 - 4ab + a + b}{b-a} D + J \right\}$
402	$\frac{3}{4b^2} \left\{ A + \frac{b^2 p(\phi) - ab}{3(b-a)p(\phi)} P - \frac{3a \cos^2 \phi + 5b \sin^2 \phi}{3p(\phi)} Q - \frac{3b - 3a - ab + ab^2}{3(b-a)} F \right.$ $\left. - \frac{(2b^2 + 5b - 4ab - 3a)(1-b)}{3(b-a)} D + J \right\}$

TABLE B.2 — The function \mathcal{M} for even s .

For $a = 1$, the expression for \mathcal{M}_1 simplifies to $(-1)^{i+j}(i+j)!$. The integral in the expression for \mathcal{M}_2 can be evaluated explicitly using e.g. the relations 2.513 of Gradshteyn & Ryzhik (1994). For $\phi = \pi/2$, it reduces to the beta function $B(i + 1/2, j + 1/2)$.

When $a < b = 1$, the elliptic integrals become elementary, so that the quantities F , D and J in eq. (B.2) reduce to

$$F = \frac{\sqrt{1-a}}{a} \ln \left[\tan \left(\frac{\pi}{4} + \frac{\phi}{2} \right) \right], \quad D = \frac{a}{1-a} F - \frac{\sin \phi}{\sqrt{1-a}}, \quad J = F - \frac{1}{\sqrt{a}} \arctan \left(\sqrt{\frac{1-a}{a}} \sin \phi \right). \quad (\text{B.5})$$

Although F diverges when $\phi \rightarrow \pi/2$, substitution of these reduced quantities in the expressions of \mathcal{M} for even s (Table B.2), shows that all terms with F cancel. For $\phi = \pi/2$, the function \mathcal{M} is thus everywhere finite, with $A = \pi/(2\sqrt{ab})$ and $P = Q = 0$.

APPENDIX C CONVERSION FROM TRUE MOMENTS TO GAUSS-HERMITE MOMENTS

We describe the conversion from the true moments of a line-of-sight velocity distribution (LOSVD) to the moments of its expansion as a Gauss-Hermite series. These Gauss-Hermite moments are used to parameterize observed LOSVDs as they are less sensitive to the often noise-dominated wings than the true moments. Because there is no simple (analytic) relation between both, we convert the projected true moments of the Abel distribution function (3.12) to Gauss-Hermite moments numerically.

One possible way is to proceed as follows: For a given set of Gauss-Hermite moments $\{\Sigma_{\text{GH}}, V_{\text{GH}}, \sigma_{\text{GH}}, h_3, h_4, \dots, h_N\}$ construct the corresponding LOSVD $\mathcal{L}_N^{\text{GH}}(v)$ (using e.g. eq. 9 of van der Marel & Franx 1993), and (numerically) calculate its moments $\mu_k^{\text{GH}} = \int_{-\infty}^{\infty} v^k \mathcal{L}_N^{\text{GH}}(v) dv$. Then find the set of Gauss-Hermite moments for which μ_k^{GH}

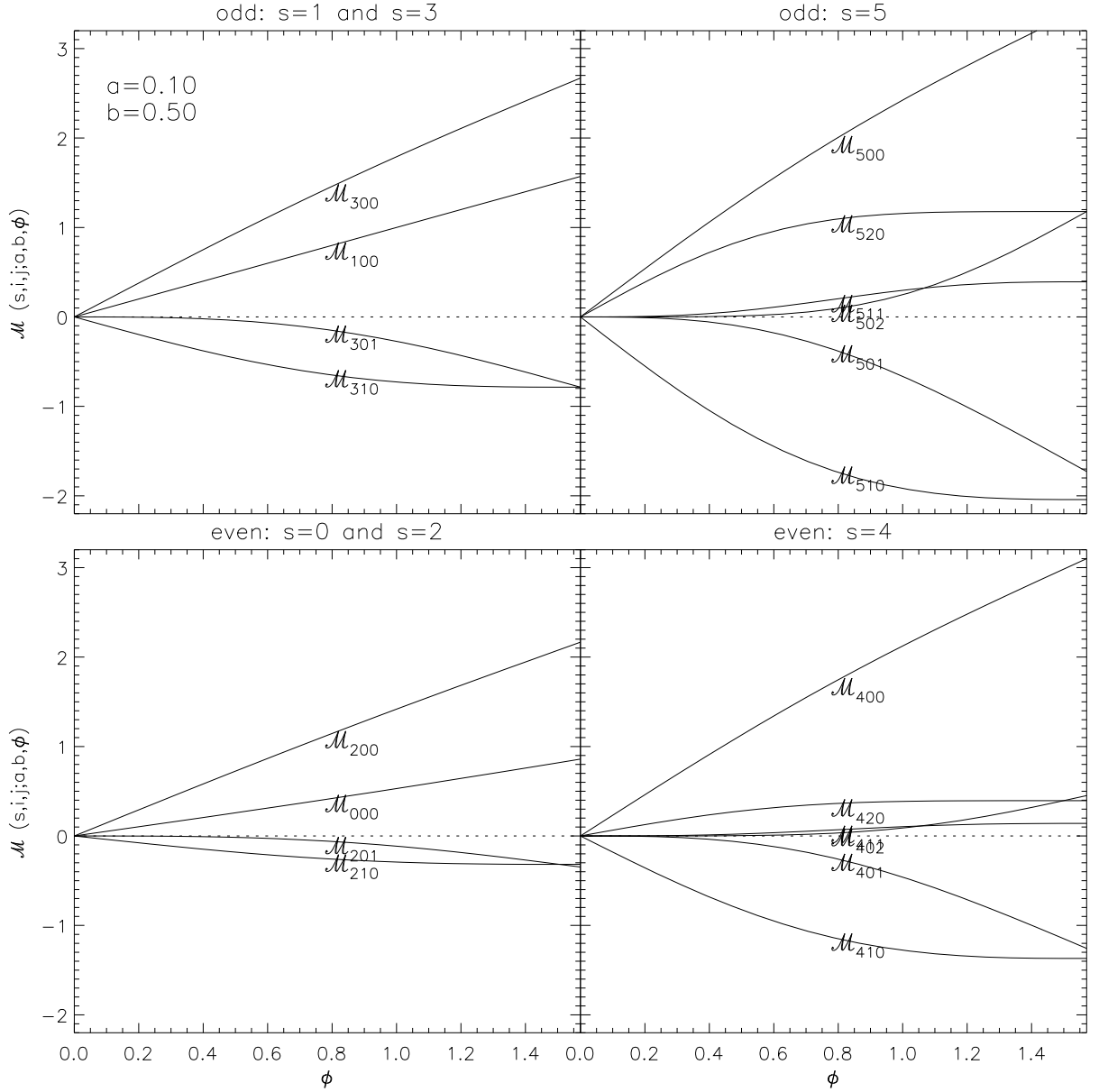


FIGURE B.1 — The function $\mathcal{M}(s, i, j; a, b, \phi)$ defined in eq. (B.1) plotted against ϕ , for $a = 0.5$ and $b = 0.8$, up to order $s = 5$. The curves in the top panels are for odd values of s corresponding to the odd velocity moments, whereas the curves in the bottom panels are for even values of s . The indices of the labels \mathcal{M}_{sij} refer to the first three parameters of the function \mathcal{M} .

($k = 0, \dots, K$) best fit the K true moments μ_k (3.12). This fit can be done e.g. by minimizing $\chi^2 = \sum_{k=1}^K [(\mu_k - \mu_k^{\text{GH}})/(\Sigma \sigma^k)]^2$. A good initial start for the set of Gauss-Hermite moments is to set the lower-order moments equal to the true moments, $\Sigma_{\text{GH}} = \Sigma$, $V_{\text{GH}} = V$, $\sigma_{\text{GH}} = \sigma$, and the higher order moments h_3, h_4, \dots, h_N to zero.

However, in practice several problems occur with the above direct fitting of the true moments. As illustrated in the right panel of Fig. C.1, the goodness-of-fit parameter χ^2 shows (many) local minima. This means it is very hard for a minimization routine to find the global minimum. It can take long before the routine converges and even

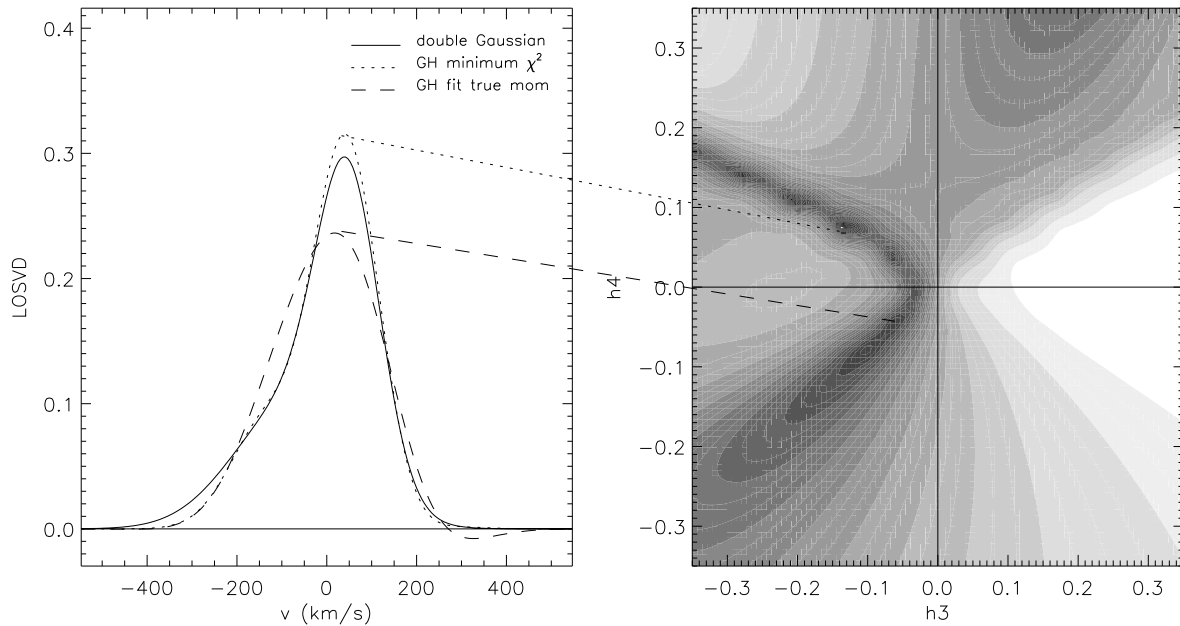


FIGURE C.1 — Derivation of the Gauss-Hermite moments of the Scorza & Bender (1995) LOSVD by fitting to its true moments. The solid curve in the left panel shows the double Gaussian representation of their LOSVD. The dotted curve is the Gauss-Hermite LOSVD of which the true moments best fit those of the double Gaussian LOSVD. This corresponds to the minimum in the goodness-of-fit parameter χ^2 , shown in the right panel. The change in grey scale from black to white represents the increase in χ^2 , as function of the higher order moments h_3 and h_4 , while minimized over the lower-order moments Σ_{GH} , V_{GH} and σ_{GH} . Besides this (global) minimum around $(h_3, h_4) \sim (-0.15, 0.07)$, there are various (broader) local minima. Hence, starting from $(h_3, h_4) = (0, 0)$, a minimization routine easily ends up in e.g. the local minimum around $(h_3, h_4) \sim (-0.05, -0.05)$, resulting in Gauss-Hermite LOSVD indicated by the dashed curve in the left panel.

then the probability is high that it ends up in one of the (in general broader) local minima. Moreover, since the higher order true moments are sensitive to the wings of the LOSVD, small (numerical) errors in the true moments can lead to (very) wrong estimates of Gauss-Hermite moments. Instead of fitting directly the true moments, an alternative method is to (re)construct the LOSVD from the true moments and then fit a Gauss-Hermite series to it.

For the (re)construction of the LOSVD from the true velocity moments, one can use the well-known Gram-Charlier series, the terms of which are simple functions of the true moments (see e.g. Appendix B2 of van der Marel & Franx 1993), but it has poor convergence properties. The terms in the Edgeworth (1905) expansion are also directly related to the true moments, but since it is a true asymptotic expansion its accuracy is controlled, so that, unlike the Gauss-Hermite and Gram-Charlier expansions, convergence plays no role (see Blinnikov & Moessner 1998 for a comparison between the expansions and for further references).

The Edgeworth expansion of the LOSVD up to order N is given by

$$\mathcal{L}_N^{\text{ED}}(v) = \Sigma \frac{e^{-\frac{1}{2}w^2}}{\sqrt{2\pi}\sigma} \left[1 + \sum_{n=3}^N D_n \right], \quad (\text{C.1})$$

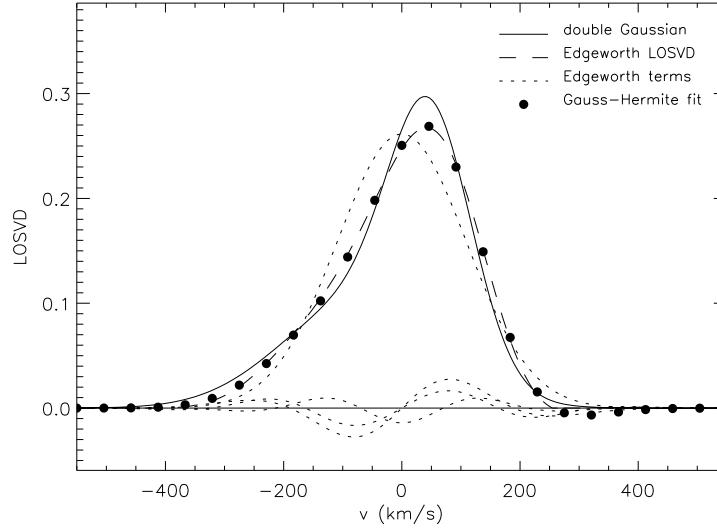


FIGURE C.2 — Derivation of the Gauss-Hermite moments of the Scorza & Bender (1995) double Gaussian LOSVD (solid curve) by fitting to the reconstructed Edgeworth LOSVD (dashed curve) from its true moments. The Gaussian and the higher order terms of the Edgeworth expansion (C.1) are shown by the dotted curves. The best-fit Gauss-Hermite LOSVD to the Edgeworth LOSVD is indicated by the filled circles.

with $w = (v - V)/\sigma$ and

$$D_n = \sum_{\{l_{i-2}\}} \mathcal{H}_{n+2(l-1)}(w) \prod_{i=3}^n \frac{1}{l_{i-2}!} \left(\frac{d_i}{i!} \right)^{l_{i-2}}. \quad (\text{C.2})$$

The Hermite polynomials \mathcal{H}_m are related to those defined by van der Marel & Franx (1993) as $\mathcal{H}_m(w) = \sqrt{m!} H_m(w/\sqrt{2})$. We have defined $l = \sum_{j=1}^{n-2} l_j$, where the sets $\{l_j\}$ are the non-negative integer solutions of the Diophantine equation $l_j + 2l_j + \dots + (n-2)l_{n-2} = n - 2$. Substituting these solutions, we find up to order $N = 5$

$$\begin{aligned} \mathcal{L}_5^{\text{ED}}(v)\Sigma \frac{e^{-\frac{1}{2}w^2}}{\sqrt{2\pi}\sigma} & \left[1 + \mathcal{H}_3(w) \frac{d_3}{3!} + \mathcal{H}_4(w) \frac{d_4}{4!} + \mathcal{H}_6(w) \frac{1}{2} \left(\frac{d_3}{3!} \right)^2 \right. \\ & \left. + \mathcal{H}_5(w) \frac{d_5}{5!} + \mathcal{H}_7(w) \frac{d_3}{3!} \frac{d_4}{4!} + \mathcal{H}_9(w) \frac{1}{6} \left(\frac{d_3}{3!} \right)^3 \right]. \end{aligned} \quad (\text{C.3})$$

The lower-order moments Σ , V and σ are equivalent to those in eq. (3.13), while the higher-order moments d_i ($i \geq 3$) are cumulants of the true moments

$$d_i = \frac{i!}{\sigma^n} \sum_{\{l_k\}} (-1)^{l-1} (l-1)! \prod_{k=1}^i \frac{1}{l_k!} \left(\frac{\mu_k}{k!} \right)^{l_k}, \quad (\text{C.4})$$

so that

$$d_3 = \xi_1, \quad d_4 = \xi_2 - 3, \quad \text{and} \quad d_5 = \xi_3 - 10\xi_1. \quad (\text{C.5})$$

The central moments ξ_1 (skewness), ξ_2 (kurtosis) and ξ_3 are related to the true moments respectively as

$$(\mu_0\sigma)^3 \xi_1 = \mu_0^2 \mu_3 - 3\mu_0 \mu_1 \mu_2 + 2\mu_1^3, \quad (\text{C.6})$$

$$(\mu_0\sigma)^4 \xi_2 = \mu_0^3 \mu_4 - 4\mu_0^2 \mu_1 \mu_3 + 6\mu_0 \mu_1^2 \mu_2 - 3\mu_1^4, \quad (\text{C.7})$$

$$(\mu_0\sigma)^5 \xi_3 = \mu_0^4 \mu_5 - 5\mu_0^3 \mu_1 \mu_4 + 10\mu_0^2 \mu_1^2 \mu_3 - 10\mu_0 \mu_1^3 \mu_2 + 4\mu_1^5. \quad (\text{C.8})$$

Substituting the line-of-sight true moments μ_k for $k = 0, \dots, K$, we can compute $\mathcal{L}_K^{\text{ED}}(v)$ at each position on the plane of the sky. By fitting a Gauss-Hermite series to $\mathcal{L}_K^{\text{ED}}(v)$, we then obtain the observables Σ_{GH} , V_{GH} , σ_{GH} and higher order moments h_3, h_4, \dots , as function of (x', y') . This method (Fig. C.2) is more accurate (and faster) than fitting the true moments directly. Still, (numerical) errors in the higher order moments might result in large (nonphysical) fluctuations in the reconstructed LOSVD. To avoid this we truncate the expansion when higher order terms exceed the lower order terms. Tests reveal that the truncation only happens in a few cases, when the Gauss-Hermite moments reach unrealistic large values.

GENERAL SOLUTION OF THE JEANS EQUATIONS FOR TRIAxIAL GALAXIES WITH SEPARABLE POTENTIALS

ABSTRACT

The Jeans equations relate the second-order velocity moments to the density and potential of a stellar system. For general three-dimensional stellar systems, there are three equations and six independent moments. By assuming that the potential is triaxial and of separable Stäckel form, the mixed moments vanish in confocal ellipsoidal coordinates. Consequently, the three Jeans equations and three remaining non-vanishing moments form a closed system of three highly-symmetric coupled first-order partial differential equations in three variables. These equations were first derived by Lynden–Bell, over 40 years ago, but have resisted solution by standard methods. We present the general solution here.

We consider the two-dimensional limiting cases first. We solve their Jeans equations by a new method which superposes singular solutions. The singular solutions, which are new, are standard Riemann–Green functions. The resulting solutions of the Jeans equations give the second moments throughout the system in terms of prescribed boundary values of certain second moments. The two-dimensional solutions are applied to non-axisymmetric disks, oblate and prolate spheroids, and also to the scale-free triaxial limit. There are restrictions on the boundary conditions which we discuss in detail. We then extend the method of singular solutions to the triaxial case, and obtain a full solution, again in terms of prescribed boundary values of second moments. There are restrictions on these boundary values as well, but the boundary conditions can all be specified in a single plane. The general solution can be expressed in terms of complete (hyper)elliptic integrals which can be evaluated in a straightforward way, and provides the full set of second moments which can support a triaxial density distribution in a separable triaxial potential.

1 INTRODUCTION

MUCH has been learned about the mass distribution and internal dynamics of galaxies by modeling their observed kinematics with solutions of the Jeans equations (e.g., Binney & Tremaine 1987). These are obtained by taking velocity moments of the collisionless Boltzmann equation for the phase-space distribution function f , and connect the second moments (or the velocity dispersions, if the mean streaming motion is known) directly to the density and the gravitational potential of the galaxy, without the need to know f . In nearly all cases there are fewer Jeans equations than velocity moments, so that additional assumptions have to be made about the degree of anisotropy. Furthermore, the resulting second moments may not correspond to a physical distribution function $f \geq 0$. These significant drawbacks have not prevented wide application of the Jeans approach to the kinematics of galaxies, even though the results need to be interpreted with care. Fortunately, efficient analytic and numerical methods have been developed in the past decade to calculate the full range of distribution functions f that correspond to spherical or axisymmetric galaxies, and to fit them directly to kinematic measurements (e.g., Gerhard 1993; Qian et al. 1995; Rix et al. 1997; van der Marel et al. 1998). This has provided, for example, accurate intrinsic shapes, mass-to-light ratios, and central black hole masses (e.g., Verolme et al. 2002; Gebhardt et al. 2003).

Many galaxy components are not spherical or axisymmetric, but have triaxial shapes (Binney 1976, 1978). These include early-type bulges, bars, and giant elliptical galaxies. In this geometry, there are three Jeans equations, but little use has been made of them, as they contain six independent second moments, three of which have to be chosen ad-hoc (see, e.g., Evans, Carollo & de Zeeuw 2000). At the same time, not much is known about the range of physical solutions, as very few distribution functions have been computed, and even fewer have been compared with kinematic data (but see Zhao 1996).

An exception is provided by the special set of triaxial mass models that have a gravitational potential of Stäckel form. In these systems, the Hamilton–Jacobi equation separates in orthogonal curvilinear coordinates (Stäckel 1891), so that all orbits have three exact integrals of motion, which are quadratic in the velocities. The associated mass distributions can have arbitrary central axis ratios and a large range of density profiles, but they all have cores rather than central density cusps, which implies that they do not provide perfect fits to galaxies (de Zeeuw, Peletier & Franx 1986). Even so, they capture much of the rich internal dynamics of large elliptical galaxies (de Zeeuw 1985a, hereafter Z85; Statler 1987, 1991; Arnold, de Zeeuw & Hunter 1994). Numerical and analytic distribution functions have been constructed for these models (e.g., Bishop 1986; Statler 1987; Dejonghe & de Zeeuw 1988; Hunter & de Zeeuw 1992, hereafter HZ92; Mathieu & Dejonghe 1999), and their projected properties have been used to provide constraints on the intrinsic shapes of individual galaxies (e.g., Statler 1994a, b; Statler & Fry 1994; Statler, DeJonghe & Smecker-Hane 1999; Bak & Statler 2000; Statler 2001).

The Jeans equations for triaxial Stäckel systems have received little attention. This is remarkable, as Eddington (1915) already knew that the velocity ellipsoid in these models is everywhere aligned with the confocal ellipsoidal coordinate system in which the motion separates. This means that there are only three, and not six, non-vanishing second-order velocity moments in these coordinates, so that the

Jeans equations form a closed system. However, Eddington, and later Chandrasekhar (1939, 1940), did not study the velocity moments, but instead assumed a form for the distribution function, and then determined which potentials are consistent with it. Lynden–Bell (1960) was the first to derive the explicit form of the Jeans equations for the triaxial Stäckel models. He showed that they constitute a highly symmetric set of three first-order partial differential equations (PDEs) for three unknowns, each of which is a function of the three confocal ellipsoidal coordinates, but he did not derive solutions. When it was realized that the orbital structure in the triaxial Stäckel models is very similar to that in the early numerical models for triaxial galaxies with cores (Schwarzschild 1979; Z85), interest in the second moments increased, and the Jeans equations were solved for a number of special cases. These include the axisymmetric limits and elliptic disks (Dejonghe & de Zeeuw 1988; Evans & Lynden–Bell 1989, hereafter EL89), triaxial galaxies with only thin tube orbits (HZ92), and, most recently, the scale-free limit (Evans et al. 2000). In all these cases the equations simplify to a two-dimensional problem, which can be solved with standard techniques after recasting two first-order equations into a single second-order equation in one dependent variable. However, these techniques do not carry over to a single third-order equation in one dependent variable, which is the best that one could expect to have in the general case. As a result, the general case has remained unsolved.

Here, we first present an alternative solution method for the two-dimensional limiting cases which does not use the standard approach, but instead uses superpositions of singular solutions. We show that this approach can be extended to three dimensions, and provides the general solution for the triaxial case in closed form, which we give explicitly. We will apply our solutions in a follow-up paper, and will use them together with the mean streaming motions (Statler 1994a) to study the properties of the observed velocity and dispersion fields of triaxial galaxies.

In Section 2, we define our notation and derive the Jeans equations for the triaxial Stäckel models in confocal ellipsoidal coordinates, together with the continuity conditions. We summarize the limiting cases, and show that the Jeans equations for all the cases with two degrees of freedom correspond to the same two-dimensional problem. We solve this problem in Section 3, first by employing a standard approach with a Riemann–Green function, and then via the singular solution superposition method. We also discuss the choice of boundary conditions in detail. We relate our solution to that derived by EL89 in Appendix A, and explain why it is different. In Section 4, we extend the singular solution approach to the three-dimensional problem, and derive the general solution of the Jeans equations for the triaxial case. It contains complete (hyper)elliptic integrals, which we express as single quadratures that can be numerically evaluated in a straightforward way. We summarize our conclusions in Section 5.

2 THE JEANS EQUATIONS FOR SEPARABLE MODELS

We first summarize the essential properties of the triaxial Stäckel models in confocal ellipsoidal coordinates. Further details can be found in Z85. We show that for these models the mixed second-order velocity moments vanish, so that the Jeans equations form a closed system. We derive the Jeans equations and find the corresponding continuity conditions for the general case of a triaxial galaxy. We then give an overview of the limiting cases and show that solving the Jeans equations for the various cases with two degrees of freedom reduces to an equivalent two-dimensional problem.

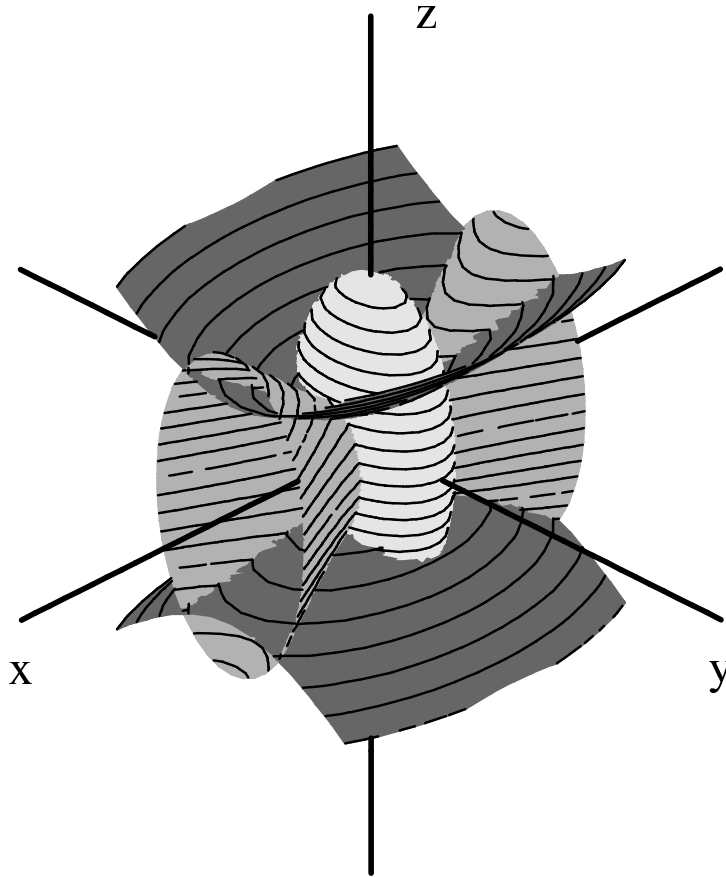


FIGURE 1 — *Confocal ellipsoidal coordinates. Surfaces of constant λ are ellipsoids, surfaces of constant μ are hyperboloids of one sheet and surfaces of constant ν are hyperboloids of two sheets.*

2.1 TRIAXIAL STÄCKEL MODELS

We define confocal ellipsoidal coordinates (λ, μ, ν) as the three roots for τ of

$$\frac{x^2}{\tau + \alpha} + \frac{y^2}{\tau + \beta} + \frac{z^2}{\tau + \gamma} = 1, \quad (2.1)$$

with (x, y, z) the usual Cartesian coordinates, and with constants α, β and γ such that $-\gamma \leq \nu \leq -\beta \leq \mu \leq -\alpha \leq \lambda$. For each point (x, y, z) , there is a unique set (λ, μ, ν) , but a given combination (λ, μ, ν) generally corresponds to eight different points $(\pm x, \pm y, \pm z)$. We assume all three-dimensional Stäckel models in this chapter to be likewise eightfold symmetric.

Surfaces of constant λ are ellipsoids, and surfaces of constant μ and ν are hyperboloids of one and two sheets, respectively (Fig. 1). The confocal ellipsoidal coordinates are approximately Cartesian near the origin and become a conical coordinate system at large radii with a system of spheres together with elliptic and hyperbolic cones (Fig. 3). At each point, the three coordinate surfaces are perpendicular to each other. Therefore, the line element is of the form $ds^2 = P^2 d\lambda^2 + Q^2 d\mu^2 + R^2 d\nu^2$, with the

metric coefficients

$$\begin{aligned} P^2 &= \frac{(\lambda - \mu)(\lambda - \nu)}{4(\lambda + \alpha)(\lambda + \beta)(\lambda + \gamma)}, \\ Q^2 &= \frac{(\mu - \nu)(\mu - \lambda)}{4(\mu + \alpha)(\mu + \beta)(\mu + \gamma)}, \\ R^2 &= \frac{(\nu - \lambda)(\nu - \mu)}{4(\nu + \alpha)(\nu + \beta)(\nu + \gamma)}. \end{aligned} \quad (2.2)$$

We restrict attention to models with a gravitational potential $V_S(\lambda, \mu, \nu)$ of Stäckel form (Weinacht 1924)

$$V_S = -\frac{F(\lambda)}{(\lambda - \mu)(\lambda - \nu)} - \frac{F(\mu)}{(\mu - \nu)(\mu - \lambda)} - \frac{F(\nu)}{(\nu - \lambda)(\nu - \mu)}, \quad (2.3)$$

where $F(\tau)$ is an arbitrary smooth function.

Adding any linear function of τ to $F(\tau)$ changes V_S by at most a constant, and hence has no effect on the dynamics. Following Z85, we use this freedom to write

$$F(\tau) = (\tau + \alpha)(\tau + \gamma)G(\tau), \quad (2.4)$$

where $G(\tau)$ is smooth. It equals the potential along the intermediate axis. This choice will simplify the analysis of the large radii behavior of the various limiting cases.¹

The density ρ_S that corresponds to V_S can be found from Poisson's equation or by application of Kuzmin's (1973) formula (see de Zeeuw 1985b). This formula shows that, once we have chosen the central axis ratios and the density along the short axis, the mass model is fixed everywhere by the requirement of separability. For centrally concentrated mass models, V_S has the x -axis as long axis and the z -axis as short axis. In most cases this is also true for the associated density (de Zeeuw et al. 1986).

2.2 VELOCITY MOMENTS

A stellar system is completely described by its distribution function (DF), which in general is a time-dependent function f of the six phase-space coordinates (\mathbf{x}, \mathbf{v}) . Assuming the system to be in equilibrium ($df/dt = 0$) and in steady-state ($\partial f/\partial t = 0$), the DF is independent of time t and satisfies the (stationary) collisionless Boltzmann equation (CBE). Integration of the DF over all velocities yields the zeroth-order velocity moment, which is the density ρ of the stellar system. The first- and second-order velocity moments are defined as

$$\begin{aligned} \langle v_i \rangle(\mathbf{x}) &= \frac{1}{\rho} \iiint v_i f(\mathbf{x}, \mathbf{v}) \, d^3v, \\ \langle v_i v_j \rangle(\mathbf{x}) &= \frac{1}{\rho} \iiint v_i v_j f(\mathbf{x}, \mathbf{v}) \, d^3v, \end{aligned} \quad (2.5)$$

where $i, j = 1, 2, 3$. The streaming motions $\langle v_i \rangle$ together with the symmetric second-order velocity moments $\langle v_i v_j \rangle$ provide the velocity dispersions $\sigma_{ij}^2 = \langle v_i v_j \rangle - \langle v_i \rangle \langle v_j \rangle$.

The continuity equation that results from integrating the CBE over all velocities, relates the streaming motion to the density ρ of the system. Integrating the CBE over

¹Other, equivalent, choices include $F(\tau) = -(\tau + \alpha)(\tau + \gamma)G(\tau)$ by HZ92, and $F(\tau) = (\tau + \alpha)(\tau + \beta)U(\tau)$ by de Zeeuw et al. (1986), with $U(\tau)$ the potential along the short axis.

all velocities after multiplication by each of the three velocity components, provides the Jeans equations, which relate the second-order velocity moments to ρ and V , the potential of the system. Therefore, if the density and potential are known, we in general have one continuity equation with three unknown first-order velocity moments and three Jeans equations with six unknown second-order velocity moments.

The potential (2.3) is the most general form for which the Hamilton–Jacobi equation separates (Stäckel 1890; Lynden–Bell 1962b; Goldstein 1980). All orbits have three exact isolating integrals of motion, which are quadratic in the velocities (e.g., Z85). It follows that there are no irregular orbits, so that Jeans’ (1915) theorem is strictly valid (Lynden–Bell 1962a; Binney 1982) and the DF is a function of the three integrals. The orbital motion is a combination of three independent one-dimensional motions — either an oscillation or a rotation — in each of the three ellipsoidal coordinates. Different combinations of rotations and oscillations result in four families of orbits in triaxial Stäckel models (Kuzmin 1973; Z85): inner (I) and outer (O) long-axis tubes, short (S) axis tubes and box orbits. Stars on box orbits carry out an oscillation in all three coordinates, so that they provide no net contribution to the mean streaming. Stars on I- and O-tubes carry out a rotation in ν and those on S-tubes a rotation in μ , and oscillations in the other two coordinates. The fractions of clockwise and counterclockwise stars on these orbits may be unequal. This means that each of the tube families can have at most one nonzero first-order velocity moment, related to ρ by the continuity equation. Statler (1994a) used this property to construct velocity fields for triaxial Stäckel models. It is not difficult to show by similar arguments (e.g., HZ92) that all mixed second-order velocity moments also vanish

$$\langle v_\lambda v_\mu \rangle = \langle v_\mu v_\nu \rangle = \langle v_\nu v_\lambda \rangle = 0. \quad (2.6)$$

Eddington (1915) already knew that in a potential of the form (2.3), the axes of the velocity ellipsoid at any given point are perpendicular to the coordinate surfaces, so that the mixed second-order velocity moments are zero. We are left with three second-order velocity moments, $\langle v_\lambda^2 \rangle$, $\langle v_\mu^2 \rangle$ and $\langle v_\nu^2 \rangle$, related by three Jeans equations.

2.3 THE JEANS EQUATIONS

The Jeans equations for triaxial Stäckel models in confocal ellipsoidal coordinates were first derived by Lynden–Bell (1960). We give an alternative derivation here, using the Hamilton equations.

We first write the DF as a function of (λ, μ, ν) and the conjugate momenta

$$p_\lambda = P^2 \frac{d\lambda}{dt}, \quad p_\mu = Q^2 \frac{d\mu}{dt}, \quad p_\nu = R^2 \frac{d\nu}{dt}, \quad (2.7)$$

with the metric coefficients P , Q and R given in (2.2). In these phase-space coordinates the steady-state CBE reads

$$\frac{d\tau}{dt} \frac{\partial f}{\partial \tau} + \frac{dp_\tau}{dt} \frac{\partial f}{\partial p_\tau} = 0, \quad (2.8)$$

where we have used the summation convention with respect to $\tau = \lambda, \mu, \nu$. The Hamilton equations are

$$\frac{d\tau}{dt} = \frac{\partial H}{\partial p_\tau}, \quad \frac{dp_\tau}{dt} = -\frac{\partial H}{\partial \tau}, \quad (2.9)$$

with the Hamiltonian defined as

$$H = \frac{p_\lambda^2}{2P^2} + \frac{p_\mu^2}{2Q^2} + \frac{p_\nu^2}{2R^2} + V(\lambda, \mu, \nu). \quad (2.10)$$

The first Hamilton equation in (2.9) defines the momenta (2.7) and gives no new information. The second gives

$$\frac{dp_\lambda}{dt} = \frac{p_\lambda^2}{P^3} \frac{\partial P}{\partial \lambda} + \frac{p_\mu^2}{Q^3} \frac{\partial Q}{\partial \lambda} + \frac{p_\nu^2}{R^3} \frac{\partial R}{\partial \lambda} - \frac{\partial V}{\partial \lambda}, \quad (2.11)$$

and similar for p_μ and p_ν by replacing the derivatives with respect to λ by derivatives to μ and ν , respectively.

We assume the potential to be of the form V_S defined in (2.3), and we substitute (2.7) and (2.11) in the CBE (2.8). We multiply this equation by p_λ and integrate over all momenta. The mixed second moments vanish (2.6), so that we are left with

$$\frac{3\langle fp_\lambda^2 \rangle}{P^3} \frac{\partial P}{\partial \lambda} + \frac{\langle fp_\mu^2 \rangle}{Q^3} \frac{\partial Q}{\partial \lambda} + \frac{\langle fp_\nu^2 \rangle}{R^3} \frac{\partial R}{\partial \lambda} - \frac{1}{P^2} \frac{\partial}{\partial \lambda} \langle fp_\lambda^2 \rangle - \langle f \rangle \frac{\partial V_S}{\partial \lambda} = 0, \quad (2.12)$$

where we have defined the moments

$$\begin{aligned} \langle f \rangle &\equiv \int f d^3p = PQR\rho, \\ \langle fp_\lambda^2 \rangle &\equiv \int p_\lambda^2 f d^3p = P^3QRT_{\lambda\lambda}, \end{aligned} \quad (2.13)$$

with the diagonal components of the stress tensor

$$T_{\tau\tau}(\lambda, \mu, \nu) \equiv \rho \langle v_\tau^2 \rangle, \quad \tau = \lambda, \mu, \nu. \quad (2.14)$$

The moments $\langle fp_\mu^2 \rangle$ and $\langle fp_\nu^2 \rangle$ follow from $\langle fp_\lambda^2 \rangle$ by cyclic permutation $\lambda \rightarrow \mu \rightarrow \nu \rightarrow \lambda$, for which $P \rightarrow Q \rightarrow R \rightarrow P$. We substitute the definitions (2.13) in eq. (2.12) and carry out the partial differentiation in the fourth term. The first term in (2.12) then cancels, and, after rearranging the remaining terms and dividing by PQR , we obtain

$$\frac{\partial T_{\lambda\lambda}}{\partial \lambda} + \frac{T_{\lambda\lambda} - T_{\mu\mu}}{Q} \frac{\partial Q}{\partial \lambda} + \frac{T_{\lambda\lambda} - T_{\nu\nu}}{R} \frac{\partial R}{\partial \lambda} = -\rho \frac{\partial V_S}{\partial \lambda}. \quad (2.15)$$

Substituting the metric coefficients (2.2) and carrying out the partial differentiations results in the Jeans equations

$$\frac{\partial T_{\lambda\lambda}}{\partial \lambda} + \frac{T_{\lambda\lambda} - T_{\mu\mu}}{2(\lambda - \mu)} + \frac{T_{\lambda\lambda} - T_{\nu\nu}}{2(\lambda - \nu)} = -\rho \frac{\partial V_S}{\partial \lambda}, \quad (2.16a)$$

$$\frac{\partial T_{\mu\mu}}{\partial \mu} + \frac{T_{\mu\mu} - T_{\nu\nu}}{2(\mu - \nu)} + \frac{T_{\mu\mu} - T_{\lambda\lambda}}{2(\mu - \lambda)} = -\rho \frac{\partial V_S}{\partial \mu}, \quad (2.16b)$$

$$\frac{\partial T_{\nu\nu}}{\partial \nu} + \frac{T_{\nu\nu} - T_{\lambda\lambda}}{2(\nu - \lambda)} + \frac{T_{\nu\nu} - T_{\mu\mu}}{2(\nu - \mu)} = -\rho \frac{\partial V_S}{\partial \nu}, \quad (2.16c)$$

where the equations for μ and ν follow from the one for λ by cyclic permutation. These equations are identical to those derived by Lynden-Bell (1960).

In self-consistent models, the density ρ must equal ρ_S , with ρ_S related to the potential V_S (2.3) by Poisson's equation. The Jeans equations, however, do not require self-consistency. Hence, we make no assumptions on the form of the density other than that it is triaxial, i.e., a function of (λ, μ, ν) , and that it tends to zero at infinity. The resulting solutions for the stresses $T_{\tau\tau}$ do not all correspond to physical distribution functions $f \geq 0$. The requirement that the $T_{\tau\tau}$ are non-negative removes many (but not all) of the unphysical solutions.

2.4 CONTINUITY CONDITIONS

We saw in §2.2 that the velocity ellipsoid is everywhere aligned with the confocal ellipsoidal coordinates. When $\lambda \rightarrow -\alpha$, the ellipsoidal coordinate surface degenerates into the area inside the focal ellipse (Fig. 2). The area outside the focal ellipse is labeled by $\mu = -\alpha$. Hence, $T_{\lambda\lambda}$ is perpendicular to the surface *inside* and $T_{\mu\mu}$ is perpendicular to the surface *outside* the focal ellipse. On the focal ellipse, i.e. when $\lambda = \mu = -\alpha$, both stress components therefore have to be equal. Similarly, $T_{\mu\mu}$ and $T_{\nu\nu}$ are perpendicular to the area inside ($\mu = -\beta$) and outside ($\nu = -\beta$) the two branches of the focal hyperbola, respectively, and have to be equal on the focal hyperbola itself ($\mu = \nu = -\beta$). This results in the following two continuity conditions

$$T_{\lambda\lambda}(-\alpha, -\alpha, \nu) = T_{\mu\mu}(-\alpha, -\alpha, \nu), \quad (2.17a)$$

$$T_{\mu\mu}(\lambda, -\beta, -\beta) = T_{\nu\nu}(\lambda, -\beta, -\beta). \quad (2.17b)$$

These conditions not only follow from geometrical arguments, but are also precisely the conditions necessary to avoid singularities in the Jeans equations (2.16) when $\lambda = \mu = -\alpha$ and $\mu = \nu = -\beta$. For the sake of physical understanding, we will also obtain the corresponding continuity conditions by geometrical arguments for the limiting cases that follow.

2.5 LIMITING CASES

When two or all three of the constants α , β or γ are equal, the triaxial Stäckel models reduce to limiting cases with more symmetry and thus with fewer degrees of freedom. We show in §2.6 that solving the Jeans equations for all the models with two degrees of freedom reduces to the same two-dimensional problem. EL89 first solved this generalized problem and applied it to the disk, oblate and prolate case. Evans et al. (2000) showed that the large radii case with scale-free DF reduces to the problem solved by EL89. We solve the same problem in a different way in §3, and obtain a simpler expression than EL89. In order to make application of the resulting solution straightforward, and to define a unified notation, we first give an overview of the limiting cases.

2.5.1 Oblate spheroidal coordinates: prolate potentials

When $\gamma = \beta$, the coordinate surfaces for constant λ and μ reduce to oblate spheroids and hyperboloids of revolution around the x -axis. Since the range of ν is zero, it cannot be used as a coordinate. The hyperboloids of two sheets are now planes containing the x -axis. We label these planes by an azimuthal angle χ , defined as $\tan \chi = z/y$. In these oblate spheroidal coordinates (λ, μ, χ) the potential V_S has the

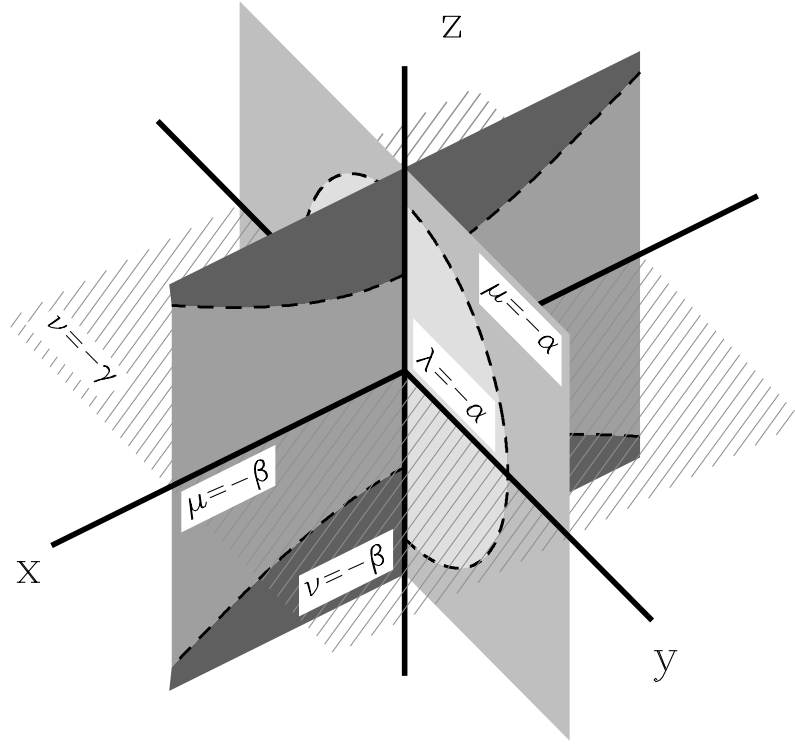


FIGURE 2 — Special surfaces inside ($\lambda = -\alpha$) and outside ($\mu = -\alpha$) the focal ellipse in the plane $x = 0$, and inside ($\mu = -\beta$) and outside ($\nu = -\beta$) the two branches of the focal hyperbola in the plane $y = 0$ and the plane $z = 0$ ($\nu = -\gamma$).

form (cf. Lynden-Bell 1962b)

$$V_S = -\frac{f(\lambda) - f(\mu)}{\lambda - \mu} - \frac{g(\chi)}{(\lambda + \beta)(\mu + \beta)}, \quad (2.18)$$

where the function $g(\chi)$ is arbitrary, and $f(\tau) = (\tau + \alpha)G(\tau)$, with $G(\tau)$ as in eq. (2.4). The denominator of the second term is proportional to $y^2 + z^2$, so that these potentials are singular along the entire x -axis unless $g(\chi) \equiv 0$. In this case, the potential is prolate axisymmetric, and the associated density ρ_S is generally prolate as well (de Zeeuw et al. 1986).

The Jeans equations (2.16) reduce to

$$\begin{aligned} \frac{\partial T_{\lambda\lambda}}{\partial \lambda} + \frac{T_{\lambda\lambda} - T_{\mu\mu}}{2(\lambda - \mu)} + \frac{T_{\lambda\lambda} - T_{\chi\chi}}{2(\lambda + \beta)} &= -\rho \frac{\partial V_S}{\partial \lambda}, \\ \frac{\partial T_{\mu\mu}}{\partial \mu} + \frac{T_{\mu\mu} - T_{\lambda\lambda}}{2(\mu - \lambda)} + \frac{T_{\mu\mu} - T_{\chi\chi}}{2(\mu + \beta)} &= -\rho \frac{\partial V_S}{\partial \mu}, \\ \frac{\partial T_{\chi\chi}}{\partial \chi} &= -\rho \frac{\partial V_S}{\partial \chi}. \end{aligned} \quad (2.19)$$

The continuity condition (2.17a) still holds, except that the focal ellipse has become a focal circle. For $\mu = -\beta$, the one-sheeted hyperboloid degenerates into the x -axis, so that $T_{\mu\mu}$ is perpendicular to the x -axis and coincides with $T_{\chi\chi}$. This gives the following

two continuity conditions

$$\begin{aligned} T_{\lambda\lambda}(-\alpha, -\alpha, \chi) &= T_{\mu\mu}(-\alpha, -\alpha, \chi), \\ T_{\mu\mu}(\lambda, -\beta, \chi) &= T_{\chi\chi}(\lambda, -\beta, \chi). \end{aligned} \quad (2.20)$$

By integrating along characteristics, Hunter et al. (1990) obtained the solution of (2.19) for the special prolate models in which only the thin I- and O-tube orbits are populated, so that $T_{\mu\mu} \equiv 0$ and $T_{\lambda\lambda} \equiv 0$, respectively (cf. §2.5.6).

2.5.2 Prolate spheroidal coordinates: oblate potentials

When $\beta = \alpha$, we cannot use μ as a coordinate and replace it by the azimuthal angle ϕ , defined as $\tan \phi = y/x$. Surfaces of constant λ and ν are confocal prolate spheroids and two-sheeted hyperboloids of revolution around the z -axis. The prolate spheroidal coordinates (λ, ϕ, ν) follow from the oblate spheroidal coordinates (λ, μ, χ) by taking $\mu \rightarrow \nu$, $\chi \rightarrow \phi$ and $\beta \rightarrow \alpha \rightarrow \gamma$. The potential $V_S(\lambda, \phi, \nu)$ is (cf. Lynden-Bell 1962b)

$$V_S = -\frac{f(\lambda) - f(\nu)}{\lambda - \nu} - \frac{g(\phi)}{(\lambda + \alpha)(\nu + \alpha)}. \quad (2.21)$$

In this case, the denominator of the second term is proportional to $R^2 = x^2 + y^2$, so that the potential is singular along the entire z -axis, unless $g(\phi)$ vanishes. When $g(\phi) \equiv 0$, the potential is oblate, and the same is generally true for the associated density ρ_S .

The Jeans equations (2.16) reduce to

$$\begin{aligned} \frac{\partial T_{\lambda\lambda}}{\partial \lambda} + \frac{T_{\lambda\lambda} - T_{\phi\phi}}{2(\lambda + \alpha)} + \frac{T_{\lambda\lambda} - T_{\nu\nu}}{2(\lambda - \nu)} &= -\rho \frac{\partial V_S}{\partial \lambda}, \\ \frac{\partial T_{\phi\phi}}{\partial \phi} &= -\rho \frac{\partial V_S}{\partial \phi}, \\ \frac{\partial T_{\nu\nu}}{\partial \nu} + \frac{T_{\nu\nu} - T_{\lambda\lambda}}{2(\nu - \lambda)} + \frac{T_{\nu\nu} - T_{\phi\phi}}{2(\nu + \alpha)} &= -\rho \frac{\partial V_S}{\partial \nu}. \end{aligned} \quad (2.22)$$

For $\lambda = -\alpha$, the prolate spheroidal coordinate surfaces reduce to the part of the z -axis between the foci. The part beyond the foci is reached if $\nu = -\alpha$. Hence, in this case, $T_{\lambda\lambda}$ is perpendicular to part of the z -axis between, and $T_{\nu\nu}$ is perpendicular to the part of the z -axis beyond the foci. They coincide at the foci ($\lambda = \nu = -\alpha$), resulting in one continuity condition. Two more follow from the fact that $T_{\phi\phi}$ is perpendicular to the (complete) z -axis, and thus coincides with $T_{\lambda\lambda}$ and $T_{\nu\nu}$ on the part between and beyond the foci, respectively:

$$\begin{aligned} T_{\lambda\lambda}(-\alpha, \phi, -\alpha) &= T_{\nu\nu}(-\alpha, \phi, -\alpha), \\ T_{\lambda\lambda}(-\alpha, \phi, \nu) &= T_{\phi\phi}(-\alpha, \phi, \nu), \\ T_{\nu\nu}(\lambda, \phi, -\alpha) &= T_{\phi\phi}(\lambda, \phi, -\alpha). \end{aligned} \quad (2.23)$$

For oblate models with thin S-tube orbits ($T_{\lambda\lambda} \equiv 0$, see §2.5.6), the analytical solution of (2.22) was derived by Bishop (1987) and by de Zeeuw & Hunter (1990). Robijn & de Zeeuw (1996) obtained the second-order velocity moments for models in which the thin tube orbits were thickened iteratively. Dejonghe & de Zeeuw (1988, Appendix D) found a general solution by integrating along characteristics. Evans (1990) gave an algorithm for solving (2.22) numerically, and Arnold (1995) computed a solution using characteristics without assuming a separable potential.

2.5.3 Confocal elliptic coordinates: non-circular disks

In the principal plane $z = 0$, the ellipsoidal coordinates reduce to confocal elliptic coordinates (λ, μ) , with coordinate curves that are ellipses (λ) and hyperbolae (μ), that share their foci on the symmetry y -axis. The potential of the perfect elliptic disk, with its surface density distribution stratified on concentric ellipses in the plane $z = 0$ ($\nu = -\gamma$), is of Stäckel form both in and outside this plane. By a superposition of perfect elliptic disks, one can construct other surface densities and corresponding disk potentials that are of Stäckel form in the plane $z = 0$, but not necessarily outside it (Evans & de Zeeuw 1992). The expression for the potential in the disk is of the form (2.18) with $g(\chi) \equiv 0$:

$$V_S = -\frac{f(\lambda) - f(\mu)}{\lambda - \mu}, \quad (2.24)$$

where again $f(\tau) = (\tau + \alpha)G(\tau)$, so that $G(\tau)$ equals the potential along the y -axis.

Omitting all terms with ν in (2.16), we obtain the Jeans equations for non-circular Stäckel disks

$$\begin{aligned} \frac{\partial T_{\lambda\lambda}}{\partial \lambda} + \frac{T_{\lambda\lambda} - T_{\mu\mu}}{2(\lambda - \mu)} &= -\rho \frac{\partial V_S}{\partial \lambda}, \\ \frac{\partial T_{\mu\mu}}{\partial \mu} + \frac{T_{\mu\mu} - T_{\lambda\lambda}}{2(\mu - \lambda)} &= -\rho \frac{\partial V_S}{\partial \mu}, \end{aligned} \quad (2.25)$$

where now ρ denotes a surface density. The parts of the y -axis between and beyond the foci are labeled by $\lambda = -\alpha$ and $\mu = -\alpha$, resulting in the continuity condition

$$T_{\lambda\lambda}(-\alpha, -\alpha) = T_{\mu\mu}(-\alpha, -\alpha). \quad (2.26)$$

2.5.4 Conical coordinates: scale-free triaxial limit

At large radii, the confocal ellipsoidal coordinates (λ, μ, ν) reduce to conical coordinates (r, μ, ν) , with r the usual distance to the origin, i.e., $r^2 = x^2 + y^2 + z^2$ and μ and ν angular coordinates on the sphere (Fig. 3). The potential $V_S(r, \mu, \nu)$ is scale-free, and of the form

$$V_S = -\tilde{F}(r) + \frac{F(\mu) - F(\nu)}{r^2(\mu - \nu)}, \quad (2.27)$$

where $\tilde{F}(r)$ is arbitrary, and $F(\tau) = (\tau + \alpha)(\tau + \gamma)G(\tau)$, as in eq. (2.4).

The Jeans equations in conical coordinates follow from the general triaxial case (2.16) by going to large radii. Taking $\lambda \rightarrow r^2 \gg -\alpha \geq \mu, \nu$, the stress components approach each other and we have

$$\frac{T_{\lambda\lambda} - T_{\mu\mu}}{2(\lambda - \mu)}, \frac{T_{\lambda\lambda} - T_{\nu\nu}}{2(\lambda - \nu)} \sim \frac{1}{r} \rightarrow 0, \quad \frac{\partial}{\partial \lambda} \rightarrow \frac{1}{2r} \frac{\partial}{\partial \lambda}. \quad (2.28)$$

Hence, after multiplying (2.16a) by $2r$, the Jeans equations for scale-free Stäckel models are

$$\begin{aligned} \frac{\partial T_{rr}}{\partial r} + \frac{2T_{rr} - T_{\mu\mu} - T_{\nu\nu}}{r} &= -\rho \frac{\partial V_S}{\partial r}, \\ \frac{\partial T_{\mu\mu}}{\partial \mu} + \frac{T_{\mu\mu} - T_{\nu\nu}}{2(\mu - \nu)} &= -\rho \frac{\partial V_S}{\partial \mu}, \\ \frac{\partial T_{\nu\nu}}{\partial \nu} + \frac{T_{\nu\nu} - T_{\mu\mu}}{2(\nu - \mu)} &= -\rho \frac{\partial V_S}{\partial \nu}. \end{aligned} \quad (2.29)$$

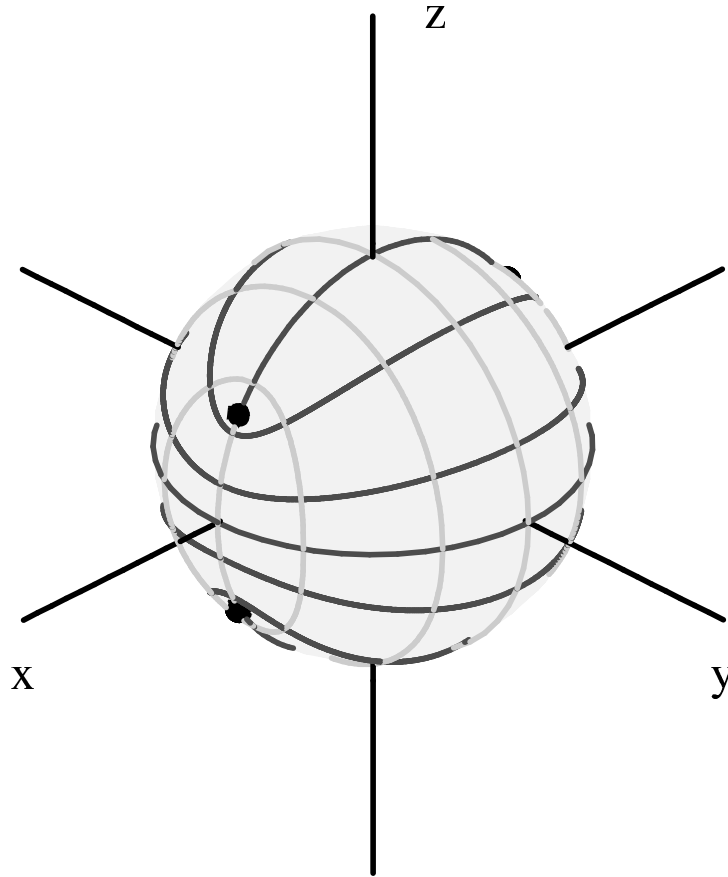


FIGURE 3 — Behavior of the confocal ellipsoidal coordinates in the limit of large radii r . The surfaces of constant λ become spheres. The hyperboloids of constant μ and ν approach their asymptotic surfaces, and intersect the sphere on the light and dark curves, respectively. These form an orthogonal curvilinear coordinate system (μ, ν) on the sphere. The black dots indicate the transition points ($\mu = \nu = -\beta$) between both sets of curves.

The general Jeans equations in conical coordinates, as derived by Evans et al. (2000), reduce to (2.29) for vanishing mixed second moments. At the transition points between the curves of constant μ and ν ($\mu = \nu = -\beta$), the tensor components $T_{\mu\mu}$ and $T_{\nu\nu}$ coincide, resulting in the continuity condition

$$T_{\lambda\lambda}(r, -\beta, -\beta) = T_{\phi\phi}(r, -\beta, -\beta). \quad (2.30)$$

2.5.5 One-dimensional limits

There are several additional limiting cases with more symmetry for which the form of V_S (Lynden-Bell 1962b) and the associated Jeans equations follow in a straightforward way from the expressions that were given above. We only mention spheres and circular disks.

When $\alpha = \beta = \gamma$, the variables μ and ν lose their meaning and the ellipsoidal coordinates reduce to spherical coordinates (r, θ, ϕ) . A steady-state spherical model without a preferred axis is invariant under a rotation over the angles θ and ϕ , so that we are left with only one Jeans equation in r , and $T_{\theta\theta} = T_{\phi\phi}$. This equation can readily be obtained from the CBE in spherical coordinates (e.g., Binney & Tremaine 1987). It also follows as a limit from the Jeans equations (2.16) for triaxial Stäckel models

or from any of the above two-dimensional limiting cases. Consider for example the Jeans equations in conical coordinates (2.29), and take $\mu \rightarrow \theta$ and $\nu \rightarrow \phi$. The stress components T_{rr} and $T_{\mu\mu} = T_{\nu\nu} = T_{\phi\phi} = T_{\theta\theta}$ depend only r , so that we are left with

$$\frac{dT_{rr}}{dr} + \frac{2(T_{rr} - T_{\theta\theta})}{r} = -\rho \frac{dV_S}{dr}, \quad (2.31)$$

the well-known result for non-rotating spherical systems (Binney & Tremaine 1987).

In a similar way, the one Jeans equation for the circular disk-case follows from, e.g., the first equation of (2.25) by taking $\mu = -\alpha$ and replacing $T_{\mu\mu}$ by $T_{\phi\phi}$, where ϕ is the azimuthal angle defined in §2.5.2. With $\lambda + \alpha = R^2$ this gives

$$\frac{dT_{RR}}{dR} + \frac{T_{RR} - T_{\phi\phi}}{R} = -\rho \frac{dV_S}{dR}, \quad (2.32)$$

which may be compared with Binney & Tremaine (1987), their eq. (4.29).

2.5.6 Thin tube orbits

Each of the three tube orbit families in a triaxial Stäckel model consists of a rotation in one of the ellipsoidal coordinates and oscillations in the other two (§2.2). The I-tubes, for example, rotate in ν and oscillate in λ and μ , with turning points μ_1 , μ_2 and λ_0 , so that a typical orbit fills the volume

$$-\gamma \leq \nu \leq -\beta, \quad \mu_1 \leq \mu \leq \mu_2, \quad -\alpha \leq \lambda \leq \lambda_0. \quad (2.33)$$

When we restrict ourselves to infinitesimally thin I-tubes, i.e., $\mu_1 = \mu_2$, there is no motion in the μ -coordinate. The second-order velocity moment in this coordinate is zero, and thus also the corresponding stress component $T_{\mu\mu}^I \equiv 0$. As a result, eq. (2.16b) reduces to an algebraic relation between $T_{\lambda\lambda}^I$ and $T_{\nu\nu}^I$. This relation can be used to eliminate $T_{\nu\nu}^I$ and $T_{\lambda\lambda}^I$ from the remaining Jeans equations (2.16a) and (2.16c) respectively.

HZ92 solved the resulting two first-order PDEs (their Appendix B) and showed that the same result is obtained by direct evaluation of the second-order velocity moments, using the thin I-tube DF. They derived similar solutions for thin O- and S-tubes, for which there is no motion in the λ -coordinate, so that $T_{\lambda\lambda}^O \equiv 0$ and $T_{\lambda\lambda}^S \equiv 0$, respectively.

In Stäckel disks we have – besides the flat box orbits – only one family of (flat) tube orbits. For infinitesimally thin tube orbits $T_{\lambda\lambda} \equiv 0$, so that the Jeans equations (2.25) reduce to two different relations between $T_{\mu\mu}$ and the density and potential. In §3.4.4, we show how this places restrictions on the form of the density and we give the solution for $T_{\mu\mu}$. We also show that the general solution of (2.25), which we obtain in §3, contains the thin tube result. The same is true for the triaxial case: the general solution of (2.16), which we derive in §4, contains the three thin tube orbit solutions as special cases (§4.6.6).

2.6 ALL TWO-DIMENSIONAL CASES ARE SIMILAR

EL89 showed that the Jeans equations in oblate and prolate spheroidal coordinates, (2.19) and (2.22), can be transformed to a system that is equivalent to the two Jeans equations (2.25) in confocal elliptic coordinates. Evans et al. (2000) arrived at the same two-dimensional form for Stäckel models with a scale-free DF. We introduce a

transformation which differs slightly from that of EL89, but has the advantage that it removes the singular denominators in the Jeans equations.

The Jeans equations (2.19) for prolate potentials can be simplified by introducing as dependent variables

$$\mathcal{T}_{\tau\tau}(\lambda, \mu) = (\lambda + \beta)^{\frac{1}{2}}(\mu + \beta)^{\frac{1}{2}}(T_{\tau\tau} - T_{\chi\chi}), \quad \tau = \lambda, \mu, \quad (2.34)$$

so that the first two equations in (2.19) transform to

$$\begin{aligned} \frac{\partial \mathcal{T}_{\lambda\lambda}}{\partial \lambda} + \frac{\mathcal{T}_{\lambda\lambda} - \mathcal{T}_{\mu\mu}}{2(\lambda - \mu)} &= -(\lambda + \beta)^{\frac{1}{2}}(\mu + \beta)^{\frac{1}{2}} \left[\rho \frac{\partial V_S}{\partial \lambda} + \frac{\partial T_{\chi\chi}}{\partial \lambda} \right], \\ \frac{\partial \mathcal{T}_{\mu\mu}}{\partial \mu} + \frac{\mathcal{T}_{\mu\mu} - \mathcal{T}_{\lambda\lambda}}{2(\mu - \lambda)} &= -(\mu + \beta)^{\frac{1}{2}}(\lambda + \beta)^{\frac{1}{2}} \left[\rho \frac{\partial V_S}{\partial \mu} + \frac{\partial T_{\chi\chi}}{\partial \mu} \right]. \end{aligned} \quad (2.35)$$

The third Jeans eq. (2.19) can be integrated in a straightforward fashion to give the χ -dependence of $T_{\chi\chi}$. It is trivially satisfied for prolate models with $g(\chi) \equiv 0$. Hence if, following EL89, we regard $T_{\chi\chi}(\lambda, \mu)$ as a function which can be prescribed, then equations (2.35) have known right hand sides, and are therefore of the same form as those of the disk case (2.25). The singular denominator $(\mu + \beta)$ of (2.19) has disappeared, and there is a boundary condition

$$\mathcal{T}_{\mu\mu}(\lambda, -\beta) = 0, \quad (2.36)$$

due to the second continuity condition of (2.20) and the definition (2.34).

A similar reduction applies for oblate potentials. The middle equation of (2.22) can be integrated to give the ϕ -dependence of $T_{\phi\phi}$, and is trivially satisfied for oblate models. The remaining two equations (2.22) transform to

$$\begin{aligned} \frac{\partial \mathcal{T}_{\lambda\lambda}}{\partial \lambda} + \frac{\mathcal{T}_{\lambda\lambda} - \mathcal{T}_{\nu\nu}}{2(\lambda - \nu)} &= -(\lambda + \alpha)^{\frac{1}{2}}(-\alpha - \nu)^{\frac{1}{2}} \left[\rho \frac{\partial V_S}{\partial \lambda} + \frac{\partial T_{\phi\phi}}{\partial \lambda} \right], \\ \frac{\partial \mathcal{T}_{\nu\nu}}{\partial \nu} + \frac{\mathcal{T}_{\nu\nu} - \mathcal{T}_{\lambda\lambda}}{2(\nu - \lambda)} &= -(-\alpha - \nu)^{\frac{1}{2}}(\lambda + \alpha)^{\frac{1}{2}} \left[\rho \frac{\partial V_S}{\partial \nu} + \frac{\partial T_{\phi\phi}}{\partial \nu} \right], \end{aligned} \quad (2.37)$$

in terms of the dependent variables

$$\mathcal{T}_{\tau\tau}(\lambda, \nu) = (\lambda + \alpha)^{\frac{1}{2}}(-\alpha - \nu)^{\frac{1}{2}}(T_{\tau\tau} - T_{\phi\phi}), \quad \tau = \lambda, \nu. \quad (2.38)$$

We now have two boundary conditions

$$\mathcal{T}_{\lambda\lambda}(-\alpha, \nu) = 0, \quad \mathcal{T}_{\nu\nu}(\lambda, -\alpha) = 0, \quad (2.39)$$

as a result of the last two continuity conditions of (2.23) and the definitions (2.38).

In the case of a scale-free DF, the stress components in the Jeans equations in conical coordinates (2.29) have the form $T_{\tau\tau} = r^{-\zeta} \mathcal{T}_{\tau\tau}(\mu, \nu)$, with $\zeta > 0$ and $\tau = r, \mu, \nu$. After substitution and multiplication by $r^{\zeta+1}$, the first equation of (2.29) reduces to

$$(2 - \zeta) \mathcal{T}_{rr} + \mathcal{T}_{\mu\mu} + \mathcal{T}_{\nu\nu} = r^{\zeta+1} \rho \frac{\partial V_S}{\partial r}. \quad (2.40)$$

When $\zeta = 2$, \mathcal{T}_{rr} drops out, so that the relation between $\mathcal{T}_{\mu\mu}$ and $\mathcal{T}_{\nu\nu}$ is known and the remaining two Jeans equations can be readily solved (Evans et al. 2000). In all other

cases, T_{rr} can be obtained from (2.40) once we have solved the last two equations of (2.29) for $T_{\mu\mu}$ and $T_{\nu\nu}$. This pair of equations is identical to the system of Jeans equations (2.25) for the case of disk potentials. The latter is the simplest form of the equivalent two-dimensional problem for all Stäckel models with two degrees of freedom. We solve it in the next section.

Once we have derived the solution of (2.25), we may obtain the solution for prolate Stäckel potentials by replacing all terms $-\rho \partial V_s / \partial \tau$ ($\tau = \lambda, \mu$) by the right-hand side of (2.35) and substituting the transformations (2.34) for $T_{\lambda\lambda}$ and $T_{\mu\mu}$. Similarly, our unified notation makes the application of the solution of (2.25) to the oblate case and to models with a scale-free DF straightforward (§3.4).

3 THE TWO-DIMENSIONAL CASE

We first apply Riemann's method to solve the Jeans equations (2.25) in confocal elliptic coordinates for Stäckel disks (§2.5.3). This involves finding a Riemann–Green function that describes the solution for a source point of stress. The full solution is then obtained in compact form by representing the known right-hand side terms as a sum of sources. In §3.2, we introduce an alternative approach, the singular solution method. Unlike Riemann's method, this can be extended to the three-dimensional case, as we show in §4. We analyze the choice of the boundary conditions in detail in §3.3. In §3.4, we apply the two-dimensional solution to the axisymmetric and scale-free limits, and we also consider a Stäckel disk built with thin tube orbits.

3.1 RIEMANN'S METHOD

After differentiating the first Jeans equation of (2.25) with respect to μ and eliminating terms in $T_{\mu\mu}$ by applying the second equation, we obtain a second-order partial differential equation (PDE) for $T_{\lambda\lambda}$ of the form

$$\frac{\partial^2 T_{\lambda\lambda}}{\partial \lambda \partial \mu} - \frac{3}{2(\lambda - \mu)} \frac{\partial T_{\lambda\lambda}}{\partial \lambda} + \frac{1}{2(\lambda - \mu)} \frac{\partial T_{\lambda\lambda}}{\partial \mu} = U_{\lambda\lambda}(\lambda, \mu). \quad (3.1)$$

Here $U_{\lambda\lambda}$ is a known function given by

$$U_{\lambda\lambda} = -\frac{1}{(\lambda - \mu)^{\frac{3}{2}}} \frac{\partial}{\partial \mu} \left[(\lambda - \mu)^{\frac{3}{2}} \rho \frac{\partial V_S}{\partial \lambda} \right] - \frac{\rho}{2(\lambda - \mu)} \frac{\partial V_S}{\partial \mu}. \quad (3.2)$$

We obtain a similar second-order PDE for $T_{\mu\mu}$ by interchanging $\lambda \leftrightarrow \mu$. Both PDEs can be solved by Riemann's method. To solve them simultaneously, we define the linear second-order differential operator

$$\mathcal{L} = \frac{\partial^2}{\partial \lambda \partial \mu} - \frac{c_1}{\lambda - \mu} \frac{\partial}{\partial \lambda} + \frac{c_2}{\lambda - \mu} \frac{\partial}{\partial \mu}, \quad (3.3)$$

with c_1 and c_2 constants to be specified. Hence, the more general second-order PDE

$$\mathcal{L}T = U, \quad (3.4)$$

with T and U functions of λ and μ alone, reduces to those for the two stress components by taking

$$\begin{aligned} T = T_{\lambda\lambda} & : \quad c_1 = \frac{3}{2}, \quad c_2 = \frac{1}{2}, \quad U = U_{\lambda\lambda}, \\ T = T_{\mu\mu} & : \quad c_1 = \frac{1}{2}, \quad c_2 = \frac{3}{2}, \quad U = U_{\mu\mu}. \end{aligned} \quad (3.5)$$

In what follows, we introduce a Riemann–Green function \mathcal{G} and incorporate the left-hand side of (3.4) into a divergence. Green’s theorem then allows us to rewrite the surface integral as a line integral over its closed boundary, which can be evaluated if \mathcal{G} is chosen suitably. We determine the Riemann–Green function \mathcal{G} which satisfies the required conditions, and then construct the solution.

3.1.1 Application of Riemann’s method

We form a divergence by defining a linear operator \mathcal{L}^* , called the *adjoint* of \mathcal{L} (e.g., Copson 1975), as

$$\mathcal{L}^* = \frac{\partial^2}{\partial\lambda\partial\mu} + \frac{\partial}{\partial\lambda} \left(\frac{c_1}{\lambda - \mu} \right) - \frac{\partial}{\partial\mu} \left(\frac{c_2}{\lambda - \mu} \right). \quad (3.6)$$

The combination $\mathcal{G}\mathcal{L}T - T\mathcal{L}^*\mathcal{G}$ is a divergence for any twice differentiable function \mathcal{G} because

$$\mathcal{G}\mathcal{L}T - T\mathcal{L}^*\mathcal{G} = \partial L/\partial\lambda + \partial M/\partial\mu, \quad (3.7)$$

where

$$\begin{aligned} L(\lambda, \mu) &= \frac{\mathcal{G}}{2} \frac{\partial T}{\partial\mu} - \frac{T}{2} \frac{\partial\mathcal{G}}{\partial\mu} - \frac{c_1 \mathcal{G} T}{\lambda - \mu}, \\ M(\lambda, \mu) &= \frac{\mathcal{G}}{2} \frac{\partial T}{\partial\lambda} - \frac{T}{2} \frac{\partial\mathcal{G}}{\partial\lambda} + \frac{c_2 \mathcal{G} T}{\lambda - \mu}. \end{aligned} \quad (3.8)$$

We now apply the PDE (3.4) and the definition (3.6) in zero-subscripted variables λ_0 and μ_0 . We integrate the divergence (3.7) over the domain $D = \{(\lambda_0, \mu_0): \lambda \leq \lambda_0 \leq \infty, \mu \leq \mu_0 \leq -\alpha\}$, with closed boundary Γ (Fig. 4). It follows by Green’s theorem that

$$\iint_D d\lambda_0 d\mu_0 (\mathcal{G}\mathcal{L}_0 T - T\mathcal{L}_0^* \mathcal{G}) = \oint_{\Gamma} d\mu_0 L(\lambda_0, \mu_0) - \oint_{\Gamma} d\lambda_0 M(\lambda_0, \mu_0), \quad (3.9)$$

where Γ is circumnavigated counter-clockwise. Here \mathcal{L}_0 and \mathcal{L}_0^* denote the operators (3.3) and (3.6) in zero-subscripted variables. We shall seek a Riemann–Green function $\mathcal{G}(\lambda_0, \mu_0)$ which solves the PDE

$$\mathcal{L}_0^* \mathcal{G} = 0, \quad (3.10)$$

in the interior of D . Then the left-hand side of (3.9) becomes $\iint_D d\lambda_0 d\mu_0 \mathcal{G}(\lambda_0, \mu_0) U(\lambda_0, \mu_0)$. The right-hand side of (3.9) has a contribution from each of the four sides of the rectangular boundary Γ . We suppose that $M(\lambda_0, \mu_0)$ and $L(\lambda_0, \mu_0)$ decay sufficiently rapidly as $\lambda_0 \rightarrow \infty$ so that the contribution from the boundary at $\lambda_0 = \infty$ vanishes and the infinite integration over λ_0 converges. Partial integration of the remaining terms then gives for the boundary integral

$$\begin{aligned} \int_{\lambda}^{\infty} d\lambda_0 \left[\left(\frac{\partial\mathcal{G}}{\partial\lambda_0} - \frac{c_2 \mathcal{G}}{\lambda_0 - \mu_0} \right) T \right]_{\mu_0=\mu} + \int_{\mu}^{-\alpha} d\mu_0 \left[\left(\frac{\partial\mathcal{G}}{\partial\mu_0} + \frac{c_1 \mathcal{G}}{\lambda_0 - \mu_0} \right) T \right]_{\lambda_0=\lambda} \\ + \int_{\lambda}^{\infty} d\lambda_0 \left[\left(\frac{\partial T}{\partial\lambda_0} + \frac{c_2 T}{\lambda_0 - \mu_0} \right) \mathcal{G} \right]_{\mu_0=-\alpha} + \mathcal{G}(\lambda, \mu) T(\lambda, \mu). \end{aligned} \quad (3.11)$$

We now impose on \mathcal{G} the additional conditions

$$\mathcal{G}(\lambda, \mu) = 1, \quad (3.12)$$

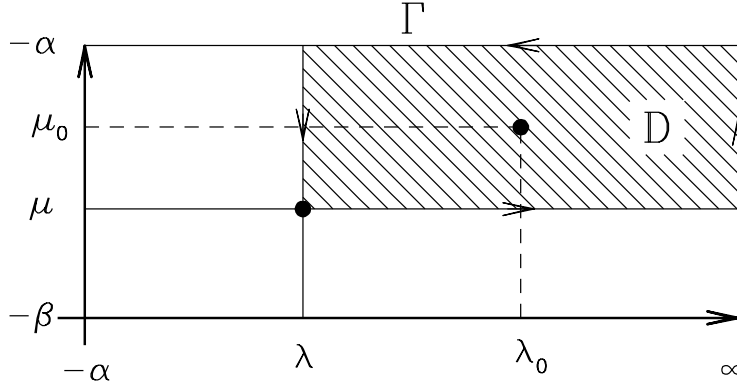


FIGURE 4 — The (λ_0, μ_0) -plane. The total stress at a field point (λ, μ) , consists of the weighted contributions from source points at (λ_0, μ_0) in the domain D , with boundary Γ .

and

$$\begin{aligned} \frac{\partial \mathcal{G}}{\partial \lambda_0} - \frac{c_2 \mathcal{G}}{\lambda_0 - \mu_0} &= 0 & \text{on } \mu_0 = \mu, \\ \frac{\partial \mathcal{G}}{\partial \mu_0} + \frac{c_1 \mathcal{G}}{\lambda_0 - \mu_0} &= 0 & \text{on } \lambda_0 = \lambda. \end{aligned} \quad (3.13)$$

Then eq. (3.9) gives the explicit solution

$$T(\lambda, \mu) = \int_{\lambda}^{\infty} d\lambda_0 \int_{\mu}^{-\alpha} d\mu_0 \mathcal{G}(\lambda_0, \mu_0) U(\lambda_0, \mu_0) - \int_{\lambda}^{\infty} d\lambda_0 \left[\left(\frac{\partial T}{\partial \lambda_0} + \frac{c_2 T}{\lambda_0 - \mu_0} \right)_{\mu_0 = -\alpha} \mathcal{G} \right], \quad (3.14)$$

for the stress component, once we have found the Riemann–Green function \mathcal{G} .

3.1.2 The Riemann–Green function

Our prescription for the Riemann–Green function $\mathcal{G}(\lambda_0, \mu_0)$ is that it satisfies the PDE (3.10) as a function of λ_0 and μ_0 , and that it satisfies the boundary conditions (3.12) and (3.13) at the specific values $\lambda_0 = \lambda$ and $\mu_0 = \mu$. Consequently \mathcal{G} depends on two sets of coordinates. Henceforth, we denote it as $\mathcal{G}(\lambda, \mu; \lambda_0, \mu_0)$.

An explicit expression for the Riemann–Green function which solves (3.10) is (Copson 1975)

$$\mathcal{G}(\lambda, \mu; \lambda_0, \mu_0) = \frac{(\lambda_0 - \mu_0)^{c_2} (\lambda - \mu_0)^{c_1 - c_2}}{(\lambda - \mu)^{c_1}} F(w), \quad (3.15)$$

where the parameter w is defined as

$$w = \frac{(\lambda_0 - \lambda)(\mu_0 - \mu)}{(\lambda_0 - \mu_0)(\lambda - \mu)}, \quad (3.16)$$

and $F(w)$ is to be determined. Since $w = 0$ when $\lambda_0 = \lambda$ or $\mu_0 = \mu$, it follows from (3.12) that the function F has to satisfy $F(0) = 1$. It is straightforward to verify that \mathcal{G} satisfies the conditions (3.13), and that eq. (3.10) reduces to the following ordinary differential equation for $F(w)$

$$w(1 - w) F'' + [1 - (2 + c_1 - c_2)w] F' - c_1(1 - c_2) F = 0. \quad (3.17)$$

This is a hypergeometric equation (e.g., Abramowitz & Stegun 1965), and its unique solution satisfying $F(0) = 1$ is

$$F(w) = {}_2F_1(c_1, 1 - c_2; 1; w). \quad (3.18)$$

The Riemann–Green function (3.15) represents the influence at a field point at (λ, μ) due to a source point at (λ_0, μ_0) . Hence it satisfies the PDE

$$\mathcal{L}\mathcal{G}(\lambda, \mu; \lambda_0, \mu_0) = \delta(\lambda_0 - \lambda)\delta(\mu_0 - \mu). \quad (3.19)$$

The first right-hand side term of the solution (3.14) is a sum over the sources in D which are due to the inhomogeneous term U in the PDE (3.4). That PDE is hyperbolic with characteristic variables λ and μ . By choosing to apply Green's theorem to the domain D , we made it the domain of dependence (Strauss 1992) of the field point (λ, μ) for (3.4), and hence we implicitly decided to integrate that PDE in the direction of decreasing λ and decreasing μ .

The second right-hand side term of the solution (3.14) represents the solution to the homogeneous PDE $\mathcal{L}T = 0$ due to the boundary values of T on the part of the boundary $\mu = -\alpha$ which lies within the domain of dependence. There is only one boundary term because we implicitly require that $T(\lambda, \mu) \rightarrow 0$ as $\lambda \rightarrow \infty$. We verify in §3.1.4 that this requirement is indeed satisfied.

3.1.3 The disk solution

We obtain the Riemann–Green functions for $T_{\lambda\lambda}$ and $T_{\mu\mu}$, labeled as $\mathcal{G}_{\lambda\lambda}$ and $\mathcal{G}_{\mu\mu}$, respectively, from expressions (3.15) and (3.18) by substitution of the values for the constants c_1 and c_2 from (3.5). The hypergeometric function in $\mathcal{G}_{\lambda\lambda}$ is the complete elliptic integral of the second kind², $E(w)$. The hypergeometric function in $\mathcal{G}_{\mu\mu}$ can also be expressed in terms of $E(w)$ using eq. (15.2.15) of Abramowitz & Stegun (1965), so that we can write

$$\mathcal{G}_{\lambda\lambda}(\lambda, \mu; \lambda_0, \mu_0) = \frac{(\lambda_0 - \mu_0)^{\frac{3}{2}}}{(\lambda - \mu)^{\frac{1}{2}}} \frac{2E(w)}{\pi(\lambda_0 - \mu)}, \quad (3.20a)$$

$$\mathcal{G}_{\mu\mu}(\lambda, \mu; \lambda_0, \mu_0) = \frac{(\lambda_0 - \mu_0)^{\frac{3}{2}}}{(\lambda - \mu)^{\frac{1}{2}}} \frac{2E(w)}{\pi(\lambda - \mu_0)}, \quad (3.20b)$$

Substituting these into (3.14) gives the solution of the stress components throughout the disk as

$$T_{\lambda\lambda}(\lambda, \mu) = \frac{2}{\pi(\lambda - \mu)^{\frac{1}{2}}} \left\{ \int_{\lambda}^{\infty} d\lambda_0 \int_{\mu}^{-\alpha} d\mu_0 \frac{E(w)}{(\lambda_0 - \mu)} \left\{ \frac{\partial}{\partial \mu_0} \left[-(\lambda_0 - \mu_0)^{\frac{3}{2}} \rho \frac{\partial V_S}{\partial \lambda_0} \right] - \frac{(\lambda_0 - \mu_0)^{\frac{1}{2}}}{2} \rho \frac{\partial V_S}{\partial \mu_0} \right\} - \int_{\lambda}^{\infty} d\lambda_0 \left[\frac{E(w)}{(\lambda_0 - \mu)} \right]_{\mu_0 = -\alpha} (\lambda_0 + \alpha) \frac{d}{d\lambda_0} \left[(\lambda_0 + \alpha)^{\frac{1}{2}} T_{\lambda\lambda}(\lambda_0, -\alpha) \right] \right\}, \quad (3.21a)$$

²We use the definition $E(w) = \int_0^{\frac{\pi}{2}} d\theta \sqrt{1 - w \sin^2 \theta}$

$$T_{\mu\mu}(\lambda, \mu) = \frac{2}{\pi(\lambda - \mu)^{\frac{1}{2}}} \left\{ \int_{\lambda}^{\infty} d\lambda_0 \int_{\mu}^{-\alpha} d\mu_0 \frac{E(w)}{(\lambda - \mu_0)} \left\{ \frac{\partial}{\partial \lambda_0} \left[-(\lambda_0 - \mu_0)^{\frac{3}{2}} \rho \frac{\partial V_S}{\partial \mu_0} \right] + \frac{(\lambda_0 - \mu_0)^{\frac{1}{2}}}{2} \rho \frac{\partial V_S}{\partial \lambda_0} \right\} - \int_{\lambda}^{\infty} d\lambda_0 \left[\frac{E(w)}{(\lambda - \mu_0)} \right]_{\mu_0 = -\alpha} \frac{d}{d\lambda_0} \left[(\lambda_0 + \alpha)^{\frac{3}{2}} T_{\mu\mu}(\lambda_0, -\alpha) \right] \right\}. \quad (3.21b)$$

This solution depends on ρ and V_S , which are assumed to be known, and on $T_{\lambda\lambda}(\lambda, -\alpha)$ and $T_{\mu\mu}(\lambda, -\alpha)$, i.e., the stress components on the part of the y -axis beyond the foci. Because these two stress components satisfy the first Jeans equation of (2.25) at $\mu = -\alpha$, we are only free to choose one of them, say $T_{\mu\mu}(\lambda, -\alpha)$. $T_{\lambda\lambda}(\lambda, -\alpha)$ then follows by integrating this first Jeans equation with respect to λ , using the continuity condition (2.26) and requiring that $T_{\lambda\lambda}(\lambda, -\alpha) \rightarrow 0$ as $\lambda \rightarrow \infty$.

3.1.4 Consistency check

We now investigate the behavior of our solutions at large distances and verify that our working hypothesis concerning the radial fall-off of the functions L and M in eq. (3.8) is correct. The solution (3.14) consists of two components: an area integral due to the inhomogeneous right-hand side term of the PDE (3.4), and a single integral due to the boundary values. We examine them in turn to obtain the conditions for the integrals to converge. Next, we parameterize the behavior of the density and potential at large distances and apply it to the solution (3.21) and to the energy eq. (2.10) to check if the convergence conditions are satisfied for physical potential-density pairs.

As $\lambda_0 \rightarrow \infty$, w tends to the finite limit $(\mu_0 - \mu)/(\lambda - \mu)$. Hence $E(w)$ is finite, and so, by (3.20), $\mathcal{G}_{\lambda\lambda} = \mathcal{O}(\lambda_0^{1/2})$ and $\mathcal{G}_{\mu\mu} = \mathcal{O}(\lambda_0^{3/2})$. Suppose now that $U_{\lambda\lambda}(\lambda_0, \mu_0) = \mathcal{O}(\lambda_0^{-l_1-1})$ and $U_{\mu\mu}(\lambda_0, \mu_0) = \mathcal{O}(\lambda_0^{-m_1-1})$ as $\lambda_0 \rightarrow \infty$. The area integrals in the solution (3.14) then converge, provided that $l_1 > \frac{1}{2}$ and $m_1 > \frac{3}{2}$. These requirements place restrictions on the behavior of the density ρ and potential V_S which we examine below. Since $\mathcal{G}_{\lambda\lambda}(\lambda, \mu; \lambda_0, \mu_0)$ is $\mathcal{O}(\lambda^{-1/2})$ as $\lambda \rightarrow \infty$, the area integral component of $T_{\lambda\lambda}(\lambda, \mu)$ behaves as $\mathcal{O}(\lambda^{-1/2} \int_{\lambda}^{\infty} \lambda_0^{-l_1-1/2} d\lambda_0)$ and so is $\mathcal{O}(\lambda^{-l_1})$. Similarly, with $\mathcal{G}_{\mu\mu}(\lambda, \mu; \lambda_0, \mu_0) = \mathcal{O}(\lambda^{-3/2})$ as $\lambda \rightarrow \infty$, the first component of $T_{\mu\mu}(\lambda, \mu)$ is $\mathcal{O}(\lambda_0^{-m_1})$.

To analyze the second component of the solution (3.14), we suppose that the boundary value $T_{\lambda\lambda}(\lambda_0, -\alpha) = \mathcal{O}(\lambda_0^{-l_2})$ and $T_{\mu\mu}(\lambda_0, -\alpha) = \mathcal{O}(\lambda_0^{-m_2})$ as $\lambda_0 \rightarrow \infty$. A similar analysis then shows that the boundary integrals converge, provided that $l_2 > \frac{1}{2}$ and $m_2 > \frac{3}{2}$, and that the second components of $T_{\lambda\lambda}(\lambda, \mu)$ and $T_{\mu\mu}(\lambda, \mu)$ are $\mathcal{O}(\lambda^{-l_2})$ and $\mathcal{O}(\lambda^{-m_2})$ as $\lambda \rightarrow \infty$, respectively.

We conclude that the convergence of the integrals in the solution (3.14) requires that $T_{\lambda\lambda}(\lambda, \mu)$ and $T_{\mu\mu}(\lambda, \mu)$ decay at large distance as $\mathcal{O}(\lambda^{-l})$ with $l > \frac{1}{2}$ and $\mathcal{O}(\lambda^{-m})$ with $m > \frac{3}{2}$, respectively. The requirements which we have imposed on $U(\lambda_0, \mu_0)$ and $T(\lambda_0, -\alpha)$ cause the contributions to $\oint_{\Gamma} d\mu_0 L(\lambda_0, \mu_0)$ in Green's formula (3.9) from the segment of the path at large λ_0 to be negligible in all cases.

Having obtained the requirements for the Riemann–Green function analysis to be valid, we now investigate the circumstances in which they apply. Following Arnold et al. (1994), we consider densities ρ that decay as $N(\mu)\lambda^{-s/2}$ at large distances. We suppose that the function $G(\tau)$ introduced in eq. (2.4) is $\mathcal{O}(\tau^{\delta})$ for $-\frac{1}{2} \leq \delta < 0$ as $\tau \rightarrow \infty$.

The lower limit $\delta = -\frac{1}{2}$ corresponds to a potential due to a finite total mass, while the upper limit restricts it to potentials that decay to zero at large distances.

For the disk potential (2.24), we then have that $f(\tau) = \mathcal{O}(\tau^{\delta+1})$ when $\tau \rightarrow \infty$. Using the definition (3.2), we obtain

$$U_{\lambda\lambda}(\lambda, \mu) = \frac{f'(\mu) - f'(\lambda)}{2(\lambda - \mu)^2} \rho + \frac{V_S + f'(\lambda)}{(\lambda - \mu)} \frac{\partial \rho}{\partial \mu}, \quad (3.22a)$$

$$U_{\mu\mu}(\lambda, \mu) = \frac{f'(\lambda) - f'(\mu)}{2(\lambda - \mu)^2} \rho - \frac{V_S + f'(\mu)}{(\lambda - \mu)} \frac{\partial \rho}{\partial \lambda}, \quad (3.22b)$$

where ρ is the surface density of the disk. It follows that $U_{\lambda\lambda}(\lambda, \mu)$ is generally the larger and is $\mathcal{O}(\lambda^{\delta-s/2-1})$ as $\lambda \rightarrow \infty$, whereas $U_{\mu\mu}(\lambda, \mu)$ is $\mathcal{O}(\lambda^{-2-s/2})$. Hence, for the components of the stresses (3.21) we have $T_{\lambda\lambda} = \mathcal{O}(\lambda^{\delta-s/2})$ and $T_{\mu\mu} = \mathcal{O}(\lambda^{-1-s/2})$. This estimate for $U_{\lambda\lambda}$ assumes that $\partial\rho/\partial\mu$ is also $\mathcal{O}(\lambda^{-s/2})$. It is too high if the density becomes independent of angle at large distances, as it does for disks with $s < 3$ (Evans & de Zeeuw 1992). Using these estimates with the requirements for integral convergence that were obtained earlier, we obtain the conditions $s > 2\delta + 1$ and $s > 1$, respectively, for inhomogeneous terms in $T_{\lambda\lambda}(\lambda, \mu)$ and $T_{\mu\mu}(\lambda, \mu)$ to be valid solutions. The second condition implies the first because $\delta < 0$.

With $V_S(\lambda, \mu) = \mathcal{O}(\lambda^\delta)$ at large λ , it follows from the energy eq. (2.10) for bound orbits that the second-order velocity moments $\langle v_\tau^2 \rangle$ cannot exceed $\mathcal{O}(\lambda^\delta)$, and hence that stresses $T_{\tau\tau} = \rho \langle v_\tau^2 \rangle$ cannot exceed $\mathcal{O}(\lambda^{\delta-s/2})$. This implies for $T_{\lambda\lambda}(\lambda, \mu)$ that $s > 2\delta + 1$, and for $T_{\mu\mu}(\lambda, \mu)$ we have the more stringent requirement that $s > 2\delta + 3$. This last requirement is unnecessarily restrictive, but an alternative form of the solution is needed to do better. Since that alternative form arises naturally with the singular solution method, we return to this issue in §3.2.6.

Thus, for the Riemann–Green solution to apply, we find the conditions $s > 1$ and $-\frac{1}{2} \leq \delta < 0$. These conditions are satisfied for the perfect elliptic disk ($s = 3, \delta = -\frac{1}{2}$), and for many other separable disks (Evans & de Zeeuw 1992).

3.1.5 Relation to the EL89 analysis

EL89 solve for the difference $\Delta \equiv T_{\lambda\lambda} - T_{\mu\mu}$ using a Green's function method which is essentially equivalent to the approach used here. EL89 give the Fourier transform of their Green's function, but do not invert it. We give the Riemann–Green function for Δ in Appendix A, and then rederive it by a Laplace transform analysis. Our Laplace transform analysis can be recast in terms of Fourier transforms. When we do this, we obtain a result which differs from that of EL89.

3.2 SINGULAR SOLUTION SUPERPOSITION

We have solved the disk problem (2.25) by combining the two Jeans equations into a single second-order PDE in one of the stress components, and then applying Riemann's method to it. However, Riemann's method and other standard techniques do not carry over to a single third-order PDE in one dependent variable, which is the best that one could expect to have in the general case. We introduce an alternative but equivalent method of solution, also based on the superposition of source points. In contrast to Riemann's method, this singular solution method is applicable to the general case of triaxial Stäckel models.

3.2.1 Simplified Jeans equations

We define new independent variables

$$\begin{aligned} S_{\lambda\lambda}(\lambda, \mu) &= |\lambda - \mu|^{\frac{1}{2}} T_{\lambda\lambda}(\lambda, \mu), \\ S_{\mu\mu}(\lambda, \mu) &= |\mu - \lambda|^{\frac{1}{2}} T_{\mu\mu}(\lambda, \mu), \end{aligned} \quad (3.23)$$

where $|\cdot|$ denotes absolute value, introduced to make the square root single-valued with respect to cyclic permutation of $\lambda \rightarrow \mu \rightarrow \lambda$. The Jeans equations (2.25) can then be written in the form

$$\frac{\partial S_{\lambda\lambda}}{\partial \lambda} - \frac{S_{\mu\mu}}{2(\lambda - \mu)} = -|\lambda - \mu|^{\frac{1}{2}} \rho \frac{\partial V_S}{\partial \lambda} \equiv g_1(\lambda, \mu), \quad (3.24a)$$

$$\frac{\partial S_{\mu\mu}}{\partial \mu} - \frac{S_{\lambda\lambda}}{2(\mu - \lambda)} = -|\mu - \lambda|^{\frac{1}{2}} \rho \frac{\partial V_S}{\partial \mu} \equiv g_2(\lambda, \mu). \quad (3.24b)$$

For given density and potential, g_1 and g_2 are known functions of λ and μ . Next, we consider a simplified form of (3.24) by taking for g_1 and g_2 , respectively

$$\tilde{g}_1(\lambda, \mu) = 0, \quad \tilde{g}_2(\lambda, \mu) = \delta(\lambda_0 - \lambda) \delta(\mu_0 - \mu), \quad (3.25)$$

with $-\beta \leq \mu \leq \mu_0 \leq -\alpha \leq \lambda \leq \lambda_0$. A similar set of simplified equations is obtained by interchanging the expressions for \tilde{g}_1 and \tilde{g}_2 . We refer to solutions of these simplified Jeans equations as *singular solutions*.

Singular solutions can be interpreted as contributions to the stresses at a fixed point (λ, μ) due to a source point in (λ_0, μ_0) (Fig. 4). The full stress at the field point can be obtained by adding all source point contributions, each with a weight that depends on the local density and potential. In what follows, we derive the singular solutions, and then use this superposition principle to construct the solution for the Stäckel disks in §3.2.6.

3.2.2 Homogeneous boundary problem

The choice (3.25) places constraints on the functional form of $S_{\lambda\lambda}$ and $S_{\mu\mu}$. The presence of the delta-functions in \tilde{g}_2 requires that $S_{\mu\mu}$ contains a term $-\delta(\lambda_0 - \lambda) \mathcal{H}(\mu_0 - \mu)$, with the step-function

$$\mathcal{H}(x - x_0) = \begin{cases} 0, & x < x_0, \\ 1, & x \geq x_0. \end{cases} \quad (3.26)$$

Since $\mathcal{H}'(y) = \delta(y)$, it follows that, by taking the partial derivative of $-\delta(\lambda_0 - \lambda) \mathcal{H}(\mu_0 - \mu)$ with respect to μ , the delta-functions are balanced. There is no balance when $S_{\lambda\lambda}$ contains $\delta(\lambda_0 - \lambda)$, and similarly neither stress components can contain $\delta(\mu_0 - \mu)$. We can, however, add a function of λ and μ to both components, multiplied by $\mathcal{H}(\lambda_0 - \lambda) \mathcal{H}(\mu_0 - \mu)$. In this way, we obtain a singular solution of the form

$$\begin{aligned} S_{\lambda\lambda} &= A(\lambda, \mu) \mathcal{H}(\lambda_0 - \lambda) \mathcal{H}(\mu_0 - \mu), \\ S_{\mu\mu} &= B(\lambda, \mu) \mathcal{H}(\lambda_0 - \lambda) \mathcal{H}(\mu_0 - \mu) - \delta(\lambda_0 - \lambda) \mathcal{H}(\mu_0 - \mu), \end{aligned} \quad (3.27)$$

in terms of functions A and B that have to be determined. Substituting these forms in the simplified Jeans equations and matching terms gives two homogeneous equations

$$\frac{\partial A}{\partial \lambda} - \frac{B}{2(\lambda - \mu)} = 0, \quad \frac{\partial B}{\partial \mu} - \frac{A}{2(\mu - \lambda)} = 0, \quad (3.28)$$

and two boundary conditions

$$A(\lambda_0, \mu) = \frac{1}{2(\lambda_0 - \mu)}, \quad B(\lambda, \mu_0) = 0. \quad (3.29)$$

Two alternative boundary conditions which are useful below can be found as follows. Integrating the first of the equations (3.28) with respect to λ on $\mu = \mu_0$, where $B(\lambda, \mu_0) = 0$, gives the boundary condition

$$A(\lambda, \mu_0) = \frac{1}{2(\lambda_0 - \mu_0)}. \quad (3.30)$$

Similarly, integrating the second of equations (3.28) with respect to μ on $\lambda = \lambda_0$ where A is known gives

$$B(\lambda_0, \mu) = \frac{\mu_0 - \mu}{4(\lambda_0 - \mu_0)(\lambda_0 - \mu)}. \quad (3.31)$$

Even though expressions (3.30) and (3.31) do not add new information, they will be useful for identifying contour integral formulas in the analysis which follows.

We have reduced the problem of solving the Jeans equations (2.25) for Stäckel disks to a two-dimensional boundary problem. We solve this problem by first deriving a one-parameter particular solution (§3.2.3) and then making a linear combination of particular solutions with different values of their free parameter, such that the four boundary expressions are satisfied simultaneously (§3.2.4). This gives the solution of the homogeneous boundary problem.

3.2.3 Particular solution

To find a particular solution of the homogeneous equations (3.28) with one free parameter z , we take as an Ansatz

$$\begin{aligned} A(\lambda, \mu) &\propto (\lambda - \mu)^{a_1} (z - \lambda)^{a_2} (z - \mu)^{a_3}, \\ B(\lambda, \mu) &\propto (\lambda - \mu)^{b_1} (z - \lambda)^{b_2} (z - \mu)^{b_3}, \end{aligned} \quad (3.32)$$

with a_i and b_i ($i = 1, 2, 3$) all constants. Hence,

$$\begin{aligned} \frac{\partial A}{\partial \lambda} &= A \left(\frac{a_1}{\lambda - \mu} - \frac{a_2}{z - \lambda} \right) = \frac{1}{2(\lambda - \mu)} \left(2a_1 A \frac{z - \mu}{z - \lambda} \right), \\ \frac{\partial B}{\partial \mu} &= B \left(\frac{b_1}{\mu - \lambda} - \frac{b_3}{z - \mu} \right) = \frac{1}{2(\mu - \lambda)} \left(2b_1 B \frac{z - \lambda}{z - \mu} \right), \end{aligned} \quad (3.33)$$

where we have set $a_2 = -a_1$ and $b_3 = -b_1$. Taking $a_1 = b_1 = \frac{1}{2}$, the homogeneous equations are satisfied if

$$\frac{z - \lambda}{z - \mu} = \frac{A}{B} = \frac{(z - \lambda)^{-\frac{1}{2} - b_2}}{(z - \mu)^{-\frac{1}{2} - a_3}}, \quad (3.34)$$

so, $a_3 = b_2 = -\frac{3}{2}$. We denote the resulting solutions as

$$A^P(\lambda, \mu) = \frac{|\lambda - \mu|^{\frac{1}{2}}}{(z - \lambda)^{\frac{1}{2}}(z - \mu)^{\frac{3}{2}}}, \quad (3.35a)$$

$$B^P(\lambda, \mu) = \frac{|\mu - \lambda|^{\frac{1}{2}}}{(z - \mu)^{\frac{1}{2}}(z - \lambda)^{\frac{3}{2}}}. \quad (3.35b)$$

These particular solutions follow from each other by cyclic permutation $\lambda \rightarrow \mu \rightarrow \lambda$, as is required from the symmetry of the homogeneous equations (3.28).

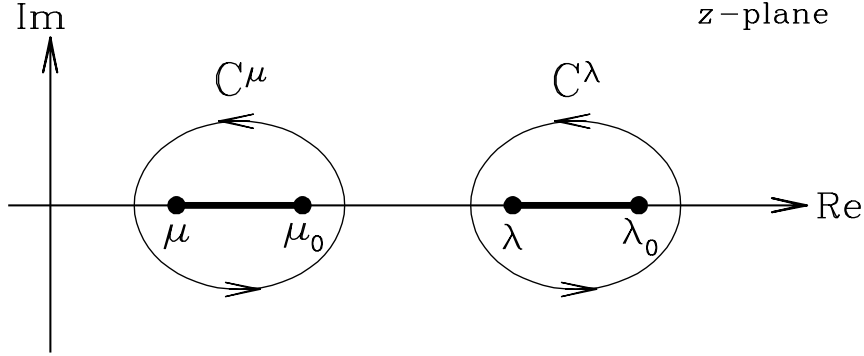


FIGURE 5 — Contours C^μ and C^λ in the complex z -plane which appear in the solution (3.37). The two cuts running from μ to μ_0 and one from λ to λ_0 make the integrands single-valued.

3.2.4 The homogeneous solution

We now consider a linear combination of the particular solution (3.35) by integrating it over the free parameter z , which we assume to be complex. We choose the integration contours in the complex z -plane, such that the four boundary expressions can be satisfied simultaneously.

We multiply $B^P(\lambda, \mu)$ by $(z - \mu_0)^{\frac{1}{2}}$, and integrate it over the closed contour C^μ (Fig. 5). When $\mu = \mu_0$, the integrand is analytic within C^μ , so that the integral vanishes by Cauchy's theorem. Since both the multiplication factor and the integration are independent of λ and μ , it follows from the superposition principle that the homogeneous equations are still satisfied. In this way, the second of the boundary expressions (3.29) is satisfied.

Next, we also multiply $B^P(\lambda, \mu)$ by $(z - \lambda_0)^{-\frac{1}{2}}$, so that the contour C^λ (Fig. 5) encloses a double pole when $\lambda = \lambda_0$. From the Residue theorem (e.g., Conway 1973), it then follows that

$$\begin{aligned} \oint_{C^\lambda} \frac{(z - \mu_0)^{\frac{1}{2}}}{(z - \lambda_0)^{\frac{1}{2}}} B^P(\lambda_0, \mu) dz &= \oint_{C^\lambda} \frac{(z - \mu_0)^{\frac{1}{2}} (\lambda_0 - \mu)^{\frac{1}{2}}}{(z - \mu)^{\frac{1}{2}} (z - \lambda_0)^2} dz \\ &= 2\pi i (\lambda_0 - \mu)^{\frac{1}{2}} \left[\frac{d}{dz} \left(\frac{z - \mu_0}{z - \mu} \right)^{\frac{1}{2}} \right]_{z=\lambda_0} \\ &= \frac{\pi i (\mu_0 - \mu)}{(\lambda_0 - \mu)^{\frac{1}{2}} (\lambda_0 - \mu)}, \end{aligned} \quad (3.36)$$

which equals the boundary expression (3.31), up to the factor $4\pi i (\lambda_0 - \mu_0)^{\frac{1}{2}}$.

Taking into account the latter factor, and the ratio (3.34) of A and B , we postulate as homogeneous solution

$$A(\lambda, \mu) = \frac{1}{4\pi i} \frac{|\lambda - \mu|^{\frac{1}{2}}}{|\lambda_0 - \mu_0|^{\frac{1}{2}}} \oint_C \frac{(z - \mu_0)^{\frac{1}{2}} dz}{(z - \lambda)^{\frac{1}{2}} (z - \mu)^{\frac{3}{2}} (z - \lambda_0)^{\frac{1}{2}}}, \quad (3.37a)$$

$$B(\lambda, \mu) = \frac{1}{4\pi i} \frac{|\mu - \lambda|^{\frac{1}{2}}}{|\lambda_0 - \mu_0|^{\frac{1}{2}}} \oint_C \frac{(z - \mu_0)^{\frac{1}{2}} dz}{(z - \mu)^{\frac{1}{2}} (z - \lambda)^{\frac{3}{2}} (z - \lambda_0)^{\frac{1}{2}}}, \quad (3.37b)$$

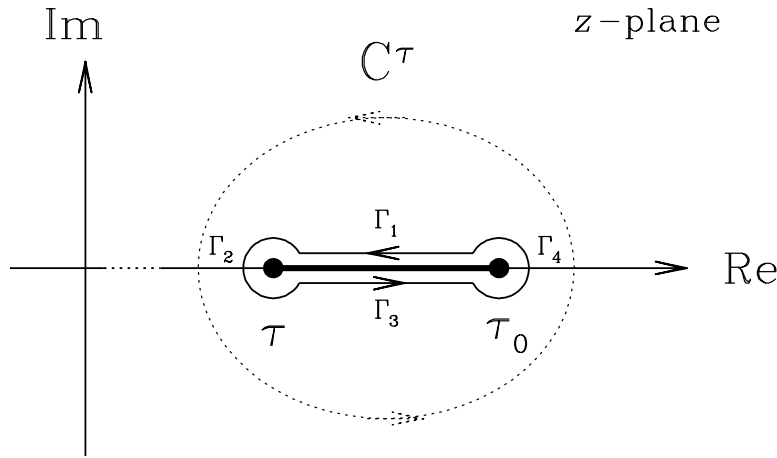


FIGURE 6 — Integration along the contour C^τ . The contour is wrapped around the branch points τ and τ_0 ($\tau = \lambda, \mu$), and split into four parts. Γ_1 and Γ_3 run parallel to the real axis in opposite directions. Γ_2 and Γ_4 are two arcs around τ and τ_0 , respectively.

with the choice for the contour C still to be specified.

The integrands in (3.37) consist of multi-valued functions that all come in pairs $(z - \tau)^{1/2-m}(z - \tau_0)^{1/2-n}$, for integer m and n , and for τ being either λ or μ . Hence, we can make the integrands single-valued by specifying two cuts in the complex z -plane, one from μ to μ_0 and one from λ to λ_0 . The integrands are now analytic in the cut plane away from its cuts and behave as z^{-2} at large distances, so that the integral over a circular contour with infinite radius is zero³. Connecting the simple contours C^λ and C^μ with this circular contour shows that the cumulative contribution from each of these contours cancels. As a consequence, every time we integrate over the contour C^λ , we will obtain the same result by integrating over $-C^\mu$ instead. This means we integrate over C^μ and take the negative of the result or, equally, integrate over C^μ in clockwise direction.

For example, we obtained the boundary expression for B in (3.36) by applying the Residue theorem to the double pole enclosed by the contour C^λ . The evaluation of the integral becomes less straightforward when we consider the contour $-C^\mu$ instead. Wrapping the contour around the branch points μ and μ_0 (Fig. 6), one may easily verify that the contribution from the two arcs vanishes if their radius goes to zero. Taking into account the change in phase when going around the two branch points, one may show that the contributions from the two remaining parts of the contour, parallel to the real axis, are equivalent. Hence, we arrive at the following (real) integral

$$B(\lambda_0, \mu) = \frac{1}{2\pi} \frac{(\lambda - \mu_0)^{\frac{1}{2}}}{(\lambda_0 - \mu_0)^{\frac{1}{2}}} \int_{\mu}^{\mu_0} \frac{dt}{(\lambda_0 - t)^2} \sqrt{\frac{\mu_0 - t}{t - \mu}}. \quad (3.38)$$

The substitution

$$t = \mu_0 + \frac{(\mu_0 - \mu)(\lambda_0 - \mu_0) \sin^2 \theta}{(\mu_0 - \mu) \sin^2 \theta - (\lambda_0 - \mu)} \quad (3.39)$$

then indeed gives the correct boundary expression (3.31).

³We evaluate the square roots as $(z - \tau)^{\frac{1}{2}} = |z - \tau|^{\frac{1}{2}} \exp i \arg(z - \tau)$ with $|\arg(z - \tau)| \leq \pi$.

When we take $\mu = \mu_0$ in (3.37b), we are left with the integrand $(z - \lambda)^{-3/2}(z - \lambda_0)^{-1/2}$. This is analytic within the contour C^μ and hence it follows from Cauchy's theorem that there is no contribution. However, if we take the contour $-C^\lambda$ instead, it is not clear at once that the integral indeed is zero. To evaluate the complex integral we wrap the contour C^λ around the branch points λ and λ_0 (Fig. 6). There will be no contribution from the arc around λ_0 if its radius goes to zero. However, since the integrand involves the term $z - \lambda$ with power $-\frac{3}{2}$, the contribution from the arc around λ is of the order $\epsilon^{-1/2}$ and hence goes to infinity if its radius $\epsilon > 0$ reduces to zero. If we let the two remaining straight parts of the contour run from $\lambda + \epsilon$ to λ_0 , then their cumulative contribution becomes proportional to $\tan \theta(\epsilon)$, with $\theta(\epsilon)$ approaching $\frac{\pi}{2}$ when ϵ reduces to zero. Hence, both the latter contribution and the contribution from the arc around λ approaches infinity. However, careful investigation of their limiting behavior shows that they cancel when ϵ reaches zero, as is required for the boundary expression $B(\lambda, \mu_0) = 0$.

We have shown that the use of C^λ and $-C^\mu$ gives the same result, but the effort to evaluate the contour integral varies between the two choices. The boundary expressions for $A(\lambda, \mu)$, (3.29) and (3.30) are obtained most easily if we consider C^λ when $\lambda = \lambda_0$ and $-C^\mu$ when $\mu = \mu_0$. In both cases the integrand in (3.37a) has a single pole within the chosen contour, so that the boundary expressions follow by straightforward application of the Residue theorem.

We now have proven that the homogeneous solution (3.37) solves the homogeneous equations (3.28), satisfies the boundary values (3.29)–(3.31) separately and, from the observation that C^λ and $-C^\mu$ produce the same result, also simultaneously.

3.2.5 Evaluation of the homogeneous solution

The homogeneous solution (3.37) consists of complex contour integrals, which we transform to real integrals by wrapping the contours C^λ and C^μ around the corresponding pair of branch points (Fig. 6). To have no contribution from the arcs around the branch points, we choose the (combination of) contours such that the terms in the integrand involving these branch points have powers larger than -1 . In this way, we can always evaluate the complex integral as a (real) integral running from one branch point to the other.

In the homogeneous solution (3.37a) for A we choose $C = C^\lambda$ and in (3.37b) for B we take $C = -C^\mu$. Taking into account the changes in phase when going around the branch points, we obtain the following expressions for the homogeneous solution

$$A(\lambda, \mu) = \frac{1}{2\pi} \frac{|\lambda - \mu|^{\frac{1}{2}}}{|\lambda_0 - \mu_0|^{\frac{1}{2}}} \int_{\lambda}^{\lambda_0} \frac{dt}{t - \mu} \sqrt{\frac{t - \mu_0}{(t - \lambda)(t - \mu)(\lambda_0 - t)}}, \quad (3.40a)$$

$$B(\lambda, \mu) = \frac{1}{2\pi} \frac{|\lambda - \mu|^{\frac{1}{2}}}{|\lambda_0 - \mu_0|^{\frac{1}{2}}} \int_{\mu}^{\mu_0} \frac{dt}{\lambda - t} \sqrt{\frac{\mu_0 - t}{(\lambda - t)(t - \mu)(\lambda_0 - t)}}. \quad (3.40b)$$

By a parameterization of the form (3.39), or by using an integral table (e.g., Byrd & Friedman 1971), expressions (3.40) can be written conveniently in terms of the complete elliptic integral of the second kind, E , and its derivative E'

$$A(\lambda, \mu; \lambda_0, \mu_0) = \frac{E(w)}{\pi(\lambda_0 - \mu)}, \quad (3.41a)$$

$$B(\lambda, \mu; \lambda_0, \mu_0) = -\frac{2wE'(w)}{\pi(\lambda_0 - \lambda)}. \quad (3.41b)$$

with w defined as in (3.16). The second set of arguments that were added to A and B make explicit the position (λ_0, μ_0) of the source point which is causing the stresses at the field point (λ, μ) .

3.2.6 The disk solution

The solution of equations (3.24) with right hand sides of the simplified form

$$\tilde{g}_1(\lambda, \mu) = \delta(\lambda_0 - \lambda)\delta(\mu_0 - \mu), \quad \tilde{g}_2(\lambda, \mu) = 0, \quad (3.42)$$

is obtained from the solution (3.27) by interchanging $\lambda \leftrightarrow \mu$ and $\lambda_0 \leftrightarrow \mu_0$. It is

$$\begin{aligned} S_{\lambda\lambda} &= B(\mu, \lambda; \mu_0, \lambda_0) \mathcal{H}(\lambda_0 - \lambda) \mathcal{H}(\mu_0 - \mu) - \delta(\mu_0 - \mu) \mathcal{H}(\lambda_0 - \lambda), \\ S_{\mu\mu} &= A(\mu, \lambda; \mu_0, \lambda_0) \mathcal{H}(\lambda_0 - \lambda) \mathcal{H}(\mu_0 - \mu). \end{aligned} \quad (3.43)$$

To find the solution to the full equations (3.24) at (λ, μ) , we multiply the singular solutions (3.27) and (3.43) by $g_1(\lambda_0, \mu_0)$ and $g_2(\lambda_0, \mu_0)$ respectively and integrate over D , the domain of dependence of (λ, μ) . This gives the first two lines of the two equations (3.44) below. The terms in the third lines are due to the boundary values of $S_{\mu\mu}$ at $\mu = -\alpha$. They are found by multiplying the singular solution (3.27) evaluated for $\mu_0 = -\alpha$ by $-S_{\mu\mu}(\lambda_0, -\alpha)$ and integrating over λ_0 in D . It is easily verified that this procedure correctly represents the boundary values with singular solutions. The final result for the general solution of the Jeans equations (3.24) for Stäckel disks, after using the evaluations (3.41), is

$$\begin{aligned} S_{\lambda\lambda}(\lambda, \mu) &= -\int_{\lambda}^{\infty} d\lambda_0 g_1(\lambda_0, \mu) \\ &\quad + \int_{\lambda}^{\infty} d\lambda_0 \int_{\mu}^{-\alpha} d\mu_0 \left[-g_1(\lambda_0, \mu_0) \frac{2wE'(w)}{\pi(\mu_0 - \mu)} + g_2(\lambda_0, \mu_0) \frac{E(w)}{\pi(\lambda_0 - \mu)} \right] \\ &\quad - \int_{\lambda}^{\infty} d\lambda_0 S_{\mu\mu}(\lambda_0, -\alpha) \left[\frac{E(w)}{\pi(\lambda_0 - \mu)} \right]_{\mu_0 = -\alpha}, \end{aligned} \quad (3.44a)$$

$$\begin{aligned} S_{\mu\mu}(\lambda, \mu) &= -\int_{\mu}^{-\alpha} d\mu_0 g_2(\lambda, \mu_0) \\ &\quad + \int_{\lambda}^{\infty} d\lambda_0 \int_{\mu}^{-\alpha} d\mu_0 \left[-g_1(\lambda_0, \mu_0) \frac{E(w)}{\pi(\lambda - \mu_0)} - g_2(\lambda_0, \mu_0) \frac{2wE'(w)}{\pi(\lambda_0 - \lambda)} \right] \\ &\quad + S_{\mu\mu}(\lambda, -\alpha) - \int_{\lambda}^{\infty} d\lambda_0 S_{\mu\mu}(\lambda_0, -\alpha) \left[-\frac{2wE'(w)}{\pi(\lambda_0 - \lambda)} \right]_{\mu_0 = -\alpha}. \end{aligned} \quad (3.44b)$$

The terms $(\mu_0 - \mu)^{-1}$ and $(\lambda_0 - \lambda)^{-1}$ do not cause singularities because they are canceled by components of w . In order to show that equations (3.44) are equivalent to the solution (3.21) given by Riemann's method, integrate the terms in $E'(w)$ by parts, and use the definitions of $S_{\tau\tau}$, g_1 and g_2 .

3.2.7 Convergence of the disk solution

We now return to the convergence issues first discussed in §3.1.4, where we assumed that the density ρ decays as $N(\mu)\lambda^{-s/2}$ at large distances and the Stäckel potential as $\mathcal{O}(\lambda^\delta)$. For the physical reasons given there, the assigned boundary stress $T_{\mu\mu}(\lambda, -\alpha)$ cannot exceed $\mathcal{O}(\lambda^{\delta-s/2})$ at large λ , giving an $S_{\mu\mu}(\lambda, -\alpha)$ of $\mathcal{O}(\lambda^{\delta-s/2+1/2})$. It follows that the infinite integrals in $S_{\mu\mu}(\lambda_0, -\alpha)$ in the solution (3.44) require only that $s > 2\delta + 1$ for their convergence. This is the less restrictive result to which we referred earlier.

The terms in the boundary stress are seen to contribute terms of the correct order $\mathcal{O}(\lambda^{\delta-s/2+1/2})$ to $S_{\lambda\lambda}(\lambda, \mu)$ and $S_{\mu\mu}(\lambda, \mu)$. The formulas for the density and potential show that $g_1(\lambda, \mu) = \mathcal{O}(\lambda^{\delta-s/2-1/2})$ while $g_2(\lambda, \mu)$ is larger and $\mathcal{O}(\lambda^{-s/2-1/2})$ as $\lambda \rightarrow \infty$. The λ_0 integrations with g_1 and g_2 in their integrands all converge provided $s > 2\delta + 1$. Hence, both $S_{\lambda\lambda}(\lambda, \mu)$ and $S_{\mu\mu}(\lambda, \mu)$ are $\mathcal{O}(\lambda^{\delta-s/2+1/2})$, so that the stress components $T_{\tau\tau}(\lambda, \mu)$ ($\tau = \lambda, \mu$) are $\mathcal{O}(\lambda^{\delta-s/2})$, which is consistent with the physical reasoning of §3.1.4.

Hence, all the conditions necessary for (3.44) to be a valid solution of the Jeans equations (3.24) for a Stäckel disk are satisfied provided that $s > 2\delta + 1$. We have seen in §3.1.4 that δ must lie in the range $[-\frac{1}{2}, 0)$. When $\delta \rightarrow 0$ the models approach the isothermal disk, for which also $s = 1$ when the density is consistent with the potential. Only then our requirement $s > 2\delta + 1$ is violated.

3.3 ALTERNATIVE BOUNDARY CONDITIONS

We now derive the alternative form of the general disk solution when the boundary conditions are not specified on $\mu = -\alpha$ but on $\mu = -\beta$, or on $\lambda = -\alpha$ rather than in the limit $\lambda \rightarrow \infty$. While the former switch is straightforward, the latter is non-trivial, and leads to non-physical solutions.

3.3.1 Boundary condition for μ

The analysis in §3.1 and §3.2 is that needed when the boundary conditions are imposed at large λ and at $\mu = -\alpha$. The Jeans equations (2.25) can be solved in a similar way when one or both of those conditions are imposed instead at the opposite boundaries $\lambda = -\alpha$ and/or $\mu = -\beta$. The solution by Riemann's method is accomplished by applying Green's theorem to a different domain, for example $D' = \{(\lambda_0, \mu_0): \lambda \leq \lambda_0 \leq \infty, -\beta \leq \mu_0 \leq \mu\}$ when the boundary conditions are at $\mu = -\beta$ and as $\lambda \rightarrow \infty$. The Riemann–Green functions have to satisfy the same PDE (3.10) and the same boundary conditions (3.12) and (3.13), and so again are given by equations (3.20a) and (3.20b). The variable w is negative in D' instead of positive as in D , but this is unimportant. The only significant difference in the solution of eq. (3.4) is that of a sign due to changes in the limits of the line integrals. The final result, in place of eq. (3.14), is

$$T(\lambda, \mu) = - \int_{\lambda}^{\infty} d\lambda_0 \int_{-\beta}^{\mu} d\mu_0 \mathcal{G}(\lambda_0, \mu_0) U(\lambda_0, \mu_0) - \int_{\lambda}^{\infty} d\lambda_0 \left[\left(\frac{\partial T}{\partial \lambda_0} + \frac{c_2 T}{\lambda_0 - \mu_0} \right) \mathcal{G} \right]_{\mu_0 = -\beta}. \quad (3.45)$$

To apply the method of singular solutions to solve for the stresses when the boundary stresses are specified at $\mu = -\beta$ rather than at $\mu = -\alpha$, we modify the singular solutions (3.27) by replacing the step-function $\mathcal{H}(\mu_0 - \mu)$ by $-\mathcal{H}(\mu - \mu_0)$ throughout. No other change is needed because both functions give $-\delta(\mu - \mu_0)$ on partial differentiation with respect to μ . The two-dimensional problem for A and B remains the

same, and so, as with Riemann's method, its solution remains the same. Summing over sources in D' now gives

$$S_{\lambda\lambda}(\lambda, \mu) = - \int_{\lambda}^{\infty} d\lambda_0 g_1(\lambda_0, \mu) - \int_{\lambda}^{\infty} d\lambda_0 \int_{-\beta}^{\mu} d\mu_0 \left[-g_1(\lambda_0, \mu_0) \frac{2wE'(w)}{\pi(\mu_0 - \mu)} + g_2(\lambda_0, \mu_0) \frac{E(w)}{\pi(\lambda_0 - \mu)} \right] - \int_{\lambda}^{\infty} d\lambda_0 S_{\mu\mu}(\lambda_0, -\beta) \left[\frac{E(w)}{\pi(\lambda_0 - \mu)} \right]_{\mu_0 = -\beta}, \quad (3.46a)$$

$$S_{\mu\mu}(\lambda, \mu) = \int_{-\beta}^{\mu} d\mu_0 g_2(\lambda, \mu_0) - \int_{\lambda}^{\infty} d\lambda_0 \int_{-\beta}^{\mu} d\mu_0 \left[-g_1(\lambda_0, \mu_0) \frac{E(w)}{\pi(\lambda - \mu_0)} - g_2(\lambda_0, \mu_0) \frac{2wE'(w)}{\pi(\lambda_0 - \lambda)} \right] + S_{\mu\mu}(\lambda, -\beta) - \int_{\lambda}^{\infty} d\lambda_0 S_{\mu\mu}(\lambda_0, -\beta) \left[-\frac{2wE'(w)}{\pi(\lambda_0 - \lambda)} \right]_{\mu_0 = -\beta}. \quad (3.46b)$$

as an alternative to equations (3.44).

3.3.2 Boundary condition for λ

There is a much more significant difference when one assigns boundary values at $\lambda = -\alpha$ rather than at $\lambda \rightarrow \infty$. It is still necessary that stresses decay to zero at large distances. The stresses induced by arbitrary boundary data at the finite boundary $\lambda = -\alpha$ do decay to zero as a consequence of geometric divergence. The issue is that of the rate of this decay. We find that it is generally less than that required by our analysis in §3.1.4.

To isolate the effect of boundary data at $\lambda = -\alpha$, we study solutions of the two-dimensional Jeans equations (2.25) when the inhomogeneous right hand side terms are set to zero and homogeneous boundary conditions of zero stress are applied at either $\mu = -\alpha$ or $\mu = -\beta$. These solutions can be derived either by Riemann's method or by singular solutions. The solution of the homogeneous PDE $\mathcal{L}T = 0$ is

$$T(\lambda, \mu) = - \int_{\mu}^{-\alpha} d\mu_0 \left[\left(\frac{\partial T}{\partial \mu_0} - \frac{c_1 T}{\lambda_0 - \mu_0} \right) \mathcal{G}(\lambda, \mu; \lambda_0, \mu_0) \right]_{\lambda_0 = -\alpha}, \quad (3.47)$$

for the case of zero stress at $\mu = -\alpha$, and

$$T(\lambda, \mu) = \int_{-\beta}^{\mu} d\mu_0 \left[\left(\frac{\partial T}{\partial \mu_0} - \frac{c_1 T}{\lambda_0 - \mu_0} \right) \mathcal{G}(\lambda, \mu; \lambda_0, \mu_0) \right]_{\lambda_0 = -\alpha}, \quad (3.48)$$

for the case of zero stress at $\mu = -\beta$.

The behavior of the stresses at large distances is governed by the behavior of the Riemann–Green functions \mathcal{G} for distant field points (λ, μ) and source points at $\lambda_0 = -\alpha$. It follows from equations (3.20) that $T_{\lambda\lambda}(\lambda, \mu) = \mathcal{O}(\lambda^{-1/2})$ and $T_{\mu\mu}(\lambda, \mu) = \mathcal{O}(\lambda^{-3/2})$. As a result, the radial stresses dominate at large distances and they decay as only the inverse first power of distance. Their rate of decay is less than $\mathcal{O}(\lambda^{\delta-s/2})$ – obtained in §3.1.4 from physical arguments – if the requirement $s > 2\delta + 1$ is satisfied. This inequality is the necessary condition which we derived in §3.2.6 for (3.44) to be a valid solution of the disk Jeans equations (3.24). It is violated in the isothermal limit.

There is a physical implication of radial stresses which decay as only the inverse first power of distance. It implies that net forces of finite magnitude are needed at an outer boundary to maintain the system, the finite magnitudes arising from the product of the decaying radial stresses and the increasing length of the boundary over which they act. That length grows as the first power of distance. Because this situation is perhaps more naturally understood in three dimensions, we return to it in our discussion of oblate models in §3.4.2. For now, lacking any physical reason for allowing a stellar system to have such an external constraint, we conclude that boundary conditions can be applied only at large λ and not at $\lambda = -\alpha$.

3.3.3 Disk solution for a general finite region

We now apply the singular solution method to solve equations (3.24) in some rectangle $\mu_{\min} \leq \mu \leq \mu_{\max}$, $\lambda_{\min} \leq \lambda \leq \lambda_{\max}$, when the stress $S_{\mu\mu}$ is given a boundary in μ , and $S_{\lambda\lambda}$ is given on a boundary in λ . This solution includes (3.44) and (3.46) as special cases. It will be needed for the large-radii scale-free case of §3.4.3.

As we saw in §3.3.1, singular solutions can easily be adapted to alternative choices for the domain of dependence of a field point (λ, μ) . Originally this was D , the first of the four quadrants into which (λ_0, μ_0) -space is split by the lines $\lambda_0 = \lambda$ and $\mu_0 = \mu$ (Fig. 4). It has the singular solution (3.27). We then obtained the singular solution for the fourth quadrant D' simply by replacing $\mathcal{H}(\mu_0 - \mu)$ by $-\mathcal{H}(\mu - \mu_0)$ in (3.27). We can similarly find the singular solution for the second quadrant $\lambda_{\min} \leq \lambda_0 \leq \lambda$, $\mu \leq \mu_0 \leq \mu_{\max}$ by replacing $\mathcal{H}(\lambda_0 - \lambda)$ by $-\mathcal{H}(\lambda - \lambda_0)$, and for the third quadrant $\lambda_{\min} \leq \lambda_0 \leq \lambda$, $\mu_{\min} \leq \mu_0 \leq \mu$ by replacing $\mathcal{H}(\lambda_0 - \lambda)$ by $-\mathcal{H}(\lambda - \lambda_0)$ and $\mathcal{H}(\mu_0 - \mu)$ by $-\mathcal{H}(\mu - \mu_0)$. We find the part of the solution of equations (3.24) due to the right hand side g terms by multiplying the first and second terms of the singular solutions by $g_1(\lambda_0, \mu_0)$ and $g_2(\lambda_0, \mu_0)$, respectively, and integrating over the relevant domain. We use $\lambda = \lambda_e$ and $\mu = \mu_e$ to denote the boundaries at which stresses are specified. We find the part of the solution generated by the boundary values of $S_{\mu\mu}$ by multiplying the singular solution (3.27), modified for the domain and evaluated at $\mu_0 = \mu_e$, by $\pm S_{\mu\mu}(\lambda_0, \mu_e)$ and integrating over λ_0 in the domain. The plus sign is needed when $\mu_e = \mu_{\min}$ and the minus when $\mu_e = \mu_{\max}$. Similarly, the part of the solution generated by the boundary values of $S_{\lambda\lambda}$ is obtained by multiplying the singular solution (3.43), modified for the domain and evaluated at $\lambda_0 = \lambda_e$, by $\pm S_{\lambda\lambda}(\lambda_e, \mu_0)$ and integrating over μ_0 in the domain. The sign is plus if $\lambda_e = \lambda_{\min}$ and minus if $\lambda_e = \lambda_{\max}$. The final

solution is

$$\begin{aligned}
S_{\lambda\lambda}(\lambda, \mu) &= S_{\lambda\lambda}(\lambda_e, \mu) - \int_{\lambda}^{\lambda_e} d\lambda_0 g_1(\lambda_0, \mu) \\
&\quad + \int_{\lambda}^{\lambda_e} d\lambda_0 \int_{\mu}^{\mu_e} d\mu_0 [g_1(\lambda_0, \mu_0)B(\mu, \lambda; \mu_0, \lambda_0) + g_2(\lambda_0, \mu_0)A(\lambda, \mu; \lambda_0, \mu_0)] \\
&\quad - \int_{\lambda}^{\lambda_e} d\lambda_0 S_{\mu\mu}(\lambda_0, \mu_e)A(\lambda, \mu; \lambda_0, \mu_e) - \int_{\mu}^{\mu_e} d\mu_0 S_{\lambda\lambda}(\lambda_e, \mu_0)B(\mu, \lambda; \mu_0, \lambda_e), \quad (3.49a)
\end{aligned}$$

$$\begin{aligned}
S_{\mu\mu}(\lambda, \mu) &= S_{\mu\mu}(\lambda, \mu_e) - \int_{\mu}^{\mu_e} d\mu_0 g_2(\lambda, \mu_0) \\
&\quad + \int_{\lambda}^{\lambda_e} d\lambda_0 \int_{\mu}^{\mu_e} d\mu_0 [g_1(\lambda_0, \mu_0)A(\mu, \lambda; \mu_0, \lambda_0) + g_2(\lambda_0, \mu_0)B(\lambda, \mu; \lambda_0, \mu_0)] \\
&\quad - \int_{\lambda}^{\lambda_e} d\lambda_0 S_{\mu\mu}(\lambda_0, \mu_e)B(\lambda, \mu; \lambda_0, \mu_e) - \int_{\mu}^{\mu_e} d\mu_0 S_{\lambda\lambda}(\lambda_e, \mu_0)A(\mu, \lambda; \mu_0, \lambda_e). \quad (3.49b)
\end{aligned}$$

This solution is uniquely determined once g_1 and g_2 are given, and the boundary values $S_{\mu\mu}(\lambda_0, \mu_e)$ and $S_{\lambda\lambda}(\lambda_e, \mu_0)$ are prescribed. It shows that the hyperbolic equations (3.24) can equally well be integrated in either direction in the characteristic variables λ and μ . Solutions (3.44) and (3.46) are obtained by taking $\lambda_e \rightarrow \infty$, $S_{\lambda\lambda}(\lambda_e, \mu_0) \rightarrow 0$, setting $\mu_e = -\alpha$ and $\mu_e = -\beta$ respectively, and evaluating A and B by equations (3.41).

3.4 APPLYING THE DISK SOLUTION TO LIMITING CASES

We showed in §2.6 that the Jeans equations for prolate and oblate potentials and for three-dimensional Stäckel models with a scale-free DF all reduce to a set of two equations equivalent to those for the Stäckel disk. Here we apply our solution for the Stäckel disk to these special three-dimensional cases, with particular attention to the behavior at large radii and the boundary conditions. This provides further insight in some of the previously published solutions. We also consider the case of a Stäckel disk built with thin tube orbits.

3.4.1 Prolate potentials

We can apply the disk solution (3.46) to solve the Jeans equations (2.35) by setting $S_{\lambda\lambda}(\lambda, \mu) = |\lambda - \mu|^{\frac{1}{2}}\mathcal{T}_{\lambda\lambda}(\lambda, \mu)$ and $S_{\mu\mu}(\lambda, \mu) = |\mu - \lambda|^{\frac{1}{2}}\mathcal{T}_{\mu\mu}(\lambda, \mu)$, and taking

$$\begin{aligned}
g_1(\lambda, \mu) &= -|\lambda - \mu|^{\frac{1}{2}}(\lambda + \beta)^{\frac{1}{2}}(\mu + \beta)^{\frac{1}{2}} \left[\rho \frac{\partial V_S}{\partial \lambda} + \frac{\partial T_{\chi\chi}}{\partial \lambda} \right], \\
g_2(\lambda, \mu) &= -|\mu - \lambda|^{\frac{1}{2}}(\lambda + \beta)^{\frac{1}{2}}(\mu + \beta)^{\frac{1}{2}} \left[\rho \frac{\partial V_S}{\partial \mu} + \frac{\partial T_{\chi\chi}}{\partial \mu} \right].
\end{aligned} \quad (3.50)$$

The boundary terms in $S_{\mu\mu}(\lambda, -\beta)$ vanish because of the boundary condition (2.36). As before, we regard the azimuthal stress $T_{\chi\chi}$ as a variable that can be arbitrarily

assigned, provided that it has the correct behavior at large λ (§3.1.4). The choice of $T_{\chi\chi}$ is also restricted by the requirement that the resulting solutions for the stresses $T_{\lambda\lambda}$ and $T_{\mu\mu}$ must be non-negative (see §2.3).

The analysis needed to show that the solution obtained in this way is valid requires only minor modifications of that of §3.2.7. We suppose that the prescribed azimuthal stresses also decay as $\mathcal{O}(\lambda^{\delta-s/2})$ as $\lambda \rightarrow \infty$. As a result of the extra factor in the definitions (3.50), we now have $g_1(\lambda, \mu) = \mathcal{O}(\lambda^{\delta-s/2})$ and $g_2(\lambda, \mu) = \mathcal{O}(\lambda^{-s/2})$ as $\lambda \rightarrow \infty$. The λ_0 integrations converge provided $s > 2\delta + 2$, and $S_{\lambda\lambda}$ and $S_{\mu\mu}$ are $\mathcal{O}(\lambda^{\delta-s/2+1})$. Hence the stresses $T_{\lambda\lambda}$ and $T_{\mu\mu}$, which follow from $T_{\tau\tau} = T_{\chi\chi} + S_{\tau\tau} / \sqrt{(\lambda - \mu)(\lambda + \beta)(\mu + \beta)}$, are once again $\mathcal{O}(\lambda^{\delta-s/2})$. The requirement $s > 2\delta + 2$ is no stronger than the requirement $s > 2\delta + 1$ of §3.2.7; it is simply the three-dimensional version of that requirement. It also does not break down until the isothermal limit. That limit is still $\delta \rightarrow 0$, but now $s \rightarrow 2$.

3.4.2 Oblate potentials

The oblate case with Jeans equations (2.37) differs significantly from the prolate case. Now $S_{\lambda\lambda}(\lambda, \nu) = |\lambda - \nu|^{\frac{1}{2}} T_{\lambda\lambda}(\lambda, \nu)$ vanishes at $\lambda = -\alpha$ and $S_{\nu\nu}(\lambda, \nu) = |\nu - \lambda|^{\frac{1}{2}} T_{\nu\nu}(\lambda, \nu)$ vanishes at $\nu = -\alpha$. If one again supposes that the azimuthal stresses $T_{\phi\phi}$ can be assigned initially, then one encounters the problem discussed in §3.3.2 of excessively large radial stresses at large distances. To relate that analysis to the present case, we use the solution (3.44) with μ replaced by ν , and with zero boundary value $S_{\nu\nu}(\lambda, -\alpha)$, and for g_1 and g_2 the right hand side of (2.37) multiplied by $|\lambda - \nu|^{\frac{1}{2}}$ and $|\nu - \lambda|^{\frac{1}{2}}$, respectively.

The estimates we obtained for the prolate case are still valid, so the stresses $T_{\lambda\lambda}$ and $T_{\nu\nu}$ are $\mathcal{O}(\lambda^{\delta-s/2})$. Difficulties arise when this solution for $S_{\lambda\lambda}$ does not vanish at $\lambda = -\alpha$, but instead has some nonzero value $\kappa(\nu)$ there. To obtain a physically acceptable solution, we must add to it a solution of the homogeneous equations (2.37) with boundary values $T_{\lambda\lambda}(-\alpha, \nu) = -\kappa(\nu) / \sqrt{-\alpha - \nu}$ and $T_{\nu\nu}(\lambda, -\alpha) = 0$. This is precisely the problem we discussed in §3.3.2 where we showed that the resulting solution gives $T_{\lambda\lambda}(\lambda, \mu) = \mathcal{O}(\lambda^{-1/2})$, and hence $T_{\lambda\lambda}(\lambda, \mu) = \mathcal{O}(\lambda^{-1})$. This is larger than $\mathcal{O}(\lambda^{\delta-s/2})$ when the three-dimensional requirement $s > 2\delta + 2$ is met. We therefore conclude that the approach in which one first selects the azimuthal stress $T_{\phi\phi}$ and then calculates the other two stresses will be unsuccessful unless the choice of $T_{\phi\phi}$ is fortunate, and leads to $\kappa(\nu) \equiv 0$. Otherwise, it leads only to models which either violate the continuity condition $T_{\lambda\lambda} - T_{\phi\phi} = 0$ at $\lambda = -\alpha$, or else have radial stresses which require external forces at large distances.

The physical implication of radial stresses which decay as only $\mathcal{O}(\lambda^{-1})$, or the inverse second power of distance, is that net forces of finite magnitude are needed at an outer boundary to maintain the system. This finite magnitude arises from the product of the decaying radial stresses and the increasing surface area of the boundary over which they act, which grows as the second power of distance. This situation is analogous to that of an isothermal sphere, as illustrated in problem 4–9 of Binney & Tremaine (1987), for which the contribution from an outer surface integral must be taken into account in the balance between energies required by the virial theorem.

There are, of course, many physical models which satisfy the continuity condition and whose radial stresses decay in the physically correct manner at large distances, but some strategy other than that of assigning $T_{\phi\phi}$ initially is needed to find them. In fact, only Evans (1990) used the approach of assigning $T_{\phi\phi}$ initially. He computed a numerical solution for a mass model with $s = 3$ and $V_S \propto \mathcal{O}(\lambda^{-1/2} \ln \lambda)$ for large λ , so

that the stresses there should be $\mathcal{O}(\lambda^{-2} \ln \lambda)$. He set $T_{\phi\phi} = -\frac{1}{3}\rho V_S$, which is of this magnitude, and integrated from $\lambda = -\alpha$ in the direction of increasing λ for a finite range. Evans does not report on the large λ behavior, and it is possible that his choice of $T_{\phi\phi}$ gives $\kappa(\nu) = 0$, but his Figure 2 especially shows velocity ellipsoids which become increasingly elongated in the radial direction, consistent with our prediction that $T_{\lambda\lambda}$ generally grows as $\mathcal{O}(\lambda^{-1})$ when the boundary value of $T_{\lambda\lambda}$ is assigned at $\lambda = -\alpha$.

A more common and effective approach to solve the Jeans equations for oblate models has been to specify the ratio $T_{\lambda\lambda}/T_{\nu\nu}$, and then to solve for one of those stresses and $T_{\phi\phi}$ (Bacon, Simien & Monnet 1983; Dejonghe & de Zeeuw 1988; Evans & Lynden-Bell 1991; Arnold 1995). This leads to a much simpler mathematical problem with just a single first-order PDE. The characteristics of that PDE have non-negative slopes $d\lambda/d\nu$, and therefore cut across the coordinate lines of constant λ and ν . The solution is obtained by integrating in along the characteristics from large λ . The continuity conditions (2.23) are taken care of automatically, the region $-\gamma \leq \nu \leq -\alpha \leq \infty$ is covered, and it is easy to verify that the stresses so obtained are everywhere positive.

3.4.3 Large radii limit with scale-free DF

We found in §2.5.4 that the first of the Jeans equations in conical coordinates (2.29) reduces to an algebraic relation for the radial stress T_{rr} . The problem that remains is that of solving the second and third Jeans equations for $T_{\mu\mu}$ and $T_{\nu\nu}$. Those equations are exactly the same as those of the disk case after we apply the coordinate permutation $\lambda \rightarrow \mu \rightarrow \nu$, and the physical domain is $-\gamma \leq \nu \leq -\beta \leq \mu \leq -\alpha$ with finite ranges of both variables. Hence, the solution (3.49) can be applied with $T_{\mu\mu}$ assigned at either $\mu_e = -\alpha$ or $\mu_e = -\beta$, and $T_{\nu\nu}$ at either $\nu_e = -\beta$ or $\nu_e = -\gamma$. For g_1 and g_2 we take the same expressions as for the disk case, i.e., the right-hand side of (3.24), but with $\lambda \rightarrow \mu \rightarrow \nu$ and multiplied by r^ζ . To obtain $T_{\mu\mu}$ and $T_{\nu\nu}$ from the $S_{\lambda\lambda}$ and $S_{\mu\mu}$ respectively, we use the transformation

$$S_{\tau\tau} = (\mu - \nu)^{\frac{1}{2}} r^\zeta T_{\tau\tau}, \quad \tau = \mu, \nu, \quad (3.51)$$

with $\zeta > 0$ the scaling factor. We can choose to specify the stress components on the two boundaries $\mu = -\beta$ and $\nu = -\beta$. For a given radius r these boundaries cover the circular cross section with the (x, z) -plane (Fig. 3). We can consider the (x, z) -plane as the starting space for the solution. It turns out that the latter also applies to the triaxial solution (§4.6.3) and compares well with Schwarzschild (1993), who used the same plane to start his numerically calculated orbits from.

3.4.4 Thin tube orbits

For infinitesimally thin tube orbits in Stäckel disks we have that $S_{\lambda\lambda} \equiv 0$ (§2.5.6), so that equations (3.24) reduce to

$$-\frac{S_{\mu\mu}}{2(\lambda - \mu)} = g_1(\lambda, \mu), \quad \frac{\partial S_{\mu\mu}}{\partial \mu} = g_2(\lambda, \mu). \quad (3.52)$$

A solution is possible only if the right hand side terms satisfy the subsidiary equation

$$g_2(\lambda, \mu) = -2 \frac{\partial}{\partial \mu} [(\lambda - \mu)g_1(\lambda, \mu)]. \quad (3.53)$$

We find below that this equation places restrictions on the form of the (surface) density ρ , and we use this relation between g_1 and g_2 to show that the disk solution (3.44) yields the right results for the stress components.

If we write the disk potential (2.24) as a divided difference, $V_S = -f[\lambda, \mu]$, we have

$$g_1 = (\lambda - \mu)^{\frac{1}{2}} \rho f[\lambda, \lambda, \mu], \quad g_2 = (\lambda - \mu)^{\frac{1}{2}} \rho f[\lambda, \mu, \mu]. \quad (3.54)$$

Upon substitution of these expressions in (3.53) we obtain a PDE in μ , of which the solution implies the following form for the density

$$\rho(\lambda, \mu) = \frac{\tilde{f}(\lambda)}{(\lambda - \mu)\sqrt{f[\lambda, \lambda, \mu]}}, \quad (3.55)$$

where $\tilde{f}(\lambda)$ is an arbitrary function independent of μ . From (3.52) and the definition (3.23) it then follows that $T_{\mu\mu}(\lambda, \mu, \nu) = -2\tilde{f}(\lambda)\sqrt{f[\lambda, \lambda, \mu]}$. The tube density that de Zeeuw, Hunter & Schwarzschild (1987) derive from the DF for thin tube orbits in the perfect elliptic disk (their eq. [4.25]) is indeed of the form (3.55).

To show that the general disk solution (3.44) gives $S_{\lambda\lambda}(\lambda, \mu) = 0$, we substitute eq. (3.53) for $g_2(\lambda, \mu)$ in (3.44a). After partial integration and using

$$2(\lambda_0 - \mu_0) \frac{\partial}{\partial \mu_0} \frac{E(w)}{\pi(\lambda_0 - \mu)} = \frac{2wE'(w)}{\pi(\mu_0 - \mu)}, \quad (3.56)$$

we find that the area integral reduces to

$$\int_{\lambda}^{\infty} d\lambda_0 \left\{ g_1(\lambda_0, \mu) - 2(\lambda_0 + \alpha) g_1(\lambda_0, -\alpha) \left[\frac{E(w)}{\pi(\lambda_0 - \mu)} \right]_{\mu_0 = -\alpha} \right\}. \quad (3.57)$$

The first part cancels the first line of (3.44a) and since from (3.52) we have that $-2(\lambda_0 + \alpha)g_1(\lambda_0, -\alpha) = S_{\mu\mu}(\lambda_0, -\alpha)$, the second part cancels the third line. Hence, we have $S_{\lambda\lambda}(\lambda, \mu) = 0$ as required. To see that the general disk solution also yields $S_{\mu\mu}(\lambda, \mu)$ correctly, we apply similar steps to (3.44b), where we use the relation

$$-2(\lambda_0 - \mu_0) \frac{\partial}{\partial \mu_0} \frac{2wE'(w)}{\pi(\lambda_0 - \lambda)} = \frac{E(w)}{\pi(\lambda - \mu_0)}. \quad (3.58)$$

We are finally left with

$$S_{\mu\mu}(\lambda, \mu) = S_{\mu\mu}(\lambda, -\alpha) - \int_{\mu}^{-\alpha} d\mu_0 g_2(\lambda, \mu_0), \quad (3.59)$$

which is just the second equation of (3.52) integrated with respect to μ .

4 THE GENERAL CASE

We now solve the system of three Jeans equations (2.16) for triaxial Stäckel models by applying the singular solution superposition method, introduced in §3.2 for the two-dimensional case. Although the calculations are more complex for a triaxial model, the step-wise solution method is similar to that in two dimensions. Specifically, we first simplify the Jeans equations and show that they reduce to a three-dimensional homogeneous boundary problem. We then find a two-parameter particular solution and apply contour integration to both complex parameters to obtain the general homogeneous solution. The latter yields the three singular solutions of the simplified Jeans equations, from which, by superposition, we construct the general solution.

4.1 SIMPLIFIED JEANS EQUATIONS

We start by introducing the functions

$$S_{\tau\tau}(\lambda, \mu, \nu) = \sqrt{(\lambda - \mu)(\lambda - \nu)(\mu - \nu)} T_{\tau\tau}(\lambda, \mu, \nu), \quad (4.1)$$

with $\tau = \lambda, \mu, \nu$, to write the Jeans equations for triaxial Stäckel models (2.16) in the more convenient form

$$\frac{\partial S_{\lambda\lambda}}{\partial \lambda} - \frac{S_{\mu\mu}}{2(\lambda - \mu)} - \frac{S_{\nu\nu}}{2(\lambda - \nu)} = g_1(\lambda, \mu, \nu), \quad (4.2a)$$

$$\frac{\partial S_{\mu\mu}}{\partial \mu} - \frac{S_{\nu\nu}}{2(\mu - \nu)} - \frac{S_{\lambda\lambda}}{2(\mu - \lambda)} = g_2(\lambda, \mu, \nu), \quad (4.2b)$$

$$\frac{\partial S_{\nu\nu}}{\partial \nu} - \frac{S_{\lambda\lambda}}{2(\nu - \lambda)} - \frac{S_{\mu\mu}}{2(\nu - \mu)} = g_3(\lambda, \mu, \nu), \quad (4.2c)$$

where the function g_1 is defined as

$$g_1(\lambda, \mu, \nu) = -\sqrt{(\lambda - \mu)(\lambda - \nu)(\mu - \nu)} \rho \frac{\partial V_S}{\partial \lambda}, \quad (4.3)$$

and g_2 and g_3 follow by cyclic permutation $\lambda \rightarrow \mu \rightarrow \nu \rightarrow \lambda$. We keep the three terms $\lambda - \mu$, $\lambda - \nu$ and $\mu - \nu$ under one square root. With each cyclic permutation two of the three terms change sign, so that the combination of the three terms is always positive real. Therefore, the square root of the combination is always single-valued, whereas in the case of three separate square roots we would have a multi-valued function.

We simplify equations (4.2) by substituting for g_1 , g_2 and g_3 , respectively

$$\begin{aligned} \tilde{g}_1(\lambda, \mu, \nu) &= 0, \\ \tilde{g}_2(\lambda, \mu, \nu) &= \delta(\lambda_0 - \lambda) \delta(\mu_0 - \mu) \delta(\nu_0 - \nu), \\ \tilde{g}_3(\lambda, \mu, \nu) &= 0, \end{aligned} \quad (4.4)$$

with

$$-\gamma \leq \nu \leq \nu_0 \leq -\beta \leq \mu \leq \mu_0 \leq -\alpha \leq \lambda \leq \lambda_0. \quad (4.5)$$

We obtain two similar systems of simplified equations by cyclic permutation of the left-hand side of (4.2). Once we have obtained the singular solutions of the simplified system with the right-hand side given by (4.4), those for the other two systems follow via cyclic permutation.

4.2 HOMOGENEOUS BOUNDARY PROBLEM

The choice (4.4) implies that the functions $S_{\tau\tau}(\lambda, \mu, \nu)$ (4.1) have the following forms

$$\begin{aligned} S_{\lambda\lambda} &= A(\lambda, \mu, \nu) \mathcal{H}(\lambda_0 - \lambda) \mathcal{H}(\mu_0 - \mu) \mathcal{H}(\nu_0 - \nu) \\ &\quad + F(\lambda, \mu) \delta(\nu_0 - \nu) \mathcal{H}(\lambda_0 - \lambda) \mathcal{H}(\mu_0 - \mu), \\ S_{\mu\mu} &= B(\lambda, \mu, \nu) \mathcal{H}(\lambda_0 - \lambda) \mathcal{H}(\mu_0 - \mu) \mathcal{H}(\nu_0 - \nu) \\ &\quad + G(\lambda, \mu) \delta(\nu_0 - \nu) \mathcal{H}(\lambda_0 - \lambda) \mathcal{H}(\mu_0 - \mu) \\ &\quad + H(\mu, \nu) \delta(\lambda_0 - \lambda) \mathcal{H}(\mu_0 - \mu) \mathcal{H}(\nu_0 - \nu) \\ &\quad - \delta(\lambda_0 - \lambda) \delta(\nu_0 - \nu) \mathcal{H}(\mu_0 - \mu), \\ S_{\nu\nu} &= C(\lambda, \mu, \nu) \mathcal{H}(\lambda_0 - \lambda) \mathcal{H}(\mu_0 - \mu) \mathcal{H}(\nu_0 - \nu) \\ &\quad + I(\mu, \nu) \delta(\lambda_0 - \lambda) \mathcal{H}(\mu_0 - \mu) \mathcal{H}(\nu_0 - \nu), \end{aligned} \quad (4.6)$$

with A, B, C and F, G, H, I yet unknown functions of three and two coordinates, respectively, and \mathcal{H} the step-function (3.26). After substituting these forms into the simplified Jeans equations and matching terms we obtain 14 equations. Eight of them comprise the following two homogeneous systems with two boundary conditions each

$$\begin{cases} \frac{\partial F}{\partial \lambda} - \frac{G}{2(\lambda - \mu)} = 0, & F(\lambda_0, \mu) = \frac{1}{2(\lambda_0 - \mu)}, \\ \frac{\partial G}{\partial \mu} - \frac{F}{2(\mu - \lambda)} = 0, & G(\lambda, \mu_0) = 0, \end{cases} \quad (4.7)$$

and

$$\begin{cases} \frac{\partial H}{\partial \mu} - \frac{I}{2(\mu - \nu)} = 0, & H(\mu_0, \nu) = 0, \\ \frac{\partial I}{\partial \nu} - \frac{H}{2(\nu - \mu)} = 0, & I(\mu, \nu_0) = \frac{1}{2(\nu_0 - \mu)}. \end{cases} \quad (4.8)$$

We have shown in §3 how to solve these two-dimensional homogeneous boundary problems in terms of the complete elliptic integral of the second kind E and its derivative E' . The solutions are

$$\begin{aligned} F(\lambda, \mu) &= \frac{E(w)}{\pi(\lambda_0 - \mu)}, & G(\lambda, \mu) &= -\frac{2wE'(w)}{\pi(\lambda_0 - \lambda)}, \\ H(\mu, \nu) &= -\frac{2uE'(u)}{\pi(\nu_0 - \nu)}, & I(\mu, \nu) &= -\frac{E(u)}{\pi(\mu - \nu_0)}, \end{aligned} \quad (4.9)$$

where u and similarly v , which we will encounter later on, follow from w (3.16) by cyclic permutation $\lambda \rightarrow \mu \rightarrow \nu \rightarrow \lambda$ and $\lambda_0 \rightarrow \mu_0 \rightarrow \nu_0 \rightarrow \lambda_0$, so that

$$u = \frac{(\mu_0 - \mu)(\nu_0 - \nu)}{(\mu_0 - \nu_0)(\mu - \nu)}, \quad v = \frac{(\nu_0 - \nu)(\lambda_0 - \lambda)}{(\lambda_0 - \nu_0)(\lambda - \nu)}. \quad (4.10)$$

The remaining six equations form a three-dimensional homogeneous boundary problem, consisting of three homogeneous Jeans equations

$$\begin{aligned} \frac{\partial A}{\partial \lambda} - \frac{B}{2(\lambda - \mu)} - \frac{C}{2(\lambda - \nu)} &= 0, \\ \frac{\partial B}{\partial \mu} - \frac{C}{2(\mu - \nu)} - \frac{A}{2(\mu - \lambda)} &= 0, \\ \frac{\partial C}{\partial \nu} - \frac{A}{2(\nu - \lambda)} - \frac{B}{2(\nu - \mu)} &= 0. \end{aligned} \quad (4.11)$$

and three boundary conditions, specifically the values of $A(\lambda_0, \mu, \nu)$, $B(\lambda, \mu_0, \nu)$, and $C(\lambda, \mu, \nu_0)$. As in §3.2.2, it is useful to supplement these boundary conditions with the values of A, B , and C at the other boundary surfaces. These are obtained by integrating the pairs of equations (4.11) which apply at those surfaces, and using the

boundary conditions. This results in the following nine boundary values

$$\begin{aligned}
A(\lambda_0, \mu, \nu) &= \frac{1}{2\pi} \left[\frac{E(u)}{(\lambda_0 - \nu)(\mu - \nu_0)} + \frac{2uE'(u)}{(\lambda_0 - \mu)(\nu_0 - \nu)} \right], \\
A(\lambda, \mu_0, \nu) &= \frac{1}{2\pi} \left[\frac{E(v)}{(\lambda_0 - \nu)(\mu_0 - \nu_0)} + \frac{2vE'(v)}{(\lambda_0 - \mu_0)(\nu_0 - \nu)} \right], \\
A(\lambda, \mu, \nu_0) &= \frac{E(w)}{4\pi(\lambda_0 - \mu)} \left[\frac{\lambda - \mu}{(\lambda - \nu_0)(\mu - \nu_0)} + \frac{\lambda_0 - \mu_0}{(\lambda_0 - \nu_0)(\mu_0 - \nu_0)} \right], \\
B(\lambda_0, \mu, \nu) &= \frac{uE'(u)}{2\pi(\nu_0 - \nu)} \left[\frac{\mu_0 - \mu}{(\lambda_0 - \mu_0)(\lambda_0 - \mu)} - \frac{\nu_0 - \nu}{(\lambda_0 - \nu_0)(\lambda_0 - \nu)} \right], \\
B(\lambda, \mu_0, \nu) &= 0, \\
B(\lambda, \mu, \nu_0) &= \frac{wE'(w)}{2\pi(\lambda_0 - \lambda)} \left[\frac{\mu_0 - \mu}{(\mu_0 - \nu_0)(\mu - \nu_0)} - \frac{\lambda_0 - \lambda}{(\lambda_0 - \nu_0)(\lambda - \nu_0)} \right], \\
C(\lambda_0, \mu, \nu) &= \frac{E(u)}{4\pi(\mu - \nu_0)} \left[\frac{\mu - \nu}{(\lambda_0 - \mu)(\lambda_0 - \nu)} + \frac{\mu_0 - \nu_0}{(\lambda_0 - \mu_0)(\lambda_0 - \nu_0)} \right], \\
C(\lambda, \mu_0, \nu) &= \frac{1}{2\pi} \left[\frac{E(v)}{(\lambda_0 - \mu_0)(\lambda - \nu_0)} - \frac{2vE'(v)}{(\mu_0 - \nu_0)(\lambda_0 - \lambda)} \right], \\
C(\lambda, \mu, \nu_0) &= \frac{1}{2\pi} \left[\frac{E(w)}{(\lambda_0 - \mu)(\lambda - \nu_0)} - \frac{2wE'(w)}{(\mu - \nu_0)(\lambda_0 - \lambda)} \right].
\end{aligned} \tag{4.12}$$

If we can solve the three homogeneous equations (4.11) and satisfy the above nine boundary expressions (4.12) simultaneously, we obtain the singular solutions (4.6). By superposition, we can then construct the solution of the Jeans equations for tri-axial Stäckel models.

4.3 PARTICULAR SOLUTION

By analogy with the two-dimensional case, we look for particular solutions of the homogeneous equations (4.11) and by superposition of these particular solutions we try to satisfy the boundary expressions (4.12) simultaneously, in order to obtain the homogeneous solution for A , B and C .

4.3.1 One-parameter particular solution

By substitution one can verify that

$$A^P(\lambda, \mu, \nu) = \frac{\sqrt{(\lambda - \mu)(\lambda - \nu)(\mu - \nu)}}{(\lambda - \mu)(\lambda - \nu)} \frac{(z - \lambda)}{(z - \mu)(z - \nu)}, \tag{4.13}$$

with B^P and C^P following from A^P by cyclic permutation, solves the homogeneous equations (4.11). To satisfy the nine boundary expressions (4.12), we could integrate this particular solution over its free parameter z , in the complex plane. From §3.2.4, it follows that, at the boundaries, this results in simple polynomials in (λ, μ, ν) and $(\lambda_0, \mu_0, \nu_0)$. This means that the nine boundary expressions (4.12) cannot be satisfied,

since in addition to these simple polynomials they also contain E and E' . The latter are functions of one variable, so that at least one extra freedom is necessary. Hence, we look for a particular solution with *two* free parameters.

4.3.2 Two-parameter particular solution

A particular solution with two free parameters z_1 and z_2 can be found by splitting the z -dependent terms of the one-parameter solution (4.13) into two similar parts and then relabelling them. The result is the following two-parameter particular solution

$$\begin{aligned} A^P &= \frac{\sqrt{(\lambda - \mu)(\lambda - \nu)(\mu - \nu)}}{(\lambda - \mu)(\lambda - \nu)} \prod_{i=1}^2 \frac{(z_i - \lambda)^{\frac{1}{2}}}{(z_i - \mu)^{\frac{1}{2}}(z_i - \nu)^{\frac{1}{2}}}, \\ B^P &= \frac{\sqrt{(\lambda - \mu)(\lambda - \nu)(\mu - \nu)}}{(\mu - \nu)(\mu - \lambda)} \prod_{i=1}^2 \frac{(z_i - \mu)^{\frac{1}{2}}}{(z_i - \nu)^{\frac{1}{2}}(z_i - \lambda)^{\frac{1}{2}}}, \\ C^P &= \frac{\sqrt{(\lambda - \mu)(\lambda - \nu)(\mu - \nu)}}{(\nu - \lambda)(\nu - \mu)} \prod_{i=1}^2 \frac{(z_i - \nu)^{\frac{1}{2}}}{(z_i - \lambda)^{\frac{1}{2}}(z_i - \mu)^{\frac{1}{2}}}. \end{aligned} \quad (4.14)$$

These functions are cyclic in (λ, μ, ν) , as is required from the symmetry of the homogeneous equations (4.11). The presence of the square roots, such as occurred earlier in the solution (3.32) for the disk case, allows us to fit boundary values that contain elliptic integrals.

To show that this particular solution solves the homogeneous Jeans equations, we calculate the derivative of $A^P(\lambda, \mu, \nu)$ with respect to λ :

$$\frac{\partial A^P}{\partial \lambda} = \frac{A^P}{2} \left(\frac{1}{\lambda - z_1} + \frac{1}{\lambda - z_2} - \frac{1}{\lambda - \mu} - \frac{1}{\lambda - \nu} \right). \quad (4.15)$$

This can be written as

$$\begin{aligned} \frac{\partial A^P}{\partial \lambda} &= \frac{1}{2(\lambda - \mu)} \left[-\frac{(z_1 - \mu)(z_2 - \mu)(\lambda - \nu)}{(z_1 - \lambda)(z_2 - \lambda)(\mu - \nu)} A^P \right] \\ &\quad + \frac{1}{2(\lambda - \nu)} \left[\frac{(z_1 - \nu)(z_2 - \nu)(\lambda - \mu)}{(z_1 - \lambda)(z_2 - \lambda)(\mu - \nu)} A^P \right]. \end{aligned} \quad (4.16)$$

From the two-parameter particular solution we have

$$\begin{aligned} \frac{B^P}{A^P} &= -\frac{(z_1 - \mu)(z_2 - \mu)(\lambda - \nu)}{(z_1 - \lambda)(z_2 - \lambda)(\mu - \nu)}, \\ \frac{C^P}{A^P} &= \frac{(z_1 - \nu)(z_2 - \nu)(\lambda - \mu)}{(z_1 - \lambda)(z_2 - \lambda)(\mu - \nu)}, \end{aligned} \quad (4.17)$$

so that, after substitution of these ratios, the first homogeneous equation of (4.11), is indeed satisfied. The remaining two homogeneous equations can be checked in the same way.

4.4 THE HOMOGENEOUS SOLUTION

In order to satisfy the four boundary expressions of the two-dimensional case, we multiplied the one-parameter particular solution by terms depending on λ_0 , μ_0 and the free complex parameter z , followed by contour integration over the latter. Similarly, in the triaxial case we multiply the two-parameter particular solution (3.35) by terms depending on λ_0 , μ_0 , ν_0 and the two free parameters z_1 and z_2 , in such a way that by contour integration over the latter two complex parameters the nine boundary expressions (4.12) can be satisfied. Since these terms and the integration are independent of λ , μ and ν , it follows from the superposition principle that the homogeneous equations (4.11) remain satisfied.

The contour integrations over z_1 and z_2 are mutually independent, since we can separate the two-parameter particular solution (4.14) with respect to these two parameters. This allows us to choose a pair of contours, one contour in the z_1 -plane and the other contour in the z_2 -plane, and integrate over them separately. We consider the same simple contours as in the disk case (Fig. 5) around the pairs of branch points (λ, λ_0) and (μ, μ_0) , and a similar contour around (ν, ν_0) . We denote these contours by C_i^λ , C_i^μ and C_i^ν respectively, with $i = 1, 2$ indicating in which of the two complex planes we apply the contour integration.

4.4.1 Boundary expressions for B

It follows from (4.12) that $B = 0$ at the boundary $\mu = \mu_0$. From Cauchy's theorem, B would indeed vanish if, in this case, in either the z_1 -plane or z_2 -plane the integrand for B is analytic within the chosen integration contour. The boundary expression for B at $\nu = \nu_0$ follows from the one at $\lambda = \lambda_0$ by taking $\nu \leftrightarrow \lambda$ and $\nu_0 \leftrightarrow \lambda_0$. In addition to this symmetry, also the form of both boundary expressions puts constraints on the solution for B . The boundary expressions can be separated in two parts, one involving the complete elliptic integral E' and the other consisting of a two-component polynomial in τ and τ_0 ($\tau = \lambda, \mu, \nu$). Each of the two parts follows from a contour integration in one of the two complex planes. For either of the complex parameters, z_1 or z_2 , the integrands will consist of a combination of the six terms $z_i - \tau$ and $z_i - \tau_0$ with powers that are half-odd integers, i.e., the integrals are of *hyperelliptic* form. If two of the six terms cancel on one of the boundaries, we will be left with an elliptic integral. We expect the polynomial to result from applying the Residue theorem to a double pole, as this would involve a first derivative and hence give two components. This leads to the following Ansatz

$$B(\lambda, \mu, \nu) \propto \frac{\sqrt{(\lambda - \mu)(\lambda - \nu)(\mu - \nu)}}{(\mu - \nu)(\mu - \lambda)} \times \oint_{C_1} \frac{(z_1 - \mu)^{\frac{1}{2}}(z_1 - \lambda_0)^{\frac{1}{2}} dz_1}{(z_1 - \nu)^{\frac{1}{2}}(z_1 - \lambda)^{\frac{1}{2}}(z_1 - \mu_0)^{\frac{1}{2}}(z_1 - \nu_0)^{\frac{3}{2}}} \times \oint_{C_2} \frac{(z_2 - \mu)^{\frac{1}{2}}(z_2 - \nu_0)^{\frac{1}{2}} dz_2}{(z_2 - \nu)^{\frac{1}{2}}(z_2 - \lambda)^{\frac{1}{2}}(z_2 - \mu_0)^{\frac{1}{2}}(z_2 - \lambda_0)^{\frac{3}{2}}}. \quad (4.18)$$

Upon substitution of $\mu = \mu_0$, the terms involving μ_0 cancel in both integrals, so that the integrands are analytic in both contours C_1^μ and C_2^μ . By choosing either of these contours as integration contour, the boundary expression $B(\lambda, \mu_0, \nu) = 0$ is satisfied.

When $\lambda = \lambda_0$, the terms with λ_0 in the first integral in (4.18) cancel, while in the second integral we have $(z_2 - \lambda_0)^{-2}$. The first integral is analytic within C_1^λ , so that there is no contribution from this contour. However, the integral over C_1^μ is elliptic and can be evaluated in terms of E' (cf. §3.2.5). We apply the Residue theorem to the second integral, for which there is a double pole inside the contour C_2^λ . Considering C_1^μ and C_2^λ as a pair of contours, the expression for B at $\lambda = \lambda_0$ becomes

$$B(\lambda, \mu, \nu) \propto -16\pi^2 \frac{\sqrt{(\lambda_0 - \mu_0)(\lambda_0 - \nu_0)(\mu_0 - \nu_0)}}{(\mu_0 - \nu_0)(\mu_0 - \lambda_0)} \times \frac{uE'(u)}{2\pi(\nu_0 - \nu)} \left[\frac{\mu_0 - \mu}{(\lambda_0 - \mu_0)(\lambda_0 - \mu)} - \frac{\nu_0 - \nu}{(\lambda_0 - \nu_0)(\lambda_0 - \nu)} \right], \quad (4.19)$$

which is the required boundary expression up to a scaling factor. As before, we keep the terms $\lambda_0 - \mu_0$, $\lambda_0 - \nu_0$ and $\mu_0 - \nu_0$ under one square root, so that it is single-valued with respect to cyclic permutation in these coordinates.

The boundary expression for B at $\nu = \nu_0$ is symmetric with the one at $\lambda = \lambda_0$, so that a similar approach can be used. In this case, for the second integral, there is no contribution from C_2^ν , whereas it can be expressed in terms of E' if $C_2 = C_2^\mu$. The first integrand has a double pole in C_1^ν . The total contribution from the pair (C_1^ν, C_2^μ) gives the correct boundary expression, up to a scaling factor that is the same as in (4.19).

Taking into account the latter scaling factor, this shows that the Ansatz (4.18) for B produces the correct boundary expressions and hence we postulate it as the homogeneous solution for B . The expressions for A and C then follow from the ratios (4.17). Absorbing the minus sign in (4.19) into the pair of contours, i.e., either of the two contours we integrate in clockwise direction, we postulate the following homogeneous solution

$$A(\lambda, \mu, \nu) = \frac{(\mu_0 - \nu_0)(\mu_0 - \lambda_0)}{16\pi^2(\lambda - \mu)(\lambda - \nu)} \sqrt{\frac{(\lambda - \mu)(\lambda - \nu)(\mu - \nu)}{(\lambda_0 - \mu_0)(\lambda_0 - \nu_0)(\mu_0 - \nu_0)}} \times \oint_{C_1} \frac{(z_1 - \lambda)^{\frac{1}{2}}(z_1 - \lambda_0)^{\frac{1}{2}} dz_1}{(z_1 - \mu)^{\frac{1}{2}}(z_1 - \nu)^{\frac{1}{2}}(z_1 - \mu_0)^{\frac{1}{2}}(z_1 - \nu_0)^{\frac{3}{2}}} \times \oint_{C_2} \frac{(z_2 - \lambda)^{\frac{1}{2}}(z_2 - \nu_0)^{\frac{1}{2}} dz_2}{(z_2 - \mu)^{\frac{1}{2}}(z_2 - \nu)^{\frac{1}{2}}(z_2 - \mu_0)^{\frac{1}{2}}(z_2 - \lambda_0)^{\frac{3}{2}}}, \quad (4.20)$$

$$B(\lambda, \mu, \nu) = \frac{(\mu_0 - \nu_0)(\mu_0 - \lambda_0)}{16\pi^2(\mu - \nu)(\mu - \lambda)} \sqrt{\frac{(\lambda - \mu)(\lambda - \nu)(\mu - \nu)}{(\lambda_0 - \mu_0)(\lambda_0 - \nu_0)(\mu_0 - \nu_0)}} \times \oint_{C_1} \frac{(z_1 - \mu)^{\frac{1}{2}}(z_1 - \lambda_0)^{\frac{1}{2}} dz_1}{(z_1 - \nu)^{\frac{1}{2}}(z_1 - \lambda)^{\frac{1}{2}}(z_1 - \mu_0)^{\frac{1}{2}}(z_1 - \nu_0)^{\frac{3}{2}}} \times \oint_{C_2} \frac{(z_2 - \mu)^{\frac{1}{2}}(z_2 - \nu_0)^{\frac{1}{2}} dz_2}{(z_2 - \nu)^{\frac{1}{2}}(z_2 - \lambda)^{\frac{1}{2}}(z_2 - \mu_0)^{\frac{1}{2}}(z_2 - \lambda_0)^{\frac{3}{2}}}, \quad (4.21)$$

$$\begin{aligned}
C(\lambda, \mu, \nu) &= \frac{(\mu_0 - \nu_0)(\mu_0 - \lambda_0)}{16\pi^2(\nu - \lambda)(\nu - \mu)} \sqrt{\frac{(\lambda - \mu)(\lambda - \nu)(\mu - \nu)}{(\lambda_0 - \mu_0)(\lambda_0 - \nu_0)(\mu_0 - \nu_0)}} \times \\
&\oint_{C_1} \frac{(z_1 - \nu)^{\frac{1}{2}}(z_1 - \lambda_0)^{\frac{1}{2}} dz_1}{(z_1 - \lambda)^{\frac{1}{2}}(z_1 - \mu)^{\frac{1}{2}}(z_1 - \mu_0)^{\frac{1}{2}}(z_1 - \nu_0)^{\frac{3}{2}}} \times \\
&\oint_{C_2} \frac{(z_2 - \nu)^{\frac{1}{2}}(z_2 - \nu_0)^{\frac{1}{2}} dz_2}{(z_2 - \lambda)^{\frac{1}{2}}(z_2 - \mu)^{\frac{1}{2}}(z_2 - \mu_0)^{\frac{1}{2}}(z_2 - \lambda_0)^{\frac{3}{2}}}. \tag{4.22}
\end{aligned}$$

The above integrands consist of multi-valued functions that all come in pairs of the form $(z - \tau)^{\frac{1}{2}-m}(z - \tau_0)^{\frac{1}{2}-n}$, for integers m and n , with τ equal to λ , μ or ν . Completely analogous to our procedure in §3.2.4, we can make the integrands single-valued by specifying, in the complex z_1 -plane and z_2 -plane, three cuts running between the three pairs (λ, λ_0) , (μ, μ_0) , (ν, ν_0) of branch points, that are enclosed by the simple contours. The integrands are now analytic in the cut plane away from its cuts and behave again as z_i^{-2} at large distances, so that the integral over a circular contour with radius going to infinity, will be zero. Hence, connecting the simple contours C_i^λ , C_i^μ and C_i^ν with this circular contour, shows that their cumulative contribution cancels

$$C_i^\nu + C_i^\mu + C_i^\lambda = 0, \quad i = 1, 2. \tag{4.23}$$

This relation allow us to make a combination of contours, so that the nine boundary expressions (4.12) are satisfied *simultaneously* (§4.4.3). Before doing so, we first establish whether, with the homogeneous solution for A and C given by (4.20) and (4.22), respectively, we indeed satisfy their corresponding boundary expressions separately.

4.4.2 Boundary expressions for A and C

The boundary expressions and the homogeneous solution of C , follow from those of A by taking $\lambda \leftrightarrow \nu$ and $\lambda_0 \leftrightarrow \nu_0$. Henceforth, once we have checked the boundary expressions for A , those for C can be checked in a similar way.

Upon substitution of $\lambda = \lambda_0$ in the expression for A (4.20), the first integrand is proportional to $z_1 - \lambda'$ and thus is analytic within the contour C_1^λ . The contribution to the boundary expression therefore needs to come from either C_1^μ or C_1^ν . The substitution

$$z_1 - \lambda_0 = \frac{\lambda_0 - \nu}{\mu - \nu} (z_1 - \mu) - \frac{\lambda_0 - \mu}{\mu - \nu} (z_1 - \nu), \tag{4.24}$$

splits the first integral into two complete elliptic integrals

$$\frac{\lambda_0 - \nu}{\mu - \nu} \oint_{C_1} \frac{(z_1 - \mu)^{\frac{1}{2}} dz_1}{(z_1 - \nu)^{\frac{1}{2}}(z_1 - \mu_0)^{\frac{1}{2}}(z_1 - \nu_0)^{\frac{3}{2}}} - \frac{\lambda_0 - \mu}{\mu - \nu} \oint_{C_1} \frac{(z_1 - \nu)^{\frac{1}{2}} dz_1}{(z_1 - \mu)^{\frac{1}{2}}(z_1 - \mu_0)^{\frac{1}{2}}(z_1 - \nu_0)^{\frac{3}{2}}}. \tag{4.25}$$

Within the contour C_1^μ , the integrals can be evaluated in terms of $E'(u)$ and $E(u)$ respectively. When $\lambda = \lambda_0$, the second integral in (4.20) has a single pole contribution from the contour C_2^λ . Together, $-C_1^\mu C_2^\lambda$, exactly reproduces the boundary expression $A(\lambda_0, \mu, \nu)$ in (4.12).

When $\mu = \mu_0$, both integrands in the expression for A have a single pole within the contour C_i^μ . However, the combination $C_1^\mu C_2^\mu$ does not give the correct boundary

expression. We again split both integrals to obtain the required complete elliptic integrals. In the first we substitute

$$z_1 - \lambda_0 = \frac{\lambda_0 - \nu_0}{\mu_0 - \nu_0}(z_1 - \mu_0) - \frac{\lambda_0 - \mu_0}{\mu_0 - \nu_0}(z_1 - \nu_0). \quad (4.26)$$

For the contour C_1^λ , the first integral after the split can be evaluated in terms of $E'(v)$. The second integral we leave unchanged. For the integral in the z_2 -plane we substitute

$$z_2 - \nu_0 = \frac{\lambda_0 - \nu_0}{\lambda_0 - \mu_0}(z_2 - \mu_0) - \frac{\mu_0 - \nu_0}{\lambda_0 - \mu_0}(z_2 - \lambda_0). \quad (4.27)$$

We take C_2^ν as contour, and evaluate the first integral after the split in terms of $E(v)$. We again leave the second integral unchanged. Except for the contour choice, it is of the same form as the integral we left unchanged in the z_1 -plane.

To obtain the required boundary expression for A at $\mu = \mu_0$, it turns out that we have to add the contribution of *three* pairs of contours, $C_1^\lambda C_2^\mu$, $C_1^\mu C_2^\nu$ and $C_1^\mu C_2^\mu$. With the above substitutions (4.26) and (4.27), the first two pairs together provide the required boundary expression, but in addition we have two similar contour integrals

$$\frac{i/8\pi}{(\lambda_0 - \nu_0)^{\frac{1}{2}}(\lambda - \nu)^{\frac{1}{2}}} \oint_{C^\tau} \frac{(z - \lambda)^{\frac{1}{2}} dz}{(z - \nu)^{\frac{1}{2}}(z - \lambda_0)^{\frac{1}{2}}(z - \nu_0)^{\frac{1}{2}}(z - \mu_0)}, \quad (4.28)$$

with contours C^λ and C^ν , respectively. The third pair, $C_1^\mu C_2^\mu$, involves the product of two single pole contributions. The resulting polynomial

$$\frac{i/8\pi}{(\lambda_0 - \nu_0)^{\frac{1}{2}}(\lambda - \nu)^{\frac{1}{2}}} \frac{2\pi i (\lambda - \mu_0)^{\frac{1}{2}}}{(\mu_0 - \nu)^{\frac{1}{2}}(\lambda_0 - \mu_0)^{\frac{1}{2}}(\mu_0 - \nu_0)^{\frac{1}{2}}}, \quad (4.29)$$

can be written in the same form as (4.28), with contour C^μ . As a result, we now have the same integral over all three contours, so that from (4.23), the cumulative result vanishes and we are left with the required boundary expression.

The expression for A at $\nu = \nu_0$ resembles the one for B at the same boundary. This is expected since their boundary expressions in (4.12) are also very similar. The first integral now has a contribution from a double pole in the contour C_1^ν . The second integral has no contribution from the contour C_2^ν . However, within C_2^μ , the second integral can be evaluated in terms of $E(w)$. We obtain the correct boundary expression $A(\lambda, \mu, \nu_0)$ by considering the pair $-C_1^\nu C_2^\mu$.

4.4.3 Combination of contours

In the previous paragraphs we have constructed a homogeneous solution for A , B and C , and we have shown that with this solution all nine boundary expressions can be satisfied. For each boundary expression separately, we have determined the required pair of contours and also contours from which there is no contribution. Now we have to find the right combination of all these contours to fit the boundary expressions simultaneously.

We first summarize the required and non-contributing pairs of contours per boundary expression

$$\begin{aligned}
A(\lambda_0, \mu, \nu) &: -C_1^\mu C_2^\lambda \pm C_1^\lambda C_2^\tau, \\
A(\lambda, \mu_0, \nu) &: +C_1^\mu C_2^\nu + C_1^\lambda C_2^\mu + C_1^\mu C_2^\mu, \\
A(\lambda, \mu, \nu_0) &: -C_1^\nu C_2^\mu \pm C_1^\tau C_2^\nu, \\
\\
B(\lambda_0, \mu, \nu) &: -C_1^\mu C_2^\lambda \pm C_1^\lambda C_2^\tau, \\
B(\lambda, \mu_0, \nu) &: \pm C_1^\mu C_2^\tau \pm C_1^\tau C_2^\mu, \\
B(\lambda, \mu, \nu_0) &: -C_1^\nu C_2^\mu \pm C_1^\tau C_2^\nu, \\
\\
C(\lambda_0, \mu, \nu) &: -C_1^\mu C_2^\lambda \pm C_1^\lambda C_2^\tau, \\
C(\lambda, \mu_0, \nu) &: +C_1^\mu C_2^\nu + C_1^\lambda C_2^\mu + C_1^\mu C_2^\mu, \\
C(\lambda, \mu, \nu_0) &: -C_1^\nu C_2^\mu \pm C_1^\tau C_2^\nu,
\end{aligned} \tag{4.30}$$

where τ can be λ , μ or ν . At each boundary separately, $\lambda = \lambda_0$, $\mu = \mu_0$ and $\nu = \nu_0$, the allowed combination of contours matches between A , B and C . This leaves the question how to relate the combination of contours at the different boundaries.

From (4.23), we know that in both the complex z_1 -plane and z_2 -plane, the cumulative contribution of the three simple contours cancels. As a consequence, each of the following three combinations of integration contours

$$C_1^\mu C_2^\mu = -C_1^\mu (C_2^\lambda + C_2^\nu) = -(C_1^\lambda + C_1^\nu) C_2^\mu, \tag{4.31}$$

will give the same result. Similarly, we can add to each combination the pairs $C_1^\lambda C_2^\mu$ and $C_1^\mu C_2^\nu$, to obtain

$$C_1^\mu C_2^\nu + C_1^\lambda C_2^\mu + C_1^\mu C_2^\mu = C_1^\lambda C_2^\mu - C_1^\mu C_2^\lambda = C_1^\mu C_2^\nu - C_1^\nu C_2^\mu. \tag{4.32}$$

The first combination of contour pairs matches the allowed range for $\mu = \mu_0$ in (4.30) and the second and third match the boundary expressions $\lambda = \lambda_0$ and $\nu = \nu_0$. This completes the proof that the expressions (4.20)–(4.22) for A , B and C solve the homogeneous equations (4.11) and satisfy the nine boundary expressions (4.12) simultaneously when the integration contour is any of the three combinations (4.32). We shall see below that the first of these combinations is preferred in numerical evaluations.

4.5 EVALUATION OF THE HOMOGENEOUS SOLUTIONS

We write the complex contour integrals in the homogeneous solutions A , B and C (4.20–4.22) as real integrals. The resulting complete hyperelliptic integrals are expressed as single quadratures, which can be easily evaluated numerically. We also express the complete elliptic integrals in the two-dimensional homogeneous solutions F , G , H and I (4.9) in this way to facilitate their numerical evaluation.

4.5.1 From complex to real integrals

To transform the complex contour integrals in (4.20)–(4.22) in real integrals we wrap the contours C^λ , C^μ and C^ν around the corresponding pair of branch points (Fig. 6). The integrands consist of terms $z - \tau$ and $z - \tau_0$, all with powers larger than -1 , except $z_1 - \nu_0$ and $z_2 - \lambda_0$, both of which occur to the power $-\frac{3}{2}$. This means that for all simple

contours C_i^τ ($\tau = \lambda, \mu, \nu; i = 1, 2$), except for C_1^ν and C_2^λ , the contribution from the arcs around the branch points vanishes. In the latter case, we are left with the parts parallel to the real axis, so that we can rewrite the complex integrals as real integrals with the branch points as integration limits. The only combination of contours of the three given in (4.32) that does not involve both C_1^ν and C_2^λ , is

$$S \equiv C_1^\mu C_2^\nu + C_1^\lambda C_2^\mu + C_1^\mu C_2^\mu. \quad (4.33)$$

We have to be careful with the changes in phase when wrapping each of the simple contours around the branch points. One can verify that the phase changes per contour are the same for all three the homogeneous solutions A , B and C , and also that the contribution from the parts parallel to the real axis is equivalent. This gives a factor 2 per contour and thus a factor 4 for the combination of contour pairs in S . In this way, we can transform the double complex contour integration into the following combination of real integrals

$$\iint_S dz_1 dz_2 = 4 \left(\int_\lambda^{\lambda_0} dt_1 \int_\mu^{\mu_0} dt_2 + \int_\mu^{\mu_0} dt_1 \int_\nu^{\nu_0} dt_2 - \int_\mu^{\mu_0} dt_1 \int_\mu^{\mu_0} dt_2 \right), \quad (4.34)$$

with t_i the real part of z_i .

We apply this transformation to (4.20)–(4.22), and we absorb the factor of 4 left in the denominators into the integrals, so that we can write

$$\begin{aligned} A(\lambda, \mu, \nu; \lambda_0, \mu_0, \nu_0) &= \frac{(\mu_0 - \nu_0)(\mu_0 - \lambda_0)\Lambda}{\pi^2(\lambda - \mu)(\lambda - \nu)} (A_1 A_2 + A_3 A_4 - A_2 A_3), \\ B(\lambda, \mu, \nu; \lambda_0, \mu_0, \nu_0) &= \frac{(\mu_0 - \nu_0)(\mu_0 - \lambda_0)\Lambda}{\pi^2(\mu - \nu)(\mu - \lambda)} (B_1 B_2 + B_3 B_4 - B_2 B_3), \\ C(\lambda, \mu, \nu; \lambda_0, \mu_0, \nu_0) &= \frac{(\mu_0 - \nu_0)(\mu_0 - \lambda_0)\Lambda}{\pi^2(\nu - \lambda)(\nu - \mu)} (C_1 C_2 + C_3 C_4 - C_2 C_3), \end{aligned} \quad (4.35)$$

where A_i , B_i and C_i ($i = 1, 2, 3, 4$) are complete hyperelliptic integrals, for which we give expressions below, and

$$\Lambda^2 = \frac{(\lambda - \mu)(\lambda - \nu)(\mu - \nu)}{(\lambda_0 - \mu_0)(\lambda_0 - \nu_0)(\mu_0 - \nu_0)}. \quad (4.36)$$

The second set of arguments added to A , B and C make explicit the position $(\lambda_0, \mu_0, \nu_0)$ of the source point which is causing the stresses at the field point (λ, μ, ν) .

4.5.2 The complete hyperelliptic integrals

With the transformation described in the previous section the expression for, e.g., the complete hyperelliptic integral A_2 is of the form

$$A_2 = \frac{1}{2} \int_\mu^{\mu_0} \frac{dt}{\lambda_0 - t} \sqrt{\frac{(\lambda - t)(t - \nu_0)}{(\mu_0 - t)(t - \mu)(\lambda_0 - t)(t - \nu)}}. \quad (4.37)$$

The integrand has two singularities, one at the lower integration limit $t = \mu$ and one at the upper integration limit $t = \mu_0$. The substitution $t = \mu + (\mu_0 - \mu) \cos^2 \theta$ removes both singularities, since $dt/\sqrt{(\mu_0 - t)(t - \mu)} = 2(\mu_0 - \mu)d\theta$.

All complete hyperelliptic integrals A_i , B_i and C_i ($i = 1, 2, 3, 4$) in (4.35) are of the form (4.37) and have at most two singularities at either of the integration limits. Hence, we can apply a similar substitution to remove the singularities. This results in the following expressions

$$\begin{aligned}
A_1 &= (\lambda_0 - \lambda)^2 \int_0^{\pi/2} \frac{\sin^2 \theta \cos^2 \theta d\theta}{x_3 \Delta_x}, & A_2 &= \int_0^{\pi/2} \frac{y_1 y_4 d\theta}{y_3 \Delta_y}, \\
A_4 &= (\nu_0 - \nu) \int_0^{\pi/2} \frac{z_2 \sin^2 \theta d\theta}{z_1 \Delta_z}, & A_3 &= \int_0^{\pi/2} \frac{y_3 y_4 d\theta}{y_1 \Delta_y}, \\
B_1 &= (\lambda_0 - \lambda) \int_0^{\pi/2} \frac{x_2 \sin^2 \theta d\theta}{x_3 \Delta_x}, & B_2 &= (\mu_0 - \mu) \int_0^{\pi/2} \frac{y_1 \cos^2 \theta d\theta}{y_3 \Delta_y}, \\
B_4 &= (\nu_0 - \nu) \int_0^{\pi/2} \frac{z_4 \sin^2 \theta d\theta}{z_1 \Delta_z}, & B_3 &= (\mu_0 - \mu) \int_0^{\pi/2} \frac{y_3 \cos^2 \theta d\theta}{y_1 \Delta_y}, \\
C_1 &= (\lambda_0 - \lambda) \int_0^{\pi/2} \frac{x_4 \sin^2 \theta d\theta}{x_3 \Delta_x}, & C_2 &= \int_0^{\pi/2} \frac{y_1 y_2 d\theta}{y_3 \Delta_y}, \\
C_4 &= (\nu_0 - \nu)^2 \int_0^{\pi/2} \frac{\sin^2 \theta \cos^2 \theta d\theta}{z_1 \Delta_z}, & C_3 &= \int_0^{\pi/2} \frac{y_2 y_3 d\theta}{y_1 \Delta_y},
\end{aligned} \tag{4.38}$$

where we have defined

$$\Delta_x^2 = x_1 x_2 x_3 x_4, \quad \Delta_y^2 = y_1 y_2 y_3 y_4, \quad \Delta_z^2 = z_1 z_2 z_3 z_4, \tag{4.39}$$

and the factors x_i , y_i and z_i ($i = 1, 2, 3, 4$) are given by

$$\begin{aligned}
x_1 &= (\lambda - \mu_0) + (\lambda_0 - \lambda) \cos^2 \theta, & x_2 &= (\lambda - \mu) + (\lambda_0 - \lambda) \cos^2 \theta, \\
x_3 &= (\lambda - \nu_0) + (\lambda_0 - \lambda) \cos^2 \theta, & x_4 &= (\lambda - \nu) + (\lambda_0 - \lambda) \cos^2 \theta, \\
y_1 &= (\mu - \nu_0) + (\mu_0 - \mu) \cos^2 \theta, & y_2 &= (\mu - \nu) + (\mu_0 - \mu) \cos^2 \theta, \\
y_3 &= (\mu - \lambda_0) + (\mu_0 - \mu) \cos^2 \theta, & y_4 &= (\mu - \lambda) + (\mu_0 - \mu) \cos^2 \theta, \\
z_1 &= (\nu - \lambda_0) + (\nu_0 - \nu) \cos^2 \theta, & z_2 &= (\nu - \lambda) + (\nu_0 - \nu) \cos^2 \theta, \\
z_3 &= (\nu - \mu_0) + (\nu_0 - \nu) \cos^2 \theta, & z_4 &= (\nu - \mu) + (\nu_0 - \nu) \cos^2 \theta.
\end{aligned} \tag{4.40}$$

For each i these factors follow from each other by cyclic permutation of $\lambda \rightarrow \mu \rightarrow \nu \rightarrow \lambda$ and at the same time $\lambda_0 \rightarrow \mu_0 \rightarrow \nu_0 \rightarrow \lambda_0$. Half of the factors – all x_i , y_1 and y_2 – are always positive, whereas the other factors are always negative. The latter implies that one has to be careful with the signs of the factors under the square root when evaluating the single quadratures numerically.

4.5.3 The complete elliptic integrals

The two-dimensional homogeneous solutions F , G , H and I are given in (4.9) in terms of the Legendre complete elliptic integrals $E(m)$ and $E'(m) = [E(m) - K(m)]/2m$. Numerical routines for $E(m)$ and $K(m)$ (e.g., Press et al. 1992) generally require the

argument to be $0 \leq m < 1$. In the allowed range of the confocal ellipsoidal coordinates, the arguments u (4.10) and w (3.16) become larger than unity. In these cases we can use transformations to express $E(m)$ and $K(m)$ in terms of $E(1/m)$ and $K(1/m)$ (e.g., Byrd & Friedman 1971).

We prefer, however, to write the complete elliptic integrals as single quadratures similar to the above expressions for the hyperelliptic integrals. These quadratures can easily be evaluated numerically and apply to the full range of the confocal ellipsoidal coordinates. The resulting expressions for the two-dimensional homogeneous solutions are

$$\begin{aligned}
 F(\lambda, \mu; \lambda_0, \mu_0) &= \frac{1}{\pi} \sqrt{\frac{\lambda - \mu}{\lambda_0 - \mu_0}} \int_0^{\pi/2} \frac{x_1 d\theta}{x_2 \sqrt{x_1 x_2}}, \\
 G(\lambda, \mu; \lambda_0, \mu_0) &= \frac{1}{\pi} \sqrt{\frac{\lambda - \mu}{\lambda_0 - \mu_0}} (\mu_0 - \mu) \int_0^{\pi/2} \frac{\sin^2 \theta d\theta}{y_4 \sqrt{y_3 y_4}}, \\
 H(\mu, \nu; \mu_0, \nu_0) &= \frac{1}{\pi} \sqrt{\frac{\mu - \nu}{\mu_0 - \nu_0}} (\mu_0 - \mu) \int_0^{\pi/2} \frac{\sin^2 \theta d\theta}{y_2 \sqrt{y_1 y_2}}, \\
 I(\mu, \nu; \mu_0, \nu_0) &= \frac{1}{\pi} \sqrt{\frac{\mu - \nu}{\mu_0 - \nu_0}} \int_0^{\pi/2} \frac{z_3 d\theta}{z_4 \sqrt{z_3 z_4}}.
 \end{aligned} \tag{4.41}$$

Again we have added two arguments to make the position of the unit source explicitly. We note that the homogeneous solutions $A(\lambda, \mu; \lambda_0, \mu_0)$ and $B(\lambda, \mu; \lambda_0, \mu_0)$ for the disk case (3.41) are equivalent to F and G respectively.

4.6 GENERAL TRIAXIAL SOLUTION

We now construct the solution of the Jeans equations for triaxial Stäckel models (4.2), by superposition of singular solutions, which involve the homogeneous solution derived in the above. We match the solution to the boundary conditions at $\mu = -\alpha$ and $\nu = -\beta$, and check for convergence of the solution when $\lambda \rightarrow \infty$. Next, we consider alternative boundary conditions and present the triaxial solution for a general finite region. We also show that the general solution yields the correct result in the case of thin tube orbits and the triaxial Abel models of Dejonghe & Laurent (1991). Finally, we describe a numerical test of the triaxial solution to a polytrope model.

4.6.1 Superposition of singular solutions

Substitution of the functions A , B , C (4.35) and the functions F , G , H , I (4.41) in expression (4.6), provides the three singular solutions of the system of simplified Jeans equations, with the right-hand side given by (4.4). We denote these by $S_2^{\tau\tau}$ ($\tau = \lambda, \mu, \nu$). The singular solutions of the two similar simplified systems, with the triplet of delta functions at the right-hand side of the *first* and *third* equation, $S_1^{\tau\tau}$ and

$S_3^{\tau\tau}$ then follow from $S_2^{\tau\tau}$ by cyclic permutation. This gives

$$\begin{aligned} S_1^{\lambda\lambda} &= B(\nu, \lambda, \mu; \nu_0, \lambda_0, \mu_0) + G(\nu, \lambda; \nu_0, \lambda_0)\delta(\mu_0 - \mu) \\ &\quad + H(\lambda, \mu; \lambda_0, \mu_0)\delta(\nu_0 - \nu) - \delta(\mu_0 - \mu)\delta(\nu_0 - \nu), \\ S_1^{\mu\mu} &= C(\nu, \lambda, \mu; \nu_0, \lambda_0, \mu_0) + I(\lambda, \mu; \lambda_0, \mu_0)\delta(\nu_0 - \nu) \\ S_1^{\nu\nu} &= A(\nu, \lambda, \mu; \nu_0, \lambda_0, \mu_0) + F(\nu, \lambda; \nu_0, \lambda_0)\delta(\mu_0 - \mu), \end{aligned} \quad (4.42a)$$

$$\begin{aligned} S_2^{\lambda\lambda} &= A(\lambda, \mu, \nu; \lambda_0, \mu_0, \nu_0) + F(\lambda, \mu; \lambda_0, \mu_0)\delta(\nu_0 - \nu), \\ S_2^{\mu\mu} &= B(\lambda, \mu, \nu; \lambda_0, \mu_0, \nu_0) + G(\lambda, \mu; \lambda_0, \mu_0)\delta(\nu_0 - \nu) \\ &\quad + H(\mu, \nu; \mu_0, \nu_0)\delta(\lambda_0 - \lambda) - \delta(\nu_0 - \nu)\delta(\lambda_0 - \lambda), \\ S_2^{\nu\nu} &= C(\lambda, \mu, \nu; \lambda_0, \mu_0, \nu_0) + I(\mu, \nu; \mu_0, \nu_0)\delta(\lambda_0 - \lambda) \end{aligned} \quad (4.42b)$$

$$\begin{aligned} S_3^{\lambda\lambda} &= C(\mu, \nu, \lambda; \mu_0, \nu_0, \lambda_0) + I(\nu, \lambda; \nu_0, \lambda_0)\delta(\mu_0 - \mu), \\ S_3^{\mu\mu} &= A(\mu, \nu, \lambda; \mu_0, \nu_0, \lambda_0) + F(\mu, \nu; \mu_0, \nu_0)\delta(\lambda_0 - \lambda) \\ S_3^{\nu\nu} &= B(\mu, \nu, \lambda; \mu_0, \nu_0, \lambda_0) + G(\mu, \nu; \mu_0, \nu_0)\delta(\lambda_0 - \lambda) \\ &\quad + H(\nu, \lambda; \nu_0, \lambda_0)\delta(\mu_0 - \mu) - \delta(\lambda_0 - \lambda)\delta(\mu_0 - \mu). \end{aligned} \quad (4.42c)$$

These singular solutions describe the contribution of a source point in $(\lambda_0, \mu_0, \nu_0)$ to (λ, μ, ν) . To find the solution of the full equations (4.2), we multiply the singular solutions (4.42a), (4.42b) and (4.42c) by $g_1(\lambda_0, \mu_0, \nu_0)$, $g_2(\lambda_0, \mu_0, \nu_0)$ and $g_3(\lambda_0, \mu_0, \nu_0)$, respectively, so that the contribution from the source point naturally depends on the local density and potential (cf. eq. [4.3]). Then, for each coordinate $\tau = \lambda, \mu, \nu$, we add the three weighted singular solutions, and integrate over the volume Ω , defined as

$$\Omega = \{(\lambda_0, \mu_0, \nu_0) : \lambda \leq \lambda_0 < \infty, \mu \leq \mu_0 \leq -\alpha, \nu \leq \nu_0 \leq -\beta\}, \quad (4.43)$$

which is the three-dimensional extension of the integration domain D in Fig. 4. The resulting solution solves the inhomogeneous Jeans equations (4.2), but does not give the correct values at the boundaries $\mu = -\alpha$ and $\nu = -\beta$. They are found by multiplying the singular solutions (4.42b) evaluated at $\mu_0 = -\alpha$, and, similarly, the singular solutions (4.42c) evaluated at $\nu_0 = -\beta$, by $-S_{\mu\mu}(\lambda_0, -\alpha, \nu_0)$ and $-S_{\nu\nu}(\lambda_0, \mu_0, -\beta)$, respectively, and integrating in Ω over the coordinates that are not fixed. One can verify that this procedure represents the boundary values correctly. The final result for the general solution of the Jeans equations (4.2) for triaxial Stäckel models is

$$\begin{aligned} S_{\tau\tau}(\lambda, \mu, \nu) &= \int_{\lambda}^{\infty} d\lambda_0 \int_{\mu}^{-\alpha} d\mu_0 \int_{\nu}^{-\beta} d\nu_0 \sum_{i=1}^3 g_i(\lambda_0, \mu_0, \nu_0) S_i^{\tau\tau}(\lambda, \mu, \nu; \lambda_0, \mu_0, \nu_0) \\ &\quad - \int_{\nu}^{-\beta} d\nu_0 \int_{\lambda}^{\infty} d\lambda_0 S_{\mu\mu}(\lambda_0, -\alpha, \nu_0) S_2^{\tau\tau}(\lambda, \mu, \nu; \lambda_0, -\alpha, \nu_0) \\ &\quad - \int_{\lambda}^{\infty} d\lambda_0 \int_{\mu}^{-\alpha} d\mu_0 S_{\nu\nu}(\lambda_0, \mu_0, -\beta) S_3^{\tau\tau}(\lambda, \mu, \nu; \lambda_0, \mu_0, -\beta), \end{aligned} \quad (4.44)$$

where $\tau = (\lambda, \mu, \nu)$. This provides the stresses everywhere, once we have specified $S_{\mu\mu}(\lambda, -\alpha, \nu)$ and $S_{\nu\nu}(\lambda, \mu, -\beta)$. At both boundaries $\mu = -\alpha$ and $\nu = -\beta$, the three stress components are related by a set of two Jeans equations, i.e., (4.2) evaluated at $\mu = -\alpha$ and $\nu = -\beta$ respectively. From §3, we know that the solution of these two-dimensional systems both will involve a (boundary) function of one variable. We need this latter freedom to satisfy the continuity conditions (2.17). This means it is sufficient to specify any of the three stress components at $\mu = -\alpha$ and $\nu = -\beta$.

4.6.2 Convergence of the general triaxial solution

As in §§3.1.4, 3.2.7 and 3.4 we suppose $G(\tau) = \mathcal{O}(\tau^\delta)$ when $\tau \rightarrow \infty$, with δ in the range $[-\frac{1}{2}, 0)$. This implies that the potential V_S (2.3) is also $\mathcal{O}(\tau^\delta)$. We assume that the density ρ , which does not need to be the density ρ_S which generates V_S , is of the form $N(\mu, \nu)\lambda^{-s/2}$ when $\lambda \rightarrow \infty$. In the special case where $\rho = \rho_S$, we have $s \leq 4$ except possibly along the z -axis. When $s = 4$ the models remain flattened out to the largest radii, but when $s < 4$ the function $N(\mu, \nu) \rightarrow 1$ in the limit $\lambda \rightarrow \infty$ (de Zeeuw et al. 1986).

From the definition (4.3), we find that $g_1(\lambda_0, \mu_0, \nu_0) = \mathcal{O}(\lambda_0^{\delta-s/2})$ as $\lambda_0 \rightarrow \infty$, while $g_2(\lambda_0, \mu_0, \nu_0)$ and $g_3(\lambda_0, \mu_0, \nu_0)$ are larger and both $\mathcal{O}(\lambda_0^{-s/2})$. To investigate the behavior of the singular solutions (4.42) at large distance, we have to carefully analyze the complete hyperelliptic (4.38) and elliptic (4.41) integrals as $\lambda_0 \rightarrow \infty$. This is simplified by writing them as Carlson's R -functions (Carlson 1977). We finally find for the singular solutions that $S_1^{\tau\tau} = \mathcal{O}(1)$ when $\lambda_0 \rightarrow \infty$, whereas $S_2^{\tau\tau}$ and $S_3^{\tau\tau}$ are smaller and $\mathcal{O}(\lambda_0^{-1})$, with $\tau = \lambda, \mu, \nu$. This shows that for the volume integral in the triaxial solution (4.44) to converge, we must have $\delta - s/2 + 1 < 0$. This is equivalent to the requirement $s > 2\delta + 2$ we obtained in §3.4 for the limiting cases of prolate and oblate potentials and for the large radii limit with scale-free DF. From the convergence of the remaining two double integrals in (4.44), we find that the boundary stresses $S_{\mu\mu}(\lambda, -\alpha, \nu)$ and $S_{\nu\nu}(\lambda, \mu, -\beta)$ cannot exceed $\mathcal{O}(1)$ when $\lambda \rightarrow \infty$.

This is in agreement with the large λ behavior of $S_{\tau\tau}(\lambda, \mu, \nu)$ that follows from the volume integral. The singular solutions $S_i^{\lambda\lambda} = \mathcal{O}(1)$ ($i = 1, 2, 3$) when $\lambda \rightarrow \infty$, larger than $S_i^{\mu\mu}$ and $S_i^{\nu\nu}$, which are all $\mathcal{O}(\lambda^{-1})$. Evaluating the volume integral at large distance gives $S_{\tau\tau}(\lambda, \mu, \nu) = \mathcal{O}(\lambda^{\delta-s/2+1})$, i.e., not exceeding $\mathcal{O}(1)$ if the requirement $s > 2\delta + 2$ is satisfied. We obtain the same behavior and requirement from the energy, eq. (2.10).

We conclude that for the general triaxial case, as well as for the limiting cases with a three-dimensional shape, the stress components $T_{\tau\tau}(\lambda, \mu, \nu)$ are $\mathcal{O}(\lambda^{\delta-s/2})$ at large distance, with the requirement that $s > 2\delta + 2$ for $-\frac{1}{2} \leq \delta < 0$. We obtained the same result for the stresses in the disk case, except that then $s > 2\delta + 1$. Both the three-dimensional and two-dimensional requirements are met for many density distributions ρ and potentials V_S of interest. They do not break down until the isothermal limit $\delta \rightarrow 0$, with $s = 1$ (disk) and $s = 2$ (three-dimensional) is reached.

4.6.3 Alternative boundary conditions

Our solution for the stress components at each point (λ, μ, ν) in a triaxial model with a Stäckel potential consists of the weighted contribution of all sources outwards of this point. Accordingly, we have integrated with respect to λ_0, μ_0 and ν_0 , with lower limits the coordinates of the chosen point and upper limits $\infty, -\alpha$ and $-\beta$, respectively. To obtain the correct expressions at the outer boundaries, the stresses must vanish when $\lambda \rightarrow \infty$ and they have to be specified at $\mu = -\alpha$ and $\nu = -\beta$.

The integration limits λ , μ and ν are fixed, but for the other three limits we can, in principle, equally well choose $-\alpha$, $-\beta$ and $-\gamma$ respectively. The latter choices also imply the specification of the stress components at these boundaries instead. Each of the eight possible combinations of these limits corresponds to one of the octants into which the physical region $-\gamma \leq \nu_0 \leq -\beta \leq \mu_0 \leq -\alpha \leq \lambda_0 < \infty$ is split by the lines through the point (λ, μ, ν) . By arguments similar to those given in §3.3, one may show that in all octants the expressions (4.35) for A , B , C , and (4.9) for F , G , H , I are equivalent. Hence, again the only differences in the singular solutions are due to possible changes in the sign of the step-functions, but the changes in the integration limits cancel the sign differences between the corresponding singular solutions. However, as in §3.3 for the two-dimensional case, it is not difficult to show that while switching the boundary conditions μ and ν is indeed straightforward, the switch from $\lambda \rightarrow \infty$ to $\lambda = -\alpha$ again leads to solutions which generally have the incorrect radial fall-off, and hence are non-physical.

4.6.4 Triaxial solution for a general finite region

If we denote non-fixed integration limits by λ_e , μ_e and ν_e respectively, we can write the triaxial solution for a general finite region as

$$\begin{aligned}
S_{\tau\tau}(\lambda, \mu, \nu) = & \int_{\lambda}^{\lambda_e} d\lambda_0 \int_{\mu}^{\mu_e} d\mu_0 \int_{\nu}^{\nu_e} d\nu_0 \sum_{i=1}^3 g_i(\lambda_0, \mu_0, \nu_0) S_i^{\tau\tau}(\lambda, \mu, \nu; \lambda_0, \mu_0, \nu_0) \\
& - \int_{\mu}^{\mu_e} d\mu_0 \int_{\nu}^{\nu_e} d\nu_0 S_{\lambda\lambda}(\lambda_e, \mu_0, \nu_0) S_1^{\tau\tau}(\lambda, \mu, \nu; \lambda_e, \mu_0, \nu_0) \\
& - \int_{\nu}^{\nu_e} d\nu_0 \int_{\lambda}^{\lambda_e} d\lambda_0 S_{\mu\mu}(\lambda_0, \mu_e, \nu_0) S_2^{\tau\tau}(\lambda, \mu, \nu; \lambda_0, \mu_e, \nu_0) \\
& - \int_{\lambda}^{\lambda_e} d\lambda_0 \int_{\mu}^{\mu_e} d\mu_0 S_{\nu\nu}(\lambda_0, \mu_0, \nu_e) S_3^{\tau\tau}(\lambda, \mu, \nu; \lambda_0, \mu_0, \nu_e), \quad (4.45)
\end{aligned}$$

with, as usual, $\tau = \lambda, \mu, \nu$. The weight functions g_i ($i = 1, 2, 3$) are defined in (4.3) and the singular solutions $S_i^{\tau\tau}$ are given by (4.42). The non-fixed integration limits are chosen in the corresponding physical ranges, i.e., $\lambda_e \in [-\alpha, \infty]$, $\mu_e \in [-\beta, -\alpha]$ and $\nu_e \in [-\gamma, -\beta]$, but $\lambda_e \neq -\alpha$ (see §4.6.3). The solution requires the specification of the stress components on the boundary surfaces $\lambda = \lambda_e$, $\mu = \mu_e$ and $\nu = \nu_e$. On each of these surfaces the three stress components are related by two of the three Jeans equations (4.2) and the continuity conditions (2.17). Hence, once one of the stress components is prescribed on three boundary surfaces, the solution (4.44) yields all three stresses everywhere in the triaxial Stäckel galaxy. The stresses on the remaining three boundary surfaces then follow as the limits of the latter solution.

4.6.5 Physical solutions

Statler (1987) and HZ92 showed that many different DFs are consistent with a triaxial density ρ in the potential V_S . Specifically, the boundary plane $\nu = -\beta$, i.e., the area outside the focal hyperbola in the (x, z) -plane (Fig. 2), is only reached by inner (I) and

outer (O) long-axis tube orbits. A split between the contribution of both orbit families to the density in this plane has to be chosen, upon which the DF for both the I and O orbits is fixed in case only thin tubes are populated, but many other possibilities exist when the full set of I- and O-orbits is included. For each of these DFs, the density provided by the I- and O-tubes can then in principle be found throughout configuration space. In the area outside the focal ellipse in the (y, z) -plane ($\mu = -\alpha$), only the O-tubes and S-tubes contribute to the density. Subtracting the known density of the O-orbits leaves the density to be provided by the S-tubes in this plane, from which their DF can be determined. This is again unique when only thin orbits are used, but is non-unique otherwise. The density that remains after subtracting the I-, O-, and S-tube densities from ρ must be provided by the box (B) orbits. Their DF is now fixed, and can be found by solving a system of linear equations, starting from the outside ($\lambda \rightarrow \infty$).

The total DF is the sum of the DFs of the four orbit families, and is hence highly non-unique. All these DFs give rise to a range of stresses $T_{\lambda\lambda}, T_{\mu\mu}, T_{\nu\nu}$, and our solution of the Jeans equations must be sufficiently general to contain them as a subset. This is indeed the case, as we are allowed to choose the stresses on the special surfaces $\nu = -\beta$ and $\mu = -\alpha$. However, not all choices will correspond to physical DFs. The requirement $T_{\tau\tau} \geq 0$ is necessary but not sufficient for the associated DF to be non-negative everywhere.

4.6.6 The general solution for thin tube orbits

For each of the three tube families in case of infinitesimally thin orbits one of the three stress components vanishes everywhere (see §2.5.6). We are left with two non-zero stress components related to the density and potential by three reduced Jeans equations (4.2). We thus have subsidiary conditions on the three right hand side terms g_1, g_2 and g_3 .

HZ92 solved for the two non-trivial stresses and showed that they can be found by single quadratures (with integrands involving no worse than complete elliptic integrals), once the corresponding stress had been chosen at $\nu = -\beta$ (for I- and O-tubes) or at $\mu = -\alpha$ (for S-tubes).

By analogy with the reasoning for the thin tube orbits in the disk case (§3.4.4), we can show that for each of the three tube families in the case of thin orbits the general triaxial solution (4.45) gives the stress components correctly. Consider, e.g., the thin I-tubes, for which $S_{\mu\mu} \equiv 0$. Apply the latter to (4.45), substitute for g_1, g_2 and g_3 the subsidiary conditions that follow from the reduced Jeans equations (4.2) and substitute for the singular solutions the expressions (4.42). After several partial integrations, we use that the homogeneous solutions A, B and C solve a homogeneous system similar to (4.11), but now with respect to the source point coordinates $(\lambda_0, \mu_0, \nu_0)$

$$\frac{\partial B(\nu, \lambda, \mu; \nu_0, \lambda_0, \mu_0)}{\partial \lambda_0} = \frac{A(\lambda, \mu, \nu; \lambda_0, \mu_0, \nu_0)}{2(\lambda_0 - \mu_0)} + \frac{C(\mu, \nu, \lambda; \mu_0, \nu_0, \lambda_0)}{2(\lambda_0 - \nu_0)}, \quad (4.46)$$

where other relations follow by cyclic permutation of $\lambda \rightarrow \mu \rightarrow \nu \rightarrow \lambda$ and $\lambda_0 \rightarrow \mu_0 \rightarrow \nu_0 \rightarrow \lambda_0$. And similar for the two-dimensional homogeneous solutions F, G, H and I

the relations follow from

$$\begin{aligned}\frac{\partial G(\mu, \lambda; \mu_0, \lambda_0)}{\partial \lambda_0} &= \frac{F(\lambda, \mu; \lambda_0, \mu_0)}{2(\lambda_0 - \mu_0)}, \\ \frac{\partial H(\mu, \nu; \mu_0, \nu_0)}{\partial \mu_0} &= \frac{I(\nu, \mu; \nu_0, \mu_0)}{2(\mu_0 - \nu_0)}.\end{aligned}\tag{4.47}$$

It indeed turns out that for $S_{\mu\mu}(\lambda, \mu, \nu)$ all terms cancel on the right hand side of (4.45). The terms that are left in the case of $S_{\lambda\lambda}$ and $S_{\nu\nu}$ are just eq. (4.2a) integrated with respect to λ and eq. (4.2c) integrated with respect to ν , respectively, and using that $S_{\mu\mu} \equiv 0$. A similar analysis as above shows that also for thin O- and S-tubes — for which $S_{\lambda\lambda} \equiv 0$ in both cases — the general triaxial solution yields the correct result.

4.6.7 Triaxial Abel models

For a galaxy with a triaxial potential of Stäckel form, the DF is a function of the three exact isolating integrals of motion, $f(\mathbf{x}, \mathbf{v}) = f(E, I_2, I_3)$ (see also §2.2). The expressions for E , I_2 and I_3 in terms of the phase-space coordinates (\mathbf{x}, \mathbf{v}) can be found in e.g. Z85. We can thus write the velocity moments of the DF as a triple integral over E , I_2 and I_3 . Assuming that the DF is function of only one variable

$$S \equiv E + wI_2 + uI_3,\tag{4.48}$$

with w and u constants, Dejonghe & Laurent (1991) show that the triple integration simplifies to a one-dimensional Abel integration over S . Even though a DF of this form can only describe a self-consistent model in the spherical case (ellipsoidal hypothesis, see, e.g., Eddington 1915), the Jeans equations do not require self-consistency.

The special Abel form results in a simple analytical relation between the three stress components (Dejonghe & Laurent 1991, their eq. [5.6])

$$T_{\mu\mu} = T_{\lambda\lambda} a_{\mu\nu} / a_{\lambda\nu}, \quad T_{\nu\nu} = T_{\lambda\lambda} a_{\mu\nu} / a_{\mu\lambda},\tag{4.49}$$

with

$$a_{\sigma\tau} = (\gamma - \alpha) + (\sigma + \alpha)(\tau + \alpha)w - (\sigma + \gamma)(\tau + \gamma)u,\tag{4.50}$$

and $\sigma, \tau = \lambda, \mu, \nu$. With these relations we find that

$$\frac{T_{\lambda\lambda} - T_{\mu\mu}}{\lambda - \mu} = \frac{T_{\lambda\lambda}}{a_{\lambda\nu}} \frac{\partial a_{\lambda\nu}}{\partial \lambda}, \quad \frac{T_{\lambda\lambda} - T_{\nu\nu}}{\lambda - \nu} = \frac{T_{\lambda\lambda}}{a_{\lambda\mu}} \frac{\partial a_{\lambda\mu}}{\partial \lambda}.\tag{4.51}$$

The first Jeans eq. (2.16a) now becomes a first-order partial differential equation for $T_{\lambda\lambda}$. This equation can be solved in a straightforward way and provides an elegant and simple expression for the radial stress component

$$T_{\lambda\lambda}(\lambda, \mu, \nu) = \sqrt{\frac{a_{\lambda_e\mu} a_{\lambda_e\nu}}{a_{\lambda\mu} a_{\lambda\nu}}} T_{\lambda\lambda}(\lambda_e, \mu, \nu) + \int_{\lambda}^{\lambda_e} d\lambda_0 \sqrt{\frac{a_{\lambda_0\mu} a_{\lambda_0\nu}}{a_{\lambda\mu} a_{\lambda\nu}}} \rho \frac{\partial V_S}{\partial \lambda_0}\tag{4.52}$$

The expressions for $T_{\mu\mu}$ and $T_{\nu\nu}$ follow by application of the ratios (4.49). If we let the boundary value $\lambda_e \rightarrow \infty$, the first term on the right-hand side of (4.52) vanishes.

The density ρ , which does not need to be the density ρ_S which generates V_S , is of the Abel form as given in eq. (3.11) of Dejonghe & Laurent (1991). If we substitute

this form in (4.52), we obtain, after changing the order of integration and evaluating the integral with respect to λ , again a single Abel integral that is equivalent to the expression for $T_{\lambda\lambda}$ that follows from eq. (3.10) of Dejonghe & Laurent (1991). Using the relations (4.49) and the corresponding subsidiary conditions for g_1 , g_2 and g_3 , it can be shown that the general triaxial solution (4.45) gives the stress components correctly.

4.6.8 Numerical test

We have numerically implemented the general triaxial solution (4.45), and tested it on a polytrope dynamical model, for which the DF depends only on energy E as $f(E) \propto E^{n-3/2}$, with $n > \frac{1}{2}$. Integration of this DF over velocity v , with $E = -V - \frac{1}{2}v^2$ for a potential $V \leq 0$, shows that the density $\rho \propto (-V)^n$ (e.g., Binney & Tremaine 1987, p. 223). This density is not consistent with the Stäckel potentials we use but, as noted in §2.3, the Jeans equations do not require self-consistency. The first velocity moments and the mixed second moments of the DF are all zero. The remaining three moments all equal $-V/(n+1)$, so that the isotropic stress of the polytrope model $T_{\text{pol}} \propto (-V)^{n+1}$.

We take the potential V to be of Stäckel form V_S (2.3), and consider two different choices for $G(\tau)$ in (2.4). The first is the simple form $G(\tau) = -GM/(\sqrt{\tau} + \sqrt{-\alpha})$ that is related to Hénon's isochrone (de Zeeuw & Pfenniger 1988). The second is the form for the perfect ellipsoid, for which $G(\tau)$ is given in Z85 in terms of complete elliptic integrals. The partial derivatives of $V_S(\lambda, \mu, \nu)$, that appear in the weights g_1 , g_2 and g_3 , can be obtained in terms of $G(\tau)$ and its derivative in a straightforward way by using the expressions derived by de Zeeuw et al. (1986).

The calculation of the stresses is done in the following way. We choose the polytrope index n , and fix the triaxial Stäckel model by choosing α , β and γ . This gives T_{pol} . Next, we obtain successively the stresses $T_{\lambda\lambda}$, $T_{\mu\mu}$ and $T_{\nu\nu}$ from the general triaxial solution (4.45) by numerical integration, where the relation between $S_{\tau\tau}$ and $T_{\tau\tau}$ is given by (4.1). We first fix the upper integration limits λ_e , μ_e and ν_e . All integrands contain the singular solutions (4.42), that involve the homogeneous solutions A , B , C , F , G , H and I , for which we numerically evaluate the single quadratures (eq. [4.35], [4.38] and [4.41]). The weights g_1 , g_2 and g_3 (4.3) involve the polytrope density and Stäckel potential. This leaves the boundary stresses in the integrands, for which we use the polytrope stress T_{pol} that follows from the choice of the DF, evaluated at the corresponding boundary surfaces. We then evaluate the general solution away from these boundaries, and compare it with the known result.

We carried out the numerical calculations for different choices of n , α , β and γ and at different field points (λ, μ, ν) . In each case the resulting stresses $T_{\lambda\lambda}$, $T_{\mu\mu}$ and $T_{\nu\nu}$ – independently calculated – were equivalent to high precision and equal to T_{pol} . This agreement provides a check on the accuracy of both our formulae and their numerical implementation, and demonstrates the feasibility of using our methods for computing triaxial stress distributions. That will be the subject of a follow-up paper.

5 DISCUSSION AND CONCLUSIONS

Eddington (1915) showed that the velocity ellipsoid in a triaxial galaxy with a separable potential of Stäckel form is everywhere aligned with the confocal ellipsoidal coordinate system in which the equations of motion separate. Lynden-Bell (1960) derived the three Jeans equations which relate the three principal stresses to the potential and the density. They constitute a highly-symmetric set of first-order partial

differential equations in the three confocal coordinates. Solutions were found for the various two-dimensional limiting cases, but with methods that do not carry over to the general case, which, as a consequence, remained unsolved.

Here, we have introduced an alternative solution method, using superposition of singular solutions. We have shown that this approach not only provides an elegant alternative to the standard Riemann–Green method for the two-dimensional limits, but also, unlike the standard methods, can be generalized to solve the three-dimensional system. The resulting solutions contain complete (hyper)elliptic integrals which can be evaluated in a straightforward way. In the derivation, we have recovered (and in some cases corrected) all previously known solutions for the various two-dimensional limiting cases with more symmetry, as well as the two special solutions known for the general case, and have also clarified the restrictions on the boundary values. We have numerically tested our solution on a polytrope model.

The general Jeans solution is not unique, but requires specification of principal stresses at certain boundary surfaces, given a separable triaxial potential, and a triaxial density distribution (not necessarily the one that generates the potential). We have shown that these boundary surfaces can be taken to be the plane containing the long and the short axis of the galaxy, and, more specifically, the part that is crossed by all three families of tube orbits and the box orbits. This is not unexpected, as HZ92 demonstrated that the phase-space distribution functions of these triaxial systems are defined by specifying the population of each of the three tube orbit families in a principal plane. Once the tube orbit populations have been defined in this way, the population of the box orbits is fixed, as it must reproduce the density not contributed by the tubes, and there is only one way to do this. While HZ92 chose to define the population of inner and outer long axis tubes in a part of the (x, z) -plane, and the short axis tubes in a part of the (y, z) -plane, it is in fact also possible to specify all three of them in the appropriate parts of the (x, z) -plane, just as is needed for the stresses.

The set of all Jeans solutions (4.45) contains all the stresses that are associated with the physical distribution functions $f \geq 0$, but, as in the case of spherical and axisymmetric models, undoubtedly also contains solutions which are unphysical, e.g., those associated with distribution functions that are negative in some parts of phase space. The many examples of the use of spherical and axisymmetric Jeans models in the literature suggest nevertheless that the Jeans solutions can be of significant use.

While triaxial models with a separable potential do not provide an adequate description of the nuclei of galaxies with cusped luminosity profiles and a massive central black hole, they do catch much of the orbital structure at larger radii, and in some cases even provide a good approximation of the galaxy potential. The solutions for the mean streaming motions, i.e., the first velocity moments of the distribution function, are quite helpful in understanding the variety of observed velocity fields in giant elliptical galaxies and constraining their intrinsic shapes (e.g., Statler 1991, 1994b; Arnold et al. 1994; Statler et al. 1999; Statler 2001). We expect that the projected velocity dispersion fields that can be derived from our Jeans solutions will be similarly useful, and, in particular, that they can be used to establish which combinations of viewing directions and intrinsic axis ratios are firmly ruled out by the observations. As some of the projected properties of the Stäckel models can be evaluated by analytic means (Franx 1988), it is possible that this holds even for the intrinsic moments considered here. Work along these lines is in progress.

The solutions presented here constitute a significant step towards completing the

analytic description of the properties of the separable triaxial models, whose history by now spans more than a century. It is remarkable that the entire Jeans solution can be written down by means of classical methods. This suggests that similar solutions can be found for the higher dimensional analogues of (2.16), most likely involving hyperelliptic integrals of higher order. It is also likely that the higher-order velocity moments for the separable triaxial models can be found by similar analytic means, but the effort may become prohibitive.

ACKNOWLEDGMENTS

This chapter owes much to Donald Lynden-Bell's enthusiasm and inspiration. This work began during a sabbatical visit by CH to Leiden Observatory in 1992, supported in part by a Bezoekersbeurs from NWO, and also by NSF through grant DMS 9001404. CH is currently supported by NSF through grant DMS 0104751. This research was supported in part by the Netherlands Research School for Astronomy NOVA. The authors gratefully acknowledge stimulating discussions with Wyn Evans during the initial phases of this work.

REFERENCES

- Abramowitz M., Stegun I. A., 1965, *Handbook of Mathematical Functions*. New York, Dover Publications [AS65]
- Arnold R., 1995, *MNRAS*, 276, 293
- Arnold R., de Zeeuw P. T., Hunter C., 1994, *MNRAS*, 271, 924
- Bacon R., Simien F., Monnet G., 1983, *A&A*, 128, 405
- Bak J., Statler T. S., 2000, *AJ*, 120, 110
- Binney J., 1976, *MNRAS*, 177, 19
- Binney J., 1978, *MNRAS*, 183, 501
- Binney J., 1982, *MNRAS*, 201, 15
- Binney J., Tremaine S., 1987, *Galactic Dynamics*. Princeton, NJ, Princeton University Press [BT87]
- Bishop J. L., 1986, *ApJ*, 305, 14
- Bishop J. L., 1987, *ApJ*, 322, 618
- Byrd P. F., Friedman M. D., 1971, *Handbook of Elliptic Integrals for Engineers and Scientists*. Springer-Verlag, Berlin Heidelberg New York, 2nd revised ed.
- Carlson B. C., 1977, *Special Functions of Applied Mathematics*. Academic Press, New York San Francisco London
- Chandrasekhar S., 1939, *ApJ*, 90, 1
- Chandrasekhar S., 1940, *ApJ*, 92, 441
- Conway J., 1973, *Functions of one complex variable*. New York, Springer-Verlag
- Copson E. T., 1975, *Partial Differential Equations*. Cambridge, Cambridge University Press [C75]
- de Zeeuw P. T., 1985a, *MNRAS*, 216, 273 [Z85]
- de Zeeuw P. T., 1985b, *MNRAS*, 216, 599
- de Zeeuw P. T., Hunter C., 1990, *ApJ*, 356, 365
- de Zeeuw P. T., Hunter C., Schwarzschild M., 1987, *ApJ*, 317, 607
- de Zeeuw P. T., Peletier R., Franx M., 1986, *MNRAS*, 221, 1001
- de Zeeuw P. T., Pfenniger D., 1988, *MNRAS*, 235, 949
- Dejonghe H., de Zeeuw P. T., 1988, *ApJ*, 333, 90
- Dejonghe H., Laurent D., 1991, *MNRAS*, 252, 606
- Eddington A. S., 1915, *MNRAS*, 76, 37
- Evans N., 1990, *Intern. J. Computer Math.*, 34, 105
- Evans N. W., Carollo C. M., de Zeeuw P. T., 2000, *MNRAS*, 318, 1131 [ECZ00]

- Evans N. W., de Zeeuw P. T., 1992, MNRAS, 257, 152
 Evans N. W., Lynden-Bell D., 1989, MNRAS, 236, 801 [EL89]
 Evans N. W., Lynden-Bell D., 1991, MNRAS, 251, 213
 Franx M., 1988, MNRAS, 231, 285
 Gebhardt K., et al. 2002, ApJ, accepted
 Gerhard O. E., 1993, MNRAS, 265, 213
 Goldstein H., 1980, Classical Mechanics. London, Addison-Wesley
 Hunter C., de Zeeuw P. T., 1992, ApJ, 389, 79 [HZ92]
 Hunter C., de Zeeuw P. T., Park C., Schwarzschild M., 1990, ApJ, 363, 367
 Jeans J. H., 1915, MNRAS, 76, 70
 Kuzmin G. G., 1973, in Proc. All-Union Conf., Dynamics of Galaxies and Clusters. ed. T. B. Omarov (Alma Ata: Akad. Nauk Kazakhskoj SSR), 71 (English transl. in IAU Symp. 127, Structure and Dynamics of Ell. Galaxies, ed. P.T. de Zeeuw [Dordrecht: Reidel], 553)
 Lynden-Bell D., 1960, PhD thesis, Cambridge University
 Lynden-Bell D., 1962a, MNRAS, 124, 1
 Lynden-Bell D., 1962b, MNRAS, 124, 95
 Mathieu A., Dejonghe H., 1999, MNRAS, 303, 455
 Oberhettinger F., Badii L., 1973, Tables of Laplace Transforms. New York, Springer-Verlag
 Press W. H., Teukolsky S. A., Vetterling W. T., Flannery B. P., 1992, Numerical Recipes. Cambridge Univ. Press, Cambridge
 Qian E. E., de Zeeuw P. T., van der Marel R. P., Hunter C., 1995, MNRAS, 274, 602
 Rix H., de Zeeuw P. T., Cretton N., van der Marel R. P., Carollo C. M., 1997, ApJ, 488, 702
 Robijn F. H. A., de Zeeuw P. T., 1996, MNRAS, 279, 673
 Schwarzschild M., 1979, ApJ, 232, 236
 Schwarzschild M., 1993, ApJ, 409, 563
 Stäckel P., 1890, Math. Ann., 35, 91
 Stäckel P., 1891, Über die Integration der Hamilton-Jacobischen Differential gleichung mittelst Separation der Variabeln. Habilitationsschrift, Halle
 Statler T. S., 1987, ApJ, 321, 113
 Statler T. S., 1991, AJ, 102, 882
 Statler T. S., 1994a, ApJ, 425, 458
 Statler T. S., 1994b, ApJ, 425, 500
 Statler T. S., 2001, AJ, 121, 244
 Statler T. S., Dejonghe H., Smecker-Hane T., 1999, AJ, 117, 126
 Statler T. S., Fry A. M., 1994, ApJ, 425, 481
 Strauss W. A., 1992, Partial Differential Equations. New York, John Wiley
 van der Marel R. P., Cretton N., de Zeeuw P. T., Rix H., 1998, ApJ, 493, 613
 Verolme E. K., et al. 2002, MNRAS, 335, 517
 Weinacht J., 1924, Math. Ann., 91, 279
 Zhao H. S., 1996, MNRAS, 283, 149

APPENDIX A SOLVING FOR THE DIFFERENCE IN STRESS

We compare our solution for the stress components $T_{\lambda\lambda}$ and $T_{\mu\mu}$ with the result derived by EL89. They combine the two Jeans equations (2.25) into the single equation

$$\frac{\partial^2 \Delta}{\partial \lambda \partial \mu} + \left(\frac{\partial}{\partial \mu} - \frac{\partial}{\partial \lambda} \right) \frac{\Delta}{2(\lambda - \mu)} = \frac{\partial \rho}{\partial \lambda} \frac{\partial V_S}{\partial \mu} - \frac{\partial \rho}{\partial \mu} \frac{\partial V_S}{\partial \lambda}, \quad (\text{A.1})$$

for the difference $\Delta \equiv T_{\lambda\lambda} - T_{\mu\mu}$ of the two stress components. Eq. (A.1) is of the form

$$\mathcal{L}^* \Delta = \frac{\partial \rho}{\partial \lambda} \frac{\partial V_S}{\partial \mu} - \frac{\partial \rho}{\partial \mu} \frac{\partial V_S}{\partial \lambda}, \quad (\text{A.2})$$

where \mathcal{L}^* is the adjoint operator defined in eq. (3.6). As in §3.1, eq. (A.1) can be solved via a Riemann–Green function.

A.1 THE GREEN'S FUNCTION

In order to obtain the Riemann–Green function \mathcal{G}^* for the adjoint operator \mathcal{L}^* , we use the reciprocity relation (Copson 1975, §5.2) to relate it to the Riemann–Green function \mathcal{G} , derived in §3.1.2 for \mathcal{L} . With $c_1 = c_2 = -\frac{1}{2}$ in this case, we get

$$\mathcal{G}^*(\lambda, \mu; \lambda_0, \mu_0) = \mathcal{G}(\lambda_0, \mu_0; \lambda, \mu) = \left(\frac{\lambda_0 - \mu_0}{\lambda - \mu} \right)^{\frac{1}{2}} {}_2F_1\left(-\frac{1}{2}, \frac{3}{2}; 1; w\right), \quad (\text{A.3})$$

where w as defined in (3.16). EL89 seek to solve eq. (A.2) using a Green's function G which satisfies the equation

$$\mathcal{L}^*G = \delta(\lambda_0 - \lambda) \delta(\mu_0 - \mu). \quad (\text{A.4})$$

That they impose the same boundary conditions that we do is evident from their remark that, if \mathcal{L}^* were the simpler operator $\partial^2/\partial\lambda\partial\mu$, G would be $\mathcal{H}(\lambda_0 - \lambda)\mathcal{H}(\mu_0 - \mu)$. This is the same result as would be obtained by the singular solution method of §3.2, which, as we showed there, is equivalent to the Riemann–Green analysis. Hence their G should match the \mathcal{G}^* of eq. (A.3). We show in §A.3 that it does not.

A.2 LAPLACE TRANSFORM

We use a Laplace transform to solve (A.4) because the required solution is that to an initial value problem to which Laplace transforms are naturally suited. The PDE is hyperbolic with the lines $\lambda = \text{const}$ and $\mu = \text{const}$ as characteristics, and its solution is non-zero only in the rectangle bounded by the characteristics $\lambda = \lambda_0$ and $\mu = \mu_0$, and the physical boundaries $\lambda = -\alpha$ and $\mu = -\beta$ (Fig. A.1). We introduce new coordinates

$$\xi = (\lambda - \mu)/\sqrt{2}, \quad \eta = -(\lambda + \mu)/\sqrt{2}, \quad (\text{A.5})$$

so that eq. (A.4) simplifies to

$$\mathcal{L}^*G \equiv \frac{\partial^2 G}{\partial\eta^2} - \frac{\partial^2 G}{\partial\xi^2} - \frac{\partial}{\partial\xi} \left(\frac{G}{\xi} \right) = 2\delta(\xi - \xi_0) \delta(\eta - \eta_0), \quad (\text{A.6})$$

where $\xi_0 = (\lambda_0 - \mu_0)/\sqrt{2}$ and $\eta_0 = -(\lambda_0 + \mu_0)/\sqrt{2}$ are the coordinates of the source point. The factor of 2 arises from the transformation of the derivatives; the product of the delta functions in (A.4) transforms into that of (A.6) because the Jacobian of the transformation (A.5) is unity. The reason for our choice of η is that $G \equiv 0$ for $\eta < \eta_0$, that is $\lambda + \mu > \lambda_0 + \mu_0$. Hence η is a time-like variable which increases in the direction in which the non-zero part of the solution propagates. We take a Laplace transform in $\tilde{\eta} = \eta - \eta_0$, and transform $G(\xi, \eta)$ to

$$\hat{G}(\xi, p) = \int_0^\infty e^{-p\tilde{\eta}} G(\xi, \tilde{\eta}) d\tilde{\eta}. \quad (\text{A.7})$$

There are two equally valid ways of taking proper account of the $\delta(\eta - \eta_0)$ in taking the Laplace transform of eq. (A.6). One can either treat it as $\delta(\tilde{\eta} - 0+)$, in which case it has a Laplace transform of 1, or one can treat it as $\delta(\tilde{\eta} - 0-)$, in which case it contributes

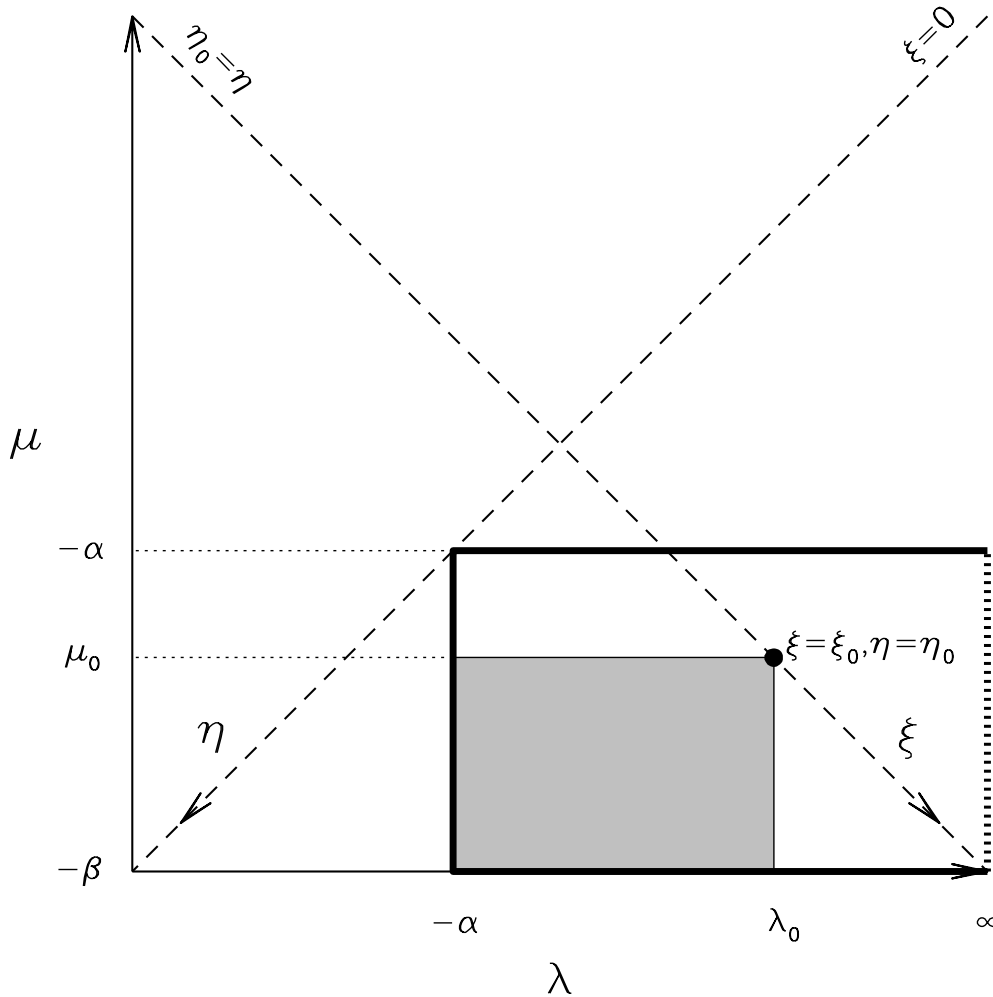


FIGURE A.1 — The physically relevant region of the (λ, μ) -plane for the determination of the Riemann–Green function G , overlaid with the new coordinates ξ and η (A.5). The dot marks the source point of the Riemann–Green function G at (λ_0, μ_0) . This function is non-zero only in the shaded region, which denotes the domain of influence in the (λ, μ) -plane of that source point. Fig. 4 on the other hand shows the (λ_0, μ_0) -plane. It is relevant to the solution for the stress at a single field point (λ, μ) . The hatched region D of Fig. 4 shows the domain of dependence of the field point, that is the portion of the source plane on which the solution at the field point depends.

a unit initial value to $\partial G/\partial\eta$ which must be included in the Laplace transform of $\partial^2 G/\partial\eta^2$ (Strauss 1992). Either way leads to a transformed equation for $\hat{G}(\xi, p)$ of

$$p^2 \hat{G} - \frac{d^2 \hat{G}}{d\xi^2} - \frac{d}{d\xi} \left(\frac{\hat{G}}{\xi} \right) = 2\delta(\xi - \xi_0). \quad (\text{A.8})$$

The homogeneous part of eq. (A.8) is the modified Bessel equation of order one in the variable $p\xi$. Two independent solutions are the modified Bessel functions I_1 and K_1 . The former vanishes at $\xi = 0$ and the latter decays exponentially as $\xi \rightarrow \infty$. We need \hat{G} to decay exponentially as $\xi \rightarrow \infty$ because $G(\xi, \eta)$ vanishes for $\tilde{\eta} < \xi - \xi_0$, and hence

its Laplace transform \hat{G} is exponentially small for large ξ . We also need \hat{G} to vanish at $\xi = 0$ where $\lambda = \mu$. The focus at which $\lambda = \mu = -\alpha$ is the only physically relevant point at which $\xi = 0$. It lies on a boundary of the solution region in the $\lambda_0 \rightarrow -\alpha$ limit (Fig. A.1). The focus is a point at which the difference Δ between the stresses vanishes, and hence G and \hat{G} should vanish there. The delta function in eq. (A.8) requires that \hat{G} be continuous at $\xi = \xi_0$ and that $d\hat{G}/d\xi$ decrease discontinuously by 2 as ξ increases through $\xi = \xi_0$. Combining all these requirements, we obtain the result

$$\hat{G}(\xi, p) = \begin{cases} 2\xi_0 K_1(p\xi) I_1(p\xi_0), & \xi_0 \leq \xi < \infty, \\ 2\xi_0 K_1(p\xi_0) I_1(p\xi), & 0 \leq \xi \leq \xi_0. \end{cases} \quad (\text{A.9})$$

We use the Wronskian relation $I_1(x)K_1'(x) - I_1'(x)K_1(x) = -1/x$ (eq. [9.6.15] of Abramowitz & Stegun 1965) in calculating the prefactor of the products of modified Bessel functions. The inversion of this transform is obtained from formula (13.39) of Oberhettinger & Badii (1973) which gives

$$G(\xi, \tilde{\eta}) = \begin{cases} \sqrt{\frac{\xi_0}{\xi}} {}_2F_1(-\frac{1}{2}, \frac{3}{2}; 1; w), & |\xi_0 - \xi| \leq \tilde{\eta} \leq \xi_0 + \xi, \\ 0, & -\infty < \tilde{\eta} < |\xi_0 - \xi|, \end{cases} \quad (\text{A.10})$$

we have (cf. eq. [3.16])

$$w \equiv \frac{\tilde{\eta}^2 - (\xi_0 - \xi)^2}{4\xi_0\xi} = \frac{(\lambda_0 - \lambda)(\mu_0 - \mu)}{(\lambda_0 - \mu_0)(\lambda - \mu)}. \quad (\text{A.11})$$

The second case of eq. (A.10) shows that G does indeed vanish outside the shaded sector $\lambda < \lambda_0$, $\mu < \mu_0$. The first case shows that it agrees with the adjoint Riemann-Green function \mathcal{G}^* of (A.3) which was derived from the analysis of §3.1.

A.3 COMPARISON WITH EL89

EL89 use variables $s = -\eta$ and $t = \xi$, whereas we avoided using t for the non-time-like variable. They consider the Fourier transform

$$\bar{G}(\xi, k) = \int_{-\infty}^{\infty} e^{-ik\tilde{\eta}} G(\xi, \tilde{\eta}) d\tilde{\eta}. \quad (\text{A.12})$$

Because $G \equiv 0$ for $\tilde{\eta} \leq 0$, we can rewrite our Laplace transform as their Fourier transform. Setting $p = -ik$ gives $\bar{G}(\xi, k) = i\hat{G}(\xi, -ik)$, and using the formulas $I_1(x) = -J_1(ix)$ and $K_1(x) = \frac{1}{2}\pi i H_1^{(1)}(ix)$, eq. (A.9) yields

$$\bar{G}(\xi, k) = \begin{cases} \pi i \xi_0 H_1^{(1)}(k\xi) J_1(k\xi_0), & \xi_0 \leq \xi < \infty, \\ \pi i \xi_0 H_1^{(1)}(k\xi_0) J_1(k\xi), & 0 \leq \xi \leq \xi_0. \end{cases} \quad (\text{A.13})$$

This formula differs from the solution for the Fourier transform given in eq. (70) of EL89. The major difference is that their solution has Hankel functions of the second kind $H_1^{(2)}(kt) = H_1^{(2)}(k\xi)$ where ours has J_1 Bessel functions. Consequently their solution has an unphysical singularity at $t = \xi = 0$, and so, in our opinion, is incorrect. Our solution, which was devised to avoid that singularity, gives a result which matches that derived by Riemann's method in §3.1.

A.4 THE SOLUTION FOR Δ

The solution for Δ using the adjoint Riemann–Green function is given by eq. (3.14) with \mathcal{G} replaced by \mathcal{G}^* and the sign of c_2 changed for the adjoint case (Copson 1975). The hypergeometric function of eq. (A.3) for \mathcal{G}^* is expressible in terms of complete elliptical integrals as

$${}_2F_1\left(-\frac{1}{2}, \frac{3}{2}; 1; w\right) = \frac{2}{\pi}[E(w) + 2wE'(w)]. \quad (\text{A.14})$$

Hence, the solution for the difference Δ between the two principal stresses is given by

$$\Delta(\lambda, \mu) = \frac{2}{\pi(\lambda - \mu)^{\frac{1}{2}}} \left\{ \int_{\lambda}^{\infty} d\lambda_0 \int_{\mu}^{-\alpha} d\mu_0 [E(w) + 2wE'(w)] (\lambda_0 - \mu_0)^{\frac{1}{2}} \left(\frac{\partial \rho}{\partial \lambda_0} \frac{\partial V_S}{\partial \mu_0} - \frac{\partial \rho}{\partial \mu_0} \frac{\partial V_S}{\partial \lambda_0} \right) - \int_{\lambda}^{\infty} d\lambda_0 [E(w) + 2wE'(w)] \frac{d}{d\lambda_0} \left[(\lambda_0 + \alpha)^{\frac{1}{2}} \Delta(\lambda_0, -\alpha) \right] \right\}. \quad (\text{A.15})$$

The determined reader can verify, after some manipulation, that this expression is equivalent to the difference between the separate solutions (3.21a) and (3.21b), derived in §3.1.

NOTE ADDED IN MANUSCRIPT

We agree with the amendment to our method of solution for Δ given in Appendix A.4. Our Green's function, while solving the differential equation, had the wrong boundary conditions.

N.W. Evans & D. Lynden-Bell

CHAPTER 6

THE EINSTEIN CROSS: LENSING VS. STELLAR DYNAMICS

ABSTRACT

We study the total mass distribution in the inner parts of the lens galaxy in the Einstein Cross by combining gravitational lensing with stellar dynamics. We obtain a realistic luminosity density of the lens galaxy by deprojecting its observed surface brightness, and we construct a lens model that accurately fits the positions and relative fluxes of the four quasar images. We combine both to build axisymmetric dynamical models that fit preliminary two-dimensional stellar kinematics derived from recent observations with the integral-field spectrograph GMOS. We find that the stellar velocity dispersion measurements with a mean value of $167 \pm 10 \text{ km s}^{-1}$ within the Einstein radius $R_E = 0.90''$, are in agreement with predictions from our and previous lens models. From the best-fit dynamical model, with I -band mass-to-light ratio $M/L = 3.6 M_\odot/L_\odot$, the Einstein mass is consistent with $M_E = 1.60 \times 10^{10} M_\odot$ from our lens model. The shapes of the density inferred from the lens model and from the surface brightness are very similar, but further improvement on the preliminary kinematic data is needed, before firm conclusions on the total mass distribution can be drawn.

1 INTRODUCTION

IN the cold dark matter (CDM) paradigm for galaxy formation (e.g., Kauffmann & van den Bosch 2002), galaxies are embedded in extended dark matter distributions with a specific and universal shape. Although we cannot directly see this dark matter, it contributes to the gravitational potential and hence it influences the dynamics of the galaxy. Measurements of rotation curves from neutral Hydrogen (HI) observations in the outer parts of late-type galaxies have provided evidence for the presence of dark matter in these systems more than two decades ago (e.g., van Albada et al. 1985). In the outer parts of early-type galaxies, however, cold gas is scarce, and evidence for dark matter in these systems has been found (mainly) from stellar kinematics (e.g., Carollo et al. 1995; Gerhard et al. 2001; but see Romanowsky et al. 2003).

A fundamental problem in using stellar kinematics for this purpose is the mass-anisotropy degeneracy: a change in the measured line-of-sight velocity dispersion can be due to a change in mass, but also due to a change in velocity anisotropy. Both effects can be disentangled by measuring also the higher-order velocity moments (Dejonghe 1988; van der Marel & Franx 1993; Gerhard 1993), but only the inner parts of nearby galaxies are bright enough to obtain the required kinematic measurements. Fitting dynamical models to such observations has provided accurate measurements of the anisotropy and M/L in the inner parts of early-type galaxies (e.g., van der Marel et al. 1991; Rix et al. 1997; Gerhard et al. 2001; Cappellari et al. 2005).

The dark matter fraction can be estimated by comparing this total (luminous and dark) M/L with the stellar (luminous) M_*/L determined by fitting stellar population models to color and absorption line-strength measurements. Due to uncertainties in the stellar population models (particularly with respect to the initial mass function), however, the dark matter fraction is not well constrained in this way.

The central dark matter profile provides a critical test of the CDM paradigm, which predicts that the inner parts of galaxies have a cuspy density $\propto r^{-\gamma}$, with power-law slope $\gamma \sim 1$ (Navarro, Frenk & White 1997). However, the observed slopes from HI rotation curves of late-type galaxies are on average much shallower, and even less is known about this apparent ‘cusp/core-problem’ in early-type galaxies (see e.g. Primack 2004 for an overview). Due to this lack of constraint, the dark matter profile in the inner parts of early-type galaxies is often restricted to the assumption that mass follows light, i.e., constant M/L .

A unique method to address the above issues is via the use of strong gravitational lensing. In combination with stellar dynamics, strong gravitational lensing can simultaneously break the mass-anisotropy degeneracy, and determine the fraction and shape of the dark matter distribution. The mass of a foreground galaxy bends the light of a distant bright object behind it, resulting in multiple images. From the separation and fluxes of the images the total mass distribution of the lens galaxy can be inferred. The luminous distribution can be obtained from the surface brightness of the lens galaxy, and dynamical models can then be constructed. Fitting the kinematics predicted by these models to the observed stellar kinematics places constraints on the free parameters, including anisotropy, stellar M_*/L and central dark matter slope γ .

Treu & Koopmans (2004, and references therein) have applied this approach to several lensing systems, of which 0047-281 (Koopmans & Treu 2003) is the best constrained case, with three spatially-resolved velocity dispersion measurements extending to about the effective radius of the lens galaxy. They measured the total mass

within the Einstein radius by fitting a singular isothermal ellipsoid to the positions of the quasar images. This total mass is then used to constrain the relative contribution to the potential from a luminous and dark matter component, both of which they assume to be a simple spherical distribution. They then compared the dispersions predicted by the spherical Jeans equations, for an ad-hoc assumption of the velocity anisotropy, with the observed dispersions. Based on a well constrained M_*/L and an upper limit on γ , they conclude that a significant amount of dark matter is present in the inner parts of the lens galaxy, with a slope flatter than the light. However, their results are limited by too few kinematic constraints (which leaves the anisotropy degenerate), and by the use of a simple spherical dynamical model.

The use of non-spherical models is important, since triaxial dark matter distributions are predicted by the CDM paradigm (e.g., Jing & Suto 2002). A triaxial geometry also seems necessary to explain the lens statistics (e.g., Oguri & Keeton 2004). Above all, most lens galaxies are significantly flattened and so cannot be well-described by spherical models. Non-spherical models provide a more realistic description of the lens galaxy, but the increase in freedom requires also (significantly) more spatially resolved kinematic measurements to constrain them. Only very few of the known strong gravitational lens systems are close enough to obtain such kinematic data, e.g., via observations with integral-field spectrographs. One of them is the gravitational lens system QSO 2237+0305, well-known as the Einstein Cross, with the lens galaxy at a redshift $z_{\text{lens}} \sim 0.04$. We have observed the Einstein Cross with the integral-field spectrograph GMOS on the Gemini-North Telescope. We combine a detailed model of the gravitational lens system with the light distribution inferred directly from the surface brightness to construct realistic non-spherical dynamical models. We then fit these models to the two-dimensional GMOS kinematics to investigate the mass distribution in the inner parts of the lens galaxy, including a possible contribution from dark matter.

In Section 2 we briefly describe the Einstein Cross and we present the photometric and kinematic observations we use in Section 3 to construct a detailed lens and dynamical model. In Section 4 we present our results. We discuss our findings in Section 5 and summarize our conclusions in Section 6. We adopt the WMAP cosmological parameters for the Hubble constant, the matter density and the cosmological constant, of $H_0 = 71 \text{ km s}^{-1} \text{ Mpc}^{-1}$, $\Omega_M = 0.27$ and $\Omega_L = 0.73$, respectively (Bennett et al. 2003), although these parameters only have a small effect on the physical scales of the lens galaxy due to its proximity.

2 OBSERVATIONS

2.1 THE EINSTEIN CROSS

The Einstein Cross is the well-known gravitational lens system QSO 2237+0305 or PGC069457 ($22^{\text{h}}40^{\text{m}}30.3^{\text{s}}$, $+03^{\circ}21'31''$). In this system, a distant quasar at $z_{\text{source}} = 1.695$ is lensed by the bulge of an early-type spiral at $z_{\text{lens}} = 0.0394$, resulting in a cross of four bright images separated by about $1.8''$.

Because the Einstein Cross has long been the closest strong gravitational lens system known, it has been very well studied since its discovery by Huchra et al. (1985). There is a wealth of ground- and space-based imaging data at all wavelengths (e.g., Falco et al. 1996; Blanton, Turner & Wambsganss 1998; Agol, Jones & Blaes 2000; Dai et al. 2003). The resulting precise measurements of the positions and relative fluxes of the quasar images can be used to construct a detailed lens model.

In contrast, kinematic data of the lens galaxy is very scarce, with only one measured central stellar velocity dispersion (Foltz et al. 1992) and two HI rotation curve measurements in the very outer parts (Barnes et al. 1999). There are several previous integral-field studies of the Einstein Cross (TIGER: Fitté & Adam 1994; INTEGRAL: Mediavilla et al. 1998; CIRPASS: Metcalf et al. 2004). However, none of these studies were concerned with the stellar kinematics of the lens galaxy, but instead investigated the quasar spectra.

2.2 IMAGING

Strong gravitational lensing occurs when a bright distant source like a quasar is sufficiently aligned with a foreground massive object such as an early-type elliptical galaxy. The lens galaxy then bends and magnifies the light from the quasar into separate images. The more precise the positions and relative fluxes of the quasar images are measured, the better the total (projected) mass distribution of the lens galaxy is constrained. Here, we use the accurate positions from the website of the CASTLES survey¹ based on *Hubble Space Telescope* (HST) imaging. Although optical flux ratios are given on this website, we use the radio fluxes provided by Falco et al. (1996), because they are in general (much) less affected by differential extinction or microlensing.

Instead of assuming a simple functional form for the light distribution as in most previous studies, we construct in § 3.1 a density model that in projection reproduces the surface brightness in detail. We measure the inclination needed to deproject the surface brightness from the flattening of the disk in a WFPC2/F555W *V*-band image (Fig. 1, left panel), retrieved from the HST-archive (1600 seconds; PI: Westphal). For the actual construction of the density model we use a WFPC2/F814W *I*-band image (Fig. 1, right panel) from the HST-archive (120 seconds; PI: Kochanek). We correct the *I*-band image for extinction following Schlegel, Finkbeiner & Davis (1998), and we convert to solar units using the WFPC2 calibration of Dolphin (2000), while assuming an absolute *I*-band magnitude for the Sun of 4.08 mag (Table 2 of Binney & Merrifield 1998). From a de Vaucouleurs $R^{1/4}$ profile fit to the *I*-band photometry in the inner 3'' bulge region, we obtain an effective radius $R_e \sim 6''$, which is consistent with previous measurements (e.g., Racine 1991).

2.3 INTEGRAL-FIELD SPECTROSCOPY

Observations of the Einstein Cross lens system were carried out using the integral-field unit of the GMOS-North spectrograph (Murray et al. 2003; Hook et al. 2004) on July 17th and August 1st 2005 as part of the program GN-2005A-DD-7. The data were obtained using the IFU two-slit mode that provides a field-of-view of 5'' \times 7''. An array of 1500 hexagonal lenslets, of which 500 are located 1' away from the main field to be used for sky subtraction, sets the 0''.2 spatial sampling. Eight individual exposures of 1895 seconds each were obtained during the two nights, resulting in a total on-source integration time of \sim 4 hours. An offset of 0''.3 was introduced between exposures to avoid bad CCD regions or lost fibers. The R400-G5305 grating in combination with the CaT-G0309 filter was used to cover a wavelength range between 7800-9200 Å with a spectral resolution of 2.8 Å (FWHM).

¹<http://cfa-www.harvard.edu/castles/>

To perform the data reduction we use an updated version of the officially distributed Gemini IRAF² package (B. Miller, priv. comm.). For each frame CuAr and Quartz Halogen (QH) lamp exposures were taken before each target for wavelength calibration and flat-fielding purposes. We bias subtract, flat-field and apply cosmic ray rejection to each science frame before the extraction of the data. An accurate flat-fielding is particularly important since at the observed wavelengths the data is affected by fringing. We minimize the effect of fringes in the final data by using the QH lamp exposures taken just before each science frame. For the cosmic ray rejection we use the *L.A. Cosmic* algorithm by van Dokkum (2001). After the extraction, we use the CuAr lamps closest to each science frame for wavelength calibration.

In order to check the range of fiber-to-fiber variations of the spectral resolution of the instrument, we measure the width of the sky lines in each fiber. As expected, the values on each fiber yield the nominal value ($2.8 \pm 0.2 \text{ \AA}$). For the sky subtraction, given the small scatter in the instrumental resolution of each fiber, we generate a single sky spectrum from all the sky fibers. This exercise, however, lead to significant residuals in the sky subtracted science frames. In each science frame, the data is grouped in blocks of science fibers surrounded by sky lenses. In an attempt to minimize the residuals in the sky subtracted frame, we subtract the averaged sky lenses closer to each group of science lenses. This approach leads to a significant improvement in the final sky subtracted results. Additionally, before the merging of the individual exposures, we homogenize each science frame for the fiber-to-fiber resolution variations by convolving each individual spectrum to an instrumental resolution of 3.2 \AA (FWHM). We also resample the individual exposures, so that they have the same starting value and sampling in wavelength. Before the merging process, we interpolate each individual frame to a common grid taking into account the small spatial offsets applied during the observations. We then sum the spectra sharing the same position in the sky to produce the final merged datacube.

3 ANALYSIS

We determine the intrinsic light distribution of the lens galaxy from its surface brightness, we fit a lens model to the quasar images, and we extract the stellar velocity and dispersion maps of the inner parts of the lens galaxy from the integral-field spectroscopic observations. These are then the ingredients for constructing an axisymmetric dynamical model of the lens galaxy.

3.1 LIGHT DISTRIBUTION

We construct a stellar luminosity density model of the lens galaxy based on its observed surface brightness with HST. For this we use the Multi-Gaussian Expansion (MGE) parametrization by Emsellem, Monnet & Bacon (1994), which describes the observed surface brightness as a sum of Gaussians. Even though Gaussians do not form a complete set of functions, in general the photometry is accurately reproduced, including ellipticity variations and non-elliptical isophotes. In Fig. 1 we show MGE fits to the *V*-band and *I*-band HST images, obtained with the software of Cappellari (2002), while masking the quasar images. Although the adopted constant-PA model

²IRAF is distributed by the National Optical Astronomy Observatories, which are operated by the Association of Universities for Research in Astronomy, Inc., under cooperative agreement with the National Science Foundation.

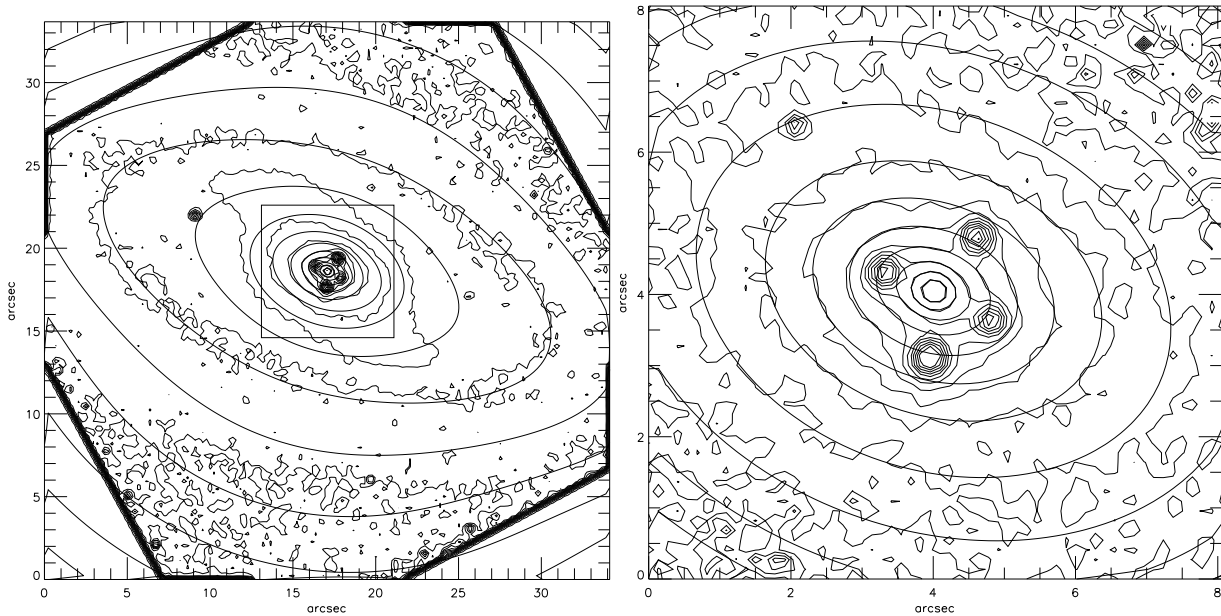


FIGURE 1 — The surface brightness of the lens galaxy in the Einstein Cross as observed with HST. Left panel: the contours of the WFPC2/F555W V -band image reveal clearly the bulge, spiral arms and bar embedded in the large-scale disk of this early-type spiral galaxy. The ellipticity measured from the MGE fit (solid contours) is used to estimate the inclination. Right panel: the central $8'' \times 8''$ of the WFPC2/F814W I -band image, of which the MGE fit (solid contours) is used to construct the stellar density model of the lens galaxy. We use the I -band image instead of the longer exposed V -band image as it tracers better the old stellar population and is less sensitive to extinction and reddening. The four quasar images are masked out during the MGE fit. The contours are in steps of 0.5 mag/arcsec^2 and the WFPC images are rotated such that North is up and East is to the left.

cannot reproduce the bar and spiral arms, it provides a very good description of the disk in the outer parts (left panel) and reproduces well the bulge in the inner parts (right panel).

The position angle (PA) of the major axis of the MGE isophotes (with respect to North through East) is $\sim 70^\circ$. This is consistent with measurements by Yee (1988), who found $\text{PA} \sim 67^\circ$ for the axis through quasar images C and D, bracketed by $\text{PA} \sim 77^\circ$ for the outer disk and $\text{PA} \sim 39^\circ$ for the bar (see also Fig. 1 of Trott & Webster 2002).

The MGE-parametrization of the surface brightness has the advantage that the deprojection can be performed analytically once the inclination i is known (Monnet, Bacon & Emsellem 1992). From the MGE fit to the V -band surface brightness of the lens galaxy (left panel of Fig. 1), we find that Gaussian components as flat as $q' = 0.4$ are required for an acceptable fit. This sets a lower limit to the inclination of $i \gtrsim 66^\circ$, which is above the value of $i \sim 60^\circ$ found by Irwin et al. (1989). Assuming a lower limit for the *intrinsic* flattening of the disk of 0.15 (e.g., Lambas, Maddox & Loveday 1992), we obtain an inclination of $i = 68^\circ$.

Given this inclination, we deproject the I -band MGE surface brightness fit, to obtain the axisymmetric stellar luminosity density $j_*(R, \theta)$ in the meridional plane of the lens galaxy, still expressed as a sum of Gaussians. The intrinsic flattening of the embedded bulge component is around 0.64.

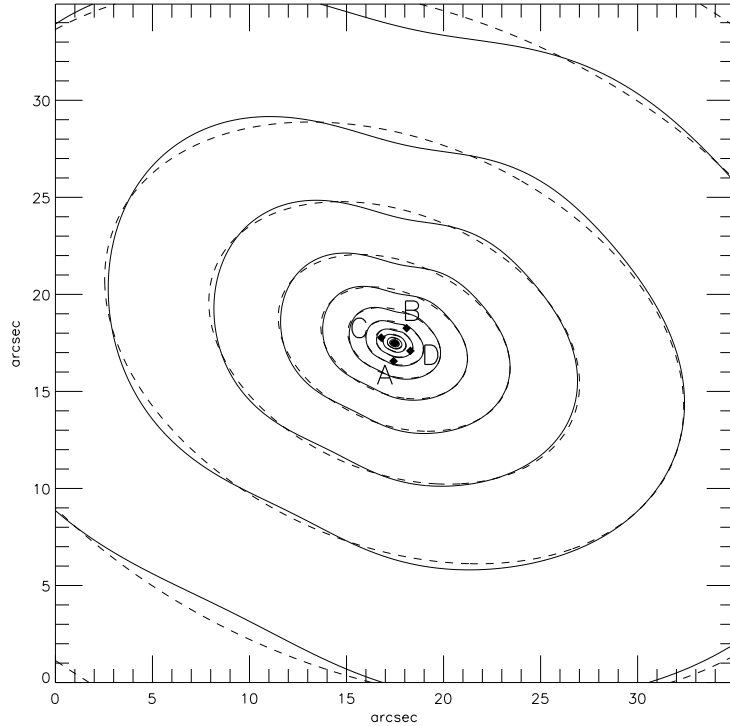


FIGURE 2 — The surface mass density from the gravitational lens model of the Einstein Cross (solid contours). The scale-free lens model fits the positions and relative fluxes of the quasar images, indicated by the filled circles. Superposed are the (dashed) contours of an MGE fit. As in Fig. 1, the contours are in steps of 0.5 mag/arcsec^2 , and North is up and East is to the left.

3.2 LENS MODEL

We use the algorithm of Evans & Witt (2003) to construct a lens model that accurately fits the (optical) positions and relative (radio) fluxes of the four quasar images (§ 2.2) in the Einstein Cross. The (projected) potential of the lens galaxy is assumed to be a scale-free function $\Phi_{\text{lens}}(R', \theta') = R'^{\beta} F(\theta')$ of the polar coordinates R' and θ' in the lens sky-plane, with $0 < \beta < 2$ for realistic models. The angular part $F(\theta')$ is expanded as a Fourier series

$$F(\theta') = \frac{1}{2} a_0 + \sum_{m=1}^{\infty} [c_m \cos(m\theta') + s_m \sin(m\theta')]. \quad (3.1)$$

We consider the models with $\beta = 1$ since they are interesting in two ways. These models have an everywhere flat rotation curve, and hence are projections of axisymmetric and triaxial generalizations of the familiar isothermal sphere. Moreover, as shown by Evans & Witt (2003), the lens model that best fits the positions and relative fluxes of the quasar images follows by straightforward matrix inversion.

The positions (R'_i, θ'_i) of the images are related to the position (ξ', η') of the quasar by the lens equation (e.g., Schneider, Ehlers & Falco 1992), which for $\beta = 1$ reduces to

$$\xi' = [R'_i - F(\theta'_i)] \cos \theta'_i + F'(\theta'_i) \sin \theta'_i, \quad (3.2)$$

$$\eta' = [R'_i - F(\theta'_i)] \sin \theta'_i - F'(\theta'_i) \cos \theta'_i. \quad (3.3)$$

The flux ratios of the images follow from their magnifications, for $\beta = 1$ given by

$$\mu_i = 1 - [F(\theta'_i) + F''(\theta'_i)]/R'_i. \quad (3.4)$$

Both equations are linear in the free parameters, i.e., the Fourier coefficients (c_m, s_m) and the quasar position (ξ', η') , so that the solution indeed follows by matrix inversion.

The Einstein Cross consists of four quasar images, resulting in 8 constraints from their positions and 3 from their flux ratios, so that in total we can constrain up to 11 free parameters. Although we can in principle fit the constraints exactly, we take into account the observational errors in the constraints (including for the positions the uncertainty in the measurement of the center of the lens galaxy). From the models that fit the constraints within the observational errors, we choose the solution with the smallest Fourier components higher than $m = 2$, as it looks most like a real galaxy. The resulting 11 best-fit parameters³ are $\xi' = 0.0696$, $\eta' = -0.0133$ for the source position with respect to the center of the lens galaxy, and $c_0 = 1.7746$, $c_2 = -0.04223$, $s_2 = 0.0428$, $c_3 = 0.0004$, $s_3 = -0.0014$, $c_4 = 0.0008$, $s_4 = 0.0009$, $c_5 = -0.0001$, $s_5 = 0.0007$, all in arcseconds.

The Fourier coefficients c_1 and s_1 are set to zero as they do not contribute to the inferred surface mass density, which follows from Poisson's equation as

$$\Sigma_{\text{lens}}(R', \theta') = \Sigma_{\text{crit}} \frac{F(\theta') + F''(\theta')}{2R'}, \quad \text{with} \quad \Sigma_{\text{crit}} = \frac{c^2 D_s}{4\pi G D_l D_{ls}}, \quad (3.5)$$

where D_l , D_s and D_{ls} are the (angular diameter) distance to the lens galaxy, the quasar source and the distance from lens to source, respectively. The contours of $\Sigma_{\text{lens}}(R', \theta')$ for the best-fit lens model of the Einstein Cross are shown in Fig. 2.

The scale-free $\beta = 1$ lens models have the further advantage that it is straightforward to compute the mass within the critical curve, which is given by

$$R_{\text{crit}}(\theta') = F(\theta') + F''(\theta'), \quad (3.6)$$

with R_{crit} in arcseconds. From the area within this critical curve, A_{crit} , it follows that

$$M_{\text{crit}} = \Sigma_{\text{crit}} A_{\text{crit}} (D_l \pi / 648000)^2, \quad (3.7)$$

where the factor in parentheses is the conversion from arcsec to pc for a given distance to the lens galaxy D_l in pc. The critical area A_{crit} (in arcsec²) can also be computed directly from the Fourier coefficients (cf. eq. 31 of Evans & Witt 2003⁴)

$$A_{\text{crit}} = \frac{1}{4} a_0^2 + \frac{1}{2} \sum_{m=1}^{\infty} (m^2 - 1)^2 (c_m^2 + s_m^2). \quad (3.8)$$

The critical mass M_{crit} also provides a good approximation of the Einstein mass M_E within the Einstein radius R_E , which can be obtained from the critical area as $R_E = \sqrt{A_{\text{crit}}/\pi}$ (in arcseconds), and describes the circle that approximately traces the positions of the quasar images.

³Although based on the same data and method, these values are slightly different than obtained by Evans & Witt (2003) due different assumptions on the errors.

⁴Their expression misses the factor half in front of the summation.

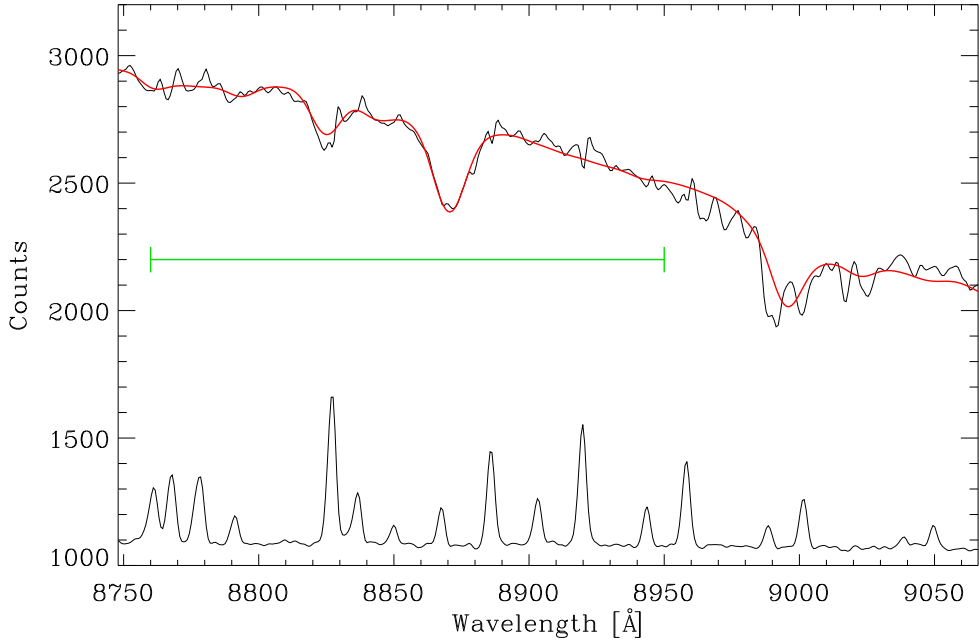


FIGURE 3 — Spectrum from the center of the lens galaxy, showing the Ca II triplet region fitted by a composite of stellar population models. The sky spectrum is shown at the bottom. The horizontal bar indicates the region included in the fit to obtain the stellar kinematics.

3.3 VELOCITY AND DISPERSION FIELDS

An accurate measurement of the mean line-of-sight velocities typically requires a signal-to-noise (S/N) ratio of 20 to match the stellar absorption lines in each spectrum. Stellar velocity dispersion measurements require higher S/N ratios to achieve the same accuracy. To measure reliable stellar kinematics we co-add the spectra using the adaptive spatial 2D-binning scheme of Cappellari & Copin (2003) to obtain in each resulting Voronoi bin a minimum S/N of ~ 40 , resulting in a total of 118 bins.

We measure the stellar kinematics of the lens galaxy using the penalized pixel-fitting algorithm of Cappellari & Emsellem (2004). We adopt the single stellar population (SSP) models of Vazdekis et al. (2003) as stellar templates. A non-negative linear combination of these templates is convolved with a Gaussian line-of-sight velocity distribution to obtain the mean line-of-sight velocity and velocity dispersion of each (binned) spectra in our merged datacube.

Fig. 3 shows the central spectrum of the lens galaxy with the best-fit SSP template (smooth line). We plot the typical sky spectrum below to indicate the regions where a possible bad sky subtraction has the strongest effect. This shows that an accurate sky subtraction is crucial given that many of the sky lines fall into the Ca II triplet absorption lines, and therefore affect our measurement of the mean line-of-sight velocity and velocity dispersion. This effect is of course stronger at larger radii in the lens galaxy, where the relative contribution from the sky is more significant.

The resulting stellar velocity V and dispersion σ fields are shown in Fig. 4, with superposed contours of the reconstructed image (obtained by collapsing the datacube in the spectral direction). The velocity field shows clear regular rotation around the projected minor axis of the bulge, with amplitude up to 100 km s^{-1} . Although the ve-

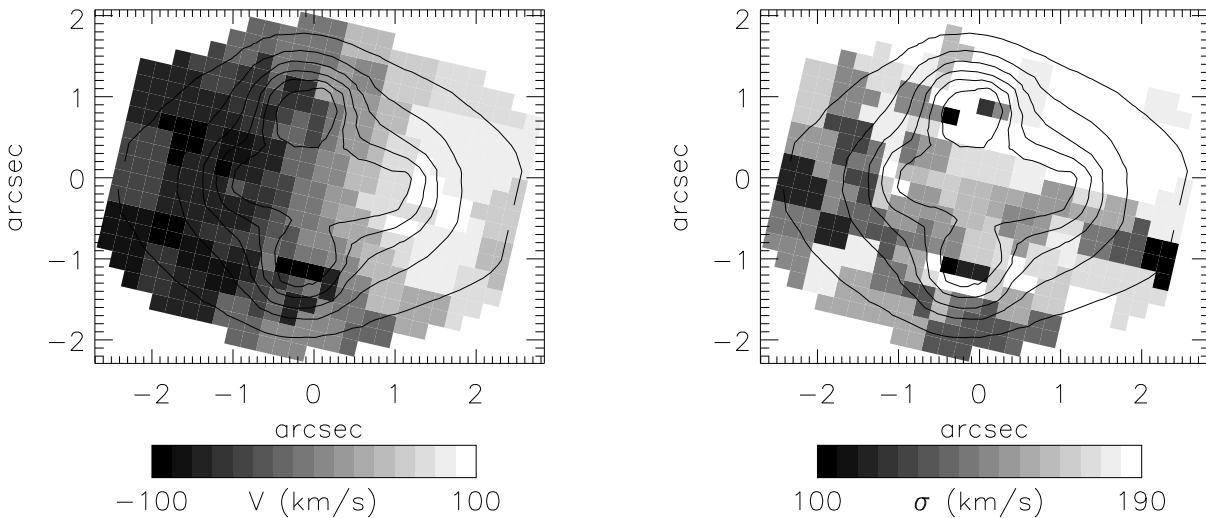


FIGURE 4 — Mean velocity and velocity dispersion field of the lens galaxy in the Einstein Cross as measured from observations with the integral-field spectrograph *GMOS* on Gemini-North. The overlaid contours of the reconstructed image show the positions of the quasar images, which affect the kinematics only very locally. The velocity field shows clear and regular rotation around the (vertically aligned) short-axis of the bulge. The velocity dispersion is fairly constant across the field, except for the region towards the upper-right, where systematic effects cause the dispersion to be overestimated. (See p. 256 for a color version of this figure.)

locity field is less well determined at the locations of the quasar images, most of their contribution has been efficiently removed during the extraction of the stellar kinematics. The dispersion field is more noisy, and is affected by systematics, in particular in the upper-right part. This is likely caused by the dominating sky lines in this region, which shift into the Ca II triplet absorption lines as a result of the corresponding positive mean velocity. The central dispersion measurements in between the quasar images, however, are robust around a value of 170 km s^{-1} (see § 5). We expect that a more detailed and careful treatment of the sky background will improve our stellar dispersion measurements, and we will investigate this in the near future. Because of the preliminary nature of the kinematic data, we limit the subsequent analysis to relatively simple axisymmetric dynamical models.

3.4 AXISYMMETRIC DYNAMICAL MODEL

For an axisymmetric model with a stellar distribution function that depends on only two integrals of motion $f = f(E, L_z)$, with E the energy and L_z the angular momentum component parallel to the symmetry z -axis, the second velocity moments are uniquely defined (e.g., Lynden-Bell 1962; Hunter 1977). They can be computed by solving the Jeans equations for a given potential and stellar density. For a given inclination i , we then obtain the line-of-sight projected second velocity moment $V_{\text{RMS}} = \sqrt{V^2 + \sigma^2}$, which can be compared with the value obtained from the observed mean line-of-sight velocity V and velocity dispersion σ .

If the potential and density are described by an MGE-parametrization, the calculation of V_{RMS} reduces to a single one-dimensional integral via eqs (61–63) of Emsellem et al. (1994), with correction for a typographical error given in Cappellari et al. (2005).

i	$\log \Sigma_0$ ($M_\odot \text{ pc}^{-2}$)	$\log \sigma'$ (arcsec)	q'
1	4.936	-1.779	0.670
2	4.971	-1.285	0.640
3	4.518	-0.915	0.650
4	4.145	-0.569	0.664
5	3.795	-0.230	0.663
6	3.460	0.105	0.667
7	3.133	0.445	0.667
8	2.836	0.814	0.665
9	2.623	1.376	0.670

TABLE 1 — The parameters of the nine Gaussians in the MGE fit to the lens model of the Einstein Cross. The second column gives the central surface mass density (in $M_\odot \text{ pc}^{-2}$) of each Gaussian component, the third column the dispersion (in arcsec) along the major axis and the fourth column the observed flattening.

i	$\log \text{SB}_0$ ($L_\odot \text{ pc}^{-2}$)	$\log \sigma'$ (arcsec)	q'
1	4.329	-3.601	0.700
2	3.935	-2.168	0.700
3	3.606	-1.444	0.700
4	3.293	-0.550	0.700
5	3.005	-0.098	0.700
6	2.845	0.530	0.700
7	2.261	1.352	0.700
8	2.160	2.111	0.414
9	1.334	2.613	0.700

TABLE 2 — The parameters of the nine Gaussians in the MGE-fit to the HST/WFPC2/F814W I-band image of the surface brightness of the lens galaxy in the Einstein Cross. The second column gives the central surface brightness (in $L_\odot \text{ pc}^{-2}$) of each Gaussian component, the third column the dispersion (in arcsec) along the major axis and the fourth column the observed flattening.

The MGE-parametrization of the lens potential follows from an MGE fit to the surface mass density $\Sigma(R', \theta')$ (3.5) of the lens model, shown by the dashed contours in Fig. 2 and with the corresponding parameters given in Table 1. Deprojection of this MGE fit provides the lens mass density from which the lens potential follows by solving Poisson’s equation. As we saw in § 3.1, the stellar luminosity density $j_\star(R, \theta)$ follows from the MGE fit to the surface brightness with the corresponding parameters given in Table 2. With the potential and density known, the only free parameter left is the inclination, for which we assume the value of $i = 68^\circ$, derived above from the ellipticity of the outer disk. When comparing the V_{RMS} predicted by the Jeans model with the observations, we also investigate a possible mass-scaling in the lens potential needed to better match the data.

Alternatively, we can build an axisymmetric Jeans model with the potential de-

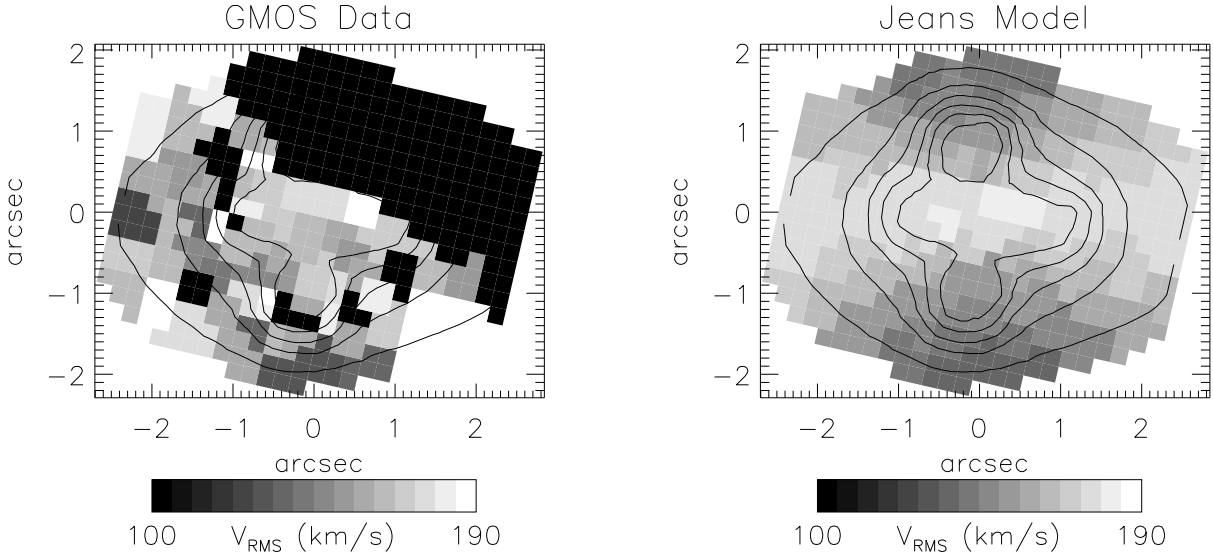


FIGURE 5 — *Two-integral axisymmetric Jeans model of the lens galaxy. Left panel: map of the second velocity moment as obtained from the observed velocity and dispersion field, where the region with systematic effects in the dispersion is excluded. Right panel: map of the second velocity moment from the best-fit Jeans model, based on the lens potential and the axisymmetric luminosity density inferred from the surface brightness.*

duced from the stellar luminosity density $j_*(R, \theta)$ instead of using the lens potential. To this end we multiply $j_*(R, \theta)$ with a constant mass-to-light ratio M/L to obtain the mass density, from which we then find the potential via Poisson’s equation. In this case we have two free parameters, i and M/L . In what follows, we refer to these axisymmetric models as *stellar* Jeans models, whereas we call the above models, based on the lens potential, *lens* Jeans models.

4 RESULTS

In the left panel of Fig. 5, we show the second velocity moment V_{RMS} map, derived from the observed velocity and dispersion field (Fig. 4). We have excluded the region that is significantly affected by systematic effects in σ (see § 3.3), leaving 66 bins out of the total of 118 bins. The right panel shows V_{RMS} as predicted by a lens Jeans model [i.e., using the (scaled) potential from the lens model] at the measured inclination $i = 68^\circ$. Across the relatively small field-of-view covered by the GMOS data, the predicted variation in V_{RMS} is small and of the order of the measurement uncertainties, so that there is only a weak indication for the ‘butterfly’ shape in the data. However, the central measurements are robust and can be used to reliably set the scaling.

We consider the region within the quasar images by selecting all bins within a radius that is half of the image separation of $1.8''$, i.e., all bins within the Einstein radius $R_E = 0.90''$. We find that the predictions of the *lens* Jeans model provide an acceptable fit to the resulting 15 dispersion measurements, although the best fit is obtained if the lens potential of the Jeans model is scaled by a factor 1.10. The best-fit *stellar* Jeans model predicts a similar butterfly shape for the projected second velocity moment. In this case the potential is inferred from the surface brightness, assuming a constant mass-to-light ratio to convert from light to mass (§ 3.4). We obtain a best-fit

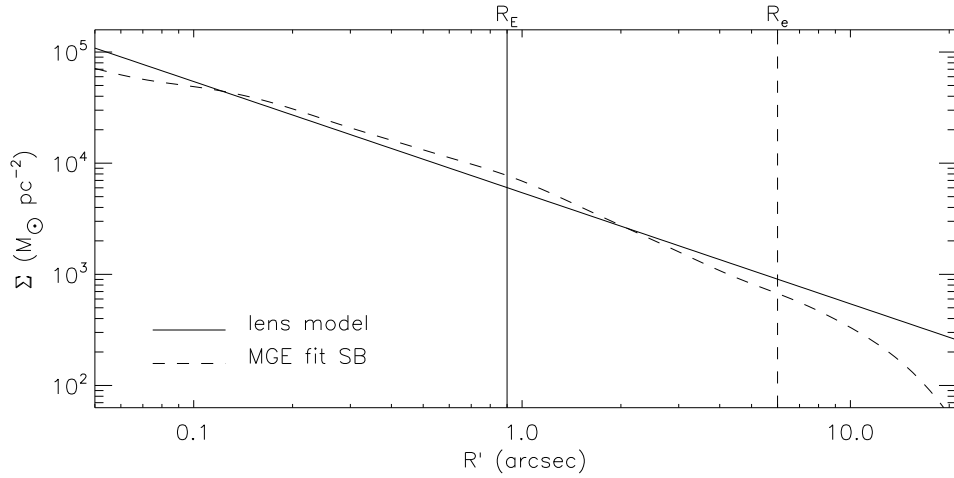


FIGURE 6 — The surface mass density profile along the major axis of the lens galaxy. The solid line is the assumed power-law slope of the lens model. The dashed line shows the profile of the MGE fit to the I -band surface brightness. The solid and dashed vertical lines indicate respectively the Einstein radius $R_E = 0.90''$ and the effective radius $R_e \sim 6''$, obtained by fitting a $R^{1/4}$ profile to the I -band photometry in the inner $3''$ bulge region.

I -band mass-to-light ratio of $M/L = 3.6 M_\odot/L_\odot$.

We compare the above best-fits by calculating the mass within the region enclosed by the critical curve R_{crit} given by eq. (3.5). This critical mass is nearly identical to the mass within the Einstein radius, which is the region of the dispersion field to which we fitted the Jeans models. For the best-fit lens Jeans model we obtain a mass of $\sim 1.76 \times 10^{10} M_\odot$. After multiplying the MGE surface brightness model with the best-fit M/L , we find for the best-fit stellar Jeans model a very similar mass of $\sim 1.75 \times 10^{10} M_\odot$. This does not mean that no dark matter is present in this region, as in both cases they are *total* masses (and *total* M/L), which in addition to the stellar mass may include a possible dark matter contribution.

At the same time, it is remarkable how similar the independent MGE fits of the surface mass density of the lens model (Fig. 2) and of the surface brightness (Fig. 1) are, and hence also their associated potentials. Both the orientation and the flattening (see fourth column of Tables 1 and 2) are comparable, suggesting that the shape of the total and stellar mass distributions are closely related. The radial profiles, shown in Fig. 6, cannot be compared in a similar way, since we assumed the power-law profile for the lens model as it is only weakly constrained by the lensing geometry. The critical mass, however, is not affected by our assumption of the power-law profile for the lens model, because it is almost independent of the lens model (e.g., Kochanek 1991; Evans & Witt 2001). The profile of the stellar dispersion can provide these constraints (e.g., Treu & Koopmans 2004). Unfortunately, due to the limited radial coverage, but mainly due to measurement uncertainties, this is not possible with the current preliminary velocity and dispersion field (but see § 6 below).

We can also compute the critical mass directly from the lens model via eq. (3.7). We find a mass of $\sim 1.62 \times 10^{10} M_\odot$, which is about 8% lower than the critical masses from the best-fit lens and stellar Jeans model, but within the measurement uncertainties. Errors of a few per cent are typically assigned to critical mass measurements directly

from the lens model, although Ferreras, Saha & Williams (2005) found errors up to 10% by considering a large ensemble of possible lens models. Still, the errors in the critical masses from the Jeans models are expected to dominate. By comparing M/L determinations from Jeans models with those from three-integral Schwarzschild models fitted to high-quality integral-field kinematics, Cappellari et al. (2005) found as a realistic lower limit on the uncertainty in these determinations a value of 6%. The 15 dispersion measurements within $R_E = 0.90''$ have a mean value of 167 km s^{-1} , with corresponding RMS value of 10 km s^{-1} , i.e., on average a 6% error, which translates into an error of about 12% in mass. Hence, we estimate a typical error of 13% in the critical mass estimates from the Jeans models. This shows that the difference in the critical mass determinations from the lens model and from Jeans models is within the expected uncertainties.

We now add the V_{RMS} measurements outside R_E , but still excluding the systematically affected upper-right region (left panel of Fig. 4). When we fit these 66 dispersion measurements with the lens and stellar Jeans models, we find again very similar values for the critical masses, but about 10% higher than before and nearly 20% higher than the critical mass directly from the lens model. The mean velocity dispersion of 166 km s^{-1} is nearly identical to that of the 15 central measurements. The corresponding RMS value increases to 15 km s^{-1} , resulting in an error on the mass of almost 20%. Although the difference between the various critical mass estimates is within the estimated uncertainties, we expect that the critical mass from the Jeans models is overestimated, mainly due to remaining systematics in the data, but also the model assumptions can have an effect (see the discussion below).

5 DISCUSSION

We find a central stellar velocity dispersion of $167 \pm 10 \text{ km s}^{-1}$, based on 15 measurements within the Einstein radius $R_E = 0.90''$. The only other direct (single) measurement of the stellar dispersion is $215 \pm 30 \text{ km s}^{-1}$ by Foltz et al. (1992). For a singular isothermal sphere lens model, we can use the relation $\Delta\theta = 8\pi(\sigma_{\text{SIS}}/c)^2 D_{ls}/D_s$ (e.g., Kochanek 2000) with a separation $\Delta\theta \sim 1.8''$ of the four quasar images, to obtain a simple estimate for the dispersion of $\sigma_{\text{SIS}} \sim 180 \text{ km s}^{-1}$. Taking into account aperture correction and a range in velocity anisotropy, van de Ven, van Dokkum & Franx (2003) converted this to a central stellar dispersion of $168 \pm 17 \text{ km s}^{-1}$. The King and de Vaucouleurs models of Kent & Falco (1988) predict a similar value of $\sim 166 \text{ km s}^{-1}$, and also Barnes et al. (1999) find a value of $165 \pm 23 \text{ km s}^{-1}$ based on their two H I rotation curve measurements. All these measurements are lower than that of Foltz et al. (1992), but in perfect agreement with ours. Their optical long-slit measurement might be affected by the very bright quasar images, whereas our measurements are in the less-affected Ca II triplet region and are spatially resolved, allowing for a clean separation of the quasar images.

A large variety of different lens models have been constructed for the Einstein Cross, most of which fit the positions of the quasar images but not their relative flux ratios. Although they predict significantly different flux ratios, the mass M_E within the Einstein radius $R_E = 0.90''$ is expected to be similar, because, as mentioned before, it is insensitive to the details of the lens model. In Table 3, we compare measurements of M_E from our analysis with values obtained from the literature, taking into account the inverse scaling with the Hubble constant. The difference between the circular

reference	M_E ($10^{10} M_\odot$)
scale-free $\beta = 1$ lens model	1.60
best-fit lens Jeans model	1.74
best-fit stellar Jeans model	1.73
Rix, Schneider & Bahcall (1992)	1.52
Wambsganss & Paczyński (1994)	1.56
Chae, Turnshek & Kehersonsky (1998)	1.58
Schmidt, Webster & Lewis (1998)	1.58
Trott & Webster (2002)	1.54
Ferreras, Saha & Williams (2005)	1.87

TABLE 3 — *Measurements of the Einstein mass M_E , i.e., the projected mass within the Einstein radius, for the Einstein Cross. The first four measurements follow from our analysis, the remaining are taken from the literature, taking into account an inverse scaling with the Hubble constant, for which we assume $H_0 = 71 \text{ km s}^{-1} \text{ Mpc}^{-1}$.*

area within R_E and the non-circular critical area causes a 1% decrease in M_E with respect to critical mass measurements we obtained in § 4. Given the typical error of a few per cent in the determination of M_E from the lens models, we conclude that the measurement from our lens model, that does fit the (radio) flux ratios, is consistent with all previous measurements. The one exception is the determination by Ferreras et al. (2005), who find a value higher than all others.

Although our two M_E values from the Jeans models fitted to the GMOS data are on average somewhat higher, they are safely within the uncertainties, given the estimated 13% error on these mass determinations. Part of the offset might be the result of our model assumptions of axisymmetry and two-integral distribution functions. Although the bar is clearly visible in the large-scale V -band image in Fig. 1, its effect in the inner bulge-dominated region is minimal, with an estimated mass contribution of only 5 per cent (Schmidt, Webster & Lewis 1998). This is supported by the observed velocity field, which shows regular rotation around the minor axis of the bulge. The two-integral assumption implies velocity isotropy in the meridional plane, which can have a direct effect on the mass estimate. Nevertheless, Cappellari et al. (2005) found that M/L determinations from axisymmetric two-integral Jeans models seem to be consistent with those obtained from three-integral Schwarzschild models. The latter models have full freedom in velocity anisotropy, but consequently more extensive and accurate kinematic observational constraints are required. When we use the $(M/L) - \sigma$ relation derived by these authors from Schwarzschild models, we find for our measured central dispersion of 167 km s^{-1} a predicted I -band $M/L \sim 3.3 M_\odot/L_\odot$. This is just 10% lower than we found from our stellar Jeans model, and implies a critical mass of $\sim 1.6 \times 10^{10} M_\odot$, equal to that measured directly from the lens model.

6 CONCLUSIONS

We have studied the total mass distribution in the inner parts of the lens galaxy in the Einstein Cross by fitting axisymmetric models based on an accurate lens model and a realistic luminosity density to spatially resolved kinematics obtained via observations with the integral-field spectrograph GMOS. We have found that the stellar velocity dispersion measurements have an average value of $167 \pm 10 \text{ km s}^{-1}$ within the

Einstein radius $R_E = 0.90''$, and are in agreement with previous predictions from lens models. The constructed scale-free lens model fits the positions as well as relative (radio) fluxes of the quasar images, and provides an Einstein mass $M_E = 1.60 \times 10^{10} M_\odot$ consistent with previous measurements.

We have obtained the luminosity density by deprojection of the surface brightness, and used it to construct axisymmetric two-integral Jeans models, which we fitted to the two-dimensional kinematic observations. Using the potential inferred from the lens model or from the luminosity density for a constant mass-to-light ratio M/L , we have found that in both cases the Einstein mass of the best-fit Jeans model is consistent with that of the lens model within the measurement uncertainties. The best-fit I -band $M/L = 3.6 M_\odot/L_\odot$ is consistent with the prediction from the $M/L - \sigma$ relation of Cappellari et al. (2005). Moreover, we have found that the M_E values from both best-fit Jeans models are the same within 1% and that the shape of the density inferred from the lens model and from the surface brightness is similar, suggesting that mass and light are similarly distributed. However, further analysis of the kinematic data, with in particular a more careful treatment of the sky background, is needed to also establish the radial profile of the mass distribution, before firm conclusions on the total mass distribution can be drawn.

Our preliminary study has shown that with integral-field spectrographs like GMOS it is possible, although very challenging, to obtain reliable spatially resolved kinematics of the lens galaxies in nearby gravitational lens systems, allowing for the unique combination of lensing and stellar dynamics to constrain the mass distribution. An even better candidate than the Einstein Cross for this kind of study is the newly-discovered gravitational lens system ESO325+G004 (Smith et al. 2005). The system is closer ($z = 0.0345$), the possible contamination from the faint quasar images is expected to be minimal, and above all, the lens galaxy is a bright giant elliptical galaxy. Hence, it becomes even feasible to measure absorption line strengths to obtain an independent estimate of the stellar mass-to-light ratio from the stellar population analysis. By improving our kinematic data on the Einstein Cross, as well as by obtaining integral-field spectroscopic observations on objects such as ESO325+G004, we expect to place constraints on the dark matter distribution in the inner parts of early-type galaxies, without being limited by ad-hoc assumptions on the geometry or velocity anisotropy.

ACKNOWLEDGMENTS

We are grateful to Jean-Rene and Matt Mountain for granting us director's discretionary time for this project and Tracy Beck for efficient and cheerful support.

REFERENCES

- Agol E., Jones B., Blaes O., 2000, ApJ, 545, 657
Barnes D. G., Webster R. L., Schmidt R. W., Hughes A., 1999, MNRAS, 309, 641
Bennett C. L., et al. 2003, ApJS, 148, 1
Binney J., Merrifield M., 1998, Galactic astronomy. Princeton, NJ, Princeton University Press
Blanton M., Turner E. L., Wambsganss J., 1998, MNRAS, 298, 1223
Cappellari M., 2002, MNRAS, 333, 400
Cappellari M., Copin Y., 2003, MNRAS, 342, 345
Cappellari M., Emsellem E., 2004, PASP, 116, 138
Cappellari M., et al 2005, MNRAS, submitted, astro-ph/0505042

- Carollo C. M., de Zeeuw P. T., van der Marel R. P., Danziger I. J., Qian E. E., 1995, *ApJ*, 441, 25
- Dai X., Chartas G., Agol E., Bautz M. W., Garmire G. P., 2003, *ApJ*, 589, 100
- Dejonghe H., 1987, *MNRAS*, 224, 13
- Dolphin A. E., 2000, *PASP*, 112, 1397
- Emsellem E., Monnet G., Bacon R., 1994, *A&A*, 285, 723
- Evans N. W., Witt H. J., 2001, *MNRAS*, 327, 1260
- Evans N. W., Witt H. J., 2003, *MNRAS*, 345, 1351
- Falco E. E., Lehar J., Perley R. A., Wambsganss J., Gorenstein M. V., 1996, *AJ*, 112, 897
- Ferreras I., Saha P., Williams L. L. R., 2005, *ApJ*, 623, L5
- Fitte C., Adam G., 1994, *A&A*, 282, 11
- Foltz C. B., Hewett P. C., Webster R. L., Lewis G. F., 1992, *ApJ*, 386, L43
- Gerhard O., Kronawitter A., Saglia R. P., Bender R., 2001, *AJ*, 121, 1936
- Gerhard O. E., 1993, *MNRAS*, 265, 213
- Hook I. M., Jørgensen I., Allington-Smith J. R., Davies R. L., Metcalfe N., Murowinski R. G., Crampton D., 2004, *PASP*, 116, 425
- Huchra J., Gorenstein M., Kent S., Shapiro I., Smith G., Horine E., Perley R., 1985, *AJ*, 90, 691
- Hunter C., 1977, *AJ*, 82, 271
- Irwin M. J., Webster R. L., Hewett P. C., Corrigan R. T., Jedrzejewski R. I., 1989, *AJ*, 98, 1989
- Jing Y. P., Suto Y., 2002, *ApJ*, 574, 538
- Kauffmann G., van den Bosch F., 2002, *Scientific American*, 286, 36
- Kent S. M., Falco E. E., 1988, *AJ*, 96, 1570
- Kochanek C. S., 1991, *ApJ*, 373, 354
- Koopmans L. V. E., Treu T., 2003, *ApJ*, 583, 606
- Lambas D. G., Maddox S. J., Loveday J., 1992, *MNRAS*, 258, 404
- Lynden-Bell D., 1962, *MNRAS*, 123, 447
- Mediavilla E., Arribas S., del Burgo C., Oscoz A., Serra-Ricart M., Alcalde D., Falco E. E., Goicoechea L. J., Garcia-Lorenzo B., Buitrago J., 1998, *ApJ*, 503, L27
- Metcalfe R. B., Moustakas L. A., Bunker A. J., Parry I. R., 2004, *ApJ*, 607, 43
- Monnet G., Bacon R., Emsellem E., 1992, *A&A*, 253, 366
- Murray G. J., Allington-Smith J. R., Content R., Davies R. L., Dodsworth G. N., Miller B., Jørgensen I., Hook I., Crampton D., Murowinski R. G., 2003, *SPIE*, 4841, 1750
- Navarro J. F., Frenk C. S., White S. D. M., 1997, *ApJ*, 490, 493
- Oguri M., Keeton C. R., 2004, *ApJ*, 610, 663
- Primack J. R., 2004, in *IAU Symp. 220: Dark Matter in Galaxies*, eds. S. D. Ryder, D. J. Pisano, M. A. Walker, and K. C. Freeman, p. 53
- Racine R., 1991, *AJ*, 102, 454
- Rix H.-W., de Zeeuw P. T., Cretton N., van der Marel R. P., Carollo C. M., 1997, *ApJ*, 488, 702
- Romanowsky A. J., Douglas N. G., Arnaboldi M., Kuijken K., Merrifield M. R., Napolitano N. R., Capaccioli M., Freeman K. C., 2003, *Science*, 301, 1696
- Schlegel D. J., Finkbeiner D. P., Davis M., 1998, *ApJ*, 500, 525
- Schmidt R., Webster R. L., Lewis G. F., 1998, *MNRAS*, 295, 488
- Schneider P., Ehlers J., Falco E. E., 1992, *Gravitational Lenses*. Springer-Verlag Berlin Heidelberg New York
- Smith R. J., Blakeslee J. P., Lucey J. R., Tonry J., 2005, *ApJ*, 625, L103
- Treu T., Koopmans L. V. E., 2004, *ApJ*, 611, 739
- Trott C. M., Webster R. L., 2002, *MNRAS*, 334, 621
- van Albada T. S., Bahcall J. N., Begeman K., Sancisi R., 1985, *ApJ*, 295, 305
- van de Ven G., van Dokkum P. G., Franx M., 2003, *MNRAS*, 344, 924 (Chapter 7)
- van der Marel R. P., 1991, *MNRAS*, 253, 710
- van der Marel R. P., Franx M., 1993, *ApJ*, 407, 525
- van Dokkum P. G., 2001, *PASP*, 113, 1420
- Vazdekis A., Cenarro A. J., Gorgas J., Cardiel N., Peletier R. F., 2003, *MNRAS*, 340, 1317
- Yee H. K. C., 1988, *AJ*, 95, 1331

THE FUNDAMENTAL PLANE AND THE EVOLUTION OF
THE MASS-TO-LIGHT RATIO OF EARLY-TYPE FIELD
GALAXIES UP TO $z \sim 1$

ABSTRACT

We analyze the Fundamental Plane (FP) of 26 strong gravitational lens galaxies with redshifts up to $z \sim 1$, using tabulated data from Kochanek et al. (2000) and Rusin et al. (2003). The lens galaxies effectively form a mass-selected sample of early-type galaxies in environments of relatively low density. We analyze the FP and its evolution in the restframe Johnson B and Gunn r bands. Assuming that early-type galaxies are a homologous family, the FP then provides a direct measurement of the M/L ratio evolution.

If we assume that the M/L ratios of field early-type galaxies evolve as power-laws, we find for the lens galaxies an evolution rate $d \log(M/L)/dz$ of -0.62 ± 0.13 in restframe B and -0.47 ± 0.11 in restframe Gunn r for a flat cosmology with $\Omega_M = 0.3$ and $\Omega_\Lambda = 0.7$. For a Salpeter (1955) Initial Mass Function and Solar metallicity these results correspond to mean stellar formation redshifts of $\langle z_* \rangle = 1.8_{-0.5}^{+1.4}$ and $1.9_{-0.6}^{+1.9}$ respectively. After correction for maximum progenitor bias, van Dokkum & Franx (2001) find a mean stellar formation redshift for cluster galaxies of $\langle z_*^{cl} \rangle = 2.0_{-0.2}^{+0.3}$, which is not significantly different from that found for the lens galaxies. However, if we impose the constraint that lens and cluster galaxies that are of the same age have equal M/L ratios and we do not correct for progenitor bias, the difference is significant and we find that the stellar populations of the lens galaxies are 10–15% younger than those of the cluster galaxies.

We find that both the M/L ratios as well as the restframe colors of the lens galaxies show significant scatter. About half of the lens galaxies are consistent with an old cluster-like stellar populations, but the other galaxies are bluer and best fit by single burst models with younger stellar formation redshifts as low as $z_* \sim 1$. Moreover, the scatter in color is correlated with the scatter in M/L ratio. We interpret this as evidence of a significant age spread among the stellar populations of lens galaxies, whereas the ages of the stellar populations of the cluster galaxies are well approximated by a single formation epoch.

1 INTRODUCTION

ONE of the central problems in astronomy is that of galaxy formation and evolution: when were the visible parts of galaxies assembled and when were the stars formed? The merging of galaxies leads to changes in their masses, and stellar evolution changes their luminosities. The evolution of the mass-to-light (M/L) ratio relates the mass and luminosity evolution.

Galaxy mass measurements are notoriously difficult. Fortunately, empirical relations such as the Tully-Fisher relation for spiral galaxies (Tully & Fisher 1977) and the Fundamental Plane (FP) for early-type galaxies (Dressler et al. 1987; Djorgovski & Davis 1987) can provide us with information on the masses and mass evolution of galaxies. The FP is a tight relation between the structural parameters and velocity dispersion, which under the assumption of homology implies that $M/L \propto M^{\frac{1}{4}}$ with low scatter (Faber et al. 1987). Due to stellar evolution the M/L ratio of a stellar population changes with redshift, and hence also the FP will change. The redshift evolution of the intercept of the FP is proportional to the evolution of the mean M/L ratio. Hence, the tightness of the FP relation makes it a very sensitive indicator of the mean age of the stellar population of early-type galaxies (van Dokkum & Franx 1996).

For cluster galaxies, the M/L ratio evolves very slowly, indicating that the stars were formed at redshifts $z \gtrsim 3$ (e.g., Kelson et al. 1997; Bender et al. 1998; van Dokkum et al. 1998). Current semi-analytical hierarchical models place the assembly time of typical early-type galaxies at much lower redshifts (e.g., Kauffmann 1996; Kauffmann & Charlot 1998; Diaferio et al. 2001). However, in hierarchical galaxy formation models the assembly time and star formation epoch are strongly dependent on the environment, with cluster early-type galaxies forming much earlier than those in the general field (e.g., Kauffmann 1996). Hence cluster early-type galaxies do not provide the most stringent tests of these models. Moreover, the measured evolution of early-type galaxies may underestimate the true evolution because of the effects of morphological evolution. If many early-type galaxies evolved from late-type galaxies at $z \lesssim 1$, the sample of early-type galaxies at high redshift is only a subset of all progenitors of present-day early-type galaxies. This would lead us to underestimate the luminosity evolution, and hence overestimate the stellar formation redshift (see van Dokkum & Franx 2001, hereafter vDF01).

Recent studies have started to explore the FP and M/L ratios of high redshift early-type galaxies in the general field. Interestingly, the FP of field early-type galaxies appears to be quite similar to that of cluster early-type galaxies out to $z \approx 0.55$ (Treu et al. 2001; van Dokkum et al. 2001), in apparent conflict with current semi-analytical models (see van Dokkum et al. 2001). However, there are indications for a significant offset between the two populations at higher redshift (Treu et al. 2002). Kochanek et al. (2000, hereafter K00) analyzed the FP and color evolution of strong gravitational lens galaxies up to $z \sim 1$. The lensing cross section is dominated by galaxies with high central velocity dispersions, and the lens galaxies effectively provide a mass-selected sample of field early-type galaxies which can be compared to optically selected samples of field and cluster galaxies. The mass-selection is important because it limits Malmquist-type biases, and it is much less sensitive to selection effects caused by morphological evolution. K00 find that the stars constituting the lens galaxies must have formed at $z \gtrsim 2$ for a flat cosmology with $\Omega_M = 0.3$ and $\Omega_\Lambda = 0.7$, and conclude that there are no significant differences between field and cluster early-type galaxies.

K00 analyze the evolution of the FP in the observed photometric bands, and their modeling necessarily includes the large variation in observed magnitudes and colors due to redshift (the “K”-correction). This complicates the measurement of the smaller effect due to evolution of (the stellar populations of) the lens galaxies. Rusin et al. (2003, hereafter R03) study the same sample of lens galaxies, with recent photometric observations included. They convert the data from observed filters into magnitudes in standard restframe bands, so that the evolution of the M/L ratio that follows from the FP (under the usual assumption that early-type galaxies are a homologous family) can be investigated instead of the evolution within the FP. This clarifies the analysis and allows for direct comparison of the results with those of other FP studies. From their M/L evolution analysis R03 find a (2σ) lower limit $z > 1.8$ for the formation of the stars in lens galaxies. Although this limit is more precise, it is similar to that of K00. Hence, R03 also conclude that the evolution measurements favor old stellar populations among field galaxies, like those of cluster galaxies, and argue against significant episodes of star formation at $z < 1$, as predicted by the semi-analytical hierarchical models.

For the analysis in this chapter we use the tabulated data of K00, extended with the recent photometric measurements as given by R03. We convert the observed surface brightnesses and colors to the restframe Johnson B and Gunn r bands. Our transformation to restframe differs from that of R03. In both approaches the modeled color between restframe band and observed filter is used to convert the observed magnitude into an estimate of the restframe magnitude. R03 obtain the modeled color for a given spectral energy distribution, whereas we use the observed color between a pair of filters to interpolate between the modeled colors for four different spectral types (Fig. 1). Moreover, while R03 use the (weighted) contribution of all observed magnitudes to determine the restframe magnitude, we select the best one with small observational error and filter close to the (redshifted) restframe band. Hence, the model dependence of our correction is small and we exclude observed magnitudes with large uncertainties, minimizing the error in the resulting restframe magnitude. We analyze the M/L evolution of the lens galaxies and compare our results with those of R03 and with results from previous studies. Additionally, we test whether age differences between the lens galaxies are significant. To this end, we study the scatter in both the M/L evolution and the restframe colors of the lens galaxies, and investigate whether the deviations are correlated.

This chapter is organized as follows. In Section 2 we determine the FP parameters, using the lensing geometry to estimate the velocity dispersion. The transformation from observed to restframe bands is described in Section 3. In Section 4, we construct the FP of the lens galaxies and present the M/L evolution derived from the FP. We estimate the age of the stellar populations of the lens galaxies by fitting single burst models to the M/L evolution in Section 5. In Section 6 we study the colors of the lens galaxies. The results are summarized and discussed in Section 7. Unless stated otherwise we assume $H_0 = 50 \text{ km s}^{-1} \text{ Mpc}^{-1}$ and a flat cosmology with $\Omega_M = 0.3$ and $\Omega_\Lambda = 0.7$. We note that our results are not dependent on the value of the Hubble constant.

2 FP PARAMETERS

The study of the FP of strong gravitational lens galaxies differs in two important aspects from that of cluster galaxies. First, the lens galaxies are individual galaxies

Name Lens	z	σ_c (km s^{-1})	σ_{c*} (km s^{-1})	r_e (kpc)	$\mu_{e,Bz}$ (mag arcsec^{-2})	$\mu_{e,rz}$
0047-2808	0.49	254 ± 26	229 ± 15	7.7 ± 0.7	21.79 ± 0.16	21.11 ± 0.28
Q0142-100	0.49	224 ± 22		4.3 ± 0.2	20.42 ± 0.05	19.64 ± 0.05
MG0414+0534	0.96	303 ± 30		8.6 ± 1.6	21.07 ± 0.17	19.97 ± 0.16
B0712+472	0.41	181 ± 18		2.8 ± 0.4	20.67 ± 0.17	19.60 ± 0.16
RXJ0911+0551	0.77	260 ± 26		7.0 ± 0.6	21.74 ± 0.17	20.75 ± 0.14
FBQ0951+2635	0.24	128 ± 13		0.9 ± 0.2	19.82 ± 0.25	19.05 ± 0.25
BRI0952-0115	0.41	117 ± 12		0.8 ± 0.2	20.00 ± 0.21	18.61 ± 0.20
Q0957+561	0.36	431 ± 43	305 ± 11	14.1 ± 1.3	22.48 ± 0.12	21.45 ± 0.11
LBQS1009-0252	0.88	198 ± 21		1.9 ± 0.3	19.81 ± 0.14	18.90 ± 0.13
Q1017-207	0.78	151 ± 16		3.1 ± 0.1	21.28 ± 0.49	20.28 ± 0.07
FSC10214+4724	0.75	241 ± 26		11.8 ± 5.2	22.97 ± 0.44	22.03 ± 0.56
B1030+074	0.60	218 ± 22		4.2 ± 0.6	21.38 ± 0.14	20.14 ± 0.25
HE1104-1805	0.73	316 ± 32		6.4 ± 1.9	21.34 ± 0.33	20.22 ± 0.30
PG1115+080	0.31	210 ± 21	288 ± 27	3.0 ± 0.1	21.23 ± 0.06	20.01 ± 0.05
HST14113+5211	0.46	190 ± 19		3.8 ± 0.4	21.70 ± 0.09	20.72 ± 0.11
HST14176+5226	0.81	292 ± 29	230 ± 14	7.5 ± 0.9	20.98 ± 0.15	20.35 ± 0.12
B1422+231	0.34	160 ± 16		2.1 ± 0.6	21.18 ± 0.25	19.93 ± 0.24
SBS1520+530	0.72	220 ± 22		3.5 ± 0.3	20.13 ± 0.17	19.36 ± 0.08
MG1549+3047	0.11	188 ± 19	242 ± 20	2.3 ± 0.2	21.39 ± 0.09	20.12 ± 0.09
B1608+656	0.63	292 ± 29		6.2 ± 1.0	20.68 ± 0.19	19.88 ± 0.15
MG1654+1346	0.25	206 ± 21		4.9 ± 0.1	21.99 ± 0.07	20.73 ± 0.05
MG2016+112	1.00	299 ± 30	328 ± 32	2.5 ± 0.3	19.22 ± 0.10	18.06 ± 0.10
B2045+265	0.87	378 ± 38		4.1 ± 1.3	20.50 ± 0.44	19.41 ± 0.30
HE2149-2745	0.50	203 ± 20		4.3 ± 0.4	20.92 ± 0.12	20.36 ± 0.12
Q2237+030	0.04	168 ± 17	220 ± 31	4.3 ± 0.8	22.37 ± 0.50	21.15 ± 0.23
HS0818+1227	0.39	251 ± 25		6.6 ± 0.2	22.18 ± 0.07	21.13 ± 0.04

TABLE 1 — FP parameters of 26 strong gravitational lens galaxies with redshifts up to $z \sim 1$. For 5 lens galaxies the redshift is not known spectroscopically, and a photometrically estimated value (in italics) is given. The velocity dispersion σ_c , within the standard aperture with a diameter of $3''.4$ at the distance of the Coma cluster, follows from the lensing geometry, assuming a singular isothermal sphere mass model and a Hernquist (1990) luminosity profile. The velocity dispersion from stellar kinematics σ_* has been measured for 7 lens galaxies (references in text). The effective radius r_e and effective surface brightness μ_e follow from fits to an $r^{1/4}$ law. To allow a direct comparison with the local FP, the effective surface brightness has been corrected to the restframe Johnson B and Gunn r band by interpolating between filters.

spread over a large range in redshifts, instead of an ensemble of galaxies at the same redshift. Additionally, whereas studies of the FP of optically selected galaxies measure velocity dispersions from spectra, for lens galaxies we use the lensing geometry to estimate this quantity. The separation between lensed images of background sources increases with the mass of the lens and is therefore a measure of the velocity dispersion. The two remaining FP parameters, the effective radius and surface brightness, are determined from surface photometry as for cluster galaxies.

2.1 VELOCITY DISPERSION

For a singular isothermal sphere (SIS) mass model the relation between the velocity dispersion of the matter distribution and the separation of the source images $\Delta\theta$ is $\Delta\theta = 8\pi(\sigma_D/c)^2 D_{LS}/D_{OS}$. Here, D_{LS} and D_{OS} are the angular diameter distances from the lens galaxy to the source and from the observer to the source. To determine these values, the redshifts of both the lens galaxy and the source are needed (e.g., Hogg 2000). If the redshift of a lens galaxy is not known spectroscopically, we adopt a photometrically estimated value¹ with a 10% uncertainty. The lens systems for which no redshift is known for the source, we exclude from our analysis. This leaves a total of 26 lens galaxies, of which 5 have a redshift that is estimated photometrically (Table 1). The velocity dispersion σ_D depends also (weakly) on cosmology through the angular diameter distances, but is independent of the value of the Hubble constant since the distances appear as a ratio.

The velocity dispersion σ_D is that of the total matter distribution, including possible dark matter, rather than the central velocity dispersion of the stellar component σ_c . For a given mass and luminosity distribution, the ratio $g \equiv \sigma_c/\sigma_D$ can be modeled by solving the single Jeans equation for a spherical system with $\sigma_\phi = \sigma_\theta$ and $\beta = 1 - \sigma_\theta^2/\sigma_r^2$ the anisotropy parameter (e.g., Binney & Tremaine 1987). The overall mass distribution is assumed to be isothermal. We model the luminosity distribution by a Hernquist (1990) profile with characteristic radius $a = r_e/1.8153$. For each lens galaxy with effective radius r_e in kpc (see Section 2.2), we integrate the resulting line of sight velocity dispersion within the Coma aperture to obtain an estimate for g , so that the stellar velocity dispersion follows as $\sigma_c = g\sigma_D$.

For the sample of 26 lens galaxies, σ_D is distributed with a (biweight²) mean of 230 km s⁻¹ and a (biweight) standard deviation of 61 km s⁻¹. In the case of an isotropic system ($\beta = 0$), the estimated stellar velocity dispersion σ_c has a mean of 223 km s⁻¹ and a standard deviation of 70 km s⁻¹. Hence, the properties of the sample of lens galaxies will be typical for early-type field galaxies close to L^* , which have a characteristic velocity dispersion around 225 km s⁻¹ (e.g., Kochanek 1994, 1996).

Several sources contribute to the uncertainty in σ_c . We account for the scatter in the image separation $\Delta\theta$, which is small and set to 2%. The error in the effective radius r_e (Table 1) contributes through the modeled ratio g . For those galaxies for which only a photometric estimate of the lens redshift z_l is available, we included an error of 10%. Since the angular diameter distance depends on redshift this error also contributes to the uncertainty in σ_c via the determination of σ_D and via the conversion of the effective radius in arcseconds into physical units of kpc. Apart from these errors in observational parameters, we want to take into account that we have made several assumptions in the modeling of the ratio g . For the 26 lens galaxies, the distribution of g has a mean of 0.90, 0.94 and 1.01 for an anisotropy parameter β of -0.5, 0 and 0.5 respectively. For each lens galaxy we apply the isotropic case $\beta = 0$, but to take the variation of g with β into account, together with the assumption of a SIS mass model and a Hernquist profile, we assume an additional error of 10% in g and hence in σ_c .

¹Obtained from the CfA-Arizona Space Telescope Lens Survey (CASTLES) web site at <http://cfa-www.harvard.edu/castles/>

²Throughout this chapter we use the biweight location and scale as estimators of the mean and standard deviation (rms) respectively. These estimators are robust for a broad range of non-Gaussian underlying populations and are less sensitive to outliers than standard estimators (e.g., Andrews et al. 1972; Beers, Flynn & Gebhardt 1990).

For 7 out of the 26 lens galaxies presented in this chapter, a velocity dispersion measured from stellar kinematics σ_{c^*} is available: 0047-2808 (Koopmans & Treu 2003), Q0957+561 (Tonry & Franx 1999; Falco et al. 1997; Rhee 1991), PG1115+080 (Tonry 1998), HST14176+5226 (Ohyama et al. 2002), MG1549+3047 (Lehár et al. 1996), MG2016+112 (Koopmans & Treu 2002) and Q2237+030 (Foltz et al. 1992). Comparing the measured velocity dispersions (Table 1) with the modeled σ_c from the lensing geometry, we find for these 7 galaxies that the ratio σ_{c^*}/σ_c is distributed with a mean of 1.07 and dispersion of 0.27. For the sample of 7 lens galaxies both methods are consistent. Due to peculiarities of the lensing system, such as the contamination of Q0957+561 by the mass distribution of the underlying cluster, the velocity dispersion from both methods can be significantly different for individual lens galaxies.

2.2 EFFECTIVE RADIUS AND SURFACE BRIGHTNESS

The lensing systems were observed with the WFPC2, NICMOS1 and NICMOS2 camera on the HST, in filters ranging from the visual F555W through the infrared F205W filter. For each system, the image with optimal contrast between the lens galaxy and the images of the background source is selected, and the effective radius r_e and the mean surface brightness within the effective radius $\langle\mu_e\rangle$ from fits to an $r^{1/4}$ law is determined. The data and model fits are described in detail by Lehár et al. (2000) and K00. Note that r_e depends slightly on cosmology due to the conversion of the effective radius from units of arcseconds from the fit into physical units of kpc. Moreover, since the lens redshift is used in the conversion, we have to take into account a (small) additional contribution to the uncertainty in r_e due to the assumed 10% error in the lens redshift in the case it is estimated photometrically (see also Section 2.1).

Here, we use the surface brightness at the effective radius μ_e (in mag arcsec⁻²), which is related to $\langle\mu_e\rangle$ by $\mu_e - \langle\mu_e\rangle = 1.393$. We also define $I_e \equiv 10^{-\mu_e/2.5}$. In the following, we refer to the filter in which the fit was made as the reference filter. The dependence of effective radius on passband due to color gradients can be ignored because of the strong correlation between μ_e and r_e (see Section 4), and we can use the observed colors (tabulated by K00) to calculate the effective surface brightness in each filter.

The effective surface brightnesses and colors are corrected for Galactic extinction with an $R_V \equiv A(V)/E(B - V) \approx 3.1$ extinction curve for a diffuse stellar medium (e.g., Cardelli, Clayton & Mathis 1989; O'Donnell 1994). The galactic extinction $E(B - V)$ is obtained from Schlegel, Finkbeiner & Davis (1998). Extinction corrections on the effective surface brightness are typically ~ 0.03 magnitudes in the reference filter, which in most cases is the F160W filter. The three galaxies MG0414+0534, MG2016+112 and B2045+265 are exceptions with significantly higher galactic extinction of 0.18, 0.14 and 0.14 magnitudes respectively.

3 TRANSFORMATION TO RESTFRAME

In order to compare the FP of the redshifted lens galaxies directly to the FP of the Coma cluster at $z = 0.023$, we calculate the effective surface brightness of the lens galaxies in restframe Johnson B band and restframe Gunn r band by interpolating between filters.

In the following example we assume that the redshifted r band falls between the WFPC2 F555W (=V) and F814W (=I) filters and the effective surface brightness is determined in the NICMOS F160W (=H) reference filter. We assume a linear relation

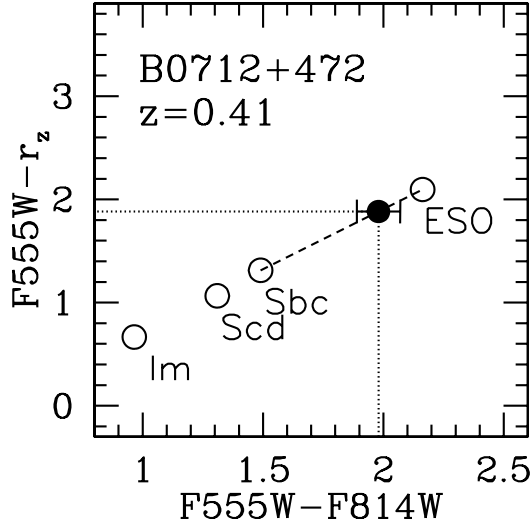


FIGURE 1 — Transformation to restframe r band by interpolation between the $F555W$ ($=V$) and $F814W$ ($=I$) filter. For four spectral types the $V - I$ and $V - r_z$ colors are modeled (open circles). With the observed $V - I$ color of the lens galaxy (filled circle) we interpolate between the modeled colors of the two nearest spectral types, to find the $V - r_z$ color of the lens galaxy.

between the AB magnitudes of the redshifted r filter and the V and I filter, so that for the restframe r magnitude of a galaxy at redshift z we can write

$$r_z = V - \alpha(V - I) - \alpha(c_V - c_I) + c_V - c_r + 2.5 \log(1 + z). \quad (3.1)$$

The constants c are the conversion constants between the standard Vega magnitudes and AB magnitudes

$$c = 2.5 \log \left(\frac{\int_0^\infty T(\nu) f_\nu^{\text{Vega}} d\nu}{\int_0^\infty T(\nu) d\nu} \right) - 48.60, \quad (3.2)$$

with f_ν^{Vega} the fluxdensity of Vega, and $T(\nu)$ the filter transmission. The transmission curves of the HST filters (including the CCD response) were obtained from STSCI³, and those of the B and r passbands were obtained from Bessel (1990) and Thuan & Gunn (1976) respectively. We used the CALCPHOT task of the STSDAS package in IRAF to calculate the conversion constants for the HST filters. The conversion constants for the B and r passband follow from Bessel (1990) and Frei & Gunn (1994) respectively. The last term in (3.1) includes the broadening of the r band with redshift and makes the magnitude behave as if it is a flux, rather than a fluxdensity.

Eq. (3.1) relates the $V - r_z$ color of a lens galaxy to its observed $V - I$ color. To determine α , we model the $V - I$ and $V - r_z$ colors for four different spectral types, E/S0, Sbc, Scd and Im, using the spectral energy distribution of Coleman, Wu & Weedman (1980). This gives four estimates of α . Using the observed $V - I$ color of the lens galaxy we interpolate linearly between the modeled colors of the two nearest spectral types (Fig. 1). In this way we obtain the best-fit $V - r_z$ color and corresponding value of α for the lens galaxy. To estimate the uncertainty in the conversion constants we compare modeled colors with those predicted by Frei & Gunn (1994). We find that the differences are small and estimate the uncertainty at 0.02 magnitudes.

³<http://www.stsci.edu/instruments/observatory/cdbs/cdbs.html>

The observed $V - H$ color is then used to relate the effective surface brightness in the reference H filter to that of the restframe r band

$$\mu_{e,r_z} = \mu_{e,H} + (V - H) - (V - r_z). \quad (3.3)$$

Similar transformations are derived for each lensing system. In cases where observations are available in more than two passbands, we calculate μ_{e,r_z} for all filter combinations and make a selection based on the following criteria: the error in μ_{e,r_z} , the wavelength difference between the redshifted r band and the observed filter, and a preference for filter pairs enclosing the redshifted r band. The latter implies an interpolation between two filters, whereas otherwise we have to extrapolate. As byproducts of our procedure we find the SEDs that provide the best fits to the observed colors of the lens galaxies. For the restframe B and r band this yields respectively 20 (77%) and 19 (73%) lens galaxies that are best fitted by the E/S0 spectral type, whereas the colors of the remaining lens galaxies are closest to the Sbc spectral type.

Since r_z in (3.1) behaves like a flux, the effective surface brightness decreases as $(1+z)^4$ with increasing redshift⁴. We correct the surface brightnesses for this cosmological dimming. For the 26 lens galaxies, the resulting values for the restframe Johnson B and Gunn r effective surface brightness μ_{e,B_z} and μ_{e,r_z} are given in Table 1, together with the other two FP parameters; the central stellar velocity dispersion σ_c and effective radius r_e . We have also included the redshift z of the lens galaxies and the velocity dispersions measured from stellar kinematics $\sigma_{c\star}$ when available.

4 FP AND M/L EVOLUTION

The Fundamental Plane has the form

$$\log r_e = \alpha \log \sigma_c + \beta \log I_e + \gamma \quad (4.1)$$

(Dressler et al. 1987; Djorgovski & Davis 1987), with r_e in kpc, σ_c in km s^{-1} and μ_e ($= -2.5 \log I_e$) in mag arcsec^{-2} . We adopt for the coefficients α and β the values derived by Jørgensen, Franx & Kjaergaard (1996) for a sample of 225 early-type galaxies in nearby clusters. They found for the Johnson B band $\alpha = 1.20 \pm 0.06$ and $\beta = -0.83 \pm 0.02$, and for the Gunn r band $\alpha = 1.24 \pm 0.07$ and $\beta = -0.82 \pm 0.02$.

We use the tabulated photometric and spectroscopic data of Jørgensen, Franx & Kjaergaard (1995a, 1995b) to construct the FP of Coma. The edge-on projection of the Coma FP in the r band is shown in Fig. 2 (small dots). A linear fit to the Coma FP yields an intercept of 9.50 ± 0.02 and 9.12 ± 0.02 for the B and r band respectively. Large symbols show the lens galaxies. The lens galaxies show a large scatter, and are offset with respect to the FP of Coma. This relative difference can be attributed to the evolution of the M/L ratios of galaxies, and the large scatter may in part be caused by the large range of redshifts spanned by the lens sample.

As usual in FP evolution studies, we assume that early-type galaxies are a homologous family, i.e. that they are structurally similar. The total mass of a galaxy (including possible dark matter) is then proportional to an effective mass $\propto \sigma_c^2 r_e$. With the total luminosity proportional to $I_e r_e^2$, the FP relation implies that the effective mass-to-light ratio $M/L \propto M^{0.24} r_e^{-0.02}$ in the r band (e.g., Treu et al. 2001). The tightness of the FP relation implies a low scatter in the M/L ratios of early-type galaxies

⁴The restframe r_z magnitude (3.1) behaves therefore as a K -corrected magnitude.

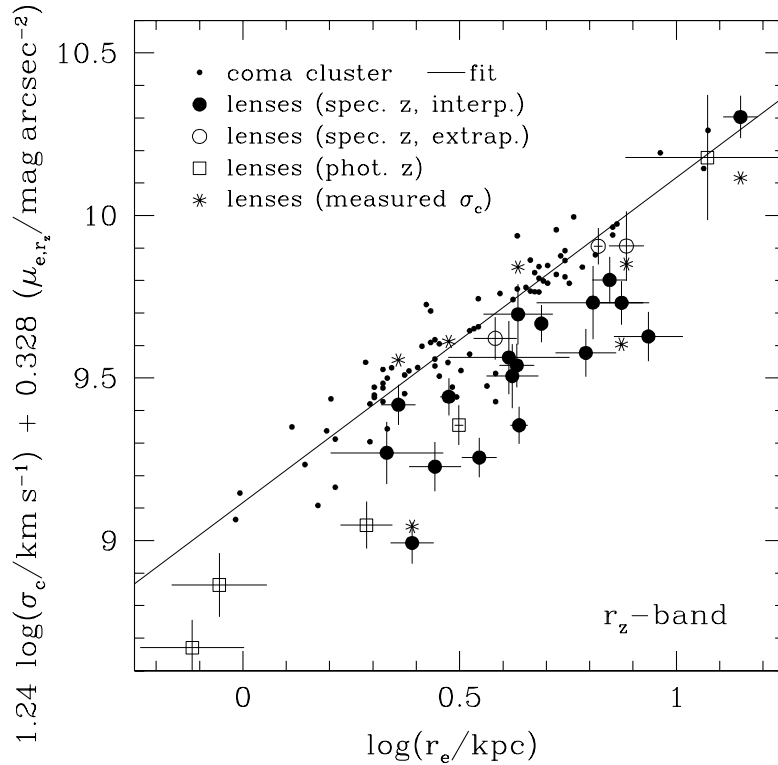


FIGURE 2 — Edge-on view of the FP in the restframe Gunn r band. The Coma cluster galaxies (small dots) and corresponding linear fit represent the local FP (Jørgensen et al. 1995a, 1995b, 1996). Lens galaxies for which the redshifts are known spectroscopically are indicated with circles. Filled circles correspond to lens galaxies for which the transformation to restframe (Section 3) was by interpolation between a pair of filters, and open circles if a modest extrapolation was needed. The open squares represent the 5 lens galaxies with a redshift that is estimated photometrically (Table 1). The transformation to restframe for these 5 galaxies was by interpolation. For 7 lens galaxies, velocity dispersions have been measured from stellar kinematics (see text for details). Asterisks show the position of these galaxies in the FP if the stellar velocity dispersion is used. The lens galaxies are offset from the Coma FP, as expected from evolution of their stellar populations.

of 23% (Faber et al. 1987; Jørgensen et al. 1996). Hence, the evolution of M/L can be well studied via the evolution of the FP.

We assume that all early-type galaxies evolve in the same way, i.e. the coefficients α and β are independent of redshift and the same for cluster and field early-type galaxies. Until now there is no convincing (observational) evidence against these assumptions, but this might change if more and deeper data become available (e.g., van Dokkum & Franx 1996; van Dokkum et al. 2001; Treu et al. 2002). If furthermore the effective radius and velocity dispersion do not change with redshift, the difference in FP intercept is due to a difference in surface brightness caused by luminosity evolution. As a result, the evolution of the intercept of the FP is proportional to the evolution of the mean M/L ratio. For each lens galaxy, the difference in FP intercept with respect to the Coma FP (Fig. 2) can be expressed as an offset in its M/L ratio relative to that of a galaxy of the same mass in Coma. Fig. 3 (two left panels) shows

the dependence of the M/L offset on redshift, in the restframe r band. The M/L ratio of lens galaxies clearly shows a trend with redshift, with the highest redshift objects having the lowest M/L ratios.

From a linear fit to the M/L ratios of the 26 lens galaxies, we find an evolution rate $d \log(M/L)/dz$ of -0.62 ± 0.13 and -0.47 ± 0.11 in restframe B and r band respectively. The intercept of the fit, $\Delta \log M/L$ at $z = 0$, is -0.01 ± 0.08 and -0.01 ± 0.06 respectively, so that locally there is no significant offset in the mean M/L ratio of the lens and cluster galaxies. If this offset is forced to be zero, we find best-fit evolution rates for the B and r band of -0.63 ± 0.06 and -0.49 ± 0.05 , which are only slightly higher than for the unconstrained fit. (The 1σ errors from the fit are smaller than for the unconstrained fit since only the slope is a fitting parameter, while the intercept is fixed to zero.) Restricting the fit to only the 21 lens galaxies with spectroscopic redshifts, has no significant effect on the results. Similarly, we find no significant differences if we exclude the lens galaxies from the fit for which a modest extrapolation was needed in the transformation to restframe band; or if for the 7 lens galaxies for which the velocity dispersion σ_{c*} measured from stellar kinematics is available, this value is used instead of the modeled σ_c from the lensing geometry.

For cluster galaxies van Dokkum et al. (1998) find in the B band an evolution rate $d \log(M/L)/dz = -0.49 \pm 0.05$. This means on average a faster evolution for the lens galaxies, but the difference is only significant if the M/L ratio of lens galaxies is forced to coincide with that of cluster galaxies at $z = 0$. The value for the cluster evolution rate by van Dokkum et al. (1998) does not take into account possible effects due to morphological evolution. If early-type galaxies were transformed from late-type galaxies at modest redshifts (e.g., Dressler et al. 1997) the early-type galaxies that were already present at high redshift are only a subset of all progenitors of low redshift early-type galaxies. As a result of this ‘‘progenitor bias’’ (vDF01) the formation redshift of morphologically selected cluster early-type galaxies may be overestimated. The lens galaxy sample is probably much less affected by progenitor bias, since they are selected on mass and not on morphology, but due to the merging of galaxies, a fraction of the progenitors may still not be accounted for. After applying the maximum correction for progenitor bias allowed by the data, vDF01 find a cluster evolution rate of $d \log(M/L)/dz = -0.56 \pm 0.05$ in the B band, similar to the evolution rate for the lens galaxies. These results suggest that, if there is no progenitor bias, field galaxies may be younger than cluster galaxies, but that such an age difference becomes less significant if we correct for possible progenitor bias.

Our results are consistent with determinations for field galaxies based on direct spectroscopic measurements of the velocity dispersions. For the B band, van Dokkum et al. (2001) arrive at an evolution rate $d \log(M/L)/dz$ of -0.59 ± 0.15 , and Treu et al. (2002) find a value of $-0.72^{+0.11}_{-0.16}$. Comparing our results for the B band with those of R03, we find that the evolution rate obtained by R03 is on average slower, but the (1σ) confidence limits still overlap. For intercepts that are allowed to vary and forced to be zero, R03 find an evolution rate of -0.54 ± 0.09 and -0.56 ± 0.04 respectively.

The error analysis and the transformation to restframe of R03 differs from ours (see also Section 1), but we cannot further investigate the effects of these differences, as R03 do not give their resulting fundamental plane parameters. However, if we add (in quadrature) an constant additional error to the observed uncertainties in the M/L ratios of the lens galaxies, the slope of the fit does decrease. Around the linear fit we

measure a (biweight) scatter of 0.17 for the B band and 0.15 for the r band⁵, which in both cases is higher than the expected scatter from the observational errors of 0.12. If we now take for the constant additional scatter the difference (in quadrature) between the measured and expected scatter, we find for the unconstrained fit in the B band an evolution rate of -0.56 ± 0.12 , almost identical to the result of R03. If the offset is forced to zero the slope changes less, giving an evolution rate of -0.61 ± 0.05 . Note that R03 rescale their input errors so that the best-fit model has a reduced χ^2 of one. They assume that the additional scatter is due to underestimated errors in the data set, whereas we propose that internal population differences cause the additional scatter. Hence, we multiply our results with the square root of the reduced χ^2 to reflect this aspect, but we do not change the uncertainties on the input data.

The additional scatter implies that the M/L ratios of the lens galaxies are not well fitted with a single evolution rate, whereas for the cluster galaxies the fit is very good (e.g., van Dokkum et al. 1998). This may be due to a significant spread in stellar population ages among field galaxies, which induces an additional scatter measured in the evolution rate $d \log(M/L)/dz$ of the lens galaxies. In the next Section, we relate the M/L evolution to stellar population ages by fitting simple single burst models. In Section 6, we then study the restframe colors of lens galaxies and their evolution. To find out whether there is a significant age spread, we also investigate scatter in color and if it is correlated with the scatter in M/L ratio.

5 STELLAR POPULATION AGES

The evolution of the M/L ratio depends on the age of the stellar population. A stellar population which formed at low redshift will evolve faster than a population formed at high redshift: the luminosity of a young population becomes rapidly fainter when short-lived massive and bright stars disappear, whereas the dimming of the light is more gradual for an old population dominated by low mass stars. We estimate the stellar population ages of lens galaxies and the age difference between lens and cluster galaxies by fitting simple single burst models to the M/L evolution.

The M/L ratio of a single burst stellar population with fixed mass evolves as

$$M/L \propto (t - t_*)^\kappa, \quad (5.1)$$

with t_* the stellar formation time, corresponding to a stellar formation redshift z_* (e.g., Tinsley & Gunn 1976). The coefficient κ depends on the Initial Mass Function (IMF) and metallicity, and also on the passband in which the luminosity is measured. For a normal IMF with Salpeter (1955) slope and Solar metallicity, $\kappa_B \approx 0.93$ and $\kappa_r \approx 0.78$ for the restframe B and r bands (Worthey 1994). Note that the predicted evolution is independent of H_0 because the age dependence of the M/L ratio is a power-law.

We first investigate if we can fit the observed M/L evolution of the lens galaxies by a single burst evolution model with the same stellar formation redshift z_* as has been derived previously for cluster galaxies (the null-hypothesis). In Section 5.2 and 5.3 we investigate the range of z_* allowed by the data.

⁵The scatter in the B band is probably higher than in the r band due to the fact that the B band is more sensitive to recent star formation.

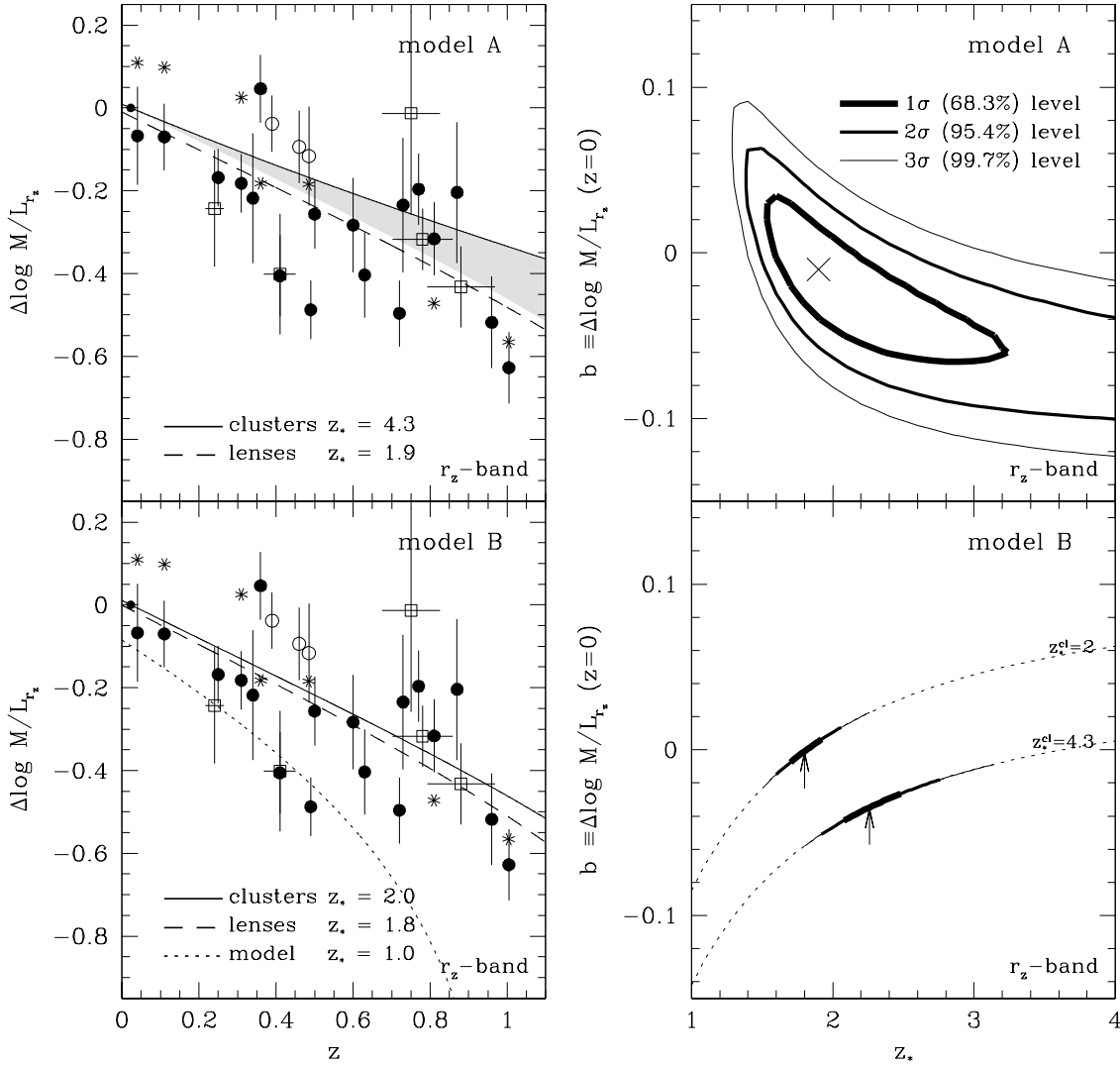


FIGURE 3 — UPPER-LEFT: The evolution of the M/L offset in the restframe Gunn r band. The small dot is the average M/L of the Coma galaxies. The lens galaxies are indicated with the same symbols as in Fig. 2. The solid line represents the single burst evolution of a stellar population formed at the mean cluster formation redshift of $z_* = 4.3$. If we correct for progenitor bias, the latter formation redshift will be lower, and hence the evolution steeper. This is indicated by the shaded region, with $z_* = 2.0$ for maximum progenitor bias correction (vdF01). The dashed line is the best fit model for the lens galaxies, with $z_* = 1.9$ and zeropoint $b \equiv \Delta \log M/L_{r_z}(z=0) = -0.01$. UPPER-RIGHT: Confidence levels (1, 2 and 3σ) for combinations of z_* and the zeropoint b when they are both allowed to vary. LOWER-LEFT: The solid line shows the evolution for a stellar population formed at $z_* = 2.0$, which is the mean cluster value after maximum progenitor bias correction. The dashed line is the model for a stellar population formed at the best-fitting star formation redshift of $z_* = 1.8$, if the lens and cluster galaxies are fitted in a self-consistent way (model B). To illustrate the effect of changing z_* we also show a model with $z_* = 1$ (dotted line). LOWER-RIGHT: Because cluster and lens galaxies are modeled self-consistently, the stellar formation redshift of the lens galaxies depends on that of the clusters z_*^{cl} . The best-fit values vary from 1.8 to 2.3 (indicated by arrows) if z_*^{cl} is increased from 2.0 to 4.3, the values for maximum and no progenitor bias correction. The errors on the best-fit parameters from the confidence levels are multiplied with the square root of the reduced χ^2 of the fit, to reflect the measured additional scatter compared to the expected scatter from the observational errors (see text and Table 2 for resulting uncertainties on b and z_*).

5.1 CAN CLUSTER GALAXIES AND LENS GALAXIES HAVE THE SAME AGE?

Before investigating more complex models we consider the case that lens galaxies and cluster galaxies have the same luminosity weighted stellar age. To determine the mean stellar formation redshift of cluster early-type galaxies $\langle z_{\star}^{cl} \rangle$ we fit a single burst model (5.1) to previously published restframe B band data for the clusters CL1358+62 (Kelson et al. 1997), CL0024+16 (van Dokkum & Franx 1996), MS2053+03 (Kelson et al. 1997) and MS1054-03 (van Dokkum et al. 1998) at redshifts 0.33, 0.39, 0.58 and 0.83, respectively, normalized with respect to the average M/L_B ratio of the local Coma cluster at $z = 0.023$ (Jørgensen et al. 1996).

To perform such a single burst fit, we minimize

$$\chi^2 = \sum_{i=1}^n \left(\frac{M/L_{\text{mod},i} - M/L_{\text{obs},i}}{\sigma(M/L_{\text{obs},i})} \right)^2, \quad (5.2)$$

with n the number of M/L observations used as constraints, $M/L_{\text{obs},i}$ the i th observation, $M/L_{\text{mod},i}$ the corresponding single burst prediction and $\sigma(M/L_{\text{obs},i})$ the uncertainty or error in this observation. To determine the confidence levels, we calculate the difference in χ^2 between a model and the overall minimum, $\Delta\chi^2 = \chi^2 - \chi_{\text{min}}^2$, to which the usual Gaussian confidence levels can be assigned (e.g., Press et al. 1992).

The resulting best-fit mean formation redshift $\langle z_{\star}^{cl} \rangle = 4.3_{-1.2}^{+3.7}$. This direct fit does not take into account possible progenitor bias. After applying the maximum correction for progenitor bias allowed by the data, vDF01 find $\langle z_{\star}^{cl} \rangle = 2.0_{-0.2}^{+0.3}$ for cluster galaxies. Therefore, we consider $2.0 < z_{\star}^{cl} < 4.3$ as a plausible range for the mean star formation epoch of cluster early-type galaxies.

We fitted single burst models with this range of formation redshifts to the restframe B and r band data of the lens galaxies. The fits improve towards higher formation epoch, but even those with maximum progenitor bias correction are rejected with nearly 100%. We can allow for an offset between M/L ratios of lens galaxies and those of cluster galaxies. We will describe this offset with the value of $\Delta \log M/L$ at $z = 0$, which we denote by b . For a stellar formation epoch ranging from 4.3 to 2.0 (no to maximum progenitor bias correction) the offset b varies from -0.12 to -0.06 for the B band, and from -0.08 to -0.03 for the r band. These models with a systematic offset fit the lens data better, but are still rejected with $> 99.9\%$ confidence.

5.2 MODEL A: UNCONSTRAINED FIT

We assume that the M/L ratios of field galaxies are independent of those of cluster galaxies, i.e. a cluster galaxy of a given age can have a very different M/L ratio than a field galaxy of the same age. This may be the case if, e.g., the metallicities of field and cluster galaxies are different at a given mass. In addition to the stellar formation redshift z_{\star} , we also have the normalization of the single burst model as free parameter. We describe this second parameter with b (see Section 5.1).

For a range of z_{\star} and b values, we fit single burst models the observed M/L values of the redshifted lens galaxies. For the r band, the 1, 2 and 3 σ limits on z_{\star} and b are shown in the upper-right panel of Fig. 3, with the minimum indicated by a cross. The best-fit values of z_{\star} and b are $1.8_{-0.5}^{+1.4}$ and -0.03 ± 0.09 for the B band, and $1.9_{-0.6}^{+1.9}$ and -0.01 ± 0.07 for the r band (Table 2). Note that the given uncertainties are 1σ errors unless noted. The M/L_r evolution that corresponds to the best-fit values is shown in the upper-left panel of Fig.3 (dashed line). Since for both B and r band the

model	B_z band	r_z band
A	1.8 (-0.5/+1.4)	1.9 (-0.6/+1.9)
B (with $z_*^{cl} = 2.0$)	1.7 (-0.1/+0.2)	1.8 (-0.2/+0.2)
B (with $z_*^{cl} = 4.3$)	2.1 (-0.2/+0.3)	2.3 (-0.3/+0.3)

TABLE 2 — The mean formation redshift $\langle z_* \rangle$ of a single burst stellar population for lens galaxies (1σ errors). Models as in Fig. 3 (see text for further details).

model parameter b is not significantly different from zero, we obtain similar best-fit values for z_* if we normalize the single burst model such that $b \equiv 0$, i.e. if we assume that locally the average M/L ratio of field and cluster galaxies is the same.

5.3 MODEL B: SIMULTANEOUS FIT TO LENS AND CLUSTER GALAXIES

Here we assume that the stellar populations of field and cluster galaxies evolve in the same way. The stellar populations of the lens galaxies may form at a different redshift than those of the cluster galaxies, but galaxies of a given age have identical M/L ratios. For the formation redshift of the stars in cluster galaxies we use the values that we obtained in Section 5.1: $z_*^{cl} = 4.3$ if not corrected for progenitor bias and $z_*^{cl} = 2.0$ after correction for maximum progenitor bias. In both cases we determine the constraints on z_* for the lens galaxies. Note that z_* and b are coupled in this model, because of the constraint that lens galaxies with the same age as cluster galaxies have identical M/L ratios. For the r band the resulting constraints on z_* (and hence b) are shown in the lower-right panel of Fig. 3, with the best fit values indicated by arrows. From maximum to no progenitor bias correction, we find z_* ranging from 1.6 to 2.4 (1σ) for the B band, and from 1.6 to 2.6 (1σ) for the r band (Table 2). For the case of maximum progenitor bias the M/L evolution that follows from the best-fit value $z_* = 1.8$ in the r band, is shown in the lower-left panel of Fig. 3 (dashed line).

5.4 SUMMARY OF RESULTS

We have demonstrated that the M/L evolution of lens galaxies cannot be fitted with models that provide good fits to cluster galaxies. The fit clearly improves if lens galaxies are allowed to be systematically offset from cluster galaxies due to metallicity differences or other systematic effects.

If we consider both this offset and the stellar formation epoch of the lens galaxies as free parameters, the best-fit single burst model in the B and r band are consistent. The resulting offset is not significantly different from zero, and although the best-fit stellar formation redshift implies for lens galaxies on average a younger stellar population than for cluster galaxies, the resulting (1σ) range of $1.3 < \langle z_* \rangle < 3.8$ is not significantly different from the formation epoch for cluster galaxies of $1.8 < \langle z_*^{cl} \rangle < 8.0$ for the full range from no to maximum progenitor bias correction.

If we impose the constraint that galaxies of the same age have the same M/L ratio irrespective of their environment, we find stellar formation redshifts for the lens galaxies of $1.6 < \langle z_* \rangle < 2.0$ if the stars in cluster galaxies formed at $z_*^{cl} = 2.0$ (maximum progenitor bias), and $1.9 < \langle z_* \rangle < 2.6$ if the stars in cluster galaxies formed at $z_*^{cl} = 4.3$ (no progenitor bias). In the latter case the stellar populations of the lens galaxies are significant younger (10–15% at the present epoch) than those of the cluster galaxies.

If the local M/L offset between lens and cluster galaxies is allowed to vary, R03 find for the stellar formation redshift of the lens galaxies a (1σ) range of $2.0 < \langle z_\star \rangle < 3.6$ from their B band analysis. Although we find a range of $1.3 < \langle z_\star \rangle < 3.2$ (model A, B band) which implies on average a somewhat younger stellar population, the results are consistent. R03 conclude that the M/L evolution rates they measure favor old stellar populations for the lens galaxies with a mean formation redshift $\langle z_\star \rangle > 1.8$ at a 2σ confidence level. We find a lower 2σ confidence limit of $\langle z_\star \rangle > 1.2$.

To test the hypothesis whether the M/L evolution of the lens galaxies can be fitted with a single burst model, we calculate the reduced χ^2 . We also compare the measured scatter around the fit with the expected scatter from the uncertainties in the M/L ratios of the lens galaxies. If we allow more freedom in the single burst models, the fit improves (lower reduced χ^2) and the measured scatter decreases. However, even the over-all best-fit single burst model is rejected with $> 99\%$ confidence and the measured scatter of 0.17 and 0.15 in B and r band is significant higher than the expected scatter of 0.12 from the observational errors. To establish whether the additional scatter is due to a significant spread in ages among field galaxies, we study in the next Section the (restframe) colors of the lens galaxies, and investigate if there is also a significant scatter in the color and if it is correlated with the scatter in their M/L ratios.

6 COLORS

If the stellar populations of lens galaxies are on average younger than those of cluster galaxies (Section 5) we expect their colors to evolve more rapidly and to be on average bluer than those of cluster galaxies. For single burst stellar populations the $B - r$ color evolves as

$$B - r = 2.5(\kappa_B - \kappa_r) \log(t - t_\star) + c, \quad (6.1)$$

with $\kappa_B - \kappa_r \approx 0.15$ (Worthey 1994) and c a normalization constant.

The left panel of Fig. 4 shows the restframe $B - r$ colors of the lens galaxies versus redshift. For the lens galaxies with open circles, a modest extrapolation was required in the transformation to either the restframe B or r band. The red outlier (at $z \sim 0.4$) is the lens BRI0952-0115, for which the observed $R - H$ (F675W-F160W) color is significantly redder than the modeled E/S0 color, and for which we had to extrapolate in the transformation to restframe B band. The single burst evolution of a stellar population formed at the mean cluster formation epoch of $z_\star^{cl} = 2.0$ (maximum progenitor bias), is drawn (solid line) through the averaged color of the coma cluster galaxies (small dot). A decline in the colors of the lens galaxies with increasing redshift is visible, in spite of the large scatter. If we fit single burst models as in Section 5 (model A and B), we find on average a younger stellar formation epoch for the lens galaxies, but the difference with the cluster galaxies is never significant. In case the stellar populations of field and cluster galaxies are assumed to evolve in the same way (model B), the evolution model with the best-fit stellar formation redshift of $z_\star = 1.7$ is shown in the left panel of Fig. 4 (dashed line). Similarly as for the single burst model fits to the M/L evolution, the fits to the color evolution are rejected with $> 99\%$ confidence, and the measured scatter is in all cases significantly higher than the expected scatter from the observational errors in the restframe colors of the lens galaxies.

To further investigate the scatter in color, we subtract the predicted colors of cluster galaxies with $z_\star^{cl} = 2.0$, from the restframe colors of the lens galaxies. Note that this choice of formation redshift corresponds to the *minimum* age difference between field

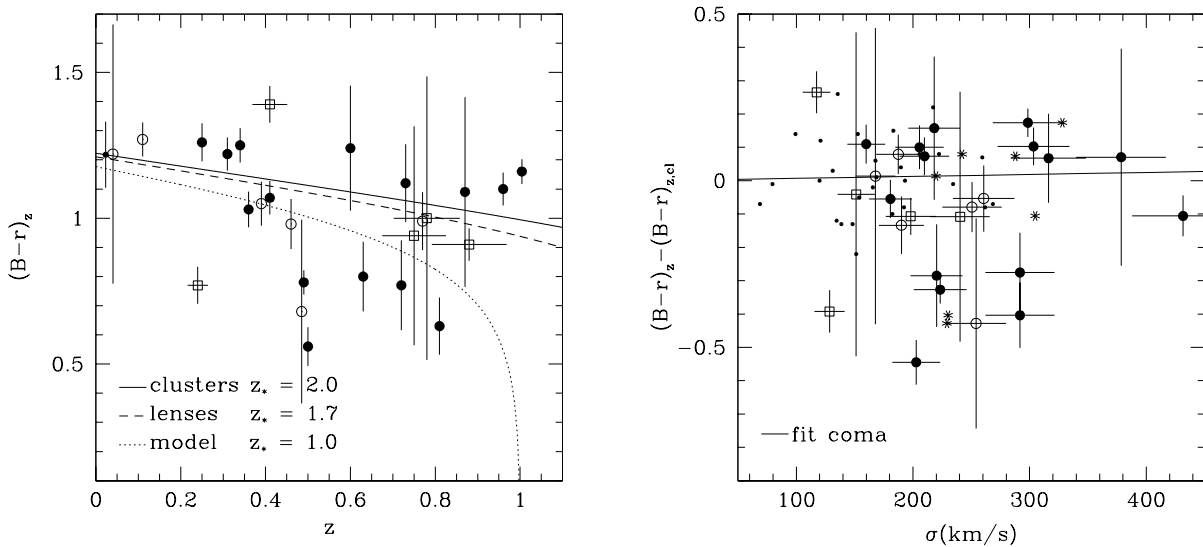


FIGURE 4 — LEFT: Evolution of the restframe $B - r$ color. The symbols correspond to those in Fig. 2, with the colors of the Coma cluster galaxies averaged (small dot). The solid line shows the evolution for a stellar population formed at $z_* = 2.0$, which is the mean cluster value after maximum progenitor bias correction. The dashed line is the model for a stellar population formed at the best-fitting star formation redshift of $z_* = 1.7$, if the lens and cluster galaxies are fitted in a self-consistent way. To illustrate the effect of changing z_* we also show a model with $z_* = 1$ (dotted line). For redshifts beyond $z \sim 0.5$ the scatter in color increases and becomes significant higher than expected from the observational errors. RIGHT: The restframe $B - r$ colors of lens galaxies, after subtracting the fiducial model for cluster galaxies with $z_*^{cl} = 2.0$, plotted versus velocity dispersion. The solid line is a linear fit to the Coma cluster galaxies. On average the colors of the lens galaxies are bluer than those of the cluster galaxies, consistent with a younger average stellar population. The scatter in the reduced colors is larger than expected from the observational errors.

and cluster galaxies. In the right panel of Fig. 4 we show the resulting residual colors plotted against velocity dispersion, with a linear fit to the Coma cluster galaxies. The lens galaxies show a large spread in their reduced colors, and are on average bluer by ~ 0.1 mag than the cluster galaxies. The bluer average color is qualitatively consistent with the on average younger ages of lens galaxies derived from the single burst model fits above and from the fits to the M/L evolution (Section 5.4). For the total sample of 26 lens galaxies, we measure a scatter in the residual colors of 0.22, that is significant higher than the expected scatter of 0.18. From the left panel of Fig. 4, we observe that the color scatter increases beyond $z \sim 0.5$. For the 15 lens galaxies with $z \gtrsim 0.5$ we measure a scatter of 0.24, whereas for the lens galaxies with $z \lesssim 0.5$ the measured scatter is only 0.16 and nearly identical to the expected scatter of 0.15 from the errors in the colors of these galaxies.

The additional measured scatter in the residual colors of the lens galaxies may indicate a significant spread in the ages of the stellar populations of the lens galaxies. We test whether the color spread is caused by a spread in ages or other effects, by investigating whether the residual colors correlate with the residual M/L ratios. In Fig. 5 we plot the color of the lens galaxies against the logarithm of their M/L ratio. For both quantities the expected evolution of a stellar population formed at $z_*^{cl} = 2.0$ was subtracted; hence a galaxy with the average color and M/L ratio of galaxies in Coma

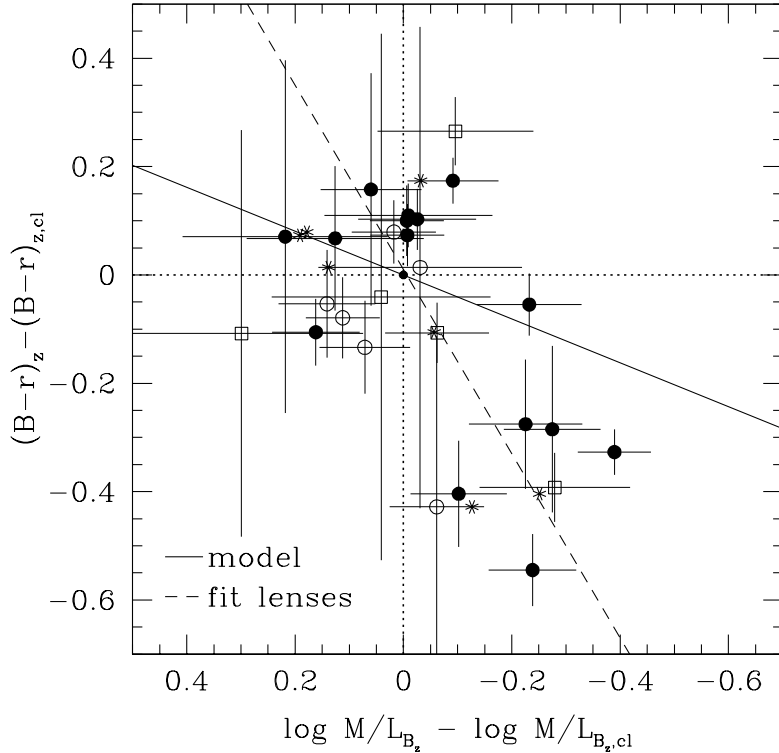


FIGURE 5 — The $B - r$ color versus M/L_r ratio, after subtracting the fiducial cluster galaxy evolution model with $z_*^{cl} = 2.0$. The symbols are the same as in Fig. 2, with the average of Coma situated in the origin. The dashed line is a linear fit to the data; the solid line shows the expected correlation between color and M/L ratio due to age variations, with slope $2.5(\kappa_B - \kappa_r)/\kappa_B \approx 0.40$. Although the slope is uncertain, the correlation between color and M/L ratio is significant at the 95% level. Hence we interpret the intrinsic scatter in the colors of the lens galaxies as a stellar population effect, probably caused by a spread in their ages.

would be located at the origin. From eq. (6.1) and (5.1) it follows that a linear relation is expected in Fig. 5, with a (time-independent) slope of $2.5(\kappa_B - \kappa_r)/\kappa_B \approx 0.40$ (solid line). The data appear to be correlated in the expected sense, albeit with large scatter. To test whether the correlation is significant we used the Spearman's rank-order correlation coefficient r_S . We find that $r_S = 0.47$, so that with $N = 26$ lenses, we can reject the hypothesis that the two quantities are uncorrelated with $> 95\%$ confidence. The only viable explanation for the correlation is age variation. If the correlation would be caused by metallicity variations, (some) field galaxies would be much less metal rich than cluster galaxies, opposite to the result by Kuntschner et al. (2002).

The colors and M/L ratios of the bluest lens galaxies are best fitted with stellar formation redshifts as low as $z_* \sim 1$. About half the lens galaxies are consistent with an old cluster-like stellar population with stellar formation redshift $z_* \gtrsim 2$. If galaxies form in a sequence of bursts, formation redshifts are indicative of the last prominent epoch of star formation. The galaxies can have older underlying stellar populations.

7 SUMMARY AND CONCLUSIONS

We studied the evolution of the M/L ratios of lens galaxies in the restframe Johnson B and Gunn r bands. For an flat cosmology with $\Omega_M = 0.3$ and $\Omega_\Lambda = 0.7$, we obtained an

evolution rate $d \log(M/L)/dz$ of -0.62 ± 0.13 in restframe B and -0.47 ± 0.11 in restframe r . Due to differences in the determination of the FP parameters and the corresponding errors, the evolution rate obtained by R03 of -0.54 ± 0.09 is slightly slower but not significantly different. Our results are consistent with determinations for field galaxies based on direct spectroscopic measurements of the velocity dispersions. For the B band, van Dokkum et al. (2001) arrive at an evolution rate of -0.59 ± 0.15 , and Treu et al. (2002) find a value of $-0.72^{+0.11}_{-0.16}$. The weighted mean of these results and our result yields an evolution rate for field early-type galaxies of -0.64 ± 0.06 in the B band. For cluster galaxies van Dokkum et al. (1998) and vDF01 find an evolution rate between $d \log(M/L_B)/dz = -0.49 \pm 0.05$ and -0.56 ± 0.05 , for minimum and maximum progenitor bias respectively. The latter value is not significantly different from the average evolution rate for the field galaxies.

We further investigated the M/L evolution in Section 5, where we related it to stellar population ages by fitting simple single burst models for a Salpeter (1955) IMF and Solar metallicity. The M/L evolution of cluster galaxies is well approximated by a mean single burst formation redshift of $z_*^{cl} = 4.3^{+3.7}_{-1.2}$, and $z_*^{cl} = 2.0^{+0.3}_{-0.2}$ after maximum progenitor bias correction (vDF01).

We first tested if these cluster models could fit the M/L evolution of the lens galaxies. This is not the case, but the fits improve if there is a systematic offset between lens and cluster galaxies of ~ -0.1 in $\Delta \log M/L$. Such an offset could be caused by, e.g., metallicity variations, systematic differences in the velocity dispersions due to the different measurement techniques, or other effects. It is interesting to note that hierarchical models have predicted such a constant offset with redshift between cluster and field galaxies (see van Dokkum et al. 2001). However, similar to van Dokkum et al. (2001), we conclude that the observed offset is much smaller than the predicted offset of $\Delta \log M/L_B \sim -0.26$.

If we next allow the stellar formation redshift z_* also to vary, we find for the best-fit single burst model that the offset is not significant from zero, together with a mean stellar formation epoch $\langle z_* \rangle$ for the lens galaxies of $1.8^{+1.4}_{-0.5}$ in the B band and $1.9^{+1.9}_{-0.6}$ in the r band. This means that on average the stellar populations of the lens galaxies are younger, but the difference with the cluster galaxies is not significant. However, if we impose the constraint that galaxies of the same age have the same M/L ratio irrespective of their environment, we find without correction for progenitor bias that the stellar populations of the lens galaxies are significant younger (10–15% at the present epoch) than those of the cluster galaxies. In the case of maximum progenitor bias the average difference ($\sim 5\%$) is not anymore significant.

From their analysis R03 obtain a (2σ) lower limit for the mean stellar formation epoch of lens galaxies of $\langle z_* \rangle > 1.8$, whereas we find that lower stellar formation redshifts are allowed, with $\langle z_* \rangle > 1.2$ as a 2σ lower limit. Nevertheless, these results disagree with the prediction of semi-analytical hierarchical galaxy formation models (e.g., Kauffmann 1996; Kauffmann & Charlot 1998; Diaferio et al. 2001) that early-type field galaxies in general have very late star formation with $z_* < 1$.

Whereas the M/L evolution of cluster galaxies is well approximated by a single burst evolution model, we found that this is not the case for the lens galaxies. All single burst models are rejected with $> 99\%$ based on the reduced χ^2 , and the measured scatter is in all cases significant higher than the expected scatter from the observational errors. The additional scatter is most likely caused by differences in the stellar population of the lens galaxies.

To investigate whether there is a significant spread in ages, we studied in Section 6 the restframe colors of the lens galaxies and their evolution. The colors of the lens galaxies are on average bluer than those of the cluster galaxies, consistent with on a younger average stellar population. We found that the measured scatter in the single burst fits to the colors is much larger than the expected scatter from the observational errors. Moreover, we showed that there is a significant correlation between the colors and the M/L_B ratios of the lens galaxies. We interpret this as evidence for a significant spread in the stellar population ages of the lens galaxies.

Whereas about half of the lens galaxies are consistent with old cluster-like stellar populations, the bluest galaxies are best fit by single burst models with young stellar formation redshifts $z_* \sim 1$. For the seven blue lens galaxies with residual colors below -0.2 mag in the right panel of Fig. 4, we found (as a byproduct of our transformation to restframe B band) that only two of them are best fitted by the E/S0 spectral type, i.e. $\sim 28\%$, whereas for the total sample we found 77% . For the r band even six of the seven blue galaxies are best fitted by the Scd spectral type, instead of the ES/0 spectral type. Three of the seven blue galaxies indeed show (some) deviations from early-type morphology. FBQ0951+2635 is an edge-on disk galaxy, SBS1520+530 is slightly irregular and B1608+656 is an apparently dusty galaxy with star forming regions. However, a homogeneous sample of quasar subtracted (NICMOS) images of the lens galaxies is needed to do a more detailed and systematic study of their morphologies. Such a study will be valuable to determine the cause of apparently younger populations in a fraction of the lens galaxies.

ACKNOWLEDGMENTS

We thank the anonymous referee for constructive and detailed comments, which improved the manuscript significantly.

REFERENCES

- Andrews D. F., Bickel P. J., Hampel F. R., Rogers W., Tukey J., 1972, Robust Estimates of Locations: Survey and Advances. Princeton University, Princeton
- Beers, T. C. and Flynn, K. and Gebhardt, K., 1990, AJ, 100, 32
- Bender R., Saglia R. P., Ziegler B., Belloni P., Greggio L., Hopp U., Bruzual G., 1998, ApJ, 493, 529
- Bessell M. S., 1990, PASP, 102, 1181
- Binney J., Tremaine S., 1987, Galactic Dynamics. Princeton, NJ, Princeton University Press
- Cardelli J. A., Clayton G. C., Mathis J. S., 1989, ApJ, 345, 245
- Coleman G. D., Wu C. ., Weedman D. W., 1980, ApJS, 43, 393
- Diaferio A., Kauffmann G., Balogh M. L., White S. D. M., Schade D., Ellingson E., 2001, MNRAS, 323, 999
- Djorgovski S., Davis M., 1987, ApJ, 313, 59
- Dressler A., Lynden-Bell D., Burstein D., Davies R. L., Faber S. M., Terlevich R., Wegner G., 1987, ApJ, 313, 42
- Dressler A., et al. 1997, ApJ, 490, 577
- Faber S. M., Dressler A., Davies R. L., Burstein D., Lynden-Bell D., Terlevich R., Wegner G., 1987, Nearly Normal Galaxies. Springer, New York, p. 175
- Falco E. E., Shapiro I. I., Moustakas L. A., Davis M., 1997, ApJ, 484, 70
- Foltz C. B., Hewett P. C., Webster R. L., Lewis G. F., 1992, ApJ, 386, L43
- Frei Z., Gunn J. E., 1994, AJ, 108, 1476
- Hernquist L., 1990, ApJ, 356, 359
- Hogg, D. W., 2000, astro-ph/9905116

- Jørgensen I., Franx M., Kjærgaard P., 1995a, MNRAS, 273, 1097
Jørgensen I., Franx M., Kjærgaard P., 1995b, MNRAS, 276, 1341
Jørgensen I., Franx M., Kjærgaard P., 1996, MNRAS, 280, 167
Kauffmann G., 1996, MNRAS, 281, 487
Kauffmann G., Charlot S., 1998, MNRAS, 294, 705
Kelson D. D., van Dokkum P. G., Franx M., Illingworth G. D., Fabricant D., 1997, ApJ, 478, 13
Kochanek C. S., 1994, ApJ, 436, 56
Kochanek C. S., 1996, ApJ, 466, 638
Kochanek C. S., Falco E. E., Impey C. D., Lehár J., McLeod B. A., Rix H. ., Keeton C. R., Muñoz J. A., Peng C. Y., 2000, ApJ, 543, 131 [K00]
Koopmans L. V. E., Treu T., 2002, ApJl, 568, L5
Koopmans L. V. E., Treu T., 2003, ApJ, 583, 606
Kuntschner H., Smith R. J., Colless M., Davies R. L., Kaldare R., Vazdekis, A., 2002, MNRAS, 337, 172
Lehár J., Cooke A. J., Lawrence C. R., Silber A. D., Langston, G. I., 1996, AJ, 111, 1812
Lehár J., et al. 2000, ApJ, 536, 584
O'Donnell J. E., 1994, ApJ, 422, 158
Ohyama Y., et al. 2002, AJ, 123, 2903
Press W. H., Teukolsky S. A., Vetterling W. T., Flannery B. P., 1992, Numerical Recipes. Cambridge Univ. Press, Cambridge
Rhee G., 1991, Nature, 350, 211
Rusin D., Kochanek, C. S., Falco E. E., Keeton C. R., McLeod B. A., Impey C. D., Lehár J., Munoz J. A., Peng C. Y., Rix H.-W., 2003, ApJ, accepted
Salpeter E. E., 1955, ApJ, 121, 161
Schlegel D. J., Finkbeiner D. P., Davis M., 1998, ApJ, 500, 525
Thuan T. X., Gunn J. E., 1976, PASP, 88, 543
Tinsley B. M., Gunn J. E., 1976, ApJ, 206, 525
Tonry J. L., 1998, AJ, 115, 1
Tonry J. L., Franx M., 1999, ApJ, 515, 512
Treu T., Stiavelli M., Bertin G., Casertano S., Møller P., 2001, MNRAS, 326, 237
Treu T., Stiavelli M., Casertano S., Møller P., Bertin G., 2002, ApJl, 564, L13
Tully R. B., Fisher J. R., 1977, A&A, 54, 661
van Dokkum P. G., Franx M., 1996, MNRAS, 281, 985
van Dokkum P. G., Franx M., 2001, ApJ, 553, 90 [vDF01]
van Dokkum P. G., Franx M., Kelson D. D., Illingworth G. D., 1998, ApJl, 504, L17
van Dokkum P. G., Franx M., Kelson D. D., Illingworth G. D., 2001, ApJl, 553, L39
Worthey G., 1994, ApJS, 95, 107

LIST OF PUBLICATIONS

REFEREED JOURNALS

General solution of the Jeans equations for triaxial galaxies with separable potentials

G. van de Ven, C. Hunter, E. K. Verolme, P. T. de Zeeuw,
2003, MNRAS, 342, 1056–1082 (Chapter 5)

The Fundamental Plane and evolution of the M/L ratio of early-type field galaxies

G. van de Ven, P. G. van Dokkum, M. Franx, 2003, MNRAS, 344, 924–934 (Chapter 7)

Radial velocities in the globular cluster ω Centauri

R. A. Reijns, P. Seitzer, R. Arnold, K. C. Freeman, T. Ingerson, R. C. E. van den Bosch,
G. van de Ven, P. T. de Zeeuw, 2005, A&A, in press, astro-ph/0509227

The dynamical distance and intrinsic structure of the globular cluster ω Centauri

G. van de Ven, R. C. E. van den Bosch, E. K. Verolme, P. T. de Zeeuw,
2005, A&A, in press, astro-ph/0509228 (Chapter 2)

A bar signature and central disk in the gaseous and stellar velocity fields of NGC 5448

K. Fathi, G. van de Ven, R. F. Peletier, E. Emsellem, J. Falcón-Barroso,
M. Cappellari, P.T. de Zeeuw, 2005, MNRAS, in press, astro-ph/0509642 (Chapter 3)

The SAURON project - IV. The mass-to-light ratio, the virial mass estimator and the fundamental plane of elliptical and lenticular galaxies

M. Cappellari, R. Bacon, M. Bureau, M. C. Damen, R. L. Davies, P. T. de Zeeuw,
E. Emsellem, J. Falcón-Barroso, D. Krajnović, H. Kuntschner, R. M. McDermid,
R. F. Peletier, R. C. E. van den Bosch, G. van de Ven,
2005, MNRAS, submitted, astro-ph/0505042

The distribution of maser stars in our Milky Way: the effect of a weak, rotating bar

H. J. Habing, M. N. Sevenster, M. Messineo, G. van de Ven, K. Kuijken:
the ROTBAR consortium, 2005, A&A, submitted

The dynamical M/L-profile and distance of the globular cluster M15

R. C. E. van den Bosch, P. T. de Zeeuw, K. Gebhardt, E. Noyola, G. van de Ven,
2005, ApJ, submitted

Recovery of three-integral galaxy models

G. van de Ven, P.T. de Zeeuw, R. C. E. van den Bosch,
2005, MNRAS, to be submitted (Chapter 4)

The Einstein Cross: lensing vs. stellar dynamics

G. van de Ven, J. Falcón-Barroso, M. Cappellari, R. M. McDermid, B. Miller,
P. T. de Zeeuw, 2005, MNRAS, to be submitted (Chapter 6)

Triaxial Schwarzschild models for elliptical galaxies

R. C. E. van den Bosch, G. van de Ven, E. K. Verolme, M. Cappellari, P. T. de Zeeuw, 2006, MNRAS, to be submitted

NON-REFEREED PAPERS

Jeans solutions for triaxial galaxies

G. van de Ven, C. Hunter, E. K. Verolme, P. T. de Zeeuw, 2003, in 'Galaxies and Chaos', eds. G. Contopoulos, N. Voglis, LNP, 626, 101–108

A SAURON view of galaxies

E. K. Verolme, M. Cappellari, G. van de Ven, P. T. de Zeeuw, SAURON team, 2003, in 'Galaxies and Chaos', eds. G. Contopoulos, N. Voglis, LNP, 626, 279–285

Orbital structure of triaxial galaxies

G. van de Ven, E. K. Verolme, M. Cappellari, P. T. de Zeeuw, 2004 in Proc. IAU Symp. 220 'Dark matter in galaxies', eds. S. D. Ryder, D. J. Pisano, M. A. Walker, K. C. Freeman, ASP San Francisco, 179–180

Two-dimensional kinematics of a bar and central disk in NGC 5448

K. Fathi, G. van de Ven, R.F. Peletier, E. Emsellem, J. Falcón-Barroso, M. Cappellari, P.T. de Zeeuw, 2005, in Proc. Island Universes conference, astro-ph/0508131

Revisiting the $(V/\sigma) - \epsilon$ anisotropy diagram of early-type galaxies using integral-field kinematics

M. Cappellari, R. Bacon, M. Bureau, R. L. Davies, P. T. de Zeeuw, E. Emsellem, J. Falcón-Barroso, D. Krajnović, H. Kuntschner, R. M. McDermid, R. F. Peletier, M. Sarzi, R. C. E. van den Bosch, G. van de Ven, 2005, astro-ph/0509470

NEDERLANDSE SAMENVATTING

STERSYSTEMEN

HET heelal ontstond in een 'oerknal', waarna het begon uit te dijen. Op plekken met net iets meer donkere materie dan in de nabije omgeving zorgde de zwaartekracht ervoor dat de donkere materie zich samentrok en daarbij gas verzamelde, waaruit zich sterren vormden. Deze eerste sterren kwamen terecht in systemen van verschillende grootte en vorm, afhankelijk van de verdeling van de donkere materie. De sterren in deze systemen evolueren: de meeste sterren doven aan het einde van hun leven uit, maar de zwaarste sterren exploderen en uit hun resten worden weer nieuwe sterren geboren. Ook de systemen zelf evolueren door onderlinge interactie en samensmelting. Dit alles leidt tot de volgende vraag: kunnen we voor de verschillende stersystemen achterhalen hoe ze zijn geëvolueerd vanaf de oerknal tot nu?

Een mogelijke onderzoeksstrategie is het waarnemen van objecten die op grote afstand staan. Doordat het licht tijd nodig heeft om afstanden af te leggen, zien we deze objecten 'terug in de tijd'. Door steeds dieper het heelal in te kijken, kunnen we dus als het ware de vorming en evolutie van deze objecten in 'omgekeerde volgorde' bekijken. Echter, met toenemende afstand wordt het licht van deze objecten snel zwakker, zodat heel grote telescopen nodig zijn, die niet alleen technisch moeilijk te realiseren zijn maar bovenal heel kostbaar zijn. Een andere manier is nabije stersystemen te bestuderen en, net als een archeoloog, op zoek te gaan naar de 'fossiele resten' van hun ontstaan en evolutie. We kunnen dan bijvoorbeeld denken aan de aanwezigheid van kleine centrale schijven, ontkoppelde kernen en tegendraads roterende schijven, welke het gevolg kunnen zijn van het samensmelten van verschillende stersystemen. Omdat de stersystemen dichtbij staan, kunnen we de bewegingen en samenstelling van de sterren in deze systemen tot in groot detail waarnemen. Door middel van het fitten van theoretische modellen (gebaseerd op de zwaartekrachtwet van Newton) aan deze waarnemingen kunnen we dan proberen deze stersystemen te reconstrueren. Hierna kunnen we als het ware stersystemen 'van binnenuit bekijken' en in hun structuur en interne bewegingen op zoek gaan naar overblijfselen, oftewel 'fossielen', die gerelateerd zijn aan hun vormingsgeschiedenis.

De geschiktste stersystemen om op zoek te gaan naar 'fossiele resten' zijn diegene waarvoor het zicht op de sterren niet bemoeilijkt, of zelfs geheel ontnomen wordt door de aanwezigheid van gas en stof, en diegene die niet 'vervuild' zijn door recente stervorming. Bolhopen zijn in dit opzicht de 'schoonste' stersystemen met in de orde van een miljoen zeer oude sterren, die zijn ontstaan uit dezelfde materie die zich samentrok vlak na de oerknal. Bovendien zijn het simpele, bijna ronde objecten, die we ook nog eens van relatief dichtbij kunnen waarnemen, omdat ze zich in onze eigen Melkweg bevinden. In deze bolhopen kunnen we (veel van) de sterren afzonderlijk waarnemen en hun individuele snelheden langs de gezichtslijn en zelfs in het vlak van de hemel bepalen. Deze laatste zogenaamde eigenbewegingen worden verkregen door heel nauwkeurig de positieverandering van de sterren in de tijd te meten. Momenteel zijn zulke metingen van de kinematica van individuele sterren alleen goed mogelijk

voor de nabijste stersystemen en voor sterren in de Melkweg zelf. Omdat wij zelf deel uitmaken van de Melkweg, is ons zicht helaas sterk vertroebeld door het aanwezige gas en stof.

In het begin van de negentiende eeuw werd duidelijk dat de Melkweg slechts één van de 'nevels' is die aan de hemel te zien zijn. Fotografische waarnemingen lieten zien dat deze sterrenstelsels in verschillende soorten voorkomen. Dit zette Hubble in 1936 aan te onder te verdelen in vier verschillende groepen naar aanleiding van hun waargenomen vorm. In het resulterende Hubble diagram (of Hubble stemvork) behoort de Melkweg tot de stelsels met een grote schijf, ook wel *spiraalen* genoemd vanwege de prominent aanwezige spiraalarmen. Aan het andere uiteinde van het diagram vinden we de *elliptische* stelsels met een (zeer) eenvoudig uitziende structuur. Tussen beide uiteindes in vinden we de *lensvormige* stelsels met een schijf en een sferoïdale verdeling van de sterren, maar geen (prominente) spiraalarmen. De vierde groep bestaat uit stelsels zonder een regelmatige vorm en deze worden dan ook heel toepasselijk *onregelmatige* stelsels genoemd. Toentertijd dacht men dat de complex uitziende spiraalstelsels evolueerden uit de schijnbaar eenvoudige elliptische stelsels. Ondanks dat we tegenwoordig weten dat de vorming en evolutie van stelsels juist in omgekeerde volgorde is, worden de spiraalstelsels nog steeds laat-type stelsels genoemd en worden de elliptische en lensvormige stelsels ook wel aangeduid als vroeg-type stelsels.

De laat-type stelsels, waartoe dus ook de Melkweg behoort, bevatten flinke hoeveelheden gas en stof en er vindt regelmatig (of zelfs continu) intensieve stervorming plaats die de omgeving als het ware 'schoonveegt', waardoor het erg lastig wordt de ontstaansgeschiedenis te achterhalen. Daarentegen bevatten vroeg-type stelsels over het algemeen weinig gas en stof en vertonen geen recente stervorming, zodat ze ideaal zijn voor het bestuderen van de vorming en evolutie van sterrenstelsels. Voor de 'nabije' (< 300 miljoen lichtjaar) vroeg-type stelsels kunnen we de fossiele resten van hun vorming in detail bestuderen. In het algemeen kunnen we de individuele sterren niet onderscheiden, maar desondanks kunnen we hun gezamenlijke licht (fotometrie) en bewegingen (kinematica) langs de gezichtslijn nauwkeurig meten.

LICHTVERDELING

De waargenomen (twee-dimensionale) lichtverdeling van vroeg-type stelsels kan in het algemeen goed beschreven worden door een set van ellipsen, ieder met hun eigen helderheid, die volgens een eenvoudige functie afneemt naarmate de straal van de ellipsen toeneemt. Hoewel de fotometrie van vroeg-type stelsels dus redelijk eenvoudig is, betekent dit niet dat ook de intrinsieke (drie-dimensionale) structuur eenvoudig achterhaald en beschreven kan worden.

De conversie van een lichtverdeling gemeten aan de hemel naar een intrinsieke lichtverdeling is in het algemeen niet uniek. Voor bolvormige objecten is deze zogenaamde deprojectie wel uniek, maar er zijn maar heel weinig stelsels die er rond uitzien en zelfs dan hoeven ze intrinsiek niet bolvormig te zijn. In het geval van afgeplatte objecten die symmetrisch zijn rond één as is de projectie alleen uniek als we zo'n *axisymmetrisch* stelsel bekijken vanuit het vlak loodrecht op de symmetrie-as. Zo'n zij-aanzicht wordt vaak aangeduid met een inclinatiehoek van 90 graden. Echter, een stersysteem in evenwicht kan net zo goed een intrinsieke vorm hebben die verschillend is langs alle drie de assen. In het geval van zo'n *triaxiaal* stelsel is de deprojectie in hoge mate niet uniek. Voor de kijkrichting zijn nu twee hoeken nodig.

Bovendien kan, in tegenstelling tot axisymmetrische objecten, de oriëntatie van de ellipsen die de lichtverdeling beschrijven, veranderen met straal. Heel snel nadat men zich dit realiseerde werd dit effect inderdaad waargenomen in elliptische stelsels, wat aantoonde dat deze stelsels niet axisymmetrisch maar waarschijnlijk triaxiaal zijn.

In het geval van axisymmetrische stelsels kan de afplatting (gedeeltelijk) veroorzaakt worden door rotatie, net als de afplatting van de Aarde. Naast deze geordende beweging, kan in een stersysteem ook de willekeurige beweging van sterren zo'n afplatting in stand houden. Deze willekeurige beweging, gemeten als de gemiddelde afwijking van de sterren van hun gemiddelde snelheid, oftewel snelheidsdispersie, gedraagt zich als een soort tegendruk die kan variëren met richting en positie binnen een stersysteem. We zeggen dan dat zo'n stersysteem anisotroop is, in tegenstelling tot een isotroop systeem waarin de dispersie overal hetzelfde is. Ondanks dat anisotropie een bepaalde vorm kan ondersteunen zoals axisymmetrie of zelfs triaxialiteit, hoeven anisotropie en vorm niet (volledig) gekoppeld te zijn. Zo kan een bolvormig systeem bijvoorbeeld ook een anisotrope snelheidsverdeling hebben.

Anisotropie en andere dynamische eigenschappen kunnen niet bepaald worden uit fotometrie alleen, maar vergen ook kinematische metingen. Toen in de midden jaren zeventig en de vroege jaren tachtig van de vorige eeuw de rotatie en de dispersie van vroeg-type stelsels werd gemeten, was één van de belangrijke conclusies dat vroeg-type stelsels in het algemeen te langzaam roteren om de afplatting volledig te kunnen verklaren. Verdere waarnemingen lieten zien dat terwijl de lichtzwakkere elliptische en de lensvormige stelsels schijfvormig zijn met duidelijke rotatie, de grote elliptische stelsels ovaler van vorm zijn met vaak nauwelijks enige rotatie. Deze tweedeling werd toegeschreven aan verschillende onderliggende dynamische structuren, waarbij de zwakkere vroeg-type stelsels isotrope roterende axisymmetrische systemen zijn en de heldere vroeg-type stelsels anisotrope triaxiale systemen zijn.

Echter, recente (N-deeltjes) simulaties van samensmeltende stelsels lijken het tegenovergestelde te suggereren voor de anisotropie: zwakkere anisotrope en heldere isotrope vroeg-type stelsels. Op basis van de intrinsieke dynamische structuur die volgt uit dynamische modellen van een serie van vroeg-type stelsels, komen wij tot dezelfde conclusies. Het is duidelijk dat zulke gedetailleerde simulaties en dynamische modellen van stelsels cruciaal zijn om hun ontstaansgeschiedenis te achterhalen. Zo'n verbetering in de bepaling van de intrinsieke dynamische structuur zou niet mogelijk zijn zonder de toevoeging van twee-dimensionale kinematische waarnemingen en realistische dynamische modellen, die hierna beide nader worden toegelicht.

TWEE-DIMENSIONALE KINEMATISCHE WAARNEMINGEN

Vroeg-type sterrenstelsels kunnen in het algemeen beschouwd worden als botsingsloze stersystemen in evenwicht. Alleen in het centrum kan de dichtheid van de sterren hoog genoeg worden zodat ze elkaars banen gaan beïnvloeden. Elders vormen de sterren een botsingsloos systeem en bewegen ze onder invloed van het gemiddelde zwaartekrachtsveld van alle andere sterren. Met uitzondering van mogelijk de buitenste delen van een stersysteem is sinds het ontstaan van het systeem genoeg tijd verstreken voor de sterren om in dynamisch evenwicht te komen. Deze aannames gelden veelal ook voor bolhopen behalve in hun kernen die vaak niet botsingsloos zijn. Als een stersysteem botsingsloos en in evenwicht is dan wordt zijn dynamische toestand volledig beschreven door de distributie functie (DF) van de sterren in de

zes-dimensionale fase-ruimte van posities en snelheden.

Van sterren in de Melkweg en die in de nabije stersystemen zoals bolhopen, kunnen we de snelheid langs de gezichtslijn en de eigenbewegingen meten als functie van hun positie aan de hemel. We missen dan alleen nog de afstand, waarvan de bepaling in het algemeen erg lastig en onzeker is. vertroebeling door gas en stof gecombineerd met beperkt ruimtelijk en snelheids oplossend vermogen van de meetinstrumenten, zorgen er bovendien voor dat waarnemingen niet compleet zijn. Desondanks zullen toekomstige ruimtemissies zoals GAIA naar verwachting voor een groot deel van de Melkweg en omgeving de zes dimensies in kaart brengen.

Al na een relatief kleine toename in afstand (in de orde van enkele duizenden lichtjaren) kunnen we geen individuele sterren meer waarnemen (althans niet met de huidige telescopen). We kunnen dan nog wel de geprojecteerde lichtverdeling en voor nabije systemen ook de gezamenlijke snelheidsverdeling van de sterren langs de gezichtslijn meten. In de meting van deze snelheidsverdeling is de laatste jaren een grote stap voorwaarts gemaakt van (één-dimensionale) spleetspectrografen naar twee-dimensionale spectrografen. Terwijl een spleetspectrograaf het licht afkomstig van een rij posities aan de hemel via een spleet verstrooit in verschillende golflengten, gebeurt dit in het geval van twee-dimensionale spectrografen via een matrix van allemaal kleine lensjes, een bundel van glasvezels of een rij van aaneengesloten spleten. Op deze manier leveren twee-dimensionale spectrografen dus een spectrum van posities in twee dimensies aan de hemel. Uit de verschuiving en de vorm van de lijnen in elk spectrum kan dan vervolgens de snelheidsverdeling van sterren en gas, tezamen met eigenschappen zoals gemiddelde leeftijd en samenstelling van de sterren, bepaald worden op verschillende plaatsen in het stelsel.

DYNAMISCHE MODELLEN

Twee-dimensionale spectroscopie heeft (letterlijk) een nieuwe dimensie toegevoegd aan de waarnemingen van vroeg-type stelsels. De resulterende kinematische kaarten geven drie-dimensionale informatie over de DF. We moeten wel rekening houden met de onzekerheden in de kaarten door de onvermijdelijke ruis. Bovendien hebben we te maken met een onbekende kijkrichting, een in het algemeen niet unieke deprojectie van de lichtverdeling, die we vervolgens ook nog moeten omzetten naar een massaverdeling via een onbekende massa-lichtkracht verhouding om de interne structuur te kunnen bestuderen. Tenslotte is er de mogelijke aanwezigheid van donkere materie, die we niet direct kunnen zien, maar wel effect heeft op de kinematica van de sterren. Dit alles beschouwend lijkt het een hopeloze zaak om de DF in de zes-dimensionale fase-ruimte te reconstrueren. Gelukkig hangt voor stersystemen in evenwicht de DF in het algemeen af van minder dan zes parameters.

INTEGRALEN VAN BEWEGING

De stelling van Jeans zegt dat de DF een functie is van de integralen van beweging. In een stationair stersysteem is de energie E altijd een integraal van beweging. Een ster met een bepaalde energie zal een baan kunnen beschrijven die reikt tot een maximale afstand vanaf het centrum van het stersysteem opgelegd door de grootte van E . Op eenzelfde manier kan behoud van hoekimpuls L verdere beperkingen opleggen. Als voor deze ster bijvoorbeeld ook de component van de hoekimpuls L_z parallel aan de z -as een integraal van beweging is, dan zal hij roterend rond de z -as een baan

beschrijven die ingeperkt is tussen een minimale en maximale straal.

In een sferische gravitationele potentiaal zijn naast E de drie componenten L behouden, maar in het geval dat ook de DF sferisch is, alleen de grootte L , omdat de richting er dan niet toe doet. De sterbanen zijn rosettes ingeperkt tussen schillen met een minimale en maximale straal in een vlak. In een axisymmetrische potentiaal voldoen de meeste sterbanen aan drie integralen van beweging: E , L_z parallel aan de symmetrie z -as en een derde integraal van beweging I_3 , waarvan de precieze uitdrukking in het algemeen onbekend is. Terwijl E en L_z er voor zorgen dat de rond de z -as roterende sterbanen zich kunnen bewegen in een volume dat de vorm heeft van een torus, zorgt I_3 voor een verdere inperking van dit volume. In het triaxiale geval zijn er naast E nog twee integralen van beweging, I_2 and I_3 , die in het algemeen beide onbekend zijn. Er is een grote variatie aan mogelijke sterbanen die bovendien kunnen roteren om ofwel de korte ofwel de lange as.

Alhoewel complexe sterbanen mogelijk zijn in de zes-dimensionale fase-ruimte, hangt de DF in het algemeen dus slechts af van drie integralen van beweging. Door nu een functionele vorm voor de DF te kiezen, kunnen alle dynamische eigenschappen van een stersysteem worden uitgerekend en vergeleken met de waargenomen lichtverdeling en kinematica. In het algemeen is de gekozen DF een functie van de bekende integralen van beweging, zoals een functie van E en L_z in het axisymmetrische geval. Deze 'twee-integraal' modellen hebben significant bijgedragen aan ons begrip van de dynamische structuur van stersystemen, maar voor meer realistische modellen moeten we ook de derde integraal van beweging meenemen. Dit is niet gemakkelijk omdat deze derde integraal in het algemeen onbekend is. Het maken van triaxiale modellen met in het algemeen twee onbekende integralen van beweging is zelfs nog gecompliceerder.

Een uitzondering hierop is de speciale familie van modellen met een gravitationele potentiaal van Stäckel vorm, waarvoor alledrie de integralen van beweging expliciet bekend zijn. Er is een grote vrijheid in de massaverdeling, maar een sterke piek in centrum van het stelsel is niet toegestaan, zodat deze modellen ongeschikt zijn voor het beschrijven van de centrale delen van sterrenstelsels met een heel zwaar zwart gat. Desondanks zijn de kinematische eigenschappen van deze modellen net zo rijk als waargenomen in vroeg-type stelsels. Verscheidene DFs zijn dan ook geconstrueerd voor deze Stäckel modellen en ze kunnen worden gebruikt om realistische modellen van sterrenstelsels te construeren, waarvan de kinematica overeenkomt met die volgend uit waarnemingen met twee-dimensionale spectrografen (Hoofdstuk 4).

SNELHEIDSMOMENTEN

Een manier om de in het algemeen onbekende integralen van beweging te omzeilen is door het oplossen van de continuïteitsvergelijking en de Jeans vergelijkingen voor de snelheidsmomenten van de DF. De continuïteitsvergelijking relateert de drie eerste momenten $\langle v_x \rangle$, $\langle v_y \rangle$ en $\langle v_z \rangle$, en de Jeans vergelijkingen relateren de negen tweede momenten, $\langle v_x^2 \rangle$, $\langle v_x v_y \rangle$, \dots , $\langle v_z^2 \rangle$, direct aan de sterdichtheid en de gravitationele potentiaal, zonder dat we de DF hoeven te kennen. Jammer genoeg zijn er in bijna alle gevallen minder vergelijkingen dan snelheidsmomenten, zodat extra aannames over de anisotropie gemaakt moeten worden.

Dit is niet nodig in het geval van Stäckel modellen in zogenaamde confocale ellipsoïdale coördinaten. In deze coördinaten geldt voor elke sterbaan in een Stäckel potentiaal dat slechts één eerste moment niet nul is, zodat de continuïteitsvergelij-

king vrij eenvoudig opgelost kan worden. Omdat alle gecorreleerde tweede momenten verdwijnen, vormen de Jeans vergelijkingen een gesloten systeem met evenveel vergelijkingen als tweede momenten. Terwijl voor het axisymmetrische geval de oplossing al enige tijd bekend is, wordt die voor het triaxiale geval afgeleid in Hoofdstuk 5.

We zijn al veel te weten gekomen over de dynamische structuur van stersystemen door hun waargenomen lichtverdeling en kinematica te modelleren met oplossingen van de continuïteitsvergelijking en Jeans vergelijkingen. Toch moeten we voorzichtig zijn omdat de oplossingen voor de snelheidsmomenten niet garanderen dat de onderliggende DF positief en dus fysisch is.

BEWEGINGSVERGELIJKINGEN

We kunnen modellen met een mogelijke niet-fysische DF vermijden, zonder de DF zelf te definiëren, door in een gegeven gravitationele potentiaal de bewegingsvergelijkingen direct op te lossen en de daaruit volgende dichtheids- en snelheidsverdeling te fitten aan de waargenomen lichtverdeling en kinematica. Analytisch is dit alleen mogelijk voor (zeer) speciale keuzes van de potentiaal, of door middel van het (linear) benaderen van de bewegingsvergelijkingen (zie Hoofdstuk 3 voor een voorbeeld). Een heel krachtige numerieke methode is afkomstig van (en vernoemd naar) Schwarzschild en is gebaseerd op het optellen van sterbanen. De methode begint met het creëren van een representatieve bibliotheek van sterbanen door de bewegingsvergelijkingen numeriek te integreren in een willekeurige potentiaal met mogelijke bijdragen van donkere materie. Daarna worden gewichten toegekend aan de sterbanen, zodanig dat de gecombineerde en geprojecteerde dichtheids- en snelheidsverdeling het beste de waargenomen lichtverdeling en (twee-dimensionale) kinematica fit. De zo gevonden verdeling van (positieve) baangewichten representeert de DF, die dus gegarandeerd overal positief is.

De afgelopen jaren hebben verschillende groepen onafhankelijke numerieke axisymmetrische implementaties van Schwarzschilds methode ontwikkeld en gebruikt om massa's van zwarte gaten, massa-lichtkracht verhoudingen, de verdeling van donkere materie en ook de DF van vroeg-type stelsels te bepalen door het in detail fitten van hun waargenomen lichtverdeling en snelheidsverdeling langs de gezichtslijn. Door ook eigenbewegingen in het vlak van de hemel toe te voegen wordt het mogelijk de afstand en dynamische structuur van nabije bolhopen te bepalen (Hoofdstuk 2). Met een (zeker niet eenvoudige) uitbreiding van Schwarzschilds methode naar triaxiale geometrie (zie o.a. Hoofdstuk 4), wordt het mogelijk elliptische stelsels te modelleren die niet-axisymmetrische kenmerken vertonen in hun waargenomen lichtverdeling (draaiing van de ellipsen) en kinematica (bijvoorbeeld om verschillende assen roterende componenten).

DYNAMISCHE STRUCTUUR EN EVOLUTIE

Hierboven hebben we drie manieren beschreven om stersystemen te modelleren, achtereenvolgens gebaseerd op een gekozen DF als functie van (bekende) integralen van beweging, op de continuïteitsvergelijking en Jeans vergelijkingen opgelost voor de snelheidsmomenten, en op de bewegingsvergelijkingen (numeriek) geïntegreerd. In deze volgorde neemt de vrijheid en flexibiliteit van de aanpak toe, maar tegelijkertijd ook de moeite (en computertijd) om het best fittende model te vinden. Vooral voor het modelleren van triaxiale stersystemen kunnen de eerste twee methoden erg nuttig

zijn om de grote parameterruimte in te perken, alvorens de algemenere maar computerintensievere Schwarzschild methode toe te passen. Een dergelijke combinatie van modelleertechnieken vormt een krachtig gereedschap om in nabije bolhopen en vroeg-type stelsels te zoeken naar fossiele overblijfselen van hun ontstaansgeschiedenis.

Voor alle dynamische modellen vormt de gravitationele potentiaal de basis. In het algemeen wordt deze verkregen uit de lichtverdeling via deprojectie en conversie van licht naar massa, voor een gegeven kijkrichting en massa-lichtkracht verhouding. Zoals we zagen is de deprojectie in het algemeen niet uniek, de kijkrichting onbekend, net zoals de massa-lichtkracht verhouding die bovendien ook nog eens niet constant hoeft te zijn bij de aanwezigheid van donkere materie. Alhoewel de gereconstrueerde potentiaal dus kan afwijken van de werkelijke, suggereren verscheidene tests dat de dynamische structuur teruggevonden wordt, mits er genoeg en nauwkeurige waarnemingen zijn (zie ook Hoofdstuk 2 en 4).

Een unieke manier om direct houvast te krijgen op de potentiaal is via (sterke) gravitatielenzen. Het licht van een verafgelegen heldere bron wordt afgebogen door een sterrenstelsel, resulterend in meerdere en versterkte afbeeldingen van de bron rondom het lensstelsel. De relatieve positie en lichtkracht van de beelden hangen af van de massaverdeling (inclusief mogelijk donkere materie) van het lensstelsel en leggen daarmee de gravitationele potentiaal (voor een groot deel) vast. Vervolgens kunnen we door een dynamisch model van het lensstelsel te maken en deze te vergelijken met de waargenomen lichtverdeling en kinematica, de donkere materie in het lensstelsel bestuderen. Slechts enkele van de tot nu toe bekende lenssystemen staan dichtbij genoeg om voldoende fotometrische en (twee-dimensionale) kinematische metingen te vergaren voor een gedetailleerde dynamische studie (Hoofdstuk 6).

Op grotere afstanden kunnen we alleen nog de globale eigenschappen van stelsels meten. En dan hebben we vaak alleen nog de fotometrische eigenschappen zoals lichtkracht, kleur en grootte tot onze beschikking, omdat kinematische metingen via spectra erg lastig worden met de sterk afnemende helderheid. Sterke gravitatielenzen zorgen hier voor een uitweg: omdat de snelheidsdispersie van een lensstelsel is gerelateerd aan zijn massa, kunnen we de (centrale waarde van de) dispersie schatten uit de onderlinge afstand van de beelden van de verafgelegen heldere bron. Als de globale eigenschappen van verschillende stelsels eenmaal bekend zijn, dan kunnen we deze stelsels met elkaar vergelijken en hun evolutie bestuderen door gebruik te maken van schalingsrelaties zoals de *Fundamental Plane* relatie. Deze nauwe relatie tussen de dispersie, grootte en lichtkracht van vroeg-type stelsels verandert met de tijd doordat de sterren in stelsels uitdoven. Door deze verandering te meten kan de massa-lichtkracht evolutie van het stelsel achterhaald worden (Hoofdstuk 7). Door zulke metingen aan de veranderingen van de globale eigenschappen van stelsels te vergelijken met gedetailleerde bepalingen van de eigenschappen van nabije stelsels, wordt het mogelijk een beter inzicht te verwerven in de dynamische structuur en evolutie van stersystemen vanaf de oerknal tot aan het heden.

DIT PROEFSCHRIFT

In HOOFDSTUK TWEE bepalen we de afstand D , inclinatie i , massa-lichtkracht verhouding M/L , en intrinsieke dynamische structuur van de bolhoop ω Centauri in onze Melkweg. Hierbij maken we gebruik van eigenbewegingen in het hemelvlak en snelheden langs de gezichtslijn van duizenden sterren in de bolhoop. We corrigeren

de gemeten snelheden voor de beweging van de bolhoop als geheel. Verder bevatten de eigenbewegingen een rotatiecomponent veroorzaakt door de relatieve draaiing van de fotografische platen waarvan ze gemeten zijn. We laten zien dat deze kunstmatige rotatie verwijderd kan worden zonder enige modellering en dat enkel de aanname van axisymmetrie volstaat. Dit levert tevens een nauwkeurige bepaling van $D \tan i$ op. De gecorrigeerde gemiddelde snelheidsvelden zijn consistent met axisymmetrische rotatie en de snelheidsdispersies duiden op significante afwijkingen van isotropie.

We modelleren vervolgens ω Centauri met een axisymmetrische implementatie van de Schwarzschild methode, die nauwkeurig de lichtverdeling fit, geen aannames maakt over de anisotropie in de bolhoop en bovendien variatie in M/L toestaat. We middelen de individuele snelheidsmetingen om effectief de parameter ruimte te kunnen doorzoeken. We voeren verscheidene tests uit met een analytisch model, waaruit blijkt dat met deze methode de afstand gemeten kan worden met een nauwkeurigheid van ongeveer 6 procent. Toepassing van de methode op ω Centauri laat zien dat M/L niet varieert met straal. Het best fittende model heeft een massa-lichtkracht verhouding (in de V -band) van $M/L_V = 2.5 \pm 0.1 M_\odot/L_\odot$ en een inclinatie van $i = 50^\circ \pm 4^\circ$, wat overeenkomt met een gemiddelde intrinsieke assenverhouding van 0.78 ± 0.03 . De gevonden afstand $D = 4.8 \pm 0.3$ kpc (afstand modulus van 13.75 ± 0.13 mag) is significant groter dan die volgt uit simpele sferische of constante-anisotropie modellen en is consistent met de canonieke waarde van 5.0 ± 0.2 kpc gemeten met behulp van fotometrische methoden. De totale massa van de bolhoop is $(2.5 \pm 0.3) \times 10^6 M_\odot$. Het best fittende model is binnen een straal van 10 boogminuten vrijwel isotroop, maar wordt naar buiten toe steeds meer tangentieel anisotroop met toenemende rotatie. Het is goed mogelijk dat deze fase-ruimte structuur veroorzaakt wordt door getijde-effecten van de Melkweg. Tenslotte laat het model in een gebied tussen 1 en 3 boogminuten een afzonderlijke schijf-achtige structuur zien, met ongeveer 4% van de totale massa.

In HOOFDSTUK DRIE analyseren we kinematische kaarten van de binnenste delen van het nabij gelegen vroeg-type spiraalstelsel NGC 5448, verkregen uit waarnemingen met de twee-dimensionale spectrograaf SAURON aan de 4.2 meter William Herschel Telescoop op La Palma. De verstoorde structuur en kinematica van het gas wijzen op duidelijke afwijkingen van simpele rotatie langs cirkels. De kinematica van de sterren is veel regelmatiger en duidt op de aanwezigheid van een kleine schijf-achtige component in een grote roterende structuur. We delen het snelheidsveld van het gas op in verschillende componenten en laten zien dat de voornaamste eigenschappen consistent zijn met een eenvoudig model met een roterende balk. Dit model is verkregen uit de analytische oplossing van de lage orde lineaire termen van de bewegingsvergelijkingen voor het geval van een zwakke roterende balk. Een aantal van de afwijkingen tussen dit model en de data worden mogelijk veroorzaakt door de asymmetrische verdeling van stof in NGC 5448.

In HOOFDSTUK VIER construeren we axisymmetrische en triaxiale modellen met een DF die afhangt van lineaire combinaties van de drie exacte integralen van beweging in een separabele Stäckel potentiaal. Voor deze zogenaamde Abel modellen kunnen we de dichtheid en snelheidsmomenten op een efficiënte manier uitrekenen en we laten zien dat ze veel van de rijke interne dynamica van vroeg-type stelsels kunnen beschrijven. We gebruiken deze modellen om de kinematische kaarten na te bootsen die volgen uit waarnemingen met twee-dimensionale spectrografen zoals SAURON. We fitten deze gesimuleerde waarnemingen met axisymmetrische en triaxiale modellen gemaakt met onze numerieke implementatie van de Schwarzschild methode.

de, terwijl we de intrinsieke vorm en kijkrichting veranderen. We concluderen dat de Schwarzschild methode ons in staat stelt de interne structuur van vroeg-type stelsels te bepalen en nauwkeurig de massa-lichtkracht verhouding te meten, maar dat extra informatie nodig is om de kijkrichting beter in te perken.

In HOOFDSTUK VIJF zetten we onze analyse van modellen met separabele potentialen voort en leiden we de algemene oplossing van de Jeans vergelijkingen af. Deze vergelijkingen relateren de tweede orde snelheidsmomenten aan de dichtheid en potentiaal van een stersysteem, zonder verder aannames over de DF. Voor algemene drie-dimensionale stersystemen zijn er drie vergelijkingen en zes onafhankelijke momenten, maar in een triaxiale Stäckel potentiaal verdwijnen de gecorelleerde momenten in confocale ellipsoïdale coördinaten. De drie Jeans vergelijkingen en drie overgebleven momenten vormen een gesloten systeem van drie symmetrische gekoppelde eerste orde partiële differentiaalvergelijkingen in drie variabelen. Meer dan 40 jaar nadat Lynden-Bell ze afleidde, geven we in dit hoofdstuk de oplossing.

We lossen allereerst de Jeans vergelijkingen in de axisymmetrische limiet op met een nieuwe methode gebaseerd op het optellen van particuliere oplossingen. Deze twee-dimensionale oplossingen passen we toe op (elliptische) schijven, oblate en prolate sferoïden en op de schaalvrije triaxiale limiet. Daarna breiden we onze methode uit naar triaxiale modellen en vinden de algemene oplossing. Deze kan uitgedrukt worden in termen van (hyper)elliptische integralen die op een efficiënte manier numeriek geëvalueerd kunnen worden. De oplossing geeft de volledige set van tweede momenten die een triaxiale dichtheidsverdeling in een separabele potentiaal kunnen ondersteunen.

In HOOFDSTUK ZES onderzoeken we de totale massaverdeling in de binnendelen van het gravitationele lensstelsel QSO 2237+0305, beter bekend als het *Einstein Cross*. In dit systeem wordt het licht afkomstig van een veraf gelegen quasar afgebogen door een vroeg-type spiraal stelsel op een roodverschuiving van $z = 0.04$, oftewel op een afstand van bijna 500 miljoen lichtjaar. We leiden de intrinsieke lichtverdeling van het lensstelsel af door de gemeten lichtverdeling aan de hemel te deprojecteren. Volgens construeren we een lensmodel dat nauwkeurig de posities en relatieve lichtkracht van de vier afbeeldingen van de quasar fit. Dan bouwen we een realistisch afgeplat dynamisch model van het lensstelsel dat voldoet aan de voorlopige kinematische waarnemingen gedaan met de twee-dimensionale spectrograaf GMOS aan de 8.2 meter Gemini Noord Telescoop op Mauna Kea. We vinden dat de gemeten snelheidsdispersie van $167 \pm 10 \text{ km s}^{-1}$ in het gebied omsloten door de quasar afbeeldingen in overeenstemming is met de voorspelde waarde uit ons en eerdere lensmodellen. Ook de massa in dit gebied dat volgt uit het model dat het beste bij de waarnemingen past is consistent met de onafhankelijk bepaalde waarde uit ons lensmodel. Tenslotte vertoont ook de vorm van geprojecteerde dichtheid van het lens model veel gelijkenis met de waargenomen lichtverdeling van het lensstelsel. Echter, verdere verbeteringen aan de voorlopige kinematische waarnemingen zijn nodig, alvorens we definitieve conclusies kunnen trekken over de total massaverdeling in het lensstelsel.

In HOOFDSTUK ZEVEN beschouwen we naast het *Einstein Cross* nog 25 andere gravitationele lenssystemen met roodverschuiving tot $z \sim 1$. Op dergelijke grote afstanden zijn we beperkt tot het bestuderen van de globale (dynamische) eigenschappen van deze lensstelsels. Ze zijn representatief voor vroeg-type veldstelsels, dat wil zeggen in een omgeving van relatief lage dichtheid aan stelsels in tegenstelling tot cluster stelsels. De *Fundamental Plane* relatie van deze lensstelsels op verschillende roodverschuivin-

gen maakt het mogelijk om de evolutie van hun massa-lichtkracht verhouding M/L te bestuderen. Als we aannemen dat de M/L van vroeg-type stelsels evolueert als een machtswet, vinden we voor de lensstelsels een evolutie $d \log(M/L)/dz = -0.62 \pm 0.13$ in de B -band. Dit betekent dat de sterren gemiddeld gevormd zijn op een roodverschuiving van $\langle z_{\star} \rangle = 1.8_{-0.5}^{+1.4}$.

Er rekening mee houdend dat op hogere roodverschuiving laat-type stelsels mogelijk nog evolueren (door samensmelting) tot vroeg-type stelsels, geldt voor sterren in cluster stelsels $\langle z_{\star}^{cl} \rangle = 2.0_{-0.2}^{+0.3}$. Dit is niet significant anders dan de lensstelsels, in tegenstelling tot voorspellingen door de huidige theoriën van de vorming van sterrenstelsels. Als we echter aannemen dat stelsels van dezelfde leeftijd gelijke M/L hebben, vinden we dat de sterpopulaties in lensstelsels gemiddeld 10–15 % jonger zijn dan die in clusterstelsels. Verder vertonen zowel de M/L waarden als de kleuren van de lensstelsels een significante spreiding. Terwijl ongeveer de helft van de lensstelsels consistent zijn met een oude sterpopulatie zoals in clusterstelsels, zijn andere lensstelsels veel blauwer met jongere sterpopulaties die mogelijk pas gevormd zijn op $z_{\star} \sim 1$. Bovendien is de spreiding in kleur gerelateerd aan die in de M/L . We zien dit als bewijs voor een significante spreiding in de leeftijden van de sterpopulaties in lensstelsels, in tegenstelling tot de oude populaties in clusterstelsels die in dezelfde periode gevormd lijken te zijn.

TOEKOMSTPERSPECTIEVEN

Een belangrijk deel van het werk gepresenteerd in dit proefschrift betreft de uitbreiding van axisymmetrische naar triaxiale modellen voor sterrenstelsels. Dit is vooral belangrijk voor de zware elliptische stelsels, waarvan vele duidelijke afwijkingen van axisymmetrie vertonen in hun kinematica gemeten met behulp van twee-dimensionale spectrografen zoals SAURON. Triaxiale modellen van deze zware elliptische stelsels, tezamen met axisymmetrische modellen van twee dozijn andere elliptische en lensvormige stelsels die al geconstrueerd zijn, zullen het mogelijk maken de fossiele overblijfselen in deze ‘schone’ vroeg-type stelsels in detail te bestuderen.

Omdat SAURON typisch de heldere binnendelen van stelsels waarneemt, hebben we extra informatie nodig om onderzoek te doen naar de uitgestrekte donkere materie verdeling zoals voorspeld door de huidige theoriën over de vorming van stelsels. We hebben gezien dat gravitatielenzen informatie verschaffen over de donkere materie, maar slechts enkele lensstelsels staan dichtbij genoeg om in detail te modelleren. Momenteel onderzoeken we het gebruik van het relatief grote waarnemingsveld van SAURON om alsnog kinematische metingen te doen in de lichtzwakke buitendelen van stelsels. Overige kinematische metingen komen voort uit waarnemingen van neutraal waterstof en van Röntgen straling, als ook de snelheden van bolhopen en planetaire nevels in de buitendelen van deze stelsels. We zijn begonnen met het uitbreiden van onze modelleer software om ook zulke discrete waarnemingen mee te kunnen nemen. Deze toevoeging is ook belangrijk met betrekking tot het modelleren van de individueel waarneembare sterren in de Melkweg en in de omliggende stersystemen.

Voor nabij gelegen bolhopen zoals ω Centauri zullen we dan in staat zijn de waargenomen snelheden van individuele sterren (in drie dimensies) direct te fitten, met eventueel zelfs de toevoeging van metingen van hun leeftijd en samenstelling. Op deze manier kunnen verschillende populaties van sterren in de fase-ruimte gescheiden worden, waarna hun structuur en dynamica afzonderlijk bestudeerd kunnen worden.

Door bovendien direct de eigenbewegingen in het centrum van bolhopen, gemeten met behulp van de Hubble Space Telescope, te fitten, kunnen we het mogelijke bestaan van zwarte gaten in bolhopen onderzoeken.

Het modelleren van de sterren in de Melkweg wordt sterk bemoeilijkt door de aanwezigheid van stof en een roterende balk. Dit laatste vereist een zeker niet vanzelfsprekende uitbreiding van onze (statische) modelleer software. In een inleidend onderzoek hebben we de zeer nauwkeurige snelheidsmetingen van meer dan duizend sterren gebruikt om aan te tonen dat met zo'n uitbreiding het binnenste van de Melkweg gemodelleerd kan worden met direct bewijs voor het bestaan van een balk. Verder zal deze uitbreiding het mogelijk maken andere roterende stelsels (met mogelijk een balk) te modelleren, waaronder de vroeg-type spiraalstelsels waargenomen met SAURON, en een link te leggen tussen de kinematica van het sterren en het gas.

De grote hoeveelheid fotometrische en kinematische data die inmiddels al beschikbaar is, zal snel toenemen met de bestaande en toekomstige instrumenten en missies, zoals RAVE, GAIA en SIM, die data van miljoenen sterren zullen opleveren, alsook VIMOS, SINFONI, MUSE en andere twee-dimensionale spectrografen, die ons zullen voorzien van twee-dimensionale data van vele nabije stelsels. Tegelijkertijd maken de snelle ontwikkeling van telescopen en de grootte van hun spiegels een steeds diepere blik in het heelal mogelijk, met een direct zicht op de evolutie en zelfs vorming van stersystemen. Het werk gepresenteerd in dit proefschrift betekent een stap vooruit in de ontwikkeling en toepassing van dynamische modellen om uit deze rijkdom aan data te achterhalen hoe stersystemen zich ontwikkeld hebben vanaf de oerknal tot de dag van vandaag.

CURRICULUM VITAE

OP zondag 2 oktober 1977 werd ik geboren in het Brabantse dorp Mill. Mijn middelbare schoolopleiding volgde ik aan het Elzendaalcollege te Boxmeer, alwaar ik in 1996 mijn Gymnasium diploma behaalde. In september van dat jaar ging ik studeren aan de Universiteit Leiden. In het eerste jaar behaalde ik de propaedeuse van de studies Sterrenkunde, Wiskunde en Infomatica, waarna ik verder ben gegaan met het doctoraalprogramma van Sterrenkunde en Wiskunde. In de zomermaanden van 2000 heb ik onderzoek gedaan aan het California Institute of Technology in Pasadena in de Verenigde Staten, onder leiding van prof. dr. P. G. van Dokkum. Terug in Leiden heb ik een gecombineerd afstudeeronderzoek gedaan op de Sterrewacht en in het Mathematische Instituut, onder leiding van prof. dr. P. T. de Zeeuw en prof. dr. ir. L. A. Peletier. De resultaten van dit onderzoek naar de oplossing van de Jeans vergelijkingen voor drie-assige systemen zijn opgenomen in hoofdstuk 5 van dit proefschrift. In september 2001 slaagde ik cum laude voor het doctoraalexamen Sterrenkunde en twee maanden later ook cum laude voor het doctoraalexamen Wiskunde.

In oktober 2001 begon ik als promovendus bij Sterrenkunde in de groep van prof. dr. P. T. de Zeeuw. In de afgelopen vier jaar heb ik onderzoek gedaan naar de dynamische structuur en evolutie van sterrenstelsels, bolhopen en andere stersystemen door theoretische modellen te construeren die de fotometrie alsook de kinematica van deze stersystemen beschrijven. De resultaten zijn beschreven in dit proefschrift en in een aantal artikelen waarvan ik mede-auteur ben (zie 'List of publications' op pagina 233). Tijdens mijn promotieonderzoek heb ik deelgenomen aan waarnemingen met de tweedimensionale spectrograaf SAURON gemonteerd aan de William Herschel Telescope op La Palma. Mijn onderzoek heb ik kunnen presenteren op conferenties in Duitsland, Frankrijk, Griekenland, Engeland, Australië en Nederland en tijdens colloquia in Nederland, Canada en de Verenigde Staten.

Al sinds mijn middelbare schooltijd heb ik met veel plezier (bij)les gegeven. Vanaf mijn tweede studiejaar ben ik student-assistent geweest bij de vakken 'Discrete Wiskunde' en 'Statistiek' en als promovendus heb ik geassisteerd bij het 'Sterrenkundig Practicum'. Daarnaast heb ik de begeleiding van de studenten Martijn Nuyten en Eveline Helder op me genomen. Erg leuk en leerzaam waren ook het bestuursjaar voor de studievereniging 'De Leidsche Flesch' en de deelname aan verscheidene commissies, waaronder de (nationale) opleidingscommissie en de publiekscontactencommissie. Dit laatste, tesamen met het organiseren van de jaarlijkse 'Nationale Wetenschapsdag' en het geven van publieke lezingen, heeft mij duidelijk gemaakt hoe belangrijk (en dankbaar) een goede interactie met het publiek is. Eenzelfde positieve interactie binnen en buiten de sterrenkunde hoop ik te mogen ervaren gedurende de komende jaren als (postdoc) onderzoeker aan Princeton University in de Verenigde Staten.

NAWOORD

ZOALS ieder kind kreeg ook ik op de lagere school de vraag wat ik later wilde worden. Dat ik nu inderdaad 'sterrenkundige' ben geworden beschouw ik als een groot voorrecht. Bij deze wil ik dan ook alle mensen die hieraan hebben bijgedragen van harte bedanken.

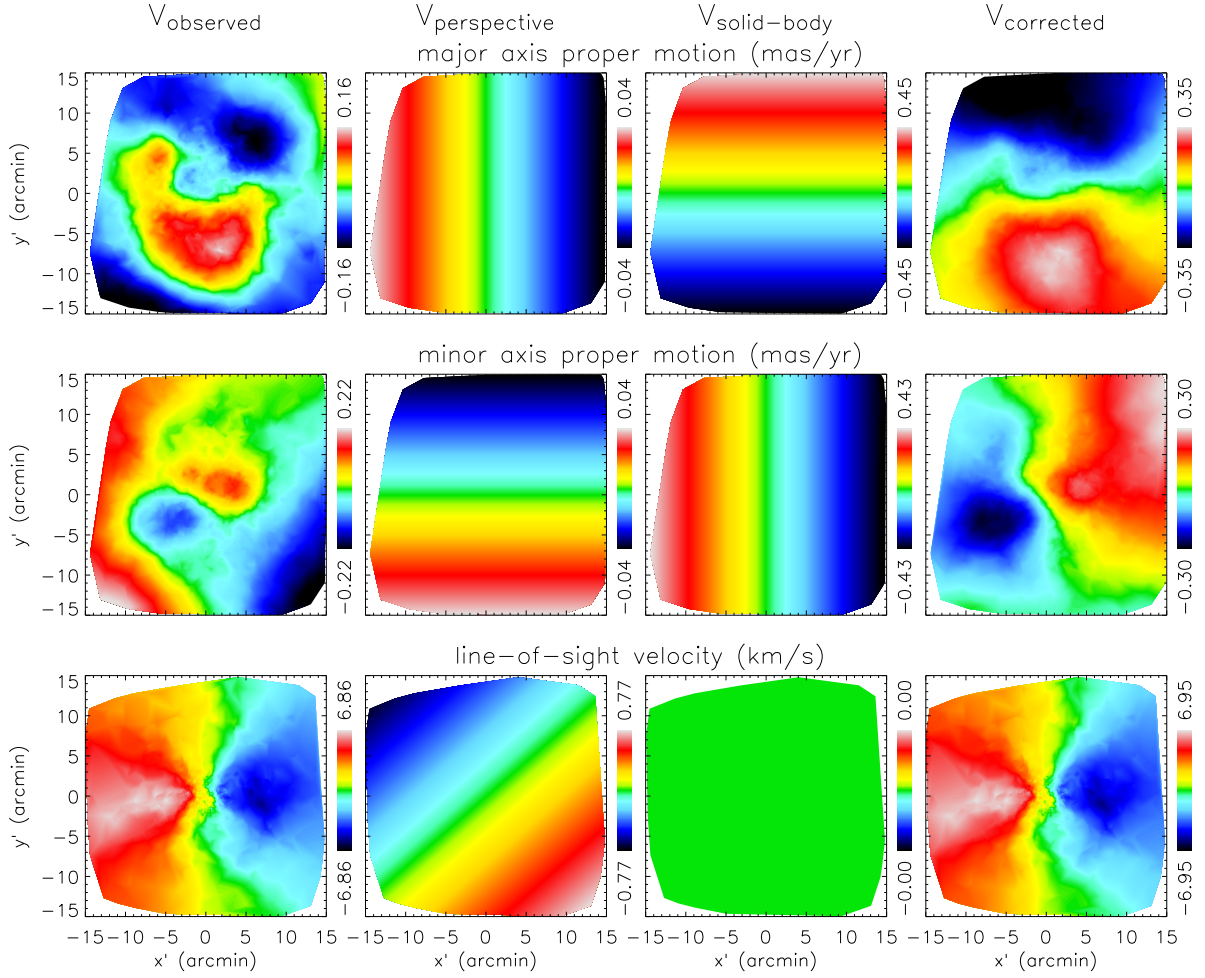
In het bijzonder ben ik veel dank verschuldigd aan mijn ouders die mij, net als mijn drie jongere zussen, altijd hebben gesteund en met raad en daad hebben bijgestaan. Familie is erg belangrijk voor mij en ik ben dan ook erg blij dat ik vanaf het begin door mijn 'schone' familie met open armen ben ontvangen.

De Leidse Sterrewacht is de afgelopen jaren voor mij eigenlijk ook een soort van familie geweest, welke zonder de hulp van de computergroep en het secretariaat uiteen zou vallen. Bij deze wil ik dan ook David, Erik, Tycho, Aart, Kirsten, Jeanne, Elise, Janet en Marja hartelijk danken voor hun onmisbare ondersteuning. De open-deur cultuur op de Leidse Sterrewacht is mij erg goed bevallen, maar maakte mijn begeleider af en toe toch wel bezorgd, wanneer, nadat iemand even langs was geweest voor een vraag, ik me weer op een nieuw project had gestort. Op dezelfde manier heb ik de afgelopen jaren genoten en veel geleerd van de vele open en kritische discussies met Ellen, Michele, Richard, Jesus, Davor, Remco, Anne-Marie en anderen binnen de vakgroep 'Dynamica van sterrenstelsels' en binnen het SAURON team. Pedro wil ik van harte bedanken voor zijn altijd intrigerende 'wiskundige vraagjes' en voor het helpen met het raamwerk en de omslag van dit proefschrift.

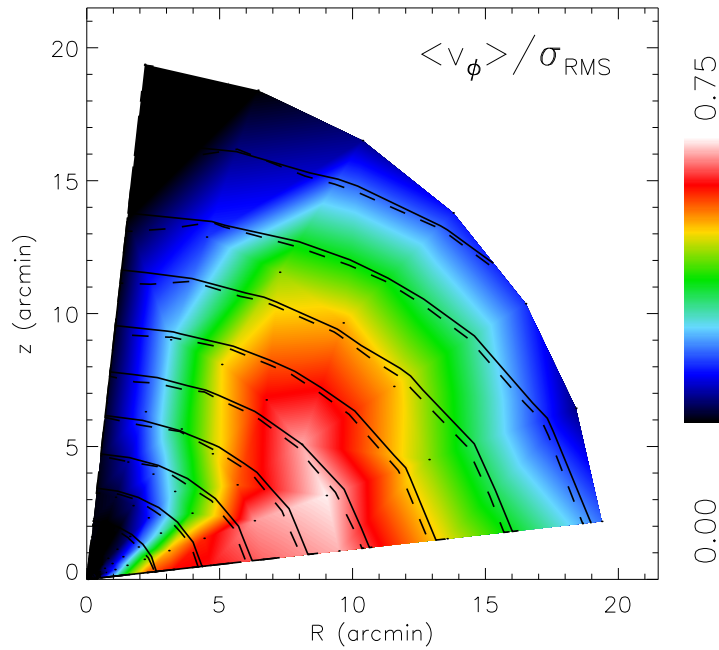
Wetenschap is niet mogelijk zonder financiële steun. Zo werd mijn onderzoekstage in Pasadena mede mogelijk gemaakt door het Hendrik Müller Fonds en zijn veel van mijn conferentie-bezoeken ondersteund door het Leids Kerkhoven Bosscha Fonds. Bovenal maakte het minimum aan financiële en bureaucratische zorgen op de Sterrewacht het voor mij mogelijk me volledig op de wetenschap te storten.

Manon, gelukkig ben jij er altijd om duidelijk te maken dat er meer is dan alleen Sterrenkunde. Bedankt voor je steun en vertrouwen en vooral voor je liefde!

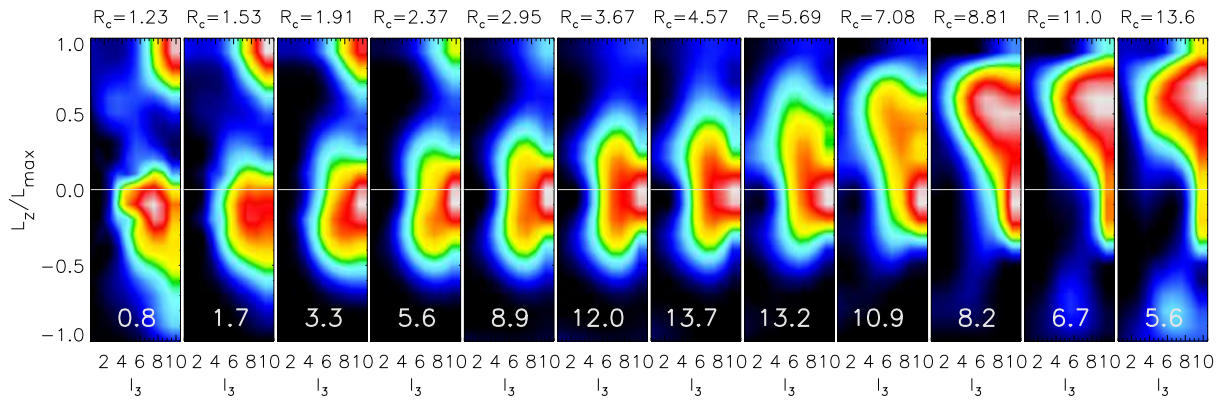
APPENDIX: COLOR FIGURES



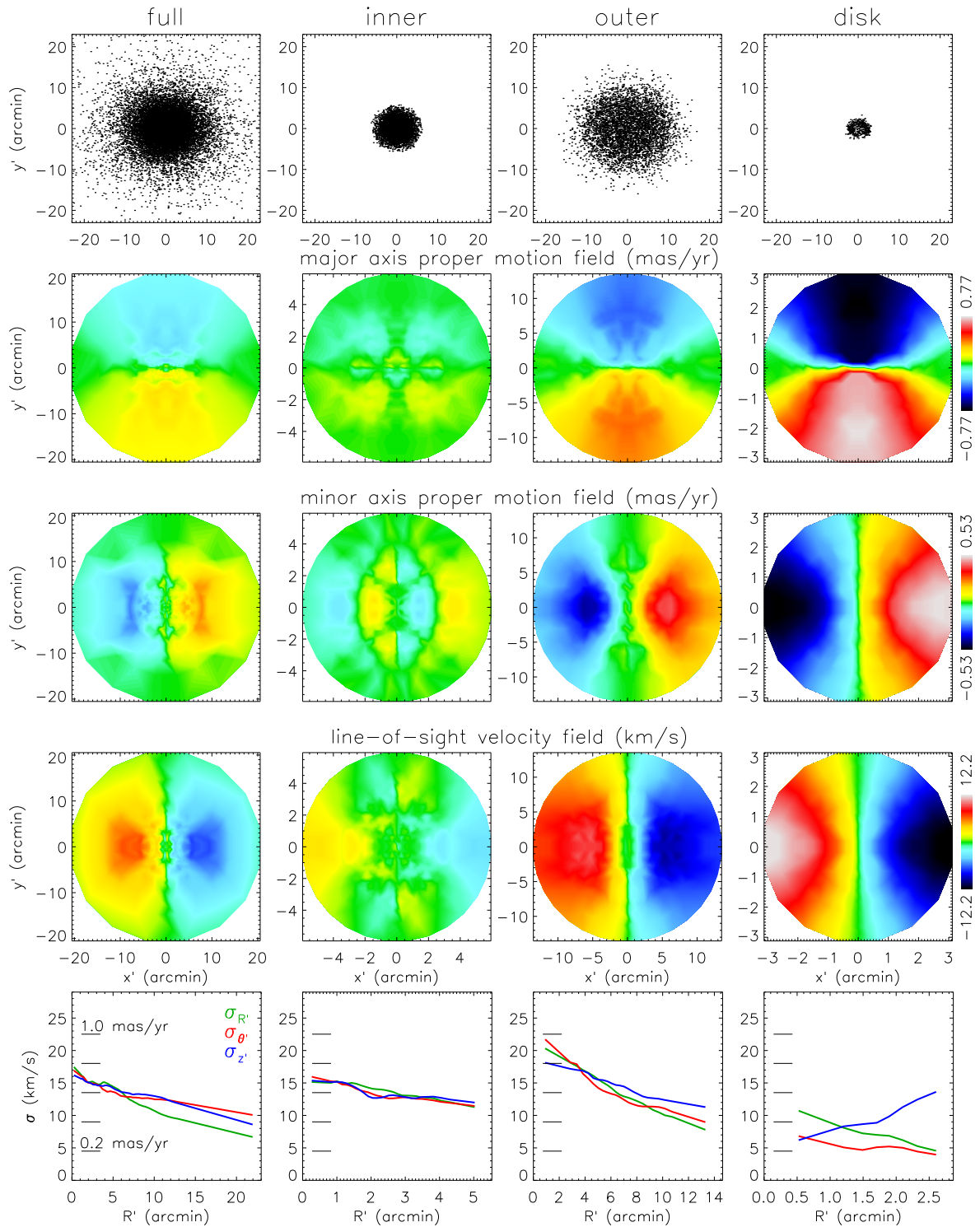
CHAPTER 2: FIGURE 6 — *The mean velocity fields of ω Cen corrected for perspective and solid-body rotation. The individual measurements are smoothed using adaptive kernel smoothening. From top to bottom: The mean ground-based proper motion in the major axis x' -direction and in the minor axis y' -direction, and the mean line-of-sight velocity. From left to right: Observed velocity fields of ω Cen, contribution from perspective rotation, contribution from solid-body rotation and the velocity fields after correcting for both. The perspective rotation is caused by the space motion of ω Cen. The solid-body rotation in the proper motions is due to relative rotation of the first and second epoch photographic plates by an amount of $0.029 \text{ mas yr}^{-1} \text{ arcmin}^{-1}$.*



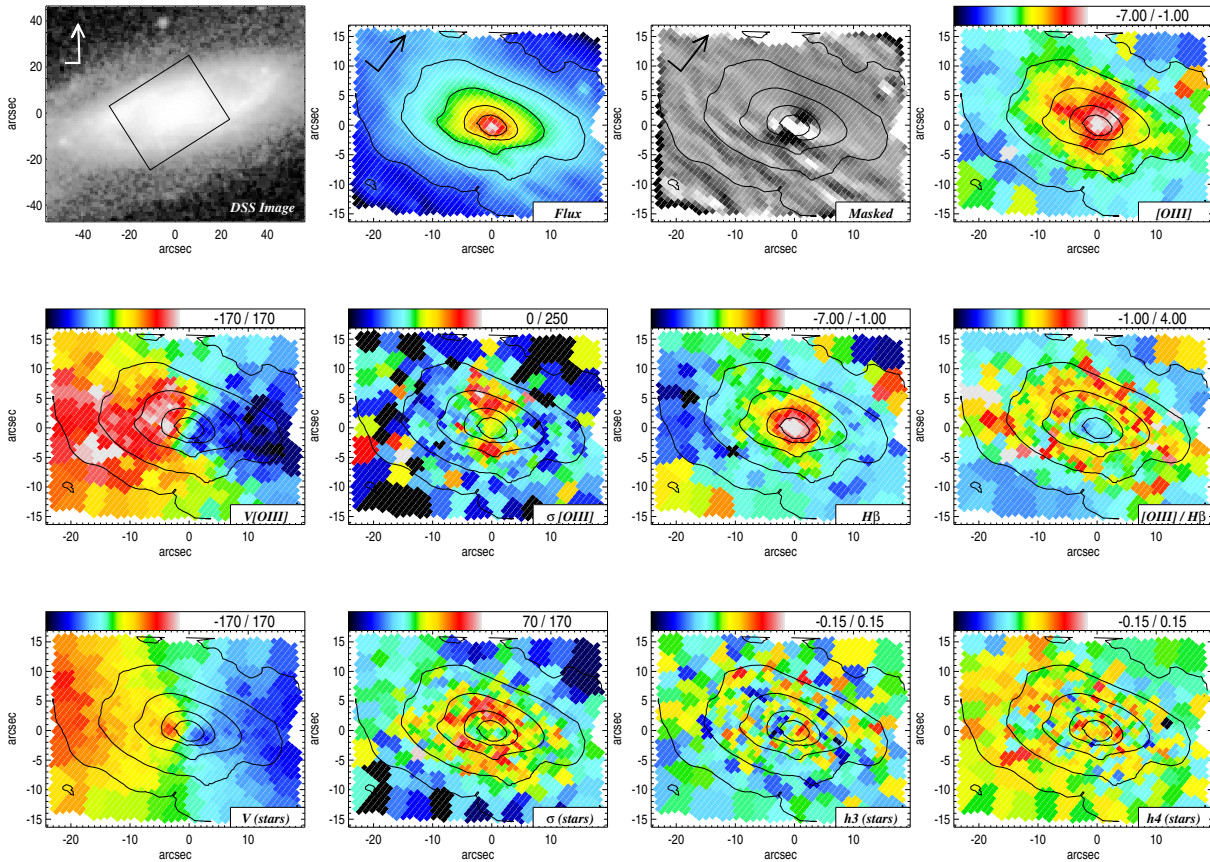
CHAPTER 2: FIGURE 17 — The colors represent the mean azimuthal rotation $\langle v_\phi \rangle$ in the meridional plane as a function of equatorial plane radius R and height z , and normalized by σ_{RMS} (excluding the axes to avoid numerical problems). The black curves are contours of constant mass density, from the mass model (solid) and from the best-fit model (dashed), showing that the mass is well fitted.



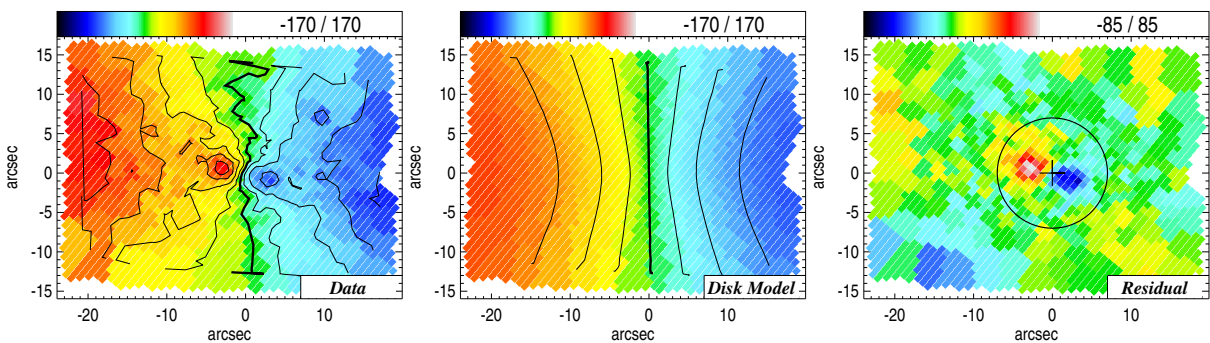
CHAPTER 2: FIGURE 19 — The orbital weight distribution for our best-fit model of ω Cen. From left to right, the panels show the orbital weight distribution at increasing distance from the center, which corresponds to increasing energy. The radius R_c of the circular orbit at the corresponding energy is given above each panel. The radial range that is shown is constrained by the observations and contains more than 90% of the total cluster mass. The vertical axis represents the angular momentum L_z in units of L_{max} , the angular momentum of the circular orbit. The horizontal axis represents the third integral I_3 , parameterized by the number of the (linearly sampled) starting angle of the orbit. Black shading corresponds to zero orbital weights, and white corresponds to the maximum orbital weight in each panel. At the bottom of each panel the fraction of the included mass with respect to the total mass is indicated (in %).



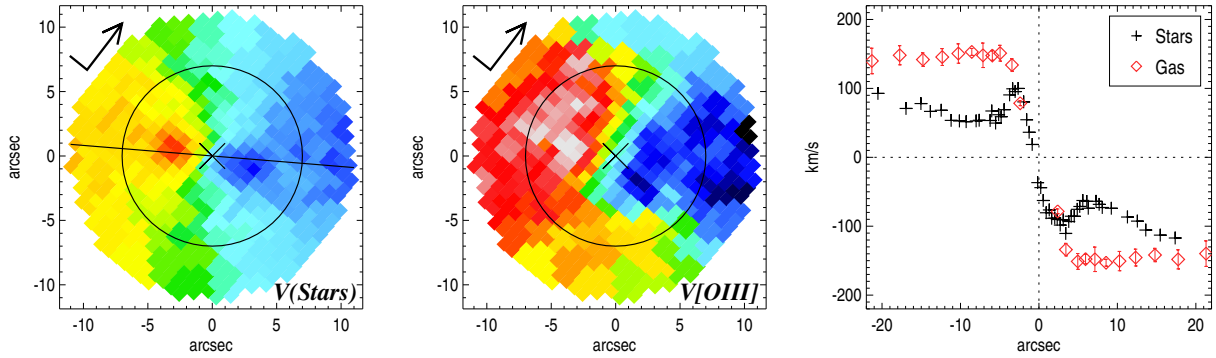
CHAPTER 2: FIGURE 20 — Kinematics of different components in the distribution function of our best-fit model for ω Cen. From left to right: full distribution function, main inner component, main outer component and separate disk component between 1 and 3 arcmin (§ 9.4). From top to bottom: spatial distribution, mean velocity fields in the direction of the major x' -axis, the minor y' -axis and the line-of-sight z' -axis, and mean velocity dispersion profiles. The radial and tangential dispersion, $\sigma_{R'}$ (green) and $\sigma_{\theta'}$ (red), are on the plane of the sky and $\sigma_{z'}$ (blue) is the line-of-sight dispersion.



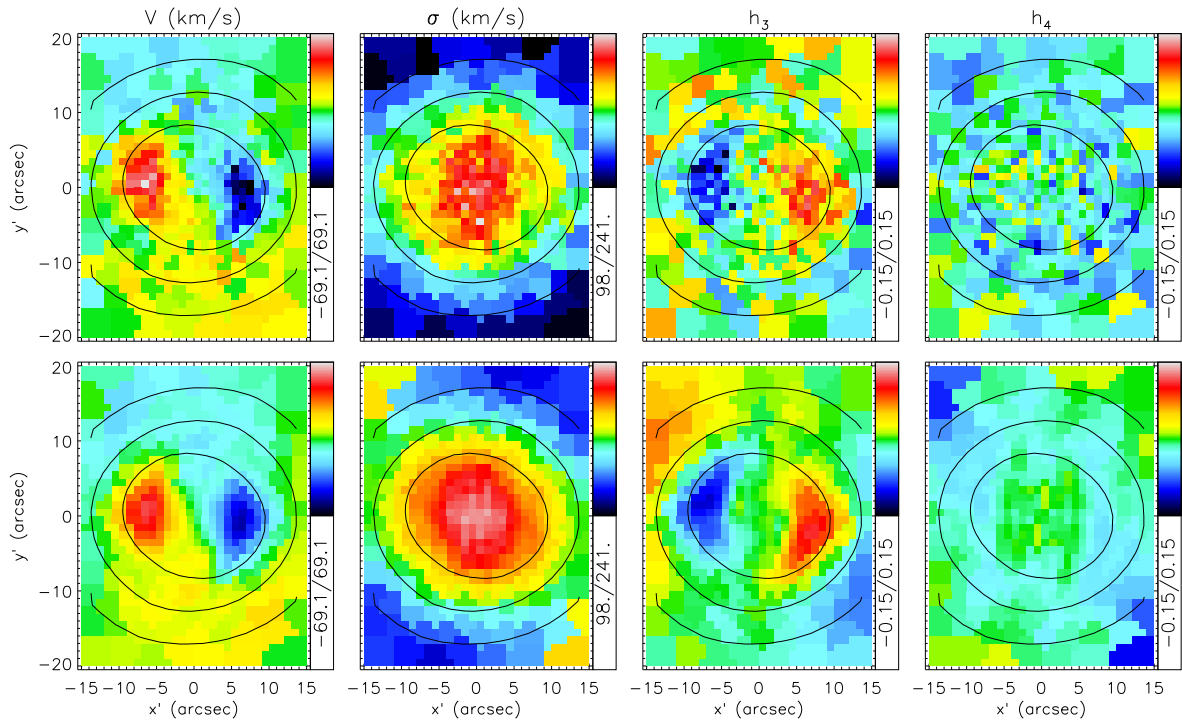
CHAPTER 3: FIGURE 1 — Top Left: Digitized Sky Survey image of NGC 5448 with SAURON footprint and north-east orientation arrow. All other panels show the SAURON data. The stellar flux map and unsharp-masked SAURON image are given in mag arcsec⁻² with arbitrary zero point, and north-east direction as indicated. The titles are indicated at the bottom right corner of each panel, and the plotting ranges are given at the top. All SAURON maps are overplotted with stellar contours in magnitude steps of 0.25, and all velocities and velocity dispersions are given in km s⁻¹.



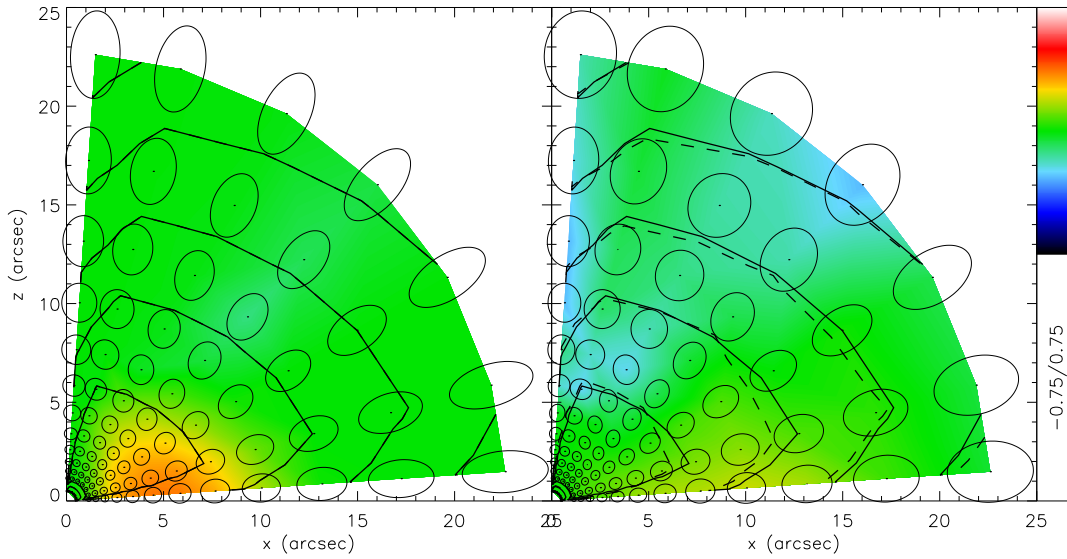
CHAPTER 3: FIGURE 3 — A thin isothermal disk model for the stellar velocity field of NGC 5448. The circle marks the 7'' region within which we find a disk-like structure. The disk model, fitted to the field outside this region, implies for the outer disk a scale length of 18'', $V_{\text{sys}} = 2002 \text{ km s}^{-1}$, and PA = 91°. The orientation of the maps is the same as in Fig. 1 of Chapter 3 (see above).



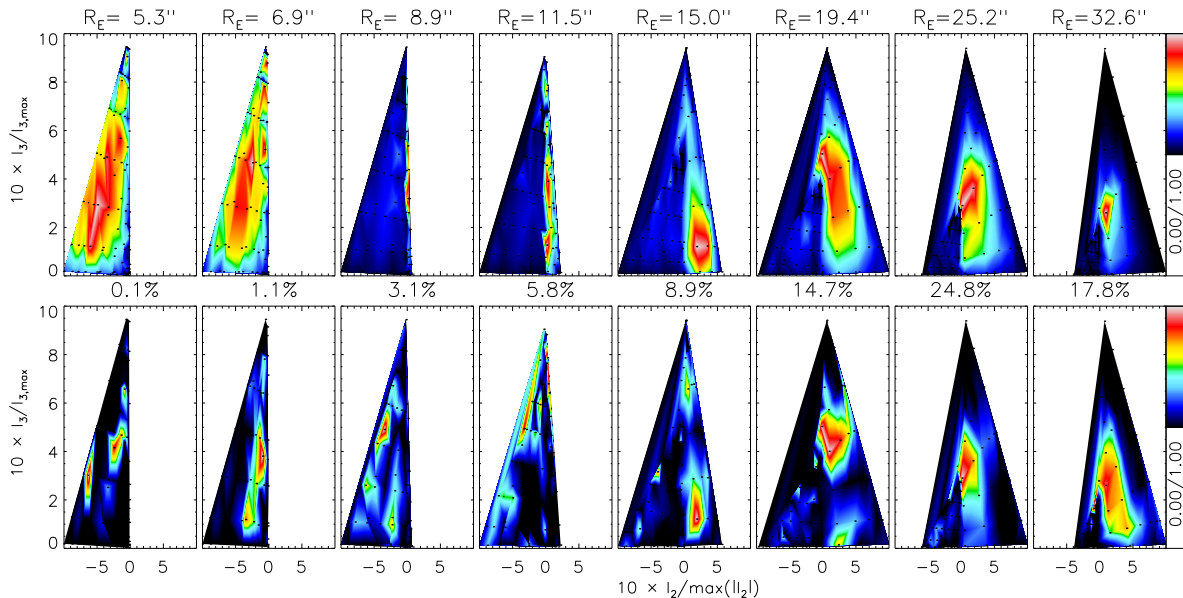
CHAPTER 3: FIGURE 5 — *Zooming into the central few arcseconds of the stellar and gaseous velocity maps of NGC 5448, using the same velocity range as in Fig. 1 of Chapter 3 (see above). Indicated are the north-east direction (arrow), the photometric PA (straight line) and the photometric center (cross). The over-plotted circle indicates the $7''$ radius for comparison with Fig. 3 of Chapter 3 (see above). In the right panel, we present the stellar rotation curve (extracted along the photometric PA) together with the gas rotation curve derived from tilted-ring decomposition.*



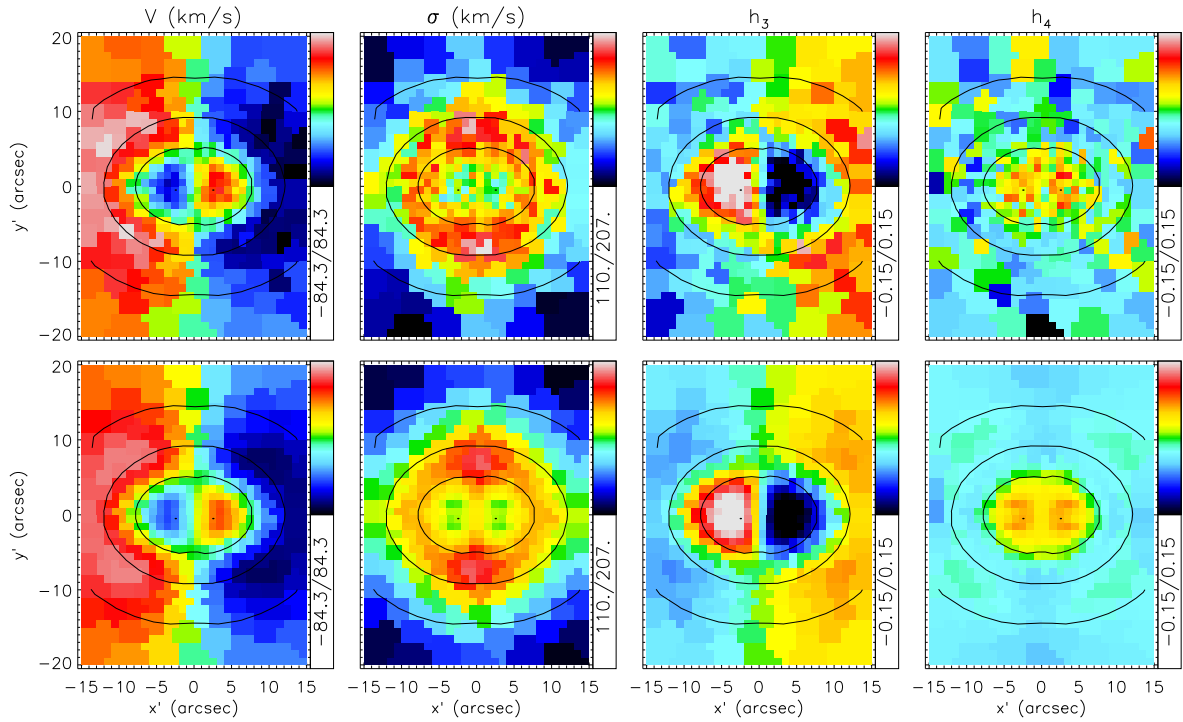
CHAPTER 4: FIGURE 6 — *Kinematic maps for a triaxial Abel model (top) and for the best-fit triaxial Schwarzschild model (bottom). From left to right: mean line-of-sight velocity V (in km s^{-1}), velocity dispersion σ (in km s^{-1}) and Gauss-Hermite moments h_3 and h_4 . The line-of-sight kinematics of the input Abel model have been converted to observables with realistic measurement errors as described in the text of Chapter 4. Isocontours of the surface brightness of the Abel model are overplotted in each map. At the right side of each map, the (linear) scale of the corresponding kinematics is indicated by the color bar, and the limits are given below.*



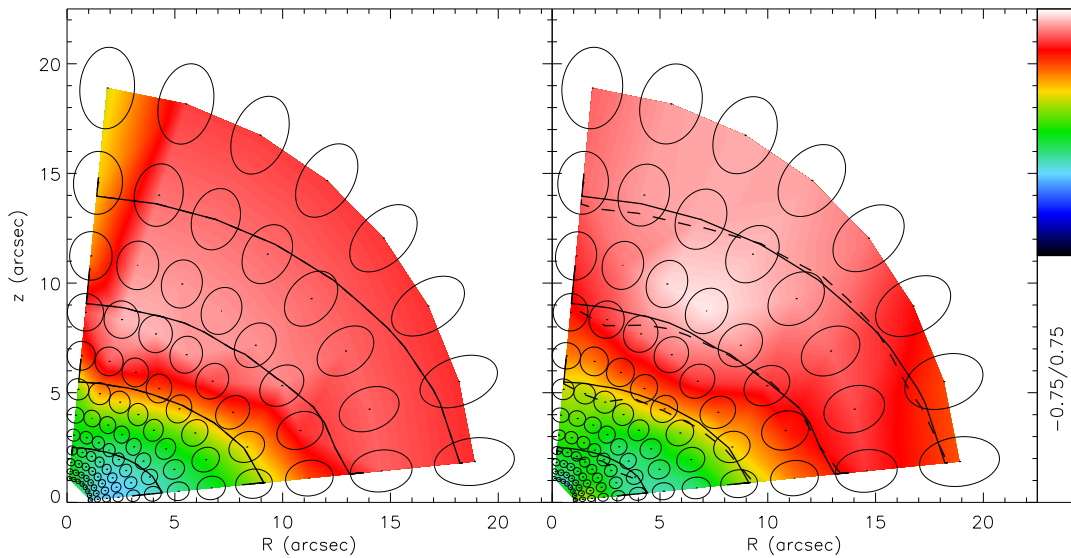
CHAPTER 4: FIGURE 9 — The colors represent the mean motion $\langle v_y \rangle$ perpendicular to the (x, z) -plane, normalized by σ_{RMS} (excluding the axes to avoid numerical problems), for a triaxial Abel model (left) and for the best-fit triaxial Schwarzschild model (right). The ellipses are cross sections of the velocity ellipsoid with the (x, z) -plane. The black curves are contours of constant mass density in steps of one magnitude, for the input Abel model (solid) and for the fitted Schwarzschild model (dashed).



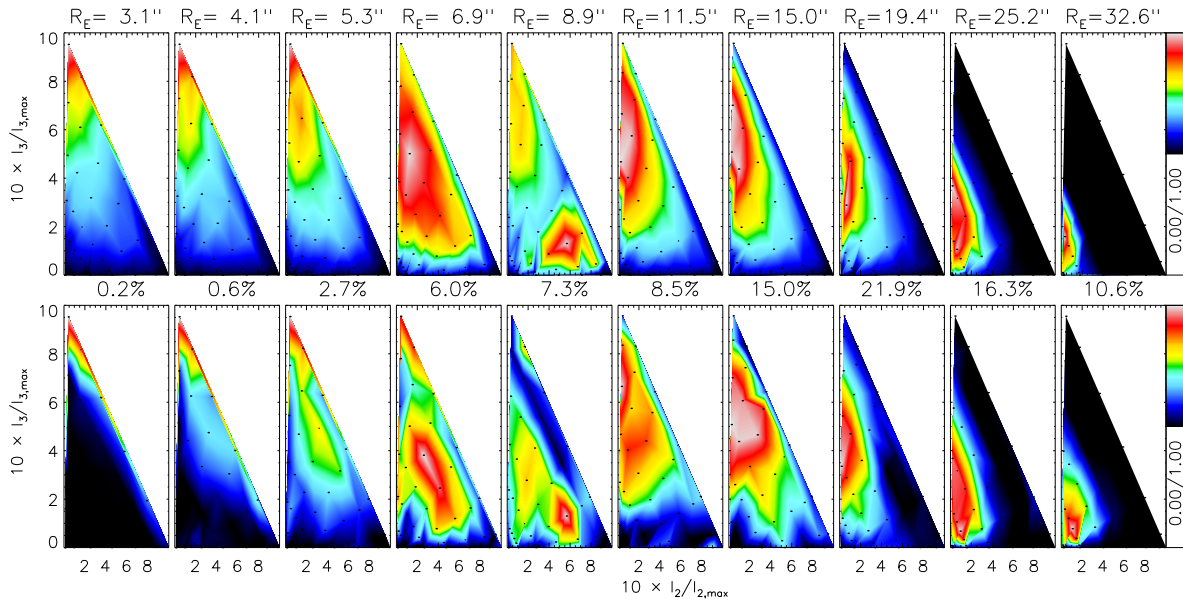
CHAPTER 4: FIGURE 11 — The orbital mass weight distribution for the input triaxial Abel model (top) and for the fitted triaxial Schwarzschild model (bottom). From left to right the energy increases, corresponding to increasing distance from the center, indicated by the radius R_E (in arcsec) of the thin short-axis tube orbit on the x -axis. The vertical and horizontal axes represent respectively the second and third integral of motion, I_2 and I_3 , normalized by their maximum amplitude (for given E). Between the two rows of panels, the fraction of the included mass with respect to the total mass is indicated (in %).



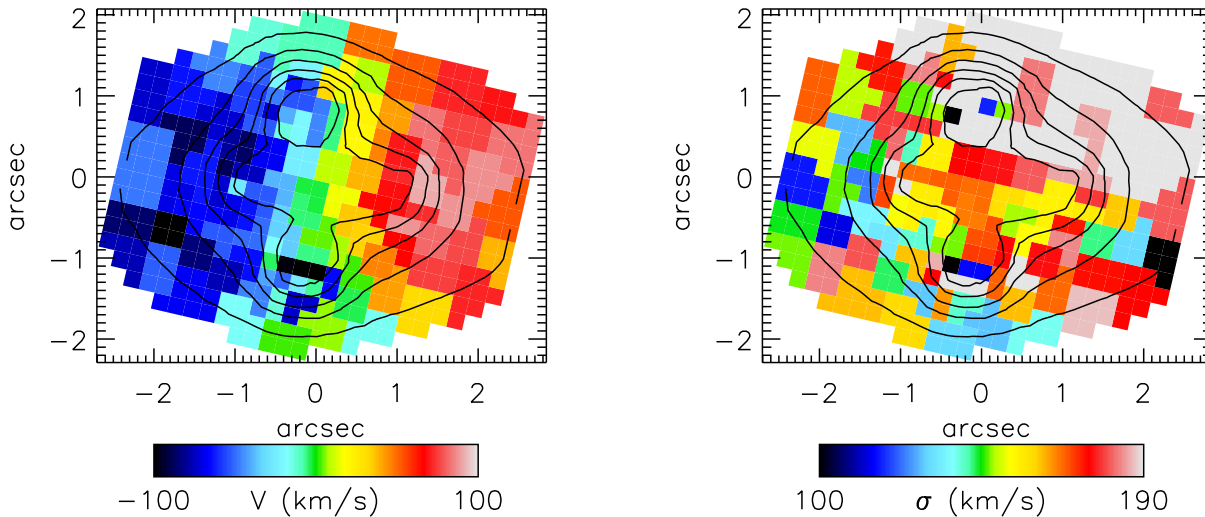
CHAPTER 4: FIGURE 7 — Kinematic maps for an oblate axisymmetric Abel model (top) and for the fitted axisymmetric Schwarzschild model (bottom), with parameters as in Fig. 6 of Chapter 4 above.



CHAPTER 4: FIGURE 13 — The mean azimuthal motion $\langle v_\phi \rangle$ perpendicular to the meridional plane, normalized by σ_{RMS} , for an oblate axisymmetric Abel model (left) and for the best-fit axisymmetric Schwarzschild model (right), with parameters as in Fig. 9 of Chapter 4 above.



CHAPTER 4: FIGURE 14 — The mass weight distribution for an oblate axisymmetric Abel model (top) and for the fitted axisymmetric Schwarzschild model (bottom). Parameters are the same as in Fig. 4 of Chapter 4 above. In this case, the second integral of motion $I_2 = \frac{1}{2}L_z^2$, where L_z is the component of the angular momentum parallel to the symmetry z -axis.



CHAPTER 6: FIGURE 4 — Mean velocity and velocity dispersion field of the lens galaxy in the Einstein Cross as measured from observations with the integral-field spectrograph *GMOS* on Gemini-North. The overlaid contours of the reconstructed image show the positions of the quasar images, which affect the kinematics only very locally. The velocity field shows clear and regular rotation around the (vertically aligned) short-axis of the bulge. The velocity dispersion is fairly constant across the field, except for the region towards the upper-right, where systematic effects cause the dispersion to be overestimated.